Superconducting, Magnetic and Transport Properties of Several Transition Metal Systems.

BY

Patricia A. Stampe

A Thesis Submitted to the Faculty of Graduate Studies
in Partial Fulfillment of the Requirements
for the degree of

DOCTOR OF PHILOSOPHY

Department of Physics
University of Manitoba
Winnipeg, Manitoba

THE UNIVERSITY OF MANITOBA

FACULTY OF GRADUATE STUDIES

*****

COPYRIGHT PERMISSION PAGE

SUPERCONDUCTING, MAGNETIC AND TRANSPORT PROPERTIES OF SEVERAL TRANSITION METAL SYSTEMS

BY

PATRICIA A. STAMPE

A Thesis/Practicum submitted to the Faculty of Graduate Studies of The University of Manitoba in partial fulfillment of the requirements of the degree of

DOCTOR OF PHILOSOPHY

Abstract

Detailed measurements of the field and temperature dependent *ac* susceptibility and resistivity have been made for several bond-disordered systems. Analysis of the susceptibility data shows the influence of disorder and spin-orbit induced anisotropy. Model calculations of the temperature dependence of the resistive anisotropy measured in low magnetic fields predict that the anisotropy should decrease linearly with increasing temperature, vanishing at T_c. The slope of this decrease is predicted to vary inversely with the degree of disorder present in the system. These calculations are compared to measurements of the anisotropy in these systems.

Similar measurements have been done on a series of 16 CuNi alloys, with concentrations between 45 and 55 at.% Ni, before and after aging. As the nickel concentration increases this system develops a ferromagnetic ground state at a critical Ni concentration, x_0. AC susceptibility and resistivity data show a decrease in T_c with decreasing Ni concentration. Detailed studies of the magnetoresistance as a function of concentration allow an accurate determination of x_0 from experimental data, and indicate a power-law dependence of sontaneous resistive anisotropy (SRA) on reduced concentration, as noticed previously near x_0 in Pd-based alloys. The SRA is essentially the difference in resistivity with a magnetic field applied parallel and perpendicular to the current, extrapolated to zero field.

Magnetic and transport measurements were done on YNi_2B_2C superconductors with partial Fe substitution at the Ni site. The strong dependence of superconducting properties on material preparation technique suggests the presence of a defect structure which enhances the critical current density in the superconducting state. The depression of T_c caused by Fe-doping is fitted to models of magnetic and non-magnetic scattering to ascertain the magnetic state of Fe in this material.

Finally, detailed studies of magnetisation and magnetoresistance were done in naturally layered $Ce(Fe_{1-x}Ru_x)_2$ and Gd_2In in the vicinity of their antiferromagnetic to ferromagnetic phase transition. The suppression of the antiferromagnetic state by applied fields causes a giant magnetoresistance (GMR) in these alloys. Attempts are made to correlate the behaviour of the magnetisation and magnetoresistance using a model successful in the interpretation of GMR in granular systems.

Acknowledgements

I wish to express my gratitude to my supervisor, Dr. Gwyn Williams, for his guidance and support during the course of this work. As well, I would like to thank my committee members, Dr. J. Charlton, Dr. R. Roshko, Dr. B. Southern and Dr. G. Tabisz. Special thanks go to Dr. H.P. Kunkel, Dr. X.Z. Zhou and Mr. X. Qi for their assistance with various areas of my research. I am also greatly indebted to the Center for Fundamental Materials Research at Michigan State University for the use of their equipment for magnetisation measurements.

Last, but not least, I would like to thank my family for their encouragement during the past few years.

Contents

Chapter 1

Introduction

The metallic elements with partially filled $3d$ and $4d$ shells are commonly referred to as the transition metals. These elements show a wide range of magnetic properties, including diamagnetism, ferromagnetism and antiferromagnetism. When these elements are alloyed with materials from their own or other groups, the resulting materials exhibit a diverse spectrum of magnetic and transport properties. This study examines several such materials, and attempts to relate the magnetic and transport phenomena found to the magnetic structure present at the microscopic level.

Magnetically ordered materials are interesting from both a fundamental and an applied perspective; this thesis focusses on the former aspect. A complete understanding of magnetic ordering is difficult to achieve, as it is a true many-body effect (the magnetic entities involved are fully interacting). The dilute alloy problem—in which the behaviour of isolated (non-interacting) moments in a non-magnetic host are studied–was initiated on the assumption that it was less complicated. However a complete understanding of the conditions under which even a single impurity develops a stable magnetic moment are still not fully resolved. Increasing the impurity concentration beyond the dilute limit leads to interactions which eventually produced a magnetically ordered ground state, the characteristics of which might be expected to be easier to model and understand than a fully interacting system. This has not proved to be true in reality. Despite these difficulties, the additional

complications accompanying the presence of both a spin ($\vec{S}$) and orbital ($\vec{L}$) component to the total moment at an impurity site are beginning to be addressed. The experimental manifestations of the presence of an orbital contribution at an essentially isolated impurity site are well established; its influence on the ordering process are not. This thesis presents an investigation of the effect of an orbital moment primarily on the transport properties of an ensemble of such moments in systems which have a magnetically ordered ground state. Although a complete understanding of the influence of this additional degree of freedom is unlikely to be achieved over the time scale of some 4–5 years, it has nevertheless be possible to obtain some general results which appear to represent some general characteristics of systems with orbital moments.

Diamagnetic atoms have no magnetic moment in zero field, i.e. $\vec{L} = \vec{S} = 0$, the most common situation among the elements. When a field is applied to these atoms, a moment is induced antiparallel to the applied field, following Lenz's law. The magnetic susceptibility of a diamagnet, $\chi = \frac{dM}{dH}$, is thus negative. In general, the diamagnetic susceptibility is very small, and has only a slight temperature dependence[1].

Atoms for which $\vec{L} \neq 0$ and/or $\vec{S} \neq 0$ have a permanent magnetic moment. If the moments are non-interacting, the system is paramagnetic. In zero applied field, the moment orientations are random and fluctuate with time, so that the net magnetisation of the system is zero. When a magnetic field is applied, the moments tend to line up parallel to the field to reduce their magnetic energy. The susceptibility of a paramagnet is normally small and positive, and obeys Curie's law,

$$\chi = \frac{C}{T} \tag{1.1}$$

More interesting results are obtained in the case in which the moments interact. The interaction may align the moments parallel to each other resulting in ferromagnetic ordering, or antiparallel to each other yielding antiferromagnetism. The moments may also form more complex arrangements, such as spin-glass or spin density wave states. A number of models developed to describe these systems are

discussed below.

Early attempts to understand systems of interacting moments led to the molecular or mean field model, originated by Weiss[2]. He noticed that in a ferromagnetic material the moments respond as though they are acted on not only by the applied field H_a, but also by another field, usually orders of magnitude larger, thus accounting for the presence of magnetic ordering at relatively high temperatures. This molecular field, which is assumed to be proportional to the magnetisation, arises from the other magnetic moments in the system. At high temperature, the thermal energy of the material is sufficiently large to overcome the coupling between moments, and the system becomes paramagnetic. The behaviour of the susceptibility in this regime, according to mean field theory, is described by the Curie-Weiss law [1],

$$\chi = \frac{C}{T - \theta} \tag{1.2}$$

where θ, the Curie temperature, is proportional to the mean field. The Weiss model can also describe an antiferromagnet which consists of two sublattices with magnetisations in opposite directions [1]. In mean field theory, the antiferromagnet also obeys the Curie-Weiss law in the paramagnetic regime, with a θ that is negative instead of positive. Although this model is simple to understand, and can be solved exactly, its predictions do not always agree well with experiment. For this reason it became necessary to develop more complex models which take into account interactions on a smaller length scale.

The mean field model as described above is purely classical, and assumes a homogeneous environment for each spin, a situation which does not normally occur in a real material. The origin of the magnetic exchange interaction is quantum mechanical, and is a direct consequence of the Pauli exclusion principle. To develop an exact, quantum mechanical model of magnetism, the Hamiltonian for the system must be considered. Heisenberg[3] proposed that, given the strength J_{ij} of the exchange interaction between two moments $\vec{S_i}$ and $\vec{S_j}$ the magnetic Hamiltonian

for a system in an applied field $\vec{H}$, is

$$\mathcal{H} = -\sum_{i \neq j} J_{ij} \vec{S}_i \cdot \vec{S}_j - \vec{H} \cdot \sum_i \vec{S}_i \tag{1.3}$$

A positive value for J_{ij} favours parallel spin arrangement, i.e. ferromagnetism, while a negative J_{ij} favours antiferromagnetic ordering. The Heisenberg model can not be solved exactly for a three dimensional lattice, however numerical solutions and approximations have been made to this model to obtain expressions for the critical temperature and the dependence of magnetisation on applied field and temperature.

Although the Heisenberg model allows for the presence of disorder in S_i and J_{ij}, solution of the model generally depends on the presence of some degree of order in the system. Although many magnetic systems are ordered, with the magnetic moments placed at equivalent lattice sites in the crystal, recent interest has been focused on bond-disordered magnets. In these systems, a given moment can feel widely varying interactions with neighbouring moments due to inhomogeneities and statistical fluctuations within the material. This competition between moments can cause magnetic frustration, particularly at low temperatures where the magnetic energy is the dominant energy term. This can result in a spin-glass state, which consists of randomly frozen magnetic moments. Although not all disordered systems exhibit a spin-glass state, they nevertheless show a variety of interesting properties, which depend on the degree of disorder present.

In part, the present study will attempt to show that the resistive anisotropy (the difference in the resistivity measured with the applied field parallel and perpendicular to the measuring current) measured in low fields (LFRA), a property which has not previously studied in detail, can be used as a tool for estimating the amount of disorder present in a magnetic system, and also as an alternative means of evaluating the critical temperature. It will be particularly interesting to study the evolution of the resistive anisotropy in a system in which the magnetic ordering is changing due to changes in concentration of the magnetic impurity.

In the copper-nickel system, when Ni is introduced into the non-magnetic Cu host, a paramagnetic system with spin clusters develops. As the nickel concentration

is increased further, the system evolves to a ferromagnetic ground state at some critical concentration value, x_0, with perhaps an intermediate mictomagnetic phase for concentrations slightly lower than x_0[4]. This type of concentration dependent behaviour is known as a percolation transition. The concentration dependence of several properties of these materials in the vicinity of this transition are well known, however recent studies of PdFe and PdNi alloys near the critical concentration[5, 6] suggested for the first time a power-law dependence of the zero temperature spontaneous resistive anisotropy as a function of concentration, although the two alloys systems have different exponent values for this apparently critical behaviour. In this study, detailed measurements of the resistive anisotropy in CuNi are done, in an attempt determine whether this critical behaviour near the percolation threshold is a universal phenomenon.

Although large Ni concentrations (~50%) are required to induce a ferromagnetic ground state in a copper matrix, only 2% Ni is needed in Pd[6]. A recently discovered family of superconductors, based on YNi_2B_2C [8] have large Ni concentrations, raising interesting questions regarding the magnetic state of Ni in this material. Normally, magnetic impurities suppress superconductivity by breaking the current-carrying Cooper pairs. These materials, however, have a critical temperature of 15K, which is high for an intermetallic superconductor. In an attempt to determine the role of Ni in the superconducting process, a comprehensive investigation of the magnetic and transport properties of the parent compound was done, as well as measurements on a series of alloys with partial substitution of Fe at the Ni sites.

The layered borocarbide compounds mentioned above show a very strong dependence of magnetic properties on the interlayer spacing[9]. This variation is reminiscent of that seen in giant magnetoresistance (GMR) multilayer systems, whose properties change dramatically with changes in the non-magnetic layer thickness [10]. Systems with giant magnetoresistance(GMR) have attracted great interest in recent years due to their potential applications in the magnetic recording industry. Most GMR systems which are currently under investigation are magnetic multilayers, which consist of alternating sputtered layers of magnetic and nonmag-

netic materials. Analysis of scattering mechanisms in these materials is complicated by the presence of interfacial scattering. Some naturally layered compounds also exhibit large magnetoresistances, and are attractive due to their natural layering which makes them easy to prepare and eliminates the analysis problems caused by interfacial scattering. A number of $CeFe_2$ pseudo-binaries have been shown to exhibit ferromagnetic to antiferromagnetic transition at which a giant magnetoresistance can occur [11, 12]. Our study of doped $CeFe_2$ concentrates on the detailed behaviour of the magnetisation and magnetoresistance of two samples of composition $Ce(Fe_{1-x}Ru_x)_2$, with x =0.07 and 0.08. Another layered intermetallic, Gd_2In, with similar magnetic behaviour is also examined. It is hoped that such detailed studies may give insight into the fundamental mechanism of the GMR phenomenon in these as well as multilayer and granular systems.

Finally, we present a detailed study of the high field magnetoresistance of CrFe and CrCo alloys containing only small amounts of Fe and Co. Cr is an antiferromagnet with a spin density wave (SDW) ground state. Previous results have shown that although both Co and Fe have local moments in these alloys, the Co moments seem to couple into the SDW structure, while the Fe moments do not[13]. Measurements of the anisotropy in the magnetoresistance were completed in an attempt to link this behaviour to the presence or absence of orbital moments at the local impurity sites, thus giving an explanation for the difference in magnetic states in these alloys.

Chapter 2

Theoretical Background

2.1 Models for Magnetic Systems

Although the mean field model described in the introduction is too crude to account for the complex behaviour of real systems, the Heisenberg model is too complex to be solved exactly, even for an ordered three dimensional lattice. In order to obtain some theoretical understanding of experimental results, several approximations and simplifications have been applied to the Heisenberg model. As well, models starting from completely different approaches have been suggested. Those results which are relevant to the materials studied are discussed briefly below.

One simplification of the Heisenberg model is the Ising model[1], which assumes the spins to be only one dimensional, so that the moments can point only parallel or antiparallel to the applied field direction. As well, the exchange constant is assumed to be a constant for all i, j. In its most general form, (1.3) can be rewritten in component notation,

$$\mathcal{H} = -\sum_{i \neq j}(\sum_{\alpha=1}^{n} J_{ij}^{\alpha} S_i^{\alpha} S_j^{\alpha}) - \sum_{i}(\sum_{\alpha=1}^{n} H^{\alpha} S_i^{\alpha})$$

, where α labels the spin components, which are of dimension n=1 for the Ising model. This model can be solved exactly on a one-dimensional lattice, and exhibits no phase transition. Onsager solved this model for a two dimensional lattice with nearest-neighbour spin interactions [14], and showed that a second order phase transition from a paramagnetic to a ferromagnetic ground state occurs at a finite

critical temperature, T_c. Phase transitions are generally classified according to Ehrenfest's scheme [15]; if the m^{th} derivative of the Gibbs free energy diverges, the transition is an 'm^{th} order transition'. The Ising model has not been solved exactly in three dimensions. Other variations of the Heisenberg model are the planar (n=2) model, in which the spins only have projections in the x-y plane, and the spherical (n=∞) model, in which the spins can lie in any position along the surface of a sphere. Various numerical approaches such as renormalisation group methods, Monte Carlo simulations, and series expansion techniques have been applied to these models in an attempt to determine their behaviour, and compare them with experimental data on real systems.

2.1.1 Critical Point Exponents

Experimentally, it has been noted that a number of physical properties seem to exhibit power law dependences on external variables in the vicinity of a phase transition. The temperature dependent relationships are commonly expressed in terms of a reduced temperature,

$$t = \frac{T - T_c}{T_c}, \tag{2.1}$$

where T_c is the transition temperature. Typical asymptotic power laws observed in the critical region of magnetic systems are [15],

$$c_H \propto t^{-\alpha} \qquad (t > 0) \tag{2.2}$$

$$c_H \propto (-t)^{-\alpha'} \qquad (t < 0) \tag{2.3}$$

$$M \propto t^{\beta} \qquad (t > 0) \tag{2.4}$$

$$M \propto t^{\beta'} \qquad (t < 0) \tag{2.5}$$

$$M \propto h^{\delta} \qquad (t = 0, h \to 0) \tag{2.6}$$

$$\chi \propto t^{-\gamma} \qquad (t > 0) \tag{2.7}$$

$$\chi \propto t^{-\gamma'} \qquad (t < 0) \tag{2.8}$$

$$\xi \propto t^{-\nu} \qquad (t > 0) \tag{2.9}$$

$$\xi \propto t^{-\nu'} \qquad (t < 0) \tag{2.10}$$

Table 2.1: Theoretical and Experimental Critical Point Exponents.

	β	γ	δ
Mean Field Theory	0.5	1	3
3D Ising	0.326	1.31	4.78
3D Heisenberg	0.365	1.386	4.80
Experimental	0.2–0.4	1.0–1.4	3–6

where c_H is the specific heat, M and χ are, respectively, the magnetisation and susceptibility, and ξ is the spin-correlation length. The spin correlation length is a measure of the correlation between spins i and j and varies as $e^{-r_{ij}/\xi}$. The divergence of ξ at the critical point thus implies the existence of long-range order. The exponents listed above are, in principle, straightforward to determine experimentally, and have been found for many different systems. Typical exponent values for magnetic systems are shown in Table 2.1. The Heisenberg and Ising model predictions for the exponents described above have been approximated numerically for a 3-dimensional lattice. Numerical results seem to indicate that the exponents calculated are only dependent on the spin symmetry and the dimensionality, d, of the system, suggesting that these exponents are independent of short-range details of the system. These exponents are tabulated in Table 2.1, as well as the values predicted by the mean field model. Although the mean field model can be solved exactly, it does not in general give exponent values which agree with experimental results, confirming that this model is too simplistic.

Although critical point exponents can be calculated numerically with the more complex models, these models give little insight into the behaviour of the system in the critical region, especially in disordered systems. For this reason, a number of different approaches have been adopted in an attempt to describe the critical behaviour.

2.1.2 Scaling Theory

Scaling theory is an approach, based completely on a heuristic argument, which differs from the models described above in that it does not attempt to derive values for the exponents, but merely establishes relationships between the various exponents and experimental variables. The basic assumption made is that the thermodynamic potentials are generalised homogeneous functions of their arguments. The definition of a generalised homogeneous function, $f(x, y)$, is that for all λ,[15]

$$f(\lambda^a x, \lambda^b y) = \lambda f(x, y) \tag{2.11}$$

Although there is no physical basis for this hypothesis, it has been justified, albeit in a somewhat non-rigorous manner by Kadanoff[16]. Kadanoff considered the Ising model (n=1) on a lattice in d dimensions, with lattice constant a and spin $S_i = \pm 1$. The Hamiltonian for an Ising system in an applied field, H, is

$$\mathcal{H} = -J \sum_{i \neq j} S_i S_j - H \sum_i S_i \tag{2.12}$$

The system is then rescaled by a factor of L, by dividing the lattice into cells of side La, where L is an integer greater than or equal to one. As $t \rightarrow 0, h \rightarrow 0$, the correlation length of the system increases, becoming much larger than the size of an individual cell. One can thus assume that within any given cell, all the spins are aligned. Thus, as t approaches 0, $a \leq La \ll \xi$, and the lattice can be redrawn, with each cell becoming a lattice site with 'cell spin' of $\pm L^d$. Since this depends on $\xi \gg La$, this procedure is valid only near the critical point ($t = 0$, $h = H/k_B T = 0$). The Hamiltonian can then be written in the same form for the new lattice, but with a redefined exchange interaction (or equivalently t) and reduced field, h, with p and q arbitrary numbers,

$$\tilde{h} = L^p h \tag{2.13}$$

$$\tilde{t} = L^q t \tag{2.14}$$

Since the Hamiltonian is of the same form in the renormalised system as for the original system, the thermodynamic potentials will also be of the same form, with

the change in scale being reflected in their arguments, i.e.

$$G(\tilde{t},\tilde{h}) = L^d G(t,h) \tag{2.15}$$

The initial step in the description of the critical behaviour is to require the Gibb's function to be a generalised function of t and h, with exponents a and b, such that

$$G(\lambda^a t, \lambda^b h) = \lambda G(t,h) \tag{2.16}$$

The magnetisation can be found from the Gibb's potential using the thermodynamic relationship

$$M(t,h) = -\frac{\partial G(t,h)}{\partial h} \tag{2.17}$$

Using the definition of a homogeneous function given in equation 2.11, the derivative of (2.16) can be written as

$$\lambda^b \frac{\partial G(\lambda^a t, \lambda^b h)}{\partial(\lambda^b h)} = \lambda \frac{\partial G(t,h)}{\partial h} \tag{2.18}$$

or, rearranging,

$$\lambda^{b-1} M(\lambda^a t, \lambda^b h) = M(t,h) \tag{2.19}$$

This relationship is often called the magnetic equation of state. Setting h=0 and $\lambda = t^{-1/a}$ in (2.19) gives

$$M(t,0) = \lambda^{b-1} M(\lambda^a t, 0) = t^{\frac{1-b}{a}} M(1,0) \tag{2.20}$$

Since $M(1,0)$ is a constant, a final expression identical to that in (2.4) is obtained, with the exponent β given by

$$\beta = \frac{1-b}{a} \tag{2.21}$$

This derivation can be repeated in the limit $t \to 0^-$ with $\lambda = (-t)^{-1/a}$, to give $\beta' = \beta$. In the scaling approach, in fact, all of the primed exponents are identical to their unprimed equivalents. Applying the same approach to the magnetic equation of state in the limit $t = 0, h \neq 0$ gives a value for δ (as defined in equation. 2.6) in terms of the exponent b,

$$\delta = \frac{b}{1-b} \tag{2.22}$$

It is also straightforward to solve for γ using the zero field susceptibility, obtained from the derivative of (2.19) with respect to h, and following the same argument used for the zero field magnetisation, resulting in

$$\gamma = \frac{2b-1}{a} \tag{2.23}$$

Parallel arguments can also be used for the specific heat, $c_H = T\left(\frac{\partial^2 G}{\partial T^2}\right)_H$ and the correlation length to obtain values for α and ν for a d-dimensional system.

$$\alpha = 2 - \frac{1}{a} \tag{2.24}$$

$$\nu = \frac{1}{ad} \tag{2.25}$$

Since the scaling hypothesis only involves the two exponents, a and b, only two exponents are needed to find all the others. One important relationship between the magnetic exponenets is the Widom equality[17],

$$\gamma = \beta(\delta - 1) \tag{2.26}$$

Also, from (2.21) and (2.23), one sees that $\gamma+\beta = b/a$. Using this and the magnetic equation of state, a useful expression for the magnetisation can be derived,

$$M(t,h) = t^{\frac{1-b}{a}} M(1, t^{-b/a}h) = t^{\beta} F\left(\frac{h}{t^{\gamma+\beta}}\right) \tag{2.27}$$

where F is a homogeneous function of field and temperature. The susceptibility is the derivative of the magnetisation with respect to field; therefore[18],

$$\chi = (t^{\beta})(t^{-(\gamma+\beta)})\dot{F}\left(\frac{h}{t^{\gamma+\beta}}\right) = t^{-\gamma}\dot{F}\left(\frac{h}{t^{\gamma+\beta}}\right) \tag{2.28}$$

This result can be rewritten in terms of its field dependence as,

$$\chi = h^{\frac{-\gamma}{\gamma+\beta}}\left(\frac{h}{t^{\gamma+\beta}}\right)^{\frac{\gamma}{\gamma+\beta}}\dot{F}\left(\frac{h}{t^{\gamma+\beta}}\right) = h^{\frac{-\gamma}{\gamma+\beta}} G\left(\frac{h}{t^{\gamma+\beta}}\right) \tag{2.29}$$

In (2.28) and (2.29), $\dot{F}\left(\frac{h}{t^{\gamma+\beta}}\right)$ is the derivative of $F\left(\frac{h}{t^{\gamma+\beta}}\right)$. The susceptibility of a ferromagnet measured in fixed field is observed to have a maximum as a function of

temperature at some temperature t_m. From equation 2.29 it can be seen that any universal feature in the susceptibility, such as a maximum or minimum, will occur at a constant value of the argument of G in different fields. This requirement gives an expression for the peak temperature t_m in terms of the field,

$$t_m \propto h^{\frac{1}{\gamma+\beta}} \tag{2.30}$$

For constant $h/t_m^{\gamma+\beta}$, one can relate the magnitude of the peak susceptibility, χ_m, to the peak temperature using equation 2.28, thus,

$$\chi_m \propto t_m^{-\gamma} \tag{2.31}$$

Also, considering the variation of the peak susceptibility as a function of field, from (2.29), gives

$$\chi_m = h^{\frac{-\gamma}{\gamma+\beta}} G\left(\frac{h}{t_m^{\gamma+\beta}}\right) \propto h^{\frac{1-\delta}{\delta}} \tag{2.32}$$

The last relationship utilizes the Widom equality. Equations 2.31 and 2.32 suggest that on increasing the applied field, the peak in the susceptibility decreases in amplitude ($\delta > 1$), and moves upwards in temperature. This general behaviour has been verified experimentally [19]. From experimental data, one can thus determine values for all the exponents using the power law relationships derived above. Only two independent exponents are required to solve for the entire set. A linear extrapolation of T_m versus $H^{1/(\gamma+\beta)}$ to zero gives a first estimate for T_c, which can then be varied slightly to provide optimum agreement between exponents.

Scaling theory is extremely versatile, since it does not predict exponent values, and is thus independent of the specific system being investigated. This allows it to be applied to a wide variety of situations. It must be remembered, however, that these expressions are valid only close to the critical point (t=0, h=0), and thus, due to experimental limitations, measured exponents may not be accurate. Plots of these exponents as a function of field and temperature often are non-constant outside the critical region. Corrections to the scaling laws can be made by including higher order terms in the postulated power law dependences[20, 21].

2.1.3 Sherrington-Kirkpatrick Model

The mean field model described earlier applies only to ordered systems with uniformly distributed spins. The problem of how to describe a system with spins distributed at random lattice sites or on a random lattice is extremely complex. This situation occurs in amorphous and dilute magnetic systems. Various models have been proposed which apply certain approximations to make it feasible to study the behaviour of the system. In 1975, Edwards and Anderson[22] studied the problem of a spin-glass, in which the spins are frozen into random orientations and the total magnetisation is zero. In dilute systems, the exchange coupling is indirect, and is described by the oscillatory RKKY interaction[23]. This interaction is caused by the polarisation of the conduction electrons by localised moments, and is predicted to vary as

$$J(r) \propto \frac{\cos(2k_F r)}{r^3} \tag{2.33}$$

Thus, depending on the separation r of any two spins, the interaction between them may be ferromagnetic or antiferromagnetic. Based on the RKKY interaction, Edwards and Anderson postulated that a site-disordered spin-glass could be modeled by a random infinite-range exchange bond distribution for moments placed at each site in a regular lattice. They chose this distribution to be a Gaussian centred on zero. Sherrington and Kirkpatrick[24] later extended this model to include other types of magnetic ordering by allowing the Gaussian to be centred about some point, J_0, with a distribution width of J. The magnitude of J_0 gives the strength of the interaction, while its width governs the amount of disorder. A perfect ferromagnet would have $J_0 > 0, J = 0$, while a spin glass would have $\eta = J_0/J < 1$. The average free energy of the system was obtained using the 'replica trick' solution, from which various properties of the system could then be derived.

In studying a system with phase transitions, one generally examines the behaviour of 'order parameters' of the system. Typically, these order parameters are observables which are non-zero only in the ordered phase. Figure 2.1 shows schematic spin arrangements for paramagnetic, ferromagnetic and spin-glass sys-

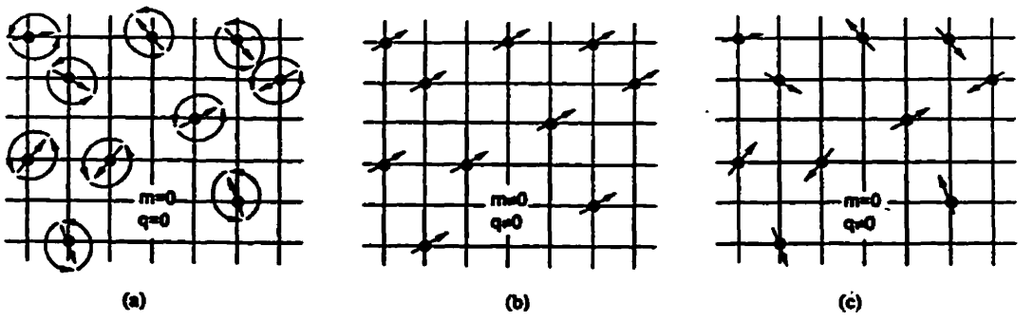

Figure 2.1: Spin arrangements for various site disordered systems. (a) paramagnet (b) ferromagnet (c) spin-glass[18]

tems, as well as postulated order parameters m and q, which are defined as

$$m = \langle\langle S_i\rangle_T\rangle_J \tag{2.34}$$

$$q = \langle\langle S_i\rangle_T^2\rangle_J \tag{2.35}$$

The symbol $\langle\rangle_T$ denotes an average over thermal fluctuations, while $\langle\rangle_J$ is an average over the exchange distribution. Obviously q is an appropriate order parameter to choose for a spin-glass, and m (which is equivalent to the magnetisation) is a good order parameter for ferromagnetism. Sherrington and Kirkpatrick derived expressions for m and q in a spin $\frac{1}{2}$ Ising system[24]; however, the thermodynamic potentials found using their approach are not well-behaved at low temperature. Southern[25] solved this model using an effective field approach instead of the replica method. The expressions obtained for m and q were the same as those of Sherrington and Kirkpatrick for S=1/2, however the thermodynamic potentials are well-behaved at all temperatures. The expressions for m and q were later generalised to a system of arbitrary spin S, by Roshko et al. [26]

$$m = \frac{1}{\sqrt{2\pi}}\int_{-\infty}^{\infty} SB_S\left[\frac{S}{k_BT}(J_0m + Jq^{1/2}\alpha + h_a)\right]e^{-\alpha^2/2}d\alpha \tag{2.36}$$

$$q = \frac{1}{\sqrt{2\pi}}\int_{-\infty}^{\infty} S^2B_S^2\left[\frac{S}{k_BT}(J_0m + Jq^{1/2}\alpha + h_a)\right]e^{-\alpha^2/2}d\alpha \tag{2.37}$$

Here, $h_a = g\mu_B H$ and $B_S(x)$, the Brillouin function for spin S is given by [1]

$$B_S(x) = \frac{2S+1}{2S}\coth\left(\frac{2S+1}{2S}x\right) - \frac{1}{2S}\coth\left(\frac{x}{2S}\right) \tag{2.38}$$

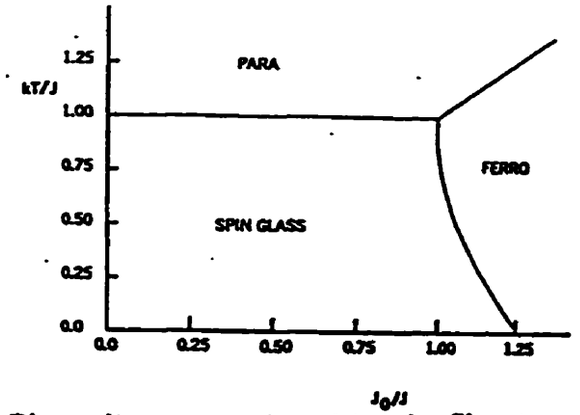

Figure 2.2: Phase diagram predicted by the Sherrington-Kirkpatrick model [24]

The spin S Ising model has 2S+1 possible values for S_i, i.e., $S_i = -S, -S+1, \ldots, S$. A phase diagram can be obtained for this model as a function of $\eta = J_0/J$ and T. The phase diagram found by Sherrington and Kirkpatrick is shown in Figure 2.2. For small η the system is a spin-glass at low temperature T/J, as would be expected; however, as the temperature is increased the system undergoes a transition to a paramagnetic state. For η >1.25 the low temperature state is ferromagnetic, with a high temperature paramagnetic state. For $1 \leq \eta \leq 1.25$, the model predicts the existence of three states, paramagnetic, ferromagnetic and spin-glass respectively, as the temperature is lowered. The transition temperature from the paramagnetic to ferromagnetic state is proportional to J_0, and the temperature for transition to the spin-glass state is proportional to J. Model calculations of the temperature dependence of the susceptibility in the ferromagnetic regime in a variety of applied fields[27] show that although the peaks obey the field and temperature dependences predicted by scaling theory, the critical exponents derived have mean field values. Thus, this model provides a qualitative method of predicting the behaviour of a disordered system in the vicinity of its critical temperature.

2.2 Electronic Transport

2.2.1 Introduction

When an electric field $\vec{E}$ is applied across a metal, a current will flow. The corresponding current density, $\vec{j}$, is given by Ohm's law,

$$\vec{j} = \sigma\vec{E} = \rho^{-1}\vec{E} \tag{2.39}$$

In general, the conductivity, σ, and the resistivity, ρ, are tensors, whose components vary from material to material. Since a perfect lattice will not scatter conduction electrons[28], a finite resistivity implies the presence of disorder. In a non-magnetic material, the disorder scattering can be separated into two contributions: scattering caused by impurities and defects, ρ_i, and scattering from lattice phonons, ρ_l. Matthiessen[29] hypothesised that these two contributions are independent of each other, so that the total resistivity can be expressed as the sum of the two terms, i.e.

$$\rho(T) = \rho_i(T) + \rho_l(T) \tag{2.40}$$

For low impurity concentrations the impurity term is generally taken to be temperature independent. Bloch[30] showed that in a pure metal the phonon component is proportional to T^5 at low temperatures and linear in T at high temperatures. Matthiessen's rule is generally obeyed quite well, however the addition of considerable amounts of alloying impurities can cause deviations from this rule[31]. Magnetic impurities cause drastic deviations from Matthiessen's rule, with the addition of a magnetic term, ρ_m, to the resistivity. At low temperature, at which the phonon term is negligible compared to the magnetic term, Matthiessen's rule, with all three components included, agrees well with experimental data. The same result is also true at high temperatures, where the phonon term dominates. At intermediate temperatures, however, Matthiessen's rule is generally not valid. In general, ρ_m depends on the type of magnetic order present in the system. At low temperature the conduction electrons are scattered from magnons, for example, giving ρ_m a temperature dependence of T^2 or $T^{3/2}$. A change in ordering is generally indicated by the

presence of an anomaly of some sort in the resistivity in the vicinity of the critical temperature. At temperatures sufficiently high to destroy any magnetic order, i.e. in the paramagnetic regime, ρ_m becomes constant and the resistivity shows only the temperature dependence of the phonon term. A number of models have been developed to explain the behaviour of ρ_m, and will be described in the following sections.

When a magnetic field is applied to a material, the electron paths are altered due to the Lorentz force, $q(\vec{v} \times \vec{B})$. At low temperatures, this will cause a small increase in the resistivity for a field applied perpendicular to the measuring current. A Hall voltage is also induced in the direction perpendicular to the current flow and the field direction. As the temperature of the system increases, electron-phonon scattering tends to reduce the effects of the applied field, as does impurity scattering. Smit[32] found that Lorentz scattering is appreciable only if the electron mean free path is on the order of, or greater than, the radius of curvature induced by the applied field. For materials in which the Lorentz effect is important, the resistivity with the magnetic field parallel to the current, $\rho_{\parallel}$, is less than that with the field applied perpendicular to the current, $\rho_{\perp}$. Kohler [33] proposed that, for an internal field, B, and residual resistivity, ρ_0, the measured magnetoresistance, $\Delta\rho = \rho(B) - \rho_0$, is a universal function of the ratio B/ρ_0, independent of the nature of the impurity. Schwerer and Silcox [34] later showed that Kohler's law holds only for materials for which a change in ρ_0 due to impurities has no effect on the crystal structure of the material, as might be expected.

The addition of magnetic impurities can have a variety of interesting effects on the magnetoresistance, in some cases causing a relative change in the resistivity of greater than 100%. The field and temperature dependence of the resistance in a system can give information on the type of magnetic structure present. The interpretation of the field and temperature dependence of the resistivity has been attempted using both localised and itinerant models, as summarised below.

2.2.2 Localised Models

Localised models are based on the picture of conduction electrons scattering from moments localised at some or all of the lattice sites. This model is applicable to rare-earth metals, whose $4f$ valence electrons lie well within the outer shells. The validity of this model is questionable for transition metal elements which have d-shells that are not as well-localised.

In the dilute limit in which the impurity moments are non-interacting, Kondo [35] showed that a minimum in the resistivity is expected at low temperature, where magnetic scattering dominates the phonon scattering. A high-order perturbation theory study of the spin-flip scattering of conduction electrons by the localised moments shows that the scattering cross-section increases with decreasing temperature at very low temperature. Competition between this effect and the phonon term (which decreases with decreasing temperature) causes a minimum in $\rho(T)$ often observed in the liquid helium temperature range.

As the magnetic impurity concentration is increased further, the moments begin to interact. At high temperature, such systems remain paramagnetic, with moments fluctuating randomly. In this region the magnetic contribution to the resistivity is a large, constant value caused by the interaction of the conduction electron spins $\vec{\sigma}$ with the local moment $\vec{S}$. If the interaction constant between the two moments is J, the paramagnetic contribution has been shown[36] to be,

$$\rho_m = \frac{k_F (mJ)^2}{4\pi e^2 z \hbar^3} S(S+1) \tag{2.41}$$

with k_F being the Fermi wave-vector and z the impurity valency. If a ferromagnetic ground state exists, the moments begin to align as the temperature is decreased through T_c, and the transverse scattering channels freeze out, decreasing ρ_m. This causes an abrupt change in the slope of $\rho(T)$ at T_c. De Gennes and Friedel [36] proposed that in this region, $\rho_m \propto \Gamma$, where Γ is the spin-spin correlation function. Fisher and Langer [37] subsequently showed that this implies a peak in $d\rho/dT$ at T_c, with $d\rho/dT$ exhibiting the same critical behaviour as the specific heat. The slow drop-off of $d\rho/dT$ above T_c which is observed in some systems is attributed to

localised spin clusters which persist to some temperature above T_c.

A system with an antiferromagnetic ground state shows remarkably different scattering behaviour. On approaching the Néel temperature, T_N, from above, an increase in the magnetic scattering is observed. This behaviour is common among the rare-earth metals whose ground states are often helical spin arrangements. If the periodicity of the spin arrangement is different from that of the lattice, gaps are induced on the Fermi surface. These 'superzone' boundaries cause a decrease in the effective number of conduction electrons at the Fermi surface, and thus increase the resistivity. The induced energy gap can be shown to be proportional to the sublattice magnetisation M(T) [38]. If the reduction of the Fermi surface area is characterised by a parameter g, the enhancement of the resistivity at T_N can be given by [38, 39]

$$\rho(T) = \frac{\rho_i(T) + \rho_l(T) + \rho_m(T)}{1 - gM(T)} \tag{2.42}$$

Sharp changes in the resistivity at the Néel temperature are observed in antiferromagnetic rare earths, as well as in chromium which has a spin-density wave state whose wave-vector is incommensurate with the lattice.

The theory of magnetoresistance has also been thoroughly investigated for localised models. The scattering Hamiltonian describing the interaction of conduction electrons with the magnetic atoms consists of several terms [40].

$$\mathcal{H}_{scatt} = \left[V + J(\vec{\sigma}\cdot\vec{S}) - \frac{D}{k_F^2}\left((\vec{S}\cdot\vec{k})(\vec{S}\cdot\vec{k'}) - \frac{S(S+1)}{3}\vec{k}\cdot\vec{k'}\right) + \ldots\right] a^{\dagger}_{\vec{k'}} a_{\vec{k}} \tag{2.43}$$

The first term represents the Coulomb interaction of the conduction electrons with the shielded ion cores, and the second is the familiar exchange Hamiltonian. A multipole expansion of the electric charge distribution shows that the first non-negligible contribution is the quadrupolar term, since in a central field electric dipole moments are zero. In the last term, D is the quadrupolar moment. $a^{\dagger}_{\vec{k'}}$ and $a_{\vec{k}}$ are the creation and annihilation operators for electrons with wave vectors $\vec{k'}$ and $\vec{k}$. From the scattering Hamiltonian the resistivity can be derived for fields applied at a particular angle to the current direction. Smit[32] deduced that, since the Coulomb and exchange terms are isotropic in a polycrystalline material, an anisotropy will

exist in the magnetoresistance only if there is spin orbit coupling in the material. The presence of spin-orbit coupling causes the non-spherical quadrupole moment D to rotate with the spin $\vec{S}$ when the field direction is changed, and thus a different scattering cross-section is presented to the conduction electrons as the field direction varies with respect to the current direction. Such effects are investigated by measuring the spontaneous resistive anisotropy(SRA), which is defined as [41]

$$\frac{\Delta\rho}{\rho_0} = \lim_{B\to 0}\left[\frac{\rho_{\parallel}(B) - \rho_{\perp}(B)}{\frac{1}{3}\rho_{\parallel}(B) + \frac{2}{3}\rho_{\perp}(B)}\right] \tag{2.44}$$

In order for an SRA to exist, therefore, there must be both a non-zero orbital moment $\vec{L}$ at the magnetic site and a (internal) field to align the spins. In the limit V≫D,J the anisotropy is given by [40]

$$\frac{\Delta\rho}{\rho_0} = \frac{D}{V}\left(\langle S_z^2\rangle - \frac{S(S+1)}{3}\right) \tag{2.45}$$

For temperatures much greater than the field, i.e. $T \gg \mu_B H/k_B$, $\langle S_z^2\rangle = \frac{S(S+1)}{3}$, and no anisotropy exists. As the temperature is decreased, $\langle S_z^2\rangle$ increases, and an anisotropy is observed.

Fert et al.[40] studied the SRA in noble metals containing small amounts of rare-earth impurities, and found that the magnitude and sign of the SRA observed was consistent with localised model predictions, i.e. the sign of the anisotropy changed when the sign of the rare earth quadrupolar moment changed, and vanished at high temperatures, confirming that this model is appropriate for rare-earth elements. In transition metals, however, the moment-bearing *d*-bands are hybridised with the *s* and *p* bands, and thus have a significant density of states at the Fermi surface. The *d* electrons can thus be quite delocalised and their scattering behaviour may be better understood using an itinerant model.

2.2.3 Itinerant Models

The itinerant electron approach is based on the two-band model proposed by Mott [42], which considers the *s* and *d* bands to be divided into spin-up and spin-down

sub-bands which conduct in parallel. This can be justified to an extent by considering the electronic band structure. The presence of an exchange field shifts the energies of the spin-up and spin-down bands with respect to each other. At the Fermi surface, the two sub-bands no longer have the same density of states, and thus have different conductivities. Mott's original model has been modified[40, 41, 43, 44] to include the effects of spin-flip scattering between sub-bands, due to the spin-orbit interaction and spin-wave scattering at low temperature. In transition metals, the conduction is modeled in terms of an isotropic $s-s$ scattering, $\rho_{ss\downarrow} = \rho_{ss\uparrow}$, and an anisotropic $s-d$ scattering $\rho_{sd\downarrow} \neq \rho_{sd\uparrow}$. Within a given sub-band, the resistivities are considered to act in series[43], an extension of Matthiessen's rule. The total resistivity for each sub-band is then,

$$\rho_{\downarrow} = \rho_{ss\downarrow} + \rho_{sd\downarrow} \tag{2.46}$$

$$\rho_{\uparrow} = \rho_{ss\uparrow} + \rho_{sd\uparrow} \tag{2.47}$$

If the spin-flip scattering is characterised by a resistivity $\rho_{\uparrow\downarrow}$, the total resistivity of the system[41] is

$$\rho_t = \frac{\rho_{\uparrow}\rho_{\downarrow} + \rho_{\uparrow\downarrow}(\rho_{\uparrow} + \rho_{\downarrow})}{\rho_{\uparrow} + \rho_{\downarrow} + 4\rho_{\uparrow\downarrow}} \tag{2.48}$$

To find the magnetoresistive anisotropy in this system, the contribution from each term must be considered. Since the anisotropy is due to spin-orbit coupling, $\lambda\vec{L}\cdot\vec{S}$, which is zero in the s bands ($\vec{L} = 0$), the $s-s$ scattering shows no anisotropy. All contributions must come from $s-d$ and spin-flip scattering. A second-order perturbation theory approach to the scattering gives an approximate expression for the anisotropy in the presence of only the exchange field, H_{ex}, between the moments[43, 45].

$$\frac{\Delta\rho}{\rho_0} \simeq \frac{\gamma[\rho_{sd\downarrow} - \rho_{sd\uparrow}]^2}{\rho_{\uparrow}\rho_{\downarrow} + \rho_{\uparrow\downarrow}(\rho_{\uparrow} + \rho_{\downarrow})} \tag{2.49}$$

Here, $\gamma \propto \lambda^2/(K^2 \pm H_{ex}^2)$, for a cubic system. The crystalline field anisotropy K is included to prevent the expression from diverging when $H_{ex} \rightarrow 0$ as T$\rightarrow$ T_c. The behaviour of this function is not obvious, due to the large number of parameters present. However, the anisotropy will vanish in the non-magnetic regime

due to the equality of the spin-up and spin-down resistivities when $H_{ex} = 0$. In the magnetic regime, $H_{ex} \neq 0$, and thus an anisotropy will be present for $\lambda \neq 0$. As the temperature approaches T_c from below, H_{ex} goes to zero. A Taylor expansion of $\rho_{sd\uparrow,\downarrow}$ near T_c gives, to first order, $\rho_{sd\uparrow,\downarrow} \simeq \rho_{sd} \pm sH_{ex}$, where s is the first derivative of ρ_{sd} with respect to field. In this limit, assuming the denominator of (2.49) to be relatively constant near T_c, the fractional anisotropy is proportional to $\gamma s^2 H_{ex}^2$. Since, in mean-field theory, $H_{ex} \propto \langle M \rangle$, which in turn is proportional to $(1 - T/T_c)^{1/2}$, the anisotropy near T_c is expected to vary linearly with temperature.

The itinerant model contains many unknowns, without which the detailed behaviour in the vicinity of T_c can not be calculated. Some of these parameters can be determined experimentally from measurements of the resistivity in ternary alloys as a function of the concentration of the two magnetic impurities[46, 47]. From these data, a value for the resistance ratio $\alpha = \rho_\downarrow / \rho_\uparrow$ can be found for a given magnetic material. With further assumptions, the expression for the SRA can be expressed in term of α, which then gives reasonable agreement to SRA values in a number of transition metal systems.

In summary, although the itinerant model may be more appropriate than the localised model for transition metals whose d-bands are not well-localised, model predictions can not be compared to experimental results without making a number of major approximations. Nevertheless, this model has shown some success in modeling the behaviour of SRA in transition metal systems and giant magnetoresistance in magnetic multilayers. The localised model, which is significantly simpler in form, is more easily fit to data, and has shown some success in modeling the behaviour of some dilute transition metal and rare-earth ferromagnets.

2.3 Superconductivity

2.3.1 Superconducting Properties

Superconducting materials are of great experimental and theoretical interest, due to their unique properties. As these systems are cooled conduction electrons form

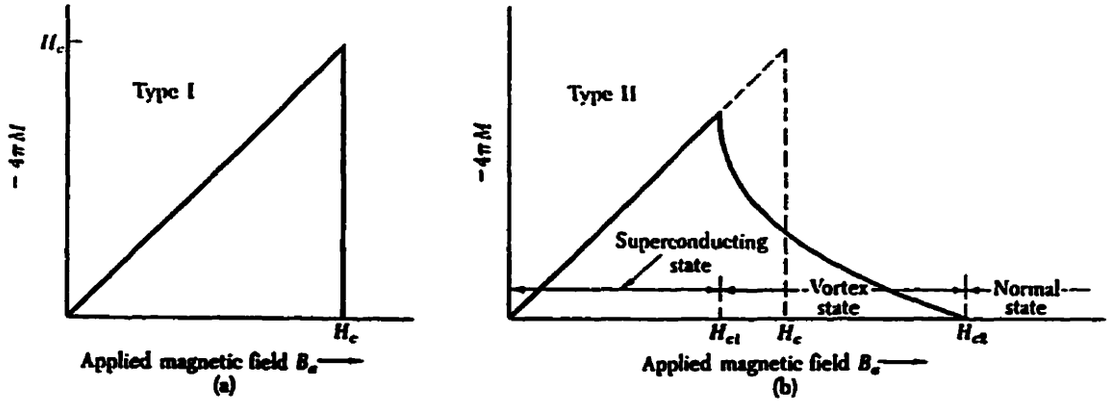

Figure 2.3: M(H) for (a) Type I and (b) Type II superconductors [28]

a collective ground state which exhibits no resistance to current flow. As well as having zero resistance, this state exhibits interesting magnetic properties. Typical M(H) plots are shown in figure 2.3 for both Type I and Type II superconductors. Type I superconductors, generally pure metals such as lead, are perfectly diamagnetic ($H=-4\pi M$) up to some critical applied field, H_c, at which the superconducting state is destroyed and the material reverts to its normal state. The total exclusion of flux in the superconducting state is called the 'Meissner effect'. Type II superconductors, which are primarily alloys, show the same behaviour up to a critical field H_{c1}, at which portions of the material become normal. The superconducting state persists up to some larger field H_{c2} in a 'vortex' state, with cores of normal material embedded in the superconducting matrix. Above H_{c2} the entire system is normal, and the magnetisation is zero. On decreasing the field, the magnetisation exhibits some hysteresis. This irreversibility is largely due to the presence of defects which pin the superconducting vortices, although it is also influenced by size effects–as the sample size increases, the area of the loop also increases. The superconducting state can also be destroyed by the application of large currents. A brief discussion of the theoretical basis for these properties is given below: a more detailed review can be found in most introductory condensed matter textbooks, for example[28, 48].

The electromagnetic properties of a superconductor can not be obtained by applying Maxwell's laws to a system with zero resistivity. H. London and F. London [49] showed that Maxwell's laws require

$$\frac{\partial}{\partial t}(\vec{\nabla} \times \vec{j} + \frac{n_s e^2}{mc}\vec{B}) = 0 \tag{2.50}$$

which is satisfied for *any* time-independent field and current density. In the above equation n_s is the density of (superconducting) electrons. On the transition to the superconducting state a perfect conductor would thus merely induce surface currents to oppose any *change* in internal flux, and not expel any pre-existing internal field. The appropriate behaviour for a superconductor can be obtained by applying the constraint

$$\vec{\nabla} \times \vec{j} = -\frac{n_s e^2}{mc}\vec{B} \tag{2.51}$$

Maxwell's equations then give equations for the behaviour of $\vec{B}$ and $\vec{j}$, showing that flux and current are surface phenomena which decrease exponentially with depth. The characteristic penetration depth is given by $\lambda = \left(\frac{mc^2}{4\pi n_s e^2}\right)^{1/2}$. The surface currents induce flux which completely screens the interior from any external fields. As $T \rightarrow T_c$, or $H \rightarrow H_c$, the density of superconducting electrons drops to zero, and flux penetrates the entire sample. For $T \ll T_c$, n_s approaches the total density of conduction electrons. Although the London result reproduces some of the observed experimental behaviour, it does not explain the origin of these effects, which lies at the microscopic level. In 1957, Bardeen, Cooper and Schrieffer (BCS) [50] formulated a theory which successfully explained the nature of the superconducting state. They proposed the presence of a weak attractive electron-electron potential, mediated by a slight overscreening (caused by lattice vibrations) of the Coulomb potential. At low temperature, this electron-phonon interaction is strong enough to form bound pairs of electrons having opposite spin, and equal but opposite wavevectors. These bound pairs are able to propagate collectively through the medium with no resistance. As the temperature is increased, thermal energy causes the pairs to dissociate, and finally, at T_c, all the electrons are in the unbound state. The application of sufficiently large fields and currents also induces pair breaking effects.

BCS theory also predicts the temperature dependence of a number of experimental observables. An exponential dependence of T_c on the attractive potential V and the electron density of states $N(E_F)$, is obtained

$$k_B T_C = 1.14\hbar\omega_D e^{-1/N(E_F)V} \tag{2.52}$$

This implies that no matter how small the attractive potential is, a superconducting state always exists at sufficiently low temperatures. In the superconducting state an energy gap, Δ, often exists at the Fermi surface, and can be measured using optical photon absorption techniques. The temperature dependence of the energy gap and the critical field in the vicinity of T_c are given by

$$\frac{\Delta(T)}{\Delta(T_c)} = 1.74\left(1 - \frac{T}{T_c}\right)^2 \tag{2.53}$$

$$\frac{H_c(T)}{H_c(0)} = 1 - \left(\frac{T}{T_c}\right)^2 \tag{2.54}$$

The penetration depth, λ, of the flux into the surface and the coherence length, ζ, can be calculated from experimentally derived parameters. The coherence length is a characteristic length over which the density of superconducting electrons is constant–even in a non-uniform applied field. A good superconductor has a low penetration depth and a high coherence length. The Ginzburg-Landau parameter $\kappa(T)$, a measure of the quality of a superconductor, is defined as

$$\kappa(T) = \frac{\lambda(T)}{\zeta(T)} \tag{2.55}$$

For Type I superconductors, $\kappa < 1$, whereas in Type II superconductors $\kappa > 1$. In Type II superconductors, κ is related to the measured critical fields as [51]

$$\kappa = \frac{H_c(T)}{\sqrt{2}H_{c2}} \tag{2.56}$$

or, [52]

$$\frac{H_{c1}(T)}{H_{c2}(T)} = \frac{\ln(\kappa(T)) + 0.5}{2\kappa^2(T)} \tag{2.57}$$

The coherence length can be related to H_{c2} in terms of the universal flux quantum $\Phi_0 = \frac{2\pi\hbar c}{2e}$[28]

$$H_{c2}^2 = \frac{1}{2\pi}\frac{\Phi_0}{\zeta^2(T)} \tag{2.58}$$

Another parameter which characterizes the usefulness of a superconductor is the critical current density J_c. This is the maximum current density which a superconductor can conduct without going normal. The critical current is obviously related to the critical field, since a current induces a field in a conductor. Using a simple model based on Ampère's law and the sample geometry, Bean[53] showed that the critical current density can be calculated from the irreversible magnetisation–the difference between the magnetisation in ascending and descending branches of the M(H) curves.

2.3.2 Impurities in Superconductors

The addition of impurities to a superconductor has the effect of introducing additional pair-breaking mechanisms. This decreases the strength of the attractive potential, and thus reduces the critical temperature for the superconducting transition, with the addition of significant amounts of impurities eventually destroying the superconducting state altogether. The sensitivity of T_c to impurity concentration depends strongly on whether the impurity is magnetic or non-magnetic, since different types of scattering result.

Several theories have been proposed to explain the effects of the introduction of transition metal impurities into superconducting hosts. One possibility is the case in which the hybridisation of the impurity d-bands with the host's s- and p-bands is sufficient to ensure no local moment exists at the impurity site. In this case, Anderson[54] showed that the scattered wave-functions can be expressed as a superposition of plane wave states. In a BCS superconductor, electrons occupy pairs of states, which scatter from the impurity. Kaiser[55] extended work done previously on this model [56], deriving equations which predict that near the critical concentration, n_c, for the destruction of superconductivity, the critical temperature is inversely proportional to the impurity concentration, c. The rate of decrease in T_c is strongly dependent on the density of states, $N_i(E_F)$, of the impurity electrons at the Fermi surface. Impurities with low $N_i(E_F)$ have only a small effect on T_c. The decrease of T_c from the pure host critical temperature, T_{c0}, as given by Kaiser

can be expressed as[57]

$$\ln\left(\frac{T_c}{T_{c0}}\right) = -\frac{(\alpha+\beta)c}{g(1-\beta c)} \tag{2.59}$$

where

$$\alpha = \frac{N_i(E_F)}{N(E_F)} \tag{2.60}$$

$$\beta = \frac{N_i(E_F)^2 U_{eff}}{(2l+1)gN(E_F)} \tag{2.61}$$

U_{eff} is the intra-impurity Coulomb repulsion between spin-up and spin-down electrons, g is the BCS coupling constant, and $2l+1$ is the orbital degeneracy of the impurity atom. This result has had some success in modeling the reduction of T_c in various systems with non-magnetic impurities [58].

With the introduction of magnetic impurities into a superconductor, a number of other pair-breaking mechanisms must be considered, in particular the effects of spin-scattering on the electrons in the Cooper pairs, the effects of the exchange field on the energies of the bound spin-up and spin-down electron pairs, and the effect of the local magnetic field on the electron paths. In 1960, Abrikosov and Gorkov [59] developed a theory describing the effects of paramagnetic (non-interacting) impurities on superconducting alloys, which assumes that the interaction between the local moment $\vec{S}$ and the electron spins $\vec{\sigma}$ is the exchange interaction, $H_{int}=2J\vec{S}\cdot\vec{\sigma}$, introduced previously. The effect of the magnetic impurities on the BCS potential is treated in the first Born approximation, and a second-order phase transition from normal to superconducting state is predicted in zero field. The model also predicts the existence of gapless superconductivity within a certain range of impurity concentration. The concentration dependence of T_c in this model is given by [60]

$$\ln\left(\frac{T_c}{T_{c0}}\right) = \Psi\left(\frac{1}{2}\right) - \Psi\left(\frac{1}{2} + \frac{0.14cT_{c0}}{n_c T_c}\right) \tag{2.62}$$

where Ψ is the digamma function. This result predicts strikingly different behaviour from the non-magnetic case (equation 2.61) near n_c, with the reduction in T_c being linear with the impurity concentration. The predictions of this model have also been verified experimentally.

Chapter 3

Experimental Methods

3.1 Sample Preparation

Due to the metallurgical diversity of the materials studied, a variety of techniques were necessary to produce the samples. The initial alloy preparation was the same for all the materials. High purity starting materials were weighed out in the appropriate stoichiometric ratios, and then melted together in an argon arc-furnace. Any melting losses were recorded, and the ingot was then inverted and remelted several times to insure homogeneity. The resulting button was then used to prepare the specimen for measurement. Samples used for transport measurements were in the form of bars, of dimensions typically (40 x 2 x 0.2) mm^3, while those used for susceptibility measurements were (16 x 2 x 0.2) mm^3 with the edges rounded so as to approximate an ellipsoid. The method of preparing these bars depended on the ductility of the material, as well as the final structural state desired. A brief summary of the starting materials and the technique followed for each alloy is given below. The specific metallurgical methods are described in detail in the following section.

3.1.1 Alloy Preparation

- PtFe: The Pt + 10 at.% Fe sample was prepared using starting materials of 99.99% purity. After alloy preparation, the sample was cold rolled to the desired thickness. After rolling, a sample was cut from the sheet, and etched

to remove possible surface contamination. The specimen was then annealed in vacuum (10^{-6} mmHg for 72 hours at 950°C), and quenched in water.

- PdCo: The Pd + 3 at.% Co sample was made using 99.999% pure Pd wire and 99.998% pure Co sheet. The ingot was cold rolled and cut, after which it was etched briefly to remove surface contamination. Prior to measurement, the sample was annealed for 30 hours in vacuum at 1000°C, and water quenched.

- FeZr: The amorphous FeZr samples were prepared at McGill University[61]. Ribbons of length 1 m, width 1–2 mm and thickness of 10–20 μm were prepared by dropping the molten metal onto a copper wheel rotating with a tangential speed of 50 m/s in an argon atmosphere. The amorphous quality of the ribbon was verified by x-ray diffraction and differential scanning calorimetry [61, 62], and crystalline phases were found to be present at less than 1%, the lower limit of detection of the methods used. A small quantity of hydrogen was introduced into one of the samples by an electrolytic process[63].

- CuNi alloys: Large ingots of 45 and 55 at.% Ni in Cu were prepared from high purity starting materials using conventional arc-melting techniques. These ingots were rolled and cut into smaller pieces with scissors. Appropriate mixtures of the two alloys were used to prepare alloys of intermediate concentrations. After cold-rolling and cutting, the samples were annealed at 950°C in an argon atmosphere for 48 hours and quenched in ice-water.

- Y-Ni-B-C superconductors: The alloys were prepared in button form using the arc-melting technique. Starting materials were 99.9% pure Y, 99.95% pure Ni, 99% pure B, 99.98% pure Fe and specpure C. All materials were weighed out in stoichiometric quantities, with an excess 2–4% of Y included to compensate for its expected preferential melting loss. The carbon, boron and yttrium were wrapped in the Ni or Fe foil to limit melting losses and to melt the carbon and boron indirectly through contact with the molten

metal. Bar-shaped samples for resistivity measurements were chill-cast from the buttons, or cut using a diamond saw. Measurements were performed on these samples both prior to and after a 12 hour anneal at 1000° C.

- $Ce(Fe_{1-x}Ru_x)_2$, $x = 0.07$, 0.08: These samples were prepared by Roy and Coles[12]. The alloys were prepared by argon arc-melting with starting materials of at least 99.99% purity. The alloys were cast into bars with square cross-sections. A complicated annealing sequence, found by trial and error to give the best samples[12], was followed: 2 days at 600° C, 5 days at 700°C, 2 days at 800°C and 1 day at 850°C. Metallographic analysis showed that impurities were present at less than 5%. X-ray diffraction showed that these samples have the C15 Laves-phase structure.

- Gd_2In: The Gd_2In sample was prepared by McAlister[64] by argon arc-melting using 99.9% pure Gd and 99.999% pure In. The resultant brittle button was cut into pieces suitable for resistivity measurements. X-ray powder diffraction showed that the alloy was single phase, with the filled NiAs structure.

- CrCo, CrFe: Samples were prepared with 1.3, 2.5, 5 and 10 at.% Fe in Cr and 2.5, 5 and 8 at.% Co in Cr. The CrCo and CrFe were prepared from high purity starting materials (Cr 99.99% pure, Co specpure, Fe 99.99% pure) in large 15 gram ingots, using successive dilution from the highest concentration alloys. Samples were cut from these ingots using a spark cutter and a diamond saw. The samples were annealed in argon atmosphere at T=950°C for 48 hours.

3.1.2 Metallurgical Techniques

Cold Rolling

Materials which are malleable can easily be cold rolled into sheets. The button, weighing 1–2 grams, was placed between protective sheets of Melinex, and its thickness was gradually reduced by successive passes through adjustable rollers. When the resultant sheet was of the desired thickness, samples could be cut from it using

a razor blade knife or a pair of scissors. Any strains induced by cold working were removed by a subsequent anneal, the details of which were highly alloy dependent.

Electric-Discharge Machining

Some of the prepared alloys were extremely brittle and thus could not be rolled into thin sheets. These materials were prepared in large ingots weighing 10–15 grams, which were then cut using electric-discharge machining (EDM)–also known as spark cutting. The ingot itself took up to one week to produce, since it had to be shaped from a round button to a cylinder 4 cm long by cutting the button lengthwise, overlapping the pieces and joining them by remelting, with the entire process repeated several times. The button was clamped to a base inside a vat of oil or kerosene, which acted as a dielectric and coolant. The base was placed at a potential of a few hundred volts. An electrically grounded metallic blade moved toward the sample, causing a spark to jump between the two metals, melting some of the sample away. In this procedure the blade never touches the sample, making EDM an important method in cases where the sample is sensitive to contamination. Also, the cut is the shape of the blade, so that complex cuts may easily be made using an appropriately shaped blade. For short or shallow cuts (up to 1 cm) a tool with a Cu blade was used. The blade was a sheet of copper about one-quarter of a millimetre thick, which was clamped and stretched between two end pieces. For longer and deeper cuts, a moving wire blade was used. The wire was 1/4 mm thick, made of high-tensile brass by Kentron. The wire ran between two spools, and was driven at a constant speed by an electric motor. The primary difficulty with this technique was that, due to the irregularity of the final ingot, it was difficult to clamp it firmly in place. Thus, slight movements of the sample due to pressure, heating and lubrication from the dielectric resulted in irregularly shaped bars. This made it difficult to accurately evaluate demagnetisation and form factors for the samples. Also, this method was extremely time consuming, requiring a minimum of two days to cut one bar from the ingot.

Diamond Saw

Due to the non-uniformity of the samples produced and the time consumed by spark-cutting, it was decided to use a diamond saw to cut some of the samples. The blade was a metal wheel with a cutting edge 3/8 of a millimetre thick, coated with diamond powder. Since this blade was wider than the EDM blade, more material was wasted, however, since the ingots could be waxed firmly to a base clamped in the required position, sample alignment was easier than with EDM. This technique produced beautiful specimens with only a few hours cutting time.

Chill-Casting

While the last two methods described above were capable of producing appropriately shaped specimens of brittle materials, they were expensive both in terms of the amount of materials and preparation time required. Also, the fifteen gram ingots were so large that a completely homogeneous alloy was difficult to obtain. For these reasons we decided to spend some time trying to develop a casting method to form small buttons into rods of the appropriate dimensions. The basic technique has been described by H.E.N. Stone[65], however, several modifications had to be made to these plans in order to produce our desired sample shape. The mold consisted of a solid copper cylinder of radius 24 mm and height 70 mm. The mold was cut in half lengthwise, the surfaces carefully machined and then a rectangular slot was machined down the centre of one half, from top to bottom, as shown in Figure 3.1. The two halves of the mold bolted together and seal with vacuum grease. The top of the mold had a shallow cone machined in its center. During the casting process, the ingot sat in the cone, the slope of which caused the molten material to flow downwards towards the slot. The bottom of the mold bolted on to a base which sat on the copper hearth of the arc furnace. The mold was cooled in part by contact with the water-cooled hearth of the furnace, but also relied on its large mass to prevent overheating. The top of the base was sealed against the mold with an o-ring. A hole drilled into the base was aligned with the slot in the mold and provided access

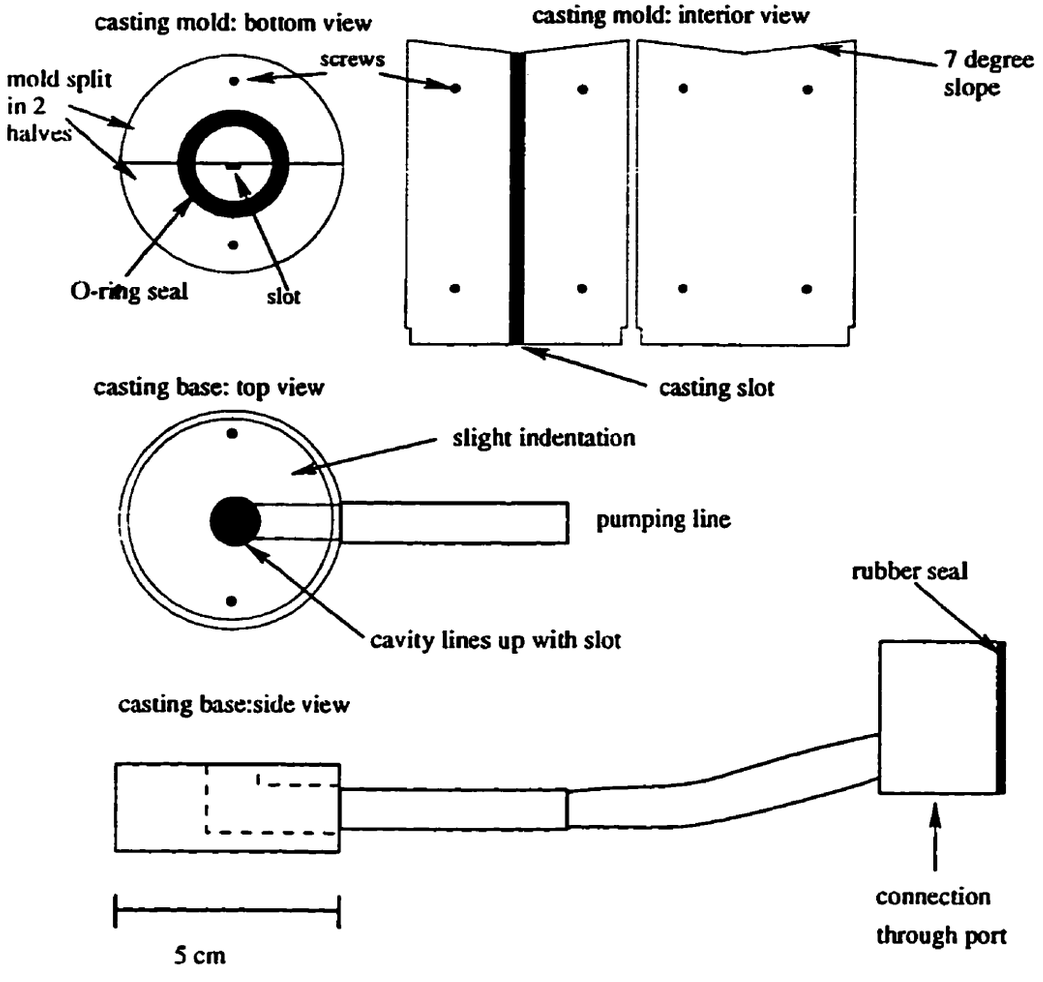

Figure 3.1: Chill-casting mold and base. Scale is as indicated above.

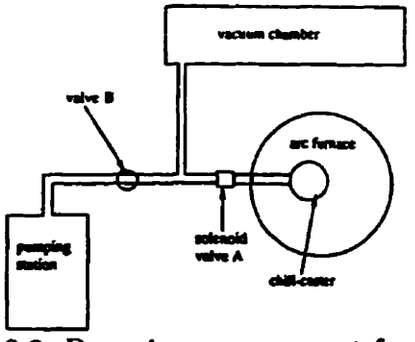

Figure 3.2: Pumping arrangement for chill-casting

for a copper pumping line which lead from the base to one of the ports on the arc furnace. This provided a vacuum line leading from the top of the copper mold to a pumping station outside the furnace. The pumping system was arranged as shown in Figure 3.2. A solenoid-activated valve directly outside the furnace isolated the mold from the pumping system while the button was being melted. Prior to the melt, a mechanical pump was used to evacuate a large cylinder. After this vacuum chamber was evacuated, valve B was closed to avoid contamination of the pump when valve A was opened. When the ingot was melted, the solenoid valve was opened and the molten metal subjected to a sudden vacuum which pulled it into the mold. The arc furnace was maintained at one-third of an atmosphere of argon during the melt. While simple in principle, this method was difficult to optimize due to the large number of parameters which could be varied. If the vacuum was too high, the molten metal flowed so rapidly that it didn't have time to solidify. If the vacuum was too low, the material didn't flow due to surface tension. Also, the success of the casting was sensitive to the time taken to melt the sample, since for longer melting times the mold will be too warm to solidify the metal as it passes down. Opening the solenoid as soon as the metal was molten gave the best results. To get a uniform sample with no voids, it was necessary to put a copper restricting shim in the lower portion of the mold. This allowed the metal to flow freely for the length of the sample desired, but impeded the flow at the bottom, preventing the metal from collecting in the base. After disassembly the copper shim could

quickly be cut from the sample using EDM (around 5 minutes). Other parameters which had to be optimised were the depth of the slot, the slope of the cone, and the amount of starting material used. We found that the molten metal would not flow into the mold for a slot thickness less than 1 mm, which is about 5 times our usual sample thickness. The optimum cone angle was found to be about 5 degrees. The ideal initial ingot consisted of approximately twice as much starting material as needed to fill the mold ($\sim$ 1g), much less than the 15g ingots which were needed for the previous methods which greatly reduces material costs. With the technique perfected, it was possible to produce long, thin, perfectly shaped bars from an ingot in minutes.

Melt-Spinning

The FeZr samples were prepared in an amorphous state. To do this, the molten metal must be cooled so rapidly that it has no time to form an ordered crystalline state. These samples were prepared at McGill University by J.O. Ström-Olsen et al.[62]. The alloy was made using the standard technique in an argon arc furnace, and amorphous ribbons were obtained from this alloy using the melt spinning technique. The alloy was melted (in argon atmosphere), and dropped on a rapidly spinning copper wheel which was maintained at liquid nitrogen temperature. The metal then solidified, cooling at a rate of 10^5 degrees per second. The resulting thin, brittle ribbons could be cut into the appropriate lengths with scissors.

Electropolishing

The samples produced by chill-casting were too thick to be mounted in our resistivity apparatus, so the thickness was reduced using an electropolishing technique. The sample was placed in an electrolyte, and connected to the anode of a power supply. A cathode of a suitable metal was placed an appropriate distance from the sample in the electropolishing tank, and voltage was applied to etch the sample to the desired thickness. The optimum values of voltage, current density and electrolyte for most alloys are tabulated in metallurgical handbooks, such as Thompson-Russell

and Edington's book on electron microscope techniques[66]. Electrolytic techniques were also used to introduce hydrogen into the lattice of the FeZr samples.

3.2 AC Resistivity and Magnetoresistance Measurements

The resistivity measurements in this study were taken using a high sensitivity *ac* difference technique. The measuring electronics were the same for all samples, but different cryostat systems were used, depending on the temperature and magnetic field ranges required. The measurement technique and principles are discussed below, along with descriptions of the various cryostats.

3.2.1 Measurement Technique

The conventional approach for measuring the resistivity of a material is the 4-probe *dc* technique. In this method one measures the current and the potential drop across the sample and obtains the resistance, R, using Ohm's law. The resistance, however, is not specific to the material measured, since it varies with the length, L, and cross-section, A, of the specimen. Normally, one quotes the resistivity, ρ, of the sample, which is obtained by multiplying the resistance by a form factor which removes the dependence on the sample's shape.

$$\rho = R\frac{A}{L} \tag{3.1}$$

For our study it is necessary to be able to measure small changes in voltage superimposed on a much larger voltage signal. DC methods tend to be sensitive to thermal emf's and contact impedances when such small values are measured. For this reason an *ac* technique is used which allows measurement of differences as small as a few parts per million of the output signal. The electronics for this system is described in detail by Muir and Ström-Olsen[67]. A 37 Hz *ac* current is supplied to the sample using a General Radio 1311A audio oscillator. The signal generator also provides the reference signal for a Princeton Applied Research HR8 lock-in

amplifier and a Kelvin-Varley DP1211 potentiometer. In order to measure small changes in the sample voltage, an initial voltage, V_0, tapped off the Kelvin-Varley divider, is subtracted from the sample voltage, so that the small difference can be amplified, and high accuracy obtained. A variometer is also placed in the circuit to remove the effects of stray capacitances and inductances in the system. This variometer consists of a primary coil of 150 turns and two secondary coils of 250 and 10 turns, allowing coarse and fine adjustment of the out of phase signal. In this manner, the lock-in can be adjusted to be completely in phase with the reference signal, so that any reasonable changes in the quadrature component will not affect the output signal. A detailed circuit diagram is shown in figure 3.3.

The basic measurement procedure was as follows. The sample was placed in the cryostat, and the system brought to the appropriate initial field and temperature conditions. Normally this meant that the sample was cooled below its critical temperature in zero magnetic field. The electronics system was then tuned, and the initial voltage, V_0, was read by opening switch A in figure 3.3, removing the back-off signal. A was closed again, and the lock-in amplifier switched to an appropriate sensitivity. It was then possible to measure small changes in the signal due to changes in the temperature, $\Delta\rho(T)$, or to changes in applied field, $\Delta\rho(H)$. For magnetoresistance measurements, the output of the lock-in and the current of the magnet power supply were read using two HP34401A multimeters. The data was collected using a computer with a GPIB card. For measurements taken as a function of temperature, data was collected automatically, except in those cryostats without an electronic temperature output. After the sample was removed from the cryostat, the form factor was measured using a Picker traveling microscope. Errors in this value could be as large as 5%, depending on sample uniformity. Using this form factor, voltage measurements could be converted to resistivity.

The experimental geometry for magnetoresistance studies is shown in figure 3.4. The current, I, flows down the length of the sample. The magnetic field was applied either parallel ($H_\parallel$) or perpendicular ($H_\perp$) to the direction of the current, as shown. The change in field direction was obtained either by rotating the sample or by

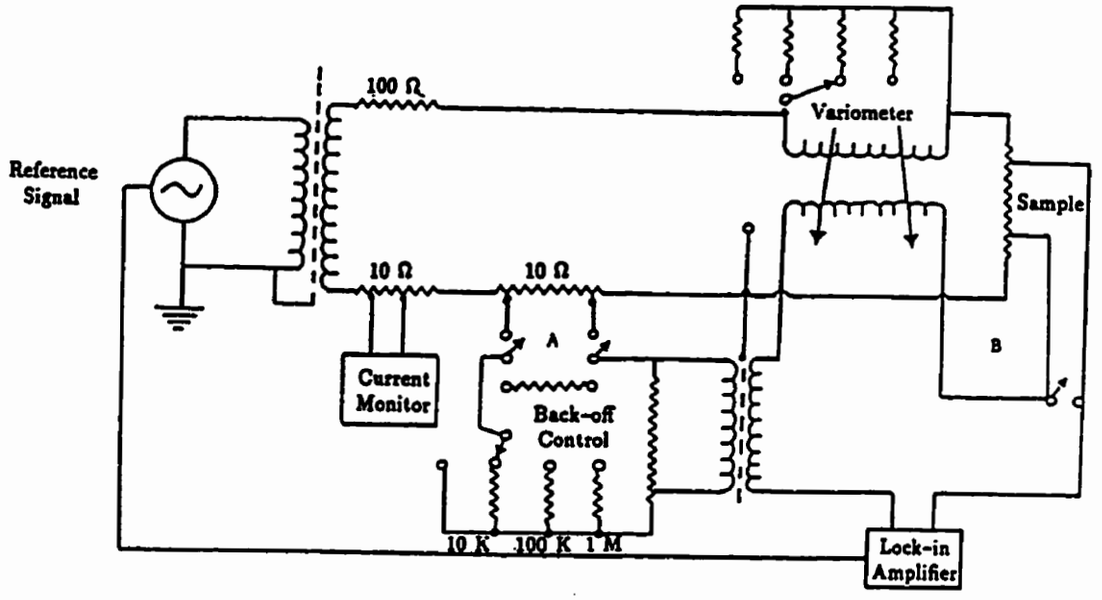

Figure 3.3: Detailed circuit diagram of *ac* resistivity measurement system [63].

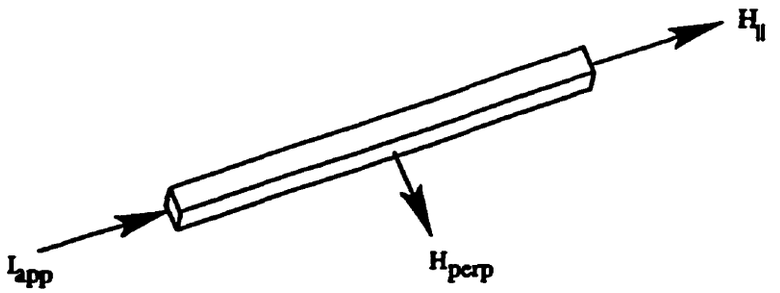

Figure 3.4: Experimental geometry for magnetoresistance measurements.

rotating the magnet which applies the field.

In the measurements described above, the *change* in voltage, ΔV, was measured. For situations in which the fractional change in $\rho(H,T)$ was required, no form-factor conversion is needed, since both numerator and denominator are multiplied by the same factors, i.e. $\Delta\rho/\rho_0 = \Delta V/V_0$. Only variations in measuring current had to be taken into account. For this reason, measurements of fractional changes could be found to an accuracy of 1 part in 10^5. Absolute measurements of $\rho(H,T)$ could have errors as high as 10% due to form factor inaccuracies and other systematic errors inherent in the *ac* technique.

3.2.2 Spontaneous Resistive Anisotropy (SRA) System

The apparatus on which the SRA was measured was made previously by Dr. H.P. Kunkel, but has not been described in detail. This system has a sample block capable of rotating through 90 degrees, so that measurements with the field parallel and perpendicular to the sample current can be taken easily. Four samples are mounted in series on this block, two on each side, as shown in figure 3.5. The block is roughly circular, with a diameter of 4.8 cm and a thickness of 0.4 cm, and is machined from a slab of Oxygen-Free High Conductivity (OFHC) copper. Each end of the sample rests on two knife edge contacts, the inner one for voltage, and the outer for current connections. These copper knife edges are electrically insulated from each other and from the copper base by layers of highly permeable cigarette paper soaked in

General Electric 7031 varnish (GE varnish). This varnish is known to have good thermal conductivity down to low temperatures. The samples are clamped to the knife-edges with a fibreglass yoke which is screwed down at either side of the sample, ensuring not only that the sample remains in good electrical contact with the knife-edges, but also that the sample does not move when subjected to thermal cycling. Any movement of the sample could result in the field and current not having the desired relative orientation. For temperature measurement and control, a Lakeshore Cryogenics CG1500 calibrated carbon-glass resistor is used in conjunction with a Lakeshore Model 520 temperature controller. The resistor is inserted directly into the sample block to reduce the possibility of thermal gradients between the samples and the thermometer. To provide warming power, a heater made of Cupron wire with nominal resistance 25 Ω at 77K is wound around the block. A pin is inserted through a hole drilled through the centre of the sample block, perpendicular to its plane. The sample block can be rotated about this axle using a lever arm, which leads upwards and through the top of the cryostat. The current and voltage wires are twisted together to reduce noise pickup, and lead down from a sealed 17-pin connector through 3/8" diameter thin walled stainless steel tubing. They exit the stainless steel tubing several inches from the bottom, and are thermally anchored by being wrapped around the tubing several times and glued down with GE varnish, ensuring that any heat passing down the leads from the top of the system will be absorbed by the helium bath, and thus not transferred to the sample block. Below this thermal anchor, the wires divide into two bundles, which enter the supporting arms, exiting near the pivot points to pass through radial bore holes to the edge of the sample block. If the wires must run around the block, they are secured with Ge varnish inside a narrow groove which runs along the edge of the block. After the samples have been mounted on the block, the probe is lowered into the cryostat and sealed at the top with an o-ring and screws. The probe sits inside a stainless steel tube 5 cm in diameter, which extends from the top to the bottom of the cryostat, where it is soldered to a double-walled copper sample can 6.2 cm in diameter with an adaptive flange. A copper plate is soldered to the bottom of the inner can

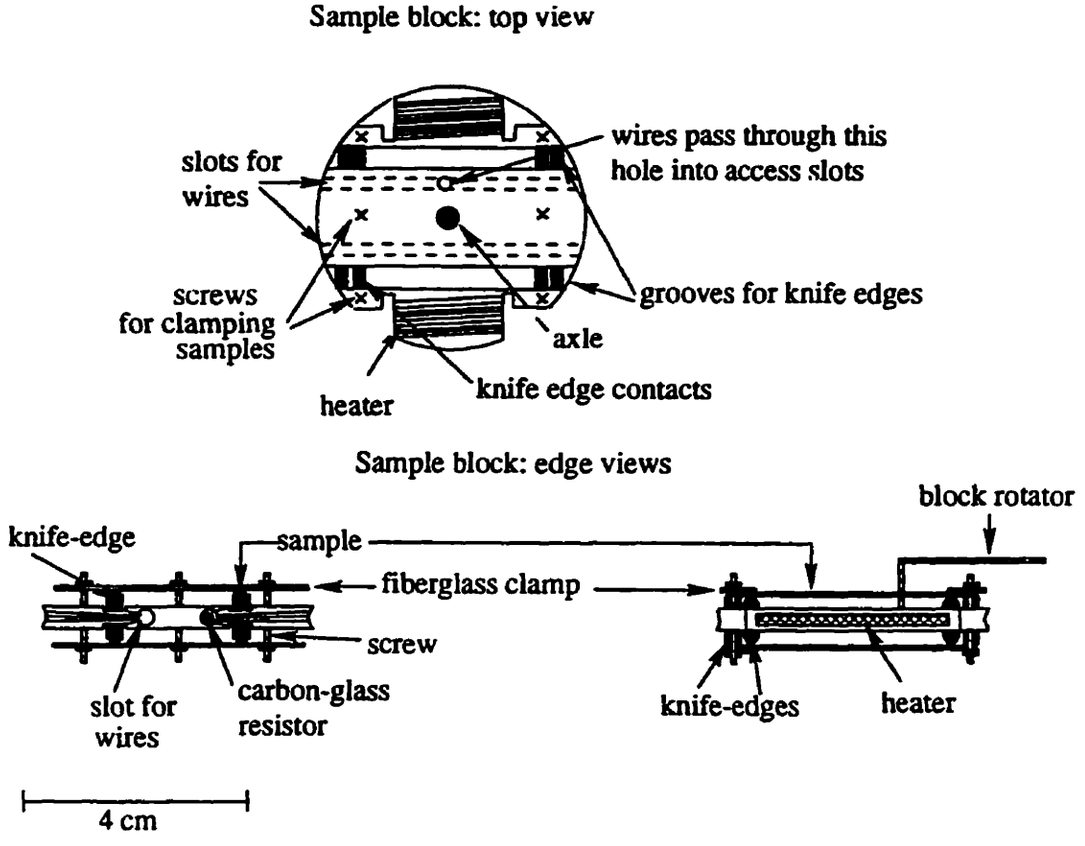

Figure 3.5: Sample block for the SRA system.

to seal it off. The space between the two walls of the can serves as the isolation space: by varying the amount of exchange gas in this space, the thermal contact between the inner can and the cooling liquids can be controlled. For this purpose, a pumping line/He gas inlet is provided with connections to mechanical and diffusion pumps. The sample can is centred in the bore of a superconducting solenoid. The solenoid is 25 cm long with a bore of 6.55 cm, and is capable of providing an axial field of up to 3 Tesla. The magnet is hung from the adaptive flange which is hard soldered to the stainless steel tube immediately above the sample can. A close-up view of this arrangement is shown in figure 3.6. Additional support rods run from this ring to the top of the cryostat. These support rods are made of stainless steel tubing, and have holes drilled in them down their length to allow free circulation when immersed in liquid helium. The solenoid is connected to the power supply through two lead-coated brass tubes, which run from the top of the cryostat to an insulated connector on the lower flange which is connected to the solenoid via insulated wires. The Pb coating becomes superconducting at liquid helium temperatures. These leads also have holes drilled in them to facilitate circulation, and are coupled to the helium return line, so that He_4 boil-off can be used to cool the leads and preserve liquid helium. The persistent switch of the solenoid is connected to an electrical feed-through outside the cryostat by thin (36 gauge), insulated Cu wires which run through one of the support rods for cooling. A number of thin copper plates are soldered to the outside of the stainless steel tube, between the tube and the wall of the helium dewar. These act as radiation shields for heat, but allow free passage of gas through a number of holes. They also act as stabilizers, preventing the system from vibrating inside the dewar. This entire unit sits inside a helium dewar with inner diameter of 10 cm. A port at the top of the cryostat allows a liquid helium transfer tube to be inserted. The transfer tube can be lowered into the system, and mates with a funnel arrangement immediately above the Cu flange. The liquid passes from the funnel through the support ring, directly cooling the solenoid. The top of the cryostat has various pumping lines attached as shown in figure 3.7. The helium dewar is suspended inside a larger liquid nitrogen dewar

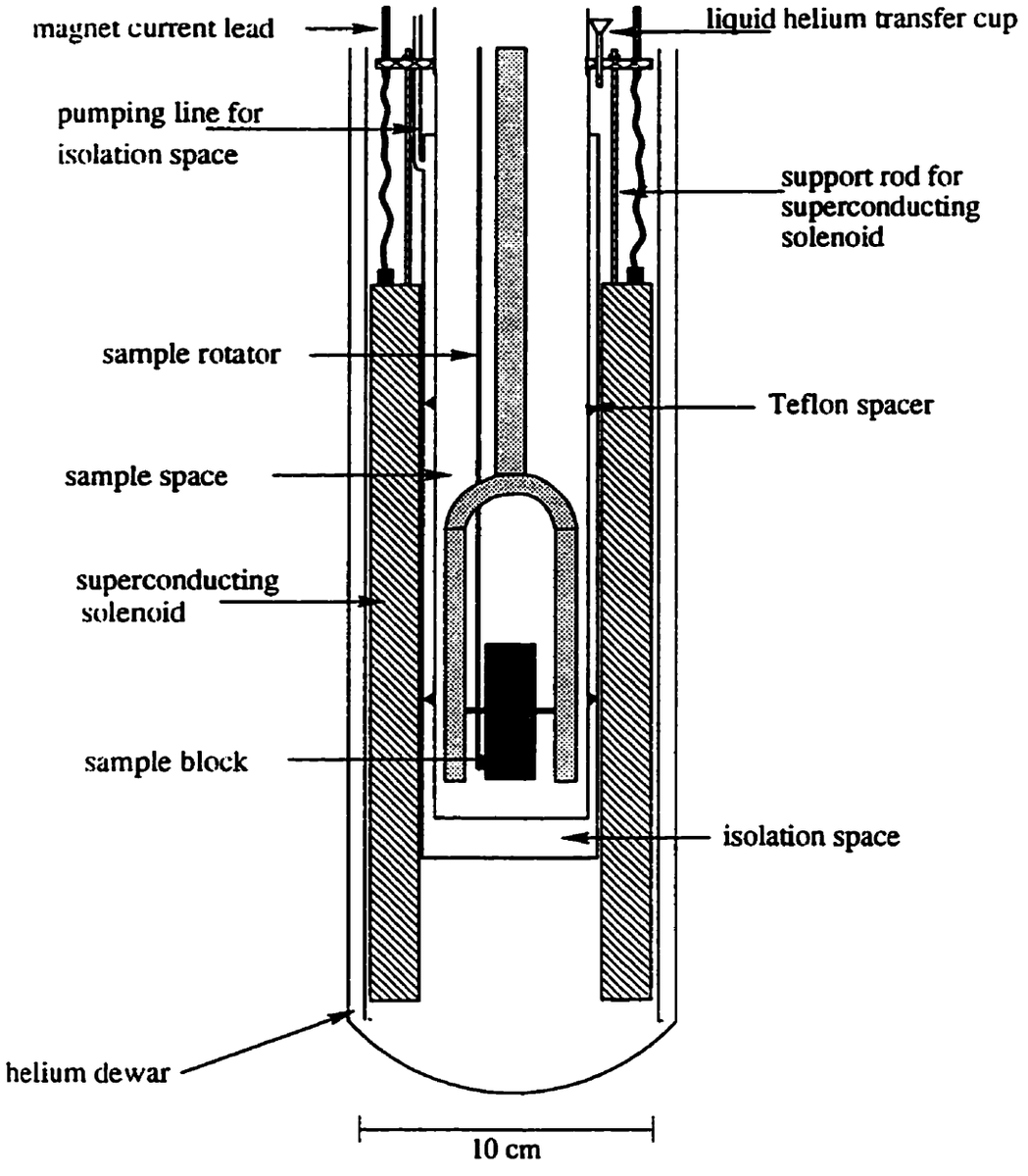

Figure 3.6: Close-up of the SRA cryostat. Scale is as indicated in the figure.

which is supported at the bottom and sides. A Helmholtz pair is positioned around the nitrogen dewar, so as to be centred about the sample block. Its magnetic field is vertical, as is that of the superconducting solenoid. These coils are used to back-off the earth's magnetic field, and to produce small magnetic fields for low field resistive anisotropy (LFRA) measurements. It was calibrated using an F.W. Bell Model 615 Gaussmeter, and was found to provide a field of 41.52 Oe/A to a maximum current of 3 Amps. In LFRA measurements, the sample is rotated from parallel to perpendicular alignments in a fixed field at various temperatures. On rotating the sample block, however, the sample temperature unfortunately changes slightly due to the proximity of the samples with the walls of the inner can when in the perpendicular orientation ($\leq$ 2 mm gap). For temperatures at which $d\rho/dT$ is large, this can cause significant errors in the measured anisotropy. Average anisotropy values are obtained by quickly rotating the samples back and forth and taking several readings. SRA measurements, in which the field is varied with the sample at a fixed temperature in one orientation are not as subject to temperature changes, as the sample is only rotated at one point, after which the temperature is stabilised. In LFRA measurements, however, the anisotropy is measured as a function of temperature, and not field. This means that the temperature is stabilised at some value, and the sample orientation is changed to measure the anisotropy. If the temperature changes while the sample is rotated, this will cause an error in the anisotropy. To improve the LFRA data, we decided to modify another cryostat used previously to measure DC resistivity as a function of temperature by designing and building a Helmholtz pair which can be rotated while the sample block remains fixed. This system is described in some detail below.

3.2.3 Low Field Resistive Anisotropy (LFRA) System

This system (modified by myself and X. Qi), was used for zero field resistivity and LFRA measurements, and operates on the same basic principles as the SRA cryostat, except that the sample block remains fixed and the magnet rotates. The sample block consisted of three layers machined from OFHC copper, each of which

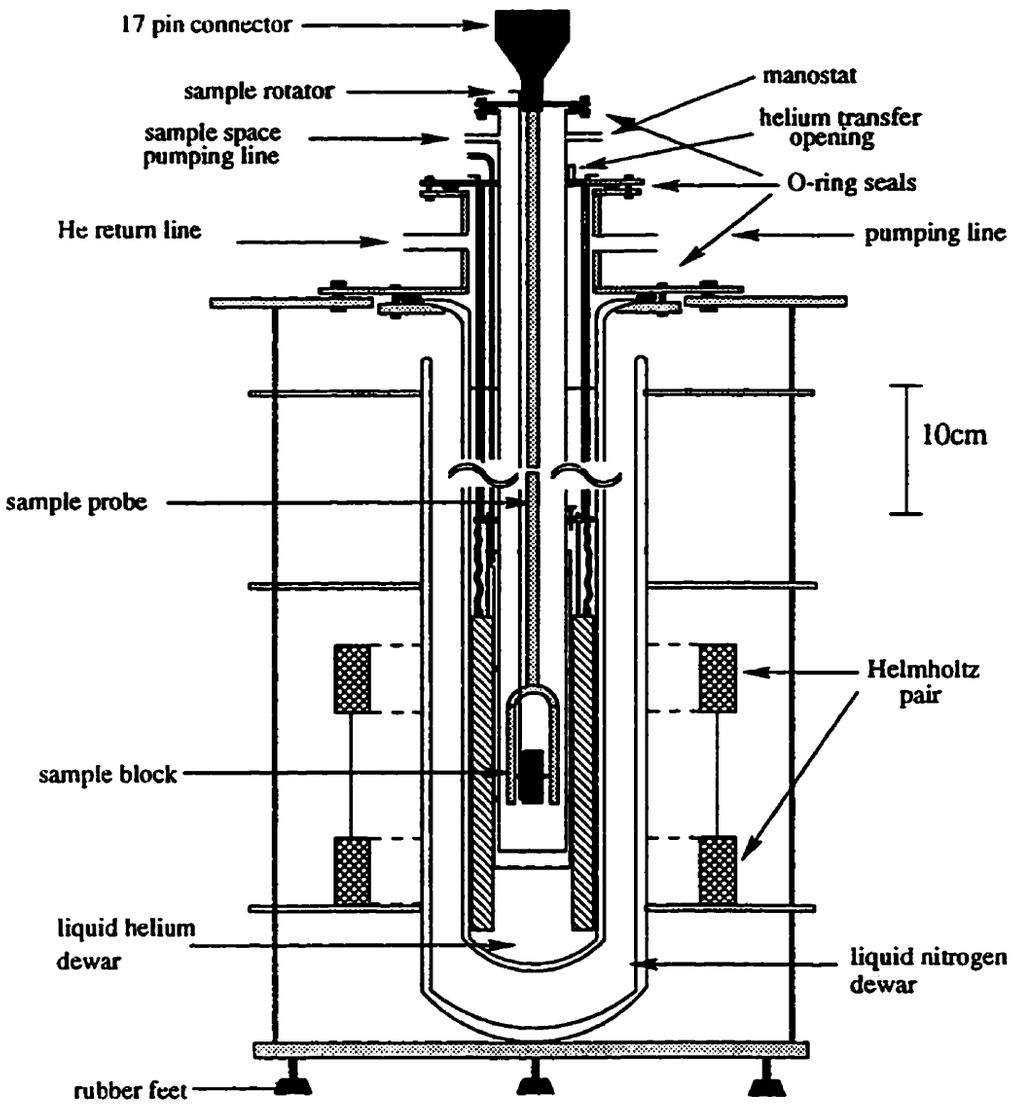

Figure 3.7: SRA cryostat and pumping lines. Scale is as indicated above.

held two samples of the same dimensions as for the SRA cryostat. These six samples were clamped to voltage knife-edges using fibreglass yokes, however the current connections were made by soldering wires to each sample, to connect them in series. The layers were soldered one above the other to a copper support to form the sample block shown in figure 3.8. A heater wire, with room temperature resistance of 500 Ω, was wrapped around this support, but was electrically insulated from it with GE varnish and cigarette paper. Temperature control was achieved using an Allen-Bradley carbon resistor as a sensor in one arm of a Wheatstone bridge circuit, and a reference resistance in the other arm. The carbon resistor was inserted into a slot machined in the central layer of the sample block. The out-of-balance signal from the Wheatstone bridge determined the current supplied to the heater. The temperature could be measured in several ways. A calibrated Lakeshore Cryogenics CG-2000 carbon-glass resistor was embedded in a hole in the sample block as shown. It was in good thermal contact with the samples, and was used over the temperature range from 4–300 K, in conjunction with a gas thermometer (below 4K temperatures were determined from the helium bath vapour pressure. A fixed volume of helium gas was admitted into the gas thermometer bulb, which was directly above the sample block, as shown in figure 3.9, and, aided by exchange gas in the sample space, was thus in good thermal contact with the samples. A change in sample temperature resulted in a change in pressure of the gas in the bulb. The bulb was connected to a Pennwalt pressure gauge by means of a continuous capillary tube, and the temperature in the sample space was then calculated from the pressure, using the ideal gas law with low-order Virial corrections. The temperature was assumed to vary linearly along the length of the tube from the sample temperature to room temperature. The drawback of using a gas thermometer is that measurements are necessarily very slow to allow the pressure to come to equilibrium along the capillary tube. The gas thermometer is also sensitive to variations in atmospheric pressure and room temperature, which must be recorded and corrected for. Measurements below 4.2 K were taken, if possible, on cooling (i.e. on pumping the He bath), since equilibrium between the bath temperature and the vapour pressure are more

easily maintained. The temperature was calculated from the vapour pressure of the helium bath, which was measured using a Datametrics Type 590 Barocell.

The sample block was suspended by three thin-walled stainless steel tubes from a supporting frame. One of the support tubes served both as a pumping line for this sample chamber and as an access port for the wires. Thirty-four wires of 36 gauge copper were inserted in a fibreglass sheath, and passed through the pumping line. A few inches above the sample block, these wires were wrapped around a large, OFHC copper thermal anchor, and secured with GE varnish. The wires then passed back through the pumping line into the sample can. Here they were wrapped around the gas thermometer bulb and then around anchor pegs on the block. The appropriate number of wires were fed through fibreglass sleeves down each side of the Cu block, exiting at the desired layer. Wires which ran along the edges of the block were fastened down with GE varnish to prevent breakage or potential grounding problems. A few spare wires were run down the side and taped to the bottom of the block. At the top of the cryostat, the sample space pumping line branches; one arm goes to the pumping system, the other separates into three feedthroughs through which the wires were passed. These feedthroughs were stainless steel disks with 12 holes drilled through each. A wire was passed through each hole, and the hole sealed with epoxy. The feedthroughs into the pumping line were sealed with an o-ring and coupling. Outside the cryostat, the wires were fed through protective plastic tubing into a box where the necessary electrical connections were made.

To provide thermal stability, a sample can was sealed around the block using an indium o-ring, after which a second can, concentric with the sample can, was sealed to an upper support using Wood's metal. The isolation space inside this second can was pumped through the central support pipe, providing a method of controlling the thermal contact between the sample space and the bath. The gas thermometer line runs through the center of the central support pipe and continues unbroken to the gauge. The third support tube is a guide for the liquid helium transfer tube (through the radiation shields) and ends in a funnel, allowing the efficient transfer of helium to the bottom of the cryostat. A liquid helium dewar

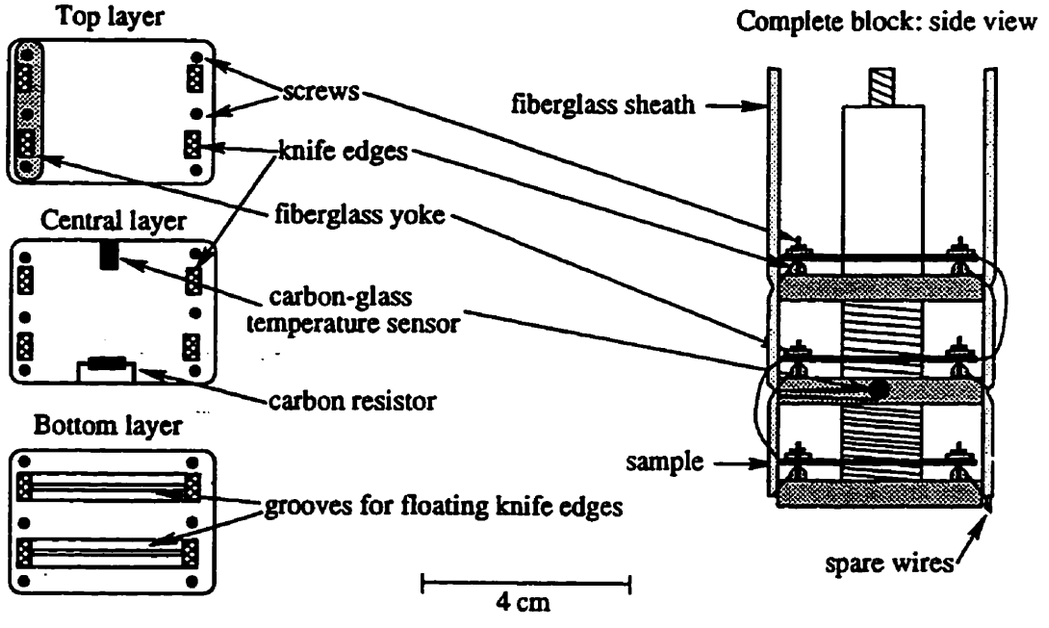

Figure 3.8: Sample block for the LFRA system.

was then raised around these cans, and sealed to the top of the supporting plate with an o-ring seal. A nitrogen dewar was suspended from a board attached to the upper frame. The bottom of this dewar was supported by a cart which carries the Helmholtz pair and its power supply. The Helmholtz pair has a radius of 20 cm and coil separation of 20.5 cm and was positioned so the sample block is centred in the magnet. The magnet produces a maximum field of 130 Oe, and has a calibration factor of 13.1 Oe/A as determined using an F.W. Bell Gaussmeter. The coils were mounted vertically on a disk supported by 23 half inch ball bearings which allow the magnet to rotate through 360°, to align exactly with the sample direction. This system is thus more flexible than the SRA system, as it permits correction for sample misalignment.

The LFRA cryostat allows accurate measurements of resistivity in zero field and in fixed fields of up to 130 Oersteds. Although the previous (SRA) system is also capable of measuring the zero field resistivity, it is more difficult to obtain a wide range of temperatures due to the large heat sink provided by the superconducting solenoid. Any temperature from 1.5 to 300 K can easily be obtained in the LFRA system, and warming and cooling rates are easy to maintain.

3.2.4 High Field Magnetoresistance System

If the magnetoresistance does not saturate in the maximum applied field of 3 Tesla available in the SRA system, it is necessary to use the high field magnetoresistance system, which has a superconducting solenoid capable of producing fields of up to 10 T. This system has been described in detail previously [63]. Temperature was controlled as described for the LFRA system above, and measured using a gas thermometer, whose bulb lies in direct contact with the sample can. The cryostat arrangement is shown in figure 3.10.

This system was used in both the longitudinal (field parallel to current) and transverse mode in this study. Due to the narrow bore of the magnet, the samples measured in the transverse mode must be less than half the length of our normal samples. After longitudinal measurements were complete, the samples were cut to

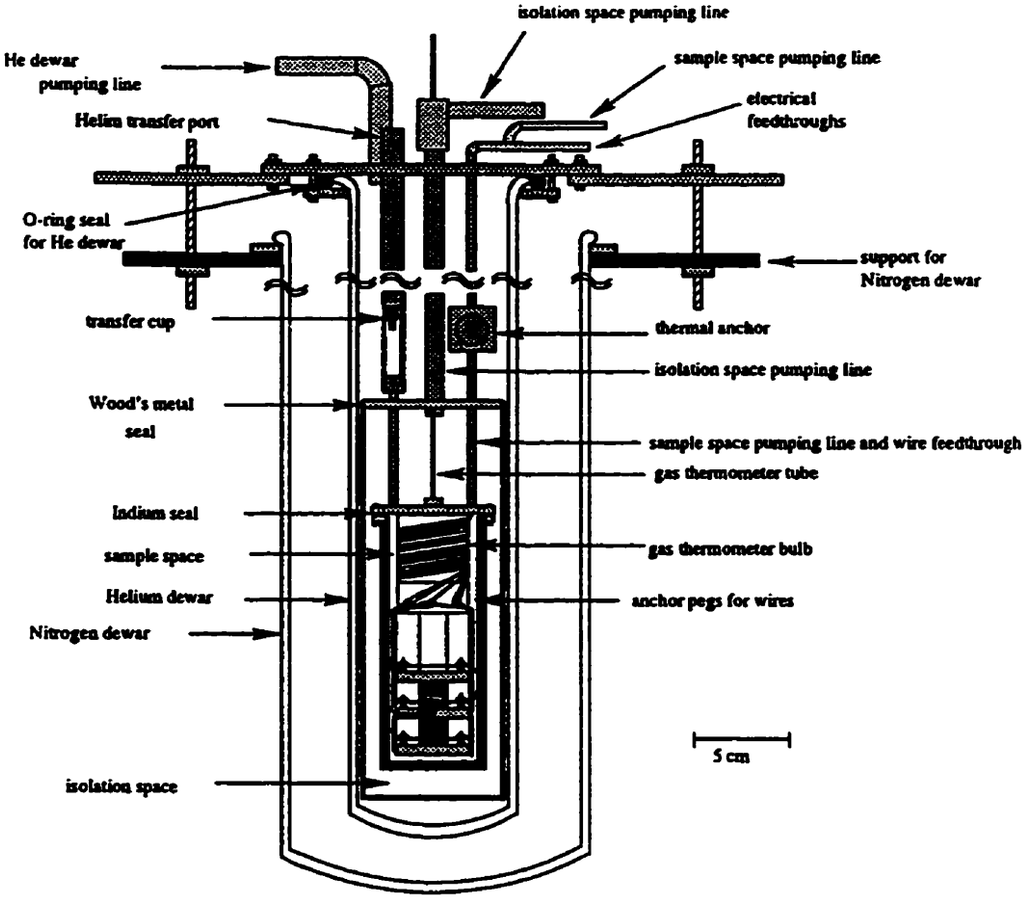

Figure 3.9: Cryostat for the LFRA system.

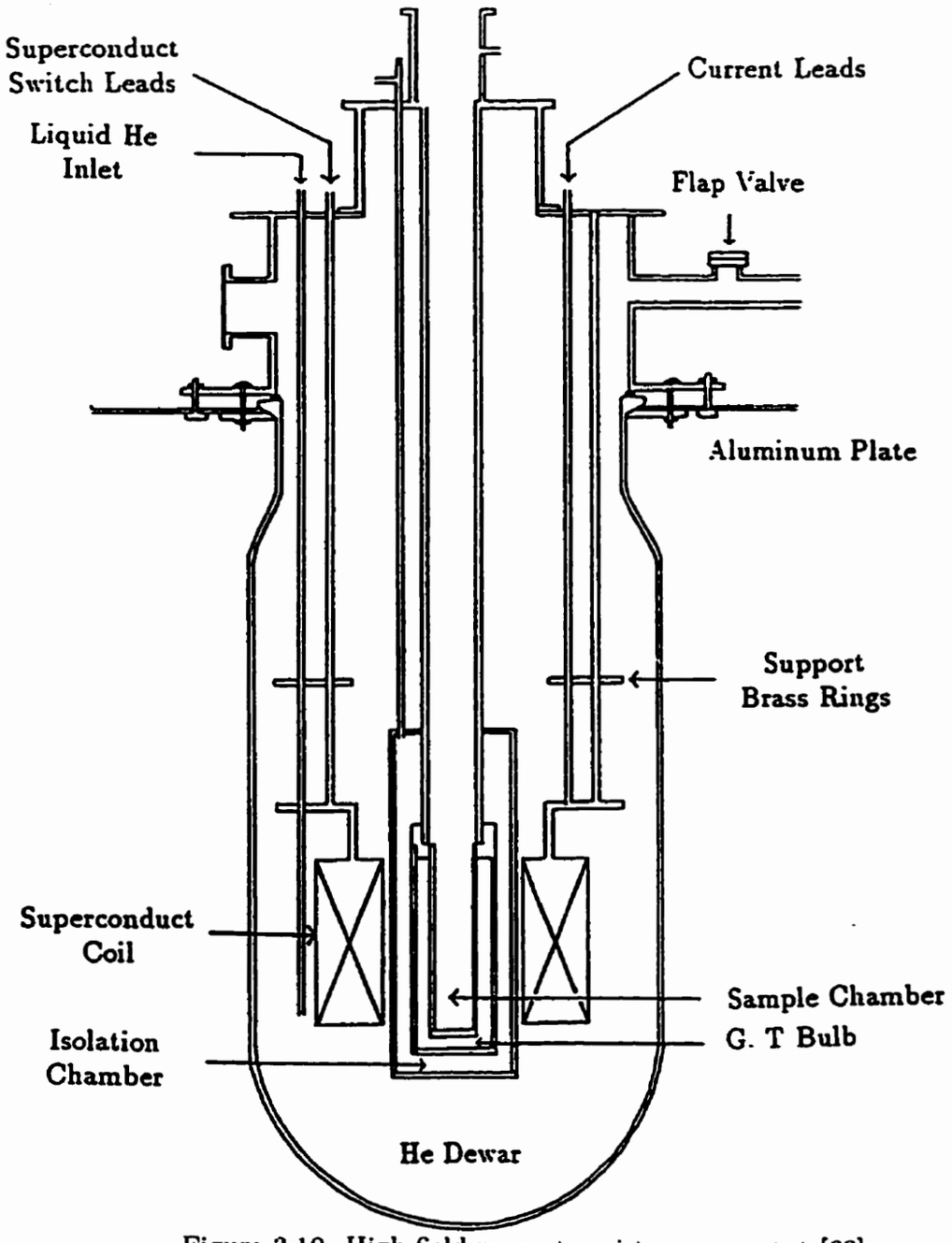

Figure 3.10: High field magnetoresistance cryostat [63].

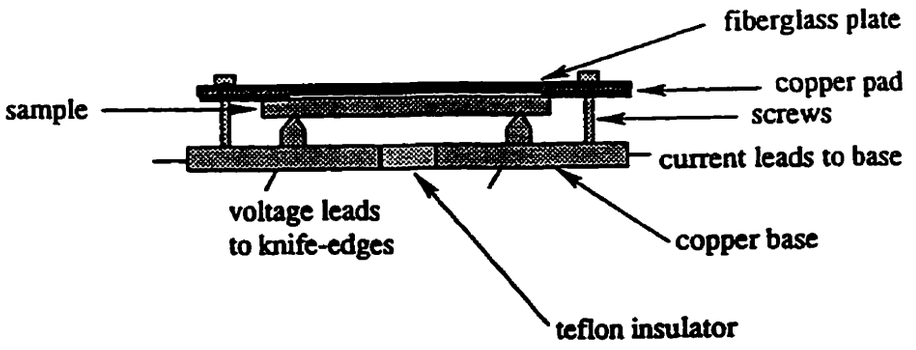

Figure 3.11: Sample mount for the high field magnetoresistance system.

the appropriate lengths for the transverse probe. In this system, the samples were again clamped to a set of voltage contacts, with current connections made by wires soldered to the ends of the samples. Pieces of indium were placed on the voltage knife-edges to maintain good contacts: a common problem in the case of brittle, non-malleable samples which can not be clamped tightly was that the contacts opened on cooling. A number of the samples measured were very short, since they were cut from brittle materials which could not be rolled or cast successfully, or were pieces obtained originally for susceptibility measurements. New sample holders compatible with the longitudinal sample probe were designed (by Dr. X.Z. Zhou) for these shorter samples. In these new sample holders the voltage knife-edges are mounted on two small pieces of Cu. The knife-edges are insulated from the Cu plates using cigarette paper and GE varnish. The copper plates are separated by a piece of mylar of the appropriate length for the sample length. These three bottom pieces are glued together with GE varnish. Printed circuit connections on a fibreglass plate clamp down on top of the sample to provide current to the sample. This printed circuit was made by etching a printed circuit board using a $FeCl_3$ solution. The current leads are soldered to each side of the lower Cu plate. The lower plate is electrically connected to the upper plate/circuit board by the screws which hold the two together, as shown in figure 3.11. Contacts are improved with small amounts of indium on the knife-edges.

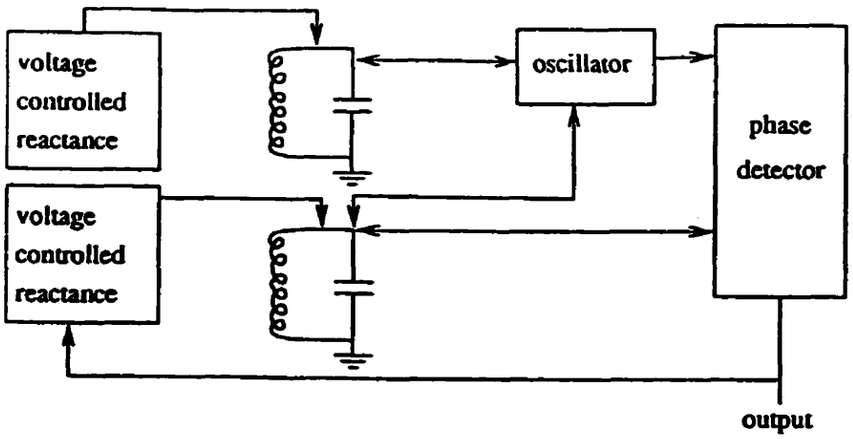

Figure 3.12: Block diagram of the *ac* susceptometer[63]

3.3 Magnetic Susceptibility Measurement

3.3.1 Susceptometer

In this study the real part of the *ac* susceptibility, $\chi = \frac{dM}{dH}$ was measured using a phase-locked magnetometer [68]. A block diagram of this device is shown in figure 3.12. The system contains two matched LC oscillators. An *ac* signal is supplied to the oscillators, producing a magnetic field in the coils, typically 50 mOe rms or less, at a frequency of 2.4 kHz. The sample is placed in the coil of one of these oscillators, causing a change in the inductance of the coil. The signals of the two oscillators are compared by a phase detector, which produces an output voltage proportional to the relative shift in the signals' phase. This signal is amplified and fed back to the sample coil through a voltage controlled reactance which controls the frequency of the oscillator. This correction signal, which is proportional to the sample's susceptibility, is the output of the susceptometer. A detailed circuit diagram is shown in Fig 3.13. The details of this system have been described previously [69]. The coils were maintained at liquid nitrogen temperatures during measurement to provide stability.

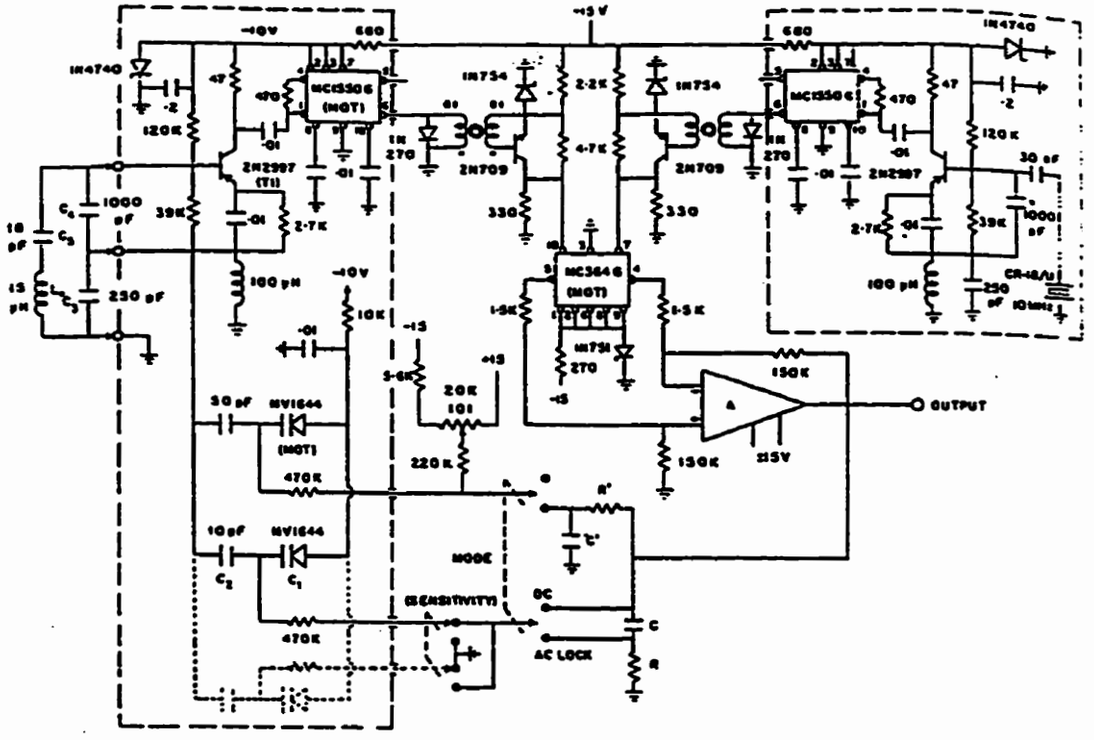

Figure 3.13: Detailed circuit diagram for the *ac* susceptometer [68].

3.3.2 AC Susceptibility Cryostat

In this system[69], the oscillator coils are mounted around the narrow tail of a liquid helium dewar. Concentric with these solenoids are another two coils with calibration factors of 215 Oe/A and 196 Oe/A which can be used individually or in series to provide *dc* biasing fields of up to 1000 Oe. The sample block and cryostat are as shown in figure 3.14. The sample was placed in a bundle of copper wires soldered to the tip of a machined OFHC Cu block. The copper braid provides good thermal contact between the sample and the temperature sensors, while allowing penetration of the *ac* driving field. A germanium resistor and a Au+0.03% Fe-chromel thermocouple are also inserted into this braid slightly above the sample. A distance of several centimetres was maintained between the sample and the thermocouple, since the thermocouple could give a slight contribution to the magnetic susceptibility. Temperatures below 30K were measured using the calibrated germanium resistor, and above 30 K using the thermocouple.

The Cu braid extends through both pick-up coils, and the sample was placed in the braid so as to be centered in the upper oscillator coil. After the probe was inserted into the susceptometer, the sample position was optimized by means of a screw, which raised and lowered the sample rod until the signal was maximized. A nichrome heater wound around the block provides warming power to the system. The sensor and heater wires pass through the rod onto which the block is soldered, and connect to the exterrnal circuit at a feedthrough attached to the top of the rod. A liquid nitrogen dewar mounted around the helium dewar was used to provide thermal isolation and cooling for the coils.

Two types of measurements were taken using this equipment. One was the temperature dependence of the susceptibility in fixed applied magnetic fields; the second was the field dependence of the susceptibility at a fixed temperature. The routine followed for the temperature sweeps was to cool the specimen from above its critical temperature in zero field. A specially designed constant current supply was used with the 215 Oe/A solenoid, to back off the vertical component of the Earth's

magnetic field while cooling. Then, a constant biasing field was applied with the same solenoid, and the sample was warmed slowly to above T_c. A second solenoid could connected in series to the first, to provide a total calibration of 401 Oe/A. The susceptometer output and the temperature sensor reading were measured on two HP3400A DMM's, which are GPIB accessible. The data was recorded by computer, and subsequently analyzed. A warming rate of 0.01–0.3 K/min was maintained, depending on the temperature range measured, with the lower rate corresponding to lower temperature ranges. Since the thermocouple was some distance from the sample, slight temperature gradients could occur. This was especially true at high temperatures, at which large heater currents had to be used. This could result in the temperatures for different biasing fields being shifted marginally from each other. In general, out of 30 or so temperature sweeps measured, 2 or 3 were shifted from the rest. The high temperature ($T \gg T_c$) paramagnetic region of all curves should overlap (since the biasing fields are so low), so these curves were corrected by introducing small temperature shifts.

For the measurement of hysteresis loops, the sample temperature was stabilised. Then, a saw-tooth function was generated by a Stanford Research Systems Model DS335 function generator, and amplified with a HP6824A *dc* power supply amplifier to a maximum current of 1A. This signal was used to drive the solenoids, thus applying a magnetic field which increased and then decreased, driving the sample around a hysteresis loop. Normally we were are uninterested in the virgin curve for these materials, so we drove the sample around at least one full loop to set the initial state before beginning data acquisition. The current through the solenoid was measured across a 1 Ω standard resistor by a HP3400A DMM and data was collected by computer.

3.3.3 Corrections to Susceptibility Data

Zero Correction

The susceptometer measures only changes in the signal and not the absolute value of the signal itself. It was thus necessary to take zero readings during the sweeps.

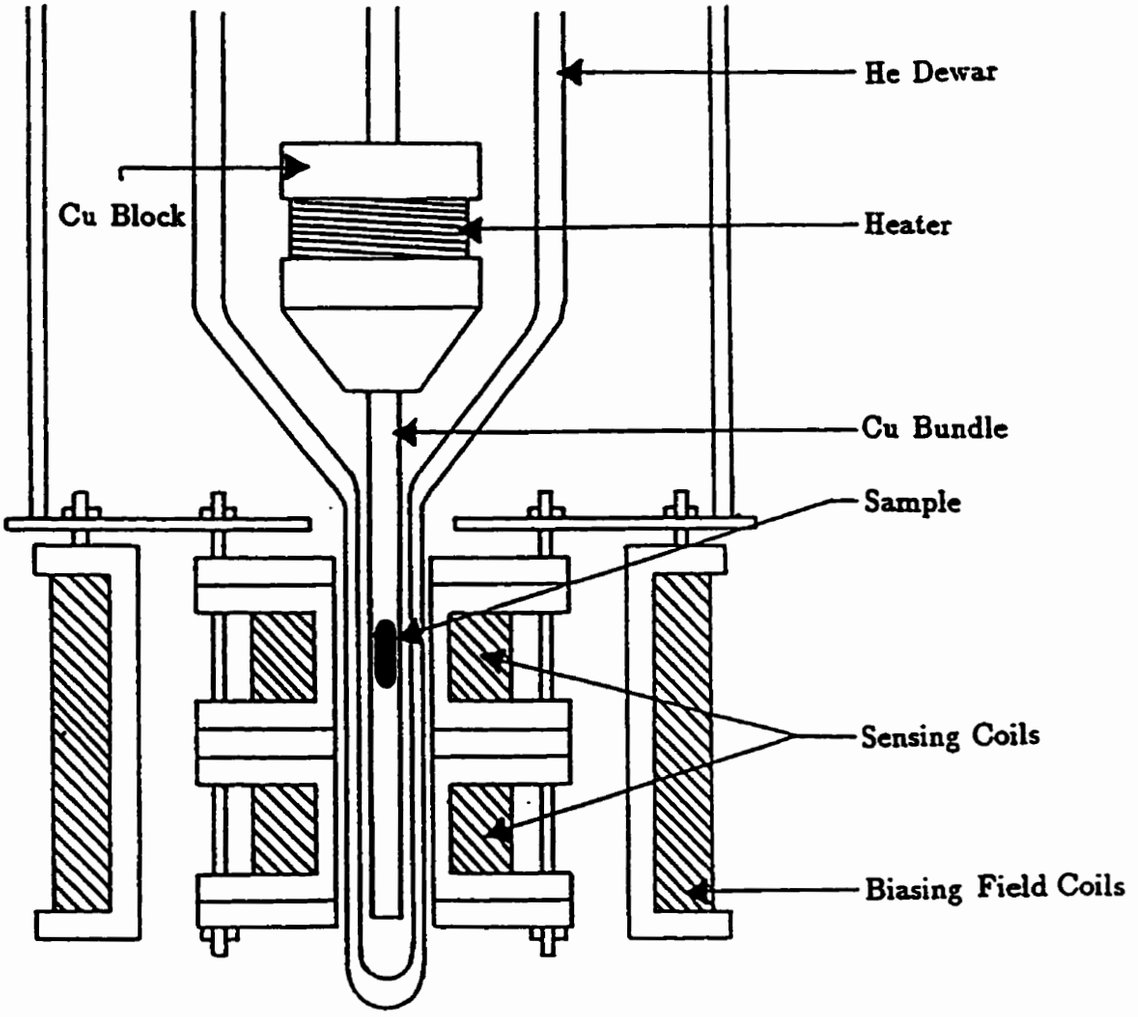

Figure 3.14: The cryostat and sample arrangement for the *ac* susceptometer [69].

A zero reading was obtained by withdrawing the sample from the top pick-up coil such that the Cu braid alone remained in the coils. The zero reading drifted significantly during measurement of small signals, and it was then necessary to take more zero readings (as often as every degree). A linear interpolation was done between sequential zeros to provide a continuous zero reference.

Background Correction

A small background contribution is present in all readings, due to magnetic contributions from the copper braid, temperature sensors and sample block. In order to correct for this background, which is a significant contribution to small signals, a background measurement was taken with the sample removed, over the entire temperature range studied. Zero readings were taken again with the sample rod extracted the same distance as previously. This background was then subtracted from the measured voltage before any conversions are done.

Calibration

To obtain the true susceptibility, it was necessary to calibrate the susceptometer, since the output of the susceptometer is merely a voltage signal proportional to the susceptibility of the sample. The simplest calibration method is to measure a material with a well-known susceptibility and find the correct conversion factor. In this case, the susceptometer was calibrated using 99.999% pure Gd_2O_3 powder. The powder was packed into tubes of varying radius and length, and the susceptometer output was recorded with the sample at liquid nitrogen temperature (77K). The actual susceptibility (in emu/g-Oe) could then be calculated using the Curie-Weiss law,

$$\chi = \frac{N\mu_{eff}^2}{3k_B(T-\theta)} \tag{3.2}$$

where N is the number of Gd atoms per gram, μ_{eff}=(7.70±0.04)μ_B, and $\theta = -13$K for antiferromagnetic Gd_2O_3 [70]. The measured signal depends on the mass of the

specimen measured, i.e.

$$\chi = \frac{cV}{m} \tag{3.3}$$

where V is the susceptometer output in volts, and c is the appropriate calibration factor. It was found that changes in the radius of the sample had little effect on the calibration factor, but that changes in the length of the sample, L, generated a linear relationship between c and L, such that[71]

$$\text{c=(0.16 emu/V-Oe-mm)L +4.5 emu/V-Oe}$$

This calibration factor determines the absolute susceptibility to an accuracy of ± 5%, however relative susceptibility values can be measured to approximately 1 part in 10^4.

Demagnetisation Correction

The measured susceptibility, χ_m, after calibration is

$$\chi_m = \frac{dM}{dH_a}, \tag{3.4}$$

however the true susceptibility is defined as

$$\chi_t = \frac{dM}{dH_i} \tag{3.5}$$

where H_i is the internal field of the specimen. The internal field can be derived from the external field, by the following expression,

$$H_i = H_a - NM \tag{3.6}$$

where N is the demagnetisation factor for the sample. The true susceptibility can be calculated from the measured susceptibility using the chain rule and equation 3.6, leading to

$$\chi_t = \frac{\chi_m}{1 - N\chi_m} \tag{3.7}$$

The demagnetisation factor for the specimen was estimated by approximating the sample by an ellipsoid whose axes are given by the sample dimensions. This approximation is somewhat crude, but is expected to give an upper limit for the demagnetisation factor[18]. The volume demagnetisation factors, in cm^3/emu, were

calculated numerically using the appropriate elliptic integrals[72], and were converted to mass demagnetisation by multiplying by the density of the sample. This then gave the true susceptibility in units of emu/g-Oe, which is independent of sample size. The demagnetisation factor was also used to calculate the internal field from (3.6), with the magnetisation calculated by numerically integrating the susceptibility as a function of field at a fixed temperature.

As can be seen from equation 3.7, the true susceptibility diverges as the measured susceptibility approaches the demagnetizing limit, $\chi_m = 1/N$. For small N, this requires large changes in magnetisation in response to the driving field. Strong local anisotropies can inhibit the rapid variation of M, leading to a true susceptibility value which does not diverge at T_c. DC susceptibility measurements are often demagnetisation limited, providing a method of estimating the demagnetizing factor of the sample.

3.4 Magnetisation Measurements

Magnetisation measurements were done by Dr. Gwyn Williams at Michigan State University using two commercial SQUID-based magnetometers (Quantum Design MPMS-2, MPMS-5). The MPMS-2 cryostat can only perform *dc* magnetisation measurements, while the MPMS-5 system can also be used for *ac* susceptibility measurements. In the *dc* measurements, the sample was pulled through three counter-wound measuring coils in the presence of a static magnetic field. In the *ac* measurements, the sample was located in the plane of one of the pickup coils, and a small tickling field was applied. This system measures not only the component of the susceptibility which is in phase with the tickling field, but also the out-of-phase component, which is a measure of energy losses in the sample. The home-built susceptometer described in section 3.3 is only capable of measuring the in-phase (real) susceptibility. Susceptibility measurements in the MPMS systems can be performed in a number of driving fields and frequencies.

The static applied field is variable from 0.1T (MPMS-2) and 0–5.5T (MPMS-5),

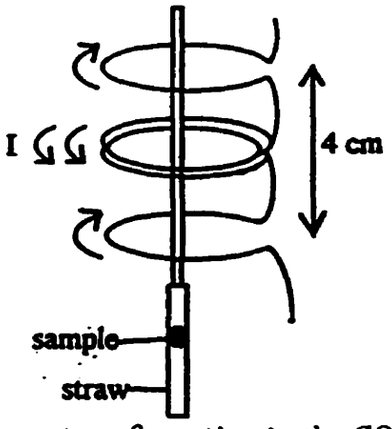

Figure 3.15: Measurement configuration in the SQUID magnetometer[73].

with residual fields of 5–7 Gauss and less than 0.1 Gauss respectively. Measurements were performed at temperatures ranging from 2K up to around 200K. Prior to each run, the sample was warmed above T_c, and then cooled to the next measuring temperature in zero field to ensure a consistent magnetic ground state and thus history independence. Measurements of magnetisation and susceptibility were done both as a function of temperature at a fixed field, and as a function of field at a fixed temperature. The measurement configuration is shown in figure 3.15[73]. The sample is mounted in a plastic straw secured to the brass tip of a hollow stainless steel sample rod. The straw is sewn through with cotton thread, so that the sample is vertical and centred in the plane of the pick-up coils. The top of the sample rod is attached to a stepping motor which moves the sample vertically during the measurement procedure. Before beginning measurements, the sample height was optimised automatically to provide the maximum signal. For *dc* measurements a 64-step, 4 cm scan was adopted. A smaller number of steps resulted in a decreased magnetisation measurement in samples with large magnetisation. This decrease was likely due to the SQUID unlocking when the slew rate of the signal is so large.

Chapter 4

Spin-Orbit Coupling in Bond-Disordered Systems

4.1 Review

As discussed previously, bond-disordered systems often exhibit strikingly different behaviour from ordered crystalline materials. Dilute and amorphous alloys are two distinct systems which exhibit bond disorder. In dilute alloys, bond disorder is caused by the addition of small amounts of magnetic impurities randomly distributed throughout the crystal lattice sites of a non-magnetic host. The exchange mechanism is generally of indirect RKKY nature, with sign and magnitude which vary with moment separation. A given moment thus feels different, often conflicting, effects from the other moments present. In some cases, this frustration leads to the formation of a spin-glass state,freezing the moments in random directions[74]. Amorphous materials are formed by the rapid cooling of a molten alloy, such that the liquid freezes into a random, non-crystalline arrangement of atoms. The moments feel random exchange fields based on their separation from other moments. A brief summary of experimental results on disordered systems is given below. More detailed discussions can be found in a number of reviews[41, 75, 76, 77]

Amorphous Alloys

Due to the presence of both chemical and structural disorder in amorphous systems, magnetic moments feel not only the influence of exchange disorder, but disordered electric fields as well[75]. In these systems, magnetic ordering will occur only when the exchange interaction between moments is large enough to overcome the strong random local anisotropies. Ferromagnetic ordering is common in transition metal-based systems, while rare earth-based systems often exhibit more complex ordering, such as ferrimagnetic and canted magnetic structures, due to their stronger anisotropies[75]. This review is limited to ferromagnetic transition metal-based amorphous alloys, with general formula T_xM_{1-x}, with T=Fe, Ni, Co and M=a metal, the type examined in this study.

T_xM_{1-x} alloys are non-magnetic up to some critical concentration, x_c, above which the system has a low-temperature ferromagnetic ground state. In general, x_c is lowest in Co-based alloys and is largest in Ni-based systems, implying that the Co-based systems are more strongly magnetic than the others. Band structure studies show that the Fe *d*-band is more strongly hybridised with the M(*sp*)-bands than the Co *d*-band, causing Fe to be more sensitive to changes in the moment separation. Small changes in separation can thus produce antiferromagnetic rather than ferromagnetic exchange[75]. As a result Fe-based alloys are weaker ferromagnets, with lower moment values than the corresponding Co alloy with the same solute concentration. As well, as the Fe concentration increases above x_c, the moment increases initially, but then decreases again. In this decreasing region, the broad distribution of Fe-Fe exchange-bonds leads to frustration which can result in a spin-glass state at low temperatures. In amorphous FeZr[78], for example, as well as in Y-Fe[75], the spin components perpendicular to an applied field freeze in random directions, leaving only longitudinal spin ordering.

The temperature dependence of the magnetisation is a good indication of the exchange coupling strength. Plotted as a function of reduced temperature, the spontaneous magnetisation of an amorphous alloy falls below that of a crystalline

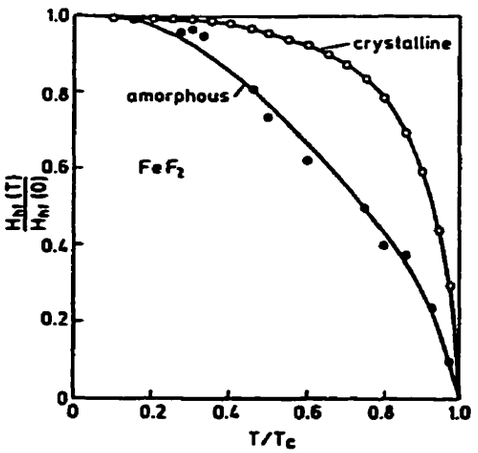

Figure 4.1: A comparison of the hyperfine fields in amorphous and crystalline FeF_2 [75]

alloy of the same composition, due to the presence of exchange disorder. This behaviour is shown in figure 4.1 for FeF_2. The critical temperature, T_c, depends strongly on the exchange disorder as well as the spin value of the transition metal. In general, fluctuations in exchange will increase T_c, as long as the coupling remains ferromagnetic. Thus, Co-based amorphous systems have higher critical temperatures than their crystalline counterparts, while Fe-based alloys, in which exchange fluctuations induce antiferromagnetic coupling, show a decrease in T_c as compared to crystalline alloys of the same concentration[75]. In both systems, however, T_c decreases monotonically as the solute concentration increases.

The critical exponents of a system are based on experimentally measured macroscopic properties. Any differences found between the exponents of crystalline and amorphous systems will be caused by the local exchange fluctuations. In general, however, crystalline and amorphous systems have the same asymptotic exponents[75], consistent with the Harris criterion [79], which states that local disorder should have no effect on the critical exponents, as long as the specific heat exponent, α, is negative. The unimportance of the local exchange fluctuations can be rationalised by considering the critical state of the system. Near T_c, the critical fluctuations are long-range, making the local fluctuations in the system insignificant. The effects of

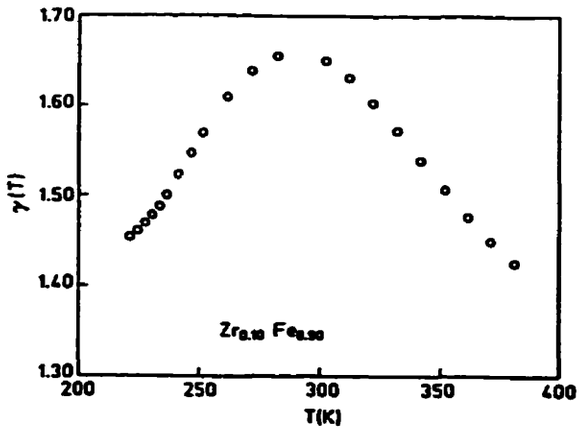

Figure 4.2: The effective susceptibility exponent, $\gamma^*(t)$, in FeZr [76]

disorder can be seen, however, in the Kouvel-Fischer effective susceptibility exponent, $\gamma^*(T) = -d\ln\chi/d\ln t$, which, plotted as a function of temperature, exhibits a non-monotonic behaviour, as shown in figure 4.2 for FeZr. The peak observed in this exponent has been noted in a number of disordered systems[80], and indicates that as one moves away from the critical point, the effective exponents change in value as a result of disorder.

Due to the lack of crystalline order, amorphous systems have very high residual resistivities, which are relatively temperature independent. This disorder also results in a highly isotropic zero field resistivity. The magnitude and sign of the isotropic (average) magnetoresistance, $\rho(H) = \frac{1}{3}\rho_{\parallel}(H) + \frac{2}{3}\rho_{\perp}(H)$, is strongly dependent on the system under study. In general, the anisotropy in the magnetoresistance is very small, and is due to the presence of spin-orbit coupling in the system. The spontaneous Hall effect, which is a measure of asymmetric scattering from the local moments, is found to be proportional to ρ^2 in these systems, indicating that the dominant scattering mechanism present is side-jump scattering[41]. The normal contribution to the Hall effect is much smaller than the spontaneous Hall effect, since the Lorentz force has little effect in a system with a short electron mean free path.

Magnetocrystalline anisotropies are low in T-M systems, and are generally only

observed in systems in which small amounts of short-range order exist [75]. Properties such as magnetostriction and coercivity are strongly dependent on anisotropies and local strains. A large positive magnetostriction is found in Fe-based systems whereas in Co-based alloys it is small and negative, again accentuating the sensitivity of the iron moments to small changes in environment. The coercive force and the transition temperature have been found to be strongly dependent on sample preparation techniques, and thus can not easily be compared from one system to another.

This review shows that a number of material properties are affected by changes in the bond-disorder of an alloy. Presumably then, measurement of such a property in samples prepared under slightly different conditions, or with slightly different concentration, should be capable of characterizing the change in disorder. In this study, we will attempt to show that the resistive anisotropy is an extremely sensitive probe of bond-disorder by measurements of amorphous H-doped FeZr samples.

Dilute Alloys

The dilute materials of interest in this study belong to a class of materials in which the impurity moments are close enough to interact, either through indirect RKKY exchange or through direct magnetic exchange. Indirect exchange often leads to spin-glass states at low temperature, due to the conflicting exchange interactions felt by the randomly-spaced moments. This is typical in noble metal matrices with $<$ 10 at.% magnetic impurities. If the matrix is 'nearly magnetic' such as Pd and, to a lesser extent, Pt, the presence of a local moment can cause polarisation of the matrix conduction band in the vicinity of the moment, resulting in a 'giant moment' system, with moments much larger in magnitude than that of the bare impurity. These giant moments are spread out in polarisation clouds which encompass many atoms, and therefore begin to interact directly at a low impurity concentration. As the impurity concentration is increased above the 'percolation limit', the concentration at which an unbroken near-neighbour chain of magnetic moments exists throughout the medium, a magnetically ordered, if somewhat inhomogeneous ground state is

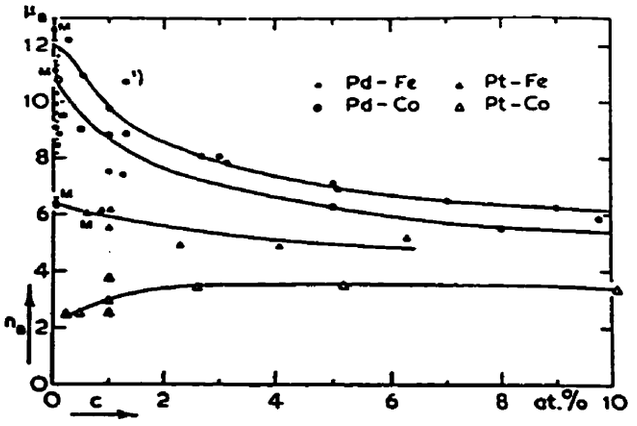

Figure 4.3: Magnetic moment (in μ_B) of some giant moment systems, from [77].

created[77]. The remainder of this review will concentrate on the properties of the giant moment systems based on Pd and Pt, which were investigated in this study.

Pd and Pt-based alloys with Fe, Ni and Co impurities have ferromagnetic ground states above a certain critical impurity concentration. Since Pt is not as strongly exchange-enhanced as Pd[41], the Pt-based alloys have smaller moments, and require a minimum solute concentration of $\sim$1 at.% in order to achieve ferromagnetic ordering. Ni, which does not exhibit a moment in isolation, requires a critical concentration of $\sim$2 at.% in Pd and $\sim$42 at.% in Pt to form a ferromagnetic ground state[41]. Mn impurities (with antiferromagnetic direct exchange), induce a spin-glass ground state in both hosts, except at very low concentrations in Pd, where it is weakly ferromagnetic[81]. Figure 4.3 compares the magnetic moment as a function of impurity concentration in a number of giant moment systems [77]. The average moment per impurity decreases at high impurity concentration due to overlap of the polarisation clouds.

The transition to the ferromagnetic state can be gradual due to the distribution of exchange coupling in these systems. The specific heat in the giant moment systems exhibits an anomaly at the critical temperature[75]. The change in magnetic specific heat, ΔC, has a gradual, wedge-shaped peak, which, with the application of a magnetic field, moves to higher temperature. At low concentration, the critical

temperature is found to be proportional to the concentration, but this dependence levels off at higher concentration, due to the decrease in average moment[41, 77].

The resistivity in these giant moment systems is generally larger than in noble metal systems, due to a combination of additional (s to d) scattering channels and enhanced coupling to local moments. As the temperature is decreased through T_c in giant moment systems, a sharp change in slope of the $\rho(T)$ curve is observed, in agreement with the prediction of section 2.2.2. This causes a peak in the $d\rho/dT$ vs T curve, which has the same behaviour as the specific heat anomaly, as predicted by Fisher and Langer[37]. An applied magnetic field induces a negative isotropic magnetoresistance in all but the systems with Ni impurities[41]. The SRA, however, is non-zero for Fe, Co, and Ni systems, indicating the presence of spin-orbit coupling at the impurity sites. Measurements of the Hall angle, related to the ratio of the spontaneous and normal Hall voltages, support the conclusions of SRA measurements. The Hall angle is zero in dilute PdFe, indicating the absence of an orbital moment at the Fe sites, but is non-zero for PdCo, PdNi, PtCo and PtFe[41].

Mössbauer studies of the various giant moment systems indicate that the giant moments persist into the paramagnetic regime. The measured hyperfine field has a positive contribution in PdCo and PdNi, again due to the presence of an orbital moment[77]. Diffuse neutron scattering experiments have shown that the matrix around the impurity is indeed polarised, up to a distance of $\sim$ 10 Å from the impurity, creating a local moment of up to $12\mu_B$ although the bare impurity moment has a magnitude of only 3–4 μ_B[76].

The presence of spin-orbit coupling in these dilute alloy systems, suggests that measurements of the resistive anisotropy are also possible in these systems. By comparing magnetic and transport measurements in these systems to those of the amorphous FeZr system, it may be possible to obtain some information about the dependence of these systems on bond-disorder, and the behaviour of the resistive anisotropy in bond-disordered crystalline materials.

4.2 Model Calculations

As indicated in the above review, measurements of the dependence of the resistivity on temperature and magnetic field can give important information about the magnetic properties of a material. Although model calculations of the behaviour of the magnetisation and magnetic susceptibility have been done for bond-disordered systems[27], the transport properties, and specifically the resistive anisotropy are not as well understood. In an effort to understand the variation of the low field resistive anisotropy (LFRA) with temperature and bond-disorder, calculations were made based on the Sherrington-Kirkpatrick (SK) model discussed in section 2.1.3. In this model, moments are located at each lattice site, but are assumed to have a Gaussian exchange distribution. One can numerically solve the resulting coupled equations for $m = \langle\langle S_z\rangle_T\rangle_J$ and $q = \langle\langle S_z\rangle_T^2\rangle_J$. Numerical integration of equations 2.36 and 2.37 was performed using Gauss-Legendre quadrature in conjunction with Newton's method, starting with initial guesses for m and q. The calculated values were substituted back into the equations, and the process is iterated until the values converge. Calculations based on this model have been done previously for the field and temperature dependence of m, q and χ[27]. The same program was extended to include calculations for the LFRA.

As shown in Section 2.2.2, the resistive anisotropy in a localised model is proportional to the quadrupolar operator,

$$\frac{\Delta\rho}{\rho} = \frac{D}{V}\left(\langle S_z^2\rangle - \frac{S(S+1)}{3}\right). \tag{4.1}$$

To calculate the LFRA, it was necessary to obtain values for $\langle\langle S_z^2\rangle_T\rangle_J$ as a function of temperature, assuming the ratio $\frac{D}{V}$ to be constant. The temperature average can be obtained using Boltzmann statistics.

$$\langle S_z^2\rangle_T = \frac{\sum_{S_i} S_i^2 e^{-aS_i/k_BT}}{\sum_{S_i} e^{-aS_i/k_BT}} = \frac{1}{Z}\frac{d^2}{dh_i^2}Z \tag{4.2}$$

In this equation the energy prefactor a is equal to $g\mu_B H$, and the denominator, Z,

in (4.2) is a finite geometrical progression, and can be rewritten as,

$$Z = \sum_{S_i=-S}^{S} e^{-h_i S_i} = \frac{\sinh\left(\frac{2S+1}{2}h_i\right)}{\sinh\left(\frac{h_i}{2}\right)} \tag{4.3}$$

with $h_i = a/k_BT$. Differentiation of (4.3) yields an expression for $\langle S_z^2\rangle_T$ of,

$$\langle S_z^2\rangle_T = S(S+1) - SB_S(Sx_i)\coth\left(\frac{x_i}{2}\right) \tag{4.4}$$

B_s is the Brillouin function and $x_i = \frac{1}{k_BT}(J_0 m + Jq^{1/2}\alpha + h_a)$, for a distribution with first and second moments J_0 and J, and applied field $h_a = g\mu_B H_a$. To obtain the site average $\langle\rangle_J$, equation 4.4 is integrated over the variable α_i, once m and q have been calculated self-consistently as described earlier. $I = << S_z^2 >_T >_J - S(S+1)/3$, is similar to the integrals for m and q,

$$I = \frac{1}{\sqrt{2\pi}}\int_{-\infty}^{\infty} d\alpha_i e^{-\alpha_i^2/2}\left[\frac{2S(S+1)}{3} - SB_S(Sx_i)\coth\left(\frac{x_i}{2}\right)\right] \tag{4.5}$$

Calculations were done for representative values of $\eta = \frac{J_0}{J}$, S and applied field as a function of reduced temperature, $t' = \frac{T}{T_c}$. These results are displayed in the following figures. Figures 4.4 and 4.5 show the variation of the quadrupolar operator as a function of the spin, S, for two different η values in ferromagnetic ($\eta > 1$) systems. These results were all calculated for a low applied field of 50 Oersteds. In all cases the quadrupolar operator is zero for temperatures greater than T_c, and approaches a limiting value dependent on S at zero temperature. The higher spin values show a greater degree of curvature at low temperature, and saturate at progressively lower temperatures as the spin value increases.

The field dependence of the calculated anisotropy is shown in Figures 4.6 and 4.7, for fixed η and spin values. Essentially no change in the anisotropy results from order-of-magnitude changes in field, indicating that the primary purpose of the small applied field is simply to provide an alignment axis for the spins. The one effect of large applied fields is to cause the anisotropy to vanish at slightly higher temperatures, since larger thermal energy is needed to overcome the effective field.

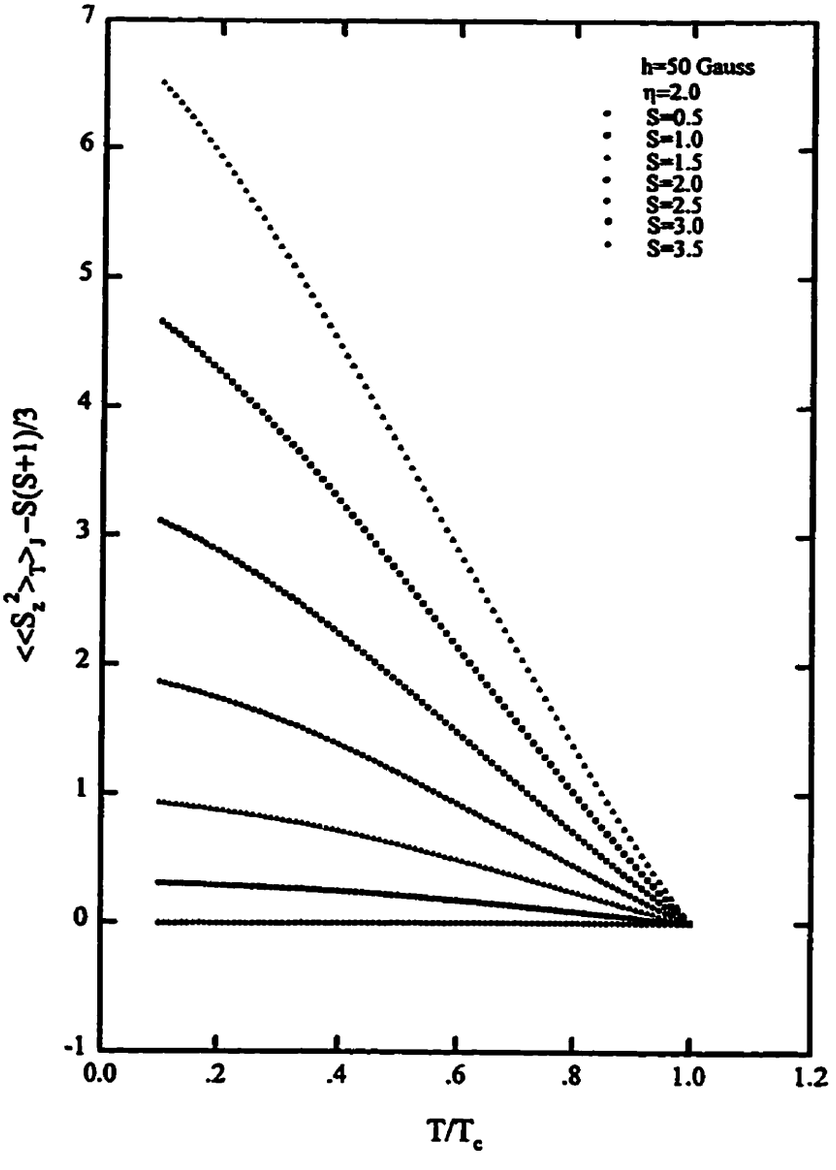

Figure 4.4: Spin dependence of the quadrupolar operator for $\eta = 2$. Spin values are as labelled, in units of μ_B.

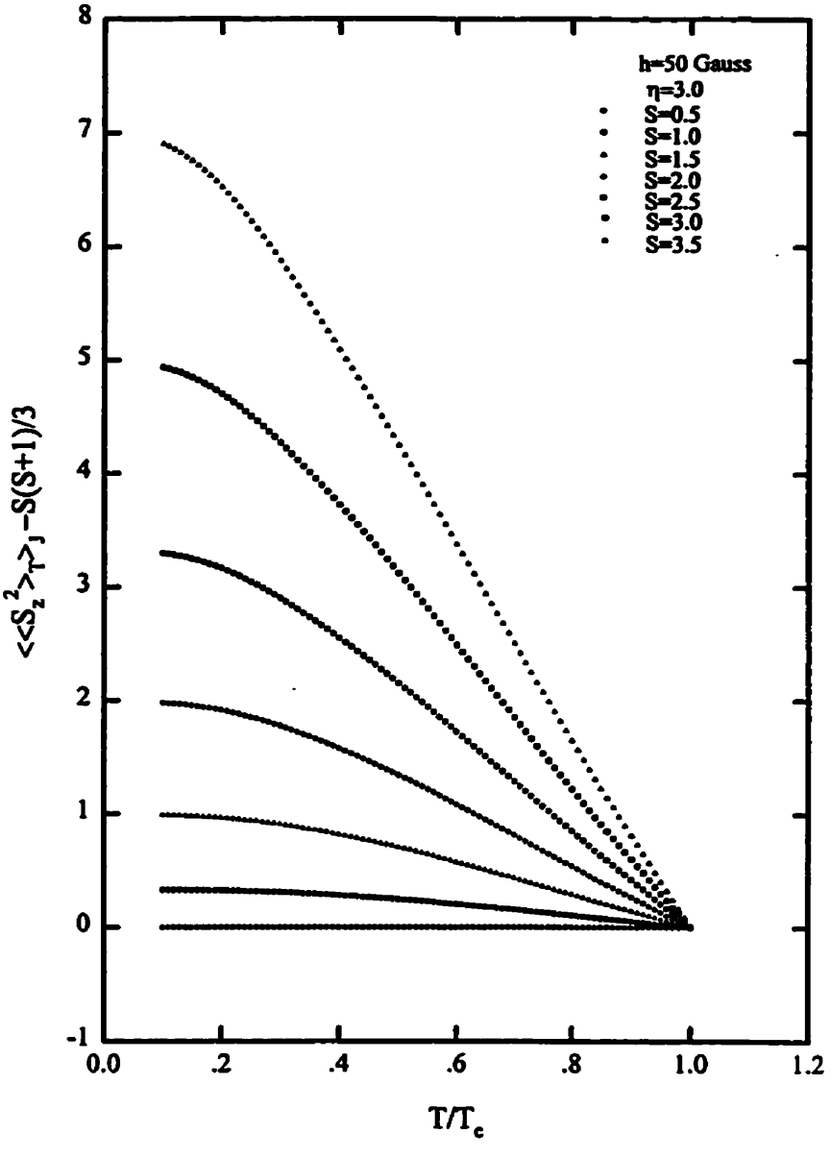

Figure 4.5: Spin dependence of the quadrupolar operator for $\eta = 3$. Spin values are as labelled, in units of μ_B.

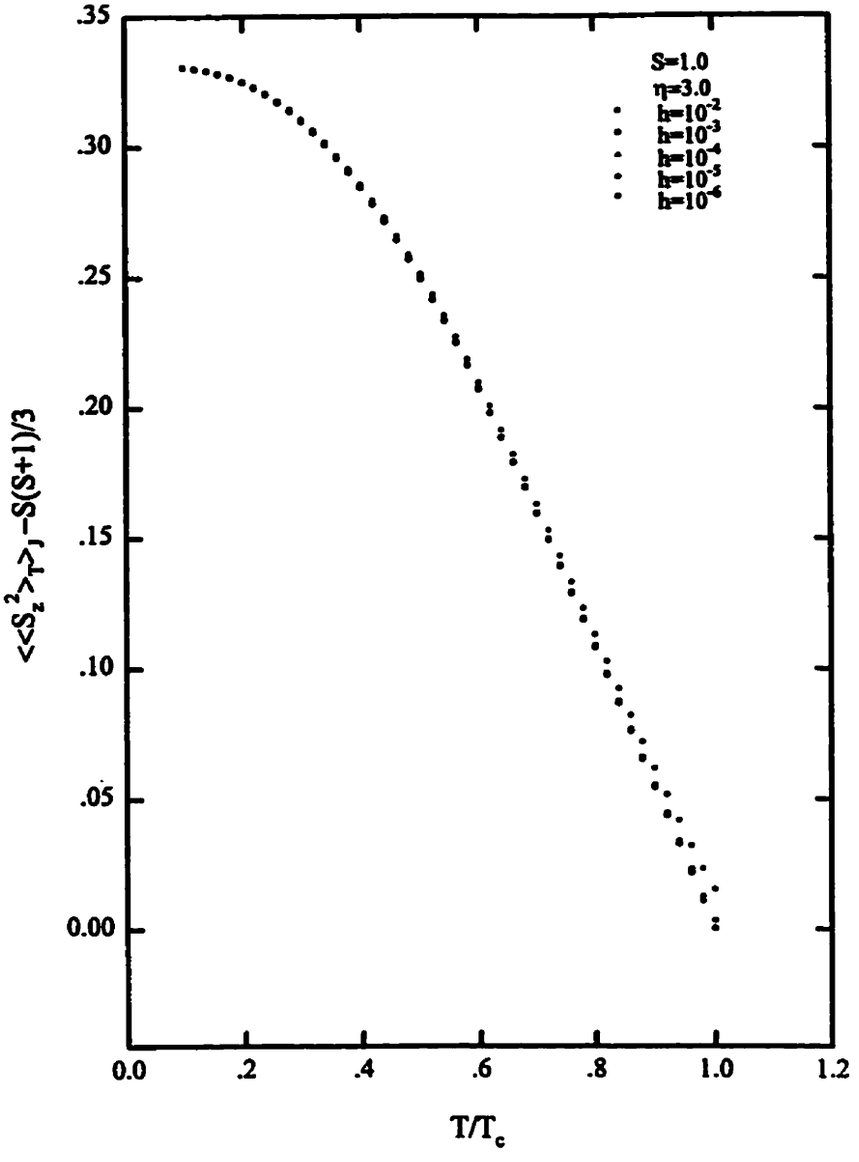

Figure 4.6: Field dependence of the quadrupolar operator for $\eta = 3$, S=1. Field values are as labelled, in units of $g\mu_B H/k_B T$. $h_a = 10^{-6}$ corresponds roughly to an applied field of 10 Oe, while $h_a = 10^{-2}$ is 10^5 Oe.

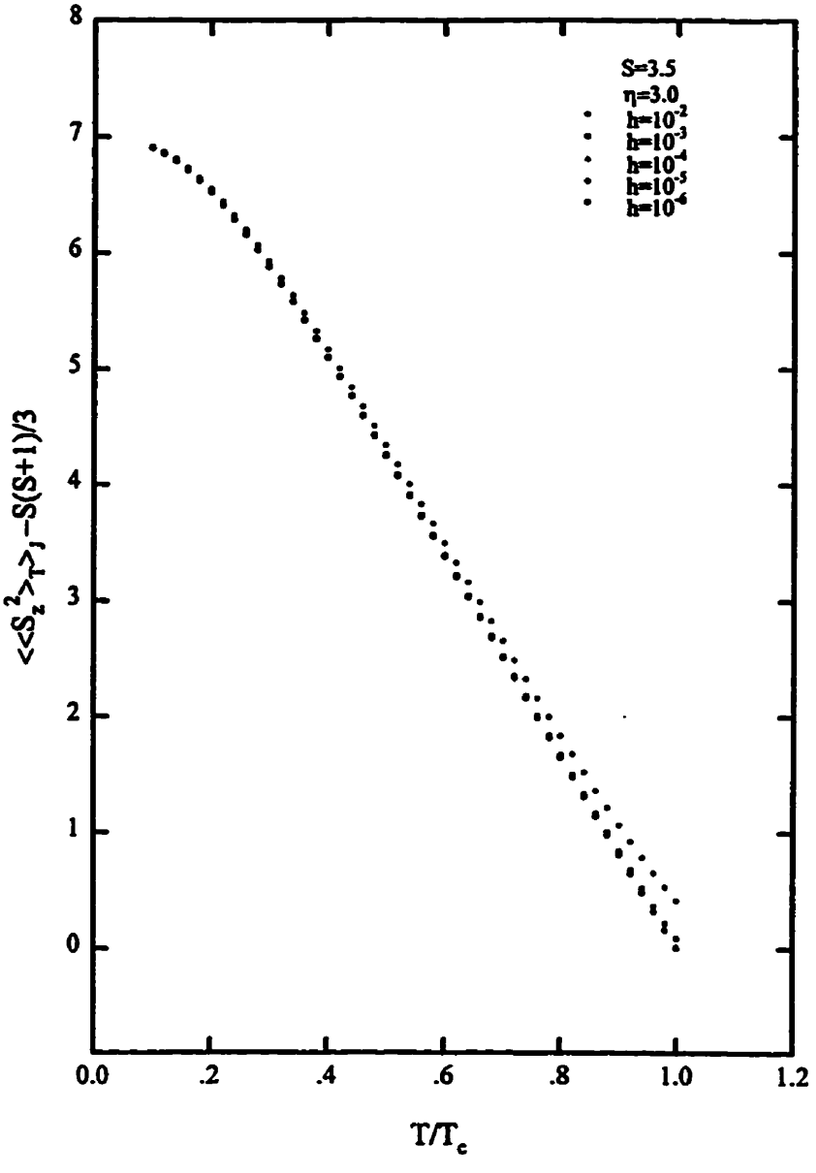

Figure 4.7: Field dependence of the quadrupolar operator for $\eta = 3$, S=3.5. Field values are as labelled, in units of $g\mu_B H/k_B T$. $h_a = 10^{-6}$ corresponds roughly to an applied field of 10 Oe, while $h_a = 10^{-2}$ is 10^5 Oe.

The most interesting results obtained from these calculations are presented in figures 4.8 to 4.10. These figures show the variation in the calculated anisotropy for a number of fixed spins as the degree of bond disorder changes. In the ferromagnetic case ($\eta > 1$) the anisotropy increases monotonically as temperature is lowered below the critical temperature, and saturates at low temperatures. Near T_c however, the curves have a linear temperature dependence, with the change in η resulting in a change in the slope of the line. In the spin-glass regime, the anisotropy shows complex behaviour, which is not presently understood. The latter curves are not shown here, as they have large negative anisotropies. This may simply reflect the inability of this mean-field model to accurately reproduce the behaviour of the complex spin-glass state. Concentrating only on the disorder dependence of the ferromagnetic systems, one can clearly see that at low temperature, the anisotropy approaches a common value of S(2S-1)/3, independent of η, and as the bond disorder increases (η decreases) the slope of the linear temperature dependence of the anisotropy near T_c decreases. This suggests that measurements of the anisotropy near the critical temperature may be a sensitive probe of the relative disorder in a system. If the absolute disorder of a reference sample is known, quantitative estimates for the disorder in related samples can be obtained. As well, the temperature intercept of the data can be used as another check on the critical temperature of the system, since the anisotropy should vanish above T_c. To verify these hypotheses, a number of bond-disordered systems were studied, as described in the following sections.

4.3 Amorphous FeZr

Transport and *ac* susceptibility measurements were performed on samples cut from melt-spun ribbons of $Fe_{91}Zr_9$, prepared as described in Section 3.1. Measurements on the sample in its as-spun state have been reported previously[82]. With the aim of discovering the effect of a slight change in bond disorder in the same specimen, these measurements were repeated on the sample after a small amount of hydrogen was introduced electrolytically. These data were then compared to earlier results.

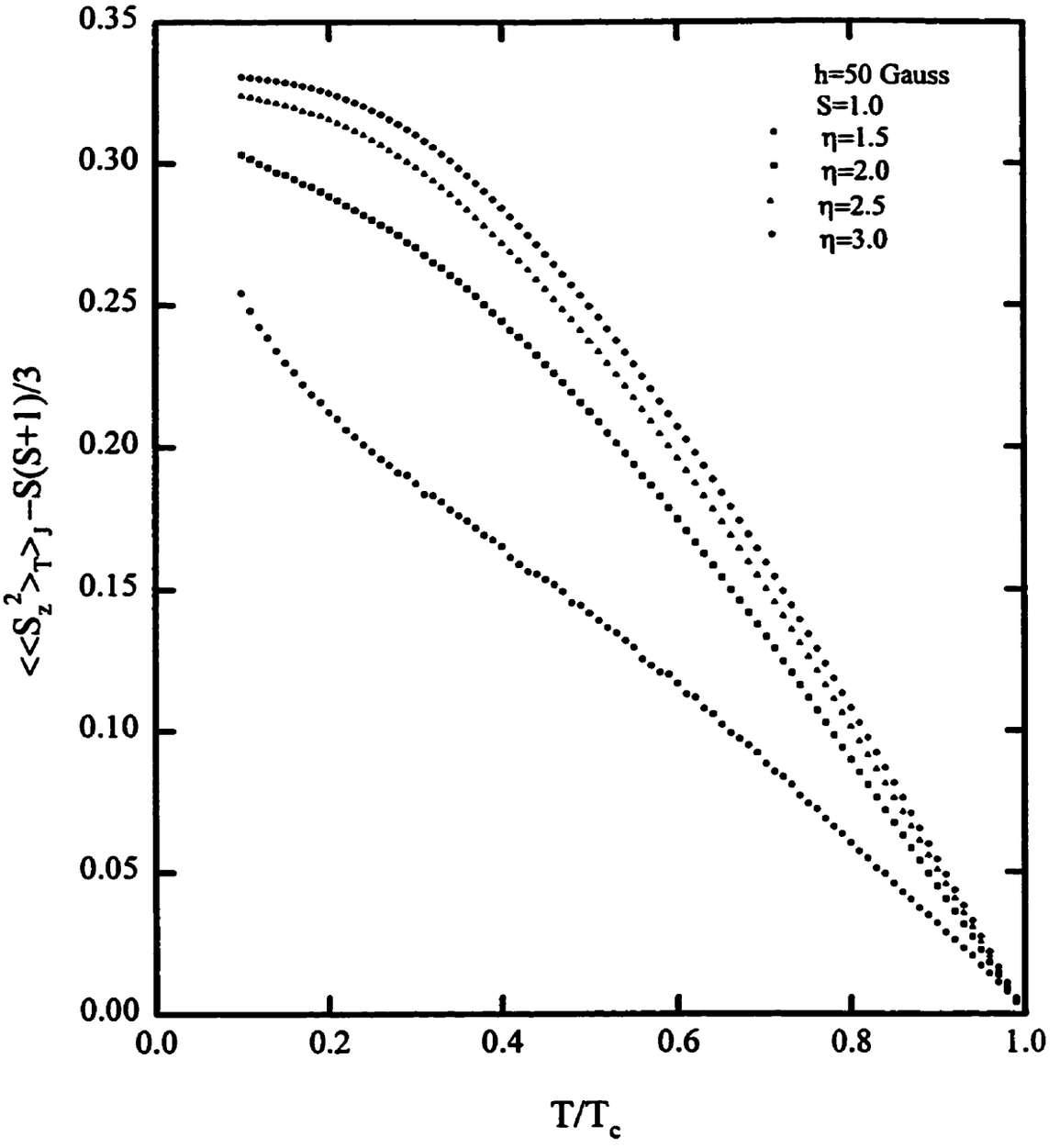

Figure 4.8: η dependence of the quadrupolar operator for H=50 Oe, S=1. η values are as labelled.

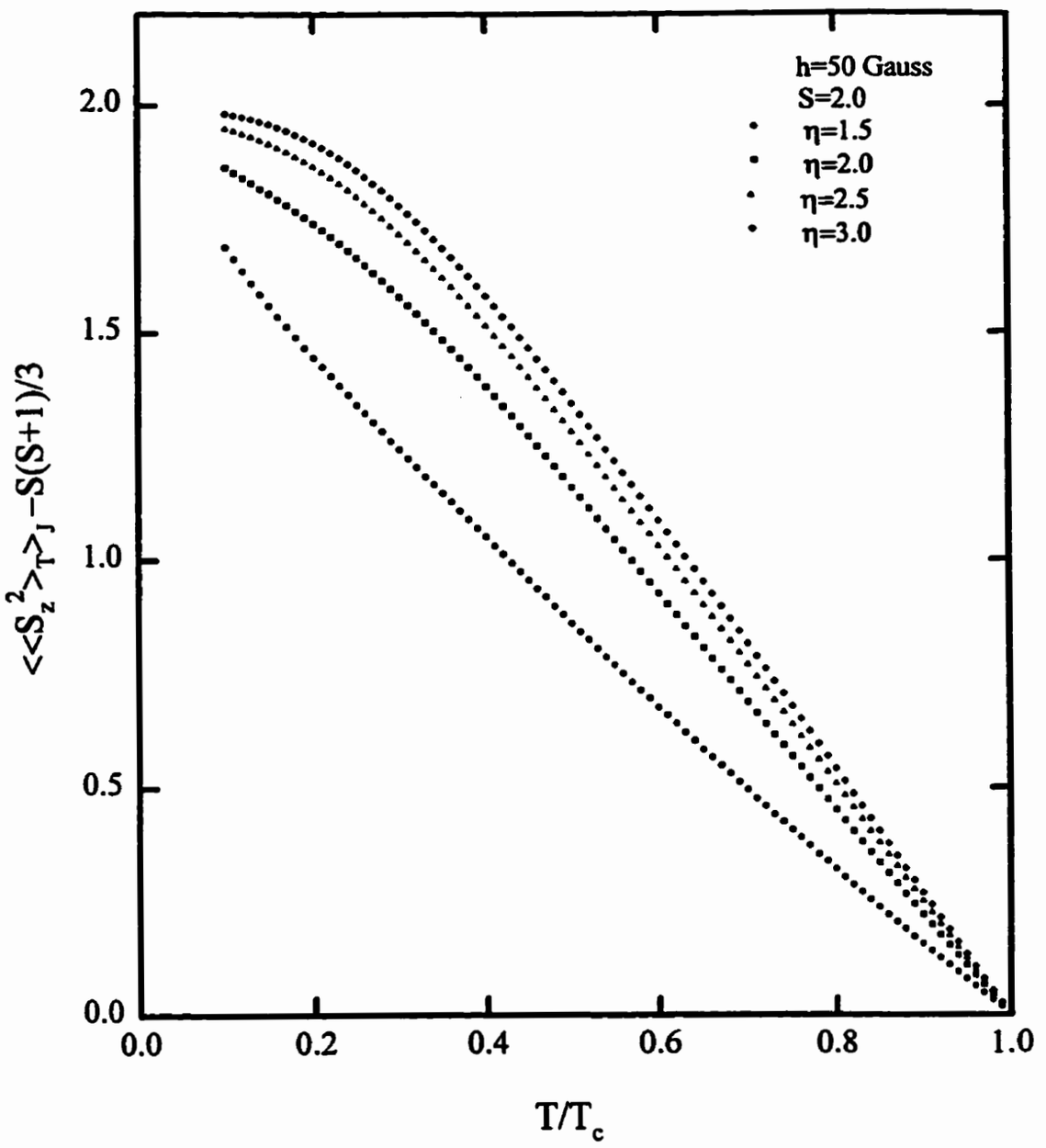

Figure 4.9: η dependence of the quadrupolar operator for H=50 Oe, S=2. η values are as labelled.

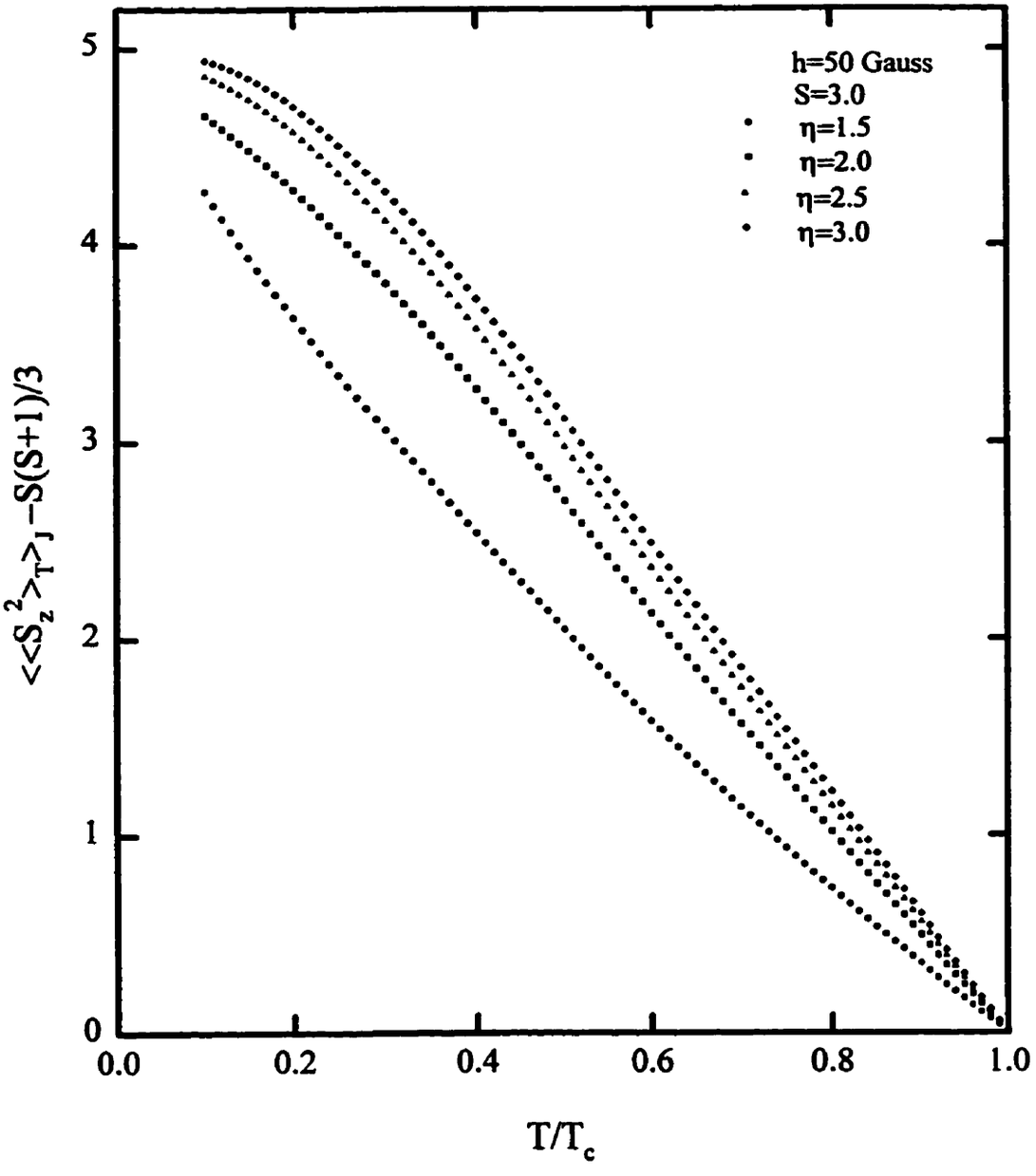

Figure 4.10: η dependence of the quadrupolar operator for H=50 Oe, S=3. η values are as labelled.

4.3.1 AC Susceptibility Measurements

A detailed study of the *ac* susceptibility of $Fe_{91}Zr_9$+H was done in the region of the paramagnetic to ferromagnetic phase transition. $Fe_{91}Zr_9$ is re-entrant, having a second transition from the ferromagnetic state to a spin-glass state at low temperature[82]. Here only the upper transition was studied, as it is in this region that our model calculations are valid. Magnetic susceptibility measurements can give an accurate value for the transition temperature, as well as values for the critical exponents of the system. The exponent values provide information on the magnetic interactions present.

The raw data was analysed as described in Chapter 3 to produce curves of the true *ac* susceptibility versus temperature in various static biasing fields. The zero field data for the $Fe_{91}Zr_9$+H sample is shown in figure 4.11. The susceptibility rises sharply as the temperature is lowered through T_c, going through a sharp peak at a temperature slightly below T_c. This Hopkinson peak results from technical contributions to the susceptibility, such as anisotropy and domain wall effects, and is not a true critical peak. The susceptibility does not approach its demagnetisation limit of 1/N (see equation 3.7), indicating the presence of substantial anisotropy, as discussed in Section 3.3.3. To observe true critical peaks, static biasing fields were applied which reduce the technical background. Figure 4.12 shows the temperature dependence of the susceptibility for $Fe_{91}Zr_9$+H in a number of small biasing fields. As the applied field was increased, the background peak was dramatically suppressed in height and temperature, until at a field of 10 Oersteds the critical peak can be seen emerging in the form of a plateau, with a clear critical peak emerging at an applied field of 25 Oersteds. The inability of small fields to resolve the critical peak is an indication of strong local anisotropy, usually resulting from the presence of spin-orbit coupling. Materials such as PdFe which do not have orbital moments at the magnetic site at low Fe concentration, typically require fields on the order of only 0.5 Oersted to bring out the critical structure[63].

Figure 4.13 shows the behaviour of the critical peak as the biasing field is in-

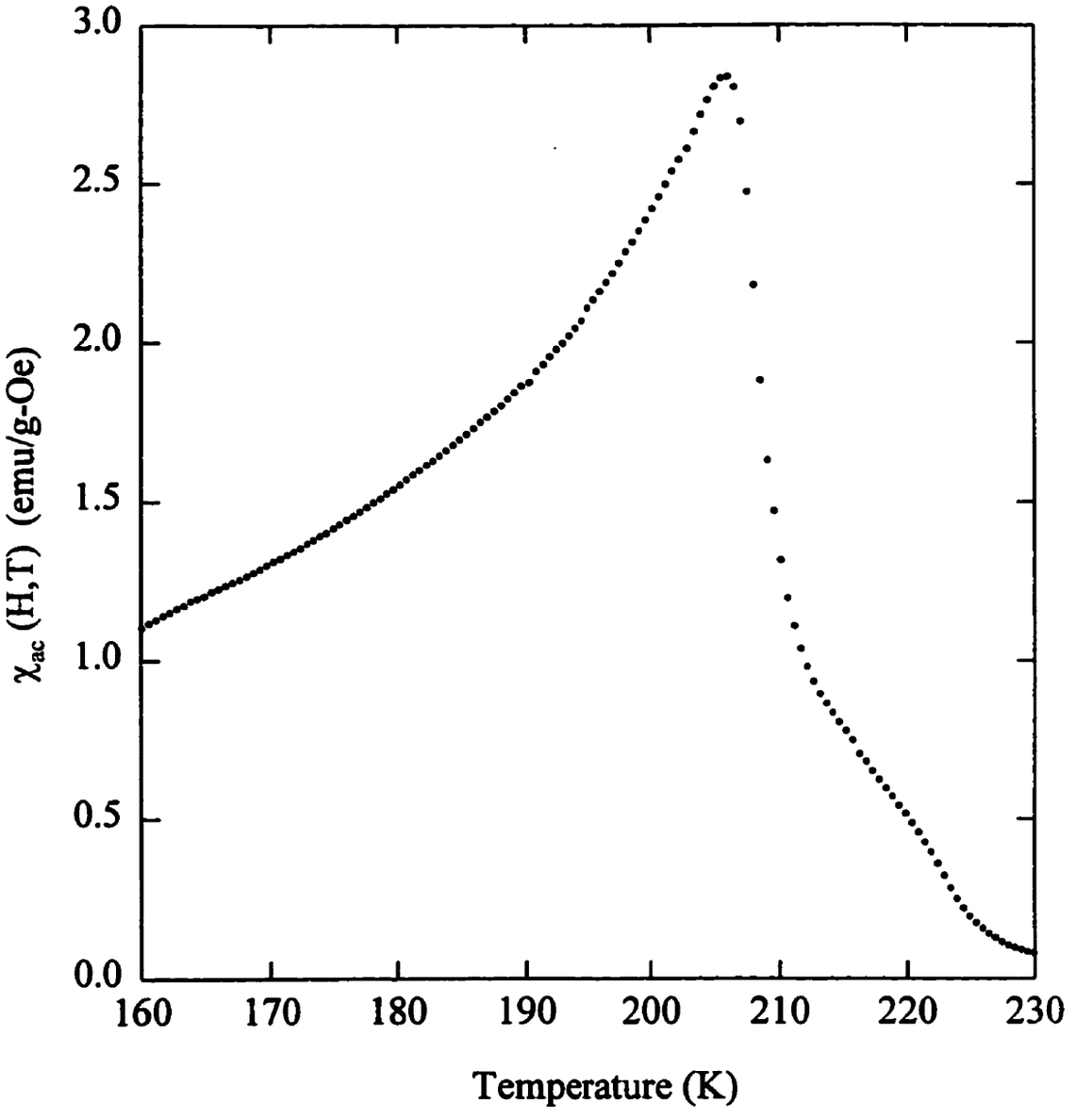

Figure 4.11: Temperature dependence of the zero field *ac* susceptibility in $Fe_{91}Zr_9$+H.

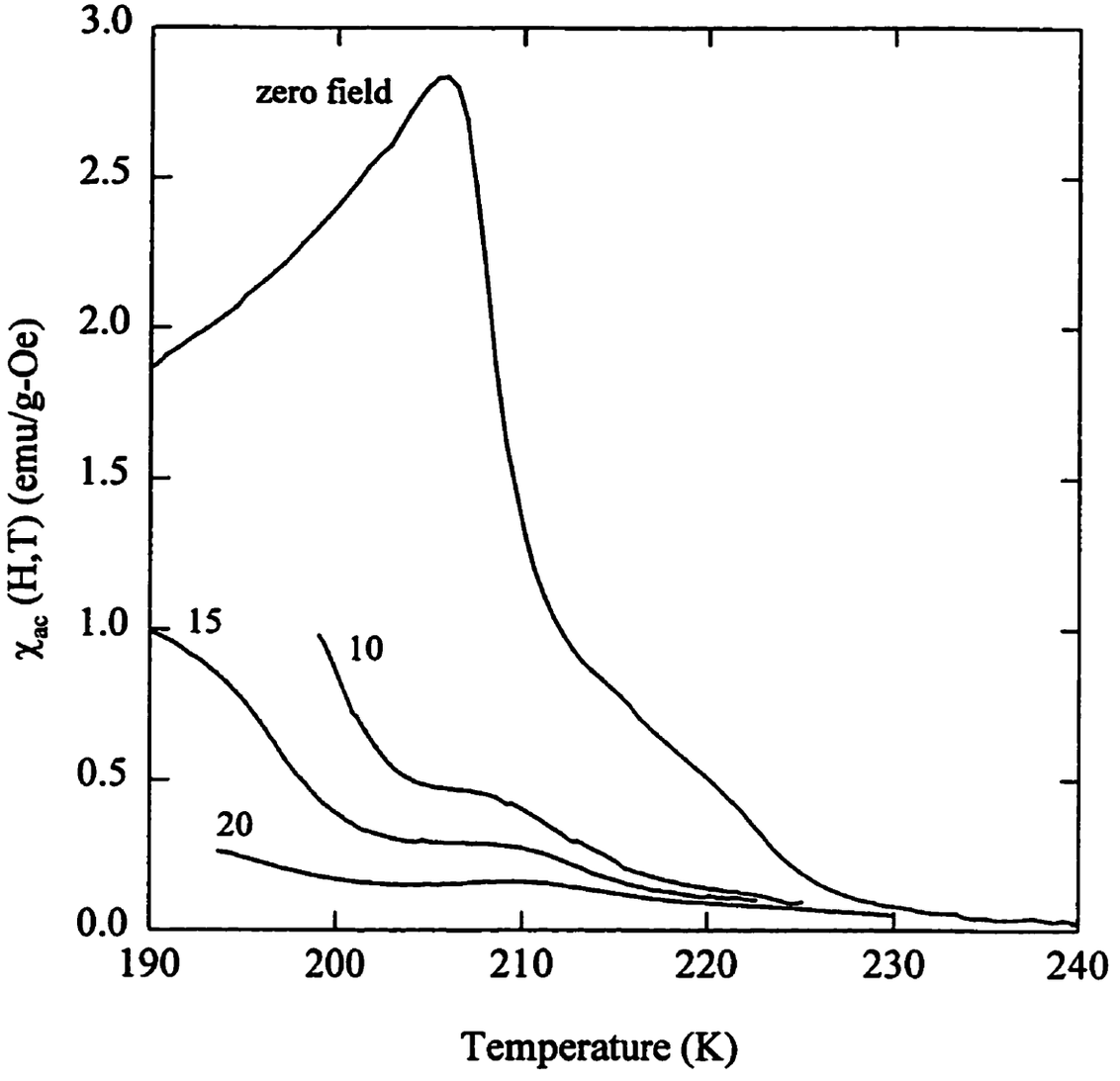

Figure 4.12: Temperature dependence of the *ac* susceptibility in $Fe_{91}Zr_9$+H in a number of small static biasing fields, as labelled, in Oe.

creased further. As predicted by scaling theory (equation 2.30), the critical peak moves upwards in temperature and decreases in magnitude as the applied field increases. By extracting peak temperatures, T_m, and amplitudes, χ_m, from the data, scaling fits were done to determine values for the critical exponents $(\gamma + \beta)$ and δ. An initial estimate for T_c was obtained by plotting the peak temperature as a function of $H^{0.571}$, where 0.571 is the 3D Heisenberg model prediction for $1/(\gamma+\beta)$. A linear fit to these data at low field (points 3–15 in this case) gave an estimate for T_c, as shown in figure 4.14. The error bars at low field result primarily from uncertainties in correctly assessing the peak position due to the size of the background contribution, while those at high field are due to scatter in the data points caused by a low signal to noise ratio. The temperature intercept, 205.7(2) K, was used as an initial estimate of T_c, from which the reduced temperature $t_m = (T_m - T_c)/T_c$ was calculated and plotted as a function of internal field on a log-log scale. As can be seen in figure 4.15, there is some curvature in the plot at high field values, although the low field data is quite linear. The asymptotic value for the so-called 'cross-over exponent', $\gamma + \beta$ was obtained in this case by fitting points 3–15 to a straight line. The cross-over line represents the line at which the system passes from field-dependent to temperature-dependent behaviour. An independent value for γ was found using equation 2.31, which relates χ_m to t_m. This plot also depends on the value chosen for T_c. The final value of γ found by fitting points 3–15 to equation 2.31 (figure 4.16), is $\gamma = 1.18(1)$, substantially lower than the 3D Heisenberg prediction of 1.386, however, the value of $\gamma+\beta$ of 1.75(1) is in excellent agreement with the 3D Heisenberg predictions. The above plots were iterated with small changes in T_c until agreement is reached, with the final T_c=205.8±2 K. The error in T_c results from the scatter in data points as well as from the error in measuring the absolute temperature. Due to calibration errors and systematic errors, the absolute temperature can be incorrect by as much as 1%, although relative temperature values are very accurate.

The Kouvel-Fisher effective γ was found from the zero field susceptibility data

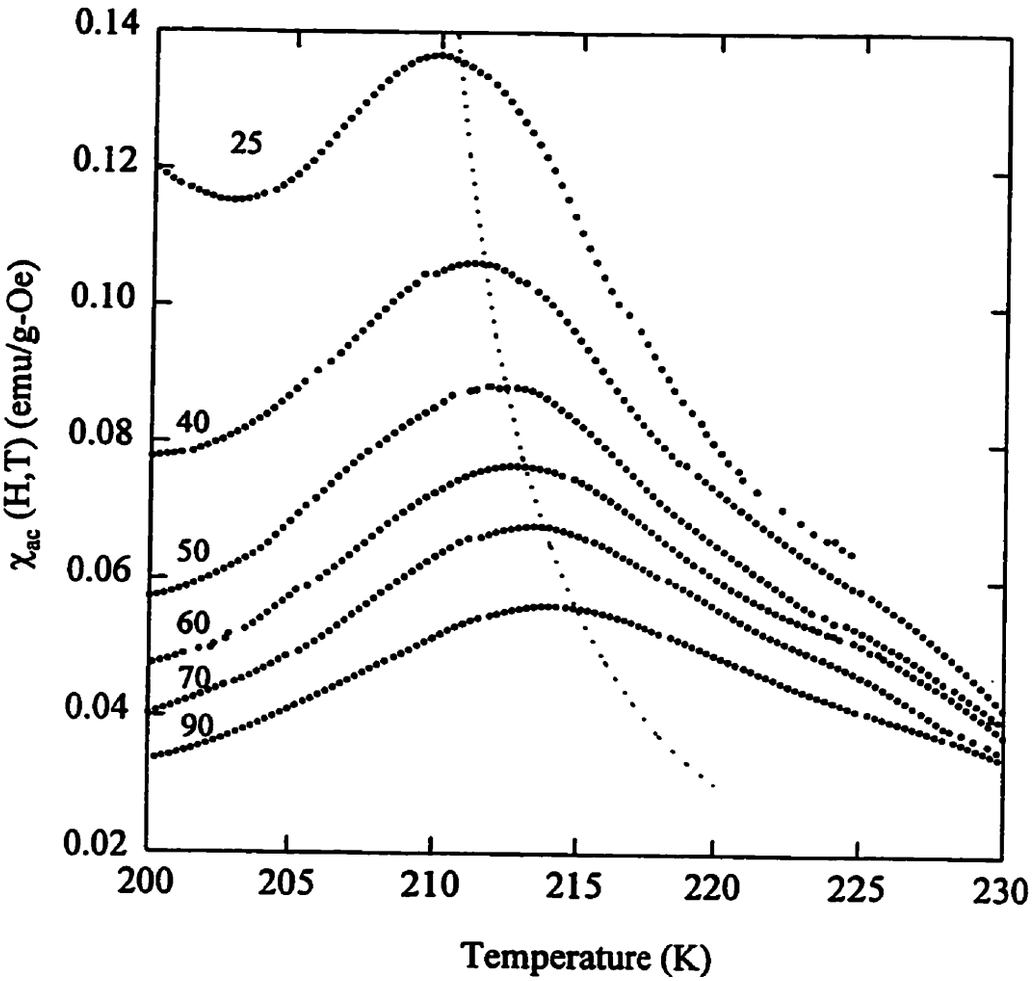

Figure 4.13: Behaviour of the critical peaks in $Fe_{91}Zr_9$+H with larger applied fields, as labelled, in Oe. The dotted line represents the cross-over line, a fit to $\chi_m \propto t_m^{-\gamma}$.

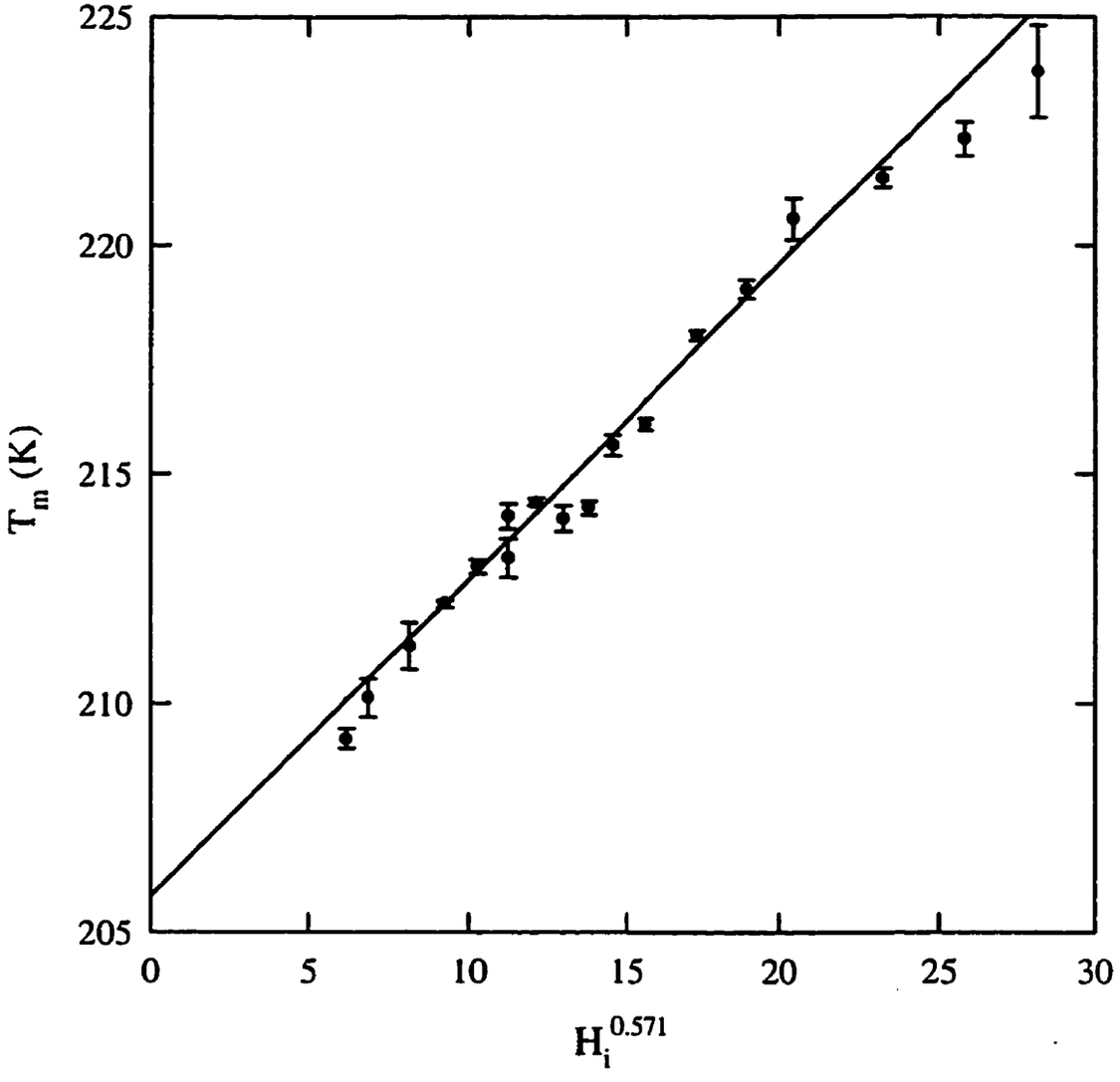

Figure 4.14: Initial estimate for T_c in $Fe_{91}Zr_9$+H, obtained from the temperatures of the critical peaks.

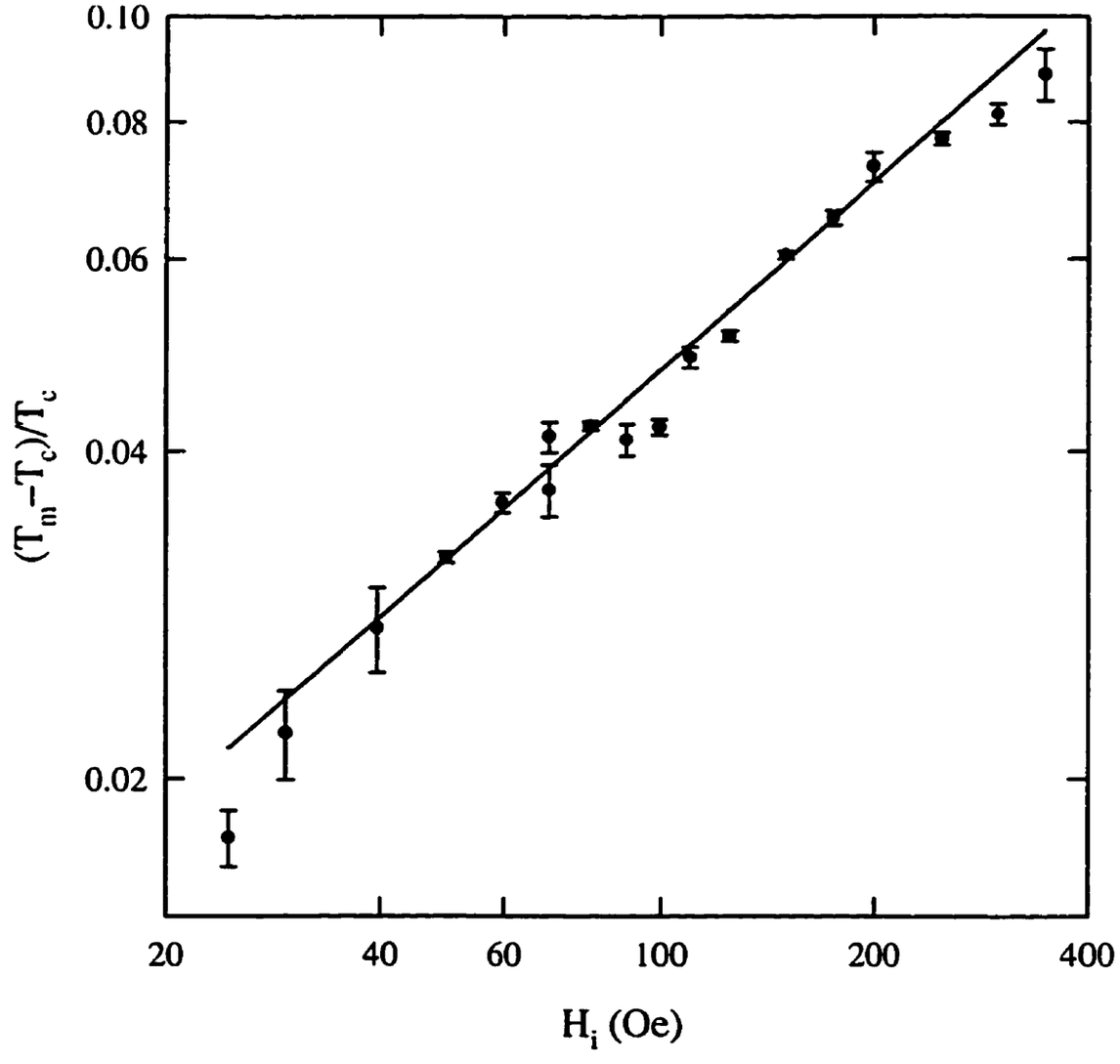

Figure 4.15: Cross-over plot for $Fe_{91}Zr_9$+H. The solid line is the best fit to the linear region, with a slope of $1/(\gamma+\beta) = 0.56(1)$.

using the relation,

$$\gamma^*(t) = -\frac{d\ln\chi}{d\ln t} \tag{4.6}$$

which was calculated and is plotted in figure 4.17 as a function of reduced temperature. The effective γ starts at a low value and rises to a peak at $t \sim 0.07$, before dropping at high temperature toward the mean field value of 1. As mentioned in section 4.1, this peaked behaviour is typical of systems with large amounts of disorder. The decrease of the exponent below the Heisenberg value as $t \rightarrow 0$ and the low value of the asymptotic γ can be explained by the fact that the zero field susceptibility does not reach the demagnetisation limit, thus decreasing the low t slope of the χ versus t curve. This is again an indication of the presence of anisotropy in the system, due to spin-orbit coupling at the Fe sites.

A value for δ was found using equation 2.32. The peak susceptibility was plotted against internal field on a log-log scale, as shown in figure 4.18. There is little curvature evident in this plot, so all data points could be fit to a straight line, yielding $\delta = 4.8(1)$, in perfect agreement with 3D Heisenberg predictions.

In conclusion, this system behaves magnetically as a 'good' ferromagnet, with asymptotic exponent values close to 3D Heisenberg values. The effects of disorder can be seen in the behaviour of $\gamma^*(t)$, as well as in the slight curvature in the other exponent plots. An estimate of the coercivity of the material at T=77 K (within the ferromagnetic region) was taken from a 'butterfly' plot of susceptibility as a function of applied field (figure 4.19). This essentially represents the local slope of the hysteresis loop for the material. Assuming that the region of highest slope in the hysteresis loop is at the coercive field, the separation between the peaks in the 'butterfly' plots is twice the coercive force, which for this material is 0.2 Oe at 77K.

4.3.2 Low Field Resistive Anisotropy

LFRA measurements were performed using the SRA apparatus described in section 3.2.2, in small biasing fields of 15, 30, 60, 90 and 120 Oersteds. Due to the large residual resistivity of these amorphous ribbons the back-off system described in

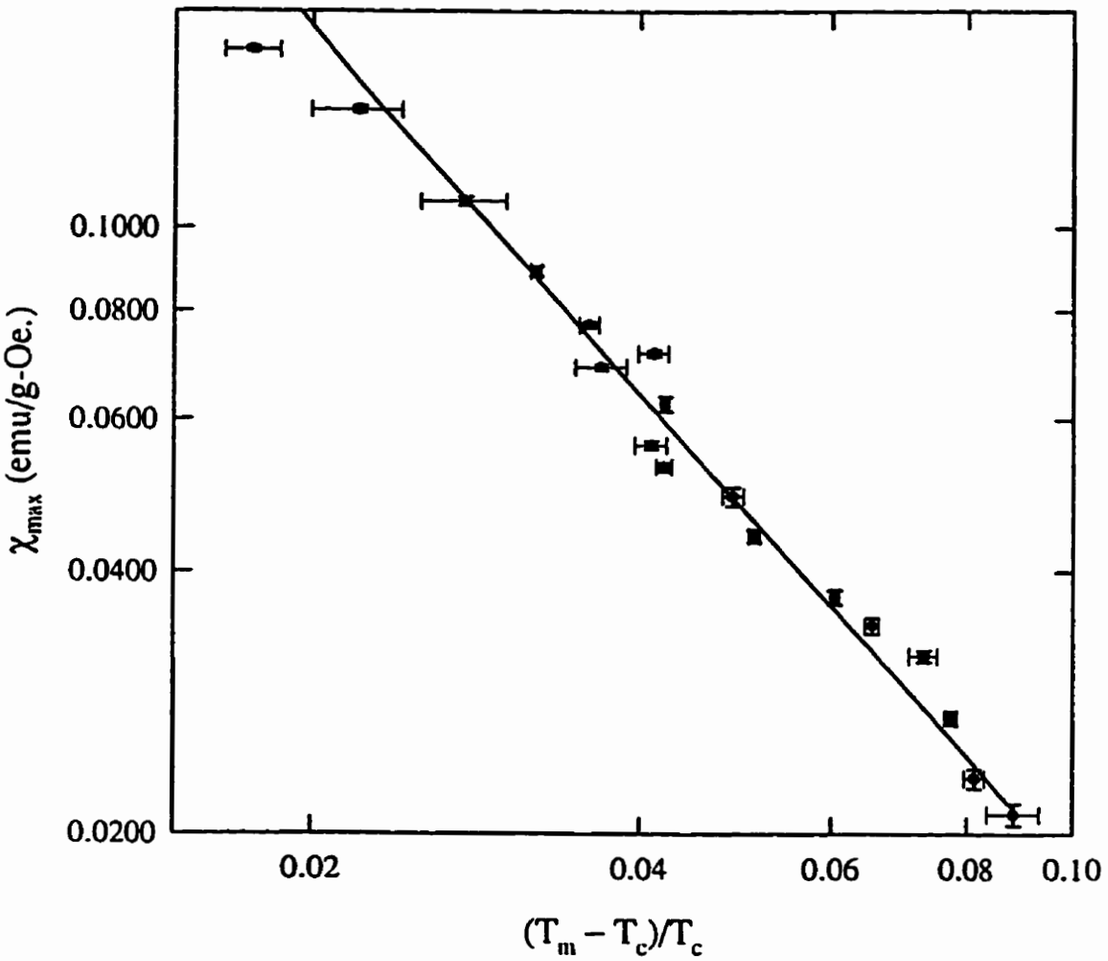

Figure 4.16: The reduced peak temperatures plotted versus the peak susceptibility. The best fit line gives a value for γ of 1.18(1).

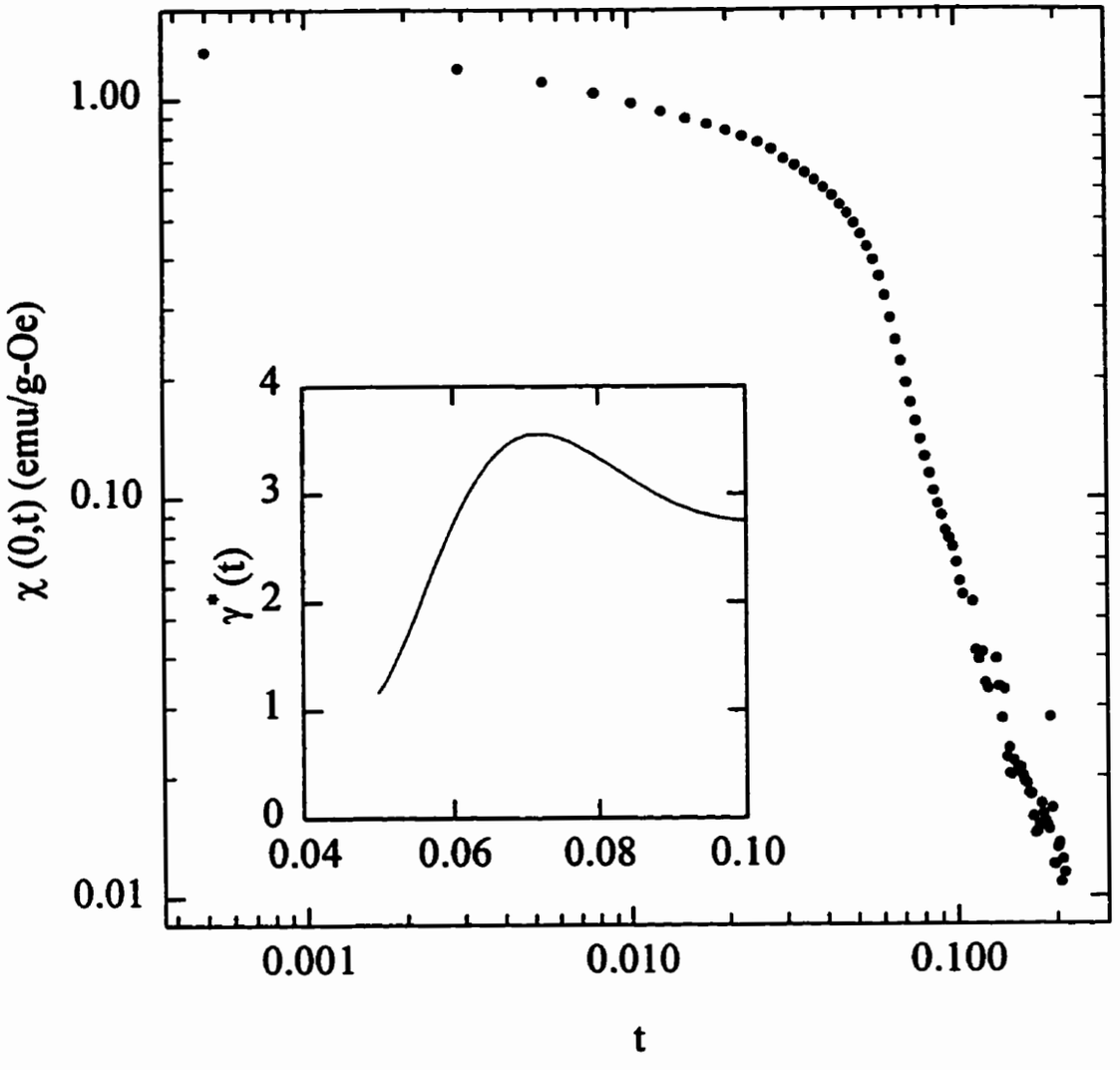

Figure 4.17: χ(0,T) plotted as a function of reduced temperature on a log-log scale. The inset shows $\gamma^*(t)$ plotted as a function of reduced temperature.

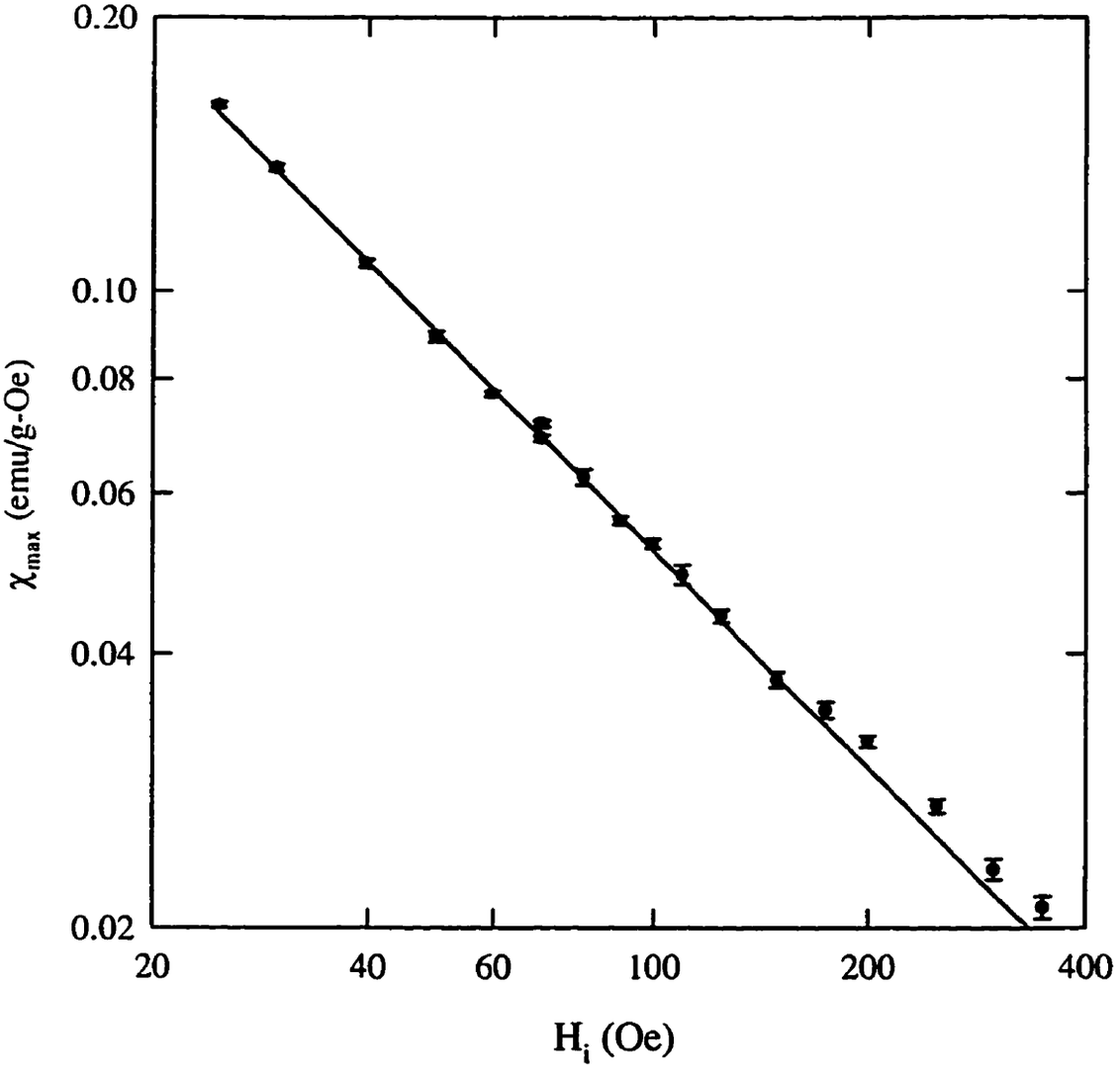

Figure 4.18: The peak susceptibility plotted as a function of internal field (Oe). The best fit line gives δ=4.8(1).

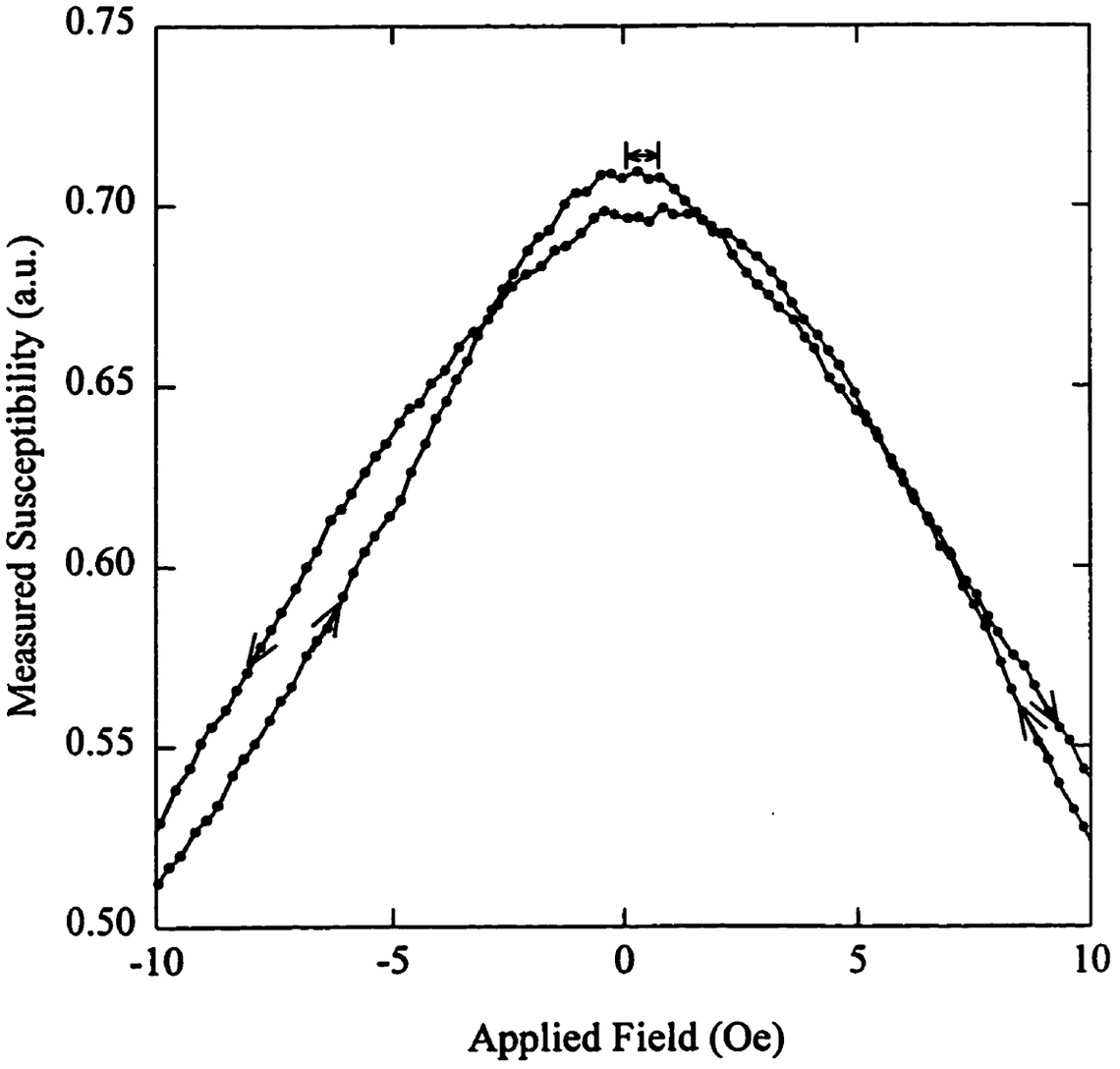

Figure 4.19: Butterfly plot of the *ac* susceptibility versus applied field in $Fe_{91}Zr_9$+H at 77K. The distance between the peaks is taken to be twice the coercive force.

section 3.2.1 was unable to completely remove this constant portion, making it impossible to tune the circuit to the sample resistance. The zero offset adjustment on the lock-in amplifier was consequently used to back-off the residual resistivity. The phase was adjusted for a maximum output signal, assuming that the resistive portion was much larger than the out-of-phase signal. Measurements were taken from 150 to 220 K, with the observed anisotropy vanishing near 210 K. The LFRA measured in 60 Oe is plotted in figure 4.20 as $(\rho_{\parallel}(H,T) - \rho_{\perp}(H,T))/\rho_0$, assuming that the residual resistivity is approximately temperature independent, as in all amorphous alloys. At all fields, the anisotropy is zero above 220K, and increases linearly as the temperature is dropped below T_c. Figure 4.21 shows a comparison between the data acquired in different fixed fields. Near T_c the points all fall on a line of the same slope. Performing a fit of the LFRA as a function of T/T_c in the linear portion of the curve (using the 60 Oersted run), yields a slope of $(21\pm1)\text{x}10^{-4}$. As the temperature decreases further below T_c, the curves become distinct, with a higher resistive anisotropy as the field is increased. This suggests that the field dependence is due to technical effects, such as domain size. The model calculations described in the previous section are based on an ideal, single-domain ferromagnet. In order for this model to be applied to a real system, the material must be single-domain at least over the mean free path of the conduction electrons. The increase in magnetic hardness (coercivity) as temperature decreases may result in smaller domain sizes, as the low applied field becomes incapable of rotating and moving the domain walls. If the applied field is increased, the domain size will remain larger than the mean free path down to lower temperature. Examining the region near T_c, we can see that the tail of the curve is also more sensitive to field than predicted by the model, with the temperature intercept moving progressively higher as the field is increased.

4.3.3 Summary

In conclusion, *ac* susceptibility measurements on hydrogenated $Fe_{91}Zr_9$ show it to be a good ferromagnet, with critical exponents in agreement with 3D Heisenberg

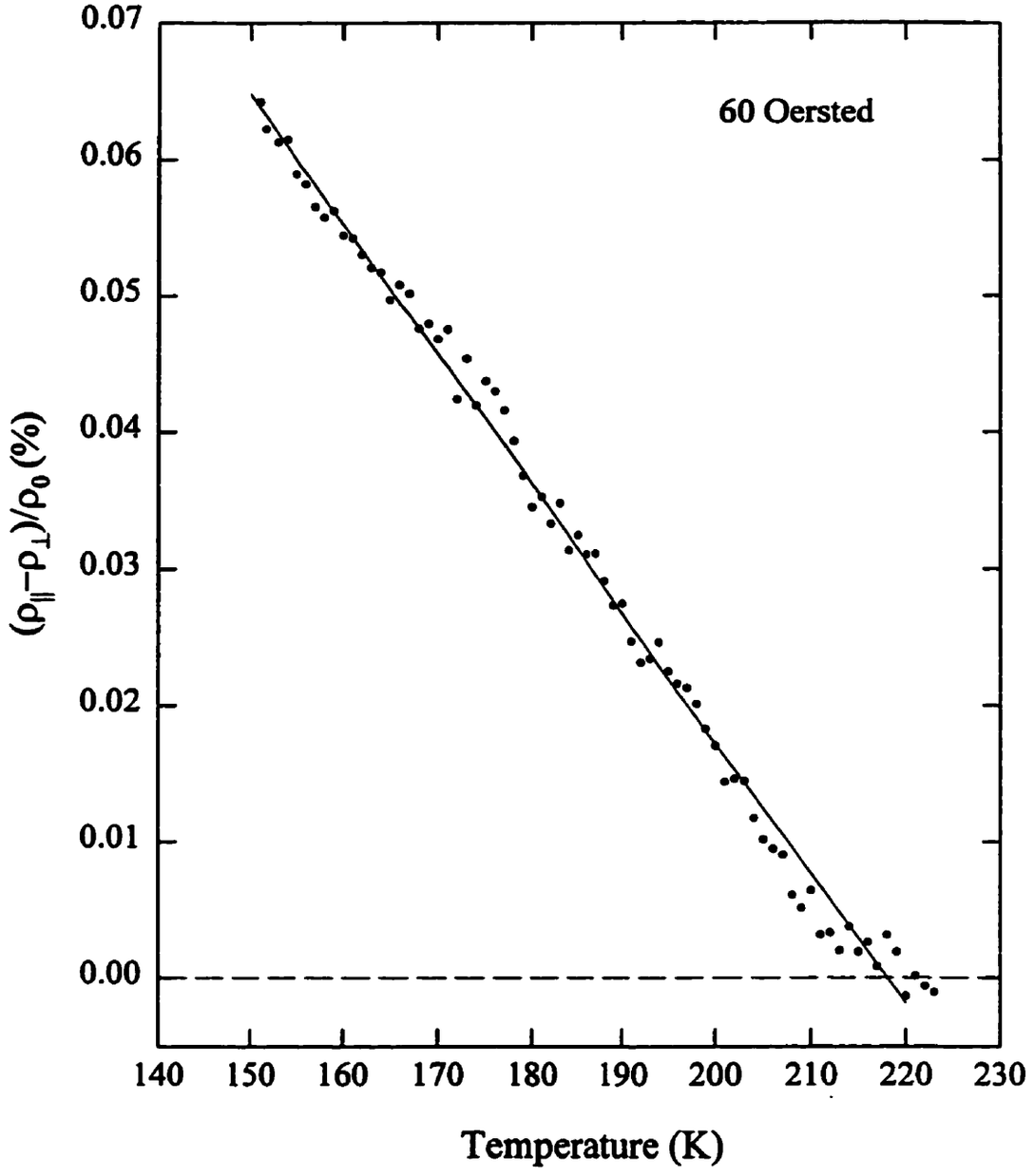

Figure 4.20: Temperature dependence of the LFRA in $Fe_{91}Zr_9$+H with H=60 Oe.

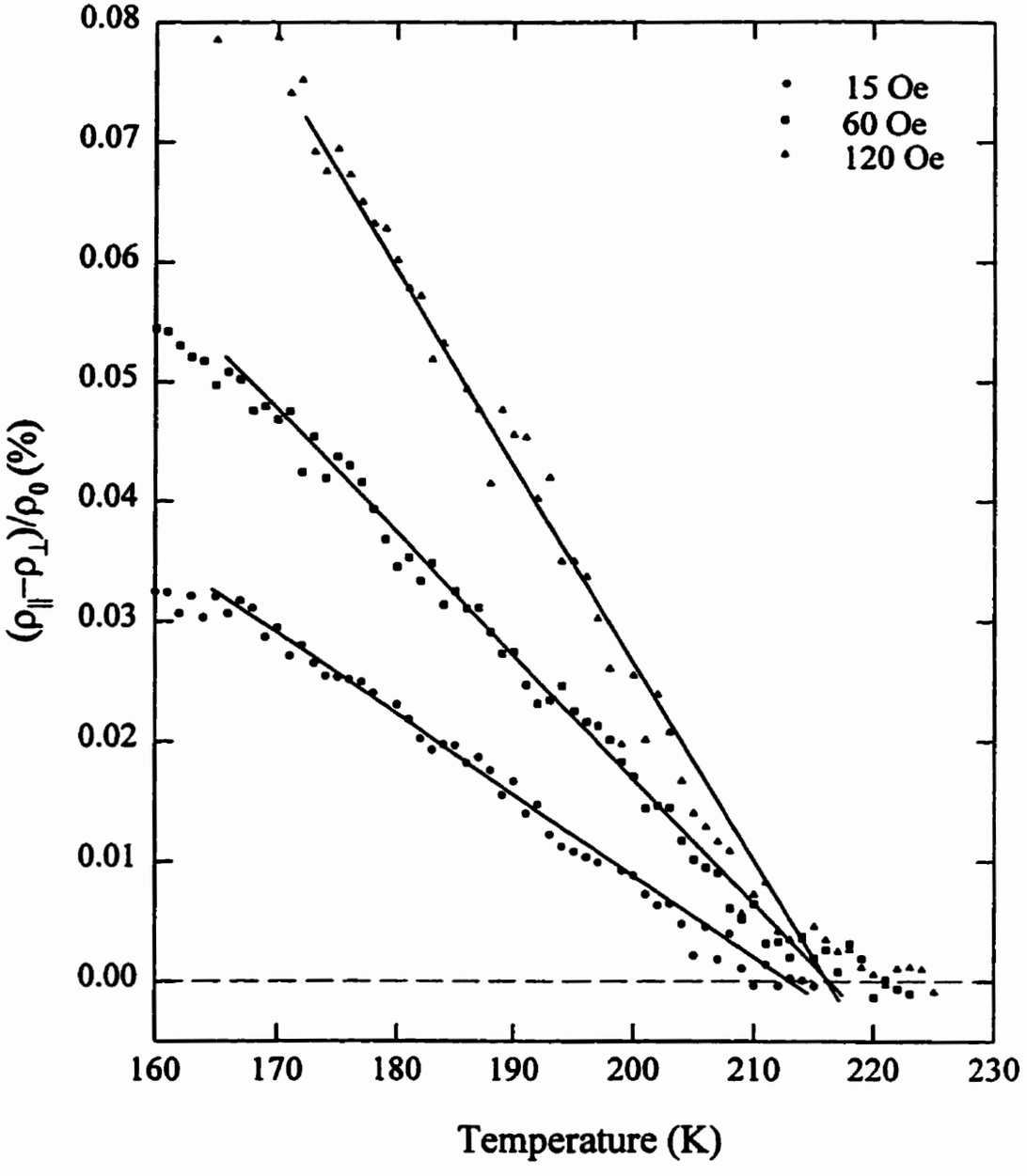

Figure 4.21: Comparison of the temperature dependence of the LFRA in $Fe_{91}Zr_9$+H with various applied fields (in Oe). The superimposed lines are guides for the eye.

Table 4.1: Fitting Parameters for the LFRA in FeZr.

	LFRA		χ_{ac}		
Sample	$T_c(K)$	$10^4 A$	$T_c(K)$	δ	$\gamma+\beta$
$Fe_{91}Zr_9$	203	16(1)	200	4.85(2)	1.75
$Fe_{91}Zr_9$+H	210	21(1)	206	4.8(2)	1.75
$Fe_{90}Zr_{10}$	235	19(1)	237	4.55(2)	1.75
$Fe_{90}Zr_{10}$+H	260	23(1)	–	–	–

model predictions. Some bond disorder is indicated by the behaviour of the effective exponents outside the critical region. The failure of the zero field susceptibility to reach its demagnetizing limit, as well as the large fields required to suppress the background indicate the presence of magnetocrystalline anisotropy, likely due to spin-orbit coupling. A non-zero LFRA is observed, confirming the presence of an orbital moment at the Fe sites. This LFRA has a linear temperature dependence immediately below T_c, in agreement with model calculations, although it exhibits stronger field dependence than predicted with the SK model, likely due to technical considerations. This data can be compared to measurements by H. Ma[82] of the LFRA of $Fe_{91}Zr_9$, $Fe_{90}Zr_{10}$ and $Fe_{90}Zr_{10}$+ H in the remanent field of an electromagnet (approximately 60 Oe). Ma's data also show a linear dependence of the anisotropy near T_c, which was also fit to the equation $\Delta\rho/\rho = -A(T/T_c)$. The introduction of hydrogen to the amorphous structure has the effect of increasing the average atomic spacing. This has been shown to increase the critical temperature for ferromagnetism[82] as can be seen in Table 4.1, and to decrease the temperature for transition to the spin-glass state, T_f. From the SK model, $T_f \propto J$ and $T_c \propto J_0$[18], so hydrogenation apparently increases the ratio $\eta = \frac{J_0}{J}$, thus decreasing the bond disorder. The model calculations in Section 4.2 would then predict that the slope, A, should increase with the addition of hydrogen, which is indeed observed. This calculation makes the assumption that the addition of hydrogen has no effect on the ratio (D/V) in equation 4.1. This assumption is believed to be valid, since

the amount of hydrogen introduced was deliberately kept small, with a change in T_c of less than 10%, compared to the change of 100% for complete hydrogenation[82]. The parameters found in these samples from susceptibility and LFRA measurement are listed in Table 4.1 for comparison. Obviously as T_c increases, A also increases. Thus, based on these results, measurements of the LFRA are shown to be sensitive to the relative amount of bond disorder present in the system.

4.4 $Pt_{90}Fe_{10}$

Detailed *ac* susceptibility and transport measurements were done on an alloy consisting of 10 at.% Fe in Pt. Measurements of $\chi(T)$ were performed in various static biasing fields, and the field dependence of the susceptibility was measured at a number of fixed temperatures. From the butterfly loops, values for the coercive force $H_c(T)$ were obtained. The zero field resistivity and its temperature derivative were also measured over a wide temperature range around T_c, and SRA values were obtained from the longitudinal and transverse magnetoresistances. Finally, measurements of the resistive anisotropy in low field were completed over a temperature range near T_c, in an attempt to verify that the agreement between the model calculations and the FeZr data is universal to disordered systems.

4.4.1 AC Susceptibility Measurements

Temperature Sweeps

Measurements of the *ac* susceptibility were done in the temperature range 150 to 200 K in a number of static biasing fields. Figure 4.22 shows the zero field susceptibility as well as the susceptibility in a number of small biasing fields. As in the FeZr sample, the zero field susceptibility does not reach its demagnetizing limit of 15 emu/g-Oe., indicating the relative hardness of the material. Internal fields of 15 Oe. were required to suppress the background contribution sufficiently to cause the emergence of a critical peak slightly above 170K, another indication of the high coercivity of this material. The *ac* susceptibility measured in a number of higher fields

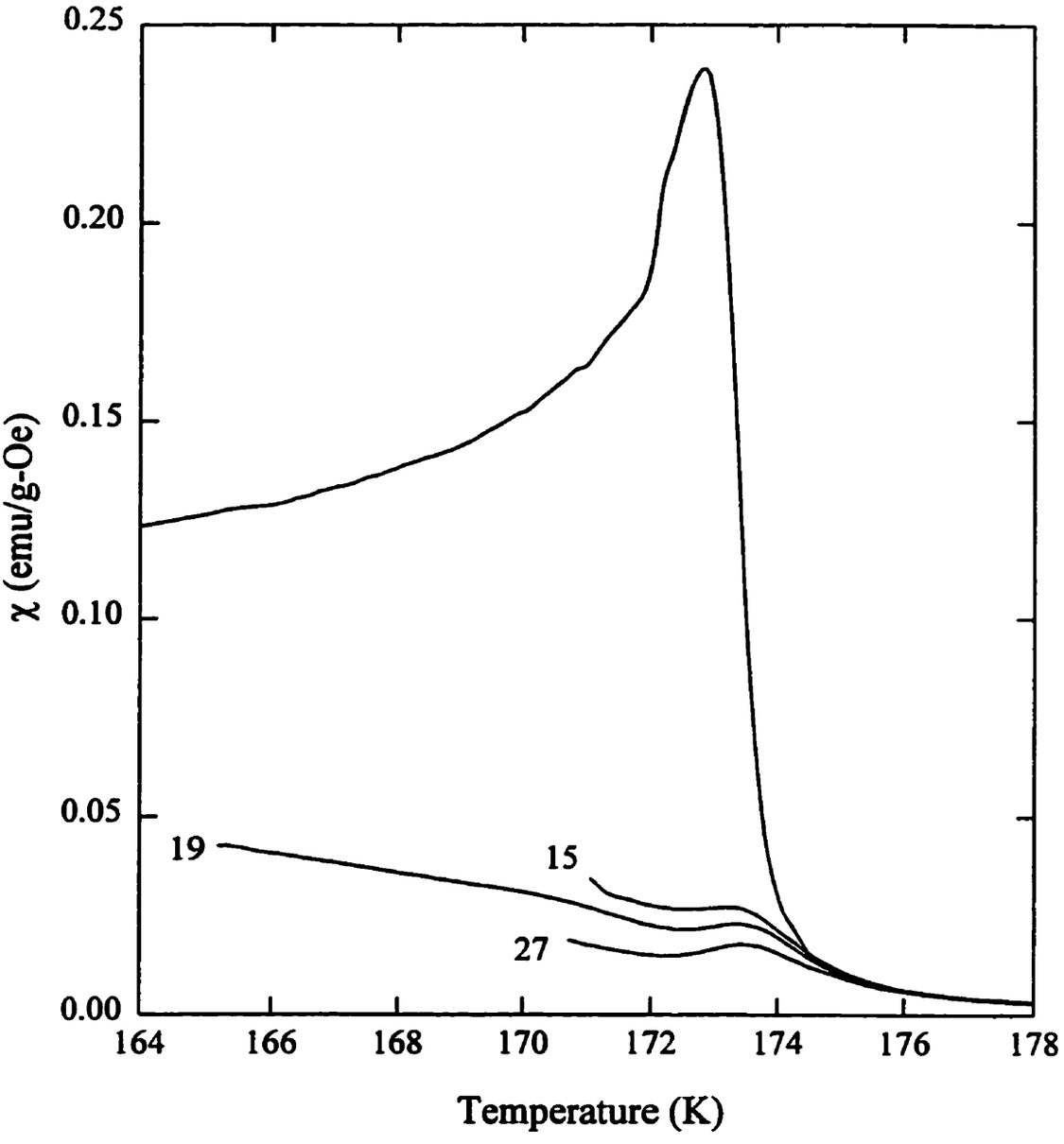

Figure 4.22: *ac* susceptibility measurements of $Pt_{90}Fe_{10}$ in zero field and a number of static internal fields, as labelled, in Oe.

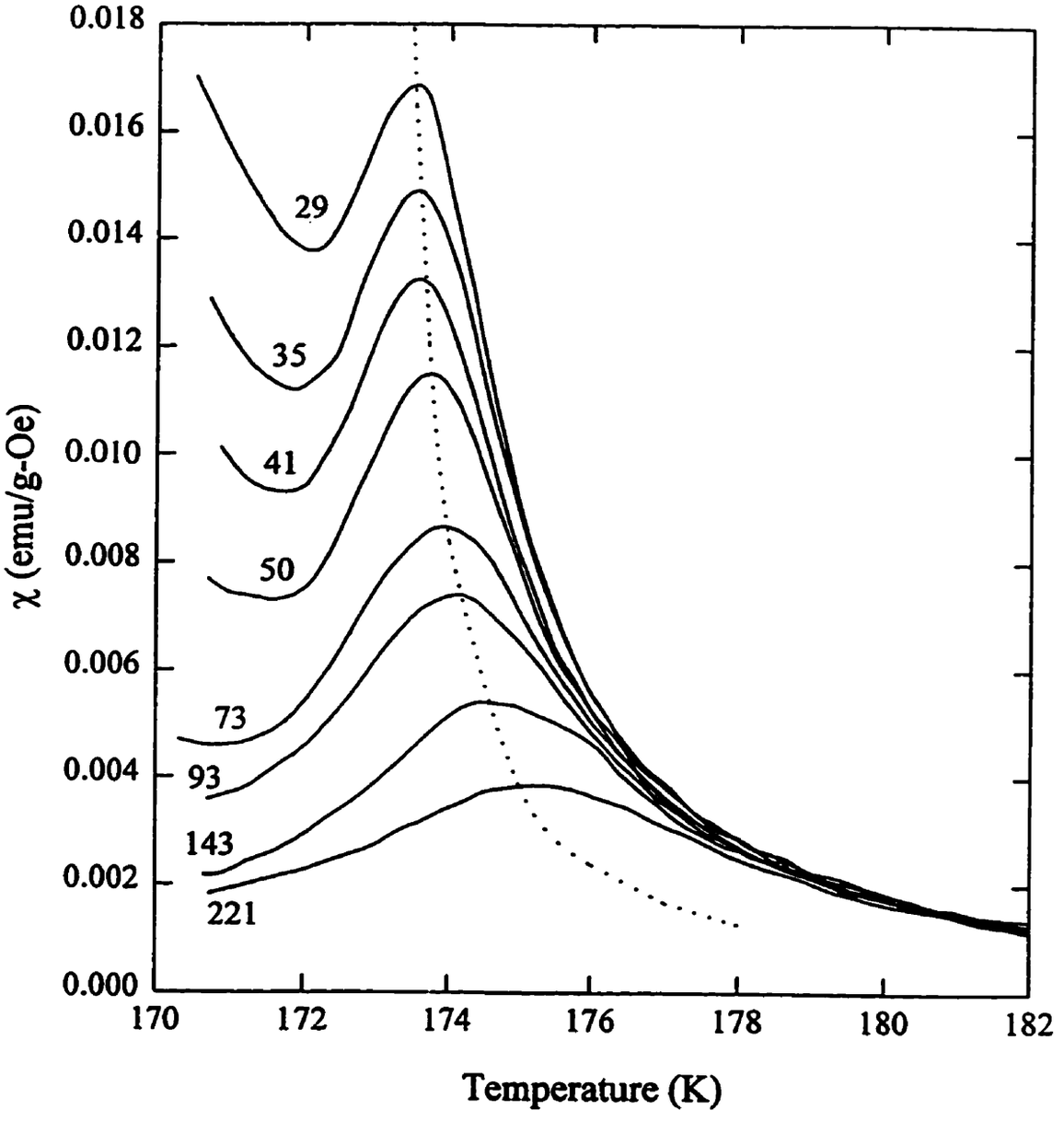

Figure 4.23: *ac* susceptibility measurements of $Pt_{90}Fe_{10}$ in a number of static internal fields, as labelled, in Oe. The dashed line is the cross-over line, a fit to $\chi_m \propto t_m^{-\gamma}$.

is shown in figure 4.23. Peak susceptibility and temperature values were extracted, and fits for the asymptotic exponents attempted as for $Fe_{91}Zr_9$+H . An approximate T_c was found by fitting T_m versus $H_i^{0.571}$, with the result T_c=172.76(1)K shown with the data in figure 4.24. Using this value for T_c, plots were done to obtain the exponents γ and $\gamma+\beta$, as explained previously. With the final value for T_c of 172.8±1.5K, the cross-over exponent was found to be $\gamma+\beta$ =1.76(1), with γ=1.31(2) (figures 4.25 and 4.26). The fits were made to all except the first point, which has a large error due to the large background contribution at low field. The effective exponent $\gamma^*(t)$ is plotted in figure 4.27. Although the values of $\gamma+\beta$ and γ are close to the 3D Heisenberg values of 1.75 and 1.386, significant amounts of curvature are present in the plots away from the critical region. The characteristic peaked structure is evident in $\gamma^*(t)$, indicating the presence of significant bond-disorder. The low t value of $\gamma^*(t)$ is well below the 3D Heisenberg value, due to the failure of the zero field susceptibility to reach its demagnetizing limit. At high t, $\gamma^*(t)$ approaches the mean field value of 1. The 'δ-plot' in figure 4.28 shows a little curvature at high field, which is common in exponent plots in disordered systems[80]. From this plot, δ was found to be 3.8(1), significantly lower than the Heisenberg value of 4.8. The curvature evident in figure 4.28 suggests that if we were able to obtain critical peaks to lower field values, the effective value for δ would be increased, although perhaps not to the 3D Heisenberg value.

Coercive Force

Butterfly loops were measured at a large number of temperatures from 120–170K, to provide estimates of the coercive field, as described for FeZr (Section 4.3.1). The coercive force, plotted in figure 4.29 as a function of temperature, is zero above 172(1) K, providing another estimate of T_c, which is in good agreement with that determined from the scaling analysis. Below T_c, H_c(T) increases rapidly, a behaviour consistent with the presence of anisotropy arising from spin-orbit coupling.

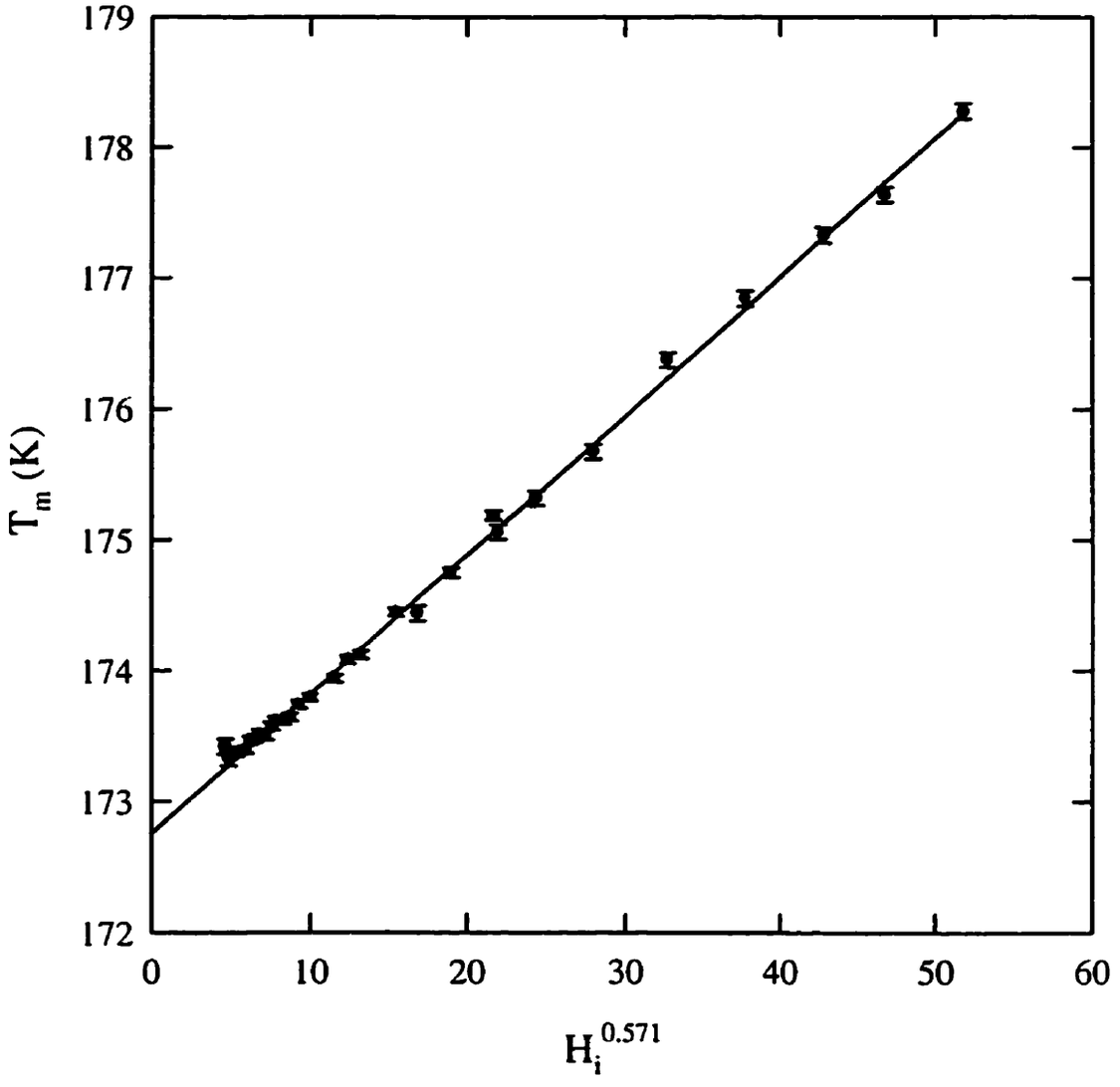

Figure 4.24: The peak temperatures plotted versus $H_i^{0.571}$ for $Pt_{90}Fe_{10}$. The best fit line gives a value for T_c of 172.76K

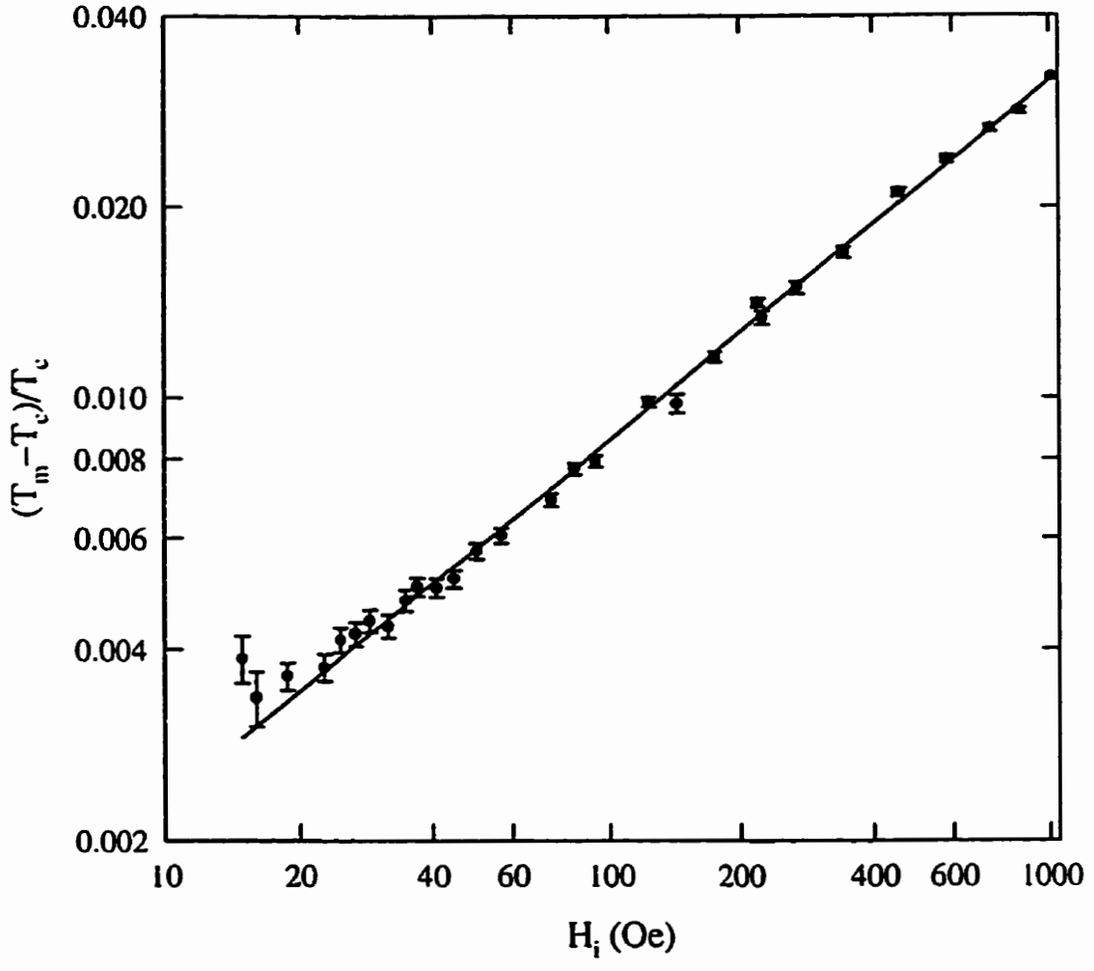

Figure 4.25: The reduced peak temperatures plotted versus H_i for $Pt_{90}Fe_{10}$. The best fit line gives a value for $1/(\gamma+\beta) = 0.567(8)$.

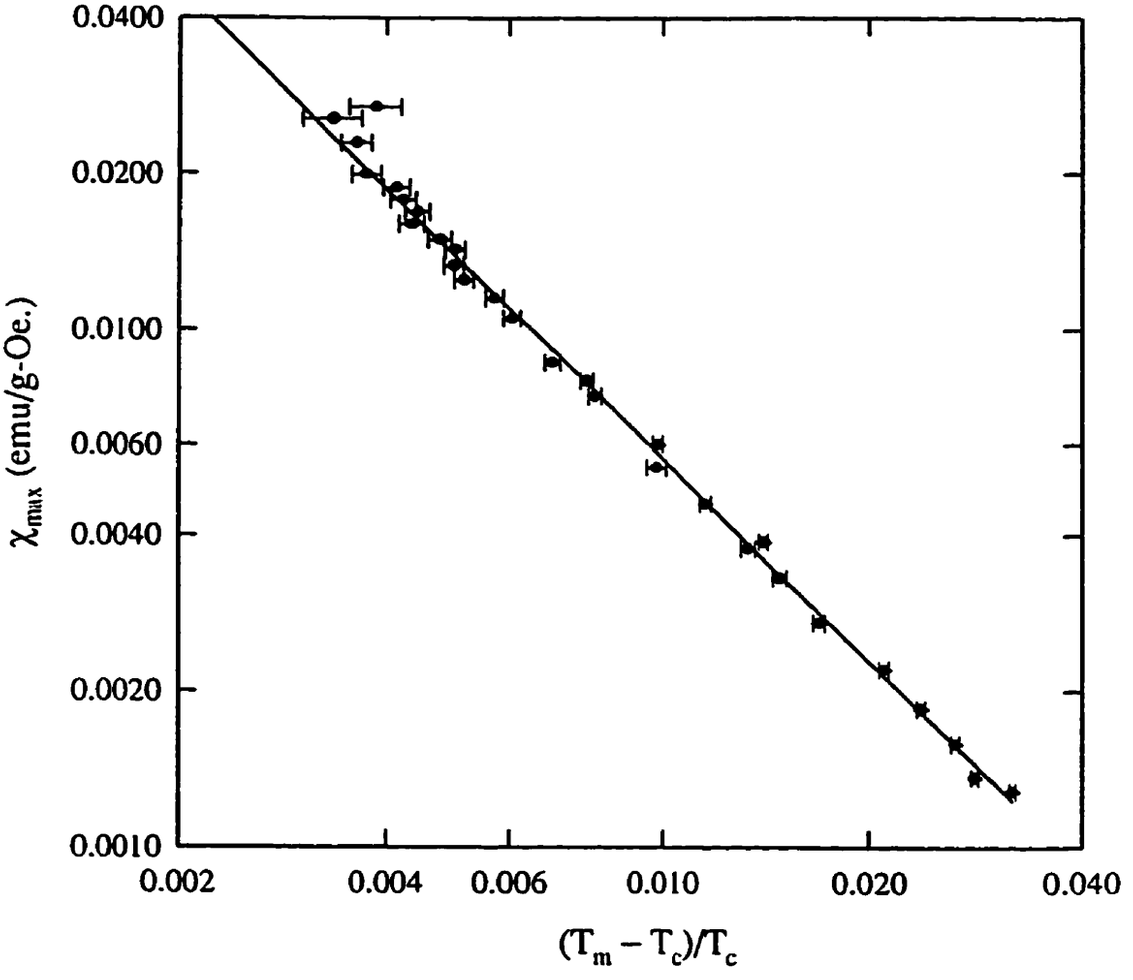

Figure 4.26: The reduced peak temperatures plotted versus the peak susceptibility for $Pt_{90}Fe_{10}$. The best fit line gives a value for γ of 1.31(2).

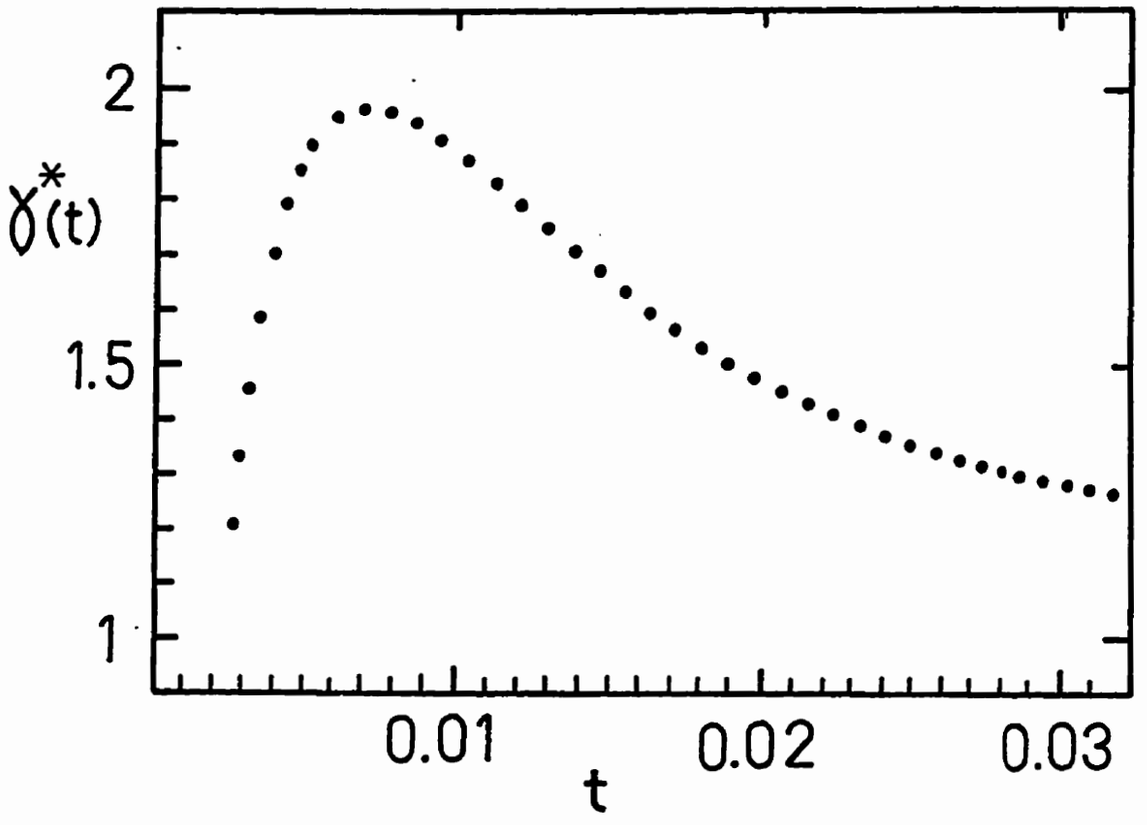

Figure 4.27: $\gamma^*(t)$ for $Pt_{90}Fe_{10}$ plotted as a function of reduced temperature with T_c=172.75 K.

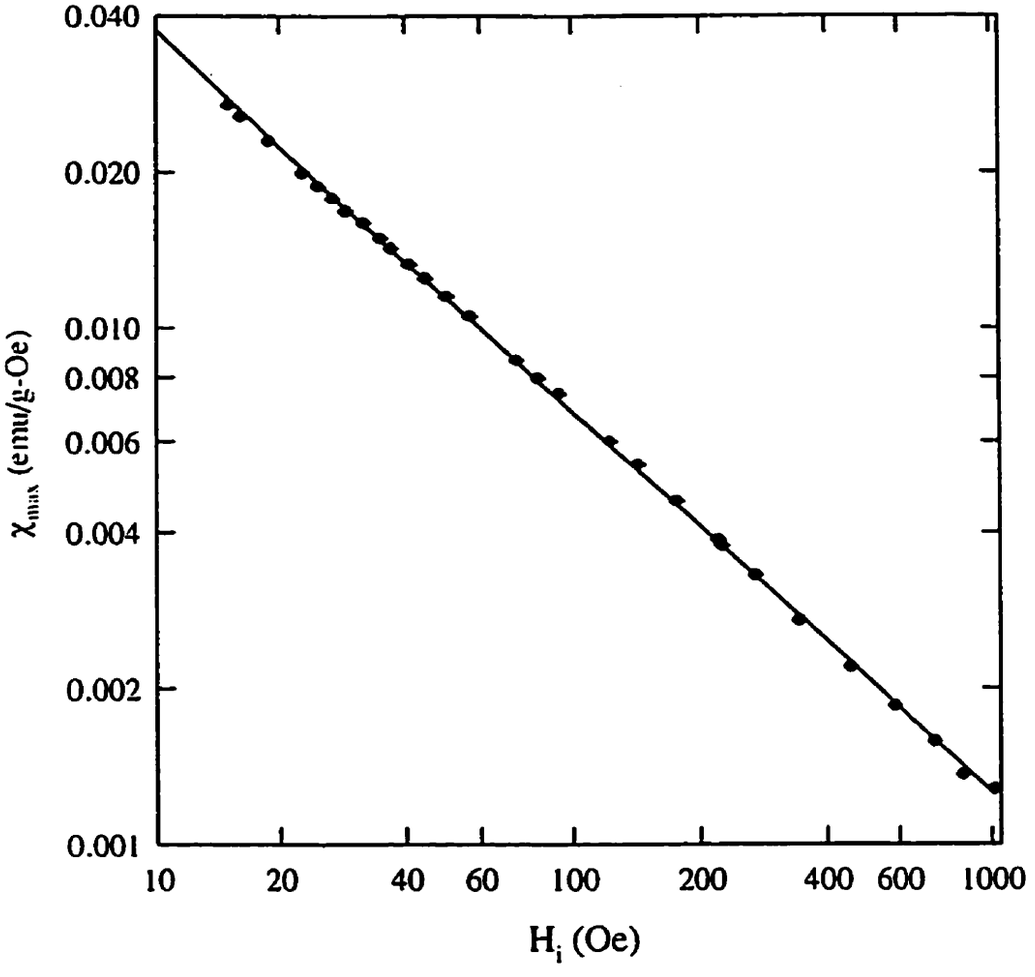

Figure 4.28: The peak susceptibility plotted as a function of internal field for $Pt_{90}Fe_{10}$. The best fit line gives δ=3.8±0.01.

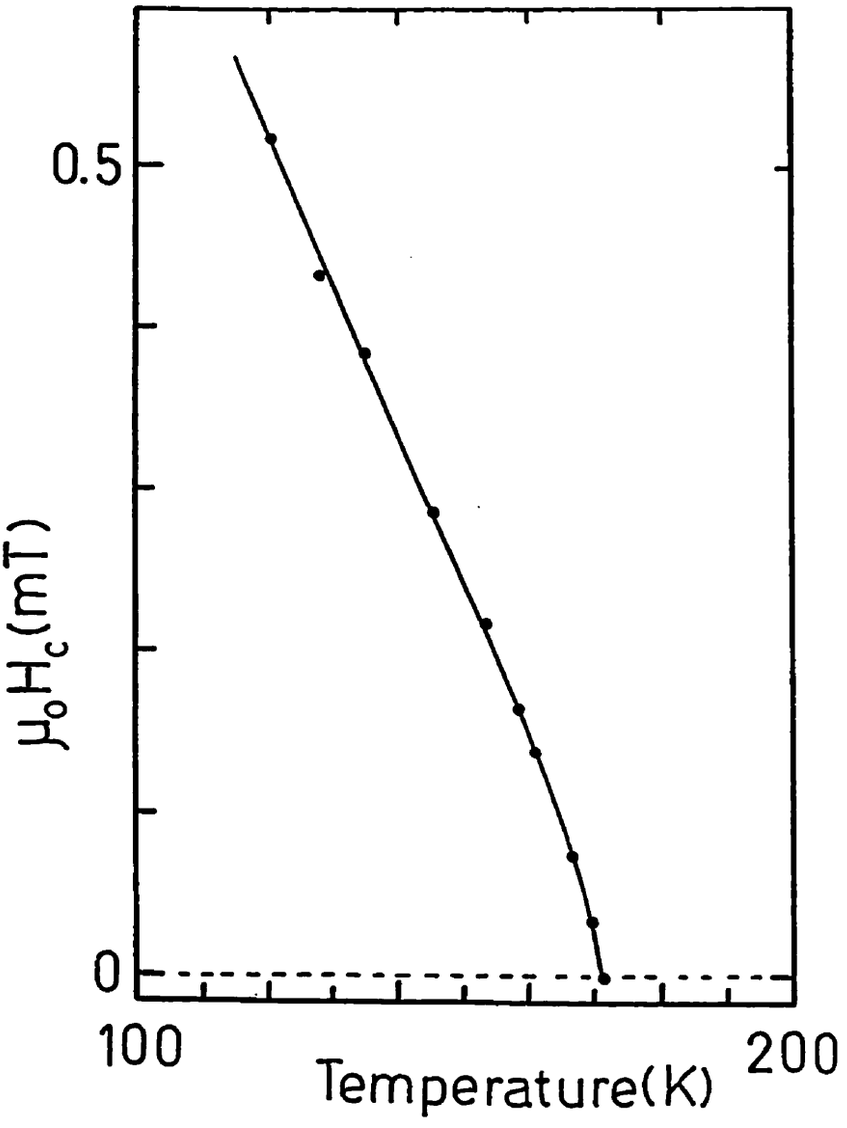

Figure 4.29: The coercive field, in Oe, as a function of temperature for $Pt_{90}Fe_{10}$.

4.4.2 Transport Measurements

Measurements of the resistivity and its temperature derivative were taken between 110 and 200 K, and plotted in figure 4.30. The resistivity shows an abrupt change in slope (a peak in $d\rho/dT$) at T_c=170±2.5K. The error incorporates the uncertainty in the absolute temperature, as well as scatter in the data itself. This estimate for T_c is in good agreement with those obtained from susceptibility measurements, which were measured in a different cryostat with different thermometry. Above T_c, $d\rho/dT$ drops rapidly to a value of 39.5 nΩ-cm/K, in agreement with that for pure Pt[83].

Magnetoresistance

Measurements of the longitudinal ($\rho_\parallel$) and transverse ($\rho_\perp$) magnetoresistance at 4.2 K are shown in figure 4.31. Both curves saturate at fields above 250 Oe, making an estimate of the SRA straightforward. Extrapolation to zero field gives an SRA of $(1.44 \pm 0.02)\%$, higher than the value of 0.7% reported previously for a lower concentration sample[84], but similar to the ~1% reported for a 16 at.% Fe sample[85]. The average magnetoresistance, $(\rho_\parallel + 2\rho_\perp)/3$ is negative, indicating that the system is not completely ordered magnetically at 4.2K.

Low Field Resistive Anisotropy

Measurements of the LFRA in $Pt_{90}Fe_{10}$ were measured as a function of temperature in the vicinity of T_c in a number of fixed fields. A typical curve is shown in figure 4.32. This curve is a plot of $(\rho_\parallel(T) - \rho_\perp(T))/\rho(T)$ versus temperature, using the measurements of $\rho(0,T)$ obtained previously.

The LFRA is zero above 170±1.5K, giving another estimate for T_c which agrees quite well with our previous estimates. Below T_c, the LFRA increases linearly as in FeZr; however, as the temperature is decreased further, the curve begins to saturate. This effect could be due to the same domain size effects which may be the cause of the variation with field in FeZr. This hypothesis is also supported by the data in figure 4.33, a summary of the LFRA in different fixed fields. The LFRA saturates

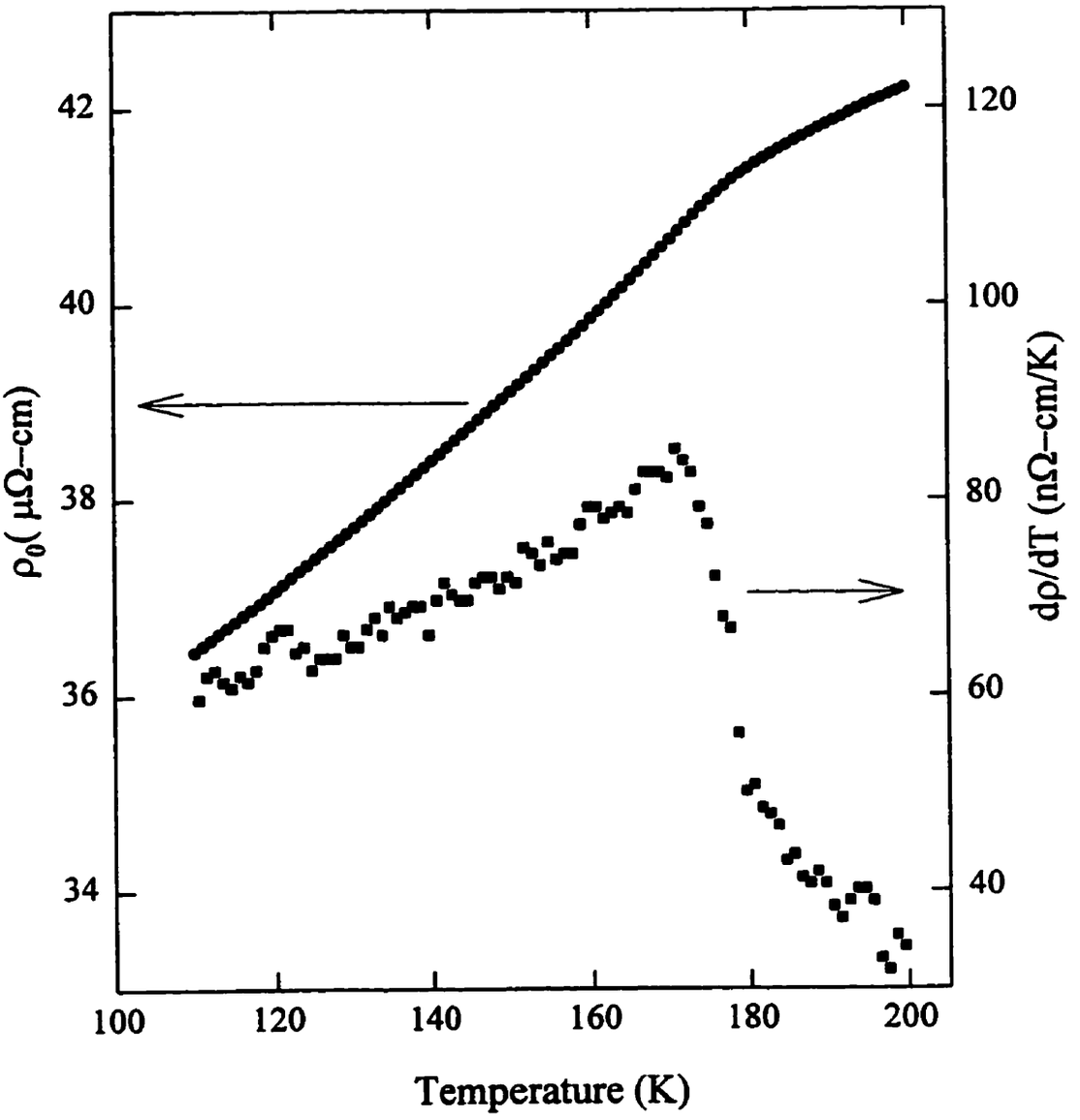

Figure 4.30: The resistivity and its temperature derivative for $Pt_{90}Fe_{10}$. The peak in $d\rho/dT$ is at 170± 2.5K.

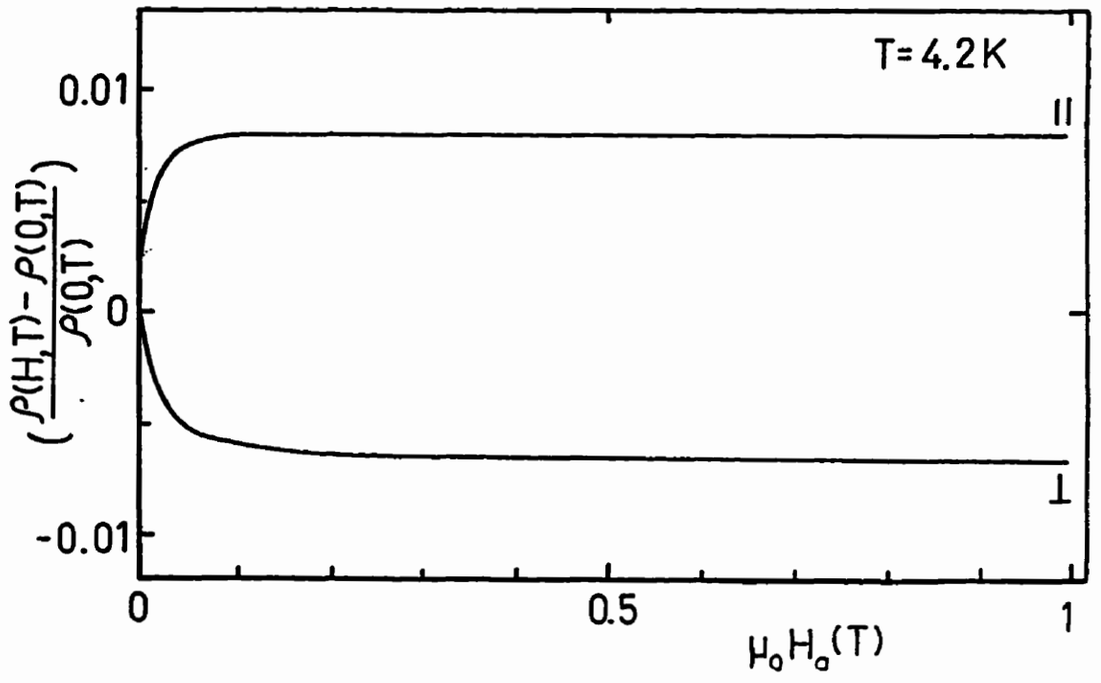

Figure 4.31: Magnetoresistance of $Pt_{90}Fe_{10}$ at 4.2K.

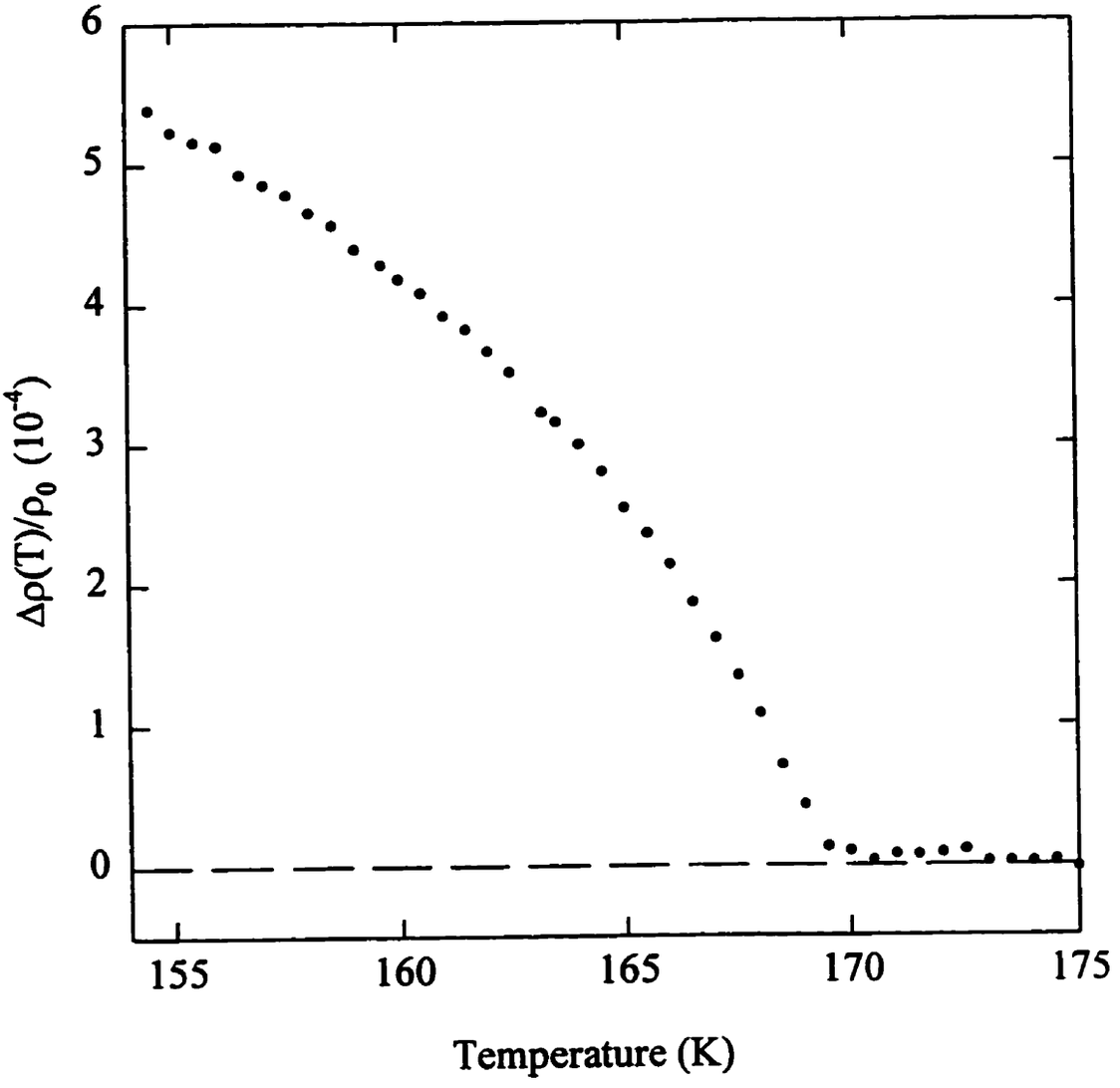

Figure 4.32: Low field resistive anisotropy of $Pt_{90}Fe_{10}$ in a static biasing field of 60 Oe.

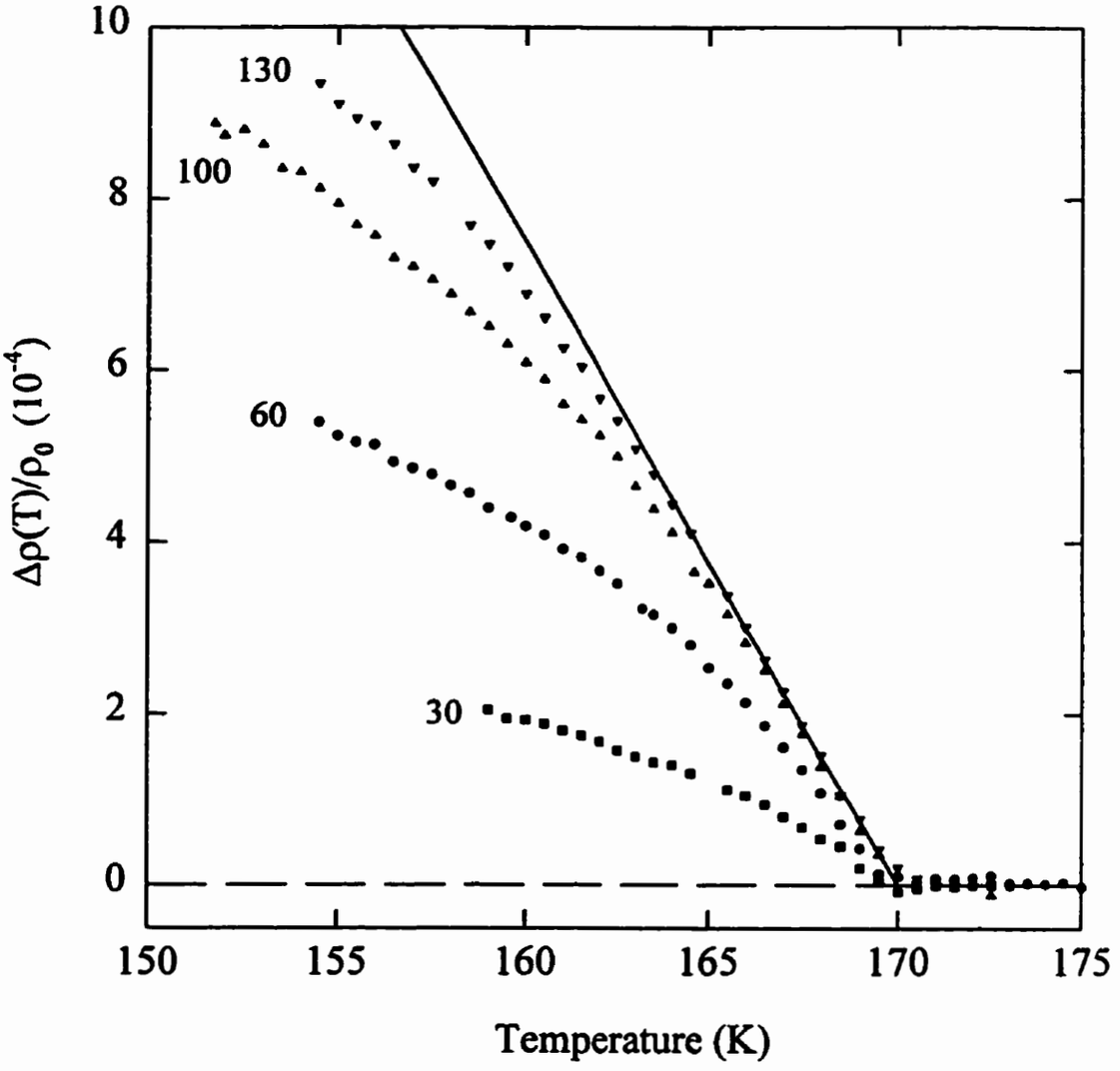

Figure 4.33: Comparison of the LFRA in $Pt_{90}Fe_{10}$ in a number of static biasing fields, as labelled, in Oe.

at higher anisotropy and lower temperatures in the higher applied fields, when the magnetic energy is able to overcome the anisotropy energy to lower temperatures. Near T_c, however, all the curves fall on approximately the same line, allowing the determination of T_c, and a unique slope.

4.4.3 Summary

Measurements of the *ac* susceptibility of $Pt_{90}Fe_{10}$ show strong evidence of the presence of an orbital moment at the Fe site. The presence of significant disorder is also obvious from the behaviour of the effective exponents outside the critical region. The resistivity shows evidence of a transition to a ferromagnetic ground state as the temperature is lowered through 170 K. Magnetoresistance measurements show a positive SRA, an indication of spin-orbit coupling. The LFRA is linear in the vicinity of T_c, in agreement with model predictions with deviations due to technical considerations at lower temperature.

4.5 $Pd_{97}Co_3$

χ_{ac}(H,T) was measured for the $Pd_{97}Co_3$ sample to characterize its critical behaviour, and to obtain values for the coercivity, as in PtFe. Various transport measurements were completed to supplement the information obtained from the magnetic measurements.

4.5.1 AC Susceptibility Measurements

Temperature Sweeps

A detailed study of the temperature dependent susceptibility was done in zero field and a number of static biasing fields. Figure 4.34 shows the behaviour of the susceptibility in zero field measured with two different driving fields, 35 and 50 mOe rms. There is some structure in the Hopkinson peak below T_c in the 35 mOe run, which is significantly decreased in the 50 mOe run. This structure is likely due to the presence of weak domain wall pinning which is overcome in the larger *ac*

field. The effect of small static biasing fields is shown in figure 4.35. A field of 60 Gauss was needed to detect a critical peak, which is an indication of the presence of considerable anisotropy, as discussed previously. The high field behaviour is shown in figure 4.36. These data were measured using a driving field of 35 mOe.

The critical peak heights and temperatures were extracted from this data, and the critical point exponents determined using the analysis method given previously. The initial estimate for T_c was found, with the linear fit shown in figure 4.37. The low field points have large errors, due to the large background present at these fields, and the resulting lack of definition of the critical peak. The peaks at higher fields are better defined, but are further from the critical point. This causes problems in the analysis for the critical exponents, as can be seen in the now familiar log-log plots. The fit for the low-field γ is shown in figure 4.38. A large amount of curvature can be noted in this plot, an indication of significant disorder and anisotropy. A fit to the first 10 field points gave a value for $\gamma = 1.0(1)$, although the 3D Heisenberg value for γ also seemed to fit quite well, within the considerable scatter. The same problem is apparent in the cross-over plot, figure 4.39, which gives a best-fit of $1/(\gamma+\beta)$=0.57(1). $\gamma^*(t)$ was determined by taking the derivative of the zero field curve. Again the peaked structure which is a signature of bond disorder is present in figure 4.40. At low temperatures, $\gamma^*(t)$ drops well below 1.386, an indication of the presence of anisotropy, as stated previously. At high t, $\gamma^*(t)$ approaches a mean field value of 1. The δ plot also shows significant curvature, with a low field fit of δ=3.1$\pm$0.1, much lower than the 3D Heisenberg value of 4.8. The curvature present suggests an increase in the effective δ at lower fields; if it were possible to determine critical peaks at lower field, a more appropriate value for δ might be found.

Coercive Field

Measurements of the coercive field were completed as a function of temperature below T_c. A typical butterfly plot is shown in figure 4.42. The values for $H_c(T)$ are plotted in figure 4.43. As in the previous sample, $H_c(T)$ increases rapidly below T_c. Coercive field measurements give a value for T_c of 137$\pm$ 1K, in good agreement

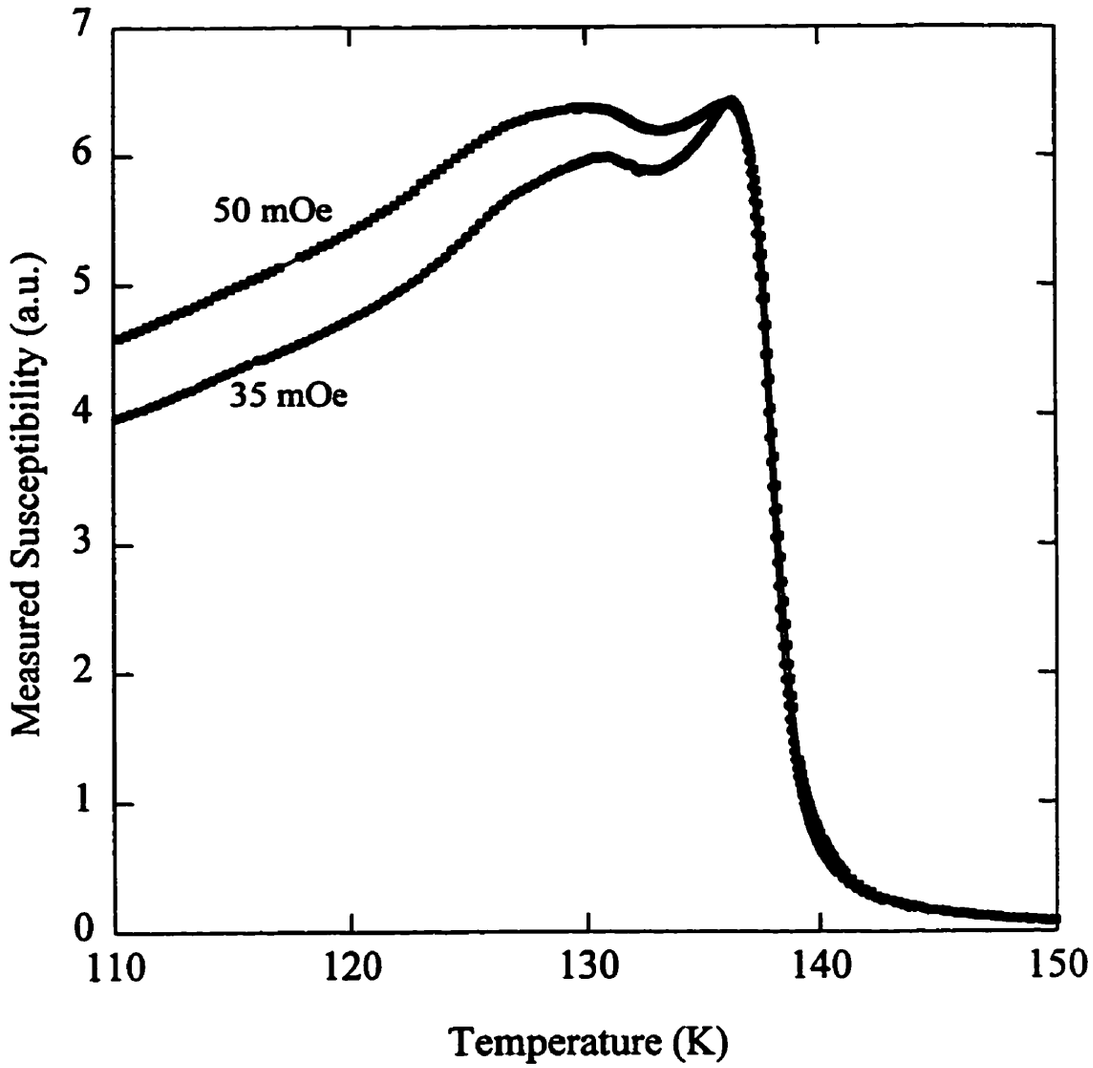

Figure 4.34: The zero field *ac* susceptibility of $Pd_{97}Co_3$ in two *ac* measurement fields, as labelled.

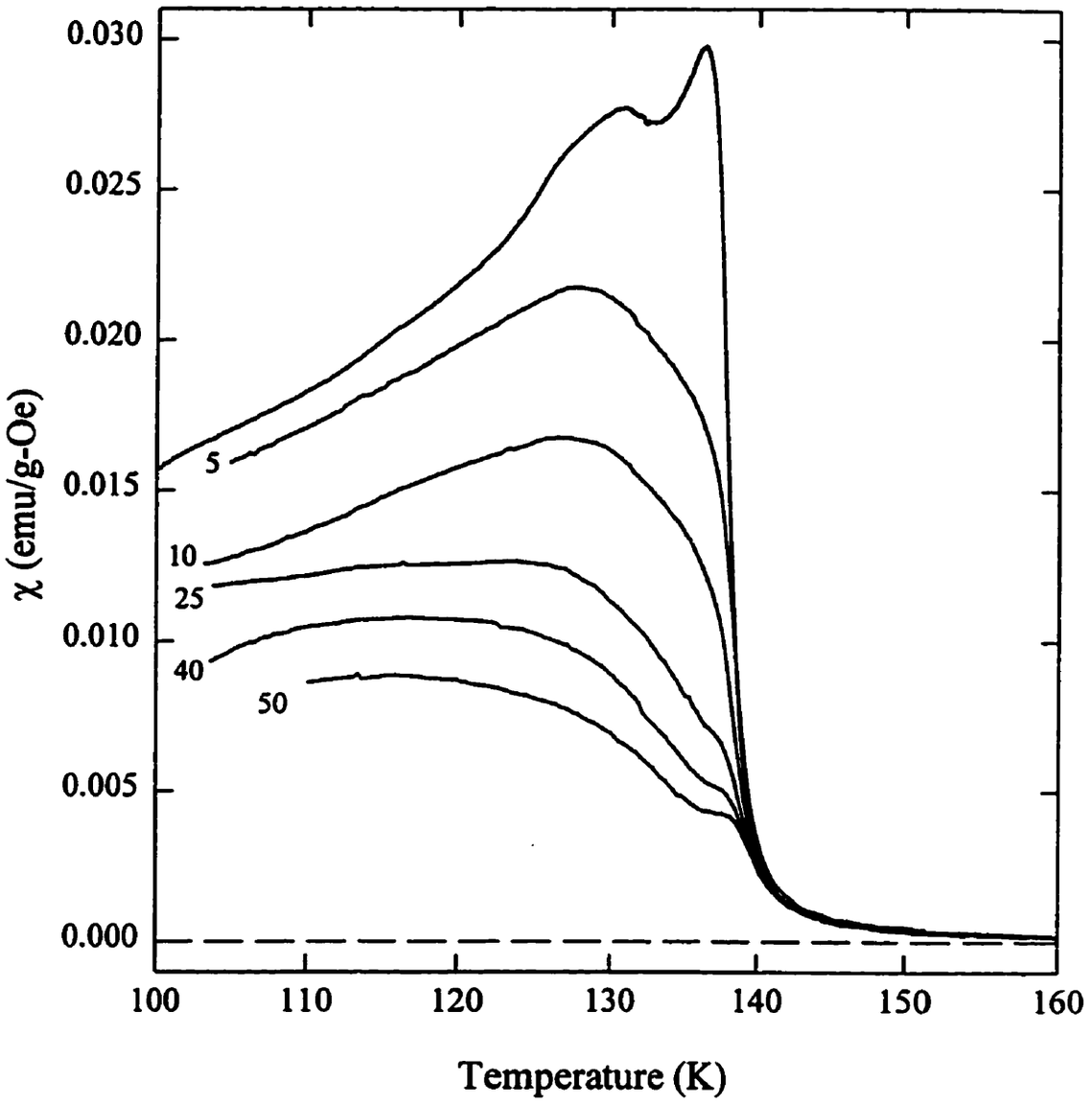

Figure 4.35: *ac* susceptibility measurements of $Pd_{97}Co_3$ in zero field and a number of static internal fields, as labelled, in Oe.

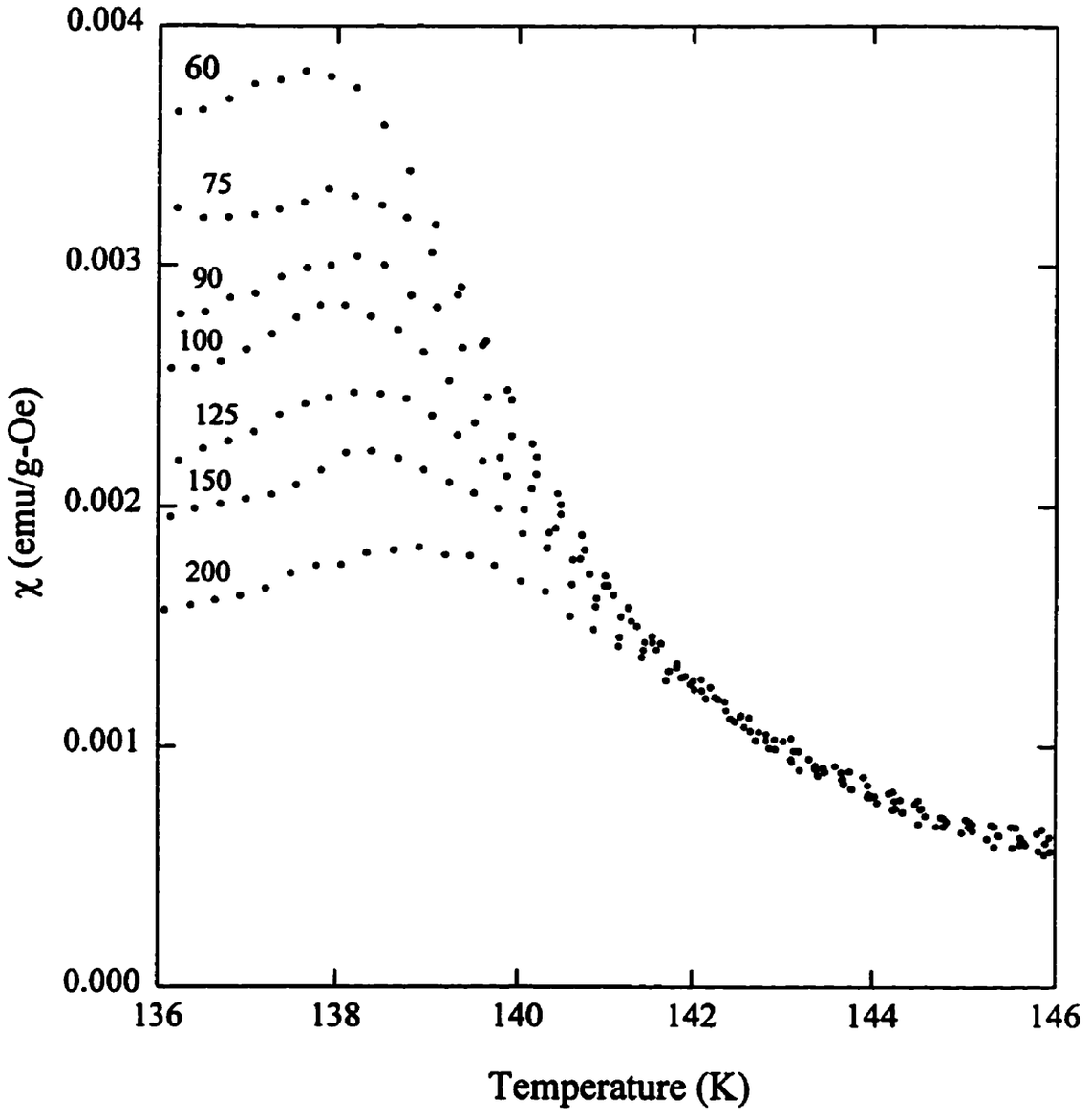

Figure 4.36: *ac* susceptibility measurements of $Pd_{97}Co_3$ in a number of biasing fields, as labelled, in Oe.

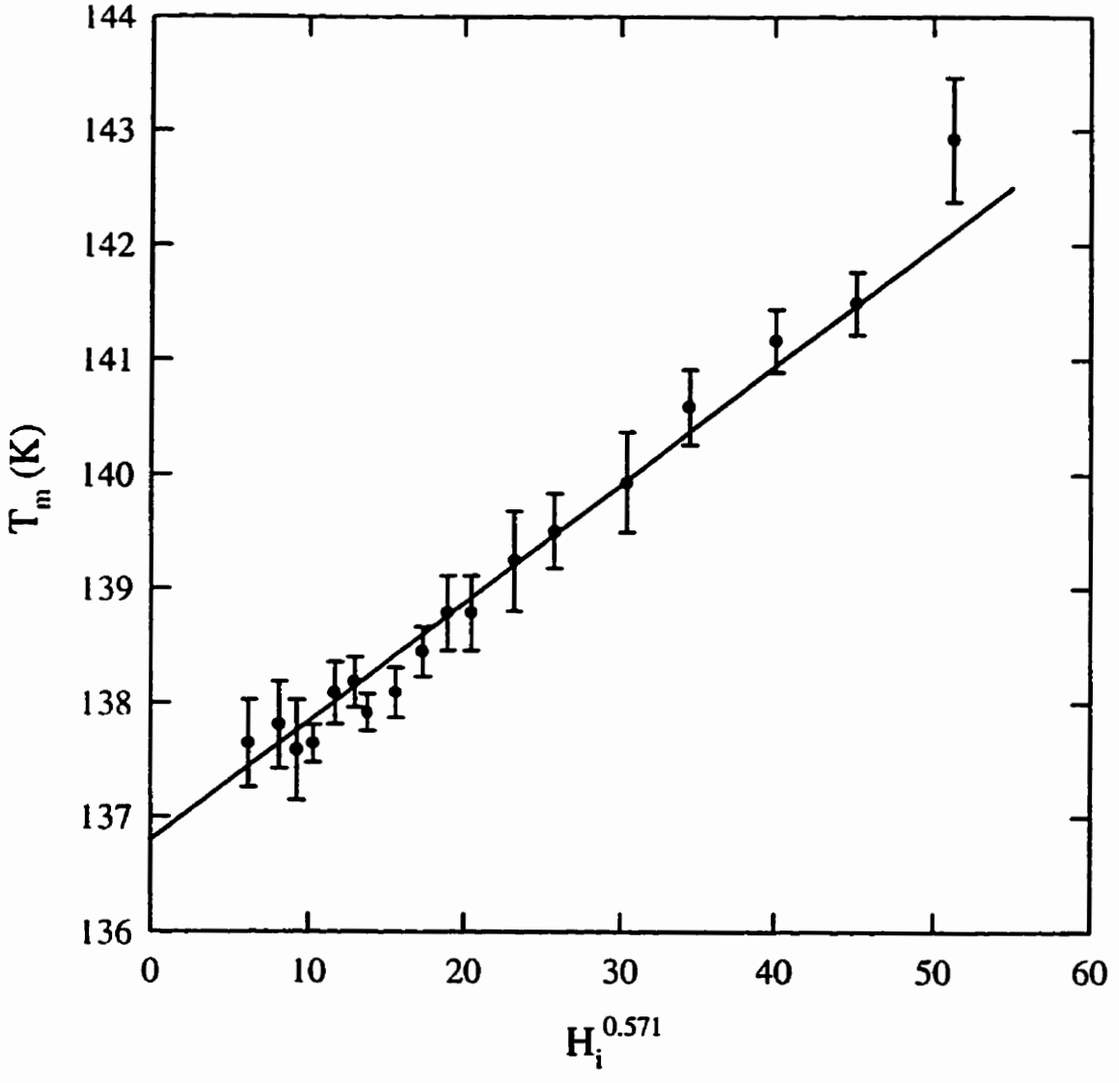

Figure 4.37: The peak temperatures plotted versus $H_i^{0.571}$ for $Pd_{97}Co_3$. The best fit line gives a value for T_c of 136.8(1)K.

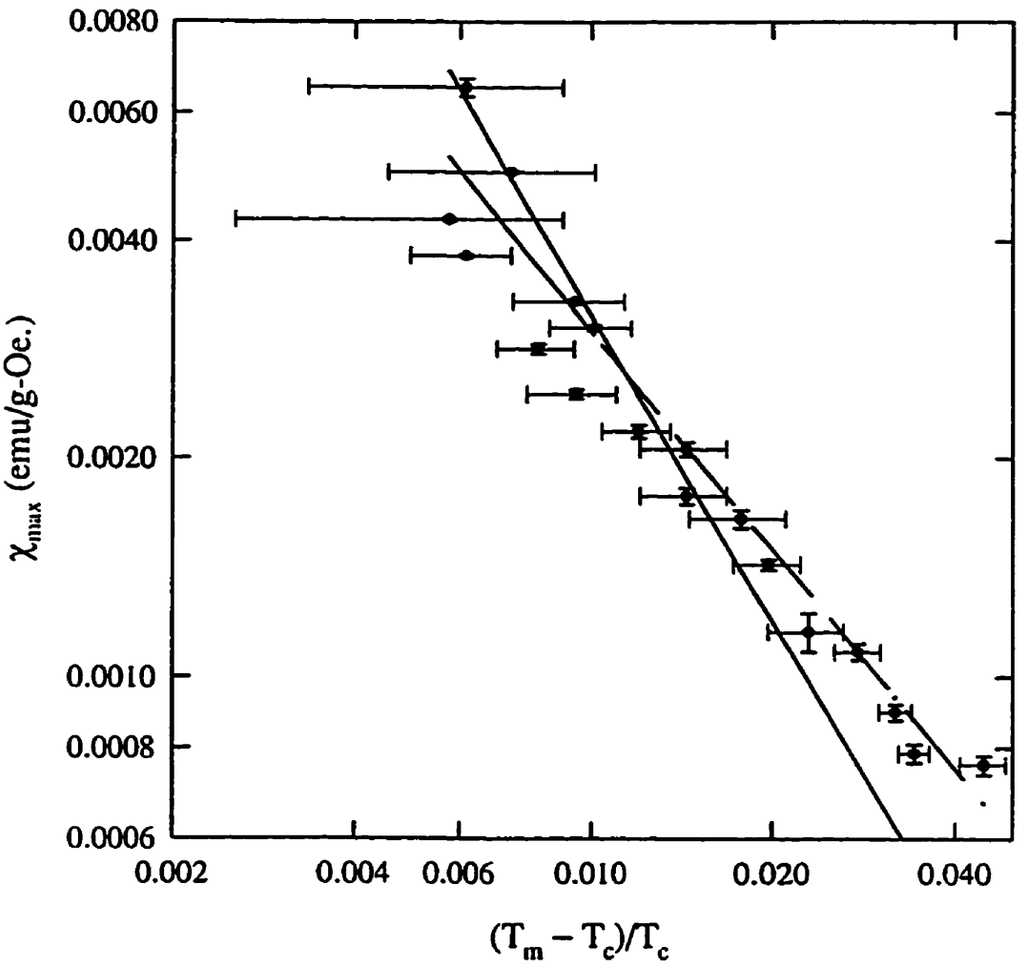

Figure 4.38: The peak susceptibility plotted versus the reduced peak temperature for $Pd_{97}Co_3$. The best fit line gives a value for γ of 1.0(1). The dotted line indicates the 3D Heisenberg prediction for γ.

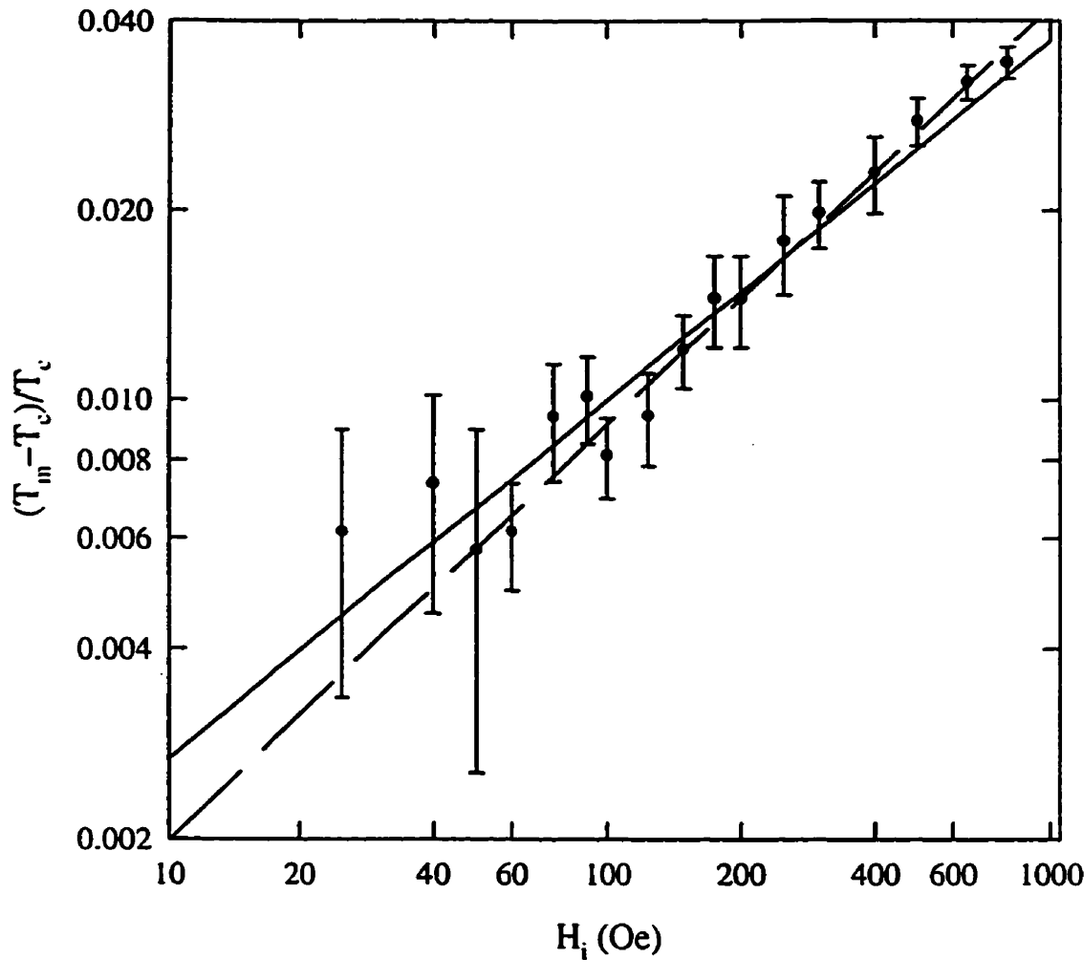

Figure 4.39: The reduced peak temperatures plotted versus H_i for $Pd_{97}Co_3$. The solid line shows the Heisenberg value for $1/(\gamma+\beta)$=1.75, while the dotted line is the mean field, $1/(\gamma+\beta)$=0.57.

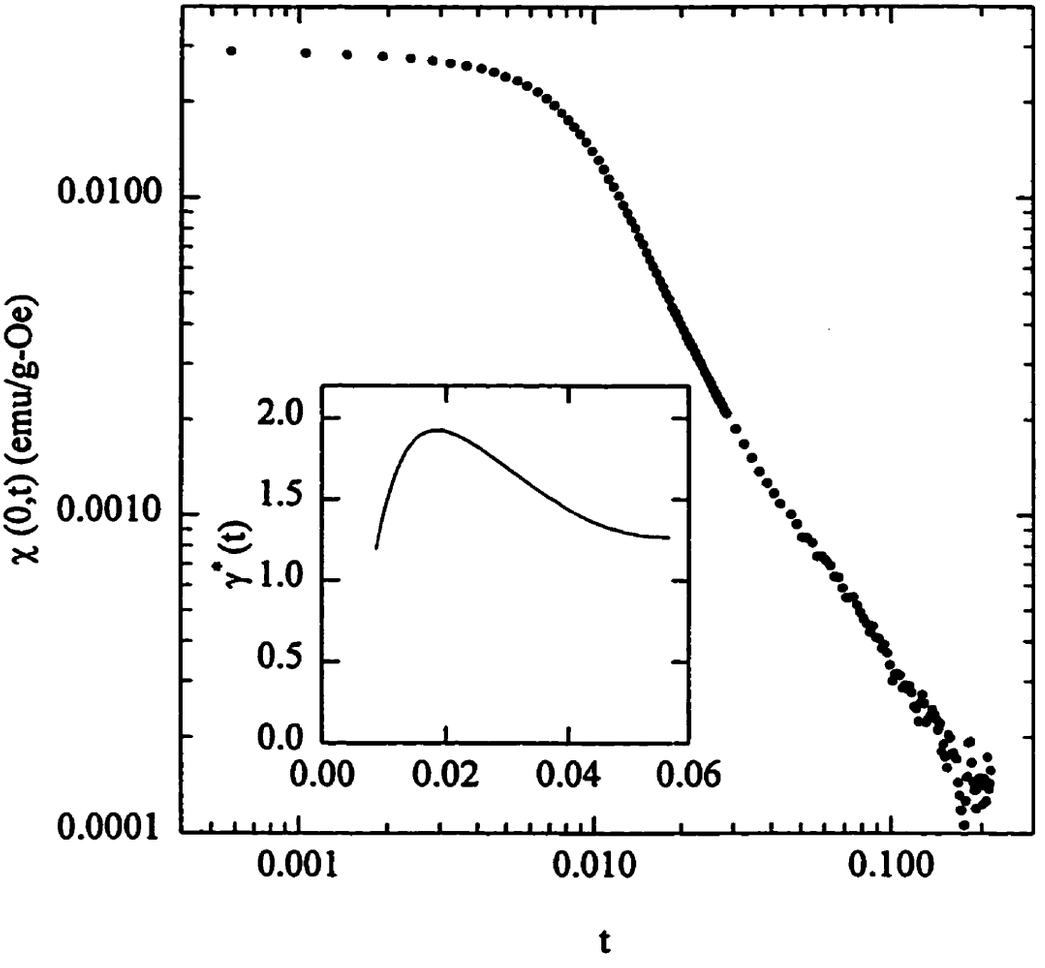

Figure 4.40: $\chi(0,T)$ plotted as a function of reduced temperature on a log-log scale. The inset shows $\gamma^*(t)$ plotted as a function of reduced temperature.

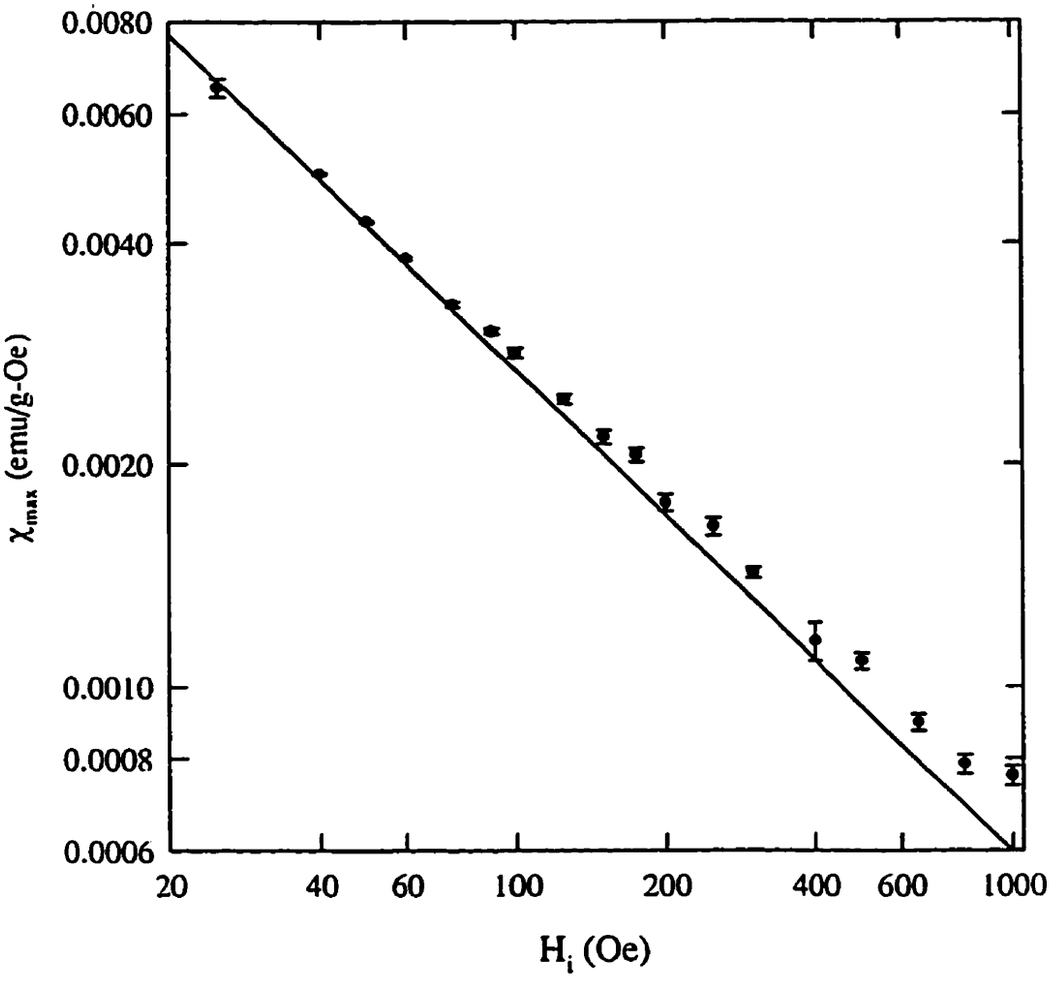

Figure 4.41: The peak susceptibility plotted as a function of internal field. The best fit line gives δ=3.1(1).

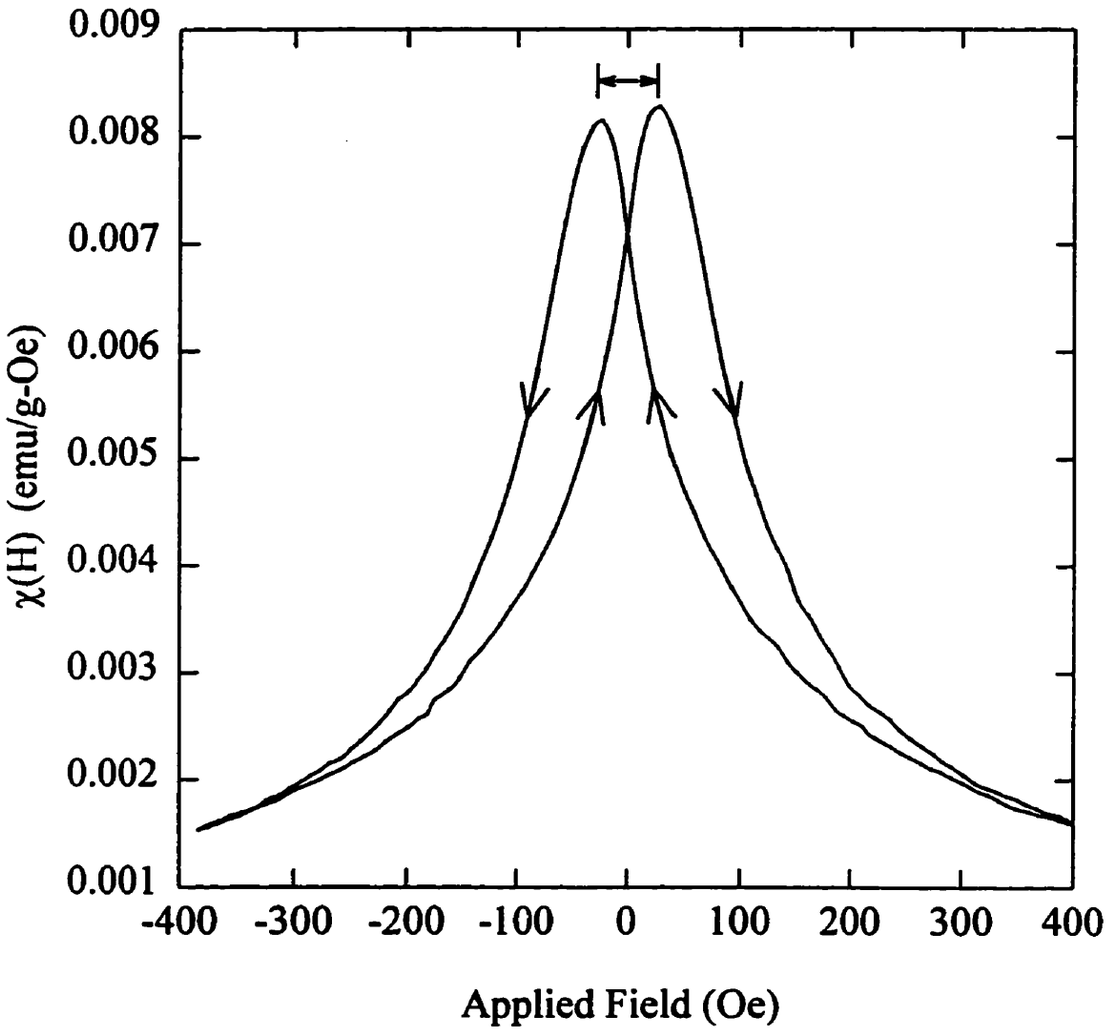

Figure 4.42: The field dependence of the *ac* susceptibility of $Pd_{97}Co_3$ at T=77K.

with that from the temperature sweeps. The presence of spin-orbit coupling can be inferred from the strong temperature dependence of the anisotropy (H_c).

4.5.2 Transport Measurements

The temperature dependence of the resistivity of $Pd_{97}Co_3$ is shown in figure 4.44. The sharp change in slope at 136^{+1}_{-2}K gives a value for T_c in agreement with the susceptibility measurements. The derivative of the resistivity has a peak at T_c, and drops rapidly above T_c to a value of 5nΩ-cm/K, slightly smaller than that for pure Pd at the same temperature[83].

Magnetoresistance

The field dependence of the resistivity of $Pd_{97}Co_3$ at 4.2K in the longitudinal and transverse configurations is shown in figure 4.45. As in $Pt_{90}Fe_{10}$, the average magnetoresistance is negative, indicating the presence of some magnetic disorder. The curves saturate at low field, giving an estimate for the SRA of $\Delta\rho/\rho = 1.70(5)\%$, in good agreement with previous results[86].

Low field resistive anisotropy

The LFRA was measured as a function of temperature in fields of 30, 60, 100 and 125 Oe. The 60 Oe curve is shown in figure 4.46, again plotted as $(\rho_{\parallel}(H,T) - \rho_{\perp}(H,T))/\rho(0,T)$. The LFRA is non-zero below T_c=137(1)K, a value for T_c in excellent agreement with the other methods. Below T_c the anisotropy shows similar behaviour to that in the $Pt_{90}Fe_{10}$, saturating at low temperatures. A comparison between the different field sweeps (figure 4.47) shows additional similarities, suggesting that in this sample as well, the anisotropy induced by spin-orbit coupling could be large enough to dominate the magnetic energy at low temperature, thus decreasing the observed LFRA.

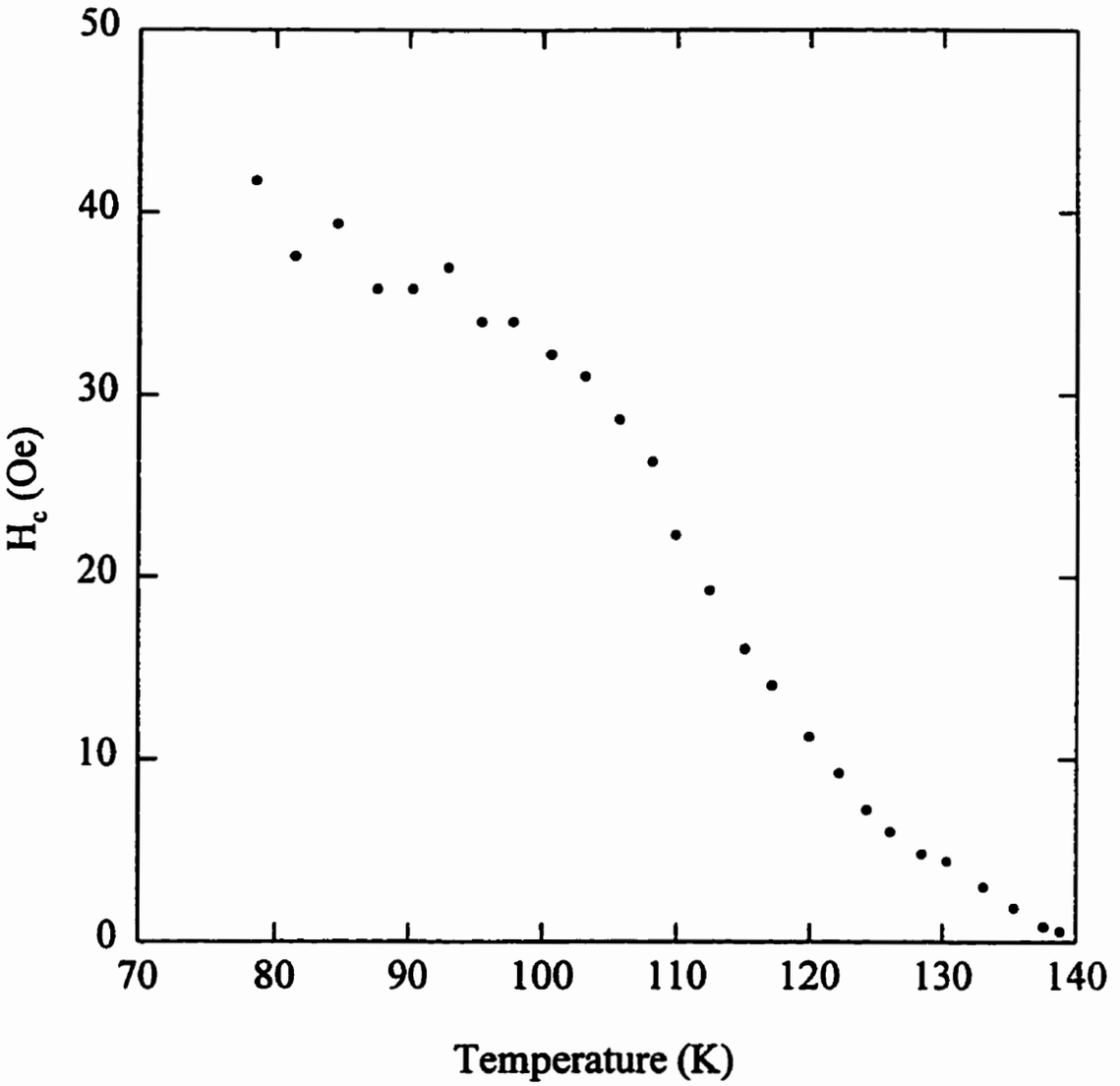

Figure 4.43: The temperature dependence of the coercive field in $Pd_{97}Co_3$.

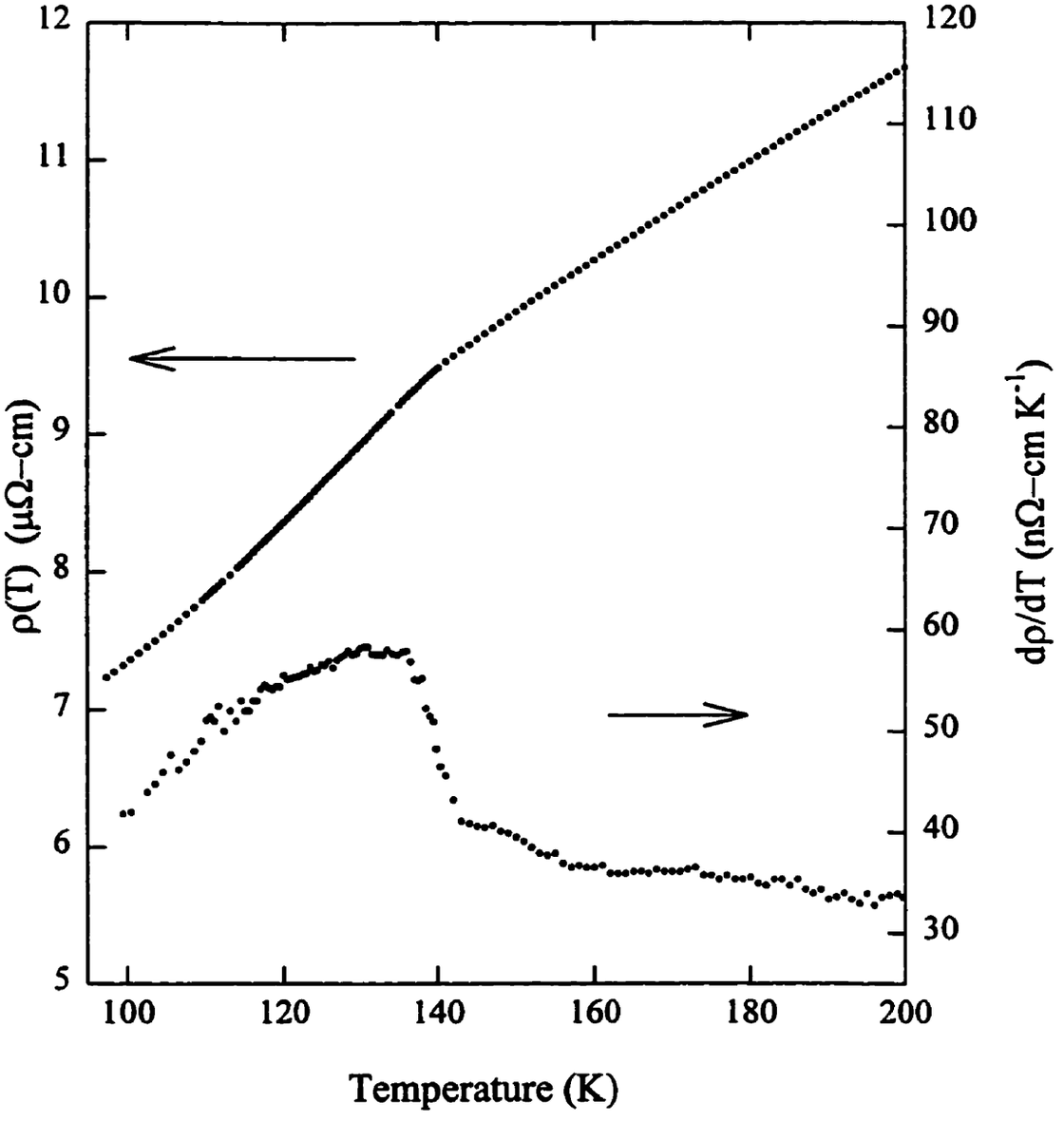

Figure 4.44: The resistivity and its temperature derivative for $Pd_{97}Co_3$. The peak in $d\rho/dT$ is at 136^{+1}_{-2}K.

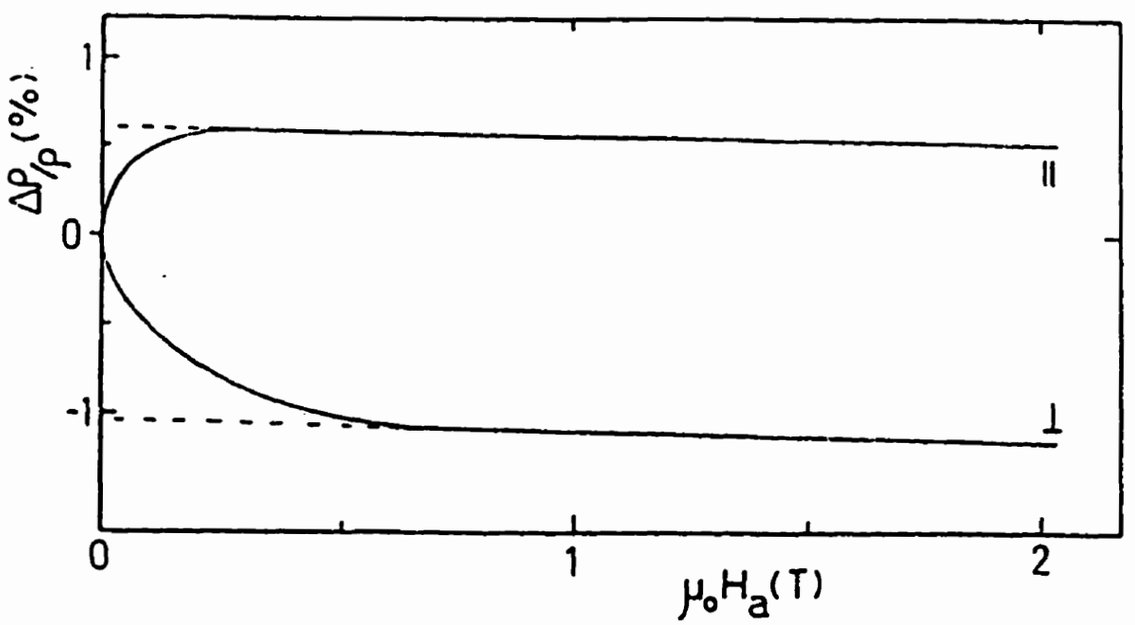

Figure 4.45: The magnetoresistance of $Pd_{97}Co_3$ at 4.2K in the longitudinal ($\rho_{\parallel}$) and transverse ($\rho_{\perp}$) modes.

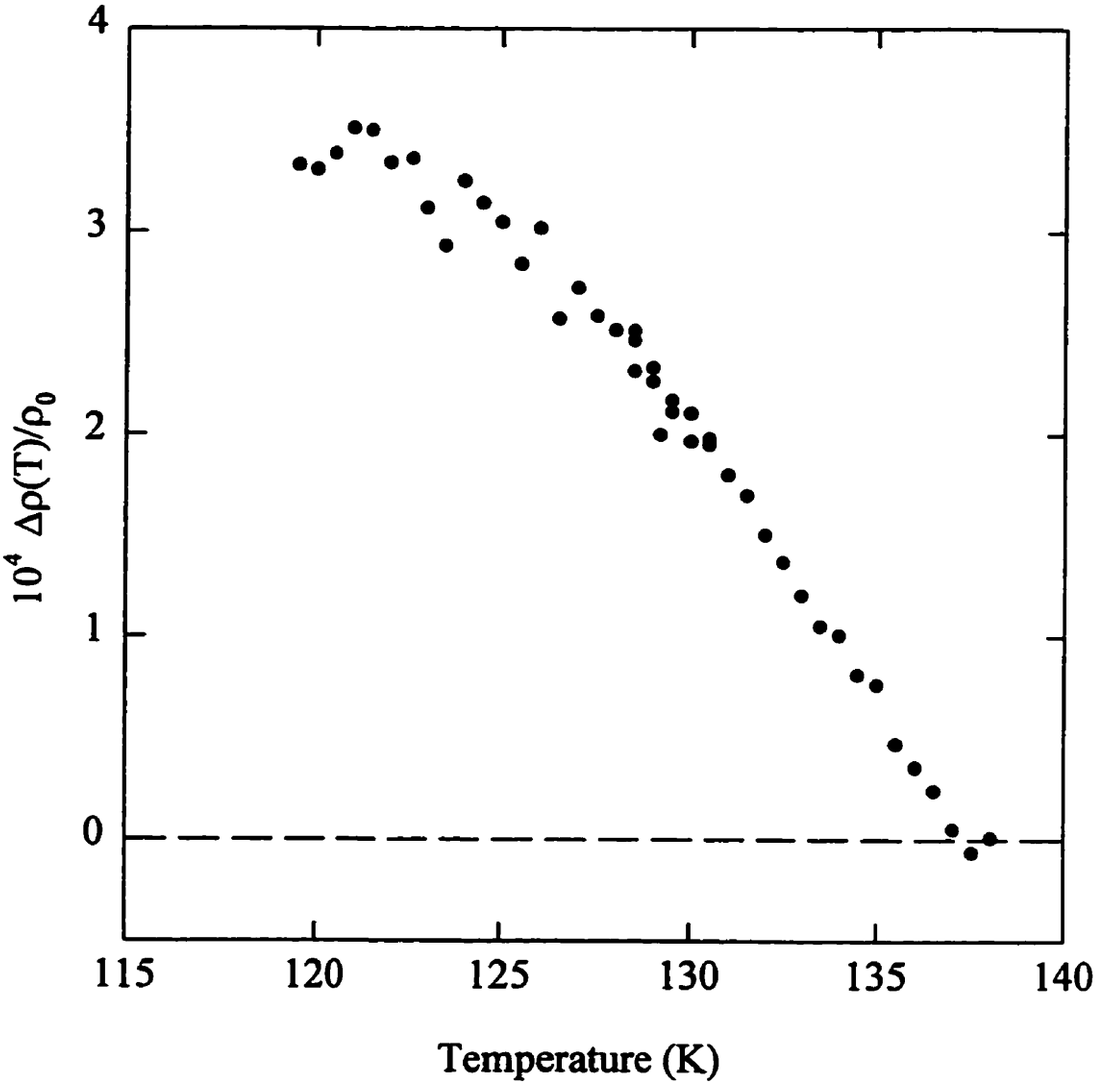

Figure 4.46: Low field resistive anisotropy of $Pd_{97}Co_3$ in a static biasing field of 60 Oe.

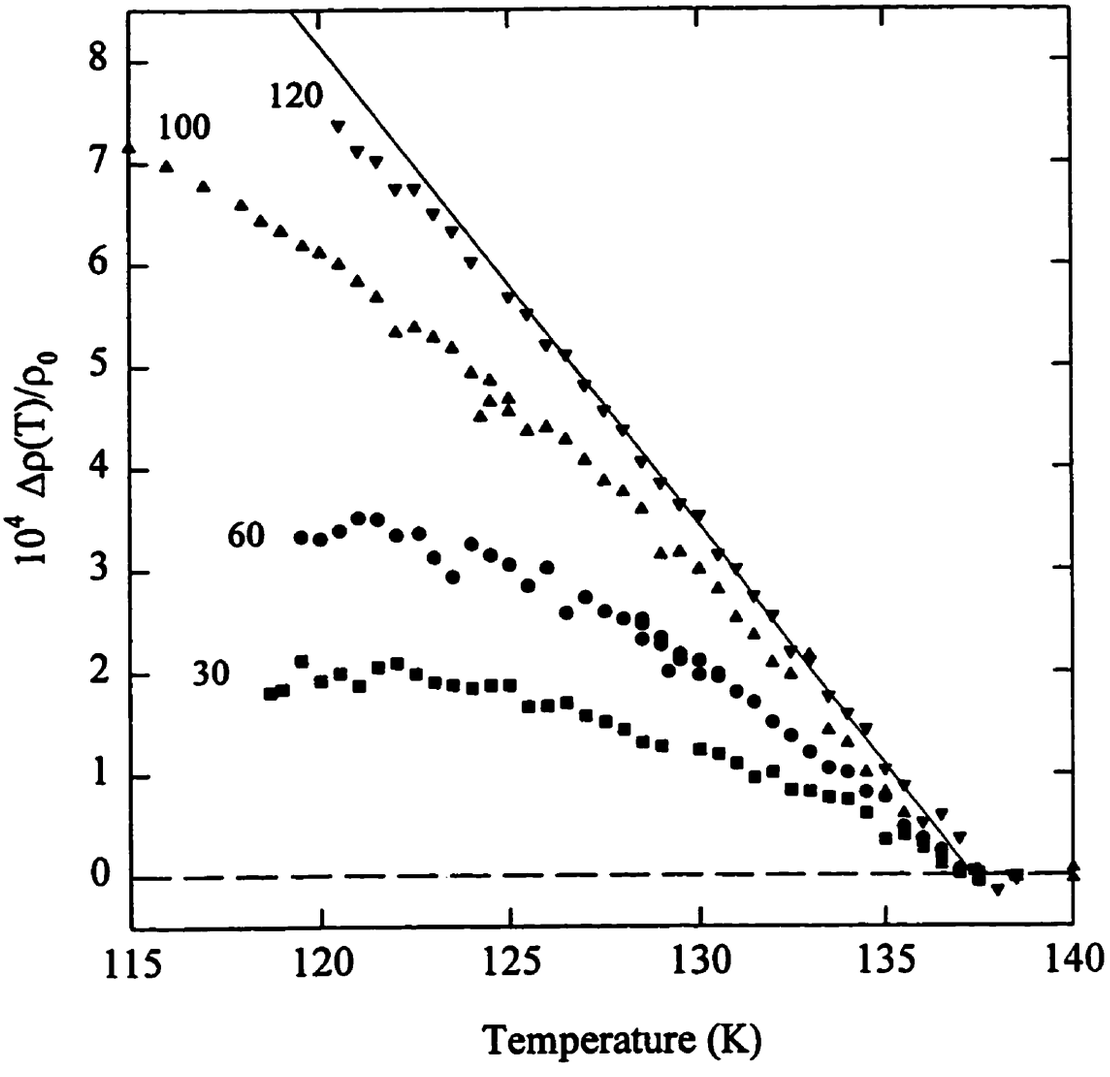

Figure 4.47: Comparison of the LFRA in $Pd_{97}Co_3$ in a number of static biasing fields, as labelled, in Oe.

4.5.3 Summary

The $Pd_{97}Co_3$ sample shows the presence of large amounts of disorder. This disorder, in conjunction with the high anisotropy complicates the evaluation of the true critical exponents. In fact, from the susceptibility data, we conclude that 3D Heisenberg or mean field exponents are equally likely. The resistivity measurements show the structure typical for the transition to a ferromagnetic state. Magnetoresistance and LFRA measurements confirm the existence of an orbital moment at the Co sites.

4.6 Conclusion

Susceptibility measurements show that all of the bond-disordered systems measured above have a transition to a ferromagnetic state from the paramagnetic state as the temperature is reduced. The presence of spin-orbit coupling at the magnetic sites is deduced from the coercivity and its rapid increase with decreasing temperature. The presence of increasing curvature in the exponent plots from FeZr to $Pd_{97}Co_3$ indicates increasing effects of disorder on the magnetic properties of the materials. Transport properties also confirm the transition to ferromagnetism, and the presence of an anisotropy in the low field magnetoresistance in this regime indicates the existence of an orbital moment, and thus spin-orbit coupling, at the magnetic site. The LFRA in various FeZr samples reproduces very well the temperature and bond-disorder dependent behaviour predicted by the model calculations in section 4.2. $Pd_{97}Co_3$ and $Pt_{90}Fe_{10}$ also exhibited a linear temperature dependence of the LFRA in the vicinity of T_c, however, the LFRA shows considerable curvature at relatively high T/T_c. The model allows for curvature only at low temperature, and virtually no dependence on field. All three systems show strong field dependence of the LFRA at low temperature, which we propose may be due to the finite domain sizes, which at low temperatures become smaller than the mean free path of the conduction electrons. The stronger curvature in the crystalline systems supports this proposal, since these materials have longer electron mean free paths, and their

resistivities will thus show a stronger dependence on domain sizes.

In conclusion, the SK model successfully predicts the general trends in the temperature and bond disorder dependent behaviour of the low field resistive anisotropy in the immediate vicinity of T_c, in bond-disordered systems. Although the LFRA is more strongly field and temperature dependent than expected, the change in the LFRA with changes in bond-disorder are as modeled. This allows the LFRA to be used as a sensitive method of examining small changes in bond-disorder within a system.

Chapter 5

Percolation Transition in CuNi

5.1 Review of Previous Results

When nickel is added to a copper matrix, an inhomogeneous ferromagnetic state evolves at a critical nickel concentration, x_0, slightly less than 50 at.%[4]. Although Fe and Co atoms generally exhibit magnetic moments in isolation, Ni does not[7]. Several theories have been postulated to explain this behaviour of nickel, such as the presence of interconfigurational fluctuations[87]. Another hypothesis is that, despite the failure to satisfy the static Hartree-Fock criterion for moment development, localised spin fluctuations exist due to local exchange[88]. In the giant moment systems discussed in Chapter 4, a minimum Ni concentration of 2.3 at.% in Pd or 42 at.% in Pt is required to induce a ferromagnetic state. Cu is not as polarizable as Pd, in that it exhibits no exchange enhancement effects, and thus requires a substantially larger Ni concentration to form a ferromagnetic ground state. $Cu_{100-x}Ni_x$ forms a binary solid solution, in which Cu and Ni atoms are randomly placed at sites on a face-centred cubic (fcc) lattice. Statistical fluctuations can result in pairs, triplets and other groupings of Ni atoms, the relative numbers of which depend on the Ni concentration. Assuming a critical number of nickel nearest neighbours (nn) to ensure a Ni moment, statistical models can be fit to experimental measurements of magnetic properties as a function of Ni concentration[89, 90]. These calculations find that a minimum of 8 Ni nn (out of a possible 12 nn in an fcc lattice) are required for moment formation in Cu. As x increases, the probability

of a cluster with 8 or more nearest neighbours increases, and thus the number of magnetic clusters increases, decreasing the inter-cluster spacing. Adjacent clusters begin to interact, at first indirectly, and then directly as clusters overlap. At the percolation threshold, an infinite chain of ferromagnetic clusters exists, forming an inhomogeneous ferromagnetic state.

The theoretical prediction of the existence of magnetic nickel clusters is supported by various experimental results for $Cu_{100-x}Ni_x$ alloys. Magnetic measurements of the paramagnetic alloys (low nickel concentration) show a rapid increase in susceptibility with increasing Ni concentration, suggesting the existence of superparamagnetism [91] due to the presence of large cluster spins which act as a single giant moment. Neutron diffraction studies for concentrations near x_0 show the presence of large magnetic clusters with giant moments as large as 10–12 μ_B, and polarisation clouds whose dimensions are larger than those of the measured chemical clusters[92]. As well, measurements of the specific heat of CuNi alloys in the ferromagnetic concentration regime show the addition of a temperature independent contribution to the normal electronic ($\propto T$) and phonon ($\propto T^3$) induced specific heats[93], i.e.

$$c_p = A + \gamma T + \beta T^3 \tag{5.1}$$

This term is consistent with thermal excitations of cluster moments and its magnitude is proportional to the concentration, i.e. proportional to the number of cluster moments present in the system.

Estimates of the critical Ni concentration (x_0) for ferromagnetic ordering in Cu range from 43–48 at.% Ni[4, 91, 92, 93, 94, 95, 96]. This scatter is due to the sensitivity of this system to heat treatment[97, 98]. Samples quenched from 900–1000°C show minimal chemical clustering, and thus low magnetisations. Subsequent heat treatments at temperatures below 600 °C result in increased chemical clustering, reflected in increased critical temperatures and magnetic moments [96, 97, 98]. Low temperature heat treatments also broaden the measured $\chi(T)$ peaks, due to the resultant large distribution of cluster sizes throughout the material[99]. Changes in the quench rate have also been found to alter the properties of the material[97, 98].

Thus only a critical concentration *range* can be specified in this system, since samples made under differing conditions show varying results. The annealing process followed in this study was chosen specifically to minimize this problem. Such metallurgical problems notwithstanding, a number of trends as a function of Ni concentration can be noted in this system.

Measurements of χ_{ac}(T) and M(H,T) have been interpreted as showing that the magnetic response at high temperature is the sum of a paramagnetic Curie-Weiss term and a temperature independent Pauli susceptibility. Calculations of the characteristic temperature, θ, in the equation

$$\chi = \frac{C}{T-\theta} \tag{5.2}$$

show an interesting trend as a function of Ni concentration. At very low x the Curie-Weiss term is negligible, since the probability of a magnetic cluster existing is very small. As x increases, the Curie-Weiss term becomes measurable, and yields a negative value for θ, consistent with antiferromagnetic exchange coupling. At higher nickel concentrations, θ becomes positive, passing through zero at $x \sim x_o$[91]. This result suggests that interactions between clusters are antiferromagnetic at large separations, caused perhaps by RKKY exchange. As x increases and the cluster separation decreases, the exchange becomes ferromagnetic due either to direct exchange or to overlap of the polarisation clouds within the first node of the RKKY exchange interaction. This is supported by measurements of resistivity as a function of temperature for a number of concentrations. At very low Ni concentration, ρ(T) has a normal, metallic temperature dependence, viz., $\propto T^5$ at low T and $\propto T$ at higher T. As x increases, a low temperature minimum develops, consistent with the Kondo effect due to conduction electron scattering from the cluster moments. At larger x, this minimum moves to lower T, and vanishes as the ρ(T) curves develop a typical ferromagnetic structure[97, 100, 101], similar to that observed in disordered alloys and shown in Chapter 4. At high temperature, T$\gg$T$_c$, the resistivity has a high temperature minimum, due likely to competition between the increasing phonon term and the decrease in spin-disorder scattering caused by the gradual

decrease of the paramagnetic cluster moments as T→625K, the Curie temperature of pure Ni[102].

The transition from ferromagnetic to antiferromagnetic coupling as x decreases through x_o raises the possibility of a mictomagnetic regime at intermediate concentrations due to frustration caused by competition between ferromagnetic and antiferromagnetic exchange. A mictomagnet is similar to a spin-glass, except that magnetic clusters take the place of the randomly frozen single moments in the spin-glass state. Boghossian et al.[103] find that a 48% Ni sample exhibits χ_{ac}(H,T) curves similar to those seen in the spin-glass regime of AuFe, and suggest that this sample is mictomagnetic. Claus et al.[104] postulate a mictomagnetic state for concentrations immediately below 46 at% Ni, based on the sudden decrease in maximum amplitude of the *ac* susceptibility data below this concentration.

In percolation-type transitions, such as may be observed in the CuNi system, a number of properties have been shown to exhibit a power law dependence on the reduced concentration, $(x-x_0)/x_0$[4]. For example, the saturation magnetisation is proportional to $((x-x_0)/x_0)^{1/2}$, while the initial susceptibility has critical exponent of -1. Detailed measurements of the spontaneous resistive anisotropy (SRA) at low temperature as a function of x in PdFe[5] and PdNi[6] alloys were interpreted as suggesting that the SRA also exhibits a percolation controlled critical behaviour, i.e.

$$\left(\frac{\Delta\rho}{\rho_0}\right)_{B\to 0} \propto \left(\frac{x-x_0}{x_0}\right)^{\Delta} \tag{5.3}$$

Although both of these systems fit the behaviour in equation 5.3 well, they have remarkably different exponents, with $\Delta \sim 1$ in PdFe and $\Delta \sim 2$ in PdNi. To verify that this power law-type critical behaviour of the SRA is a universal feature in percolation transitions, despite the different exponents exhibited, measurements of similar systems with magnetic impurities are necessary.

In this study, detailed *ac* susceptibility measurements have been done on a series of CuNi alloys to characterize the evolution of the magnetic state with increasing Ni concentration. Detailed magnetoresistance measurements have also been done to determine whether the SRA shows critical behaviour at the percolation threshold.

Finally, studies of the low field resistive anisotropy were done before and after aging the samples. Comparison of these results gives important information on the effects of aging on the bond-disorder in the material.

5.2 Experimental Results and Discussion

The sixteen $Cu_{100-x}Ni_x$samples measured in this study range in concentration from x=45 to x=55. After sample preparation as described in Section 3.1, the samples were annealed in argon atmosphere for 48 hours at 950°C and quenched into ice-water. The quench rate was maintained as constant as possible from one sample to the next, however, due to the extreme sensitivity of this system to heat treatment, some variation in final state was noticeable even in samples of the same size and concentration annealed together. This result could be due to slightly different quench rates for samples at different locations in the tube. This effect is small, but may cause some scatter in the results, as will be discussed later.

For the purpose of clarity, the experimental results have been divided into three sections. The detailed *ac* susceptibility results will be discussed first, followed by the transport measurements. Finally a brief study on the effects of aging on the LFRA measurements will be presented.

5.2.1 AC Susceptibility Measurements

The field and temperature dependent *ac* susceptibility (χ_{ac}(H,T)) was measured as described in Section 3.3 for all 16 samples. From these data, quantitative analysis was performed using the scaling relations (Section 2.1.2) to give values for the critical exponents, γ, $\gamma+\beta$, and δ, as well as the critical temperature. The trends in these values as a function of Ni concentration will be described in detail, however the detailed behaviour of χ_{ac}(H,T) will be examined only for 3 representative samples. Plots of the data and analysis for the remainder of the samples appear in Appendix A.

General Features

The general behaviour of χ_{ac}(H,T) in the higher concentration samples is very similar to that seen in the disordered compounds, FeZr, PtFe and PdCo, discussed in Chapter 4. As the temperature decreases towards T_c, the zero field susceptibility increases rapidly, reaching a maximum (the Hopkinson peak) at a temperature, T_H, slightly lower than T_c. Below this temperature the susceptibility drops rapidly, an effect attributed to the temperature dependence of the coercivity of the system. The height of the Hopkinson peak is only 0.35 emu/g-Oe in the 55 at.% Ni sample (less than one-tenth of the demagnetisation limited value, N^{-1}), and decreases in amplitude essentially monotonically with decreasing Ni concentration. This trend will be discussed in more detail later. As discussed earlier (Section 3.3.3) the demagnetisation factor was obtained by approximating the sample as an ellipsoid, and performing elliptic integrals.

The higher concentration samples were magnetically quite hard, requiring applied fields on the order of 40 Oe to suppress the background contribution sufficiently to allow observation of critical peaks. Above this field, the Hopkinson peak was rapidly depressed both in height and temperature, and the non-critical (regular) contribution became negligible. This behaviour is shown in figure 5.1 for the 54 at.% Ni sample. With the background contribution removed, the critical peak decreased in amplitude and moved to higher temperature as the applied field was increased, as predicted by the scaling relationships. From critical peaks such as those in figure 5.2, one can extract values for χ_m and T_m to use in the scaling relationships. The critical temperature was estimated by plotting the peak temperature as a function of $H_i^{0.571}$ (0.571 being the 3D Heisenberg value for $1/(\gamma+\beta)$). This plot is quite linear, as demonstrated in figure 5.3, with only the first two points (H_i=40 and 50 Oe) falling slightly off the line. This deviation at low field is understandable, since the large background contribution present at these fields distorts the critical peak, causing errors in the estimated value of T_m. A straight line fit to these data gave an intercept of T_c=78.4 K. Using this value for T_c, the

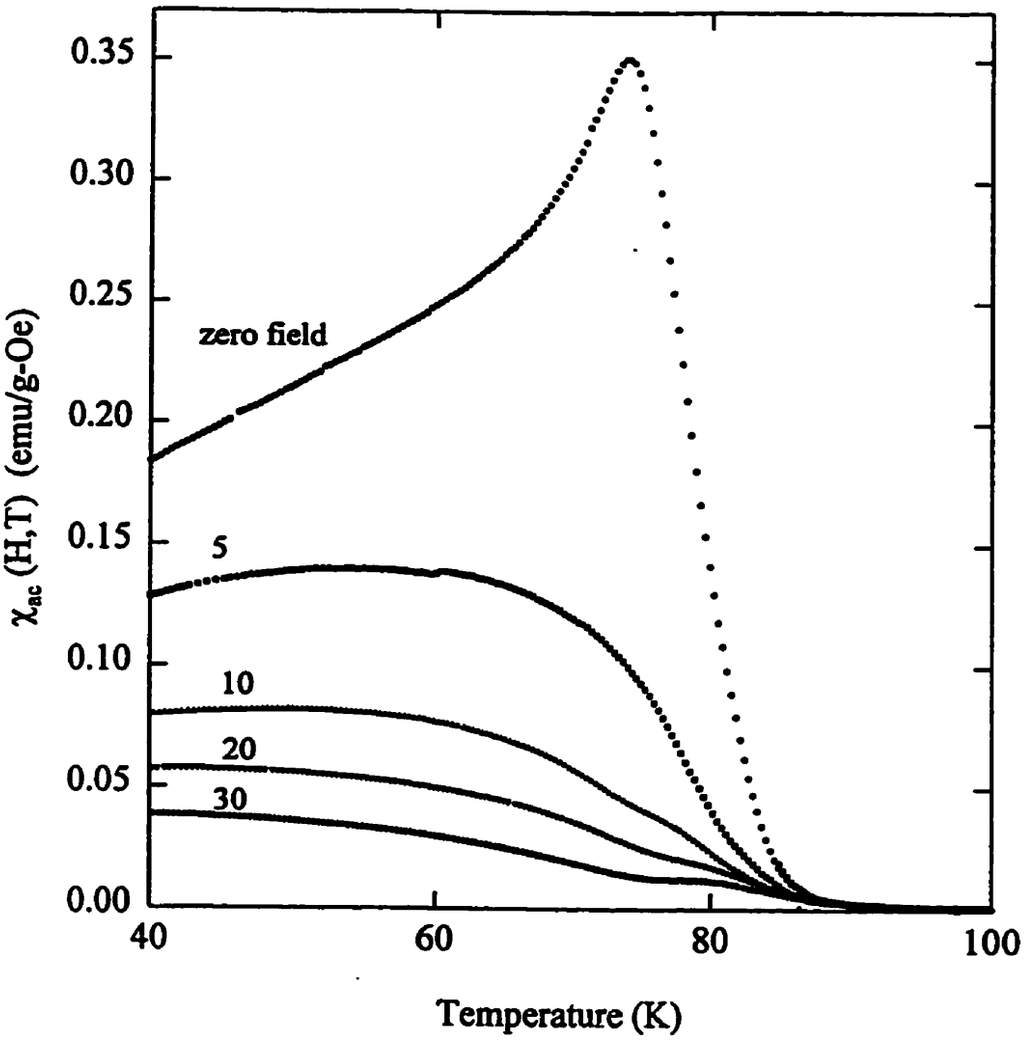

Figure 5.1: The temperature dependence of the *ac* susceptibility in fixed biasing fields as labelled, in Oe, for the x=0.54 sample.

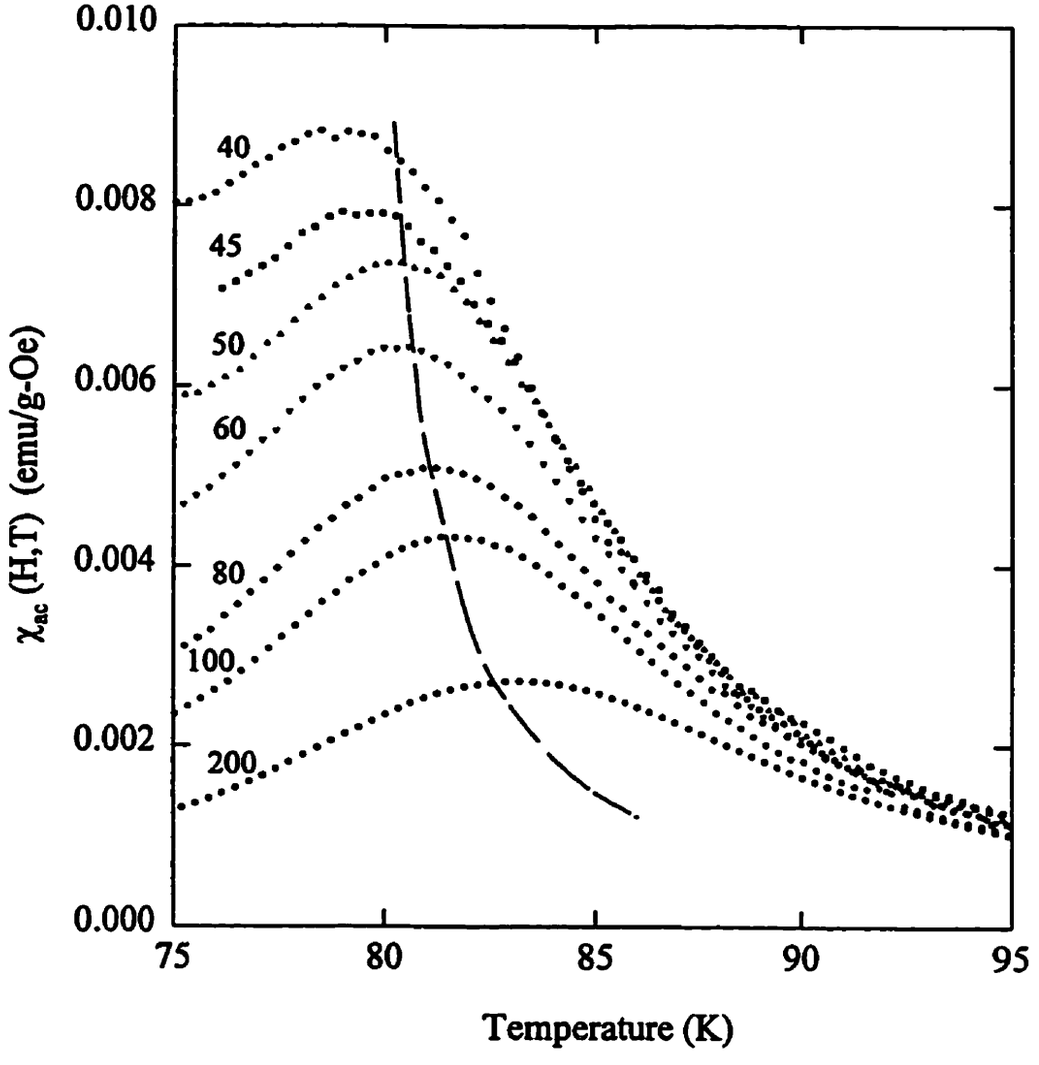

Figure 5.2: The temperature dependence of the *ac* susceptibility in fixed biasing fields as labelled for the x=0.54 sample. The dotted line represents the crossover line. $\chi_m \propto t_m^{-\gamma}$.

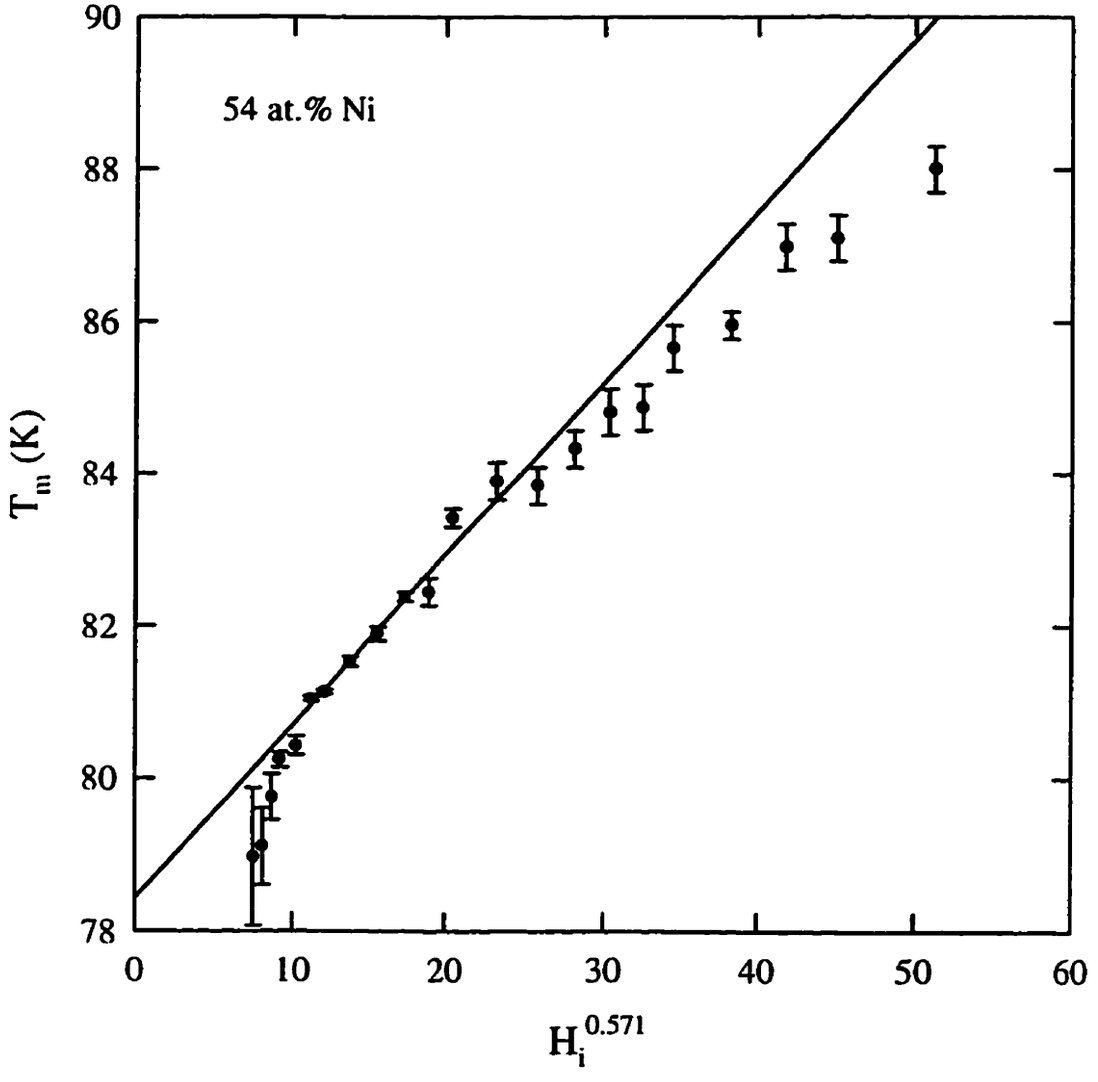

Figure 5.3: Peak temperature as a function of internal field to the power of 0.571 for $Cu_{100-x}Ni_x$ with x=0.54. The superimposed line represents a fit to the data with T_c=78.4.

effective γ, $\gamma^*(t) = -d\ln(\chi(0,t))/d\ln(t))$ was found by fitting a curve to the zero field susceptibility for t >0 and differentiating to find the local slope, i.e. $\gamma^*(t)$. This is demonstrated in figure 5.4, in which $\chi(0,T)$ is plotted against t on a log-log scale for x=0.54, with the inset showing the derivative. The derivative has the peak structure common in systems with disorder, as discussed in Chapter 4. At low t, γ^*(t) falls below the value of 1.386 predicted by the 3D Heisenberg model, due to the failure of the zero field susceptibility to reach its demagnetisation limited value, as discussed earlier (section 4.3.1). After going through a peak at a reduced temperature slightly higher than 0.1, the effective γ falls toward the mean field value of 1 at high temperature (not shown in this figure). Although this behaviour is similar to that seen, for example, in PtFe and PdCo, the height of the peak in $\gamma^*(t)$ is larger here, reaching a value of 4 in this sample. Values for the cross-over exponent, $\gamma+\beta$, and the zero-field susceptibility exponent, γ, were also found for the 54 at.% sample, as in Chapter 4. Figure 5.5 is a plot of reduced peak temperature, t_m, as a function of internal field on a log-log scale. The data is quite linear, with only the first two points falling off the line, and a line with the 3D Heisenberg predicted slope of $1/(\gamma+\beta)$=0.57(3) is consistent, within scatter, to the data. The asymptotic γ was found similarly, fitting a straight line to the peak susceptibility as a function of peak reduced temperature on a log-log scale, as in figure 5.6. These data are consistent with γ=1.386(60), as predicted by the 3D Heisenberg model.

The 'δ plot' (figure 5.6) for the x=0.54 sample shows little curvature, and a straight line fit gives a value for δ=4.2$\pm$0.1, slightly lower than that of 4.8 predicted by the 3D Heisenberg model. This low value is likely due to the high coercivity of this sample, which again prevents true asymptotic field dependence from being determined by obscuring the low-field critical peaks. A hypothetical fit of the low field data with a δ= 4.8 is shown by the dashed line in the plot to be a reasonable approximation of the data at very low field.

Figures 5.8 through 5.13 show the corresponding plots for a sample with 49.5 at.% Ni. The exponent plots show considerable curvature, as did those for $Pt_{90}Fe_{10}$ and $Pd_{97}Co_3$, so that only points at low biasing fields are fit to a straight line, as

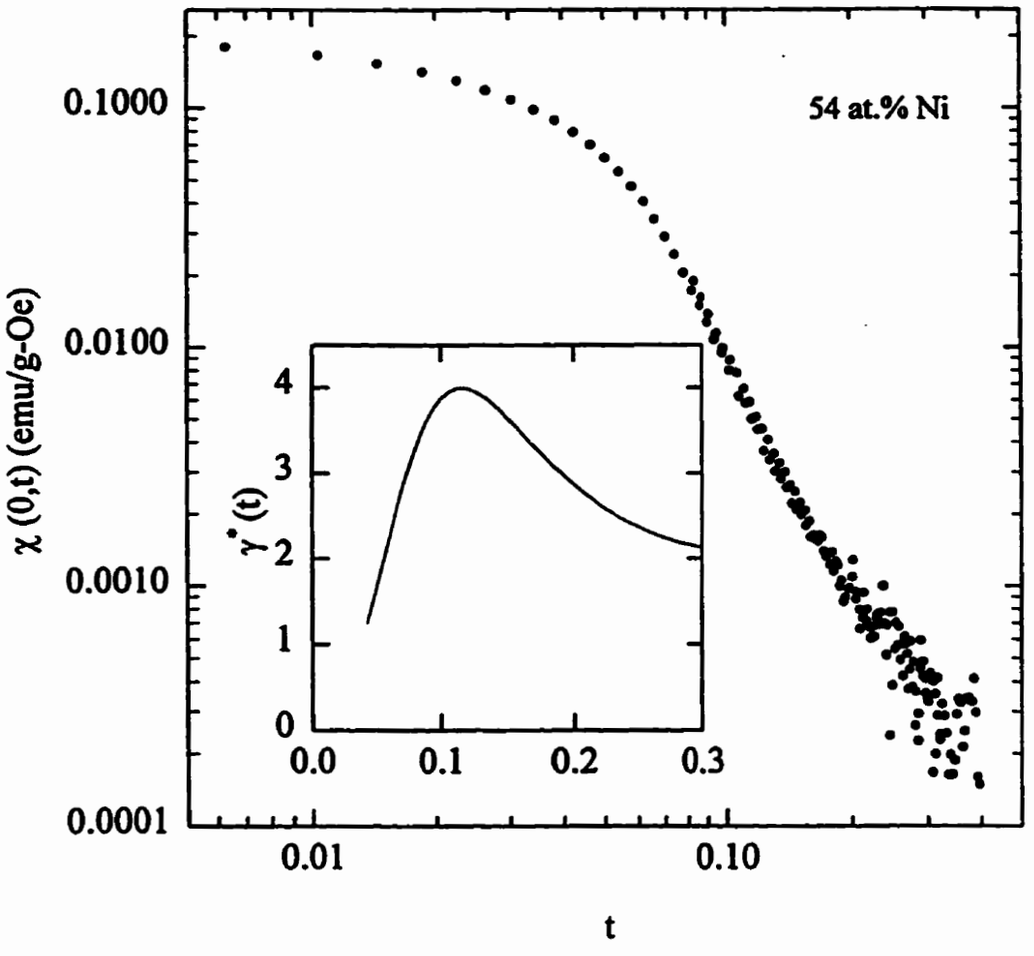

Figure 5.4: The zero field susceptibility as a function of reduced temperature for the 54 at.% Ni sample. The inset shows the calculated effective exponent, $\gamma^*(t)$.

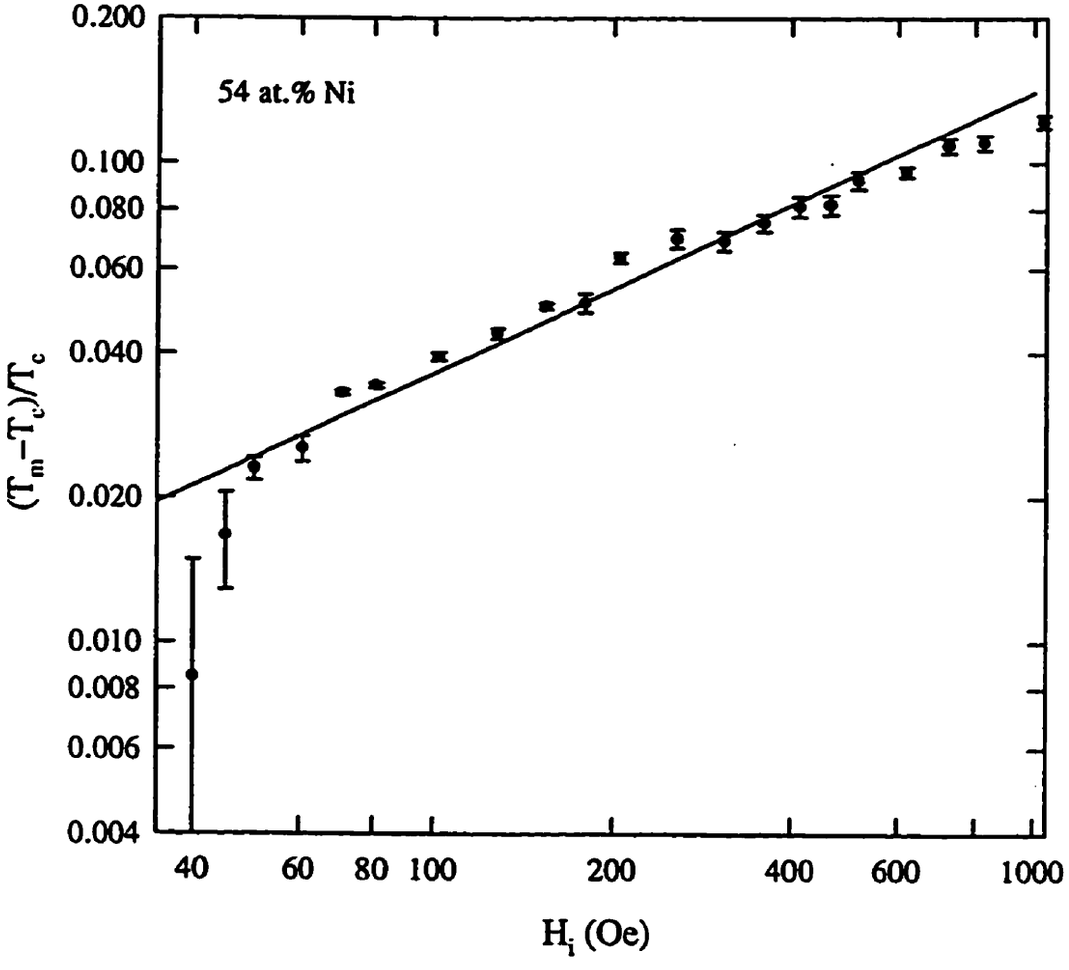

Figure 5.5: Reduced peak temperature as a function of internal field for x=0.54. The superimposed line represents the 3D Heisenberg prediction, $1/(\gamma+\beta)$=0.571.

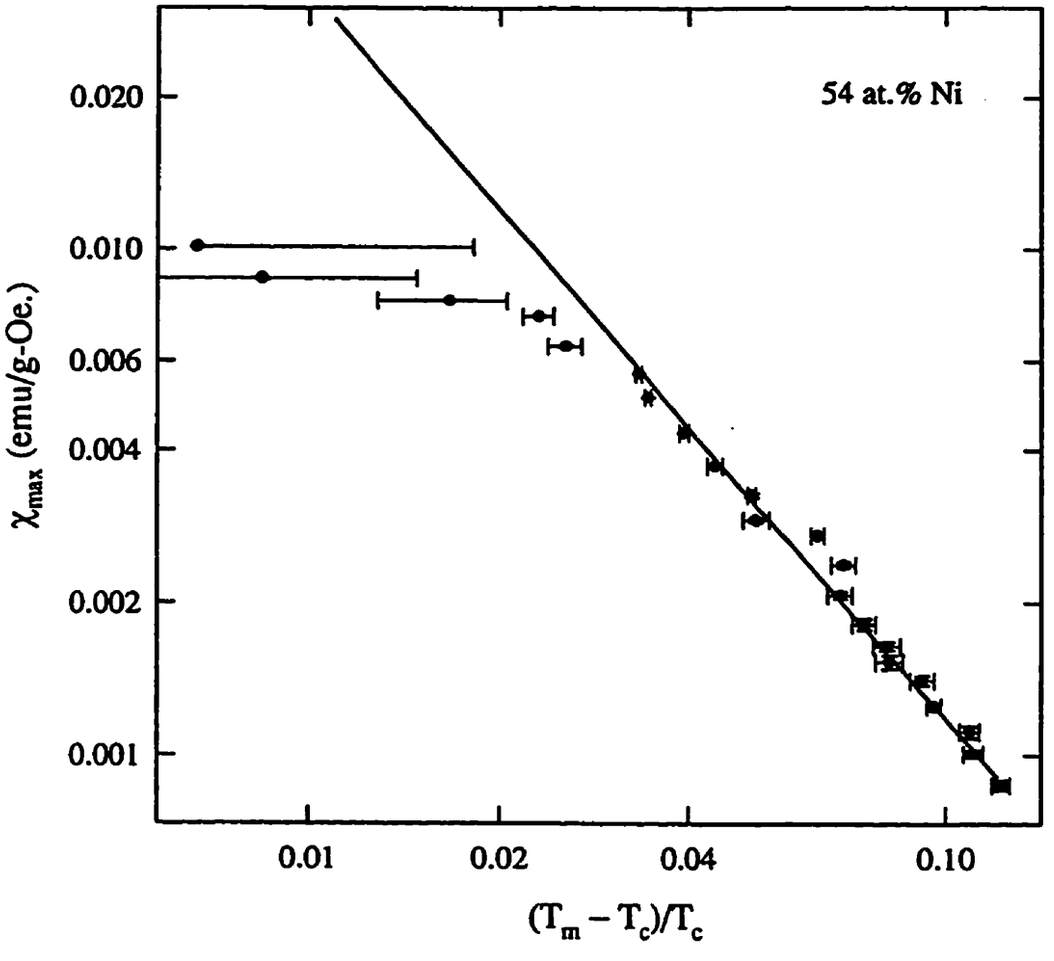

Figure 5.6: Peak susceptibility as a function of reduced peak temperature for the 54 at.% Ni sample. The superimposed line represents the 3D Heisenberg value for γ=1.386.

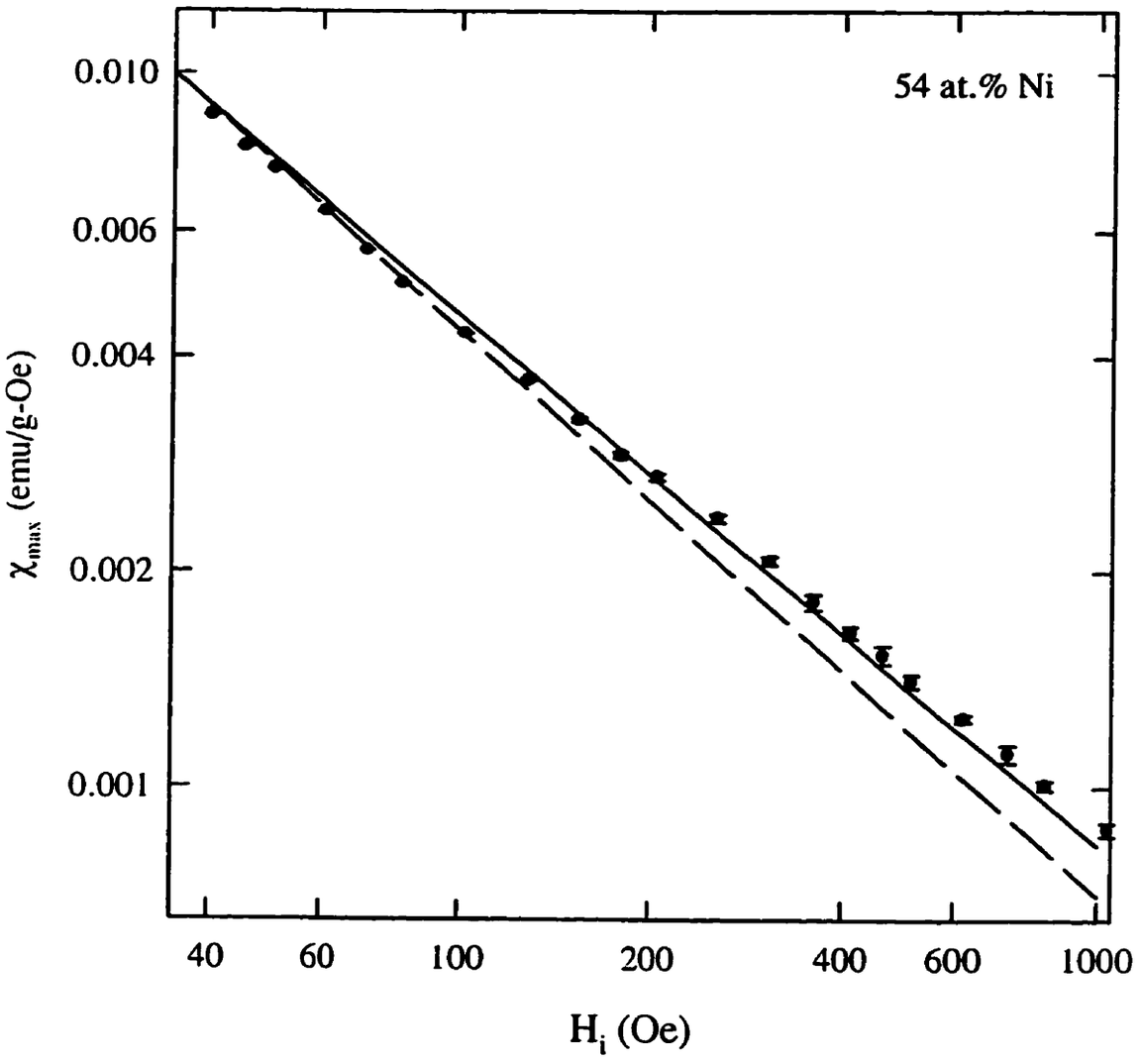

Figure 5.7: Peak susceptibility as a function of internal field for the 54 at.% Ni sample. The solid line represents a fit to the data with δ=4.2(1). The dashed line shows a fit calculated using the 3D Heisenberg exponent, δ=4.8.

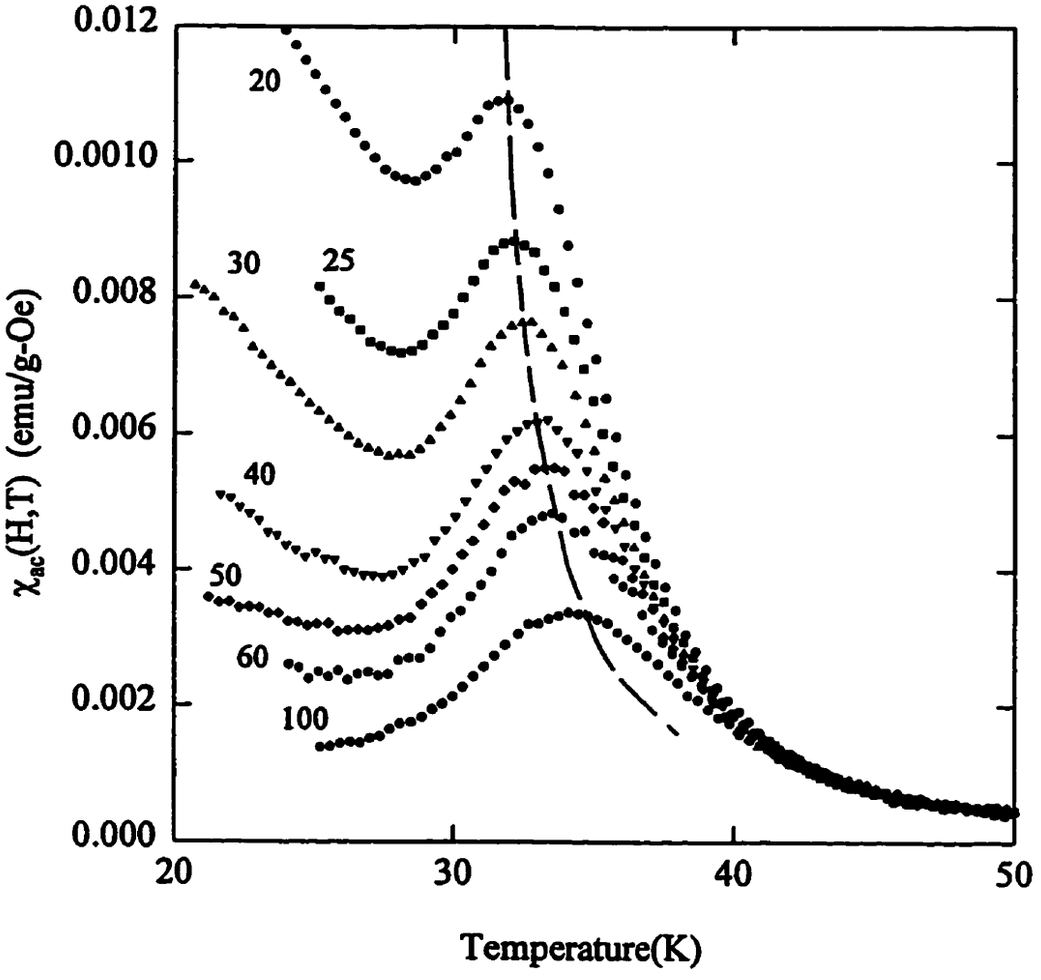

Figure 5.8: The temperature dependence of the *ac* susceptibility in fixed biasing fields as labelled, in Oe, for the x=49.5 sample. The dashed line represents a fit to the cross-over line, $\chi_m \propto t_m^{-\gamma}$

the exponents represent the asymptotic behaviour (i.e. H$\rightarrow$ 0, $t \rightarrow$ 0). This sample is magnetically softer than the higher concentration samples, allowing critical peaks to be observed in fields of only 7 Oe. Fits for the other exponents gave reasonable values for data in the range 7–50 Oe. With T_c=29.4(2) (figure 5.9), the effective γ plotted in figure 5.10 shows the peaked structure associated with bond-disorder, with a peak height of 3.8. The value found for T_c is only marginally above the temperature, T_H, at which the Hopkinson peak has its maximum. Traditionally, T_c is taken to be the temperature of the inflection point on the χ(0,T) plot. In the higher concentration range, this inflection point agrees well with the value of T_c found from detailed analysis of the critical behaviour, however as the concentration is decreased, the critical temperature moves closer to T_H. This trend was also noticed in the dilute PdMn system as a function of increasing Mn concentration (i.e. towards the limit of ferromagnetic instability)[105], and could potentially be a feature common to systems with ferromagnetic percolation transitions. The cross-over plot, shown in figure 5.11, has a linear region extending from approximately 7–50 Oe, whose slope is equal to the 3D Heisenberg value (0.571) within the considerable scatter. At higher fields, the t_m fall below this line, consistent with the increase of $\gamma^*(t)$ outside the critical regime seen in figure 5.10. This increase in $\gamma^*(t)$ can also be seen in the γ plot (figure 5.12), the low t slope of which can be fit well with the 3D Heisenberg γ=1.386. At high t, however, the slope increases dramatically, consistent with the increase in the calculated $\gamma^*(t)$ shown in figure 5.10.

The slope of the δ plot decreases steadily with increasing field. Two lines can be drawn on the plot (figure 5.13) yielding low field and a high field values for δ. The low field δ of 8.4(3) is considerably higher than the 3D Heisenberg value, due possibly to the presence of a considerable technical background in the lower field runs. This larger background could be caused by an increase in coercivity of the sample (although only small fields are required to resolve the critical peaks), or alternatively could be due to the smearing of the transition caused by variations in local environment within a macroscopic sample or from one sample to the next.

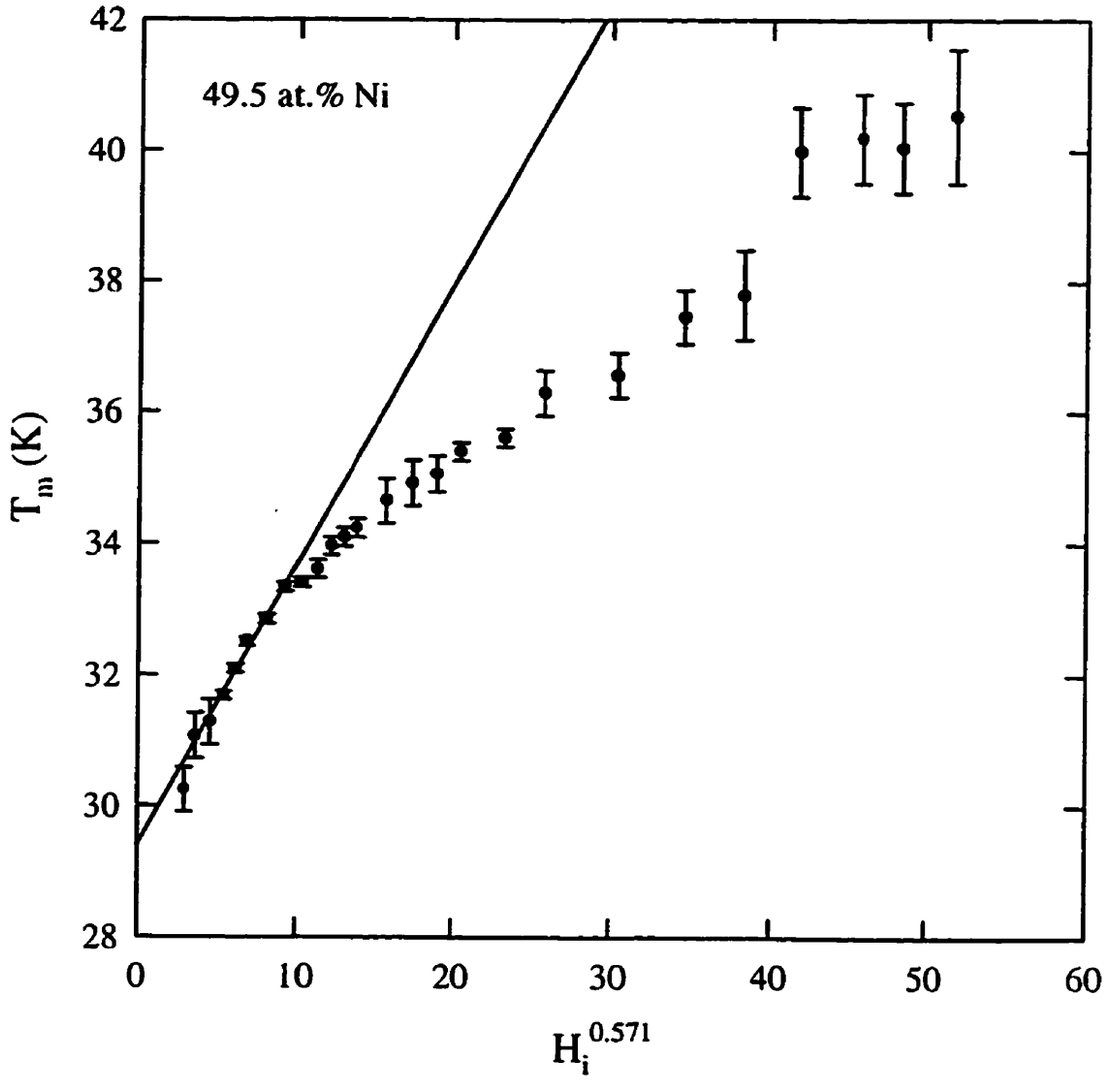

Figure 5.9: Peak temperature as a function of internal field to the power of 0.571 for $Cu_{100-x}Ni_x$ with x=49.5. The superimposed line represents a fit to the data with T_c=29.4(2).

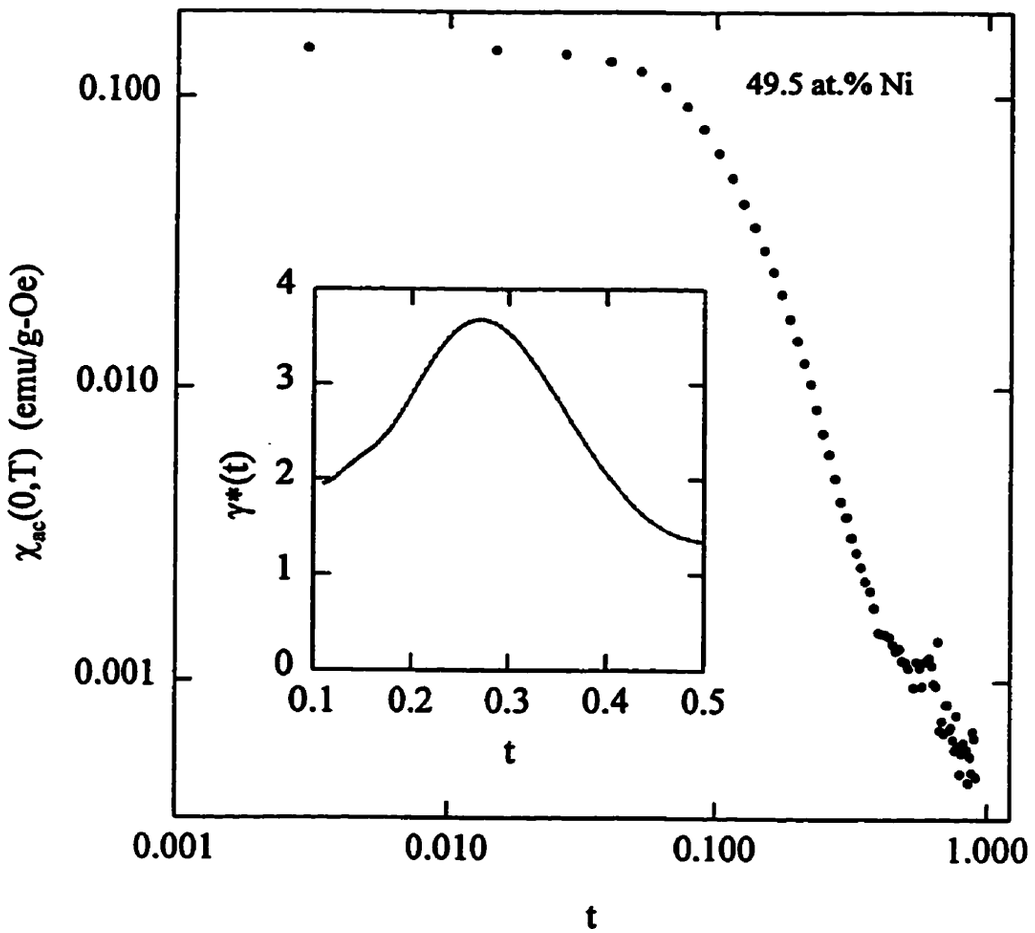

Figure 5.10: The zero field susceptibility as a function of reduced temperature for the 49.5 at.% Ni sample. The inset shows the calculated effective exponent, $\gamma^*(t)$.

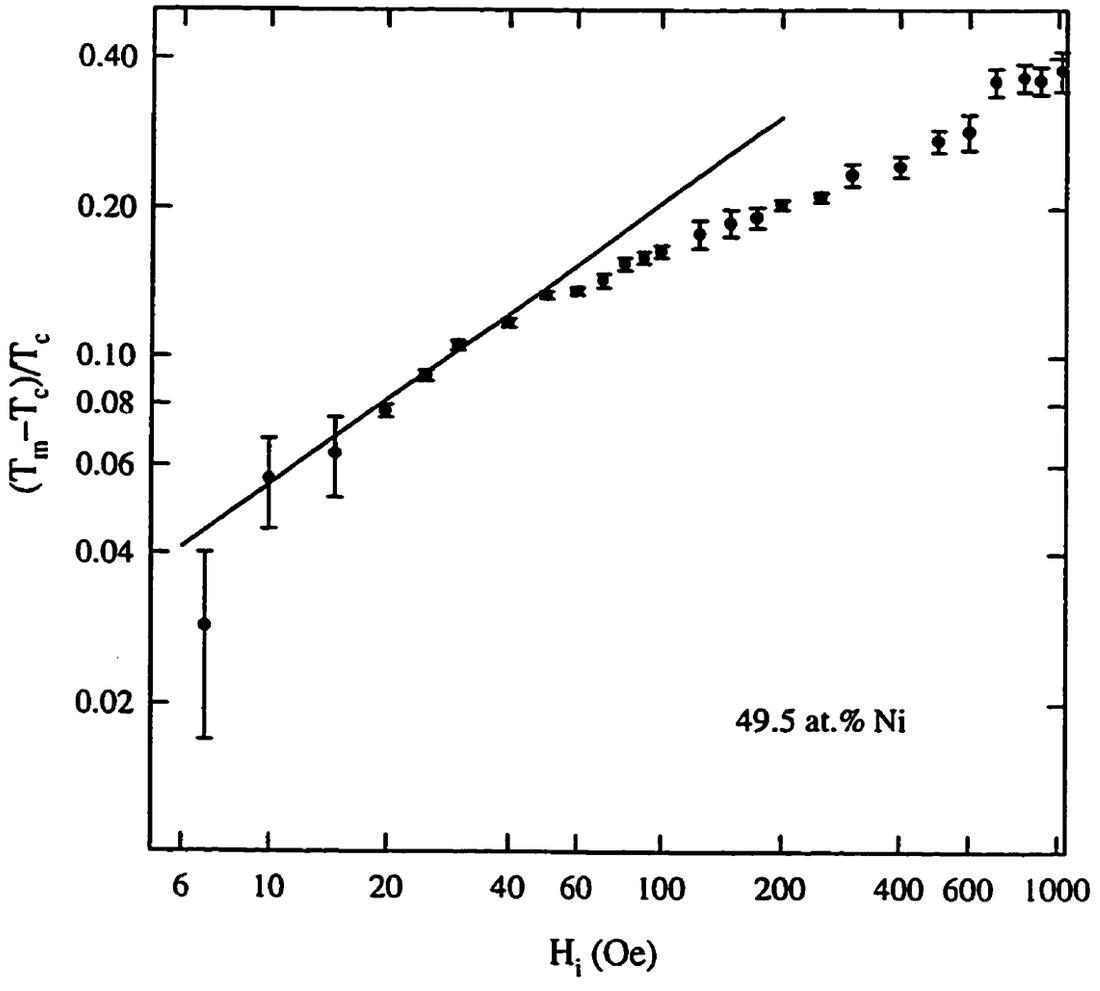

Figure 5.11: Reduced peak temperature as a function of internal field for x=49.5. The superimposed line represents a fit to the data with $1/(\gamma+\beta)$=0.571.

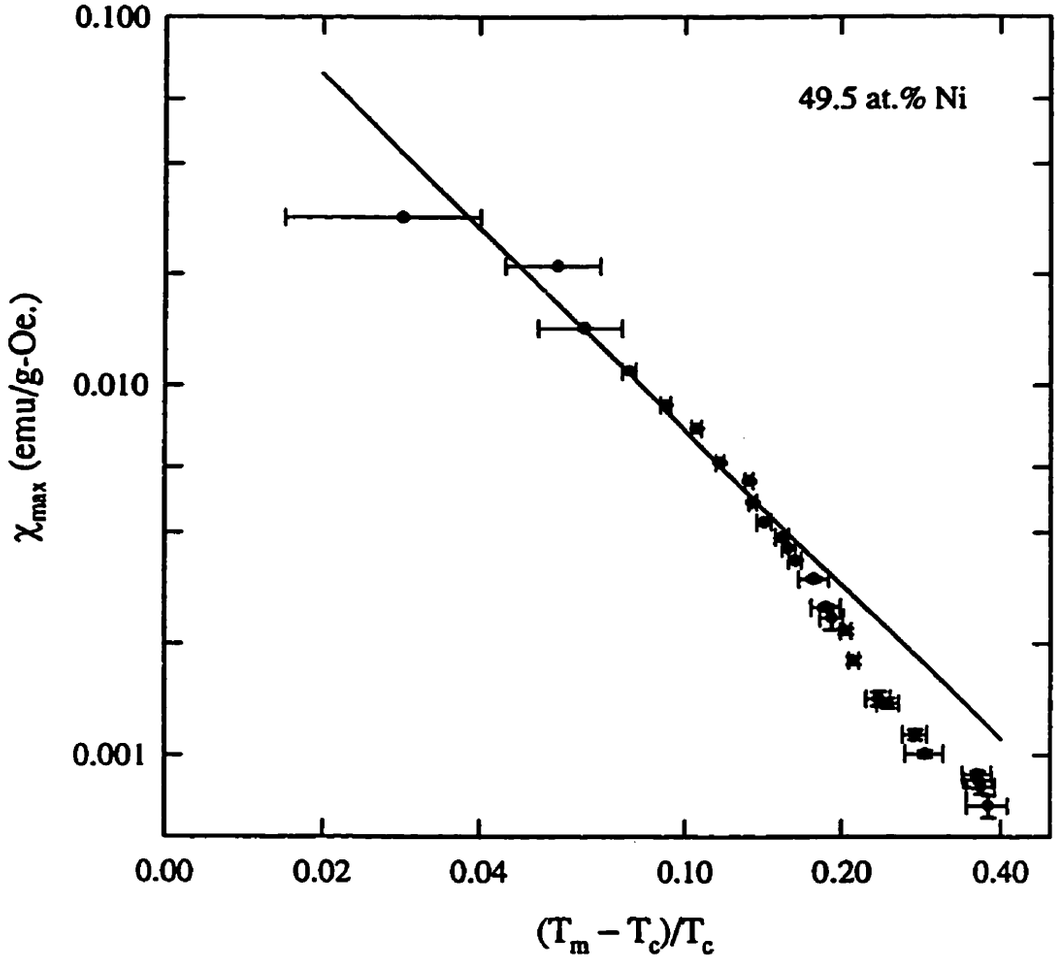

Figure 5.12: Peak susceptibility as a function of reduced peak temperature for the 49.5 at.% Ni sample. The superimposed line represents a fit to the data with γ=1.386.

Due to the rapid suppression of the susceptibility with applied field, several pieces of sample had to be inserted in the susceptometer to give high signal-to-noise ratios at high field. As discussed above, even samples cut from the same piece of material and annealed in the same tube showed differences in critical behaviour, due to the sensitivity of the alloy to quench rate [98]. Although this large value for the low field δ may be due to changes in the magnetic behaviour, it can most likely be attributed to technical effects, particularly in those systems for which $\delta < 0$ (see later dicussion). Similarly high values for δ_{lf} were observed previously in the PdGd system[106], which also has low field δ's of 10 or higher due to large amounts of curvature in the exponent plots. The high field data were fit quite well with a mean field δ=3, again similar to the PdGd system.

The samples with the three lowest Ni concentrations, x=45, 45.5, and 46, showed anomalous behaviour in that only one peak in χ_{ac}(H,T) was observed, in fields of up to 1000 Oe. Fig 5.14 shows the evolution of the *ac* susceptibility peak in small fields for the 46 at.% sample. An internal field of 0.5 Oe decreased the Hopkinson peak amplitude and broadened it, however the peak remained at approximately the same temperature as in the zero field run. The same behaviour was evident in fields of 1 and 2 Oe. As the internal field increased above 5 Oe, the peak temperature and magnitude appeared to follow scaling predictions. At no point, however, does one see the evolution of a critical peak as seen in the higher concentration samples, for example in figure 5.8. We then examined the behaviour of the critical exponents, on the assumption that the observed peaks originate from critical fluctuations rather than technical contributions. In the following plots, the open symbols represent those peaks which do not appear to obey the scaling relations.

The anomalous behaviour of the first few peaks can be seen clearly in the T_c plot (figure 5.15). The first few points (open symbols), at very low field, remain at approximately constant T, however at higher field T_m increases as expected, giving a value for T_c=5.67 K, with a second change in curvature at even higher field, as seen in the more concentrated materials. γ^*(t) (figure 5.16) still shows the peaked behaviour, however the peak location has moved to high temperature ($t > 1$).

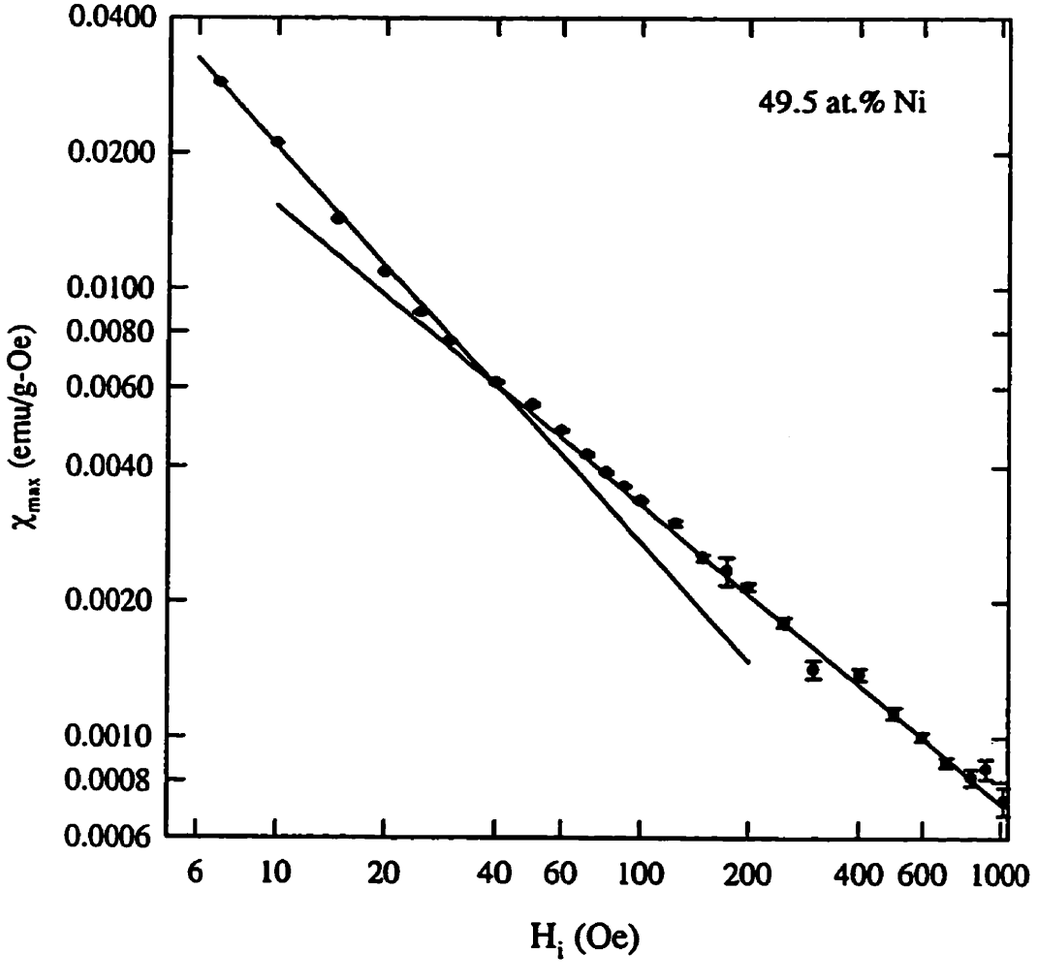

Figure 5.13: Peak susceptibility as a function of internal field for the 49.5 at.% Ni sample. The superimposed lines represent fits to the data with δ_{lf}=8.4(3), and δ_{hf}=3.0(1)

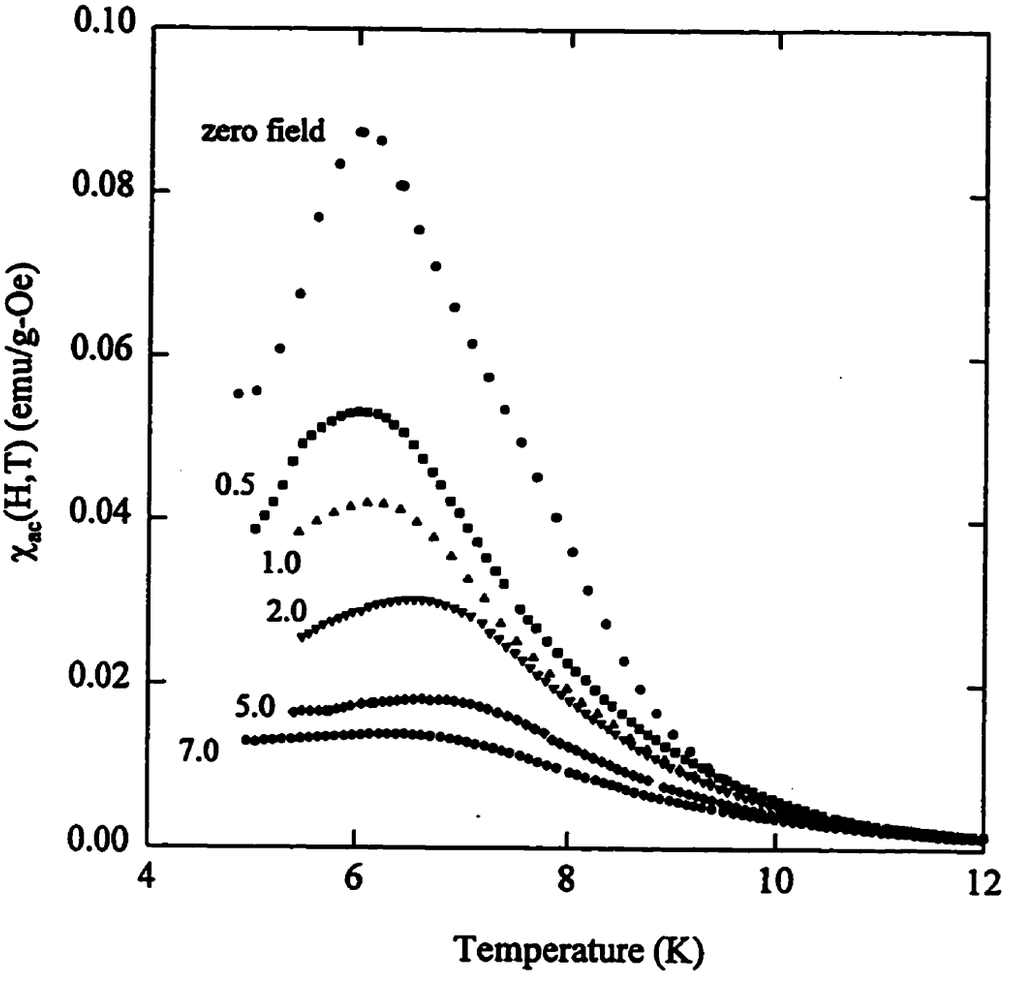

Figure 5.14: The temperature dependence of the *ac* susceptibility in low biasing fields as labelled, in Oe, for the x=46 sample.

At lower Ni concentration, $\gamma^*_m(t)$ decreases, to less than 2 in the 45 at% sample, a value similar to that seen in a number of other disordered systems, including those in Chapter 4. The plots for the cross-over exponent and the asymptotic γ (figures 5.17 and 5.18) show curvature as in the previous sample, with low field slopes consistent with 3D Heisenberg predictions. The disagreement of the high field/temperature data with the 3D Heisenberg values suggests an increase in $\gamma^*(t)$ with t, as seen in figure 5.16. The 'δ-plots' for these lower concentrations show the opposite curvature to that observed in the higher concentration samples, i.e. the low field slope is *smaller* than the high field slope. Figure 5.19 illustrates this for the x=46 samples, with fits of δ_{lf}=1.69(2) and δ_{hf}=3.70(5). δ_{hf} is similar to that seen in the intermediate concentration ranges, however the low value of δ_{lf} is anomalous. One possible reason for this is that, at low fields, the observed peak could be a superposition of both the Hopkinson and the critical peak, each with a different field and temperature dependence. As noted above, as the nickel concentration decreases the critical temperature moves progressively closer to T_H, probably causing an overlap at low concentration. Furthermore, the lower concentration samples may be more sensitive to small differences in quench rate, and the observed smearing of the two peaks into one broad peak could also be caused by the approximately 8 different pieces of sample used exhibiting slightly different susceptibilities. Along similar lines, the presence of large fluctuations of cluster size as $x \rightarrow x_0$ as observed by neutron scattering measurements[92], could contribute to this effect. In these low concentration samples, the susceptibility shows features consistent with the presence of critical fluctuations at a second order phase transition, although here only one broad peak in χ_{ac}(H,T) is observed.

The detailed behaviour and trends in exponents for the individual samples will be discussed in the following section.

Comparison and Discussion

Changes in the magnetic state as a function of concentration can often be deduced from plots of various parameters as a function of concentration. Figure 5.20, in

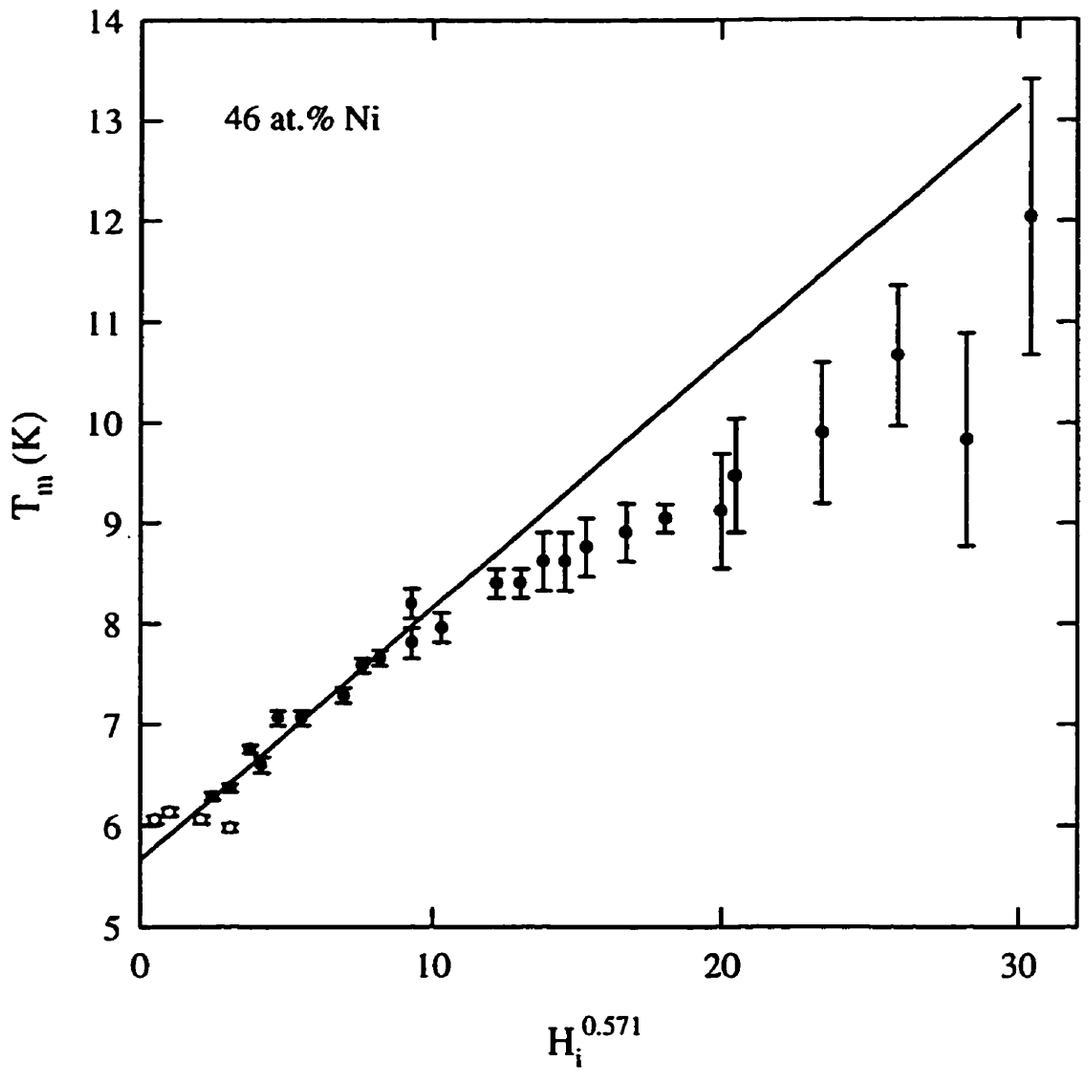

Figure 5.15: Peak temperature as a function of internal field to the power of 0.571 for $Cu_{100-x}Ni_x$with x=46. The superimposed line represents a fit to the data with T_c=5.67(3).

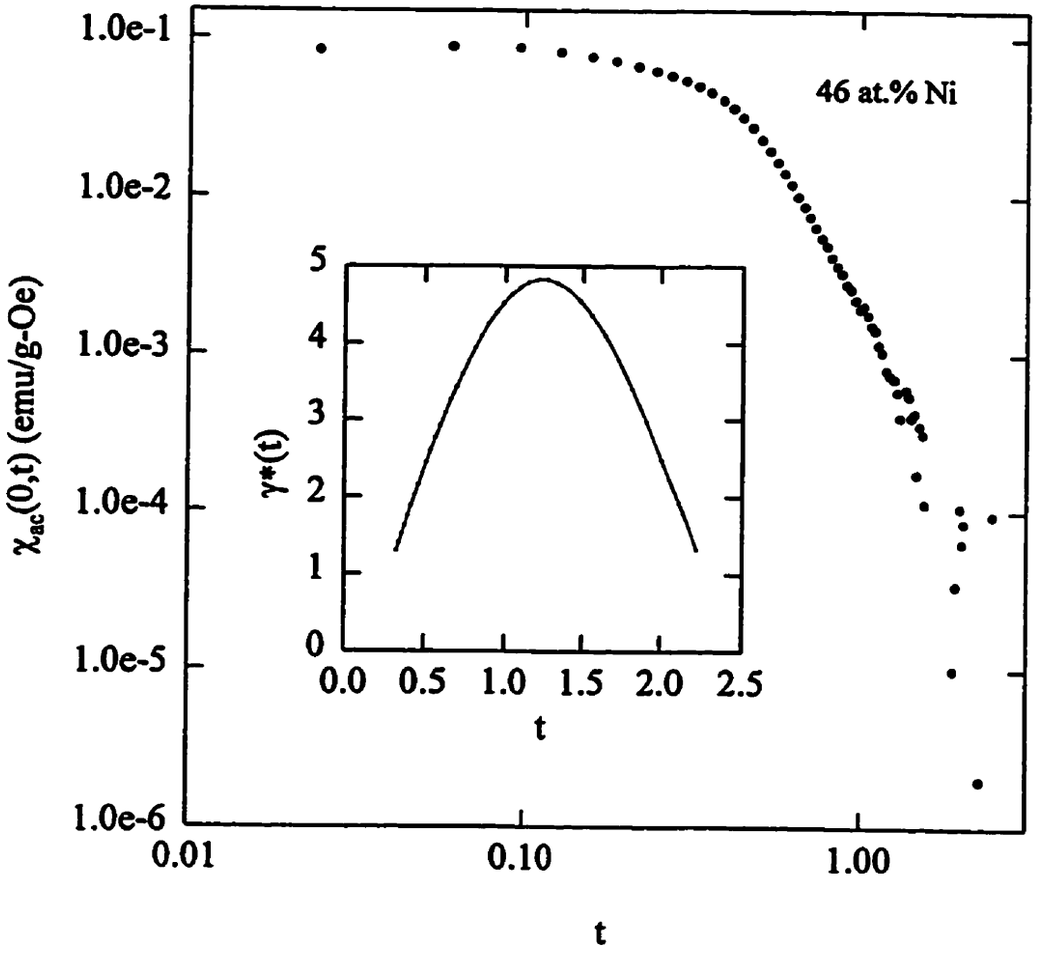

Figure 5.16: The zero field susceptibility as a function of reduced temperature for the 46 at.% Ni sample. The inset shows the calculated effective exponent, $\gamma^*(t)$.

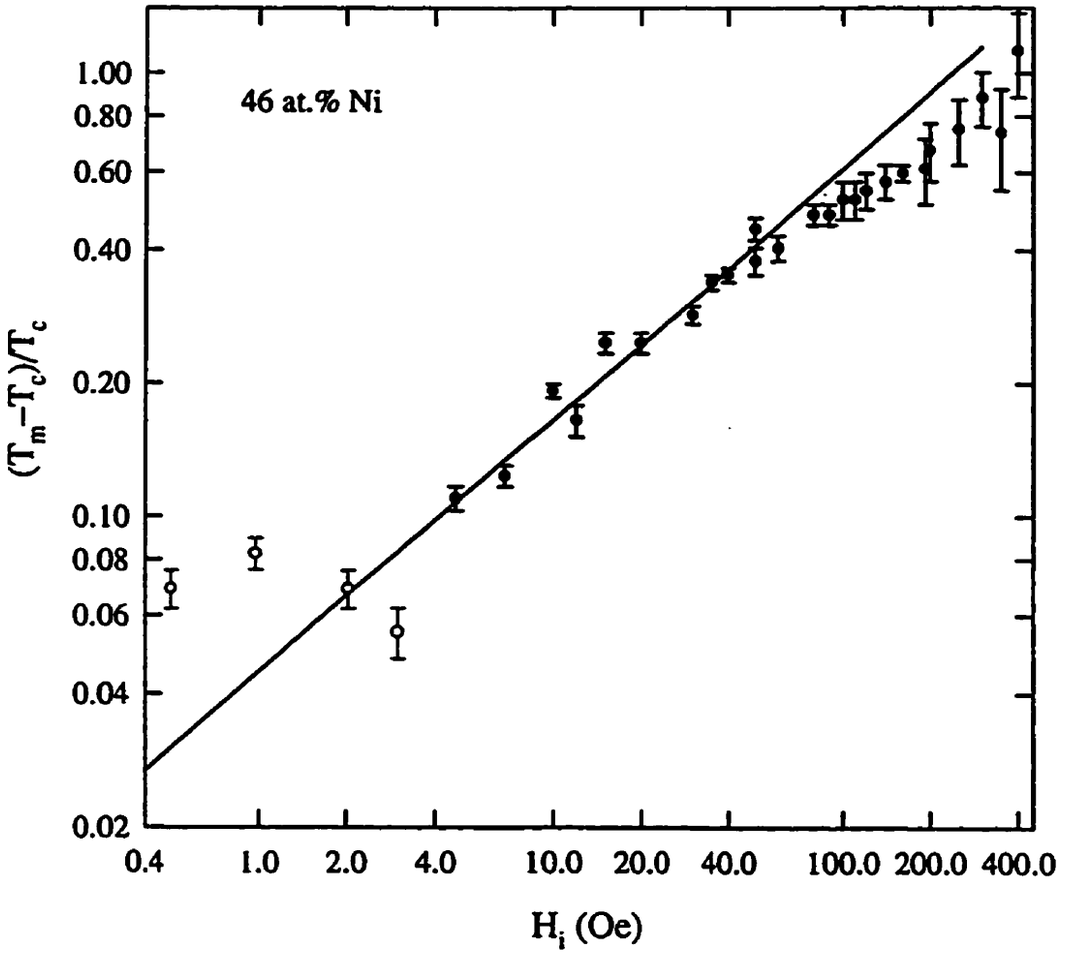

Figure 5.17: Reduced peak temperature as a function of internal field for x=46. The superimposed line represents a fit to the data with $1/(\gamma+\beta)$=0.571.

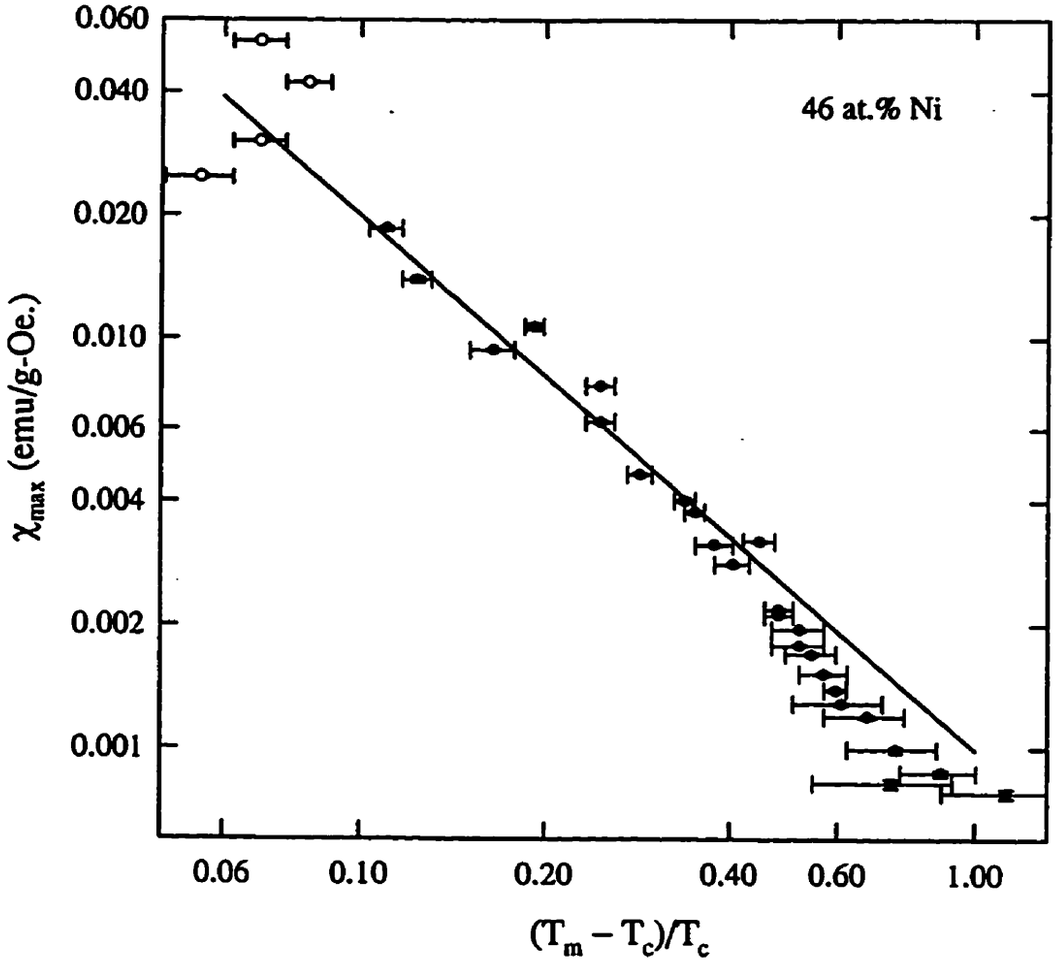

Figure 5.18: Peak susceptibility as a function of reduced peak temperature for the 46 at.% Ni sample. The superimposed line represents a fit to the data with γ=1.386.

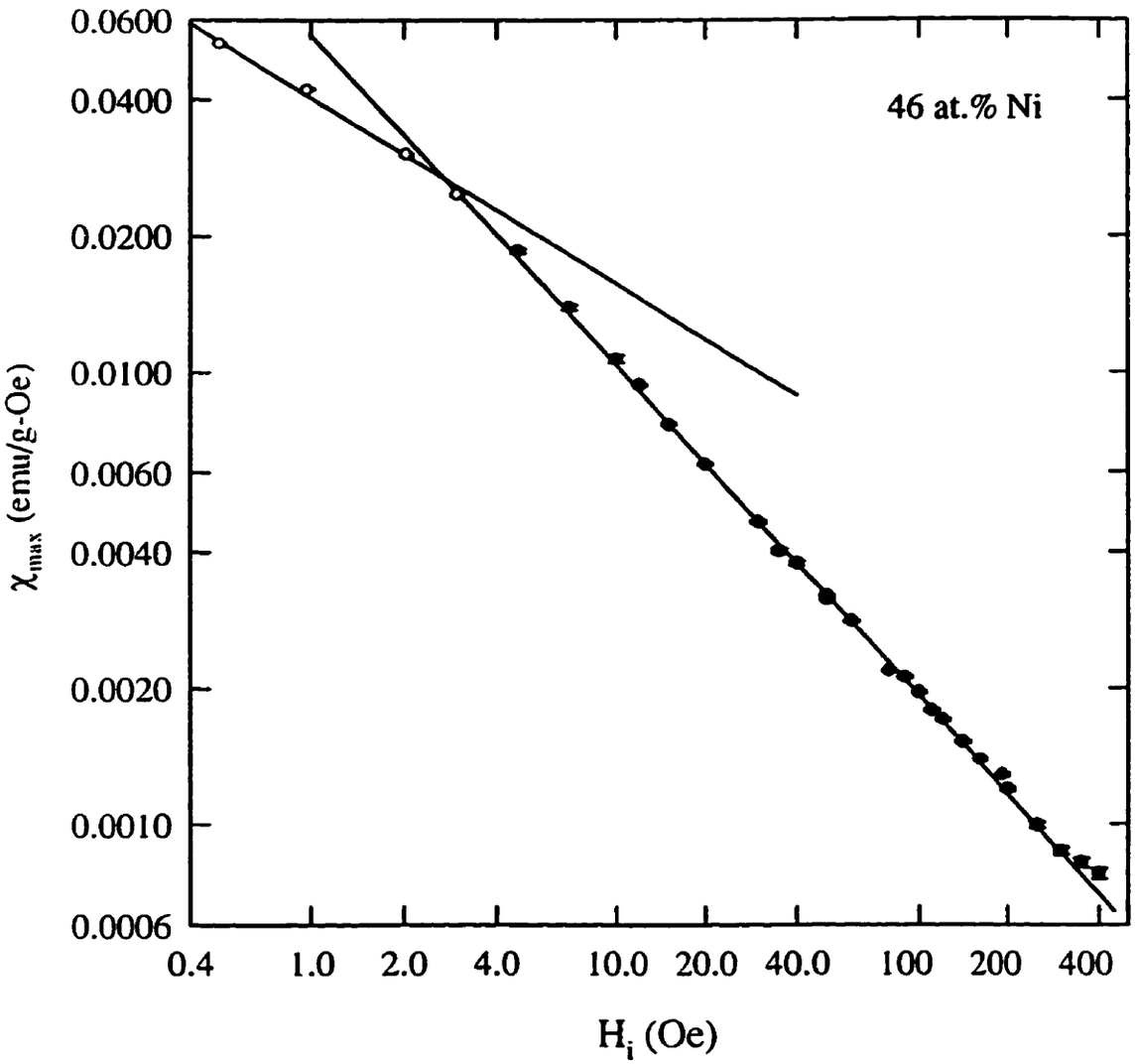

Figure 5.19: Peak susceptibility as a function of internal field for the 46 at.% Ni sample. The superimposed lines represent fits to the data with δ_{lf}=1.69(2), and δ_{hf}=3.70(5).

which the zero field *ac* susceptibility is plotted as a function of temperature for the $Cu_{100-x}Ni_x$samples, illustrates the evolution of ferromagnetism with increasing Ni concentration. For clarity, not all of the curves are shown. The ferromagnetic state obviously becomes more stable with increasing x, since both T_c and the peak height increase essentially monotonically with Ni concentration. The small variation in χ_m evident from 47–50% Ni is slightly larger than the absolute uncertainty in the susceptibility, and is likely due to slight differences in quench rate, which cause inconsistencies between samples. The height of the Hopkinson peak in the zero field *ac* susceptibility is examined in more detail in figure 5.21. χ_m increases rapidly between 50 and 54 at.% Ni, and drops slightly above 54 at.%. The peak height in the region between 47 and 50% Ni is essentially constant, but falls precipitously below 47 at.% Ni. χ_m in the 45% sample is only $\sim$1/20 of that at 55% Ni. This latter decrease suggests a critical concentration only slightly lower than 45%. For comparison, the inset of Figure 5.21 shows similar data for PdNi near the critical concentration (extracted from data published by Wang et al. [107]). The PdNi system is not as sensitive to preparation technique as the CuNi, and is thus a good benchmark against which to compare the trends observed in the $Cu_{100-x}Ni_x$ system. These data show surprisingly good agreement, including the small initial increase with decreasing concentration from 5 to 4.5 at.% Ni in Pd (c.f. 55-54% here). χ_m then drops rapidly to a plateau regime, which is terminated by an abrupt drop at 2.4 at.% Ni–immediately above the critical concentration x_0=2.25–2.3[6]. The peak susceptibility, however, is approximately an order of magnitude lower in the Pd based system than in CuNi, scaling approximately with the ratio of their respective Ni concentrations. From this we might infer that the magnetic behaviour in these two systems is rather similar, likely a percolation-type transition in both, and indicates a critical concentration for Ni in Cu of slightly less than 45 at.%.

The final values of T_c as deduced from susceptibility data are summarised in Table 5.1, along with various exponent values; $T_c(x)$ is plotted in figure 5.22. T_c increases essentially monotonically with increasing concentration, fitting well to a linear dependence for x >46, with a slope $\frac{dT_c}{dx} \sim 8.6$ K/at.% Ni, considerably lower

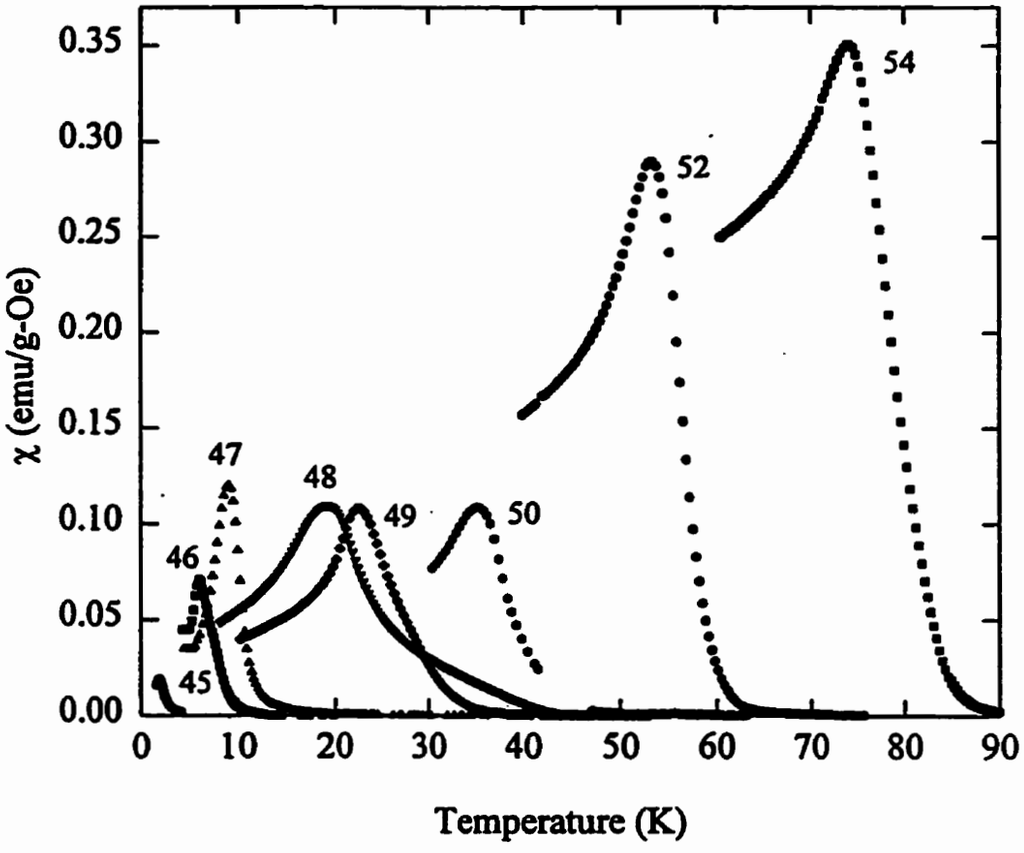

Figure 5.20: Temperature dependence of the zero-field *ac* susceptibility in $Cu_{100-x}Ni_x$ with x as labelled.

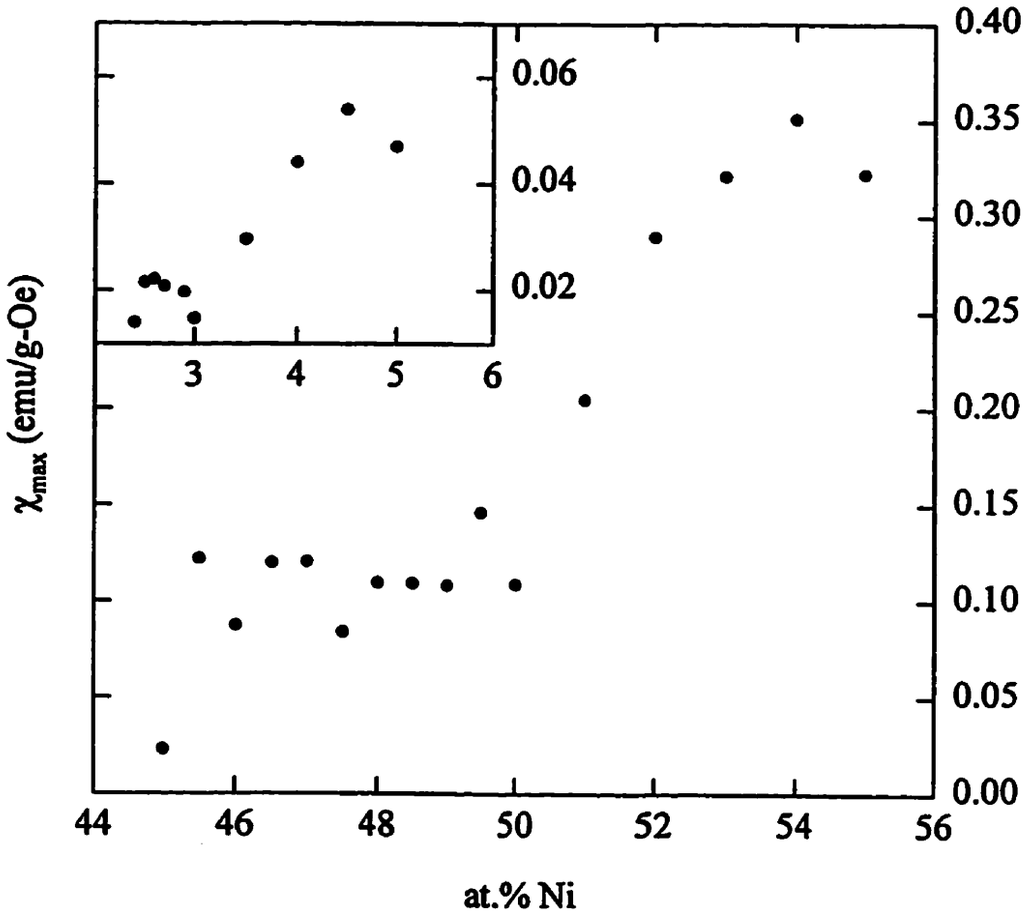

Figure 5.21: The height of the Hopkinson maximum as a function of Ni concentration. The inset shows similar data for PdNi[107].

Table 5.1: Summary of Temperature Dependence of Susceptibility Peaks in $Cu_{100-x}Ni_x$

at.% Ni	T_c(K)	$\gamma+\beta$	γ	γ_m^*	t_m
45.0	1.7(3)	1.75(3)	1.00(5)	1.5	1.5
45.5	4.2(1)	2.1(1)	1.39(10)	6.4	1.16
46.0	5.6(1)	1.75(20)	1.39(10)	5.0	1.15
46.5	8.1(2)	1.75(30)	1.39(20)	3.0	0.60
47.0	9.8(2)	1.75(20)	1.39(10)	4.2	1.6
47.5	13.1(3)	1.75(20)	1.39(10)	4.2	0.59
48.0	20.1(4)	1.75(20)	1.16(6)	—	—
48.5	25.1(6)	1.75(10)	1.39(20)	7.3	0.56
49.0	22.2(6)	1.75(10)	1.8(1)	5.9	0.59
49.5	29.4(6)	1.75(20)	1.39(10)	3.7	0.27
50.0	33.3(7)	1.75(30)	1.39(10)	4.8	0.34
51.0	39.1(8)	1.75(70)	1.39(20)	5.4	0.23
52.0	55.4(11)	1.75(7)	1.39(5)	3.8	0.12
53.0	62.8(13)	1.75(20)	1.39(10)	2.7	0.06
54.0	78.4(20)	1.75(10)	1.39(6)	4.0	0.11
55.0	83.2(20)	1.75(20)	1.39(10)	2.6	0.06

than that of 30K/at.% Ni found by Ododo and Coles[4], using primarily data with x >50. These authors suggest that the curvature evident below 50 at.% Ni is due to mictomagnetic contributions to the magnetic state at low concentration, which do not vanish completely until above 50 at.% Ni. This 'mictomagnetic' region corresponds to the plateau in the $\chi_{max}(x)$ plot. The cross-over exponent (Table 5.1), however, shows little evidence of a change in state at x=50, having instead an approximately constant value of 1.75. The asymptotic γ also seems consistent, within error, with the 3D Heisenberg value except at intermediate ($x = 0.48, 0.49$) and low concentration (45 at% Ni). The sudden drop from the 3D Heisenberg exponent to the mean field value of 1 between 45.5 and 45 at% Ni, indicates, perhaps, the proximity of the x=45 sample to the critical concentration. $\gamma_m^*(t)$ is plotted as a function of Ni concentration in figure 5.23. The peak in γ^* moves

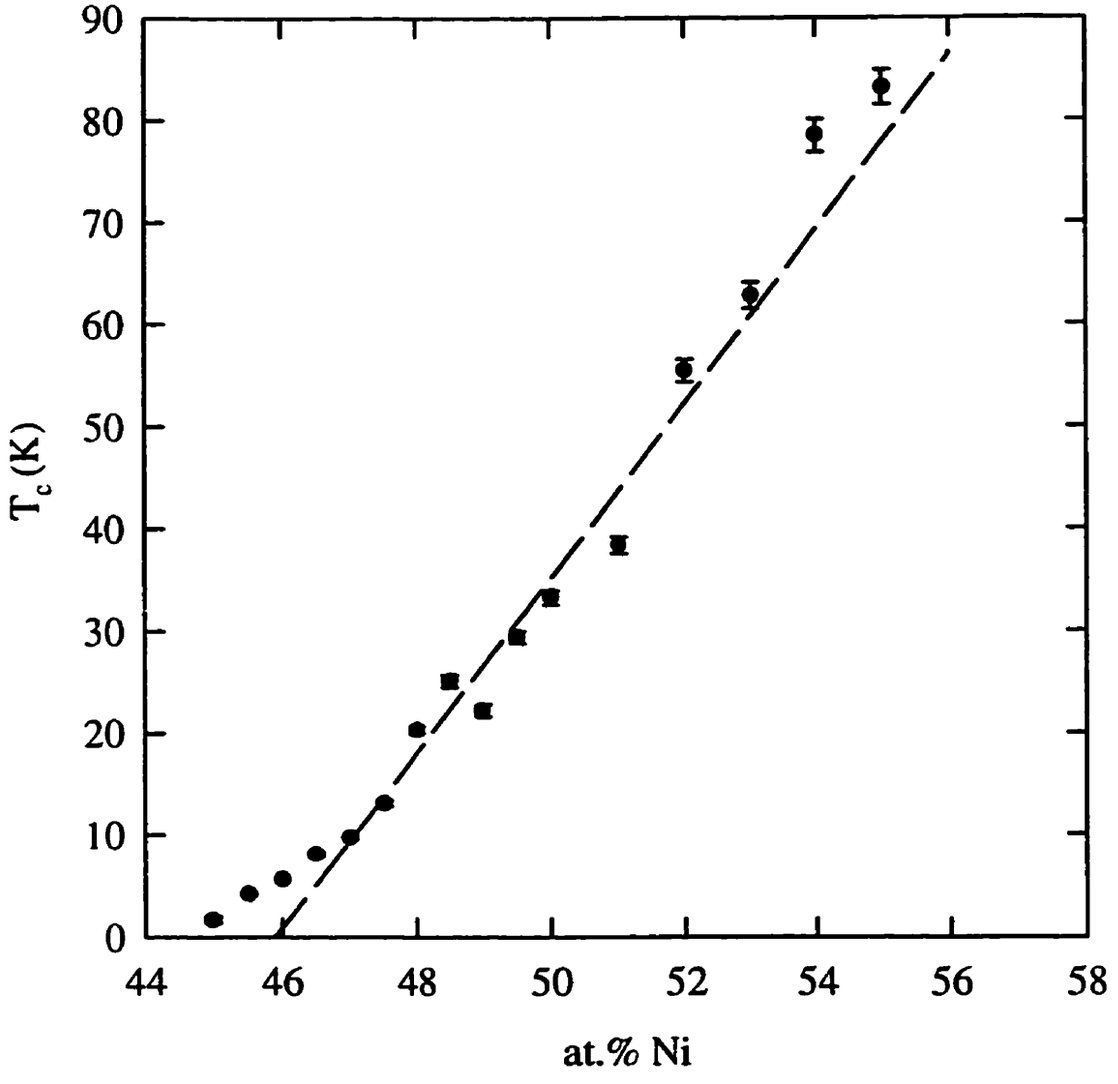

Figure 5.22: T_c as a function of Ni concentration as determined from *ac* susceptibility data. The dashed line indicates a fit to $T_c(x)$ ($x \geq 46$) with dT_c/dx=8.6 K/at.% Ni.

Table 5.2: Summary of Delta Plot Results for the $Cu_{100-x}Ni_x$samples

at.% Ni	δ_{lf}	δ_{hf}	H_c(Oe)
45.0	1.47(2)	3.00(1)	0.29(2)
45.5	2.00(4)	3.00(2)	0.11(2)
46.0	1.69(2)	3.70(5)	0.49(2)
46.5	5.8(2)	3.56(5)	0.54(2)
47.0	4.8(3)	3.8(1)	0.82(2)
47.5	12(1)	3.7(1)	1.5(2)
48.0	8.6(6)	2.13(2)	1.3(2)
48.5	—	3.73(5)	0.86(2)
49.0	—	3.00(8)	1.1(2)
49.5	8.4(3)	3.00(8)	1.1(2)
50.0	10.2(4)	3.00(7)	1.1(2)
51.0	4.80(6)	1.98(2)	1.0(2)
52.0	—	3.18(1)	0.91(5)
53.0	—	4.2(2)	0.86(5)
54.0	—	4.17(5)	1.3(2)
55.0	—	3.25(9)	1.7(2)

to higher reduced temperature as x decreases, similar to the trend observed in the PdNi system. The peak value of γ^* shows no consistent trend, although it does decrease rapidly as $x \rightarrow 45$. In PdNi, the maximum in γ^* was largest around 3 at.%, which is close to the upper end the 'plateau' regime of its $\chi_m(x)$ plot. The considerable scatter in figure 5.23(a) does not preclude a peak in $\gamma^*_m(t)$ around x=49, at approximately the end of the plateau in this system.

Table 5.2 lists the values for the high and low field δ and the coercive force for the sample, as determined from 'butterfly' plots measured at 4.2K (1.5K for x=45 and 45.5). Figure 5.24 shows the dependence of H_c on the concentration, with the inset showing a typical 'butterfly' curve for the 49.5 at% Ni sample. $H_c(x)$ decreases to approximately zero at 45 at.% Ni, another indication that $x_0 \sim 45$.

Some trends can also be observed in the values of δ. The low-field slope of the δ plot shows a non-uniform increase with decreasing x, approaching very large values

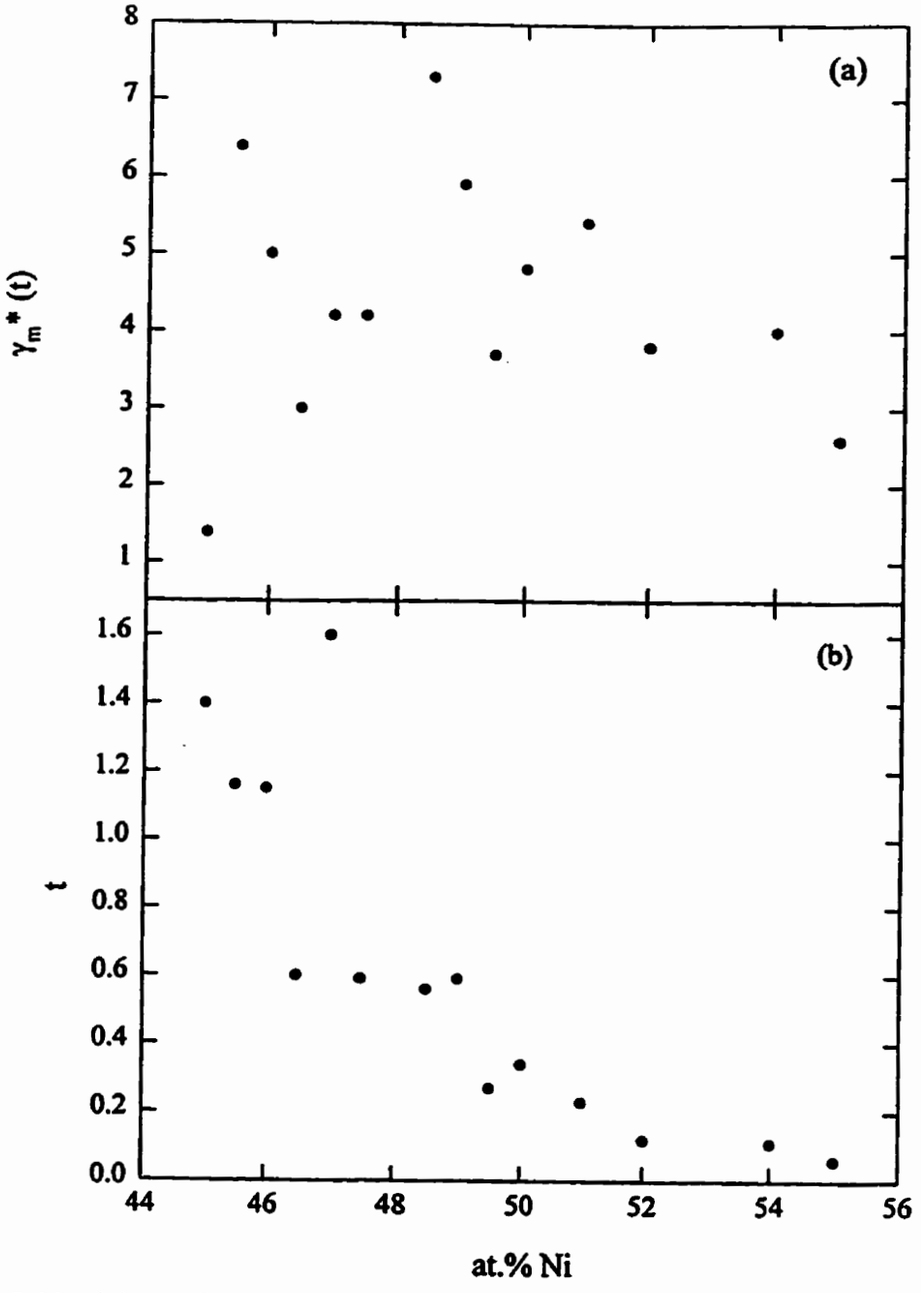

Figure 5.23: (a) $\gamma_m^*(t)$ as a function of Ni concentration for $Cu_{100-x}Ni_x$. (b) The temperature at which the peak in $\gamma^*(t)$ occurs as a function of Ni concentration.

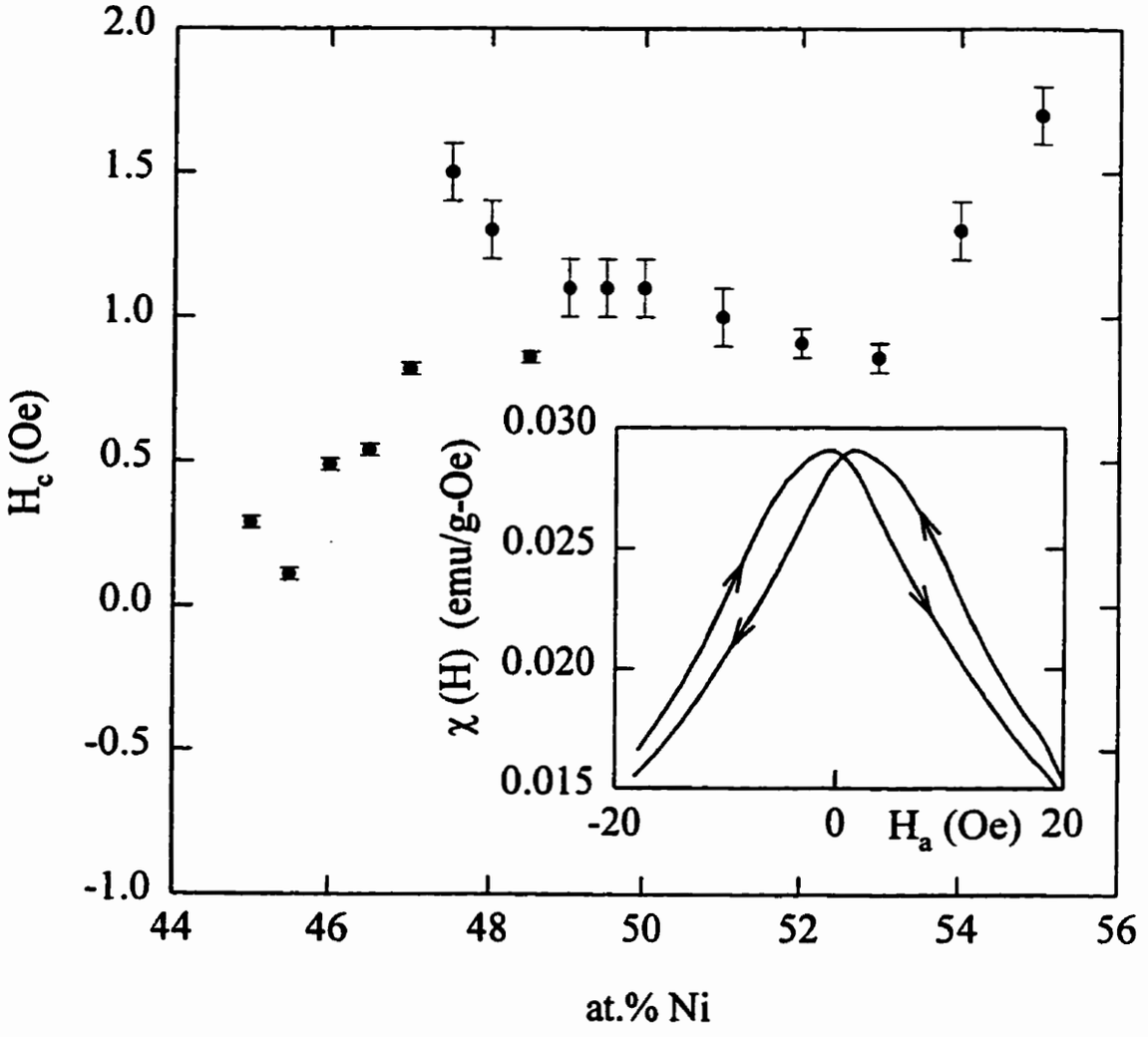

Figure 5.24: Coercive force as a function of concentration for the CuNi system. These values are estimated from butterfly loops, as explained in the text. The inset shows a butterfly loop for the x=49.5 at.% Ni sample at 4.2K.

in the range 48–49 at%Ni–in fact, for these samples the slope of the δ-plot, $\frac{1}{\delta} - 1$, is greater than 1, i.e. $\delta < 0$, which is unphysical. This result is likely due to the large background contribution to the low field data which obscures the true low field behaviour. The scatter in the δ_{lf} values corresponds roughly to the abrupt changes in the coercive force, although the latter changes may also be influenced by changes in sample preparation conditions. Below 48%, δ_{lf} increases to 3D Heisenberg values, and then drops suddenly to 2 due to the anomalous behaviour of the low field data in the three lowest concentration samples. By contrast, PdNi showed a continuous decrease in δ_{lf} with decreasing x from $\sim$ 4.1 at 5% Ni to $\sim$ 2.7 at the lowest ferromagnetic concentration[63]. We suggest that the large variation observed in the present system may be an artifact due to additional metallurgical complications. For $x = 55$, 54 and 53, there is no significant curvature in the δ fit, and all points can be fit, to give a value for δ which increases from 3.3 to 4.8 (the 3D Heisenberg prediction) at 53 at.%. Below 53%, the curvature present greatly reduces δ_{hf}, with several of the samples having δ_{hf} of 3, the mean field value. There is, however, no noticeable trend in these values, although comparison with the $H_c(x)$ plot indicates that there may be correlations between δ_{hf} and the changes in the coercive force. δ_{hf} shows no consistent trend with x, as was also found in PdNi[6].

In summary, the CuNi system shows many similarities to the PdNi system, with the general features of the *ac* susceptibility in both systems indicative of a second order paramagnetic to ferromagnetic phase transition. The detailed behaviour is more complicated in CuNi, however, due possibly to the difficulties in sample preparation discussed earlier. The 48% sample, in fact, shows a number of anomalous exponents, as can be seen from Tables 5.1 and 5.2, suggesting additional problems with this sample. Nevertheless, the overall trends in the general behaviour as well as in specific features of the susceptibility data indicate a change in the system slightly below 50 at.% Ni, with a complete loss of ferromagnetic character close to 45 at.% Ni.

Table 5.3: Summary of Residual Resistivity and Form Factors for $Cu_{100-x}Ni_x$

x (at.% Ni)	form factor (10^{-3}cm)	$\rho_0(\mu\Omega-cm)$
45.0	1.08	44(2)
45.5	1.18	43(2)
46.0	1.38	44(2)
46.5	1.36	42(2)
47.0	1.06	37(2)
47.5	1.36	38(2)
48.0	1.59	43(2)
48.5	1.25	42(2)
49.0	1.68	42(2)
49.5	0.752	40(2)
50.0	1.47	42(2)
51.0	1.26	42(2)
52.0	0.429	38(2)
53.0	1.46	40(2)
54.0	1.32	39(2)
55.0	1.27	39(2)

5.2.2 Transport Measurements

Residual Resistivity

Resistance measurements were taken at fixed temperatures of 1.5 and 4.2K in fields of up to 30 kOe in the SRA cryostat (Section 3.2.2). Sample dimensions were measured and used to calculate the form factors, as done previously. Using these form factors and initial voltage measurements, values for ρ_0 were obtained, as listed in Table 5.3. The large errors of $\pm$ 5% are due both to uncertainties in form factor and to systematic errors inherent in the *ac* measuring technique. Overall, the residual resistivity seems to be decreasing with increasing nickel concentration (averaging out the scatter), as expected in this composition range[4]. The magnitude of the residual resistivity agrees approximately with previously published results[4, 97, 100, 101].

Magnetoresistance and Spontaneous Resistive Anisotropy

To avoid errors resulting from uncertainties in form factor, the fractional rather than the absolute magnetoresistance was calculated. This magnetoresistance is shown in figure 5.25 both as a function of applied field, H, and induction B(= H + 4πM− NM) for the 55 at.% sample. Magnetisation data were obtained from previous published work[4, 94]. Obviously the correction is negligible, causing shifts smaller than 1% at high field. Thus extrapolations to H=0 are essentially equivalent to extrapolations to B=0 in this sample, with both branches (parallel and perpendicular) extrapolating to B=0 at H=0. Similar plots were done for the 50 and 45 at.% samples, for which conversion from applied field to induction also resulted in insignificant changes. The magnetoresistance data are thus plotted as a function of applied field rather than induction in the following figures. Figure 5.26 compares the magnetoresistance for two representative samples, with 45 and 55 at.% Ni. These data were measured at 1.5 K, the lowest measuring temperature. The magnetoresistance plots for the remaining samples are shown Appendix A. At all concentrations, $\rho_{\parallel} > \rho_{\perp}$, in contrast to the PdNi system, in which $\rho_{\perp} > \rho_{\parallel}$[6], and in agreement with measurements by Kaul[108] for samples with more than 70 at.% Ni. The isotropic magnetoresistance, $(2\rho_{\perp} + \rho_{\parallel})/3$ is negative, consistent with the reduction of spin-disorder scattering by a magnetic field. At the highest Ni concentration (55%), $\rho_{\parallel}$ increases initially at low field, followed by a linear decrease for fields greater than 400 Oe. $\rho_{\perp}$ has a sudden decrease followed by a linearly decreasing region above 400 Oe, as in the parallel configuration. The slope of this linear region remains large as x decreases and the anisotropy (i.e. the separation between the two curves), decreases rapidly, until, at 45% Ni, there is no measurable anisotropy at 4.2K, and only a very small anisotropy at 1.5K. For the higher concentrations, 1.5K$\ll$T$_c$, and thus the data at 4.2K differs very little from that at 1.5K, and is not shown here. One can find values for the spontaneous resistive anisotropy from the magnetoresistance curves, using equation 2.44 viz.,

$$\frac{\Delta\rho}{\rho_0} = \lim_{B\to 0}\left(\frac{\rho_{\parallel}(B) - \rho_{\perp}(B)}{\frac{1}{3}(\rho_{\parallel} + 2\rho_{\perp})}\right) \tag{5.4}$$

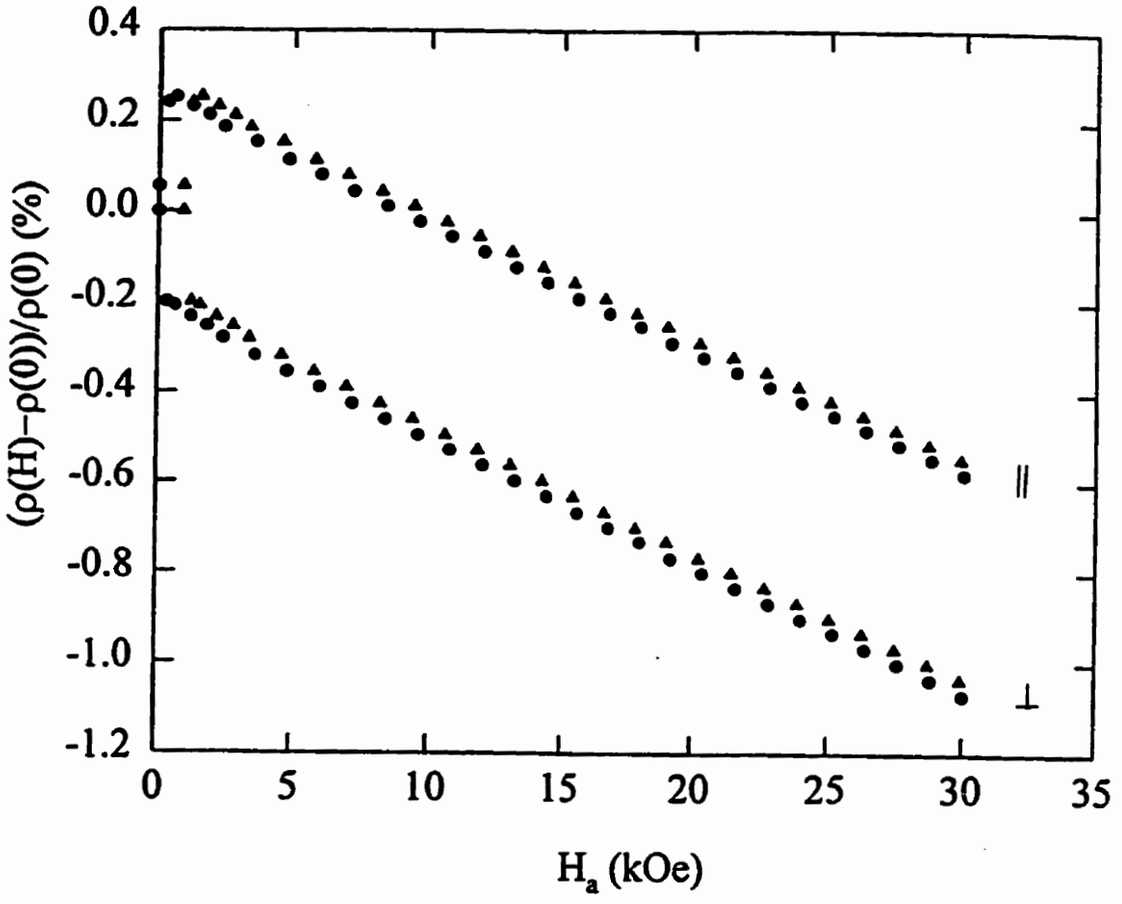

Figure 5.25: Magnetoresistance as a function of applied field (circular symbols) and induction (triangular symbols) for the 55 at.% sample, as measured at a fixed temperature of 1.5 K.

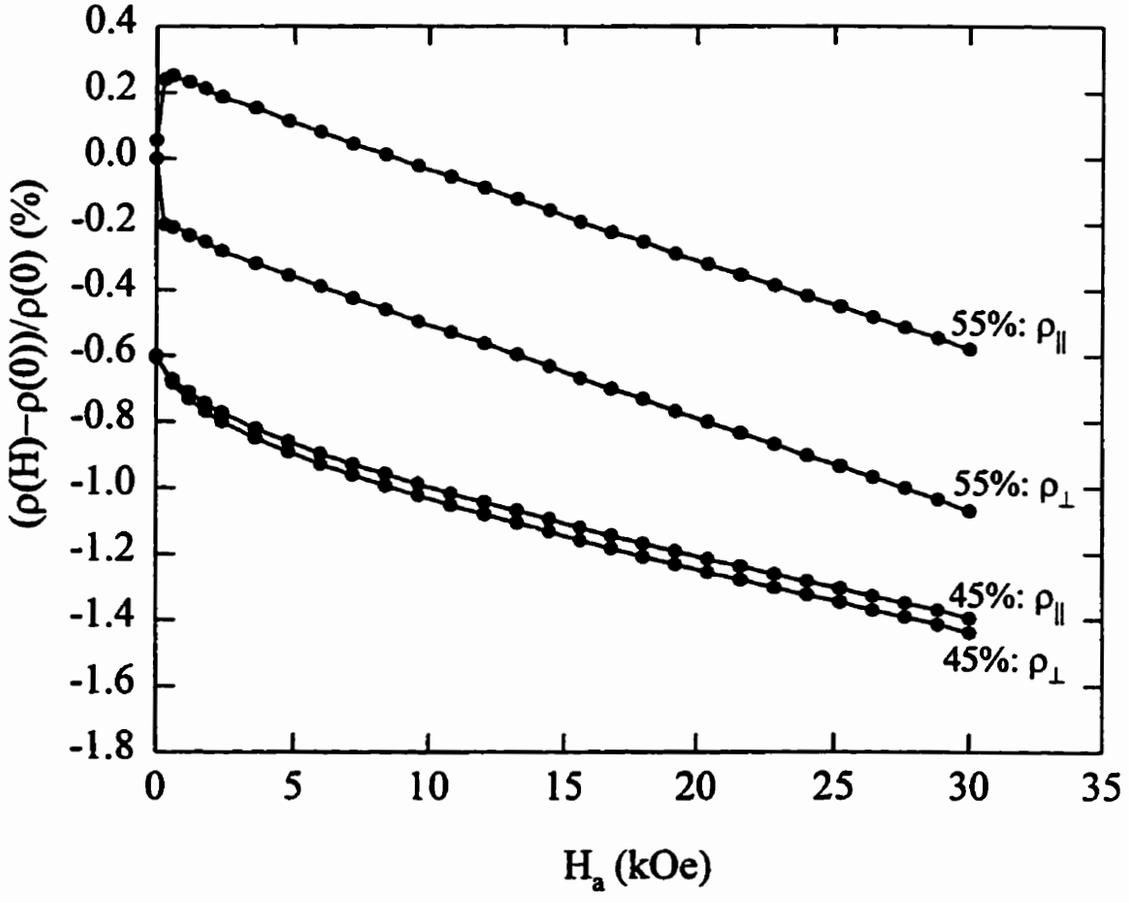

Figure 5.26: A comparison of the magnetoresistances at 1.5 K for the 45 and 55 at.% samples, as labelled. The curves for $x = 0.45$ have been offset by 0.6% for clarity.

In the $Pt_{90}Fe_{10}$ and $Pd_{97}Co_3$ samples discussed in Chapter 4, the magnetoresistance saturates at high field and the SRA can be obtained by simple extrapolation of the high field data back to B=0 (or equivalently H=0 in these systems). This high field extrapolation is the traditional method of obtaining values for the SRA[41], and works well for the 55 at.% Ni sample, as demonstrated by the dashed lines in figure 5.27, giving an SRA of $\Delta\rho/\rho_0$=0.0046(1) or 0.46%. This extrapolation method remains appropriate and yields accurate values for the SRA in nickel concentrations as low as 49%. Below this concentration the large high field slope of the curves in conjunction with the small anisotropy results in large errors in the extrapolated SRA, as demonstrated for the 47 at.% Ni sample in figure 5.28(a). The two sets of lines shown in this plot represent slightly different extrapolations to H=0 for both $\Delta\rho_{\parallel}(H)/\rho_0$ and $\Delta\rho_{\perp}(H)/\rho_0$. One is the best fit to the high field points, while the other slope is within error of the first. Although the difference in the slope between lines is small, the slope itself is large, causing a significant difference in the SRA determined at H=0: 0.05% and 0.07%; the difference between which is greater than the SRA in the lowest concentration samples. Thus, as $x \rightarrow x_0$, the extrapolation method can not reliably determine the magnitude of the SRA, and, indeed, at the lowest concentrations can not even correctly determine the sign of the anisotropy. A second method of determining the anisotropy is to plot the difference between the MR in the two modes as a function of field. This direct subtraction of the two magnetoresistances is valid, since in these samples the demagnetisation corrections are negligible, i.e. $B_{\parallel}(H) \simeq B_{\perp}(H) \simeq H$. Since the two curves are essentially parallel in the high field region, these data (shown in figure 5.28(b) for the 47% sample) yield a curve which, through extrapolation to H=0, gives $\Delta\rho/\rho_0$=0.06(1)%, in good agreement with the estimates obtained using the two curve extrapolation method. As the concentration decreases yet further, even this method develops considerable errors. As well, notwithstanding the extrapolation to B=0, the large applied fields can enhance the intrinsic polarisation of the system, significantly increasing the measured SRA. Thus, a non-zero anisotropy may be observed at high fields even for $x < x_0$ due to field-induced polarisation.

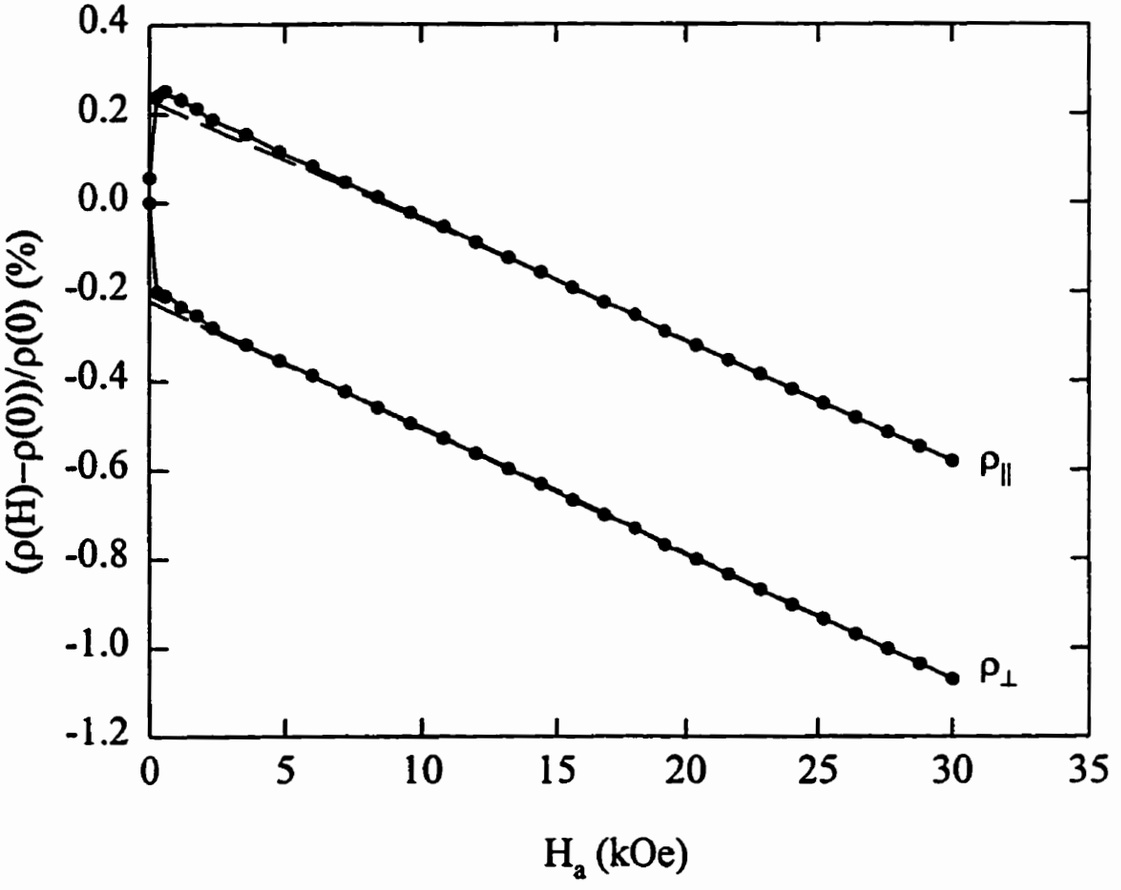

Figure 5.27: The magnetoresistance as a function of field at 1.5 K for the 55 at.% Ni sample. The dashed lines illustrate the extrapolation method used to obtain the spontaneous resistive anisotropy (SRA).

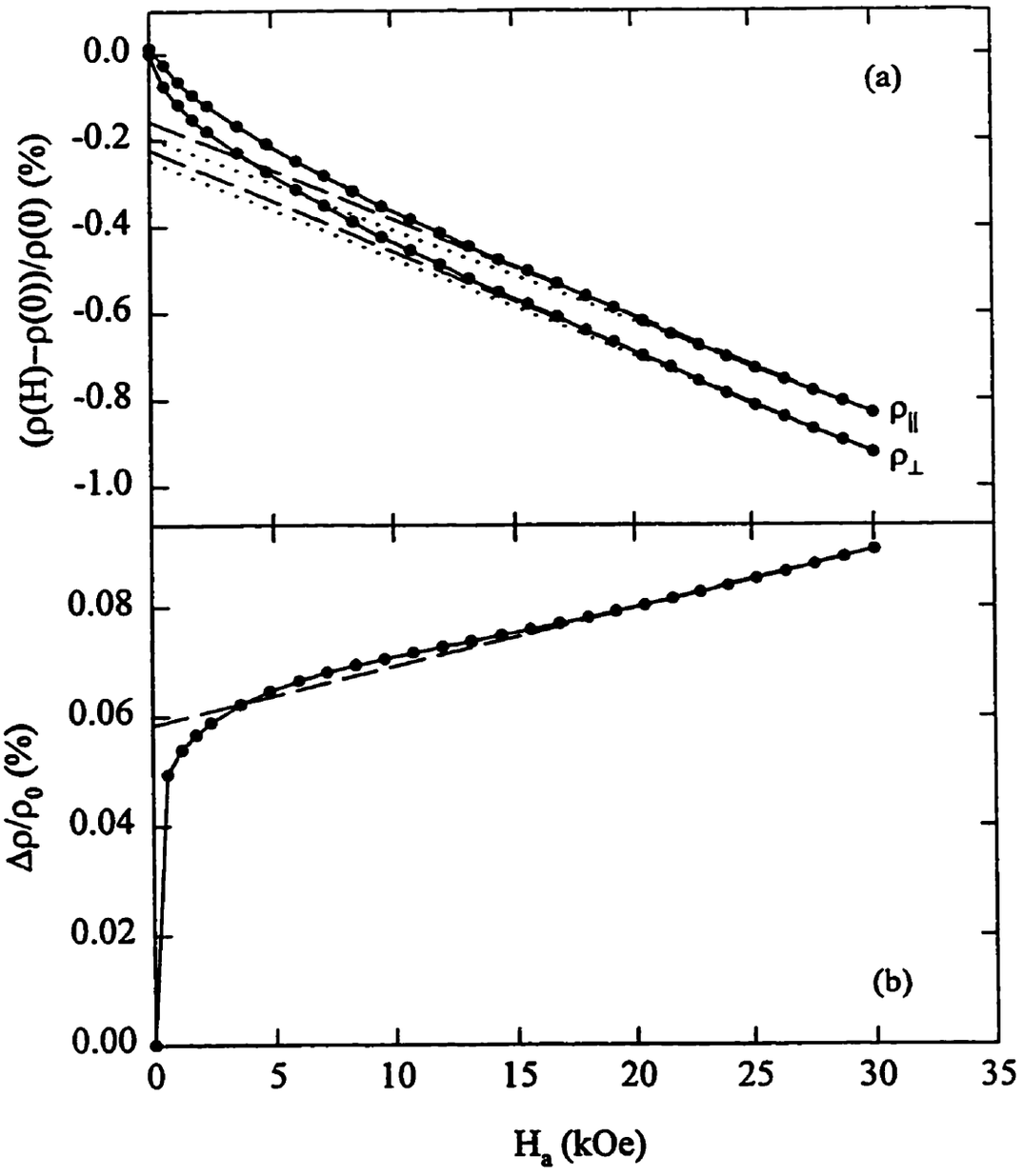

Figure 5.28: (a) The magnetoresistance in the 47 at.% Ni sample at 1.5 K. The two sets of lines are both good fits to the high field data, giving different values for the SRA. (b) The anisotropy in magnetoresistance as a function of field at 1.5 K for the 47 at.% Ni sample, showing the extrapolation method used to obtain the SRA.

For the low Ni concentration samples, a new technique for finding the SRA is thus required. The similarity of the magnetic properties of this system to those in the PdNi system suggest that comparison of their magnetoresistances may help solve the problem. Although the sign of the anisotropy is different in these two systems, i.e. $\rho_{\parallel} < \rho_{\perp}$ in PdNi, the magnetoresistance in the two systems exhibits a similar rapid decrease in anisotropy coupled with a rapid increase in the high field slope with decreasing Ni concentration[6]. Thus, the PdNi system exhibits the same difficulty in obtaining accurate estimates of the SRA in the vicinity of x_0. In PdNi, a minimum in $\rho_{\parallel}$ (H) was observed at some value of applied field, H_m; this field approached zero as $x \rightarrow x_0$. The anisotropy at this field was observed to give SRA values in good agreement with values obtained using the traditional technique in the concentration range over which the latter is valid[107], supporting the reliability of the estimates based on $\Delta\rho(H_m)$. A corresponding feature exists in $\rho_{\parallel}$ in $Cu_{100-x}Ni_x$, namely the presence of a maximum at a field, H_m, which also exhibits the desirable property of decreasing to zero at x_0, so that estimates based on it are made in progressively decreasing fields as $x \rightarrow x_0$, thus minimising potentially perturbing effects of externally applied fields. The maximum in $\rho_{\parallel}(H)$ can be seen clearly in figure 5.29, the low field magnetoresistance in the 47% sample. H_m drops from ~400 Oe at 55 at.% Ni to ~5 Oe at 45 at.% Ni. This means that the perturbing effects of the external field are minimal near H_m as $x \rightarrow x_0$, allowing the presence of an SRA to be accurately deduced using this alternate method.

The values of the SRA obtained using these three methods are listed in Table 5.4 as a function of nickel concentration. At high concentrations the values obtained from all three estimates agree within error, although generally the value obtained using the maximum in the parallel magnetoresistance is lower than that obtained using the conventional technique, a reassuring result as it is expected generally that measurements at larger fields will show larger anisotropies, due to externally enhanced spin polarisation. Also, although the first two methods (A and B in Table 5.4) exhibit considerable scatter from sample to sample, the SRA found using the third method decreases monotonically with Ni concentration. Thus, the latter

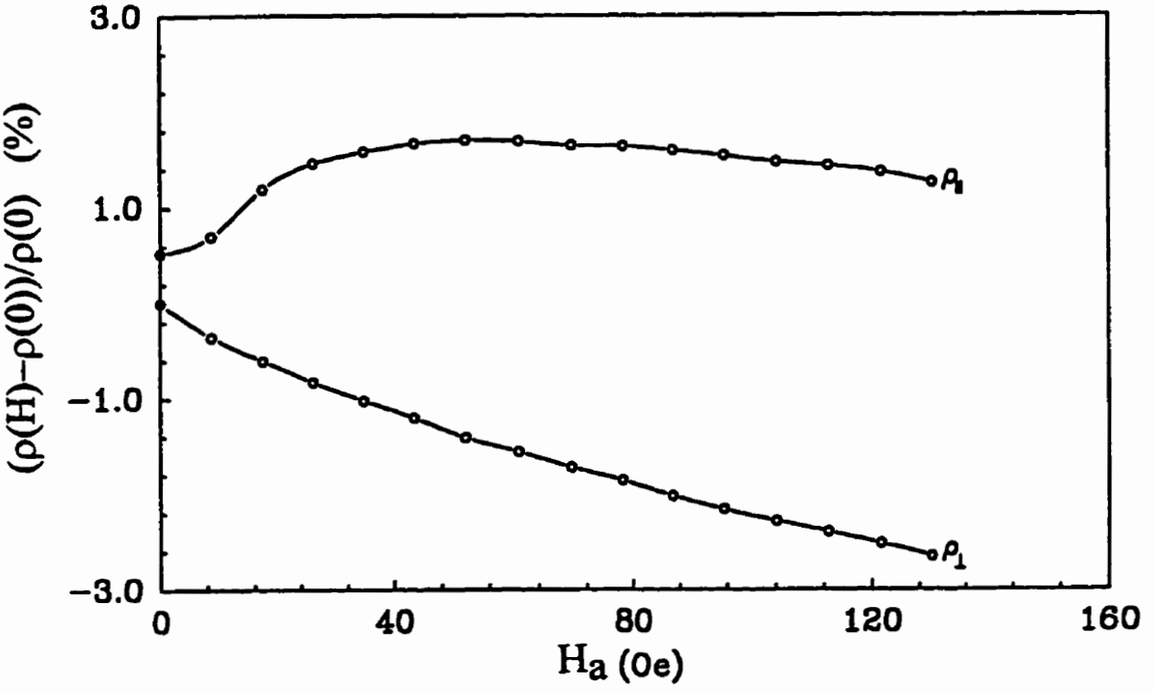

Figure 5.29: The low field portion of the 47 at.% Ni magnetoresistance data, clearly showing the maximum in $\rho_{\parallel}$.

Table 5.4: Summary of SRA Data in $Cu_{100-x}Ni_x$, found using A: conventional extrapolation techniques, B: difference extrapolation and C: anisotropy at H_a^m.

at.% Ni	A (%)	B(%)	C(%)
45.0	–	–	0.0011(4)
45.5	–	–	0.0034(4)
46.0	–	–	0.015(2)
46.5	–	–	0.033(2)
47.0	–	0.06(4)	0.030(3)
47.5	–	0.10(5)	0.056(2)
48.0	–	0.11(6)	0.084(2)
48.5	–	0.14(2)	0.11(1)
49.0	0.14(1)	0.14(1)	0.13(1)
49.5	0.22(1)	0.22(1)	0.16(1)
50.0	0.17(1)	0.17(1)	0.16(1)
51.0	0.23(2)	0.22(2)	0.20(1)
52.0	0.31(2)	0.30(2)	0.23(1)
53.0	0.36(2)	0.36(2)	0.35(1)
54.0	0.45(2)	0.46(2)	0.43(1)
55.0	0.46(2)	0.48(2)	0.46(1)

method probably provides a more reliable estimate of the SRA over the entire range of x. The SRA obtained using this technique are plotted versus concentration in figure 5.32. As in PdNi[6] the rapid decrease of the SRA with concentration is consistent with a power law dependence on the reduced concentration. Clearly, fitting equation 5.3 requires knowledge of x_0, with the *ac* susceptibility analysis suggesting an x_0 slightly less than 45 at.% Ni. This is supported by a comparison of the low field magnetoresistance at fixed temperatures of 1.5 and 4.2K for the lowest x samples (figure 5.30 and 5.31). While the 45.5% sample has a clear anisotropy at *both* measuring temperatures, the 45% sample shows no difference between the parallel and perpendicular magnetoresistance in low field at 4.2K, however at 1.5K there *is* an anisotropy. This indicates clearly that the 45% sample is ferromagnetic at 1.5K but not at 4.2K, suggesting that the critical concentration is only slightly lower than 45. The SRA data were fit to equation 5.3 using a number of values for x_0, with x_0=44.5 giving the best fit, in our opinion. This is illustrated in figure 5.33 which plots the SRA as a function of reduced concentration on a log-log scale. The data at high Ni concentration deviates slightly from the linear behaviour, as might be expected so far from the critical region. One must also take into account the fact that, since the SRA is expected to be temperature dependent, especially in the vicinity of T_c, the measured anisotropy at 1.5K may not accurately reflect the true anisotropy at T=0. This consideration is important for those samples with T< 10K. Thus, the lower x data may have a slightly smaller SRA than the true, T=0, values, suggesting that the critical concentration may be slightly lower than that suggested from the data at these concentrations. Fitting equation 5.3 to all data points (equivalent to decreasing x_0) yields Δ=2.0(1), while fitting only the points at lower concentration gives Δ=2.2(1). The low x fit should be more appropriate, considering the asymptotic nature of (5.3). These values for Δ are in excellent agreement with that of 2.25 found for PdNi[6]. This agreement suggests that the SRA near the percolation concentration exhibits critical behaviour, with a universal exponent $\Delta \sim 2$ for those alloys with an orbital moment. As discussed in Section 4.1, dilute PdFe moments have no orbital moment at the impurity site, and

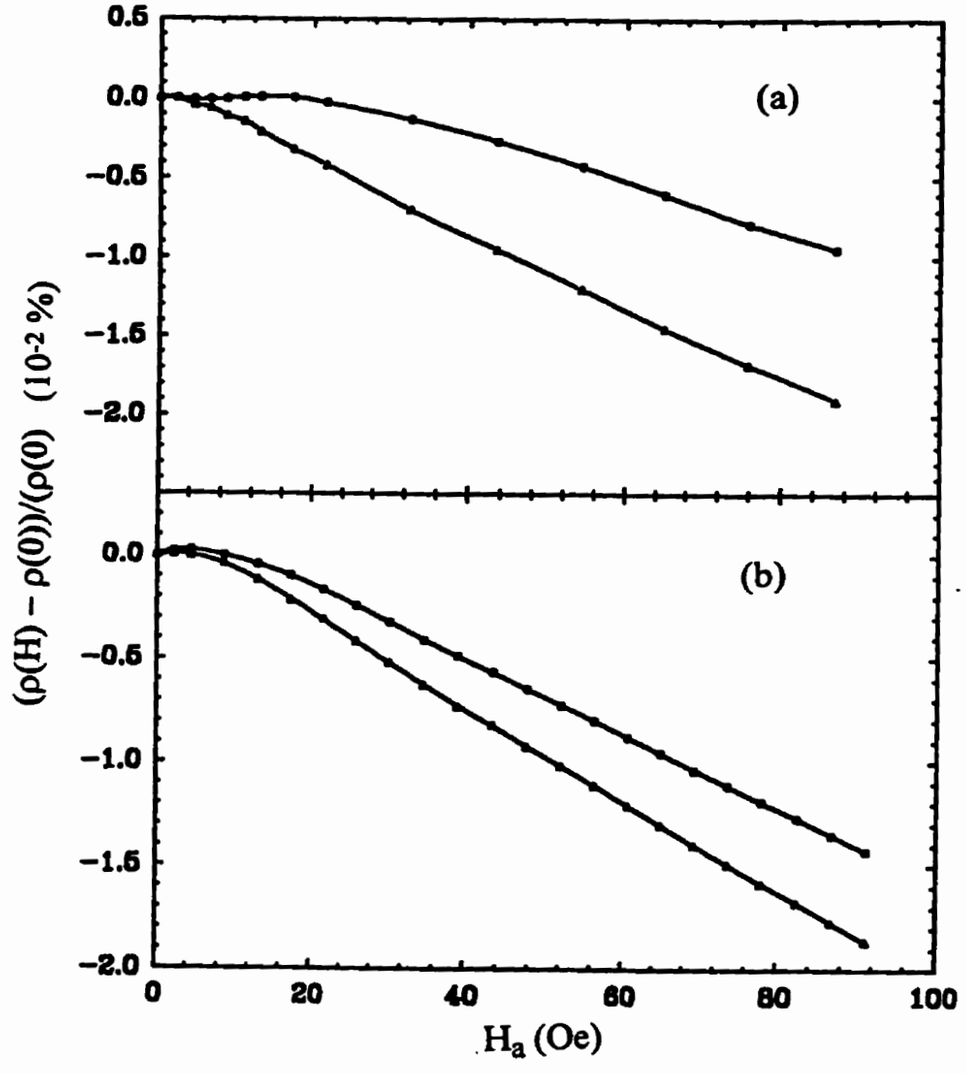

Figure 5.30: The low field magnetoresistance in the 45.5 at.% Ni at fixed temperatures of (a) 1.5 K and (b) 4.2K.

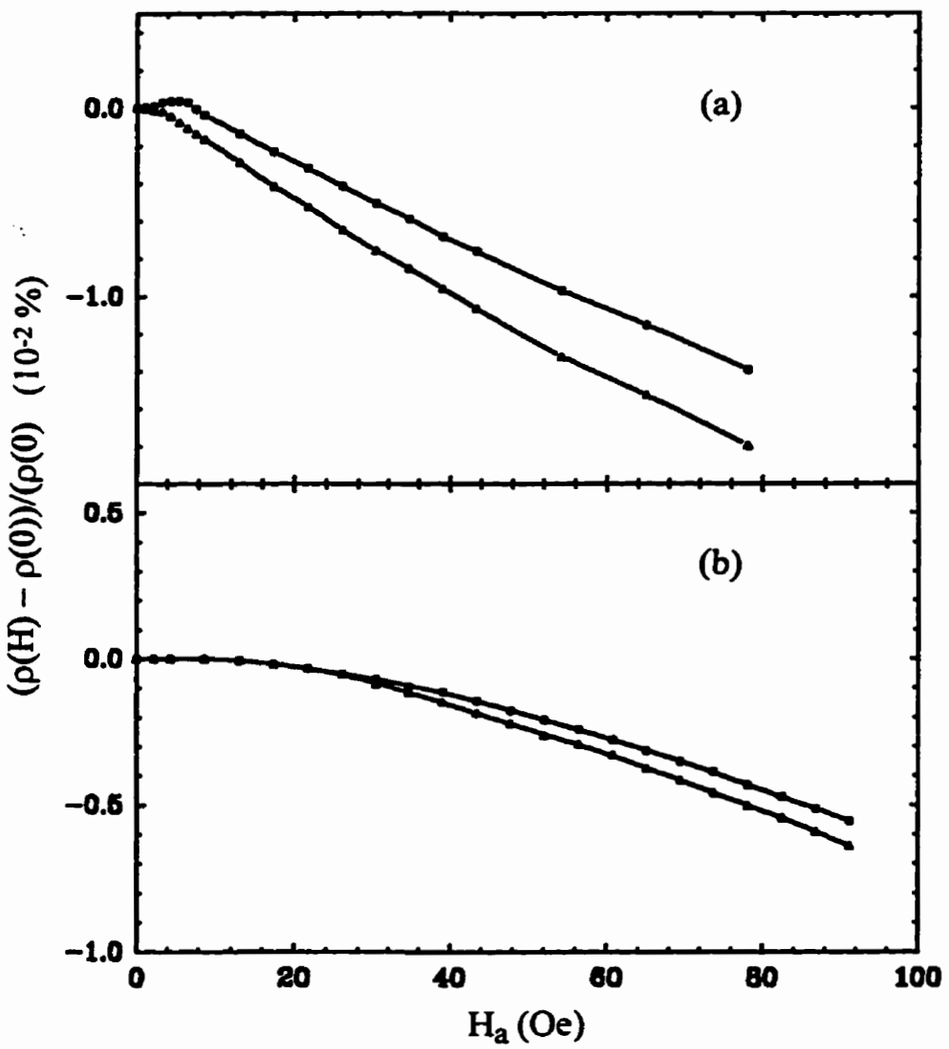

Figure 5.31: The low field magnetoresistance in the 45 at.% Ni at fixed temperatures of (a) 1.5 K and (b) 4.2K.

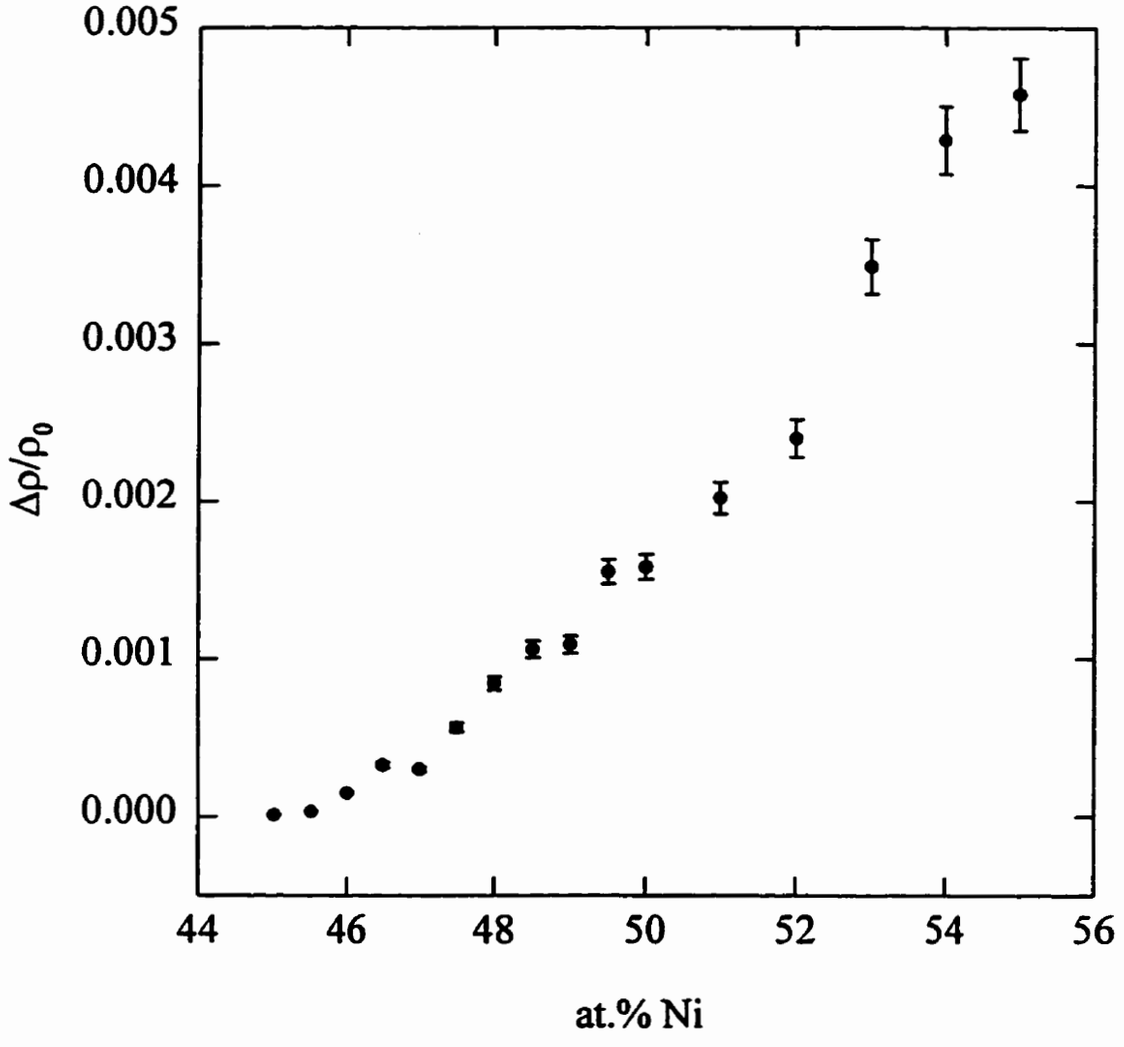

Figure 5.32: The SRA at 1.5 K as a function of Ni concentration.

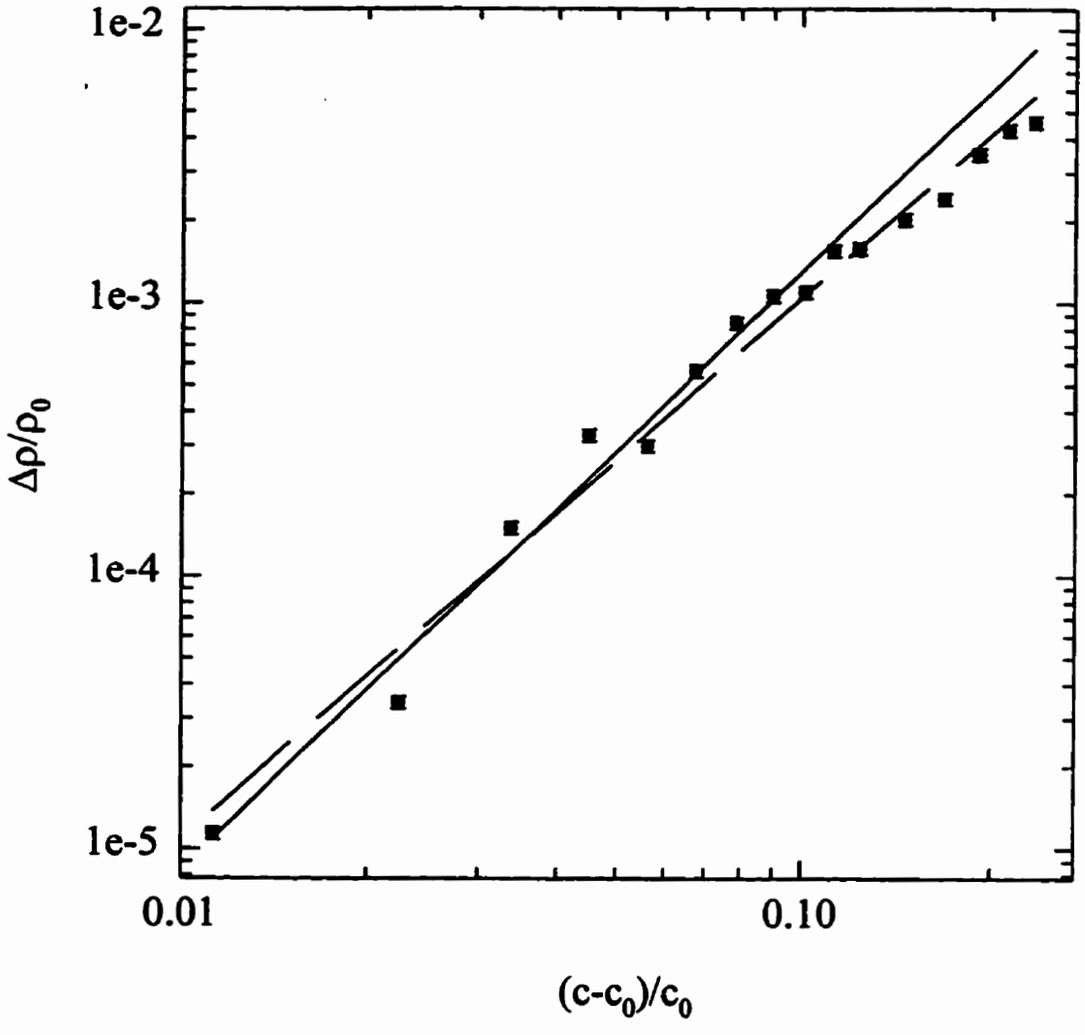

Figure 5.33: The SRA at 1.5 K as a function of reduced concentration, with x_0=44.5. The solid line is a fit to equation 5.3 with Δ=2.2, while the dashed line has Δ=2.0.

the SRA observed is due to spin-orbit coupling in the exchange-split Pd d-bands[5]. Further studies on the percolation transition in other alloy systems, perhaps with Co as the impurity, need to be done to reinforce this claim.

ρ(T) and the Low Field Resistive Anisotropy

The temperature dependence of the resistivity and the low field resistive anisotropy (LFRA) were measured in the LFRA cryostat described in section 3.2.3. Starting at a temperature well below T_c ($\leq 0.9T_c$), these data were collected using the following method: the temperature was stabilised at the lowest measuring temperature, and the absolute voltage across the sample (V_0) was measured. A field was then applied ($\sim$ 100 Oe), and the magnet was rotated so as to obtain the highest voltage output. This ensures that the magnetic field is parallel to the current (the longest sample dimension), based on models in which the anisotropy varies as the quadrupolar operator, i.e. $\propto \cos^2\theta$, where θ is the angle between the current and field directions. The voltage at this angle was recorded, after which the magnet was rotated by 90 degrees, so as to have the field perpendicular to the measuring current, and the voltage was recorded once more. Due to noise, two rotation averaging was employed to obtain the anisotropy $\Delta V = V_{\parallel} - V_{\perp}$. The temperature was then stabilised at a slightly higher temperature, and the change in voltage with temperature was measured on the most sensitive scale capable of accomodating the change. This allowed accurate determination of V_0(T) simply by adding these small changes. The anisotropy was measured at the new temperature, and the temperature was increased once more. This process was repeated until the anisotropy vanishes for temperatures above the critical temperature.

By definition the LFRA is given by

$$\frac{\Delta\rho(T)}{\rho_0} = \frac{\rho_{\parallel}(T) - \rho_{\perp}(T)}{\rho_0(T)} \tag{5.5}$$

As usual, this was calculated from the measured data using $\Delta\rho(T)/\rho_0 = \Delta V/V_0$, thus avoiding problems due to inaccuracies in form factor. The absolute resistivity $\rho_0(T)$ was obtained by multiplying V_0(T) by the appropriate form factor, calculated

from the sample dimensions. These data were taken using a different cryostat from that used to obtain the residual resistivities, and, since data were, in general, not taken at 4.2K, no attempt was made to compare the absolute value of the resistivities found in the two systems. $\rho(T)$ and $\Delta\rho(T)/\rho_0(T)$ are discussed for three representative samples in the following section. The remainder of the data can be found in Appendix A. Figures 5.34 and 5.35 show the data for the 55 at.% Ni sample. $\rho(T)$ has a 'knee' at T_c, characteristic of a paramagnetic to ferromagnetic transition. The derivative of $\rho(T)$ (inset of figure 5.33) was calculated using a point-to point difference method, i.e. $\Delta\rho/\Delta T$, and has a low temperature plateau followed by a sharp decrease above T_c, rather than the peaked structure seen in the samples in Chapter 4. The temperature at which this drop-off begins is taken to be T_c, giving a value for T_c of 83.1(8) K in the 55% sample, within error of that found from *ac* susceptibility data (83.2 K). As predicted by the model calculations shown in Section 4.2, the LFRA (figure 5.35) decreases linearly with increasing temperature, although some curvature is present near T_c. A linear fit of the low temperature region gives a temperature intercept of T_c=84.8±K, higher than that obtained from ρ(T). Since both sets of data were obtained simultaneously under the same conditions of field and temperature in the same cryostat, the difference between these temperatures is taken to be the error in the estimate of T_c from the LFRA data, and the linear fits are done over ranges which allow best agreement with T_c from *ac* susceptibility. An intermediate temperature regime (0.6–0.85 T_c) is thus used to obtain the straight line fit for T_c. These estimates, however, fail to take into account the clear presence of the high temperature 'tail' evident in these figures. Such tails most probably arise from short range order (generally associated with a decreasing coherent length above T_c), which may have an enhanced profile in this system due to the metallurgical difficulties involved. This 'tail' in the data is more pronounced than that observed in the disordered compounds in Chapter 4, perhaps reflecting inhomogeneities over the length of the sample. To compensate for the biasing effects of short range order, particularly on T_c estimates, a line is fit to the tail region, and T_c is taken to be the temperature at which the two lines intersect,

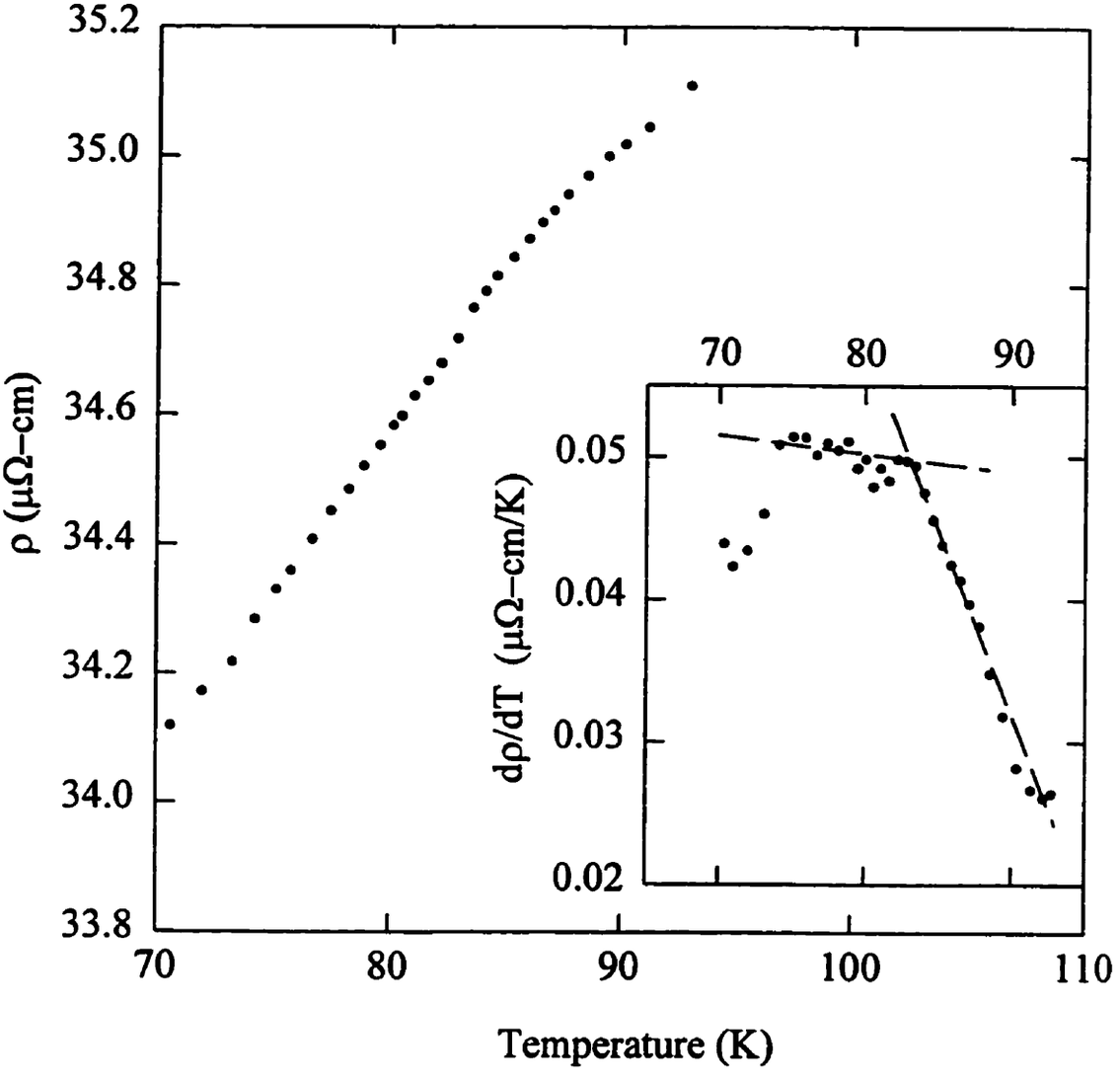

Figure 5.34: $\rho(T)$ for the 55 at.% Ni sample. The inset shows the temperature derivative of the resistivity, with T_c=83.1(8)K.

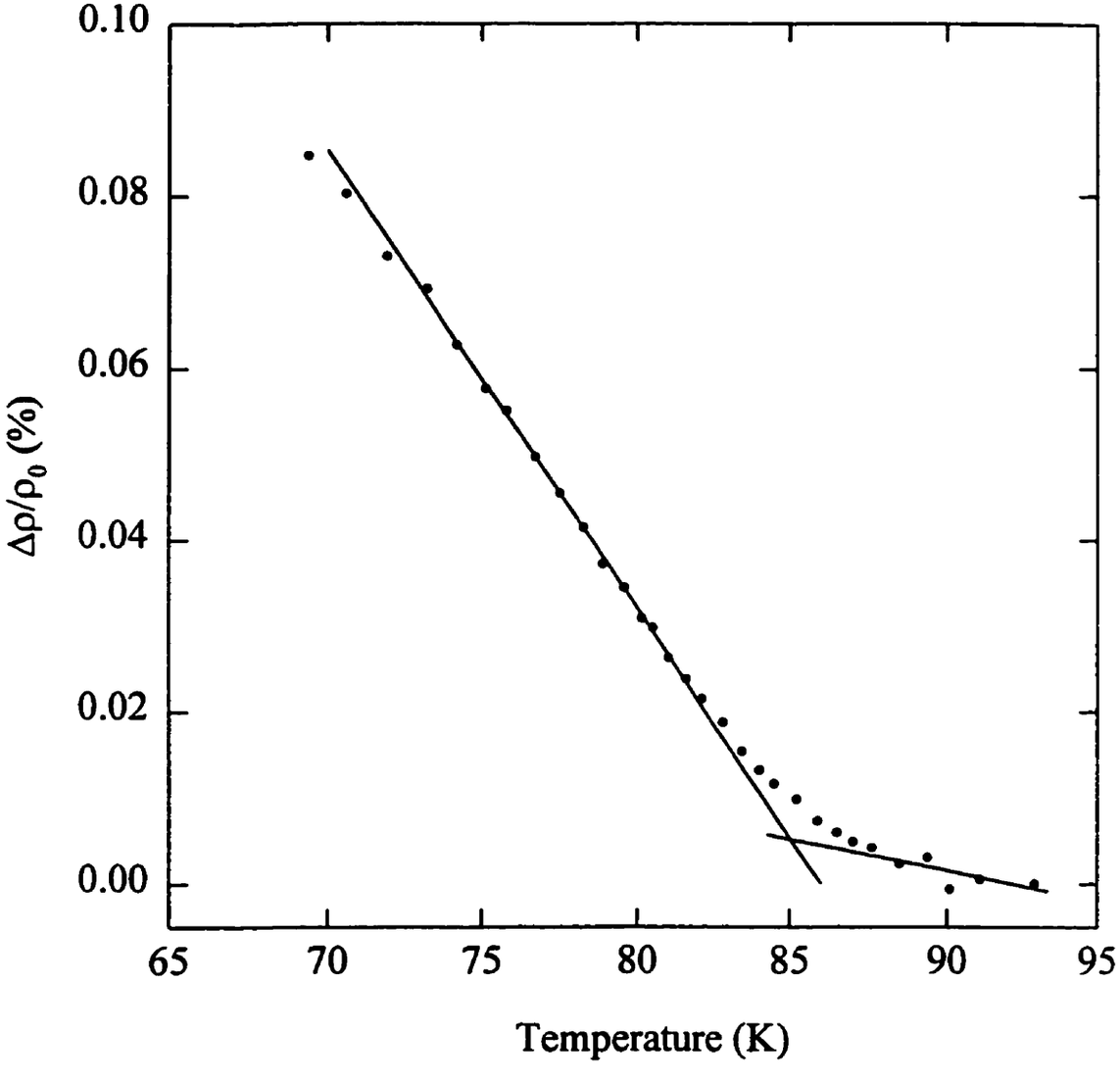

Figure 5.35: The low field resistive anisotropy (LFRA) for the 55 at.% Ni sample. The superimposed lines give T_c =84.8±1 K.

giving T_c much closer to that of the ρ(T). Similar curves are shown for the 50 and 46 at.% samples (figures 5.36–5.39). The resistivity data in the 45 and 45.5 at.% Ni samples (figure 5.40) show evidence of a slight decrease in resistivity above T_c, as seen in previous resistivity measurements for samples with $x \sim x_0$[109], again indicating $x_0 \sim 45$. As well, the slope of the resistivity seems to decrease smoothly with increasing temperature from the lowest measuring temperature, thus allowing no estimate of T_c from the behaviour of the derivative. On average, the values of T_c found in the CuNi system are in agreement with those found from susceptibility, indicating a good agreement between the thermometry in the two cryostats.

After T_c was determined in the manner described above, the data were plotted as a function of reduced temperature $t = T/T_c$ to allow comparison between the anisotropy for different Ni concentrations. A comparison for three samples (x=55, 50 and 47) is shown in figure 5.41. Obviously the anisotropy at a fixed reduced temperature decreases with decreasing nickel concentration, and thus the slope of the linear region also decreases with x. The data were fit, as in chapter 4, to the equation,

$$\frac{\Delta\rho}{\rho_0} = -A\left(\frac{T}{T_c}\right). \tag{5.6}$$

The values of T_c found using both $\rho(T)$ and the LFRA are summarised in Table 5.5, along with the slopes A found from the fits. The slope, A, increases with increasing Ni concentration from a value of approximately zero for x=0.45. From the model calculations in Chapter 4, the increase in the slope implies a decrease in the amount of bond-disorder, as would indeed be expected with the addition of Ni to the system. Although we were not able to attain low enough temperatures to observe the evolution of the anisotropy with temperature in the 45% sample, the data are consistent with $T \geq T_c$, i.e. in the tail regime. An attempt to obtain a value from T_c from the anisotropy data gives a value for T_c of 3.8K, twice that found from susceptibility data.

The LFRA data fits well to a straight line at low temperature, showing little evidence of the curvature observed in this regime in $Pd_{97}Co_3$ and $Pt_{90}Fe_{10}$, which was attributed to domain effects (Sections 4.4 and 4.5). Since the residual resistivity

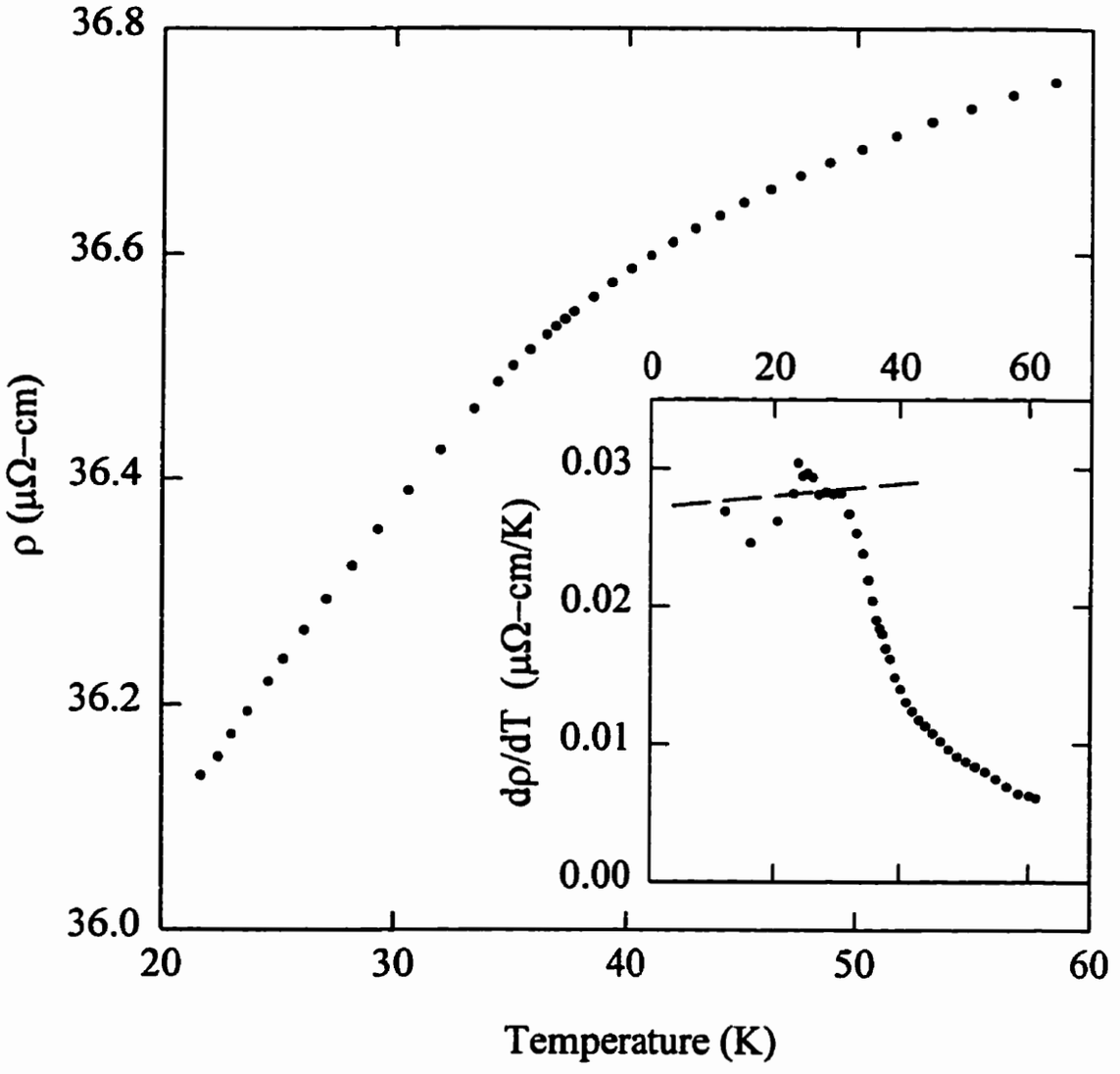

Figure 5.36: $\rho(T)$ for the 50 at.% Ni sample. The inset shows the temperature derivative of the resistivity, with T_c=31.5(8)K.

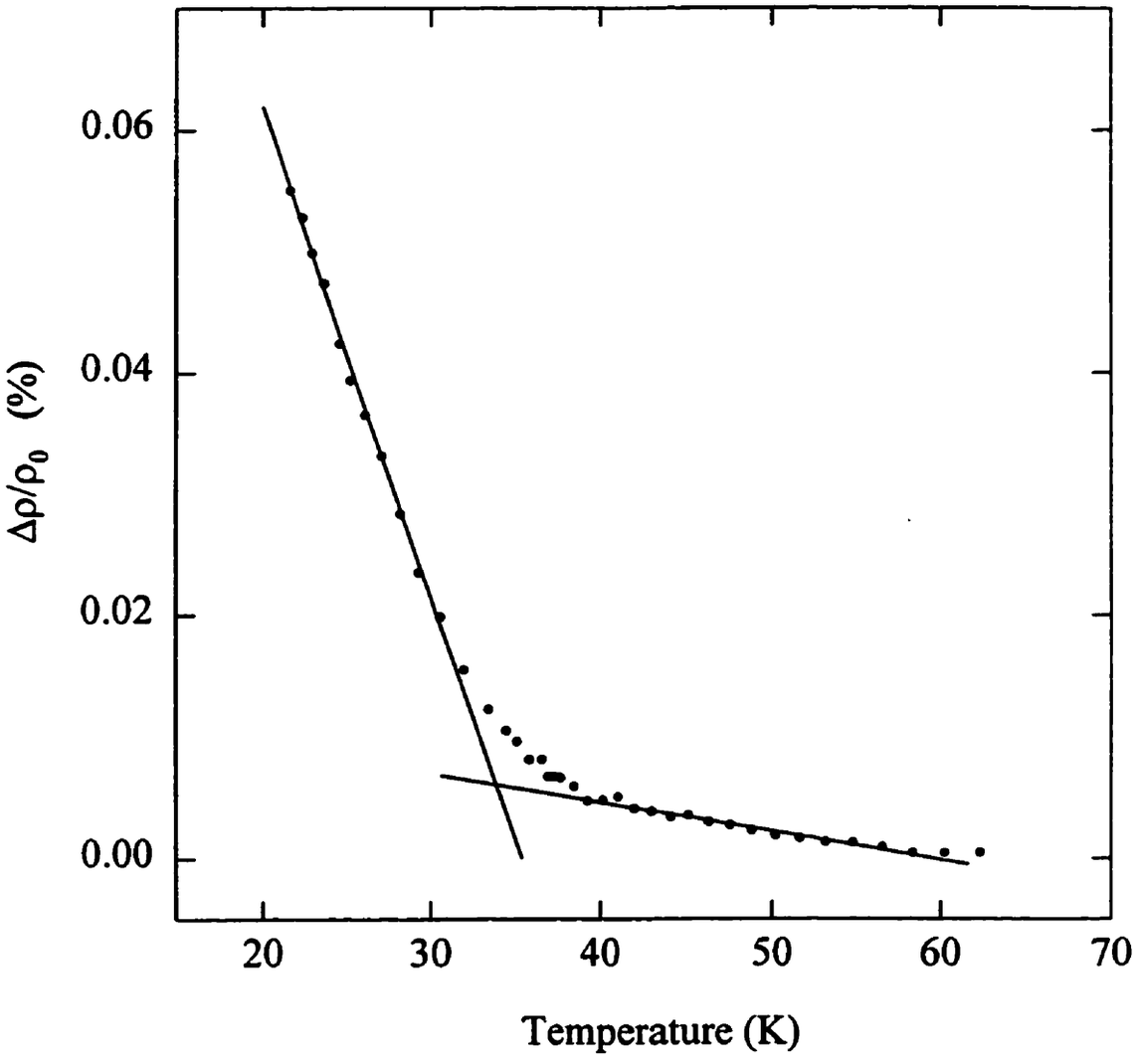

Figure 5.37: The low field resistive anisotropy (LFRA) for the 50 at.% Ni sample. The superimposed lines give T_c=33.4±1K.

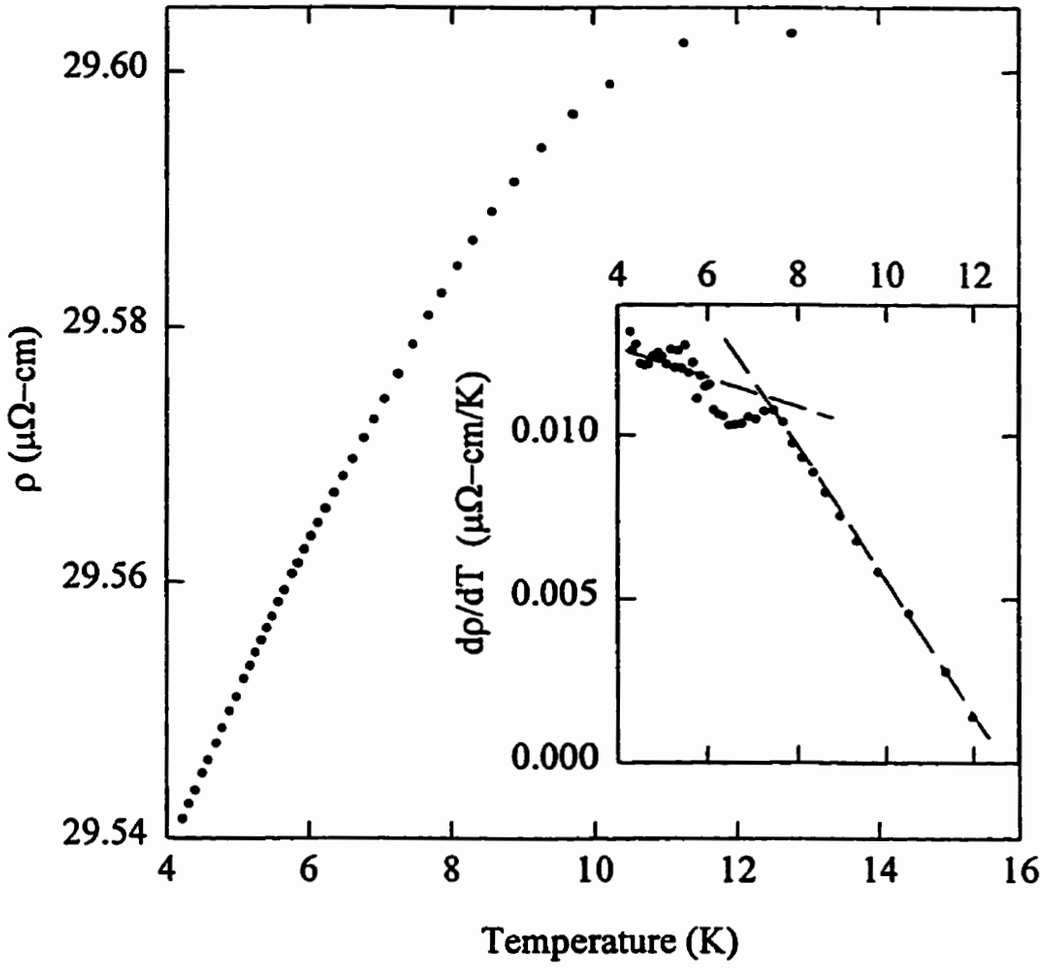

Figure 5.38: $\rho(T)$ for the 46 at.% Ni sample. The inset shows the temperature derivative of the resistivity, with T_c=7.2(5)K.

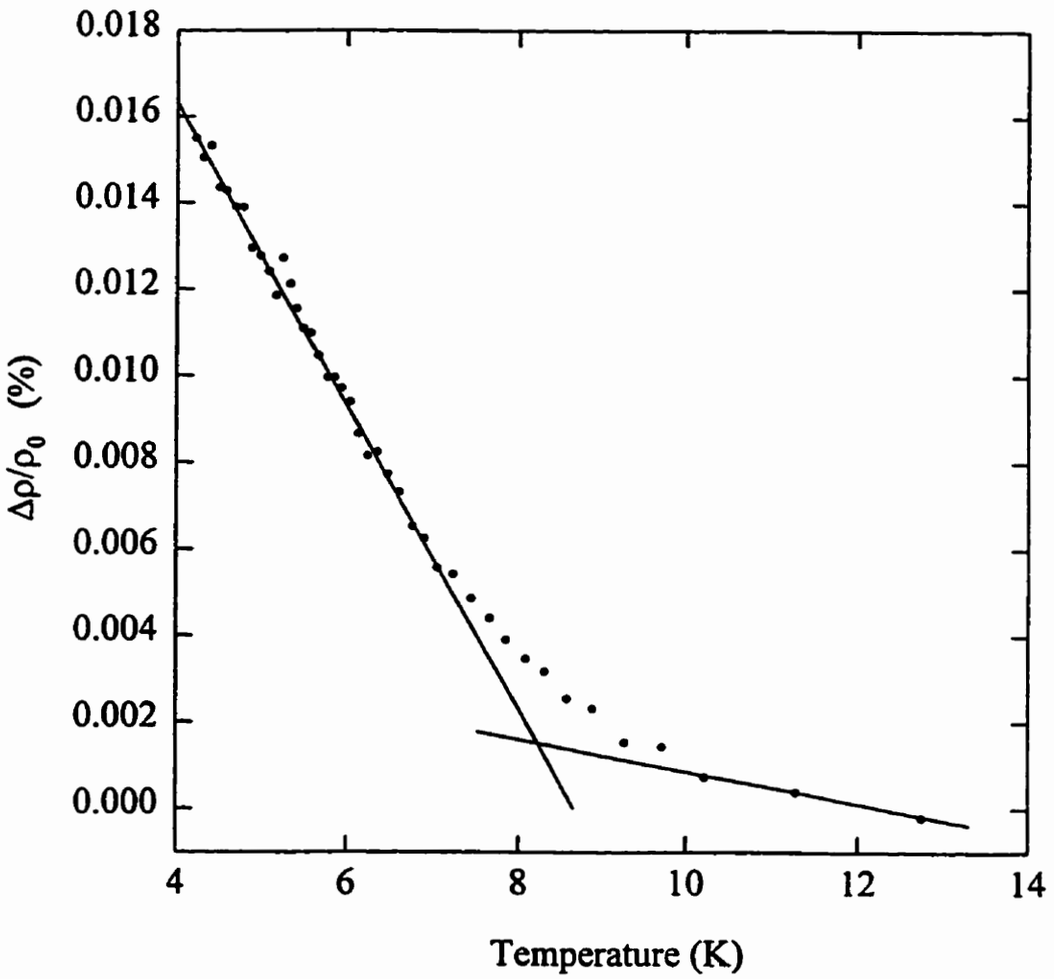

Figure 5.39: The low field resistive anisotropy (LFRA) for the 46 at.% Ni sample. The superimposed lines give T_c =8.2(5)K.

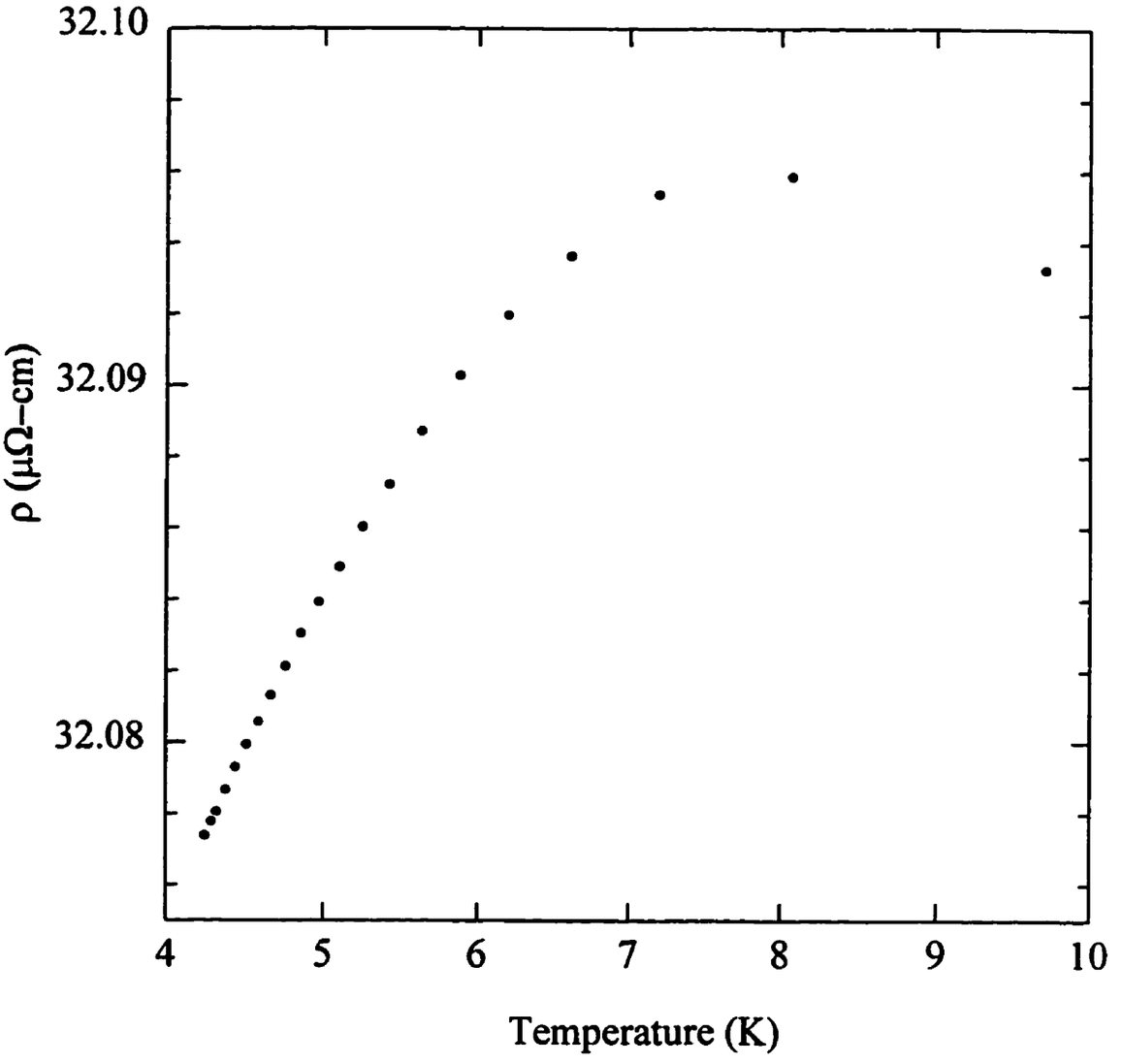

Figure 5.40: The resistivity of the sample with 45.5 at.% Ni in Cu, showing the decrease in resistivity above T_c.

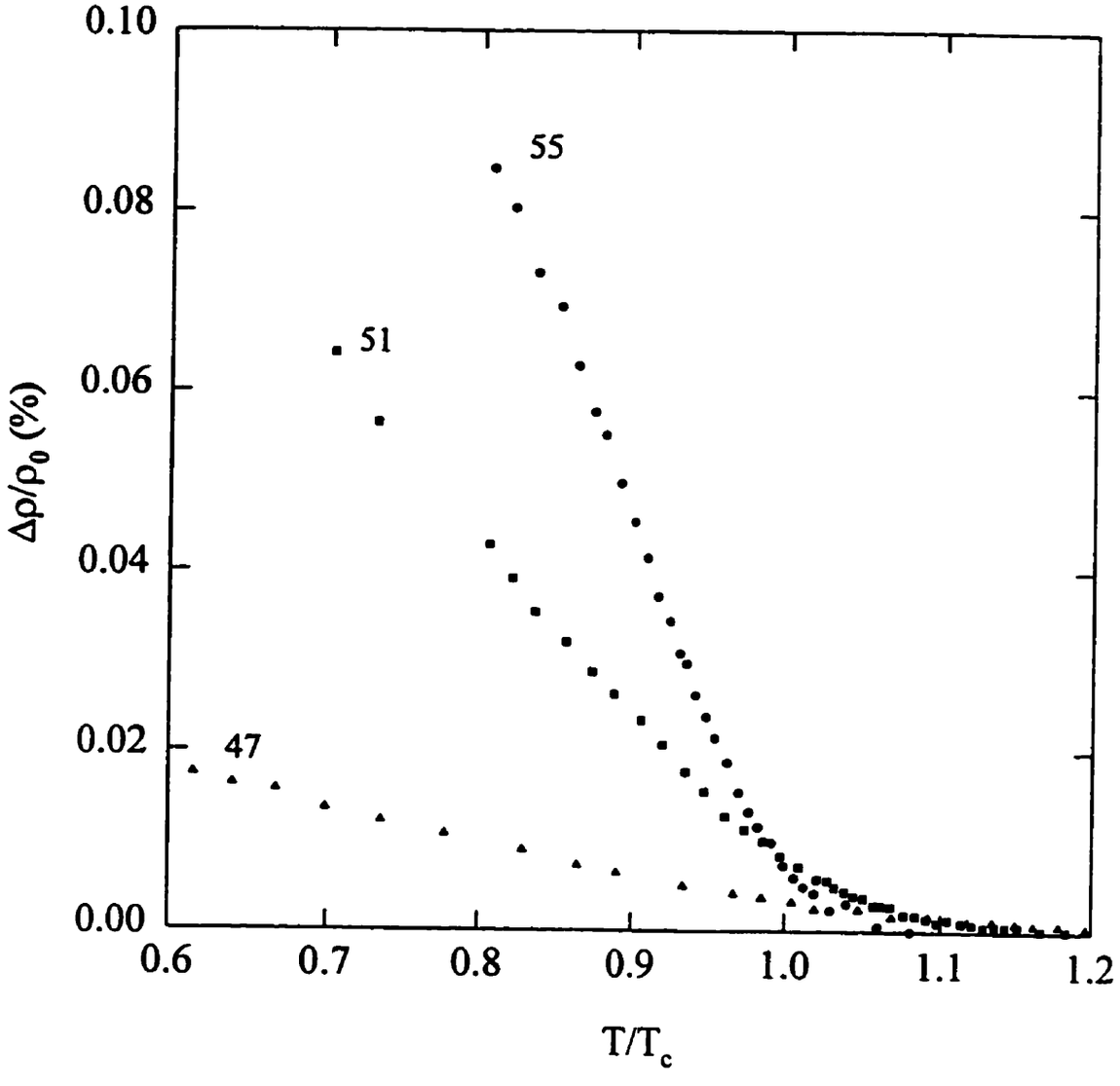

Figure 5.41: The LFRA as a function of reduced temperature for 3 Ni concentrations, as labelled.

Table 5.5: Variation of T_c and the slope A as obtained from LFRA measurements.

x	T_c(K) from $\rho(T)$	T_c(K) from LFRA	A (10^{-3})
45.0	–	3.8(10)	0.0684
45.5	–	5.6(10)	0.169
46.0	7.2(5)	8.2(5)	0.303
46.5	9.3(5)	10.5(6)	0.429
47.0	10.3(5)	10.4(7)	0.444
47.5	11.9(10)	14.6(20)	0.627
48.0	19.6(5)	20.2(8)	0.957
48.5	23.0(5)	23.9(8)	1.14
49.0	22.4(6)	24.8(9)	1.11
49.5	28.8(6)	30.4(9)	1.58
50.0	31.5(7)	33.4(10)	1.43
51.0	40.6(7)	40.4(10)	2.17
52.0	55.0(8)	57.9(10)	2.46
53.0	68.3(8)	67.6(10)	3.60
54.0	82.5(8)	86.0(10)	3.62
55.0	83.1(8)	84.8(10)	4.59

in this system is approximately the same as in the latter system, the mean free path of the conduction electrons will be similar. The coercive force at 4.2K ranges from 0.1–1 Oe in the CuNi samples, much lower than the values of 5 Oe found in $Pt_{90}Fe_{10}$ at temperatures much higher than 4.2K (in general H_c decreases with increasing temperature). This suggests that the curvature observed at low temperature in $Pt_{90}Fe_{10}$ and $Pd_{97}Co_3$ is indeed an artifact due to the domain size becoming smaller than the mean free path at low temperature.

In summary, then, the LFRA in CuNi agrees well with the model predictions in Ch. 4. Critical temperatures from the resistivity and the low field resistive anisotropy data agree well with those found from susceptibility data, suggesting a critical concentration x_0 slightly less than 45.

5.2.3 Effects of Aging on $Cu_{100-x}Ni_x$

As discussed in the review, the properties of CuNi alloys have been shown to be strongly dependent on the heat treatment and quench rate of the specimens. As well, a sample aged for 3 years at room temperature was shown to exhibit a considerable change in transport properties[109]. Detailed studies of sample properties as a function of annealing temperature, time, quench rate, cold-working and irradiation have been done by various groups. In general, it is agreed that samples quenched from high temperature (> 600°C) have a random distribution of nickel atoms. Over long periods of time at room temperature and during low temperature heat treatments, the Ni atoms tend to cluster together. Hedman and Mattuck[97] suggest that annealing at 200°C causes clustering to occur at a slow but measurable rate, while at higher temperatures the clusters quickly reach an equilibrium size. Although the *ac* susceptibility and resistivity have been shown to depend in a complicated manner on annealing time and temperature, T_c generally increases after aging[97]. This study attempts to find the effects of small changes in cluster size on the low-field resistive anisotropy, and relate these changes to changes in the bond-disorder by comparisons to model predictions.

Direct comparisons between as-quenched and aged specimens are only realistic

for small changes in the sample state, since the model in Chapter 4 assumes no significant changes in the band structure, as discussed in section 4.3.2. For this reason, it was initially decided to age the specimens at room temperature alone, so as to have more control over the aging process (after the specimens were quenched from the 900°C anneal, they were maintained at liquid nitrogen temperature to reduce aging effects).

For this aging study, the *ac* susceptibility was used as a sensitive probe of changes in T_c. Temperature sweeps in zero field and 40 Oe were done on the specimen in its as-quenched state, after which the specimen was removed to sit at room temperature for a certain period of time, and remeasured. None of the specimens showed any measurable aging at room temperature after periods of up to 1 week, so it was decided to try a low temperature anneal at 200°C. After being aged for a certain length of time, the samples were removed from the furnace and allowed to cool at room temperature. These slow cools proved to be irreversible. This is clearly shown by the data in figure 5.42(a), which plots the evolution of the 40 Oe temperature sweep in the 48% sample for successive anneals of 1+1+2+4 hours (with a slow cool after each). The total change in the peak temperature after 8 hours total aging is less than that shown in figure 5.42(b) for a virgin samples annealed for 2 hours. The only effects of a further anneal after a slow cool had been done were to broaden slightly the susceptibility peak and to decrease slightly the peak amplitude. Table 5.6 lists the temperatures of the peak in the 40 Oe susceptibility data for the six aged samples, before and after treatment, as well as the aging treatment followed. The six samples examined (55, 50, 48, 47, 46 and 45 at.% Ni) covered the entire concentration range studied, however little difference in the effects of aging as a function of concentration was observed. The change in peak temperature after the anneal was less than 10% in all the samples, roughly equivalent to the changes in the FeZr samples after partial hydrogenation.

The resistivity samples were subjected to the same annealing treatment as for the susceptibility samples, and the low field resistive anisotropy was measured in the same manner as previously. Once more we could not attain sufficiently low

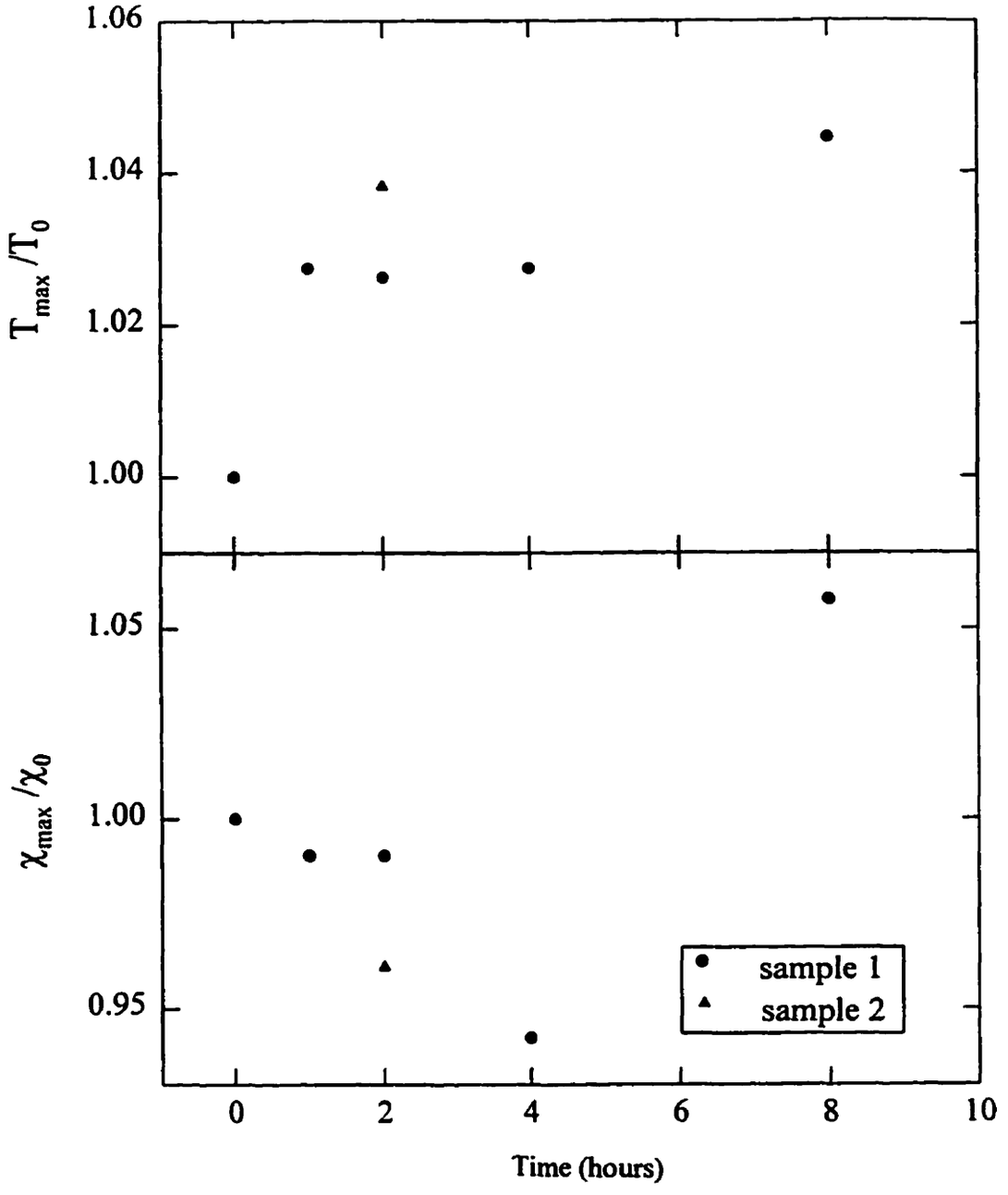

Figure 5.42: The evolution of the peak temperature (upper graph) and susceptibility (lower graph) for x=0.48 in a fixed field of 40 Oe, as a function of total time annealed at 200° C (plotted as a fraction of the initial temperature/susceptility for the as-quenched sample). Sample 1 was annealed for 8 hours total, with quenches after each time period shown. Sample 2 was annealed only once, for 2 hours and quenched. The irreversibility of a quenching is shown by the plateau in both parameters after the initial quench for sample 1.

Table 5.6: Change in peak temperature of the 40 Oe *ac* susceptibility with aging in $Cu_{100-x}Ni_x$.

x	T_p(K)	anneal time at 200°C	$T_p'(K)$
45.0	4.83	2 hours	5.0
46.0	6.85	2 hours	7.10
47.0	10.6	2 hours	11.6
48.0	22.4	2 hours	23.6
50.0	38.3	2 hours	39.6
55.0	82.5	2+4 hours	85.6

temperatures to study the behaviour of the 45 at.% Ni sample, however, good data were obtained for the remaining 5 samples. T_c estimates were obtained from plots of $\rho(T)$ and from linear fits to the LFRA. The values found using these two methods are summarised in Table 5.6, with the data on the as-quenched specimens included for comparison. Again, the value of T_c as obtained from the LFRA data is within error of that obtained from $\rho(T)$. After aging, the 46% sample shows the same behaviour at high temperature as the 45 and 45.5% samples before aging, i.e. a decrease in resistivity and no evident 'kink' in the curve from which to obtain T_c. Due to uncertainties in form factors, no effort is made to compare the magnitude of the residual resistivities before and after aging. The $\rho(T)$ curves are very similar to those in section 5.3.2, and can be found in Appendix A.

Using the values of T_c listed in Table 5.6, the LFRA data obtained before and after aging can be compared on the same graph by plotting as a function of reduced temperature T/T_c, as done in the previous section. Fitting this data to equation 5.6, values for the slope A were obtained. In general A does not change after aging (figure 5.43–5.47), except in the lowest concentration samples. This suggests that although the critical temperature has increased (which in the model in Chapter 4 implies an increase in the first moment J_0 of the exchange distribution), there is no overall change in the bond-disorder of the system, as determined by this technique. Thus, although the Ni atoms are forming clusters, there has been no

Table 5.7: Change in T_c with aging in $Cu_{100-x}Ni_x$, as determined from transport measurements

	as-quenched			aged		
x	T_c(K) ρ	T_c(K) LFRA	$A(10^{-3})$	T_c(K) ρ	T_c(K) LFRA	$A(10^{-3})$
46	7.2	8.2	0.30	–	8.6	0.33
47	10.3	10.5	0.44	9.8	11.3	0.43
48	19.6	20.2	0.96	19.5	21.4	0.96
50	31.5	33.4	1.4	31.1	35.2	1.4
55	83.1	84.8	4.6	86.4	87.5	4.6

noticeable change in the bond-disorder on the length scale set by the resistivity measurements. The *ac* susceptibility measurements of the aged samples support this proposal, showing little change in peak height, indicating very small changes in overall magnetic moment. This agreement once again suggests that measurements of the LFRA may successfully indicate changes in the overall bond-disorder of a material on the length scale of resistivity measurements.

5.3 Conclusion

In conclusion, *ac* susceptibility measurements showed the $Cu_{100-x}Ni_x$ samples measured to be ferromagnetic, with the presence of considerable disorder indicated by curvature in the exponents. The presence of an orbital moment at the Ni site was indicated by the magnetic hardness of the samples, which decreases with decreasing Ni concentration. General trends in the susceptibility data showed that this system is very similar to the PdNi system, and comparison suggests a critical (percolation) concentration near 45 at.% Ni. This conclusion is supported by measurements of the magnetoresistance as a function of concentration, from which we were able to deduce a power law dependence of the SRA on reduced concentration (with a critical concentration of 44.5% Ni) and the exponent Δ was found to be the same as in PdNi. This suggests that this exponent value may be universal for systems with

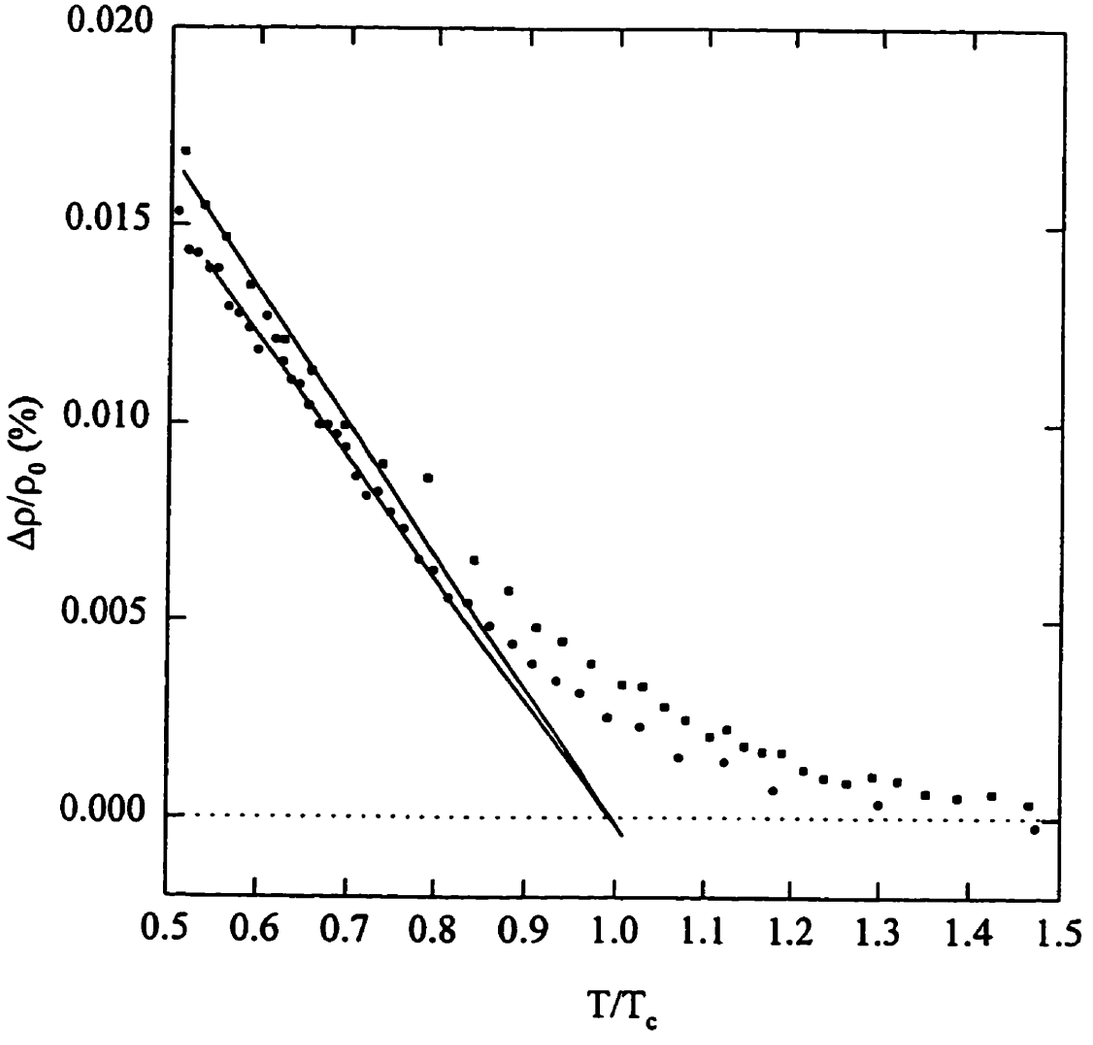

Figure 5.45: The LFRA as a function of reduced temperature before and after aging for x=46, as labelled. The solid lines are fits to equation 5.6, with slightly different values for A before and after aging. The solid circles are for the as-quenched samples, while the square symbols denote the aged sample.

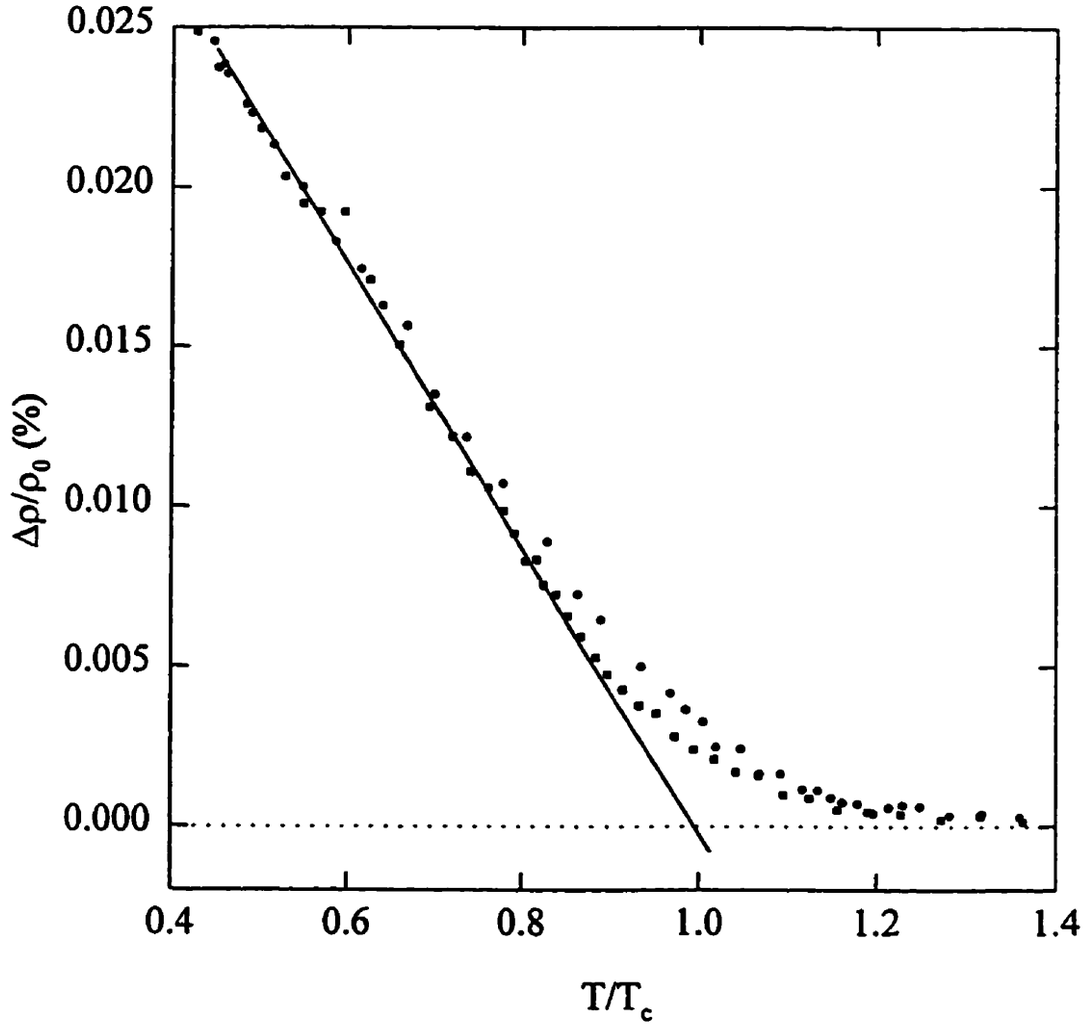

Figure 5.44: The LFRA as a function of reduced temperature before and after aging for x=47, as labelled. The solid line is a fit to equation 5.6, with the same value of A before and after aging. The solid circles are for the as-quenched samples, while the square symbols denote the aged sample.

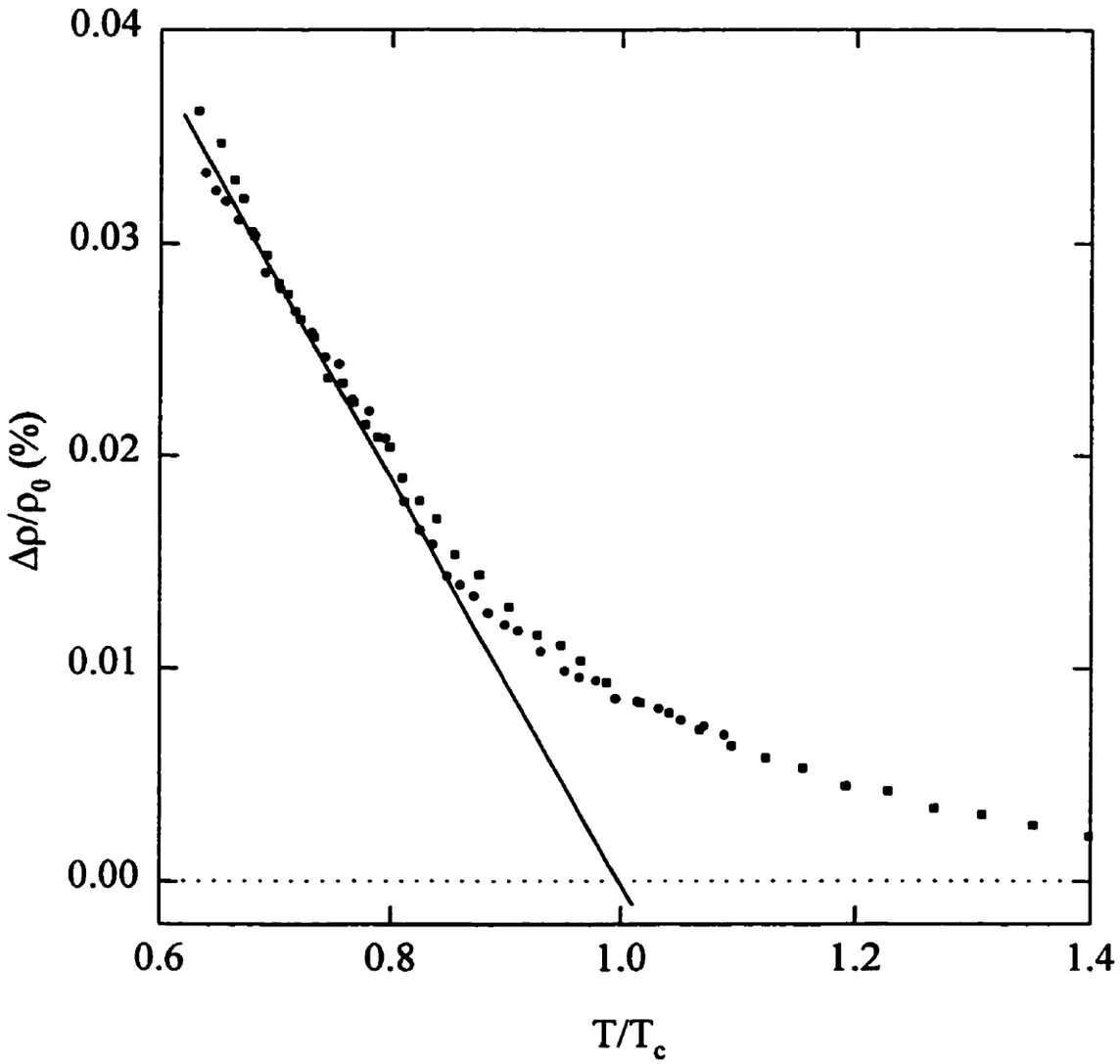

Figure 5.45: The LFRA as a function of reduced temperature before and after aging for x=48, as labelled. The solid line is a fit to equation 5.6, with the same value of A before and after aging. The solid circles are for the as-quenched samples, while the square symbols denote the aged sample.

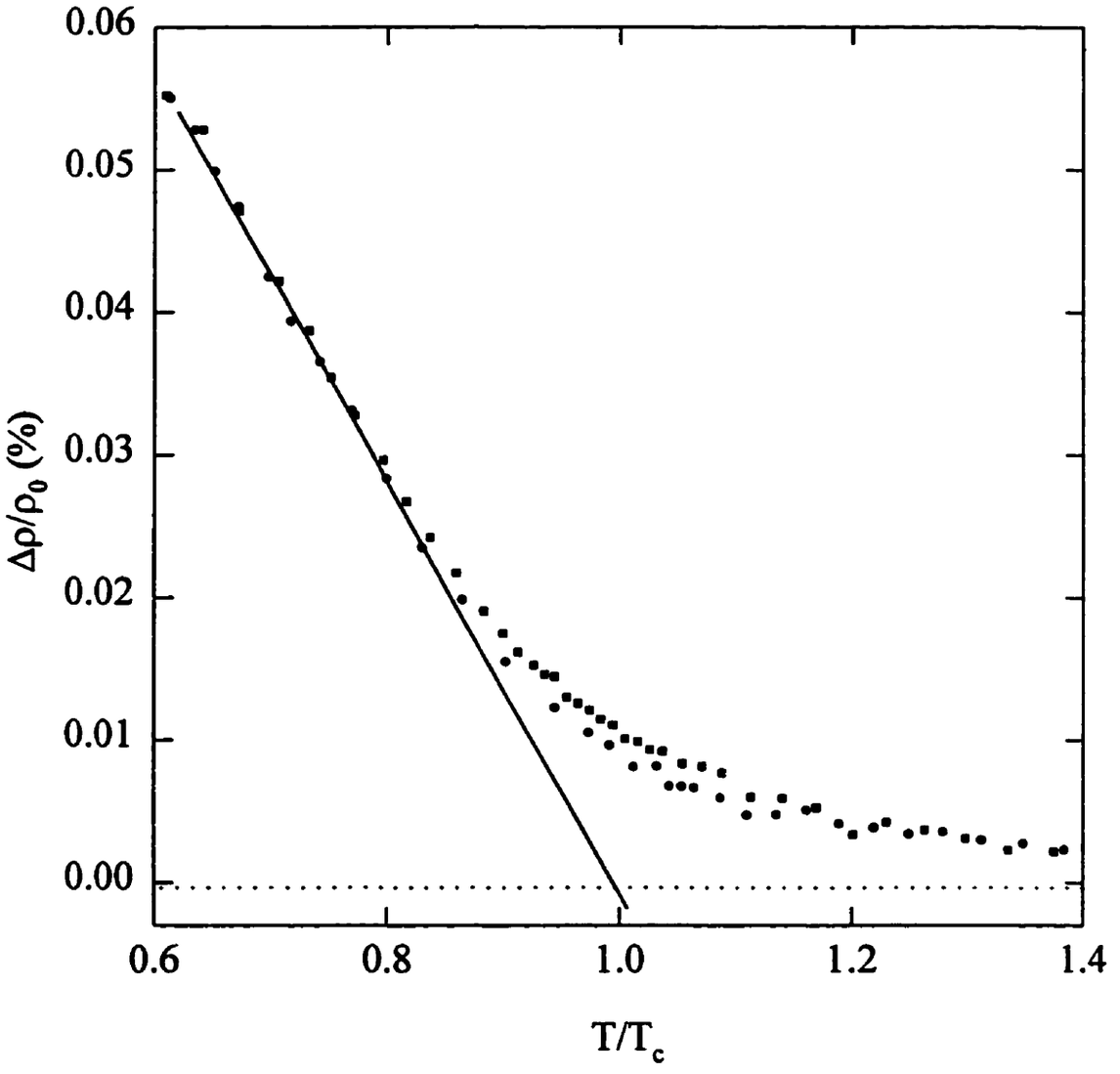

Figure 5.46: The LFRA as a function of reduced temperature before and after aging for x=50, as labelled. The solid line is a fit to equation 5.6, with the same value of A before and after aging. The solid circles are for the as-quenched samples, while the square symbols denote the aged sample.

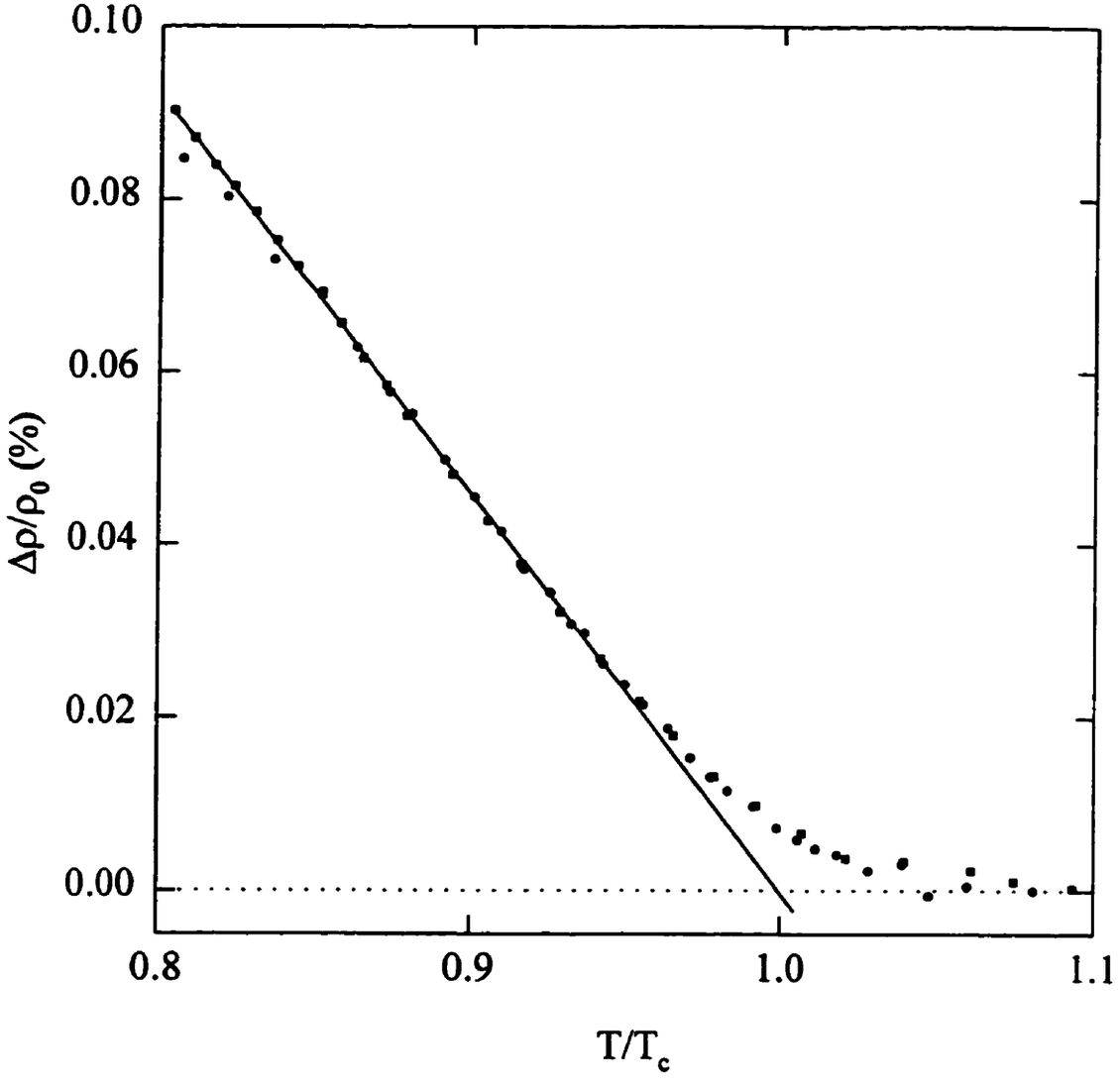

Figure 5.47: The LFRA as a function of reduced temperature before and after aging for x=55, as labelled. The solid line is a fit to equation 5.6, with the same value of A before and after aging. The solid circles are for the as-quenched samples, while the square symbols denote the aged sample.

orbital moments. Further studies of the SRA in materials with dilute Co impurities would be interesting, however these would be difficult due to the low concentration of Co required for ferromagnetism. Measurements of resistivity and LFRA found values for T_c in $Cu_{100-x}Ni_x$ which agree within error with those from susceptibility, and suggest that the percolation transition is slightly below 45%. The slope of the LFRA as a function of reduced concentration was found to increase rapidly with increasing Ni concentration, which suggests a decrease in bond-disorder. After aging, however, the slope of the LFRA did not change, indicating that any changes in the disorder present in the system are not noticeable on the length scale of resistivity measurements.

Chapter 6

Superconductivity in Borocarbides

6.1 Review

As discussed in Chapter 5, Ni does not exhibit a magnetic moment in isolation. This property of Ni raises interesting questions regarding the role of Ni in a family of alloys with formula $(RC)_m(NiB)_n$, where R=rare earth. The magnetic properties of these materials depends on the specific rare earth and on the interlayer spacing. A number of the m=1, n=2 compounds are superconducting, with R=Lu having a T_c of 16.6 K [8], remarkably high for an intermetallic compound containing Ni. The substitution of Pd in the Ni site enhances T_c slightly; the compound $YPd_5B_3C_x$ has T_c=23K, equal to the highest T_c previously recorded for an intermetallic compound[110]. As discussed in Chapter 2, the presence of magnetic atoms in superconductors generally suppresses T_c substantially due to pair breaking effects, however the substitution of Ni for Pd results in only a slight decrease in T_c. Speculation has thus arisen as to whether Ni plays some role in the superconducting process, or whether this high T_c is produced primarily by the high frequency phonons associated with the light B and C constituents. This review section concentrates on the 1-2 compounds RNi_2B_2C and the effects of substitution in the various sites.

The RNi_2B_2C family has a body-centred tetragonal crystal structure (I4/mmm) with alternating Ni_2B_2 and RC layers stacked along the c axis[111, 112], and stabilised by vertical B-C-B interlayer bonds. The unit cell, containing two formula

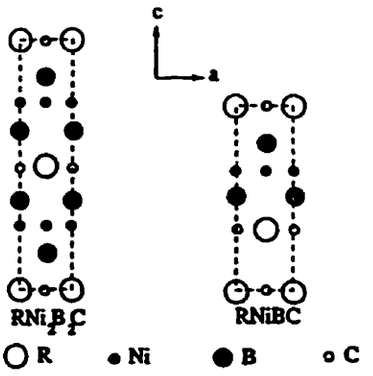

Figure 6.1: Projection on the ac plane of the tetragonal crystal structure of RNi_2B_2C and RNiBC, from [9].

units, is shown in figure 6.1. The T_c's of various borocarbide superconductors are listed in Table 6.1. Of the series RNi_2B_2C, R=Lu has the highest T_c of 16.6K[8], slightly higher than that of YNi_2B_2C. The substitution of some magnetic rare earths such as holmium and erbium depresses T_c only slightly from that of R=Lu, however the presence of R=Dy, Ce, Gd and Sm completely destroys superconductivity. The small effect of the former substitutions suggests a weak coupling between the rare-earth $4f$ electrons and the conduction electrons. Interestingly, $YbNi_2B_2C$ has recently been shown to be a heavy fermion system, however it is not superconducting down to 0.34K[113].

Various measurements have established that YNi_2B_2C is a Type II superconductor of conventional BCS character, i.e. the superconductivity is due to electron-phonon interactions. Many results have been published, with specific heat[112, 119, 120], magnetic[52, 112, 121] and transport[8, 122] measurements giving values for various parameters of the superconducting state. The scatter present in published values of T_c, H_{c1} and H_{c2} suggests that these may be sensitive to sample quality and preparation technique, making it important for a complete set of data to be obtained from one sample.

The high T_c found in this material has been attributed primarily to the presence

Table 6.1: Superconducting Properties of Rare Earth Borocarbides

Compound	T_c	Reference(s)
$YPd_5B_3C_x$	22.6-23K	[110, 114]
$ThPd_2B_2C$	14.5K	[115]
$ThPt_2B_2C$	6.5K	[115]
$LaPt_2B_2C$	11.0K	[116]
$LuNi_2B_2C$	16.6K	[8]
YNi_2B_2C	15.2-15.6K	[8, 112]
$TmNi_2B_2C$	11.0K	[8, 117]
$ErNi_2B_2C$	10.5K	[8, 118]
$HoNi_2B_2C$	8.0	[8]
$ThNi_2B_2C$	6.0K	[115]

of a sharp peak in the density of states at the Fermi level, as shown by band structure calculations[123]. The large contribution to this peak from the nickel $3d$ bands suggests that the superconducting state will be sensitive to substitutions of different transition metals in the Ni site. As the number of valence electrons varies, the Fermi energy moves away from the peak (using a rigid band approach), decreasing the density of states of the system, and thus decreasing T_c. This has been verified experimentally, with substitutions of the transition metal elements Ru, Fe and Co at the Ni site causing a dramatic suppression of T_c[124, 125, 126].

A number of the measured T_c's in $YNi_{1-x}M_xB_2C$ are plotted as a function of x in figure 6.2. Bud'ko et al.[124] find that $T_c(x)$ decreases linearly as a function of dopant concentration at relatively low concentration, with extrapolated critical concentrations of x_0=0.08, 0.095, and 0.14 for Ru, Fe and Co respectively. The T_c's observed upon Fe, Ru and Co substitution agree well with suppression of T_c due to changes in the density of states at the Fermi level. Bud'ko et al. also note that chemical pressure due to changes in lattice parameter and bond angle upon substitution of impurities will affect T_c, as will the decrease in the normal electron mean free path[124]. As discussed previously, Fe and Co impurities generally bear magnetic moments, even when dissolved in a non-magnetic host. It is interesting to deter-

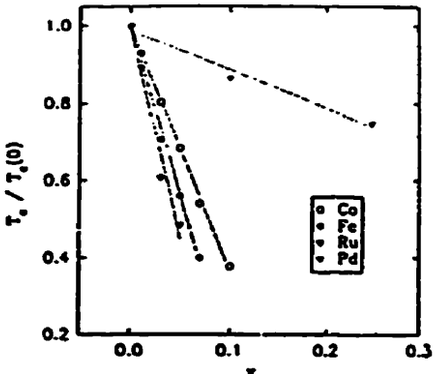

Figure 6.2: Effects of doping at the Ni site on the critical temperature in YNi_2B_2C superconductors[124].

mine whether Fe and Co substitutions act as magnetic scattering sites or as simple impurities in YNi_2B_2C. In a recent detailed study of $Y(Ni_{1-x}Co_x)_2B_2C$, Hoellworth et al.[125] find that at high Co concentrations $T_c(x)$ is *not* well-described by a straight line, and fit their data to the BCS equation for $T_c \propto \theta_D \exp[-1/N(E_F)V]$, as described earlier in Chapter 2 (equation 2.52). Values for θ_D and $N(E_F)$ were calculated from magnetic and specific heat measurements, with V, the interaction potential, taken to be constant. The data is in excellent agreement with the equation, suggesting that the primary effects of the Co on T_c are *not* due to magnetic scattering effects. Schmidt et al.[126] also find a non-linear decrease in T_c with Co concentration, and fit this to Kaiser's equation for scattering from non-magnetic *d*-states, as in equation 2.59. The values obtained for $N_i(E_F)$ and U_{eff} from this fit are close to the static Hartree-Foch criterion for magnetism ($N_i(E_F)U_{eff} \geq 1$), i.e. the impurities are almost magnetic. Measurements of the static magnetic susceptibility, however, showed no change in paramagnetic moment as a function of Co concentration, and thus Schmidt et al. conclude that the change in T_c is not caused by magnetic pair-breaking effects of possible moments at the cobalt impurity sites.

6.2 YNi_2B_2C

Samples of YNi_2B_2C were prepared in button form as described in Chapter 3. These polycrystalline samples could be measured in button form for *ac* susceptibility measurements, however bar-shaped samples were required for transport measurements. These bars were produced by chill-casting followed by an anneal at 1000° C. The annealing process was found to elevate T_c, as well as changing other sample properties, as will be discussed later. X-ray powder diffraction spectra of the arc-melted buttons before and after annealing show little change, with the pattern indexing to the I4/mmm structure with a=3.5351(6)Å and c=10.5598(26)Å, in good agreement with the structure published by Siegrist et al.[111]. There was no evidence of any impurity phases in our x-ray spectra. The diffraction patterns for the as-cast and annealed bars are shown in figure 6.3(a) and 6.3(b), with the reflections indexed to the filled $ThCr_2Si_2$ structure as in 6.3(b). The effect of annealing on the cast samples is to decrease slightly the background in the diffraction spectrum, presumably due to the removal of strains induced during the casting process. A variety of measurements were then done on these samples to find a set of superconducting parameters and to determine their dependence on preparation technique.

6.2.1 Magnetic Measurements

AC Susceptibility

The zero field *ac* susceptibility of the arc-melted buttons was measured in the cryostat described in section 3.2.2, using a 30 mOe rms driving field at a frequency of 2400 Hz. The results for the unannealed and annealed samples are plotted together in figure 6.4 for comparison. Both samples are perfect diamagnets at low temperature, with a mass susceptibility of -0.137 emu/g-Oe. The onset temperature for superconductivity is raised by the annealing process from 14.6 to 15.3K, with the latter value in good agreement with previously published values of T_c[8, 112]. The transition width, characterised by the temperature over which the susceptibility drops from 90% to 10% of its high temperature value, decreases from 0.9 to 0.7K

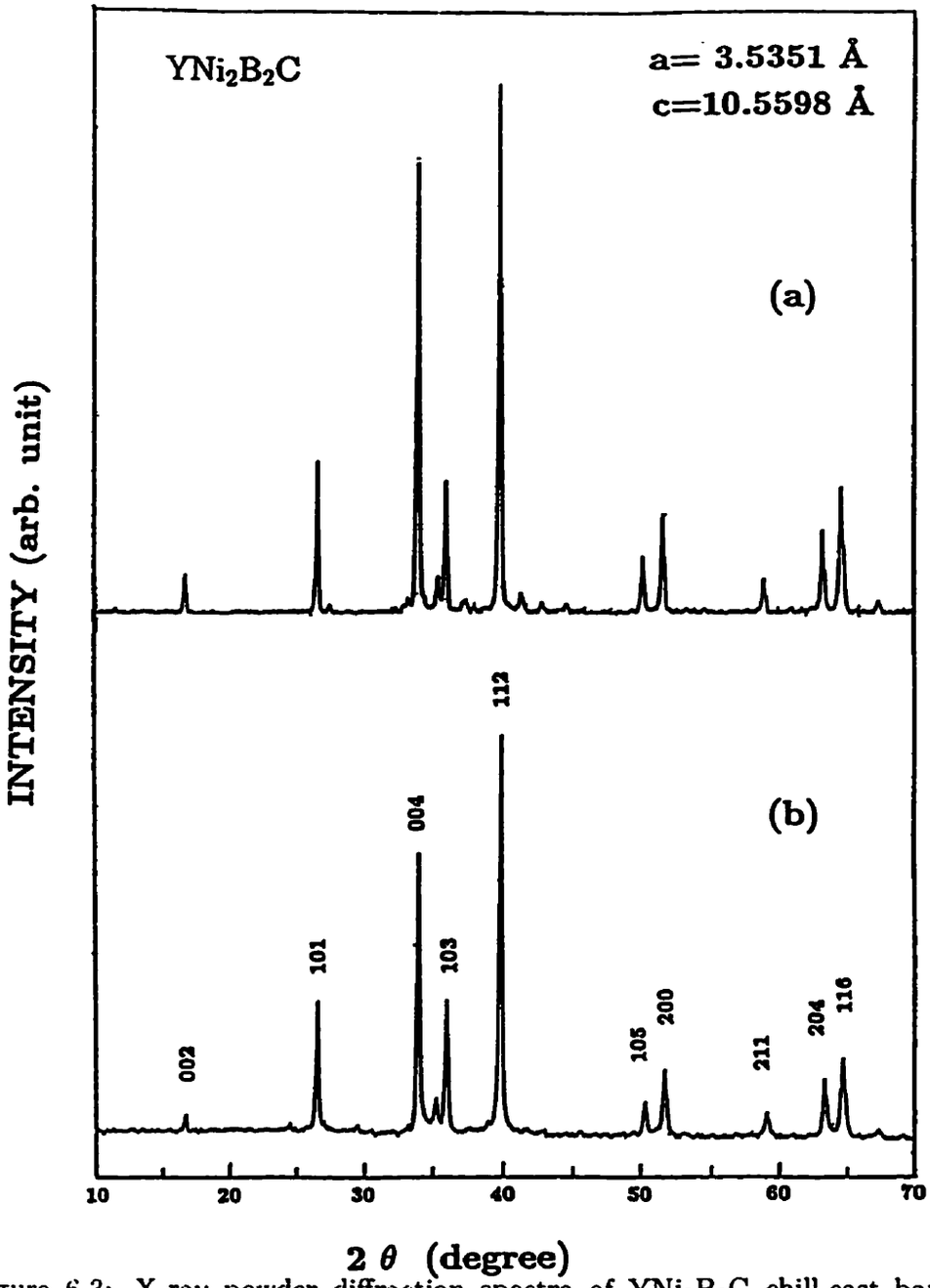

Figure 6.3: X-ray powder diffraction spectra of YNi_2B_2C chill-cast bars (a) as cast;(b) annealed. The lines are indexed as in (b) to the I4/mmm structure.

after annealing, an indication of an increase in sample homogeneity. Measurements of the chill-cast bars show a significant depression of T_c from that found in the buttons: even after annealing T_c is lower than in the buttons. This result, demonstrated by the susceptibility data in figure 6.5, suggests that the casting procedure may introduce defects to the material which act as additional pair-breaking scattering centres. The annealing procedure increases the onset temperature for the superconducting state from 10.9 to 14.2K, a much larger change than was observed in the buttons. As in the buttons, the 10–90% transition width decreases slightly after annealing, with ΔT dropping from 0.8 to 0.7K. The zero field susceptibility of the cast bars was measured at a wide range of driving field frequencies–5 and 1500 Hz in the Quantum Design Magnetometers, and at 2400 Hz in the home-built system. No change was observed in T_c between cryostats or with frequency, a result which verifies the accuracy of the thermometry in the two cryostats–absolute temperatures measured in different systems may have errors as large as 1%. The in-phase(χ') and out-of-phase(χ'') component of the zero-field susceptibility measured at 5 Hz in the annealed specimen are reproduced in figure 6.6. χ' shows an onset of superconductivity at 14.2K, with χ'' exhibiting an anomaly at a temperature slightly below the onset, as observed in some high-T_c superconductors.

Magnetisation

The field dependence of the magnetisation was measured in fields of up to 5.5 Tesla at a number of fixed temperatures between 2K and T_c in the chill-cast samples. To minimize the demagnetisation corrections, the biasing field was applied along the longest sample dimension. Typical M(H) plots measured for the two samples in increasing and decreasing field are shown in figure 6.7 and 6.8. The general features of M(H) are those of an imperfect Type II superconductor, with a large irreversibility due to flux pinning at defect sites. Values for the critical fields H_{c1} and H_{c2} can be extracted from the magnetisation data. In an ideal Type II superconductor, H_{c1} is the field at which the sample is no longer perfectly diamagnetic (i.e. $H \neq -4\pi M$). Above H_{c1} the magnetisation increases, and becoming zero at $H=H_{c2}$. In these

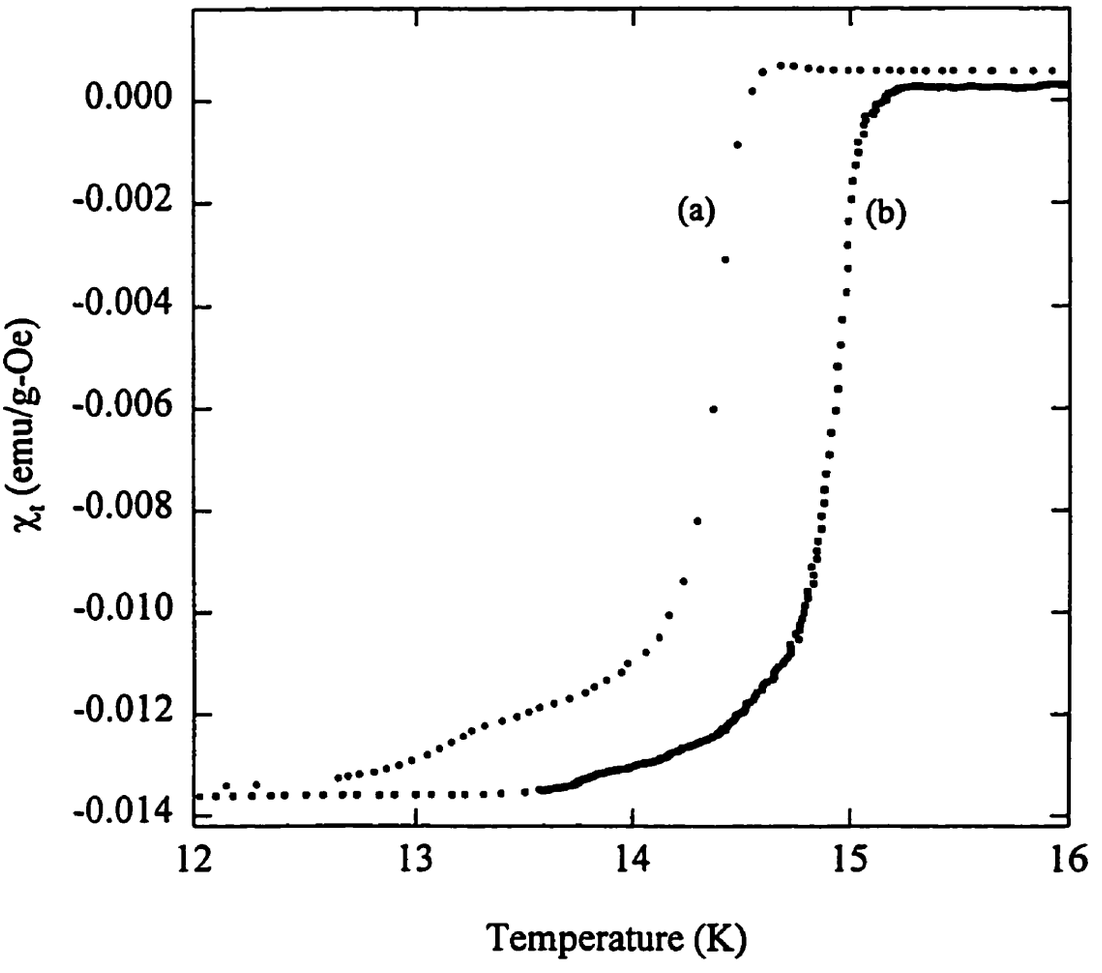

Figure 6.4: Zero field *ac* susceptibility measurement of the arc melted buttons of YNi_2B_2C (a) as cast;(b) annealed.

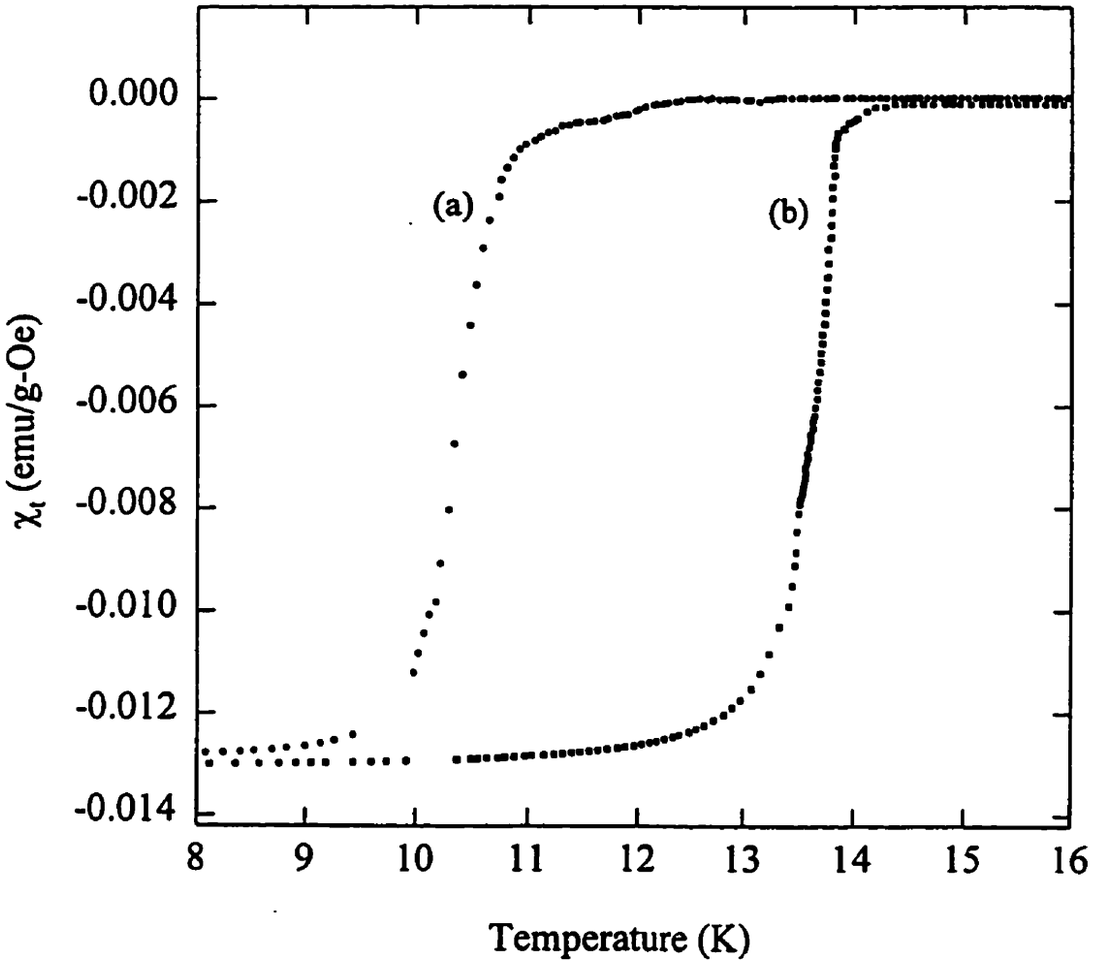

Figure 6.5: Zero field *ac* susceptibility measurement of the chill-cast samples of YNi_2B_2C (a) as cast;(b) annealed.

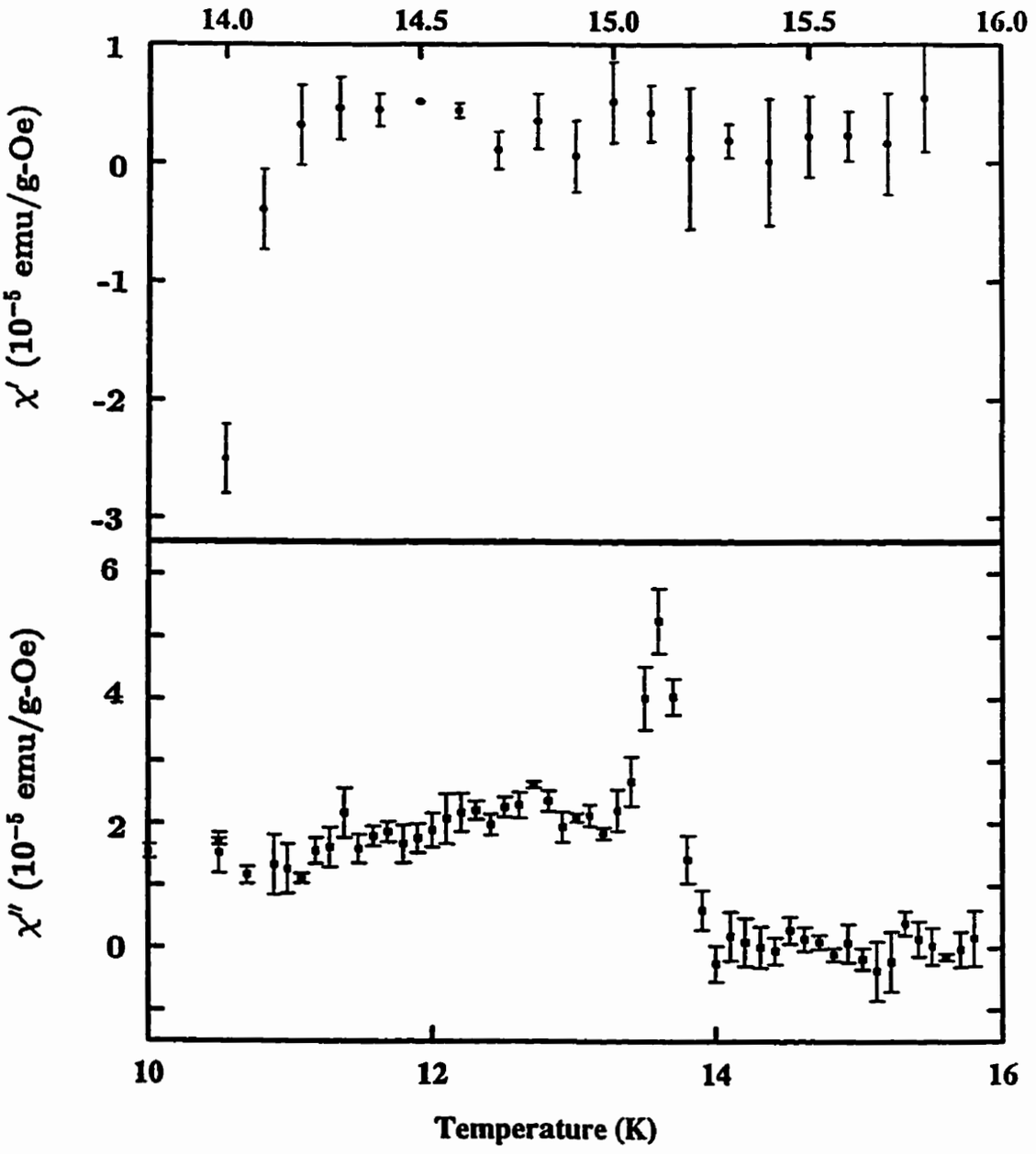

Figure 6.6: Zero field *ac* susceptibility measurement in 5 Hz of chill-cast and annealed YNi_2B_2C (upper) in-phase susceptibility; (lower) out-of-phase susceptibility.

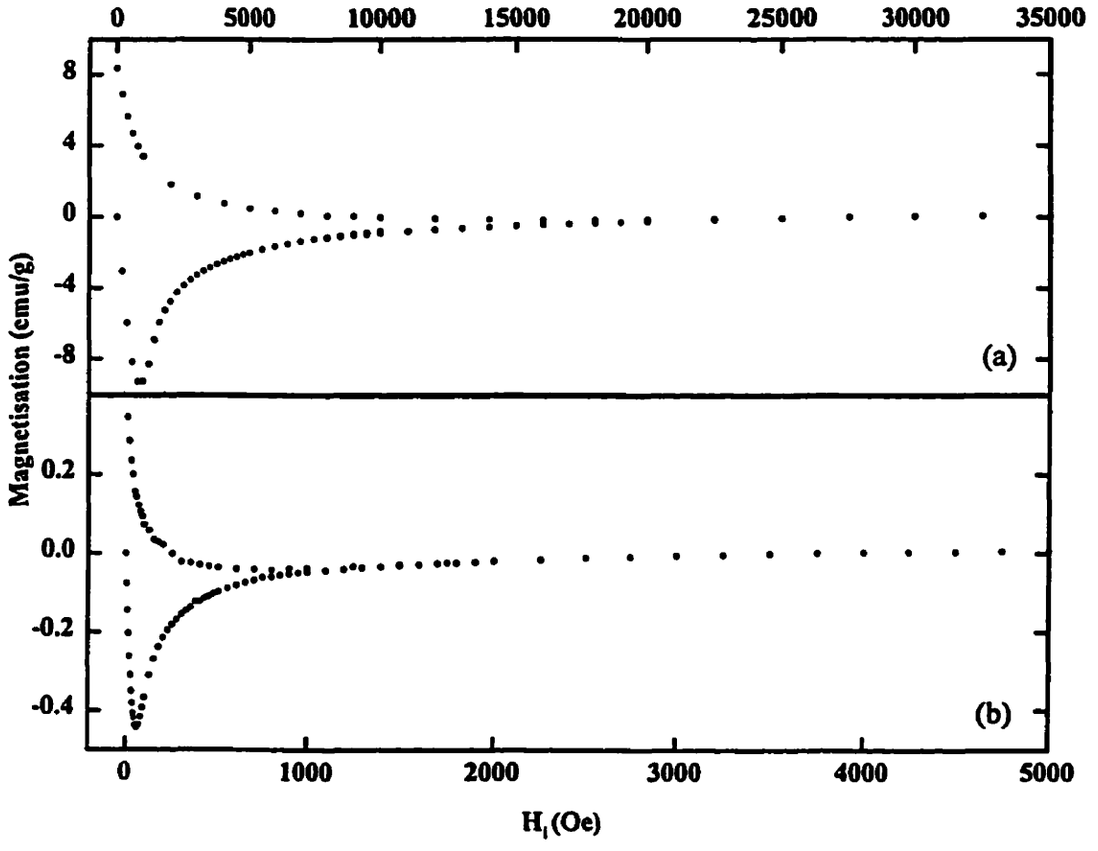

Figure 6.7: Magnetisation as a function of increasing and decreasing field in the as-cast bar of YNi_2B_2C at fixed temperatures of (a) 1.95 K (b) 9.7 K.

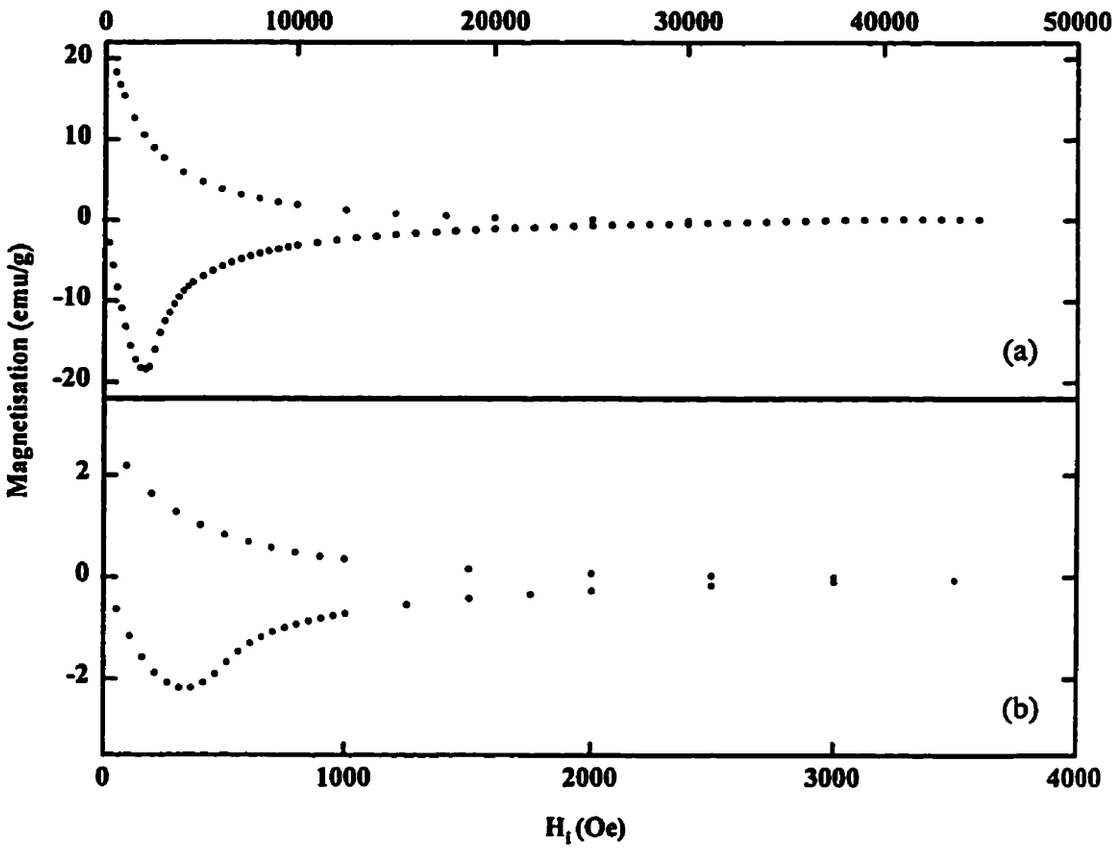

Figure 6.8: Magnetisation as a function of increasing and decreasing field in the annealed bar of YNi_2B_2C at fixed temperatures of (a) 1.95 K (b) 11.5 K.

samples, however, M(H) deviates from linear at significantly lower fields than at the minimum in the magnetisation. This could be due to the presence of a non-uniform field inside the sample (caused by a non-uniform demagnetizing field) which induces certain areas to enter the 'vortex' state before others, causing the gradual, rounded transition observed in our data. This non-linear behaviour could also be caused by defects in the system which change the response of the material from ideal Type II behaviour. Estimates of H_{c1} can be obtained by interpolation of the data to find the field at which the magnetisation deviates from the linear diamagnetic behaviour. Alternatively, the data can be fit to the expected behaviour of an ideal Type II superconductor, as shown in figure 6.9, and H_{c1} can be taken to be the turnover point between the superconducting and the vortex state. The data obtained using these two approaches are plotted in fig 6.10 and 6.11 for the as-cast and annealed samples respectively. As expected, the second estimate is higher than the first, however the ratio of the two values of $H_{c1}(T)$ is roughly constant with temperature.

In both samples H_{c1}(T) increases as the temperature is lowered below T_c, and appears to bend over slightly toward saturation as the temperature goes to zero. Neither set of data, however, follows the $1-(T/T_c)^2$ behaviour predicted for a BCS superconductor. H_{c1}(T) is significantly higher in the annealed sample than in the as-cast sample, and both sets of data are enhanced by factors of 2–20 from previously published values[52, 127].

By definition, H_{c2} is the field at which the magnetisation becomes zero, and can be estimated by a linear interpolation of the data to M=0. The presence of a small paramagnetic contribution to this data complicates analysis, as it affects the zero crossing point, and subtraction of the paramagnetic component is error-prone due to the small field dependence of M(H) in this regime. Extrapolations based on the Ginzburg-Landau relation, $M \propto (H - H_{c2})$, and the London equation, $M \propto \ln\left(\frac{H}{H_{c2}}\right)$, fail due to the presence of curvature in M vs. H and M vs. ln(H) plots. At the transition from the vortex state to the normal state, the slope of the magnetisation should change abruptly. By plotting the local field derivative of the measured M(H), values of H_{c2} can be deduced from the field at which the

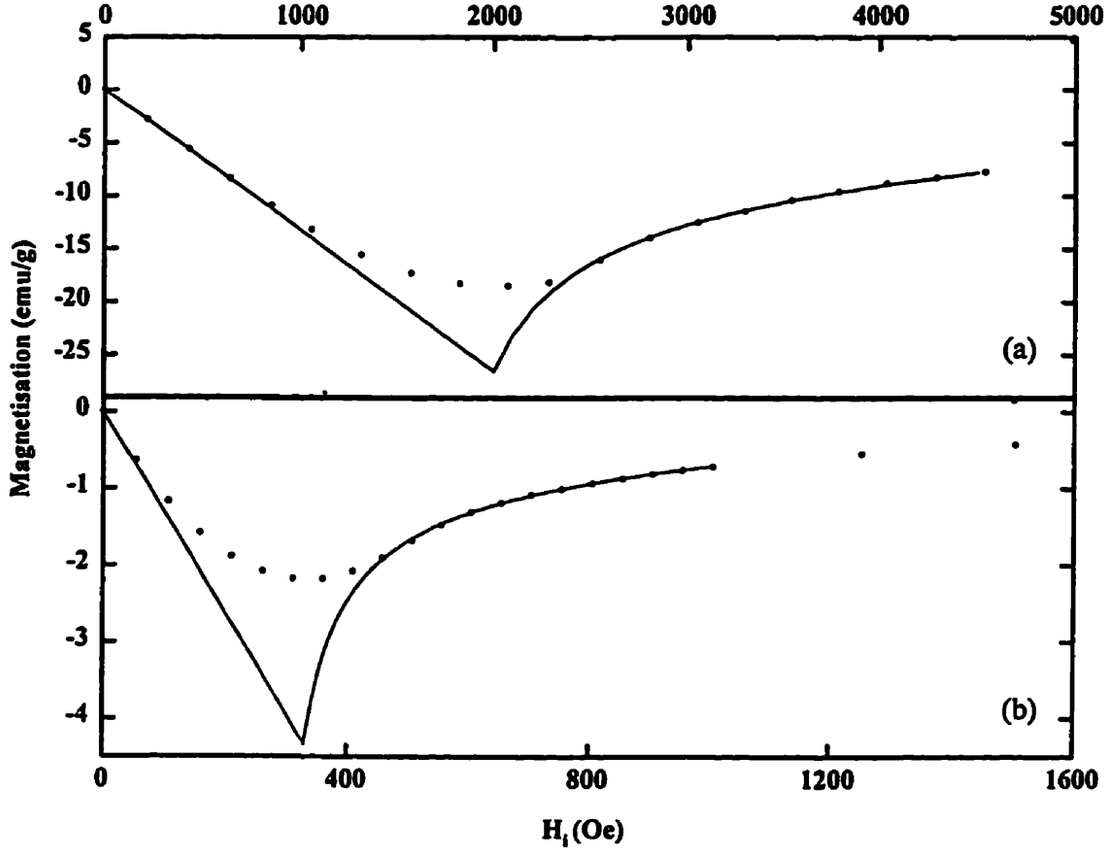

Figure 6.9: A fit of the magnetisation as a function of increasing field in the annealed bar of YNi_2B_2C at fixed temperatures of (a) 1.95 K (b) 11.5 K to that expected for an ideal Type II superconductor.

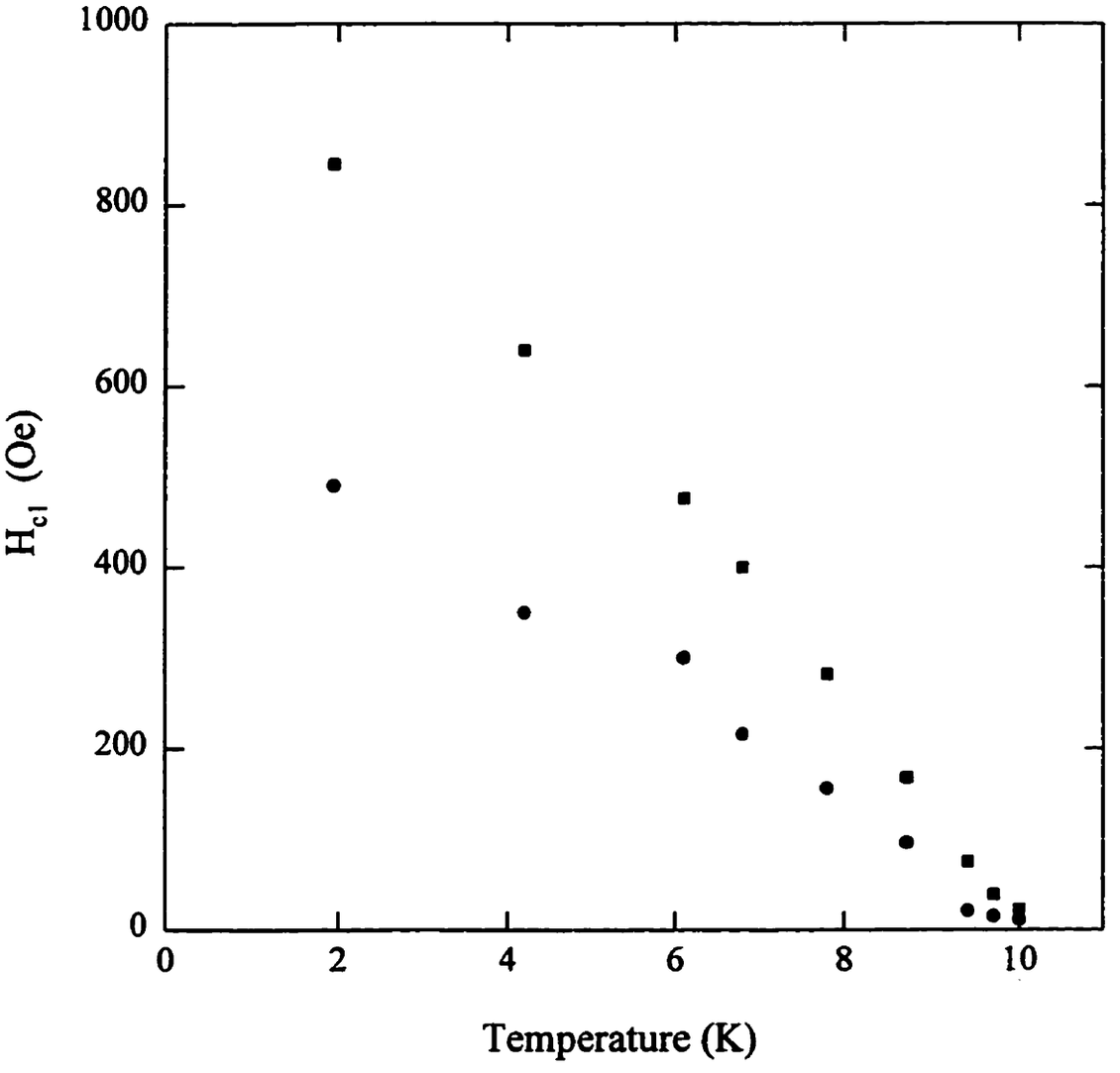

Figure 6.10: Estimates of $H_{c1}(T)$ in the as-cast bar of YNi_2B_2C; the lower data is estimated from the point of deviation from linear behaviour, the upper from fits as in figure 6.9, as described in the text.

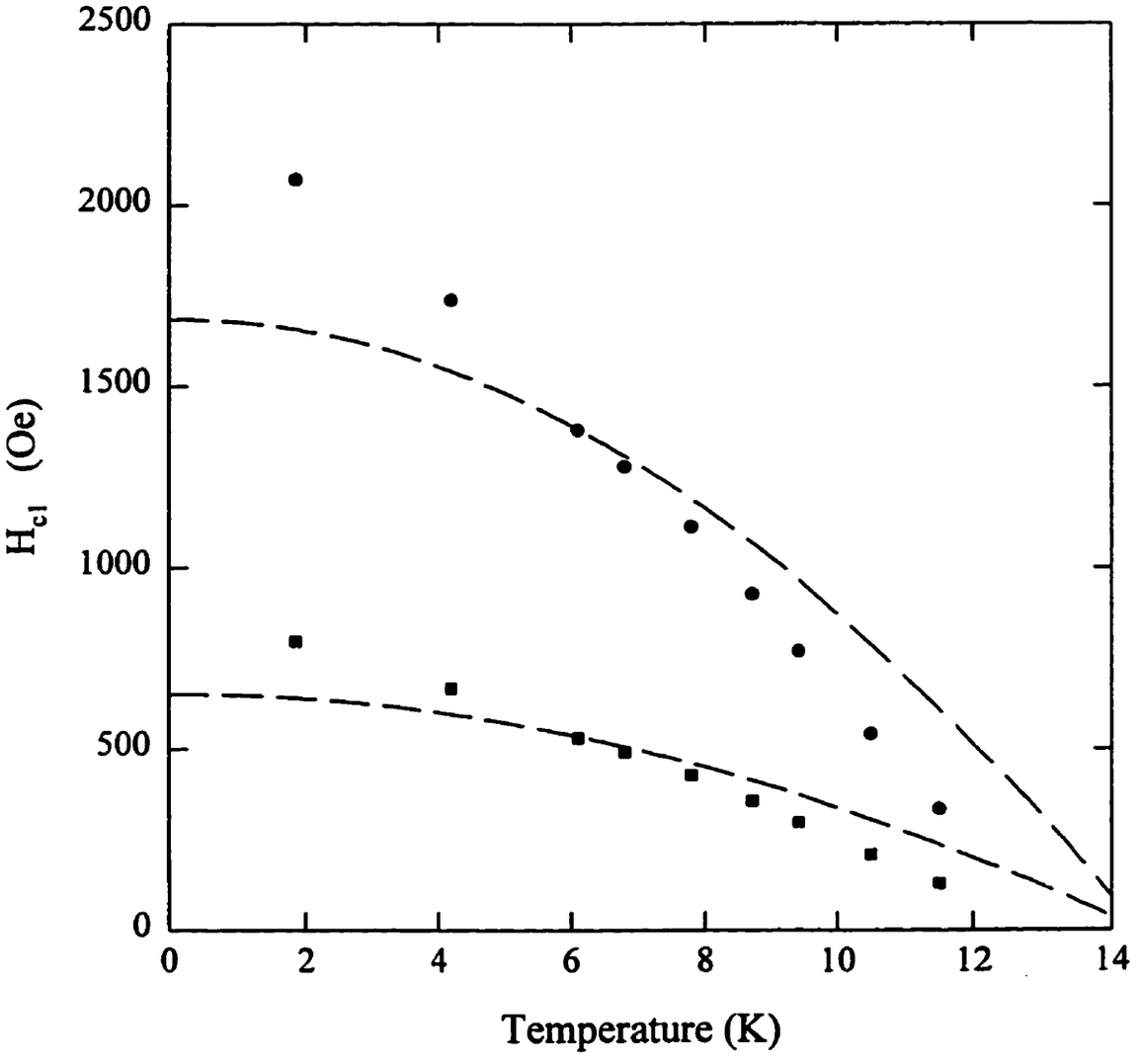

Figure 6.11: Estimates of $H_{c1}(T)$ in the chill-cast and annealed bar of YNi_2B_2C; the lower data is estimated from the point of deviation from linear behaviour, the upper from fits as in fig 6.9, as described in the text. The dashed lines show a fit to the predicted BCS behaviour, $H_{c1}(T) \propto 1-(T/T_c)^2$.

slope exhibits an anomaly (at high field). Again, $H_{c2}(T)$ is larger in the annealed sample than in the unannealed sample, as can be seen in figures 6.12 and 6.13. In contrast with the predictions of BCS theory, $H_{c2}(T)$ does *not* saturate as $T \rightarrow 0$, in fact, the slope seems to increase as the temperature decreases, an effect which also been noticed in some high-T_c superconductors. Although Prozarov et al. saw saturation in $H_{c2}(T)$ as temperature went to zero[52], other experimentalists found that $H_{c2}(T)$ showed no sign of saturating[121, 127], in agreement with our results. Our values of $H_{c2}(T)$ obtained from magnetisation measurement for the unannealed sample are in general lower than those obtained by other groups, however those for the annealed sample are comparable to previous results[52, 112, 121, 127].

Transport Measurements

Transport measurements were done in the high field magnetoresistance cryostat described in Section 3.2, with the magnetic field applied parallel to the *ac* measuring current along the longest sample dimension, as for the magnetisation measurements. The use of the same sample for both magnetisation and resistivity measurements allows direct comparison between data taken at the same value of applied field. The temperature dependence of the resistivity of the as-cast and annealed samples are compared in figure 6.14. The large decrease in the normal state resistivity after annealing indicates a significant reduction in defects, as does the increase in T_c. The as-cast sample has an onset of superconductivity at 11.0 K (midpoint 10.2 K), while the annealed sample has an onset of 14.2 K (midpoint 13.9 K). These temperatures agree well with those found from susceptibility data. The transition in the annealed sample is very sharp, with ΔT=0.3K, as opposed to 0.7K in the as-cast sample, again reflecting the reduction of defects in the material after annealing. The normal state resistivity $\rho(T \geq T_c)$ of $\simeq$ 16.6 $\mu\Omega$-cm is much higher than the value of 2.5$\mu\Omega$-cm measured by Cava et al.[8]. This wide variation in normal state resistivities is not uncommon in high-T_c superconductors. In fact, reported resistivities for the borocarbide $YPd_5B_3C_{0.3}$ range from 6–80 $\mu\Omega$-cm [8, 127].

The field dependence of the magnetoresistance at fixed temperatures below T_c is

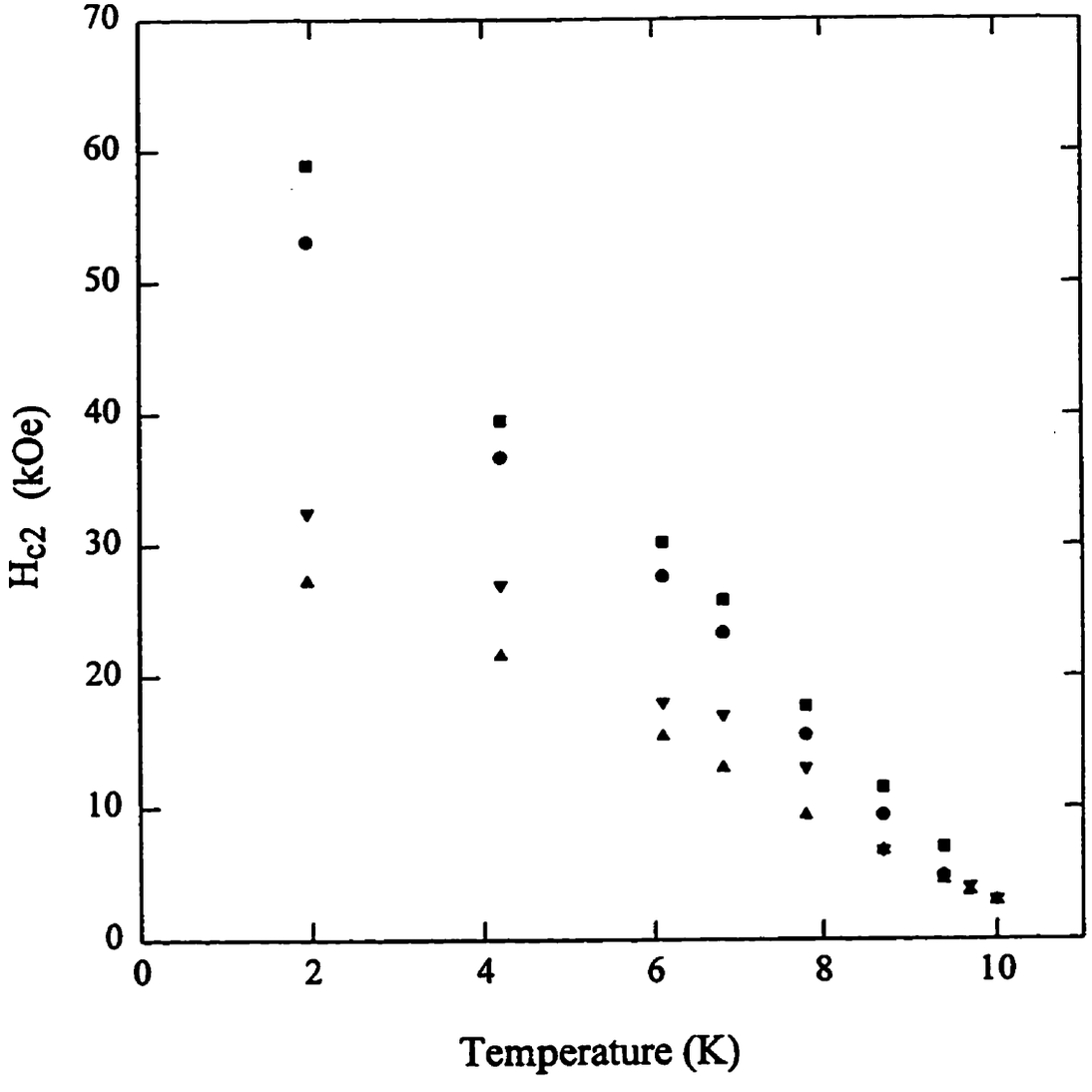

Figure 6.12: Estimates of $H_{c2}(T)$ in the as-cast bar of YNi_2B_2C: (●) 10% restoration of $\rho(0,T)$; (■) peak in $d\rho/dH$; (▲) M=0; (▼) sudden change in dM/dH.

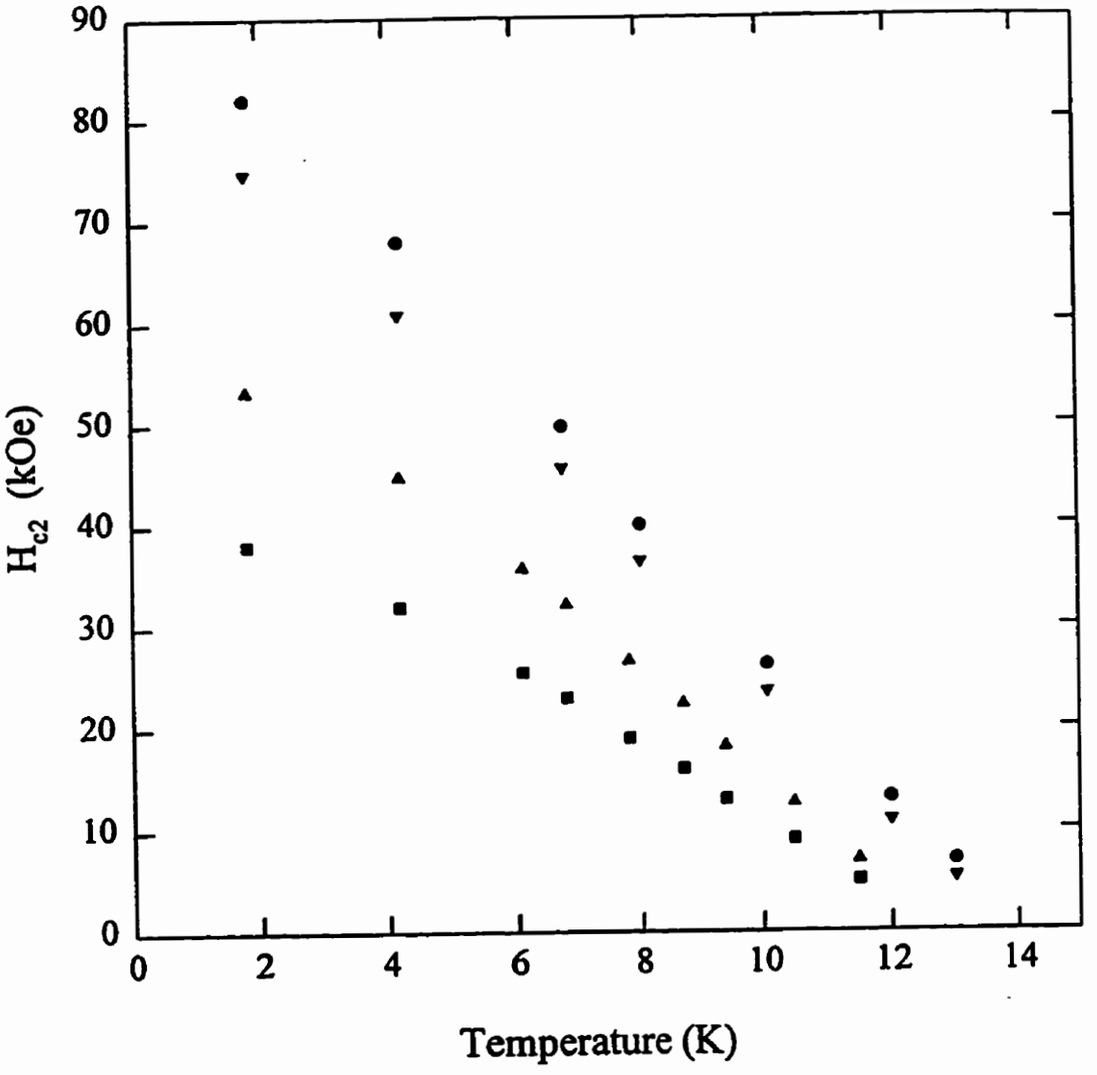

Figure 6.13: Estimates of $H_{c2}(T)$ in the chill-cast and annealed bar of YNi_2B_2C: (▼) 10% restoration of $\rho(0,T)$; (●) peak in $d\rho/dH$; (■) M=0; (▲) sudden change in dM/dH.

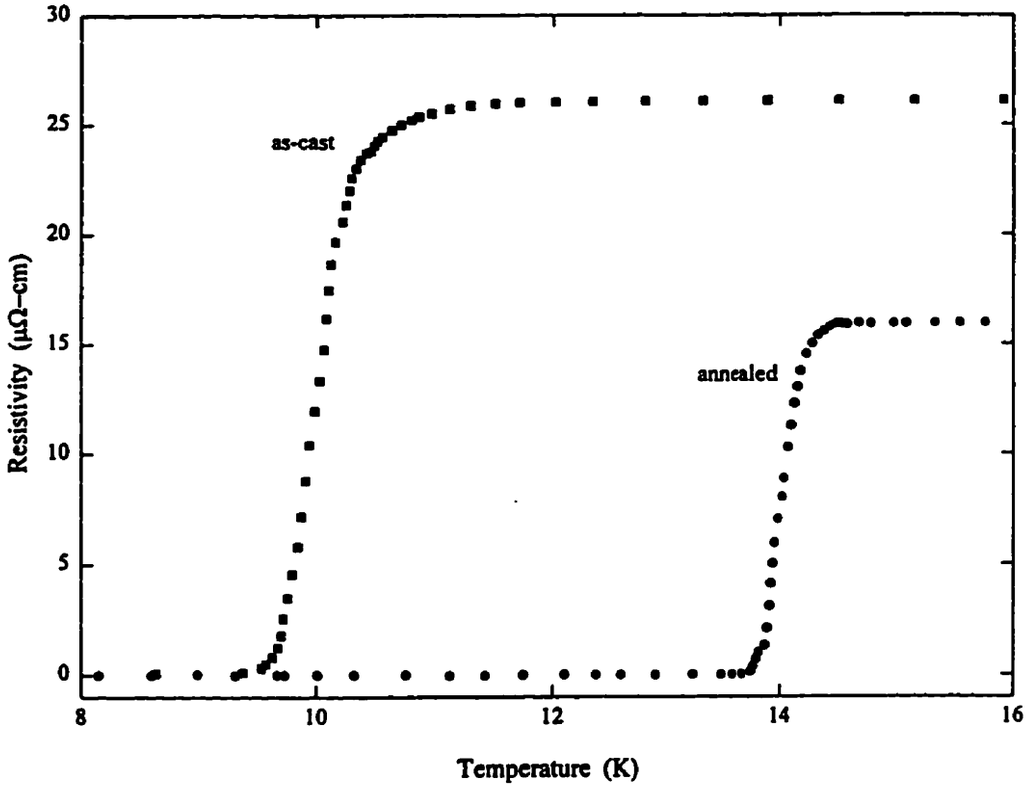

Figure 6.14: Comparison of the zero field resistivities in the as-cast sample and the annealed sample, as labelled.

summarised in Figures 6.15 and 6.16. In each case, the sample is superconducting at low field, and the resistivity rises towards its normal state value for H>H_{c2}. The transition width (in field) for the restoration of $\rho(H,T)$ to its normal state value of $\rho(0,T \geq T_c)$ increases gradually with decreasing temperature, although the most dramatic effect observed is the sharp increase in H_{c2}(T) as T decreases. H_{c2}(T) is typically estimated from $\rho(H,T)$ data using one of two methods: (i) H_{c2}(T) is taken to be the field which restores $\rho(H,T)$ to 10% of its $\rho(0,T \geq T_c)$ value, or (ii), H_{c2}(T) is taken as the field which restores $\rho(H,T)$ to 50% of its $\rho(0,T \geq T_c)$ value. This second approach is essentially equivalent to taking the field at which $\rho(H,T)$ has a maximum slope in these data. To allow direct comparison, these values are plotted with the estimates of H_{c2}(T) from the magnetisation data in figures 6.12 and 6.13. The estimates of H_{c2}(T) from resistivity measurements are higher than those taken from magnetisation measurements, however the same lack of saturation at low temperature is observed in both sets of curves. As seen in the magnetisation data, H_{c2}(T) is higher in the annealed sample than in the as-cast bar. The magnitude of H_{c2}(T) from resistivity data in the annealed sample agree well with those found, also from resistivity measurements, by Takagi et al.[122], but are higher than those found by other groups[52, 127].

Superconducting Parameters: λ, ξ and J_c

Superconductors are generally evaluated using a number of parameters, two of which are the skin-depth λ, the correlation length ξ. The ratio of these two parameters gives the Ginzburg-Landau parameter κ. Estimates for λ and ξ can be found from the H_{c1}(T) and H_{c2}(T) data, in the following manner. κ can be obtained using equation 2.57[52].

$$\frac{H_{c1}(T)}{H_{c2}(T)} = \frac{\ln(\kappa(T)) + 0.5}{2\kappa^2(T)} \tag{6.1}$$

From the two sets of H_{c1}(T) (magnetisation and resistivity), two values for κ(T) were found, with errors arising from the spread of H_{c2}(T) values. ξ was then found

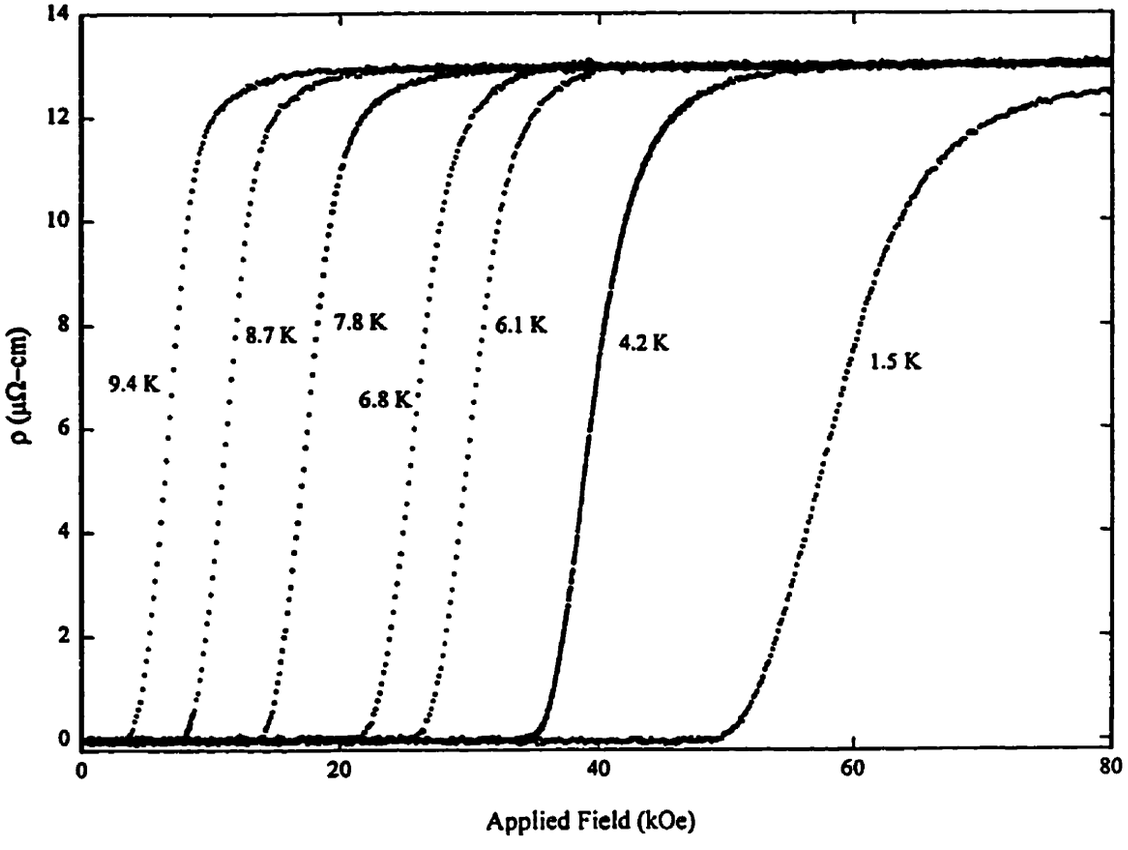

Figure 6.15: Resistivity as a function of increasing field in the as-cast bar of YNi_2B_2C at a number of fixed temperatures, as labelled.

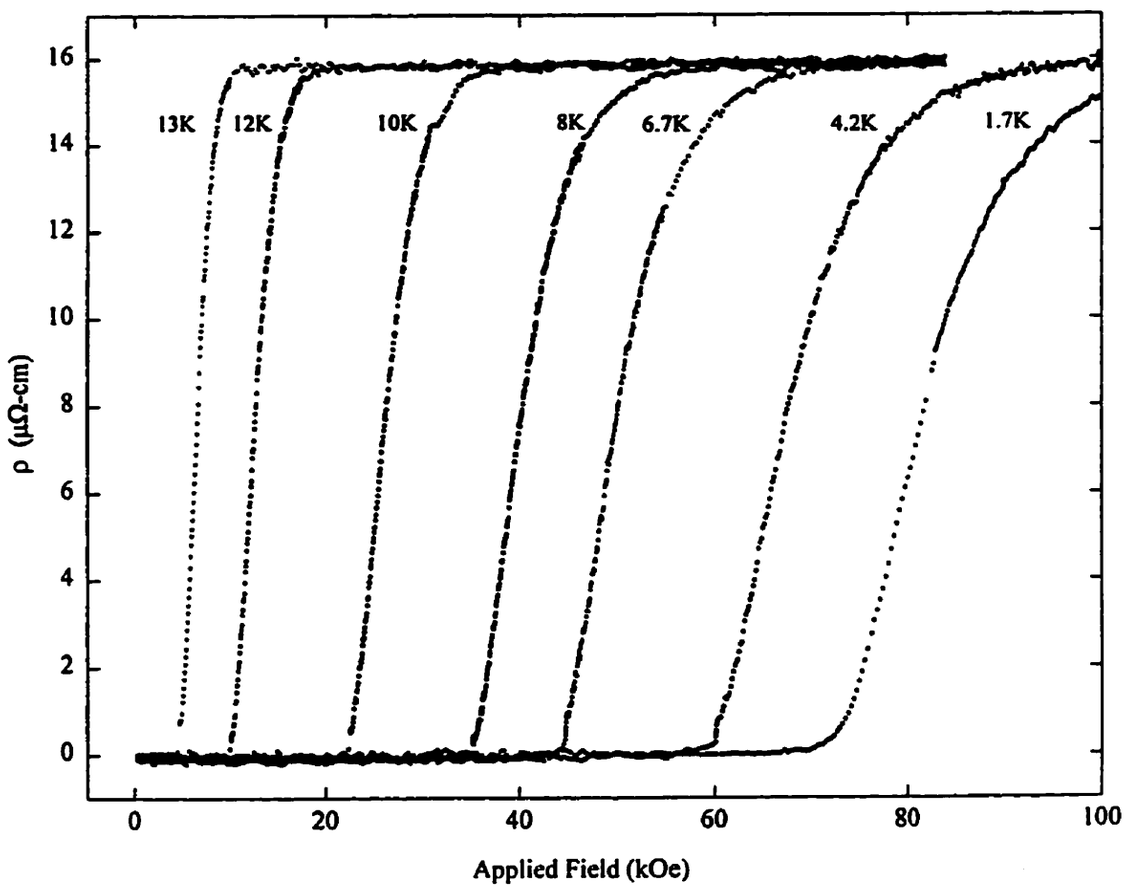

Figure 6.16: Resistivity as a function of increasing field in the annealed bar of YNi_2B_2C at a number of fixed temperatures, as labelled.

Table 6.2: Superconducting Parameters of YNi_2B_2C Chill-cast Bars.

Parameter	As-cast sample	Annealed sample
κ (magnetisation H_{c1})	8±2	10±2
κ (magnetoresistance H_{c1})	6±1	4±2
ξ	(0.7–1.1)x10−6cm	(0.6–0.9)x10−6cm
λ	(4.2–6.6)x10−6cm	(4.8–7.2)x10−6cm

using equation 2.58,

$$\xi(T) = \left(\frac{\phi_0}{2\pi H_{c2}(T)}\right)^{1/2}. \tag{6.2}$$

The spread in ξ(T) resulting from the different H_{c2}(T) values gives rise to a range of λ values (found using $\lambda = \kappa\xi$). The values derived for these parameters are summarised in Table 6.2 for both samples. The estimates for λ in both samples are lower than those measured by Prozarov et al.[52], but the ξ values are similar. This means that the value for κ in these chill-cast samples is lower than that measured by Prozarov et al.

Another important parameter in evaluating the practicality of a superconductor is its critical current density, i.e. the maximum current it can carry without going normal. This can be evaluated from the sample geometry and magnetisation measurements, using the Bean model[53]. This model assumes that the critical current can be induced by *any emf*, no matter how small. Thus, the sample will have a uniform critical current density, J_c, which penetrates into the sample to a depth determined by the value of the applied field,which decreases linearly with depth, by Ampere's law. Assuming the sample to be a semi-infinite slab of thickness D, J_c can be calculated from the irreversible magnetisation, the difference between the magnetisation in the ascending and descending branches of the magnetisation data,

$$J_c \sim \frac{20 M_{irr}}{D} \tag{6.3}$$

The factor of 20 arises from the combination of constants from Ampere's law.

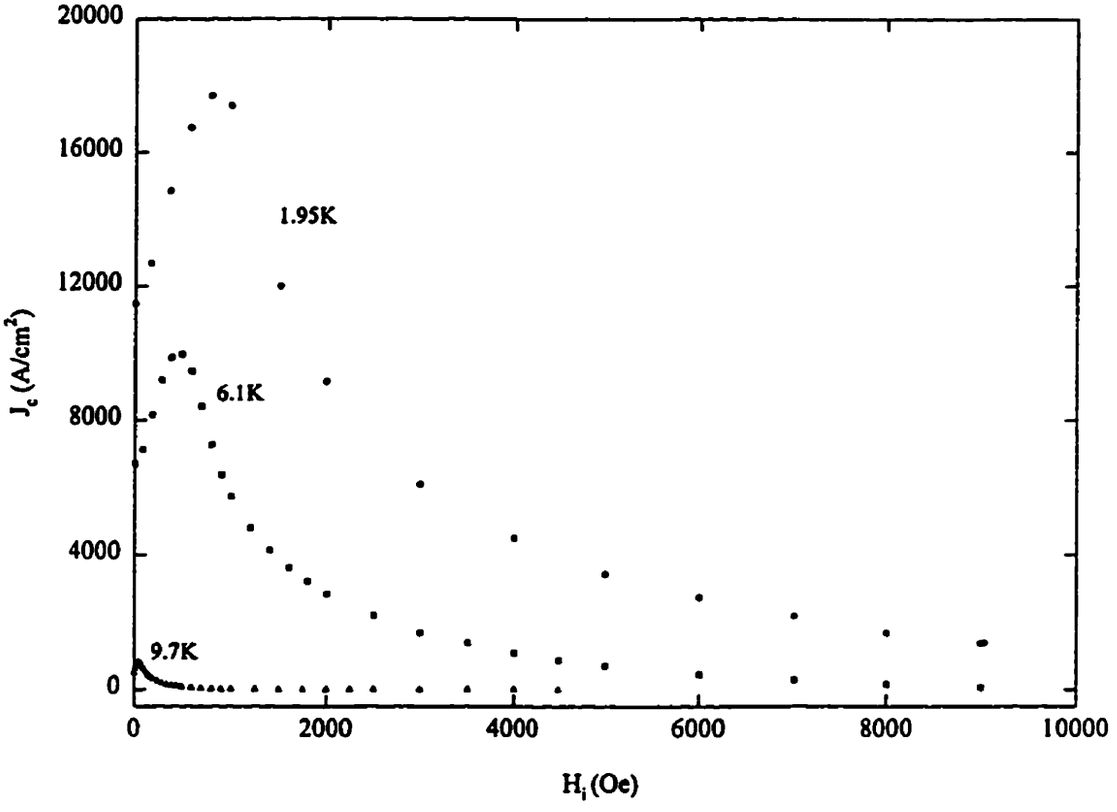

Figure 6.17: J_c as a function of field in the as-cast bar of YNi_2B_2C at a number of fixed temperatures, as labelled.

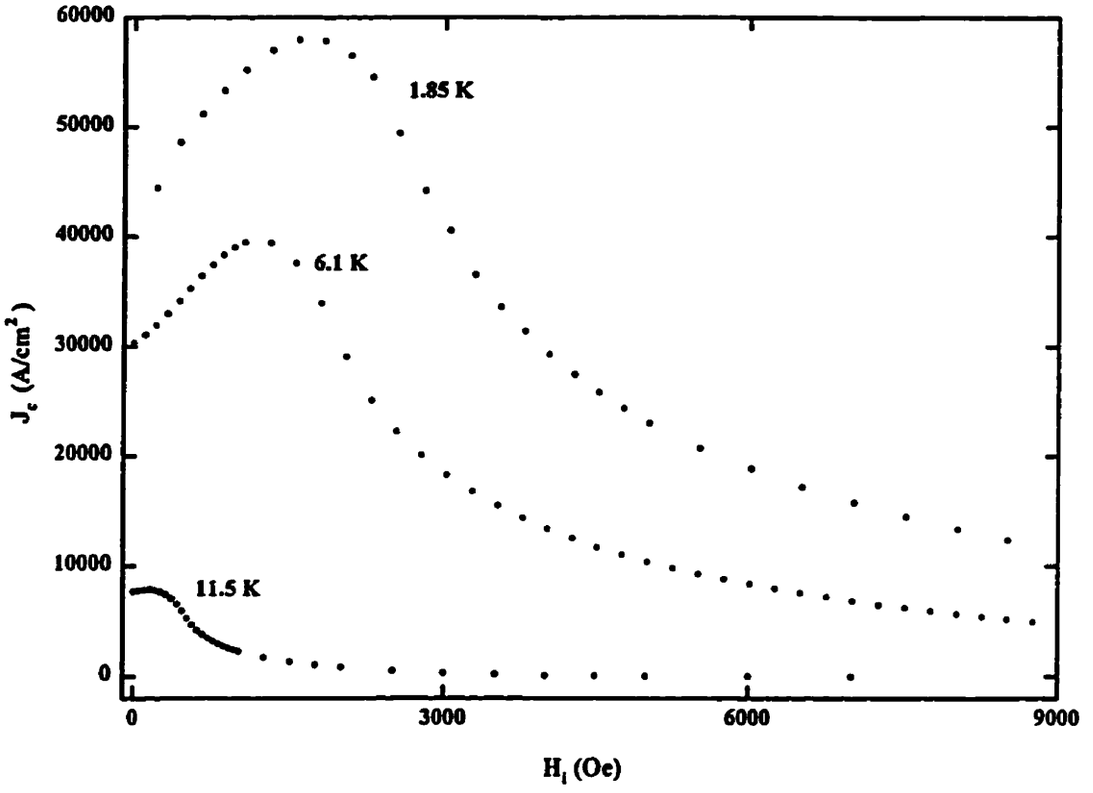

Figure 6.18: J_c as a function of field in the annealed bar of YNi_2B_2C at a number of fixed temperatures, as labelled.

A number of the J_c curves are shown in figures 6.17 and 6.18 for the chill-cast samples before and after annealing. Since the annealed sample had a larger irreversibility in the magnetisation, it also has a larger critical current density, some 2–5 times larger than previously published data[52, 112]. The maximum in the J_c vs H plot reflects the large value of H_{c1} in these materials. The increase in J_c after annealing is not understood, since removing defects typically *increases* the reversibility of the magnetisation and thus decreases the critical current. We suggest that the combination of chill-casting followed by annealing has introduced some type of defect structure which enhances the critical current density (c.f. high T_c oxide superconductors[129]), and thus the practicality of this superconductor.

6.3 $Y(Ni_{1-x}Fe_x)_2B_2$

A number of studies have been done on the effects of Co substitution in the Ni site of YNi_2B_2C, concluding that the Co acts as a simple impurity rather than a magnetic scattering centre. The effects of Fe doping have not been analyzed in as much detail. Measurements of Bud'ko et al. on $Y(Ni_{1-x}Fe_x)_2B_2$ with x=0, 0.01, 0.03, 0.05 and 0.07 showed a linear decrease in $T_c(x)$ with increasing x, as did their low x Co doping. Extension of these measurements to higher Co doping by Hoellworth et al.[125] and Schmidt et al.[126], as detailed in the review, showed curvature developing in the $T_c(x)$ plot as x approached the critical concentration for the complete suppression of superconductivity, x_0. For this reason, we prepared a series of $Y(Ni_{1-x}Fe_x)_2B_2C$, with $0 \leq x \leq 0.1$, to determine whether the behaviour of $T_c(x)$ follows the same pattern as the Co data, or whether it remains linear to x_0 as suggested by Bud'ko et al. Since chill-casting the samples causes large changes in the properties of the parent compound, as described in the previous section, the doped samples were prepared by cutting bars from the arc-melted button with a diamond saw. The resulting samples displayed exactly the same properties as the buttons from which they were cut, allowing direct comparison with the results of Bud'ko et al.

6.3.1 AC Susceptibility

$T_c(x)$ was determined from *ac* susceptibility measurements. Figure 6.19 shows a comparison of the zero field χ_{ac} data for x=0.01, 0.02, 0.05 and 0.1. As x increases, T_c clearly drops rapidly, and the transition width ΔT increases steadily. $T_c(x = 0.1)$ is well below 4.2K, suggesting that the critical concentration x_0 of Fe is slightly above 0.1. From figure 6.19 it can also be seen that the amount of diamagnetic shielding decreases as x increases, ranging from 100% shielding for the parent compound (as shown in the previous section) to only 90% for x=0.1. A slight temperature dependent paramagnetism also develops with increasing x, as can be seen in figure 6.20, a plot of χ_{ac}(H,T) in the $x = 0.01$ sample, suggesting that the Fe impurities do indeed have magnetic moments. Values for T_c were extracted from these data using two methods: firstly by taking the onset temperature of the drop in the zero field susceptibility, and secondly as the temperature at which the maximum in $d\chi(0,T)/dT$ occurs. These $T_c(x)$ are plotted in figure 6.25 with the data obtained from transport measurements on a number of these specimens, as described in the following section.

6.3.2 Transport Measurements

Transport properties were also measured for a number of these doped compounds. These measurements show that the presence of Fe impurities at the Ni site not only decreases the temperature at which the sudden drop in resistivity occurs, it also increases the resistivity in the normal state, at a rate of $d\rho/dx$=3–4$\mu\Omega$-cm/at.% Fe. This can be seen in figure 6.21, which compares $\rho(0,T)$ for the x=0, 0.02 and 0.05 compounds. Values for T_c were taken from these data in the same manner as from the χ_{ac}(0,T) plot, namely (i) the temperature of the onset of the drop in resistivity and (ii) the temperature of the peak in $d\rho/dT$.

The magnetoresistance measured at a number of fixed temperatures below T_c is plotted for the $x = 0.02$ and $x = 0.05$ samples in figures 6.22 and 6.23 respectively. As in the parent compound, the critical field H_{c2} drops dramatically as T goes to

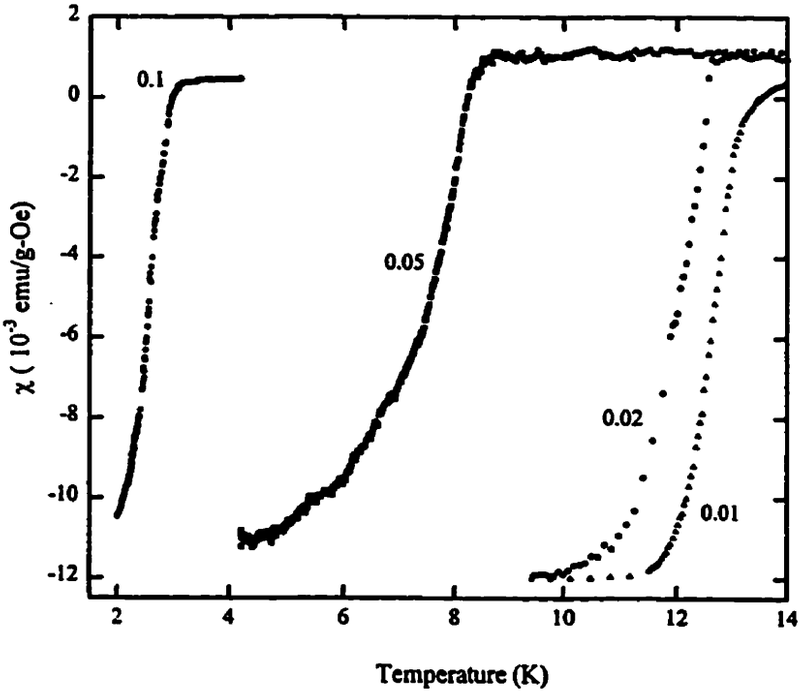

Figure 6.19: A comparison of the zero field χ_{ac} for $Y(Ni_{1-x}Fe_x)_2B_2$ with x=0.01, x=0.02, x=0.05 and x=0.1.

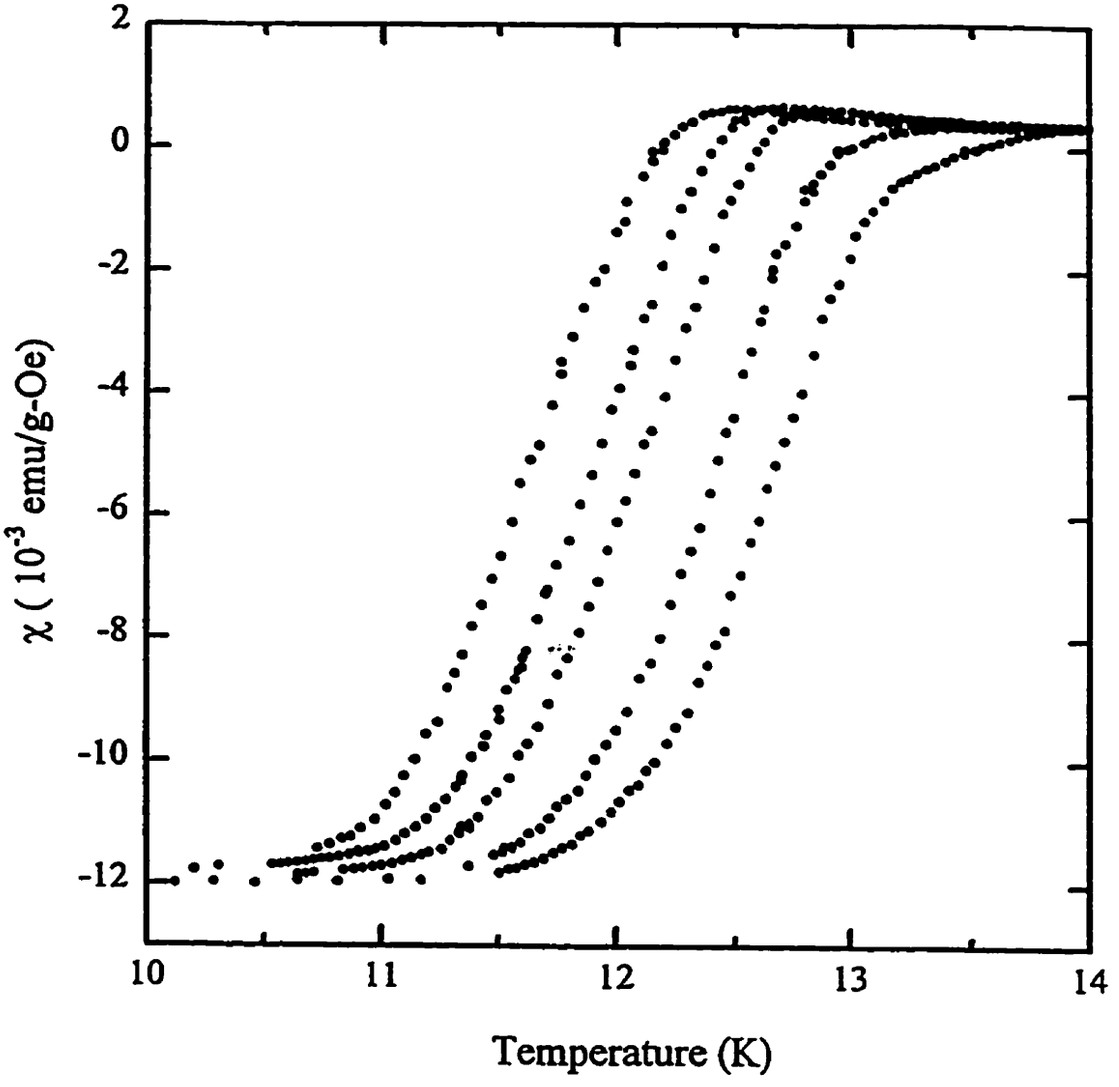

Figure 6.20: χ_{ac}(H,T) for $Y(Ni_{1-x}Fe_x)_2B_2$ with x=0.01 in a number of fixed static biasing fields, from right to left: 0, 100, 500, 750 and 1000 Oe.

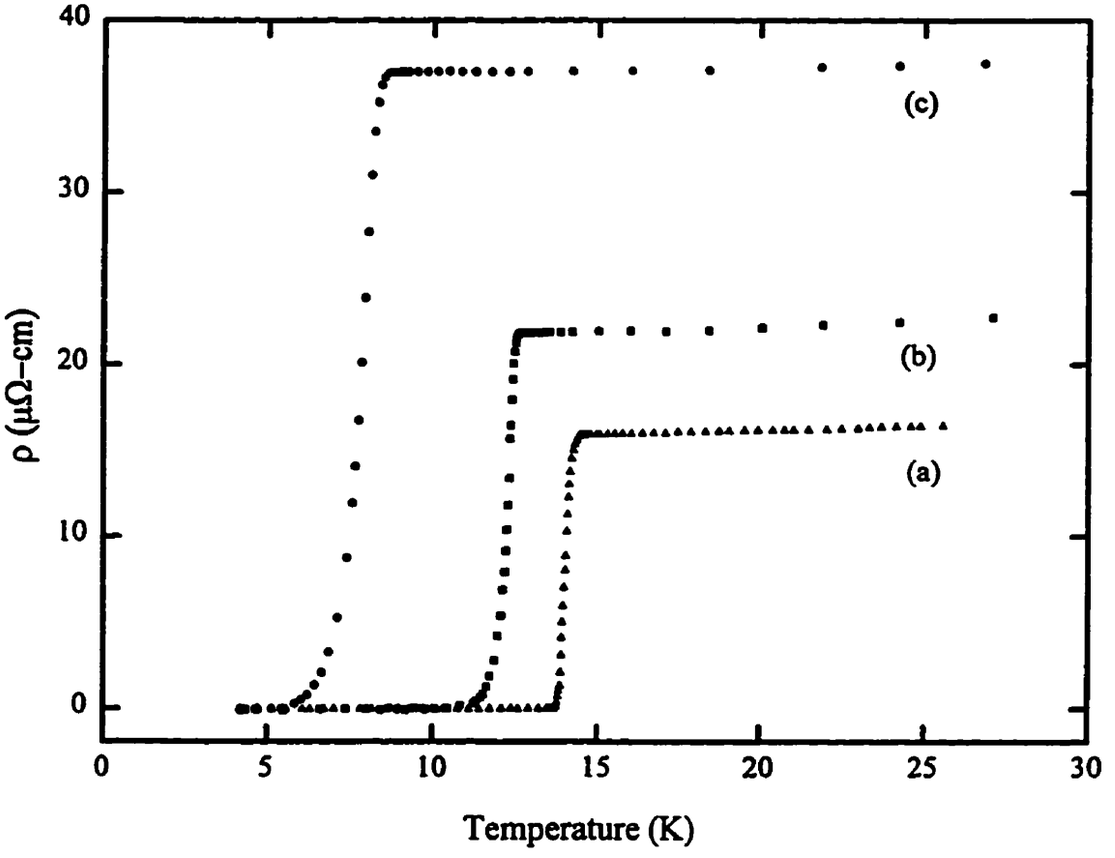

Figure 6.21: A comparison of the zero field resistivity for $Y(Ni_{1-x}Fe_x)_2B_2$ with (a) x=0, (b) x=0.02 and (c) x=0.05.

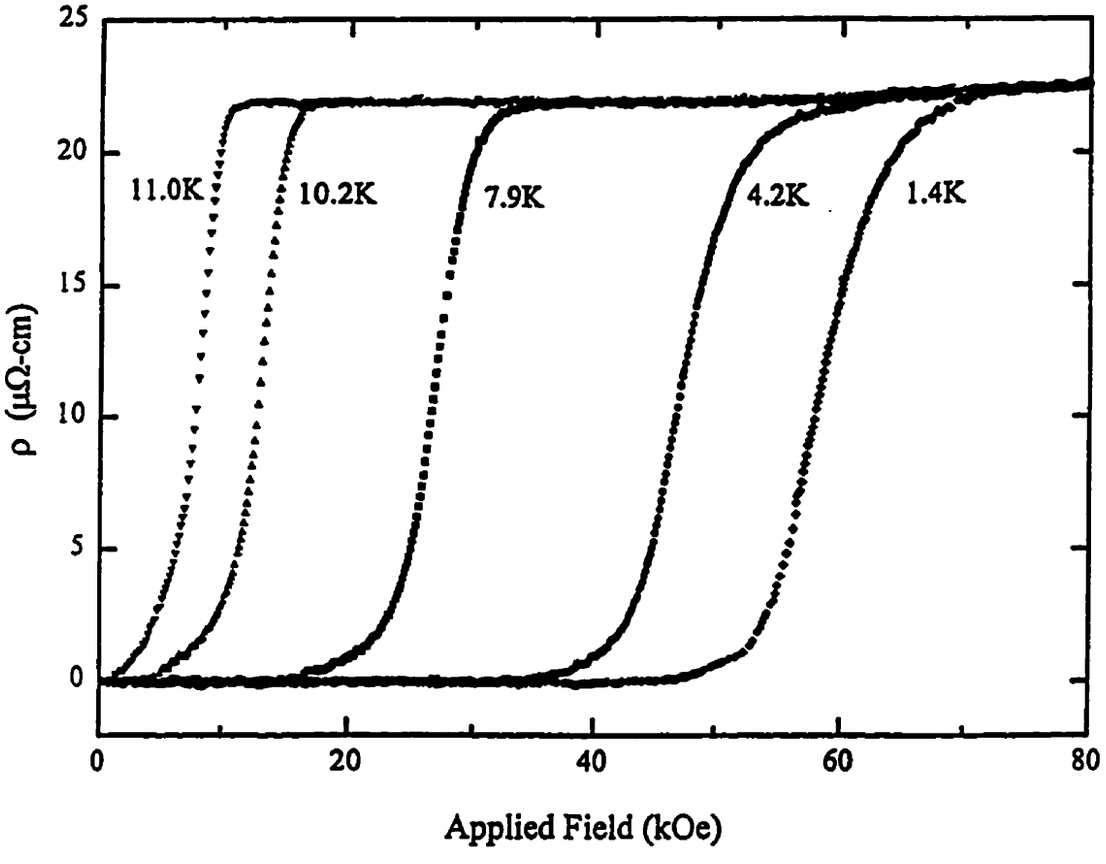

Figure 6.22: ρ(H,T) for $Y(Ni_{1-x}Fe_x)_2B_2$ with x=0.02 at a number of fixed temperatures, as labelled.

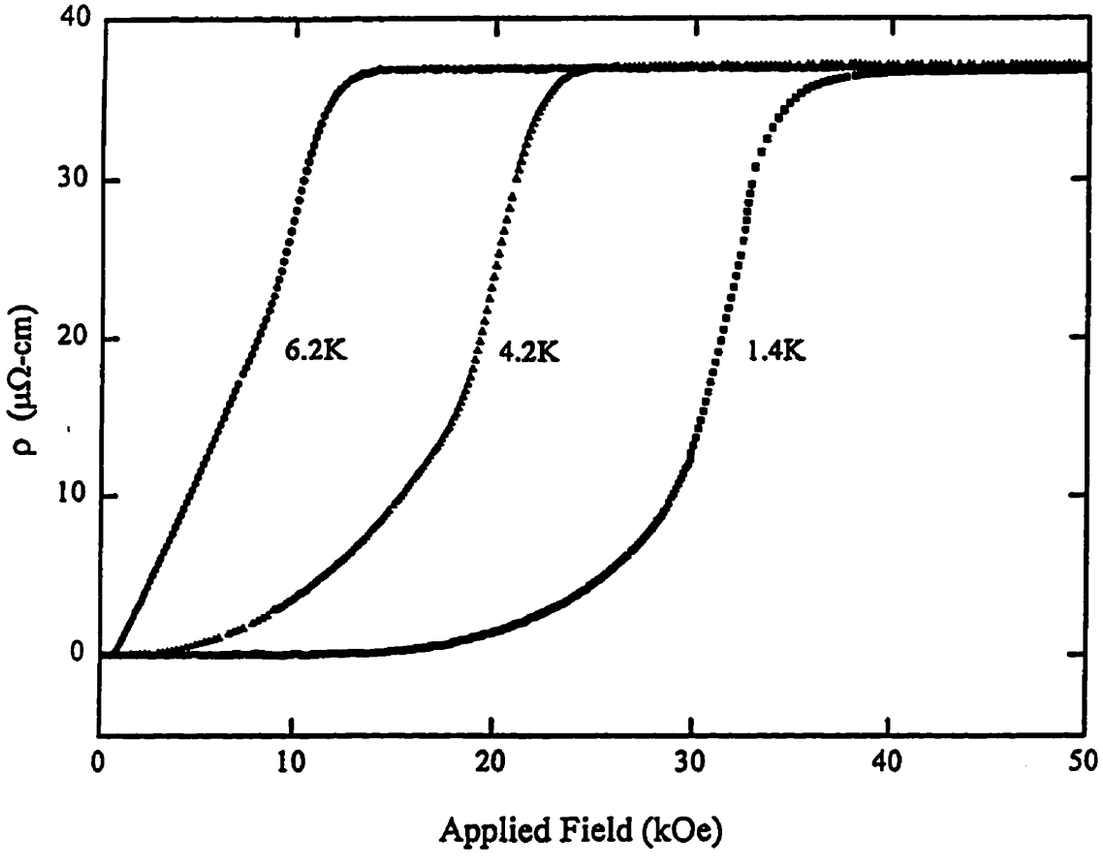

Figure 6.23: ρ(H,T) for $Y(Ni_{1-x}Fe_x)_2B_2$. with x=0.05 at a number of fixed temperatures, as labelled.

T_c^-. $H_{c2}(T)$ shows no indication of saturating at zero temperature, as was observed in the parent compound. Values for $H_{c2}(T)$ are compared for these two samples in figure 6.24, with the values extracted from the $\rho(H,T)$ curves as previously. $H_{c2}(T)$ is much larger in the x=0.02 sample than in the x=0.05 sample, however the $H_{c2}(T)$ and T_c values in the x=0.02 sample are comparable to those in the chill-cast bar of the parent compound, suggesting perhaps a similar amount of disorder scattering.

6.3.3 Suppression of T_c

The various values of $T_c(x)$ found from our data are plotted in figure 6.25 along with those published previously by Bud'ko et al.[124]. In general our data agree quite well with the previous results, and have less scatter. The dashed and solid lines in figure 6.25 are fits to two different types of scattering behaviour. The dashed line models the behaviour of the Fe impurities as non-magnetic scattering centres while the solid line is a fit to scattering from paramagnetic impurities. While neither line appears to fit the data well, the solid curve is perhaps a better fit in the high concentration regime. Note that in this figure x is replaced by the concentration c in atomic percent, where $c = x/3$. A discussion of the results of the two model fits is below.

The dashed line is a fit to the Kaiser scattering model, as done by Schmidt et al.[126] for Co doping. The data is fit to equations 2.59–2.61, with $N(E_F)$=0.34 states/eV atom spin and g=0.27 (the BCS coupling constant) from previously published data[128]. This fit returns parameters of U_{eff}=2x10^6 eV and $N_i(E_F)$ = 0.6x10^{-5} states/eV atom spin. These results are obviously bizarre, with the low density of states and very high U_{eff} yielding $N_i(E_F)U_{eff}$ >1, i.e. the static Hartree-Fock criterion for magnetism is satisfied. Thus, although this equation, which assumes non-magnetic impurities, fits the data fairly well, the fitting results suggest that this model is not a good representation of the data, and that the impurities may have paramagnetic moments in direct contradiction of the model assumptions.

The solid line is a fit to the Abrikosov-Gorkov equation in Chapter 2 (equation

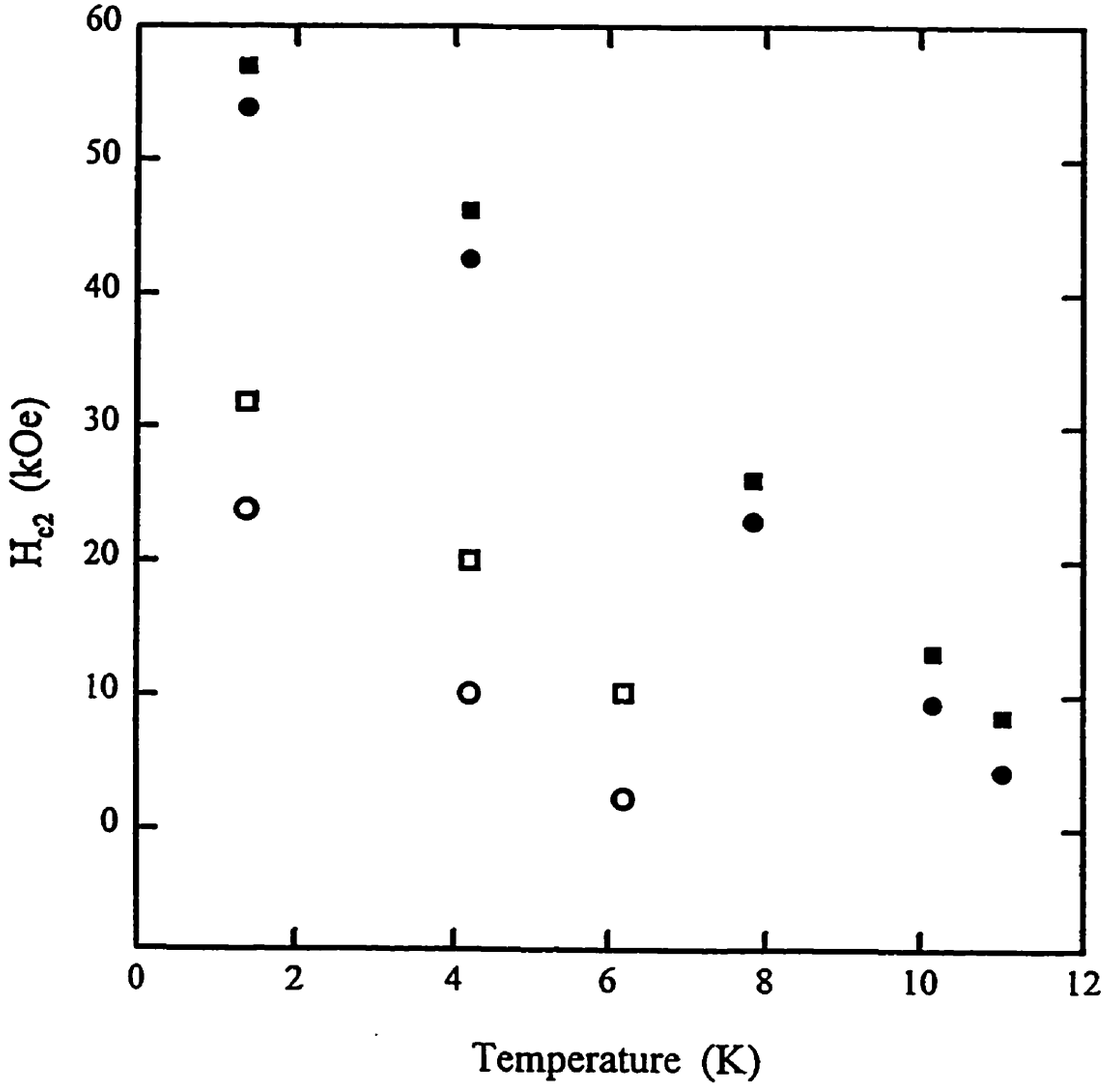

Figure 6.24: Estimates of $H_{c2}(T)$ in $Y(Ni_{1-x}Fe_x)_2B_2$ with x=0.05 (bottom curves) and x=0.02 (top curves); In each set of curves, the lower data is estimated from the 10% restoration of $\rho(0,T)$ while the upper is from the temperature of the peak in $d\rho/dH$.

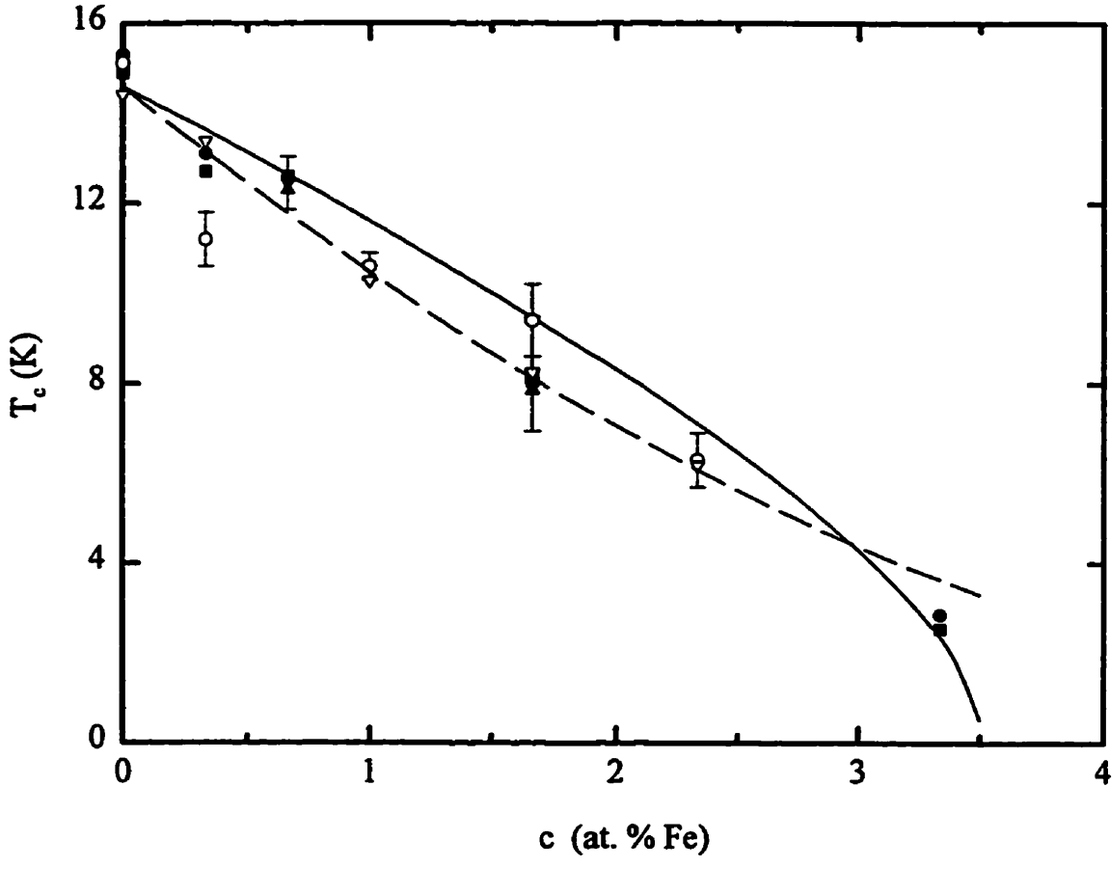

Figure 6.25: T_c as a function of Fe concentration for $Y(Ni_{1-x}Fe_x)_2B_2$. The open symbols are estimates of T_c from Bud'ko et al.[124], while the solid symbols are from the current study: estimated from (■) susceptibility onset, (●) maximum in $d\chi/dT$, (▲) resistivity onset, (▼) maximum in $d\rho/dT$.

2.62) for the suppression of T_c by paramagnetic impurities, namely,

$$\ln\left(\frac{T_c}{T_{c0}}\right) = \Psi\left(\frac{1}{2}\right) - \Psi\left(\frac{1}{2} + \frac{0.14cT_{c0}}{T_c}\right) \tag{6.4}$$

T_{c0} is 15.6K, T_c for the parent compound, and Ψ is the digamma function. A fit to this curve gives a critical concentration c_0=3.5 at.% (x=0.105), and the curvature of this fit at high c seems to better fit the data than the Kaiser model, shown by the dashed curve. Our data seem to fit the theory for non-magnetic and magnetic impurity scattering equally well, with perhaps a leaning towards magnetic scattering based on the high c curvature. Measurements are inconclusive, as Bud'ko et al. claim[124] (based on unpublished Mössbauer data) that the Fe impurities have no moment, however our data suggest that Fe *may* carry a moment in $Y(Ni_{1-x}Fe_x)_2B_2$.

6.4 Conclusion

In conclusion, YNi_2B_2C is shown to exhibit properties of an imperfect Type II superconductor. Preparing the samples using the chill-casting process introduces defects in the structure which suppress the superconducting state. After annealing, the superconducting state is enhanced and the normal state resistivity is decreased substantially, suggesting a decrease in the defects. However, the irreversibility in the magnetisation is also enhanced after annealing, a result which usually arises from an *increase* rather than a decrease in the inhomogeneity of the sample. We suggest that this contradiction indicates the formation of some type of stable defect structure during the annealing process, which increases the irreversibility considerably, greatly improving the current carrying capacity of the material.

Finally, the effects of Fe doping at the Ni site on the suppression of T_c show that, in contradiction to previously published work[124], the Fe impurities may carry magnetic moments. The existence of such a moment is supported by the susceptibility measurements of the doped samples, in which a slight paramagnetic susceptibility is observed. Further work, possibly a Mössbauer study of these materials, needs to be done in order to state conclusively whether or not such a moment exists.

Chapter 7

Giant Magnetoresistance in Layered Intermetallics

7.1 Review

The application of a magnetic field to a metal changes its resistivity slightly, due to the action of the Lorentz force on the conduction electrons. In magnetically ordered materials, this small positive magnetoresistance may be overwhelmed by larger effects due to changes in the magnetic structure with applied field. For example, the materials studied in Chapter 4 show a negative isotropic magnetoresistance caused by the alignment of spins along the field direction, and thus a reduced spin-disorder scattering. Recently, field-induced resistivity changes of more than 100%[1] have been observed in magnetic multilayer systems. These materials have become the focus of a great deal of research, due to their potential applications in the magnetic recording industry and elsewhere.

Magnetic multilayers are formed by the successive deposition of magnetic and non-magnetic layers on a substrate using molecular beam epitaxy (MBE) or sputtering techniques. The relative orientation of the magnetisation in adjacent magnetic layers is a function of the thickness of the intermediate non-magnetic layer. This separation dependence has been explained using an extended version of RKKY

[1]Some authors calculate the magnetoresistance ratio using $\Delta\rho/\rho=(\rho(H)-\rho(0))/\rho(H)$, rather than $\Delta\rho/\rho=(\rho(H)-\rho(0))/\rho(0)$ as done here. This method allows values of >100% to be reported.

exchange coupling[10]. If neighbouring magnetic layers are aligned antiferromagnetically, the resistance of the material is large, since both spin-up and spin-down electrons will be scattered as they pass through the layers. When a magnetic field is applied to the material, magnetizing all layers along the field direction, an abrupt decrease in the resistivity occurs, since only one spin channel is scattered substantially in this configuration. The magnitude of the magnetoresistance depends not only on the ordering of the layers and the coupling between the layers but also depends in a complicated manner on the roughness of the interface between the layers—since the layers are only on the order of 10–100 Å thick, interfaces constitute a non-negligible fraction of the volume. This complicates the analysis of the mechanics of the scattering[10].

Manganese perovskites, with general formula $A_xB_{1-x}MnO_3$ (A=La, rare earth, B= Ca, Mg, Pb etc.) also show giant magnetoresistance[130]. These materials have field induced metal-insulator transitions, and can exhibit changes in resistance as high as 1000% within this region. The magnetic structure in these compounds can be very complicated, causing a cascade of transitions to occur as a function of applied field. This results in very complicated relationships between the magnetisation and magnetoresistance.

Some intermetallic compounds have a naturally layered magnetic structure, exhibiting both antiferromagnetic and ferromagnetic ordering as a function of temperature, combined with metamagnetic behaviour, in which the transition to the antiferromagnetic state is suppressed by an applied magnetic field. Large magnetoresistances are observed in a number of these materials, particularly in the region of the metamagnetic transition. These materials are particularly interesting since they are naturally layered, and thus are quickly and easily prepared and have no interface scattering effects to complicate the analysis of the results. The present study focuses on the magnetoresistance and the magnetisation near the metamagnetic transition in two such layered materials: doped $CeFe_2$ and Gd_2In. An attempt is made to correlate the behaviour of these two properties in the vicinity of this transition, an important step in the understanding of the GMR phenomenon in these

compounds as well as multilayer and perovskite systems.

$CeFe_2$ is a cubic Laves phase compound which orders ferromagnetically at low temperature. This compound is interesting due to its low critical temperature of 237K and low moment per Fe atom of $1.2\mu_B$–strikingly smaller than those for other RFe_2 (R=rare earth) compounds[131]. This, as well as the presence of a small anomaly in the low temperature *ac* susceptibility[132] suggests an instability in the ferromagnetic structure of $CeFe_2$. Indeed, neutron diffraction measurements[133] have shown the presence of some canting in the spin structure at low temperature, indicating a tendency towards antiferromagnetic ordering. Neutron diffraction studies also indicate the existence of a small moment at the Ce site, aligned antiferromagnetically with the Fe moment. Band structure calculations suggest that the small Fe moment is the result of the hybridisation of the Ce $4f$ electrons with the Fe $3d$ electrons[134]. This is supported by the abnormally large value of the specific heat coefficient γ (approximately four times larger than that for YFe_2[135]), typical of systems with such hybridisation. Neutron diffraction analysis based on these band structure calculations gave a moment per Fe atom of $1.1(3)\mu_B$, in excellent agreement with the measured moment[133]. The presence of hybridisation suggests that the magnetic structure may be strongly dependent on the occupancy of the Fe site. Substitution of other transition metals at the Fe site is found to destabilize the ferromagnetic state, in some cases completely destroying the ferromagnetism. A large number of these doped compounds have been studied, with general composition $Ce(Fe_{1-x}M_x)_2$, and M=Co, Pd, Ru, Rh, and Al, for example. The addition of Co, Al and Ru has been shown to destabilize the lattice, suppressing T_c and destroying ferromagnetism at low temperature.

Neutron diffraction studies of $Ce(Fe,Co)_2$, with less than 30% Co substitution, indicate a transition from ferromagnetic to antiferromagnetic ordering at low temperature, accompanied by a rhombohedral distortion of the crystal lattice[136, 137, 138]. Alloys with more than 30 percent cobalt substituted in the iron sites remain ferromagnetic down to helium temperatures. No moment was detected at the cerium sites in any of these alloys. Neutron diffraction and Mössbauer measurements[139]

for those compounds with less than 30% Co substitution show a continuous reorientation of the moments from the [100] direction in the ferromagnetic state to the [111] direction in the antiferromagnetic state. The antiferromagnetic state consists of layers of ferromagnetically aligned Fe spins in (111)-type planes, with antiferromagnetic coupling between adjacent layers. In the transition region between these two states, competition between the ferromagnetic and antiferromagnetic components results in a canted spin arrangement. T_c and T_N are indicated by anomalies in specific heat[135] and resistivity[140] measurements. The resistivity measurements show a change in slope at T_c, as expected at a paramagnetic to ferromagnetic transition. At T_N the resistivity rises sharply as antiferromagnetic ordering sets in, reminiscent of the effects of superzone boundaries in antiferromagnetically ordered rare earths (section 2.2.2)[38, 39]. On cooling, the magnetisation and *ac* susceptibility increase abruptly at T_c followed by a rapid decrease at T_N, with T_N dramatically suppressed by the application of large magnetic fields[140]. Sufficiently large applied fields pull the layers from antiparallel to parallel arrangements, producing a sudden increase in M(H) as the system becomes ferromagnetic. As the temperature is increased toward T_N, the field, H_m, required to drive this metamagnetic transition drops monotonically to zero.

$Ce(Fe_{1-x}Al_x)_2$ alloys also show the presence of an antiferromagnetic phase at low temperature. Neutron diffraction studies[138] indicate that the transition to the antiferromagnetic state consists of a continuous spin reorientation, with competition between ferromagnetic and antiferromagnetic components leading to a gradual transition. The coexistence of ferromagnetic and antiferromagnetic components extends over a much larger temperature range in the aluminum-doped alloys than for the cobalt-doped alloys. Substitutions of x=0.01 and 0.02 Al do not result in the complete suppression of ferromagnetism at low temperature[138]. With x=0.035 Al, the two competing states coexist for almost 70K, with the system becoming antiferromagnetically ordered below 50K[138, 141]. Detailed magnetisation and transport measurements have been done by Radha et al.[143] on $Ce(Fe_{0.92}Al_{0.08})_2$, showing that the ferromagnetic and antiferromagnetic transitions are so close that the fer-

romagnetic state is barely established before the onset of antiferromagnetism, in agreement with neutron diffraction results[138]. The proximity of the two transitions results in cusp-like M(T) and χ(T) curves. Alloys with more than 8% Al in the Fe sites have a direct transition from a paramagnetic high temperature state to an antiferromagnetic ground state[138, 139]. Measurements of M(H), the field dependence of the magnetisation, at fixed temperatures in a number of samples[141, 143] show that the field, H_m, necessary to induce the transition to the ferromagnetic state decreases almost linearly as the temperature increases to T_N. In addition, measurements by Radha et al.[143] on x=0.08 Al indicate the presence of a large (up to 10%) magnetoresistance in the temperature region (80–150K) in which the FM and AFM regimes overlap. At high temperature ($T>T_N$) the magnetoresistance decreases, with the resistivity showing only a small negative field dependence consistent with the reduction of spin-disorder scattering due to field induced spin alignment in a slightly disordered ferromagnet.

Detailed measurements have also been done on Ru-doped $CeFe_2$. Studies by Roy and Coles[12] show that samples with x=0.01 and 0.033 Ru substitution do not have well-developed antiferromagnetic ground states, but those with higher Ru concentrations (up to around x=0.08) have a ferromagnetic regime followed by a transition to a low temperature antiferromagnetic regime. Compounds with x >0.08 show behaviour similar to that of the x =0.08 Al sample with strong overlap of the regimes, and thus a loss of ferromagnetic character as the Ru composition increases. Figure 7.1 shows a phase diagram of the Ru doped system as deduced from a number of studies.

Temperature dependent resistivity measurements[12] for samples in the intermediate concentration range, $0.033 \leq x \leq 0.08$, show a change in slope at the temperature of the paramagnetic-ferromagnetic transition. At lower temperatures, the resistivity rises sharply to a peak and then decreases once again, the now-familiar behaviour at a transition to an antiferromagnetic state. Detailed linear and non-linear *ac* susceptibility measurements by Wang et al.[11], on samples with x=0.07 and 0.08 determined critical temperatures in good agreement with those measured

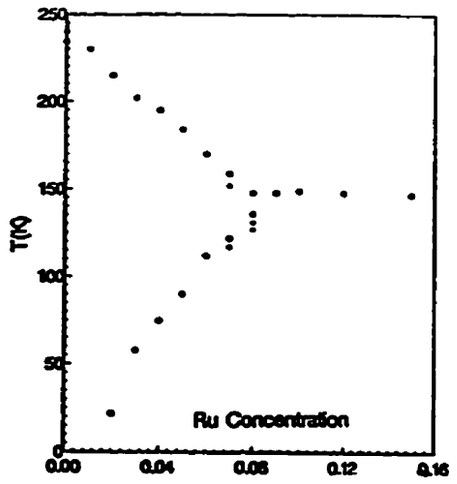

Figure 7.1: Phase diagram of the $Ce(Fe_{1-x}Ru_x)_2$ system [71].

previously by Roy and Coles. The zero field susceptibility increases rapidly as the temperature decreases towards T_c , and then drops sharply back to zero as the temperature is lowered further through T_N. The existence of a peak in the non-linear susceptibility near the lower transition at 115K in the x=0.07 sample and a possible peak at 124K in the x=0.08 sample, are characteristic of peaks found at the lower transition of reentrant spin-glass systems, suggesting a similarity in the dynamics of these transitions. Detailed measurements of the field and temperature dependent resistivity and magnetisation, as done for the Al-doped samples, are needed for these samples to determine the behaviour of these features in the region of the metamagnetic transition,and to search for the presence of a giant magnetoresistance.

Gd_2In, another layered intermetallic, has a more complex magnetic structure than the doped $CeFe_2$. The hexagonal cell (symmetry $6_3/mmc$) consists of a layered ABACA structure stacked along the c axis as shown in figure 7.2[64, 144]. The A layers consist of only Gd atoms placed at the cell corners. The crystallographically inequivalent B and C layers each contain one Gd and one In atom located inside the unit cell. The Gd moments in different layers are located in different environments, a much more complicated situation than in doped $CeFe_2$, in which all Fe atoms lie in identical sheets.

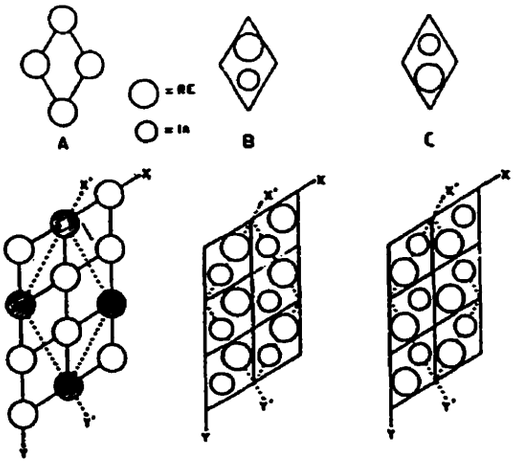

Figure 7.2: Layered crystal structure of Gd_2In, from [144].

Published magnetisation[64, 145, 146, 147] and resistivity [64] data are very similar to those seen in the doped $CeFe_2$, and indicate that this system also undergoes two magnetic phase transitions. At high temperature the system is paramagnetic with ferromagnetism developing as the temperature is lowered through 190K. At ~100K, Gd_2In undergoes a further transition to a low temperature state, the structure of which is currently unknown. The low temperature transition is identified by a sudden drop in magnetisation and by a sudden increase in the zero field resistivity as the temperature is lowered to below 100K. The *ac* susceptibility also drops in this temperature regime (although not to zero) as observed in the $CeFe_2$. The application of a small magnetic field suppresses this transition to lower temperatures, while a moderately large field can completely remove the low temperature state, indicating that the low temperature state is metamagnetic[64, 145, 146, 147]. Although the magnetic structure of the doped $CeFe_2$ compounds is well known, there continues to be some disagreement as to the structure of the two low temperature states in Gd_2In. Neutron scattering experiments to ascertain the magnetic structure for Gd_2In have not been done, due to the large absorption cross-section of Gd for thermal neutrons. Certain conclusions can however be made based on the crystal structure and other arguments. Mössbauer spectroscopy of ^{119}Sn substituted at

the In sites[148] was interpreted as showing ferromagnetic coupling in *both* the low temperature regimes. Tm_2In, crystallographically equivalent to Gd_2In, is known to be ferromagnetic at low temperature, with all the Tm moments lying in the basal plane, which suggests a similar ferromagnetic state in Gd_2In [64]. However, low field magnetisation measurements in Gd_2In show a low-field limited slope, which Jee et al.[147] interpret as indicating a spiral magnetic structure as found in MnSi[149] for the intermediate temperature phase, rather than the simple Tm_2In structure. The decrease in magnetisation at 100K suggests a loss of ferromagnetism, indicating that the low temperature state has at least partial antiferromagnetic coupling. The simplest structure possible is one similar to doped $CeFe_2$, i.e. ferromagnetic intra-planar coupling with antiferromagnetic interplanar coupling. Since the Gd moments in different layers have different environments, this structure would result in a ferri-magnetic rather than an antiferromagnetic state[64]. McAlister's measurements of the low temperature magnetisation of Sm_2In[150], a ferrimagnetic compound with exactly the same crystal structure as Gd_2In, show a very different temperature dependence of the magnetisation than that measured in Gd_2In[64], suggesting that Gd_2In does *not* have this simple structure. McAlister suggested instead a spiral antiferromagnetic structure[64], with the Gd moments lying in or out of the basal plane. The detailed magnetisation and magnetoresistive data taken in this study will be compared with those of $Ce(Fe_{1-x}Ru_x)_2$, for which the magnetic structure is known, in the hope that information about the magnetic ordering in Gd_2In can be gained.

7.2 $Ce(Fe_{1-x}Ru_x)_2$, x=0.07, 0.08

Magnetic and transport measurements were taken on the $Ce(Fe_{0.93}Ru_{0.07})_2$ and $Ce(Fe_{0.92}Ru_{0.08})_2$ samples used in a previous *ac* susceptibility study by Wang et al[11]. For convenience these samples will be referred to within this section as simply 7% and 8%, respectively. Magnetisation and magnetoresistance measurements were performed with the biasing field applied along the longest sample dimension in all

cases. The use of the same sample in both magnetisation and magnetoresistance measurements means that, at a given external field, H_a, the internal field will be the same in both sets of data. Magnetoresistance measurements were done in the high-field cryostat described in section 3.2.4. Magnetisation measurements were taken with the SQUID magnetometer (Section 3.4), using a 64 step, 4 cm scan. Due to the large magnetisation of these samples, attempts to decrease the step number caused the SQUID to unlock because of the resulting high slew rate.

7.2.1 Resistivity and Magnetoresistance

Figures 7.3 and 7.4 show the temperature dependence of the zero field resistivities of the 7% and 8% samples respectively. In both cases the general features of the resistivity agree well with those measured previously by Roy and Coles on pieces cut from the same sample[12]. The absolute values of the resistivities are, however, lower than those found by Roy and Coles, likely due to the annealing procedure followed by Wang et al.[11], as described earlier (section 3.1.1). The transition from paramagnetism to ferromagnetism is indicated by a change in slope of the resistivity at T_c . A sudden rise in resistivity at a lower temperature indicates the onset of antiferromagnetism. For the 7% sample, the temperature derivative of ρ(T) near T_c has a peak at 155±2K, in good agreement with the T_c of 152±1.5K estimated from susceptibility measurements. The zero field *ac* susceptibility measured by Wang et al.[11] has been superimposed on the resistivity data to provide a direct comparison of the agreement between the two measurements. The vertical arrows in the figures indicate the values of T_c and T_N derived from the susceptibility data. The onset of the sharp increase in resistivity occurs at approximately 116K, close to the temperature (112–115K) at which a peak in the non-linear susceptibility was observed[11]. Estimates of the transition temperatures, T_c and T_N, from the same features in the 8% sample are (131±1)K and (126±2)K, in good agreement with the susceptibility estimates of (131.3±1.3)K and 123–124K, respectively. In the 7% sample, the low temperature resistivity anomaly stretches over 10K, whereas in the 8% sample, the resistivity rises over an interval of only 6K. This difference

in transition width could indicate that the ferromagnetic state in the 7% sample is more stable than in the 8%, likely due to the proximity of T_c and T_N in the 8% compound–ferromagnetic order is barely established before the onset of antiferromagnetism. The application of a static biasing field of 72 kOe has similar effects on the resistivity in both samples (lower curves in figures 7.3 and 7.4). The temperature of the lower transition is greatly suppressed–by 38K in the 7% sample and by 15K in the 8%. At temperatures below this transition, a slight positive magnetoresistance is observed, consistent with that expected due to the Lorentz force. A large negative magnetoresistance is exhibited in the region of the anomaly in the zero field resistivity and persists well into the ferromagnetic regime. The magnetoresistance in the ferromagnetic regime amounts to 2.2% in the 7% sample and as much as 5% in the 8% sample. This negative MR is due to a decrease in spin-disorder scattering caused by the ordering of magnetic moments by the applied field, and persists up to the highest measuring temperature ($\sim$ 200K) attainable in this cryostat with the superconducting magnet in persistent mode at full field.

The magnetoresistance was measured at a number of fixed temperatures between 1.5 and 150K in fields of up to 84 kOe. Several of these curves, for temperatures in the vicinity of T_N, are summarised in figures 7.5 and 7.6, for the 7% and 8% samples respectively. The trends in both samples are the same. Above the Néel temperature (figure 7.6(a), for example) a small, negative magnetoresistance exists, consistent with the field induced reduction of thermal magnons (i.e. the reduction of spin-disorder scattering). Well below T_N (figure 7.6(g)) the resistivity goes through an initial plateau region, before dropping sharply at the metamagnetic field (the field necessary to induce the transition to ferromagnetism), and saturating at high field. The magnetoresistance is largest (as much as 20%) in the vicinity of the peak in the zero field resistivity. As the temperature is decreased below T_N, the metamagnetic field becomes larger, until at low temperature the transition can not be driven by the largest available field. This behaviour will be discussed in more detail later.

The presence of considerable hysteresis was observed in the magnetoresistance of both samples, as was noticed previously in the Al-doped $CeFe_2$[143]. Figure

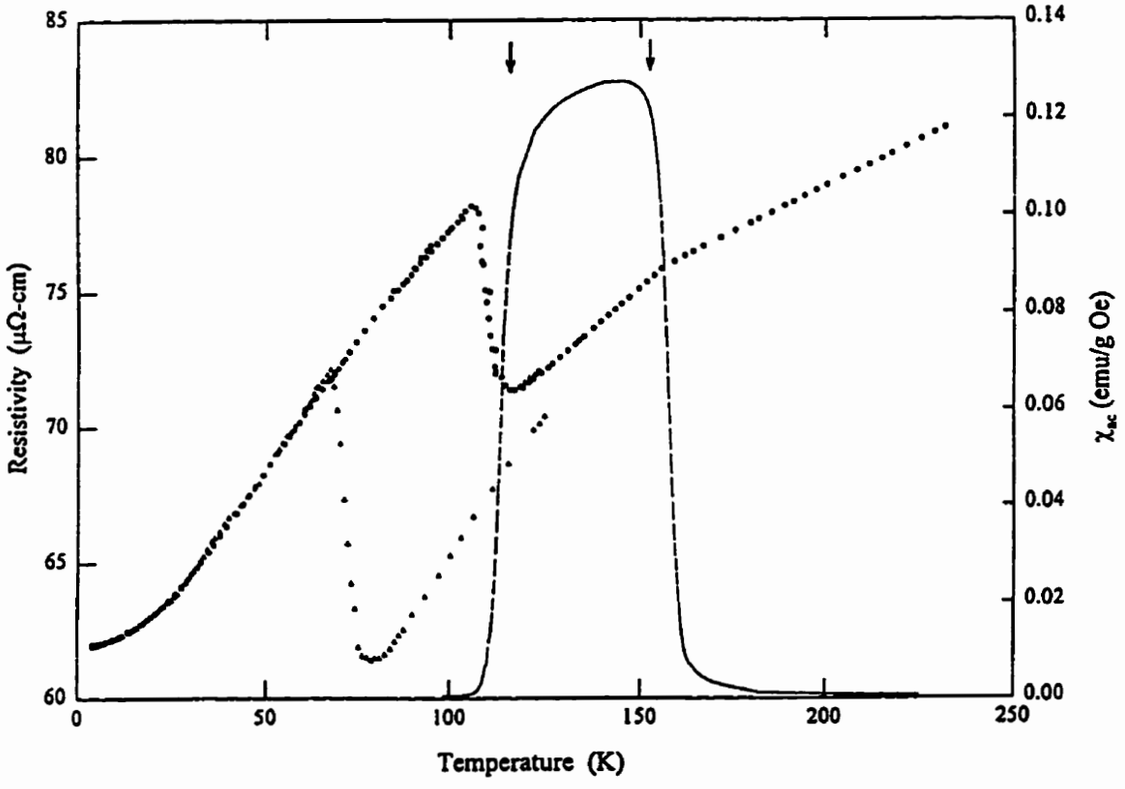

Figure 7.3: The resistivity of $Ce(Fe_{0.93}Ru_{0.07})_2$ as a function of temperature in zero applied field (upper curve) and in a static biasing field of 72 kOe (lower curve). The superimposed dashed curve is the true *ac* susceptibility in zero field[11], with the vertical arrows indicating the transition temperatures found from the susceptibility analysis.

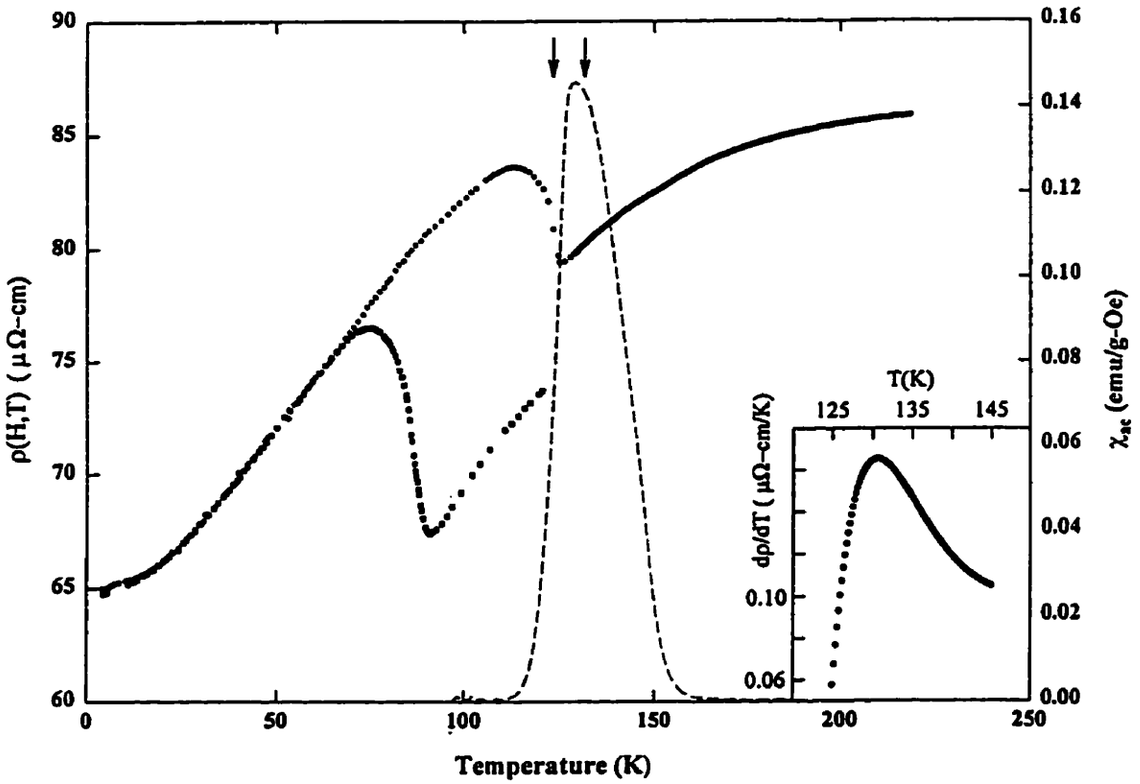

Figure 7.4: The resistivity of $Ce(Fe_{0.92}Ru_{0.08})_2$ as a function of temperature in zero applied field (upper curve) and in a static biasing field of 72 kOe (lower curve). The superimposed dashed curve is the experimental *ac* susceptibility is zero field[11], with the vertical arrows indicating the transition temperatures found from the susceptibility analysis.

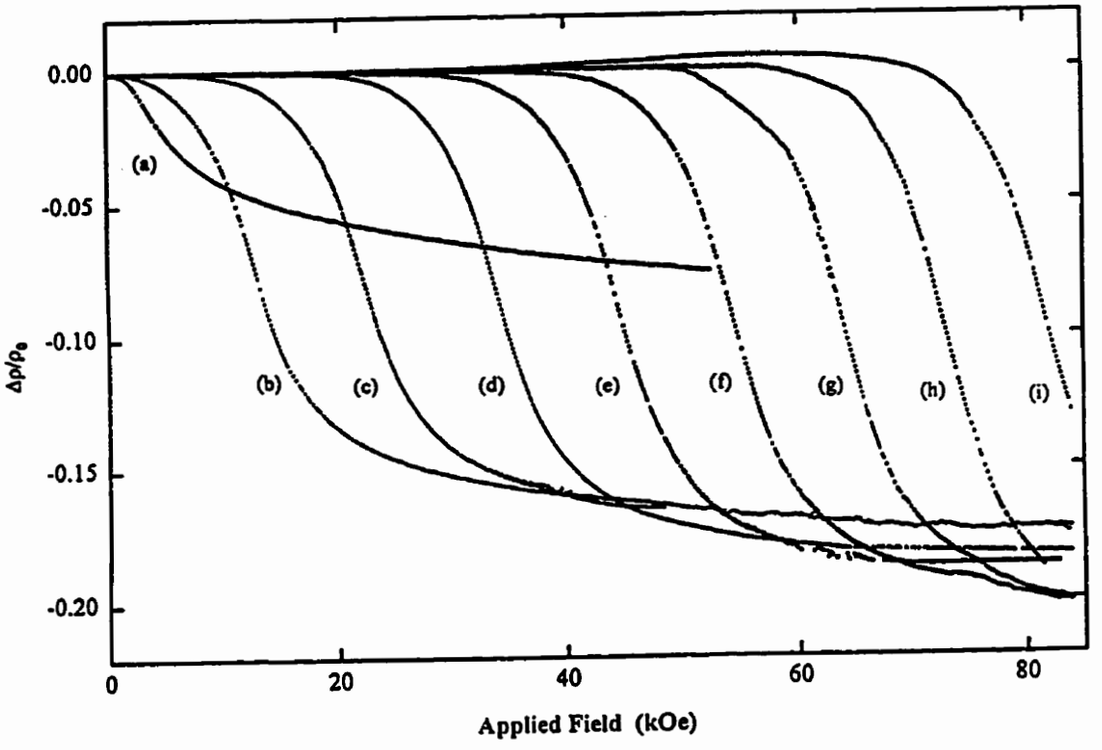

Figure 7.5: The magnetoresistance of $Ce(Fe_{0.93}Ru_{0.07})_2$, expressed as the ratio $\Delta\rho/\rho_0$, at a number of fixed temperatures; (a) 114.1K, (b) 107.5 K, (c) 101.7 K, (d) 95.3 K, (e) 90.6 K, (f) 84.0 K, (g) 78.2 K, (h) 72.6 K, and (i) 67.0 K.

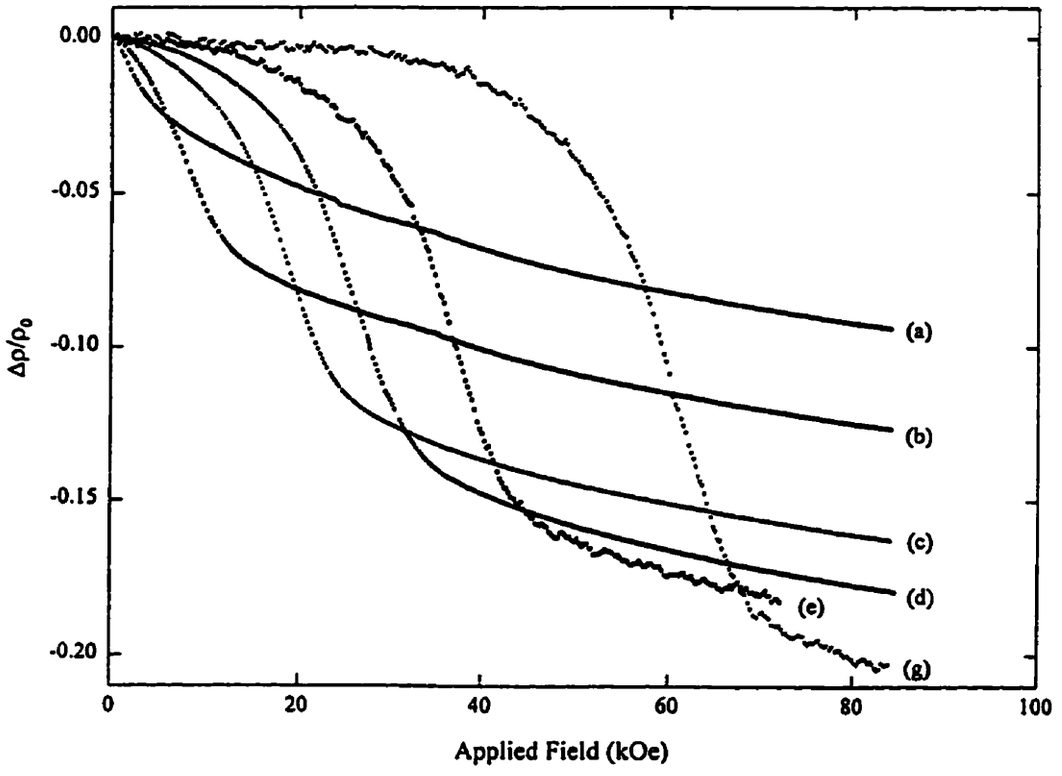

Figure 7.6: The magnetoresistance of $Ce(Fe_{0.92}Ru_{0.08})_2$, expressed as the ratio $\Delta\rho/\rho_0$, at a number of fixed temperatures;(a) 129.2 K, (b) 125.8 K, (c) 120.6 K, (d) 117.3 K, (e) 110.9 K and (g) 98.5 K.

7.7 shows a typical magnetoresistance loop for the 7% sample, measured first in increasing and then decreasing field. The loops for the 8% sample are similar, and are not shown here. Two types of data were extracted from these hysteresis loops: the dependence of the onset field for hysteresis with temperature, $H_{hys}(T)$, and the temperature dependence of the maximum loop width, $\Delta H_{hys}(T)$. A summary of these data for the two samples are plotted in figures 7.8 and 7.9. In both samples $H_{hys}(T)$ and $\Delta H_{hys}(T)$ decrease as the temperature approaches T_N from below. The onset of hysteresis occurs at zero field for temperatures above 108K in the 7% sample and above 117K in the 8% sample, slightly lower than their Néel temperatures of 112–115K and 124K respectively, as determined from *ac* susceptibility measurements[11]. The hysteresis itself, $\Delta H_{hys}(T)$, does not vanish completely until slightly above T_N. The flattening in $\Delta H_{hys}(T)$ observed at low temperature is likely caused by the inability of the highest applied field to saturate the magnetoresistance.

7.2.2 Magnetisation

The field dependence of the magnetisation was measured in fields of up to 55 kOe at fixed temperatures from 2 to 200K. M(H) curves in $Ce(Fe_{1-x}Ru_x)_2$ and $Ce(Fe_{0.92}Ru_{0.08})_2$ are shown in figures 7.10 and 7.11 at a number of fixed temperatures near T_N. After a sharp initial increase, the reason for which is not fully understood, the low temperature M(H) curves (67.0 K, the lowest temperature curve in figure 7.10, for example), exhibit a low field plateau region with essentially zero slope. When the applied field reaches the metamagnetic field, the magnetisation again rises sharply as the system becomes ferromagnetic. At high field, the magnetisation levels off, but does not saturate to the highest available measuring field. As the temperature increases toward T_N, the field required to induce the metamagnetic transition decreases monotonically. At temperatures above T_N, the magnetisation has a large low-field slope but flattens out at higher field. In this ferromagnetic regime the magnetisation does not saturate to the highest measuring field, however extrapolation of the magnetisation at these temperatures to $1/H=0$ (i.e. $H=\infty$) can be done to estimate the saturation moment in these samples. This

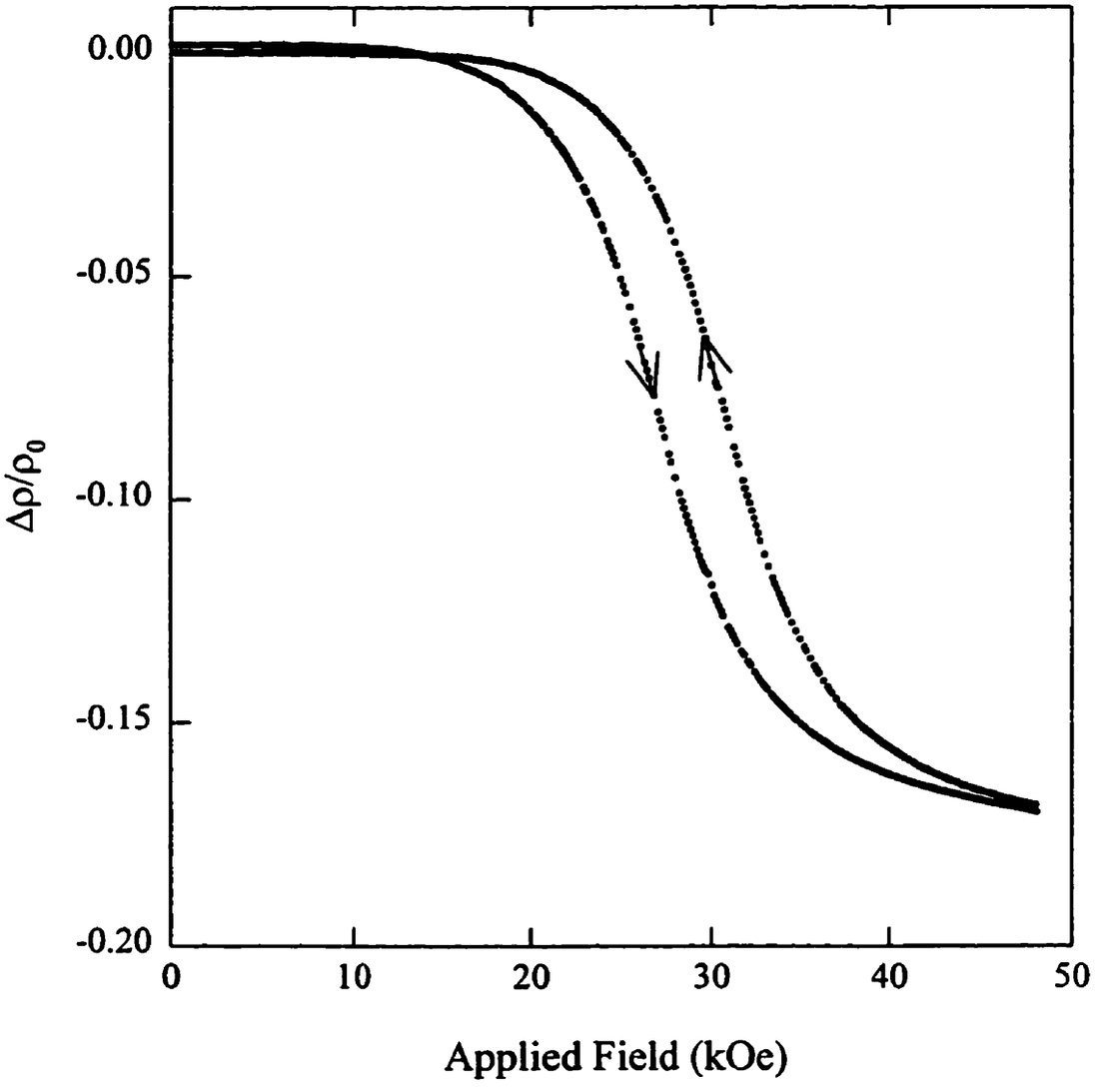

Figure 7.7: The magnetoresistance of $Ce(Fe_{0.93}Ru_{0.07})_2$,at a fixed temperature of 78.2 K, measured in increasing followed by decreasing field, with the path of the loop indicated by the arrows.

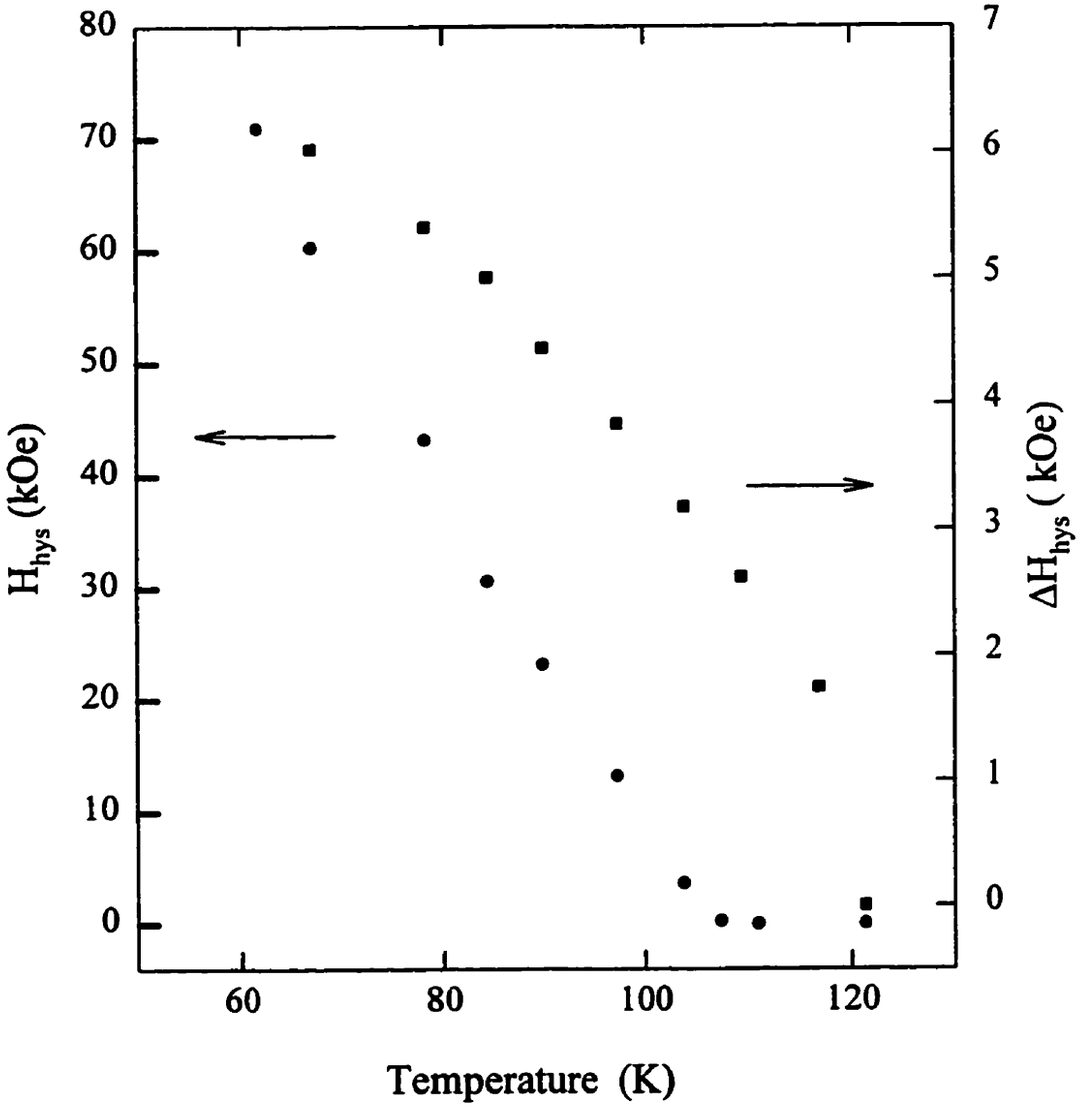

Figure 7.8: The temperature dependence of the onset field for hysteresis, $H_{hys}(T)$, and the width of the hysteresis loop, $\Delta H_{hys}(T)$, in $Ce(Fe_{0.93}Ru_{0.07})_2$.

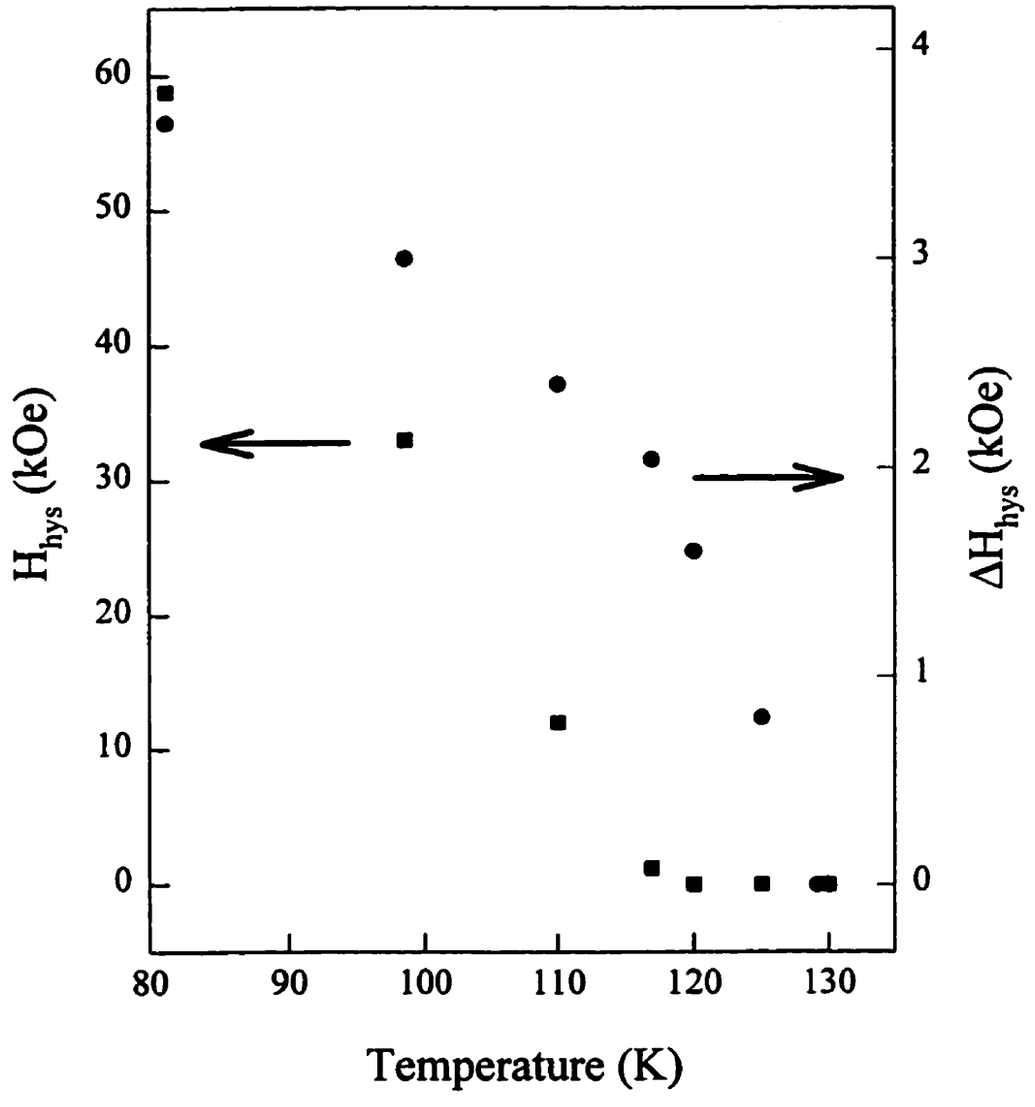

Figure 7.9: The temperature dependence of the onset field for hysteresis, $H_{hys}(T)$, and the width of the hysteresis loop, $\Delta H_{hys}(T)$, in $Ce(Fe_{0.92}Ru_{0.08})_2$.

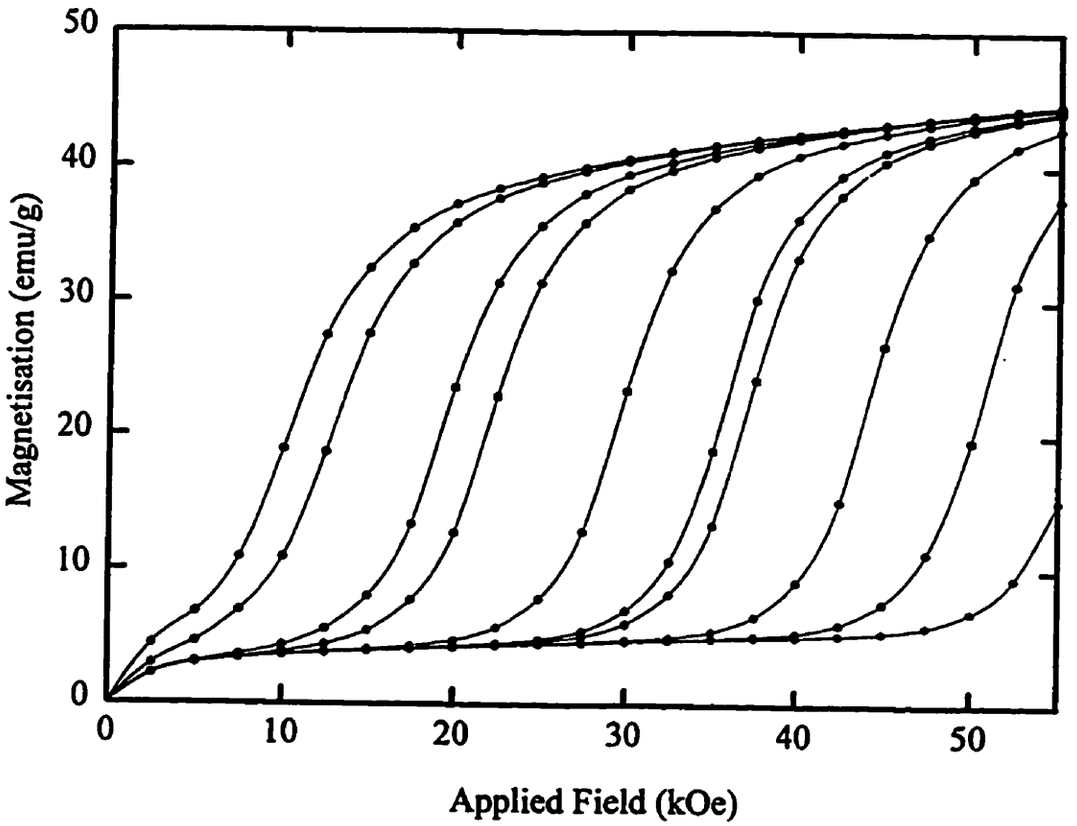

Figure 7.10: The magnetisation of $Ce(Fe_{0.93}Ru_{0.07})_2$ at a number of fixed temperatures. from left to right: 103.8 K, 101.7 K, 97.2 K, 95.3 K, 89.7 K, 85.2 K, 83.9 K, 78.2 K, 72.6 K and 67.0 K.

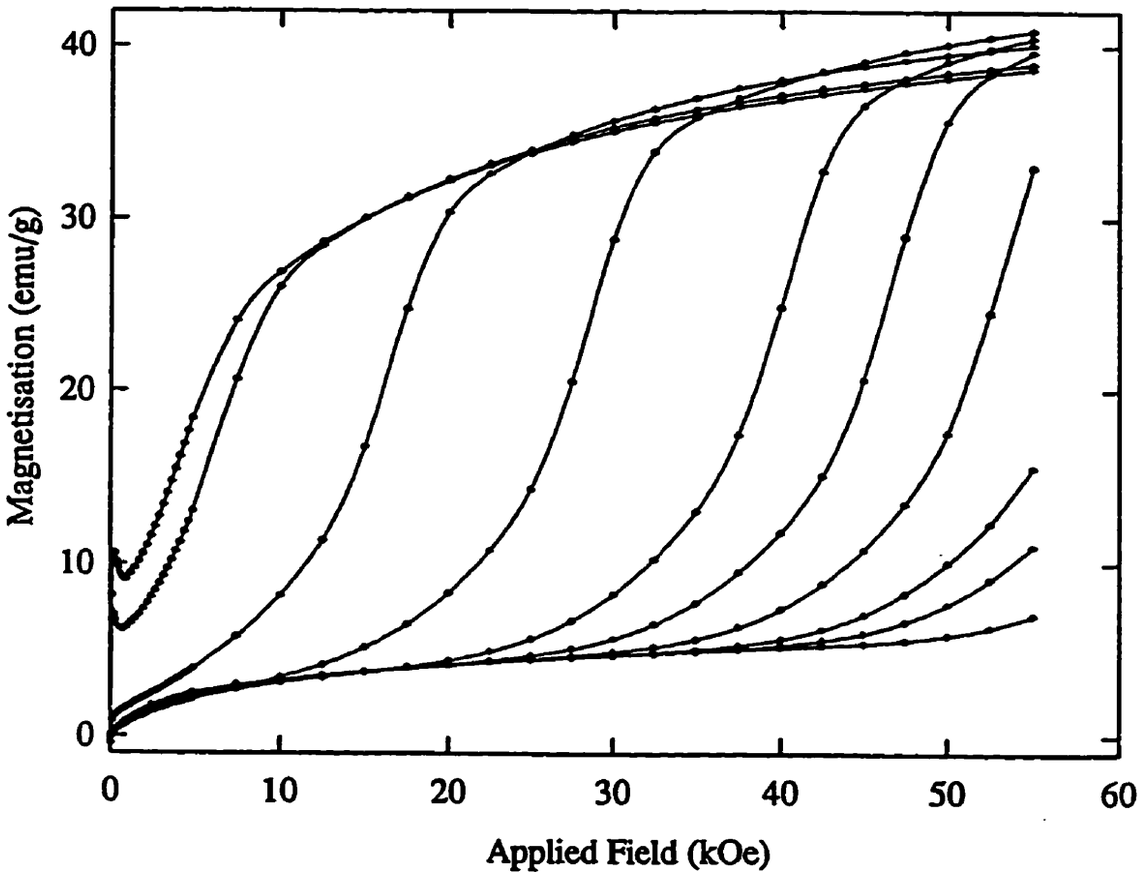

Figure 7.11: The magnetisation of $Ce(Fe_{0.92}Ru_{0.08})_2$ at a number of fixed temperatures, from left to right: 123.0 K, 121.5 K, 114.0 K, 105.0 K, 96.2 K, 91.2 K, 86.2 K and 81.2 K.

technique yields a moment per formula unit of $2.25\mu_B$ for the 7% and $2.1\mu_B$ in the 8% sample, both lower than the $2.4\mu_B$ per formula unit measured for the parent compound. This result supports the existence of a destabilizing influence of the dopant on the $CeFe_2$ ferromagnetic state.

An interesting feature of the magnetisation is the anomalous behaviour at very low fields within the antiferromagnetic regime. As shown in figure 7.12 for the 7% sample, the magnetisation has a high initial slope, then flattens out to a plateau before once again increasing sharply at H_m. This behaviour is also evident in the low field magnetisation of $Ce(Fe_{0.92}Al_{0.08})_2$ [143], and $Ce(Fe_{0.80}Co_{0.20})_2$[140]. Radha et al. suggest that the large low field slope may be due to the presence of a slight impurity phase in the Al doped sample. X-ray diffraction measurements on the Ru samples[12] show no presence of an impurity phase, however, suggesting that this behaviour may be due to some aspect of the antiferromagnetic ordering.

7.2.3 Temperature Dependence of the Metamagnetic Field

Both the magnetisation and magnetoresistance data show the presence of a metamagnetic transition induced by large applied fields. Radha et al. determined the dependence of the metamagnetic field on temperature for $Ce(Fe_{0.92}Al_{0.08})_2$ [143], estimating H_m from the field at which the magnetoresistance first becomes negative, or the field at which the magnetisation begins to increase sharply above the plateau region. This description is somewhat qualitative. A more quantitative method would be to take as the metamagnetic field, the field at which the magnetisation or magnetoresistance data has the largest slope. To determine this, the magnetisation and magnetoresistance data (in the form of $\Delta\rho/\rho_0$) were fit using a routine which selects the best fit from a base of some 3000 equations. The resulting functions were differentiated with respect to field, and plotted in figures 7.13 and 7.14 for the 7 and 8% samples. These curves show distinct peaks from which the metamagnetic field can be found. The derivatives in figures 7.13 and 7.14 indicate that the magnitude of the maximum slope of the magnetoresistance and magnetisation curves is constant below T_N, dropping off rapidly in the ferromagnetic regime in

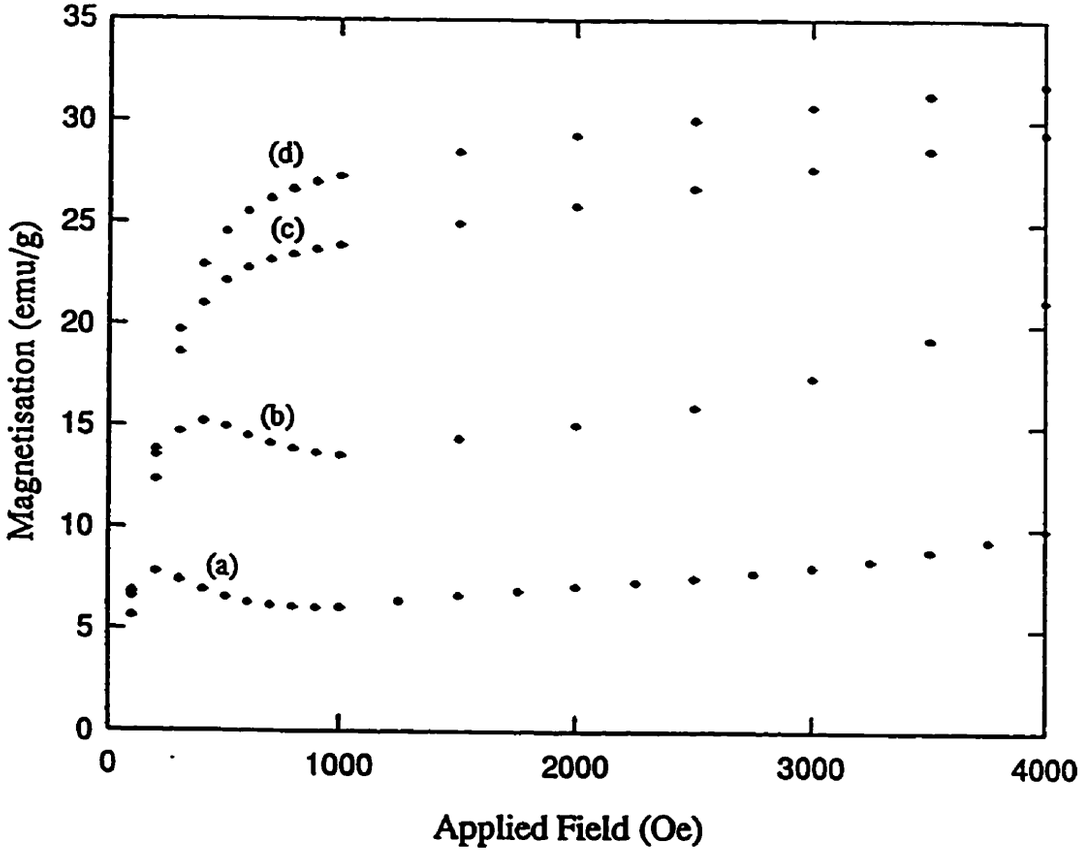

Figure 7.12: The low field magnetisation of $Ce(Fe_{0.93}Ru_{0.07})_2$ at a number of fixed temperatures around the metamagnetic transition, $T_N \simeq 115K$.;(a) 109.0 K, (b) 111.0 K, (c) 114.0 K and (d) 116.8 K: note the disappearance of the low field anomaly above T_N.

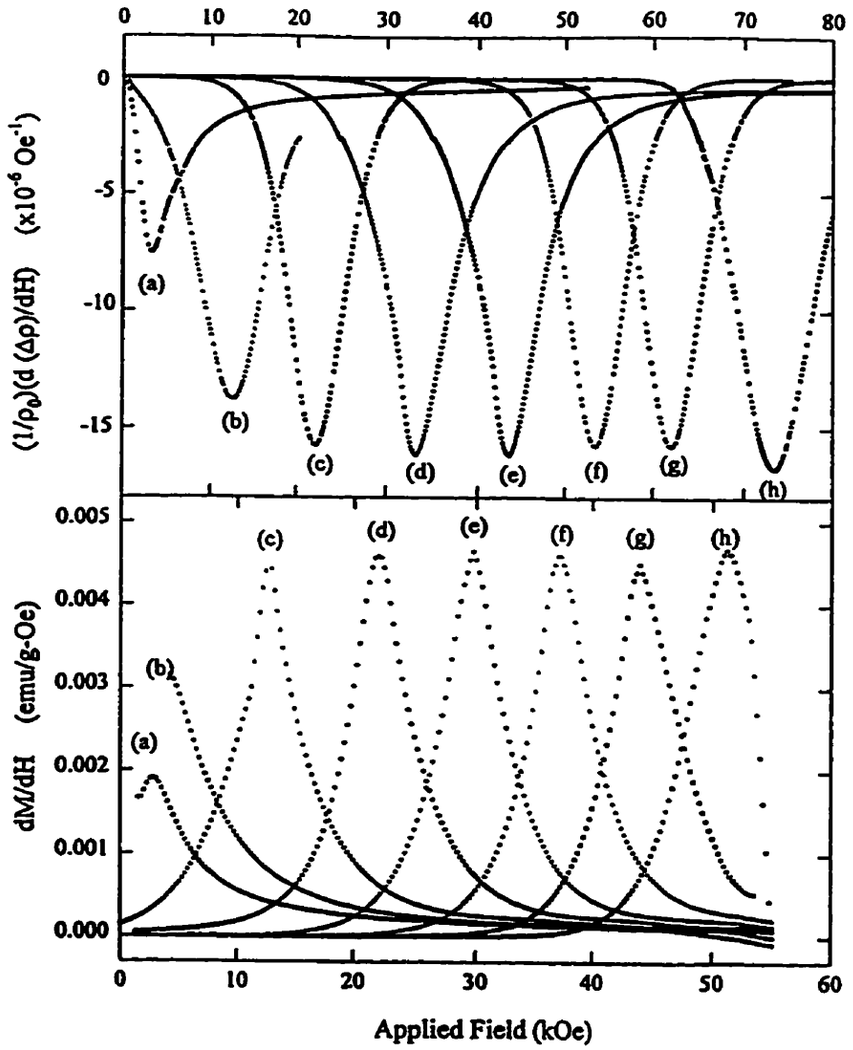

Figure 7.13: The derivatives (upper) $1/\rho_0(d\Delta\rho/dH)$ at a number of fixed temperatures: (a) 114.1 K, (b) 107.5 K, (c) 101.7 K, (d) 95.3 K, (e) 90.6 K, (f) 84.0 K, (g) 78.2 K and (h) 72.6 K; and (lower) dM/dH at a number of fixed temperatures: (a) 114.1 K, (b) 107.5 K, (c) 101.7 K, (d) 95.3 K, (e) 89.7 K, (f) 83.9 K, (g) 78.2 K and (h) 72.6 K $Ce(Fe_{0.93}Ru_{0.07})_2$.

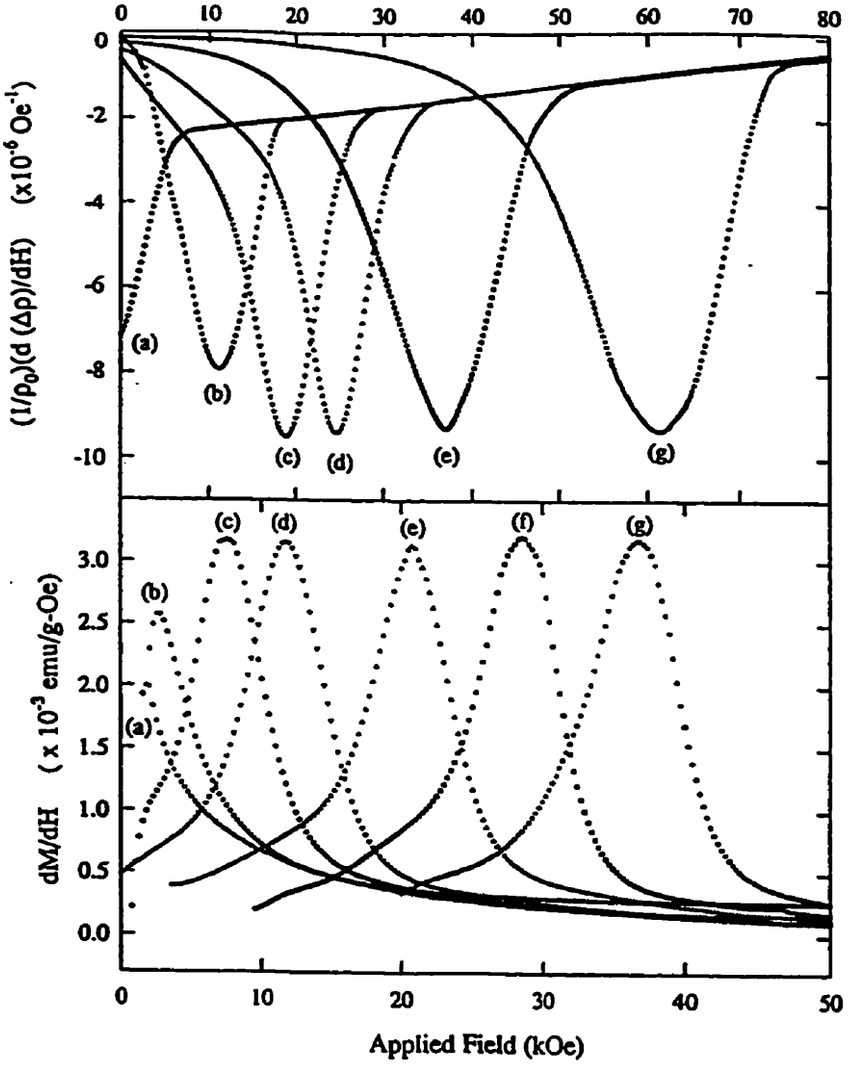

Figure 7.14: The derivatives (upper) $1/\rho_0(d\Delta\rho/dH)$ at temperatures of: (a) 129.2 K, (b) 124.5 K, (c) 120.6 K, (d) 117.3 K, (e) 110.9 K and (g) 98.5 K.and (lower) dM/dH at temperatures of ;(a) 129.2 K, (b) 125.8 K, (c) 120.5 K, (d) 117.3 K, (e) 110.8 K, (f) 105.0 K and (g) 98.9 K for $Ce(Fe_{0.92}Ru_{0.08})_2$.

Table 7.1: Fitting Parameters for H_m versus T Phase Diagrams in $Ce(Fe_{1-x}Ru_x)_2$

	$Ce(Fe_{0.93}Ru_{0.07})_2$		$Ce(Fe_{0.92}Ru_{0.08})_2$	
Estimate type	a(kOe/K)	T_N(K)	a(kOe/K)	T_N(K)
MR onset	1.6	115	1.7	120
MR derivative	1.7	115	2.2	129
MG onset	1.1	107	1.3	125
MG derivative	1.3	112	1.5	127

MR=magnetoresistance; MG=magnetisation

both samples. It is also apparent that at any given temperature, the magnetisation data yield considerably lower metamagnetic fields than the corresponding magnetoresistance data. This behaviour is reflected in the H_m versus T phase diagrams for the two samples (figures 7.15 and 7.16). Not only is there a difference between the estimates of H_m obtained via the two methods described above (i.e. using the onset field and the derivative), but there is a large difference between the metamagnetic fields found from the magnetisation and magnetoresistance data. The H_m versus T curves are all roughly linear, with some curvature evident in the magnetoresistance data in the 7% sample and in the magnetisation data in the 8% sample. When fit to a linear temperature dependence, $H_m = a(T_N - T)$, best fit slopes of 1.1–1.7 kOe/K are found for the 7% sample and 1.3–2.2 kOe/K for the 8% samples. These are larger than the estimates of 0.9 kOe/K in $Ce(Fe_{0.92}Al_{0.08})_2$[143], and similar to the 1.6 kOe/K found for $Ce(Fe_{0.80}Co_{0.20})_2$ [140]. These linear fits can also be used to give estimates for T_N, as tabulated in Table 7.1. For the 7% sample the H_m(T) curves deduced from the position of maximum slope in the magnetoresistance give values for T_N close to those found from susceptibility and zero field resistivity measurements, whereas the magnetisation results are further off. This suggests that magnetoresistance may be a more sensitive probe of internal structure than magnetisation measurements. The 8% data shows considerably more scatter than the 7% data, likely a consequence of the proximity of T_N and T_c in the former material.

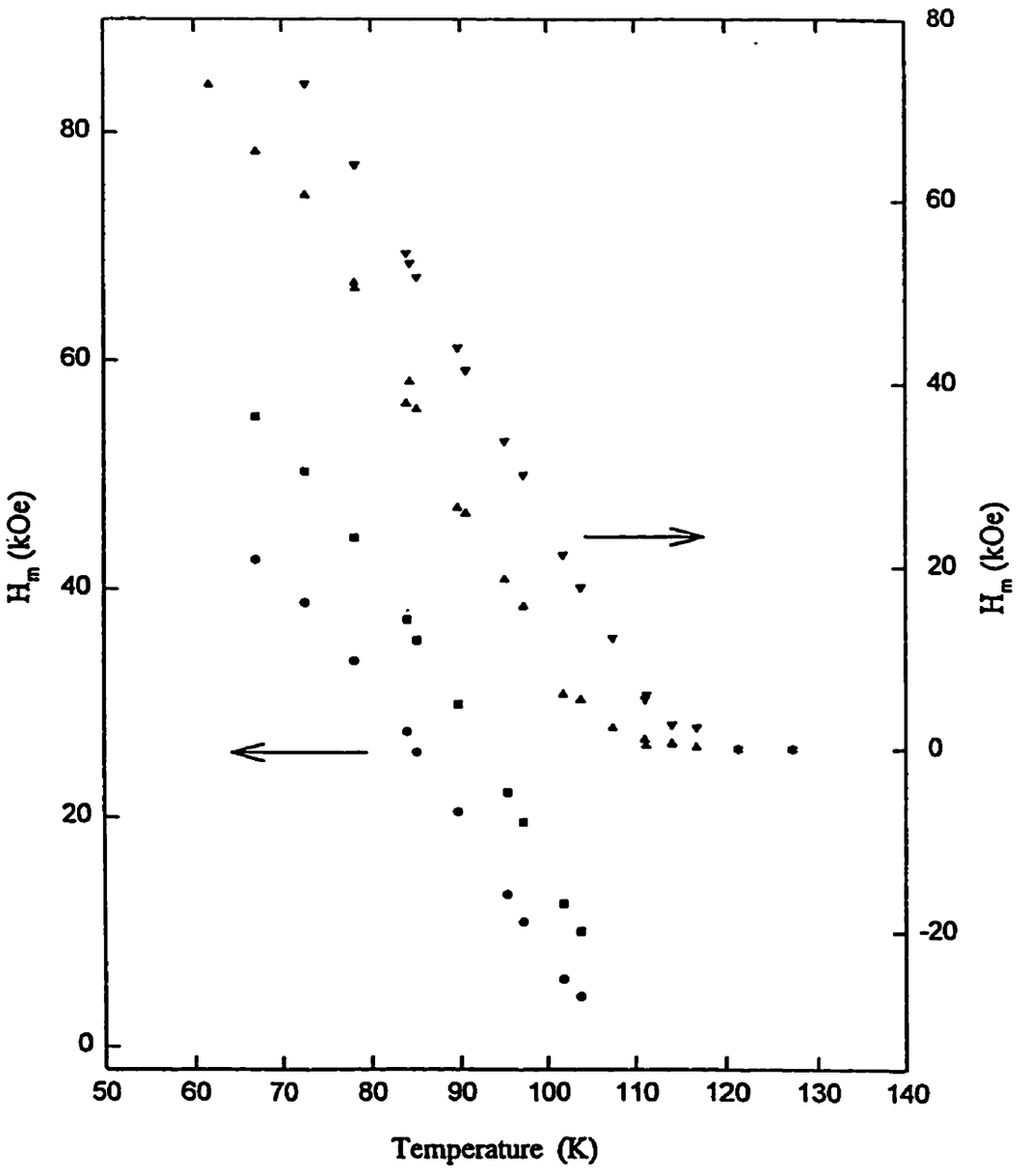

Figure 7.15: H_m-T phase diagram for $Ce(Fe_{0.93}Ru_{0.07})_2$. The left axis corresponds to $H_m(T)$ estimates from magnetoresistive data, while the right corresponds to the magnetisation data.

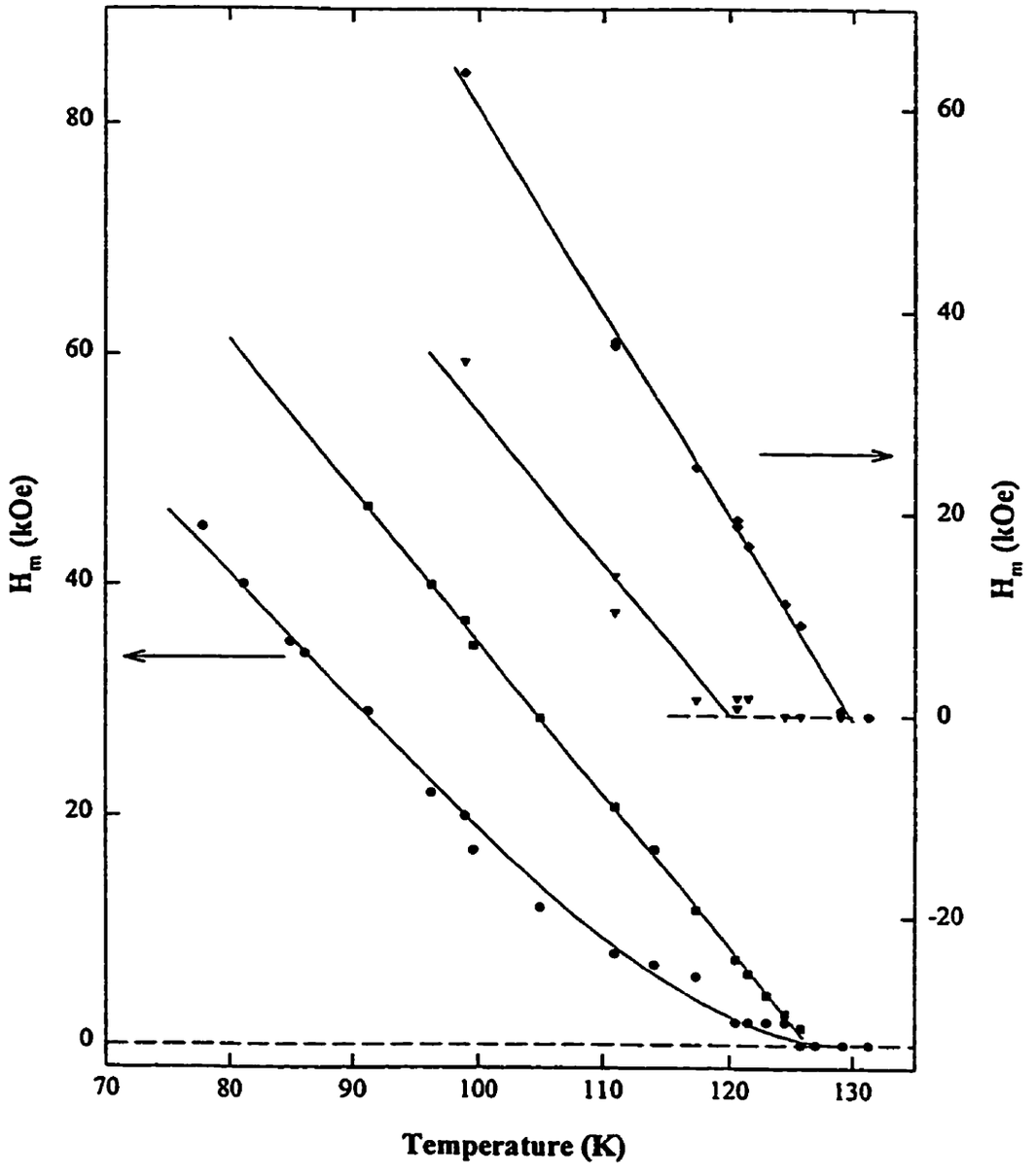

Figure 7.16: H_m-T phase diagram for $Ce(Fe_{0.92}Ru_{0.08})_2$. The left axis corresponds to $H_m(T)$ estimates from magnetoresistive data, while the right corresponds to the magnetisation data. The lines are guides to the eye.

In fact, some of the estimates for T_N are almost as high as T_c in the 8% sample.

7.2.4 Summary

In summary, the magnetoresistance and magnetisation data in doped $CeFe_2$ show many similarities to systems with Al and Co doping. A giant magnetoresistance is found in the vicinity of the metamagnetic transition, due to the dramatic suppression of this transition by applied fields. Plots of H_m(T) show a large difference between the corresponding magnetic and transport characteristic fields, however the temperature dependence is similar in these sets of data. This suggests that it may be possible to relate the behaviour of the magnetoresistance and the magnetisation at the metamagnetic transition.

7.3 Gd_2In

Detailed magnetisation and resistance measurements were done on the Gd_2In sample using the same measurement conditions as for the $Ce(Fe_{1-x}Ru_x)_2$ systems. The specimen used in both the magnetisation and magnetoresistance measurements was cut from a sample prepared earlier by McAlister[64], and was also used in a previous *ac* susceptibility study[151]. The use of the same specimen for both transport and magnetic measurements ensures that data at the same applied field in both sets of data can be compared directly.

7.3.1 Resistivity and Magnetoresistance

The zero field resistivity, $\rho(0,T)$, of Gd_2In is reproduced in figure 7.17, as well as the resistivity measured in a fixed static biasing field of 72 kOe applied along the longest sample dimension. The zero field *ac* susceptibility data measured previously in the same sample[151] is included to allow direct comparison between features. The general features of ρ(0,T) are similar to those observed in the doped $CeFe_2$ samples, and to those measured previously by McAlister[64]. The paramagnetic to ferromagnetic transition is indicated by the knee in ρ(0,T) near 190K. The temperature derivative

of this resistivity (shown in the inset, figure 7.17(b)) has a peak at T_c=186.5±1K, in excellent agreement with the value of 187±1K (indicated by the vertical arrow in figure 7.17) determined by an analysis of the critical behaviour of the magnetic susceptibility[151]. At lower temperatures the resistivity begins to rise sharply, beginning at a temperature of 96±1K and peaking at approximately 93 K, as can be seen more clearly in inset (a) of figure 7.17. The onset temperature of this resistive anomaly is in exact correspondence with the midpoint (96±1K) of the sharp drop in *ac* susceptibility with decreasing temperature, and with the peak in the coefficient a_2(H) of the non-linear *ac* susceptibility[154]. McAlister[64] previously obtained an estimate for the metamagnetic transition temperature, T_m=99.5±1K, based on the anomaly in the temperature derivative of the resistivity near the lower transition. The 72 kOe biasing field completely suppresses the antiferromagnetic state, as shown in the lower curve in figure 7.17. The applied field decreases the resistivity at all temperatures, although the magnetoresistance is much smaller in the ferromagnetic regime than at low temperatures.

The field dependence of the resistivity was measured at 15 fixed temperatures between 1.5 and 120K. The behaviour of these curves in the vicinity of T_m is summarised in figure 7.18. Within the ferromagnetic regime (for example, curve (a)), the magnetoresistance is small ($\sim$ 6%) and negative, consistent with a field-induced decrease in spin-disorder scattering. At 4.2 K (figure 7.19), the magnetoresistance saturates at a large negative value (29%) at high field. The general features of the curves are similar to those seen in $Ce(Fe_{1-x}Ru_x)_2$: after a low field plateau, the magnetoresistance has an abrupt drop-off at H_m, followed by a slowly decreasing high field region. At 1.5 and 4.2K this magnetoresistance saturates abruptly at fields of 50–60 kOe. As the temperature is increased from 4.2K towards the metamagnetic transition temperature, the field required to drive the transition decreases, as was observed in the doped $CeFe_2$. The detailed behaviour of these plots will be discussed later.

The doped $CeFe_2$ samples measured previously[143, 152, 153] show a large hysteresis in the magnetoresistance within the antiferromagnetic regime. A similar

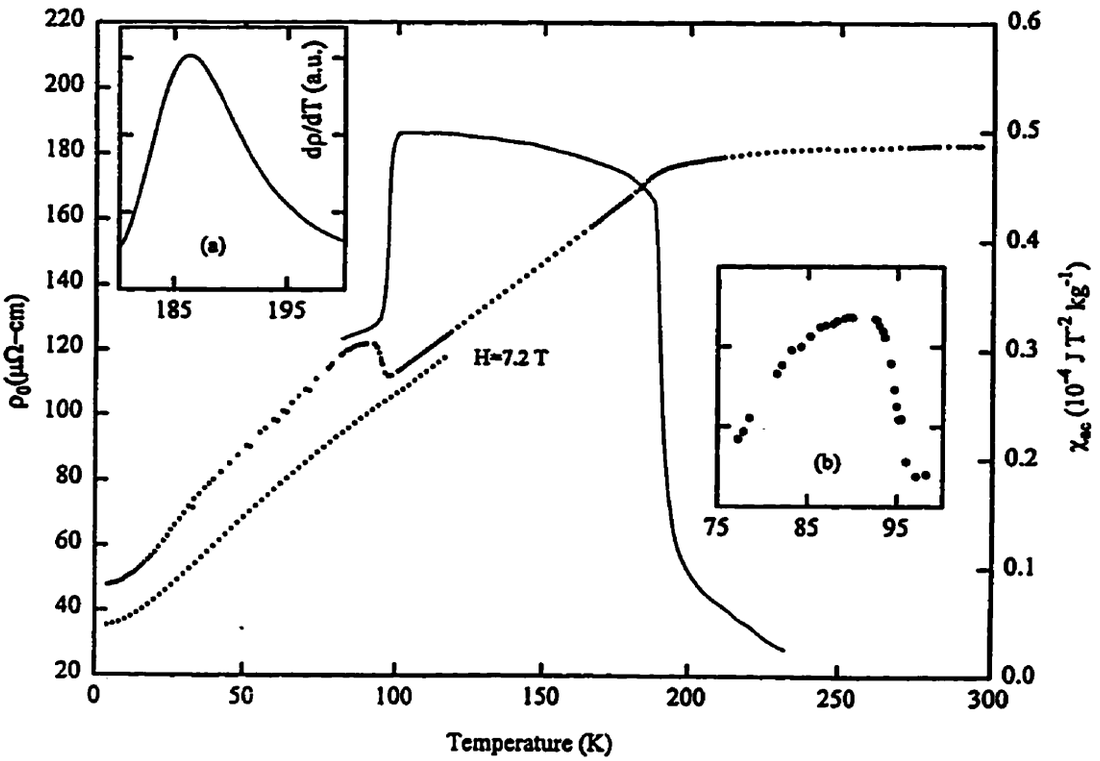

Figure 7.17: The resistivity of Gd_2In measured in fixed biasing fields of zero(upper curve) and 72 kOe (lower curve). Inset (a) shows the low temperature anomaly in the resistivity on a larger scale, while inset (b) shows the resistivity derivative at the upper transition, yielding a value for T_c of 186.5±0.1K.

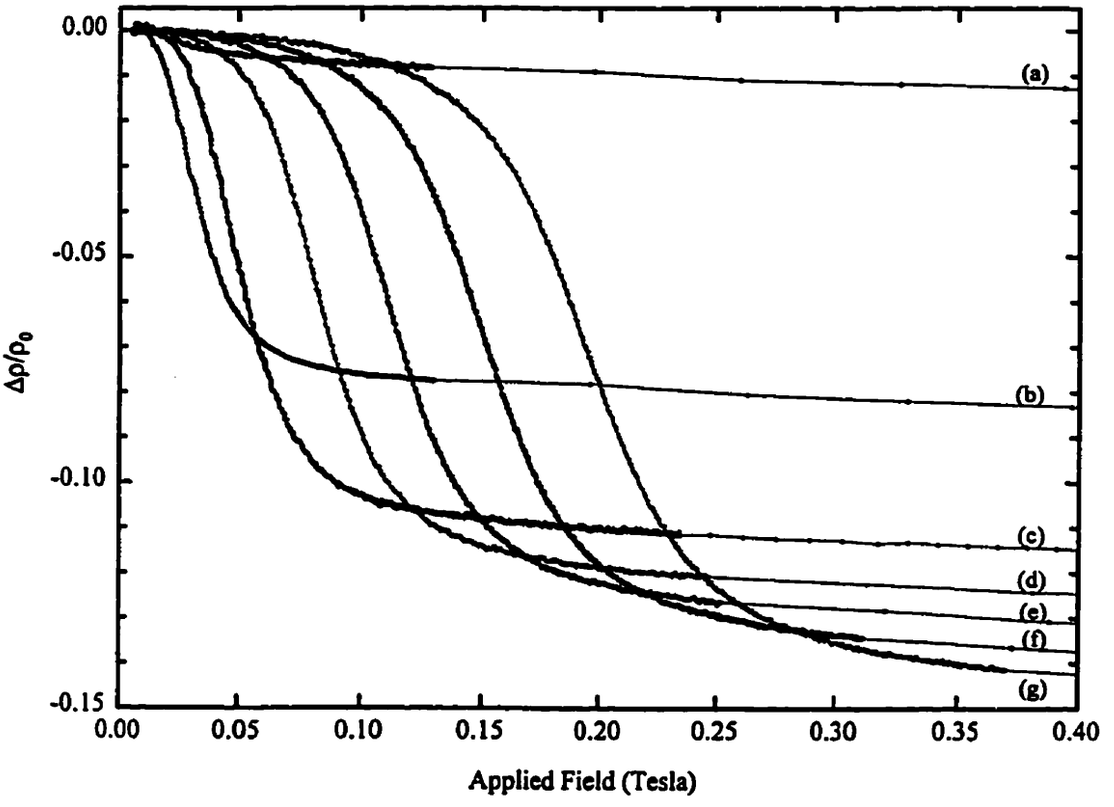

Figure 7.18: Magnetoresistive curves for Gd_2In at a number of fixed temperatures (a) 98.8 K, (b) 96.0 K, (c) 92.7 K, (d) 90.2 K, (e) 87.9 K, (f) 84.6 K and (g) 81.3 K.

magnetoresistance loop in Gd_2In at a fixed temperature of 4.2K is shown in figure 7.19. This curve, however, shows extremely small hysteresis–the loop width is only 1 kOe, compared to greater than 6 kOe in the $Ce(Fe_{1-x}Ru_x)_2$ samples at considerably higher temperatures. The lack of significant hysteresis in this compound could be due to the lack of an orbital moment at the Gd site, and thus the absence of spin-orbit coupling in the material. This would greatly reduce the crystalline anisotropy, and thus the hysteresis, since hysteresis measures primarily the coercivity of a material. Alternatively, differences in magnetic structure between Gd_2In and $Ce(Fe_{1-x}Ru_x)_2$ could be responsible for this disparity, by influencing the amount of hysteresis associated with the metamagnetic transition.

7.3.2 Magnetisation

The field dependence of the magnetisation was measured at a number of fixed temperatures from 2 to 140K in applied fields of up to 55 kOe. Figure 7.21 reproduces those curves measured in the vicinity of T_m, and the inset shows a typical low temperature magnetisation curve. The low temperature magnetisation has a rapid initial increase, similar to that observed in doped $CeFe_2$[143, 152, 153], which is not completely understood at present. As the field increases further, the magnetisation appears to approach saturation temporarily, as seen in the doped $CeFe_2$. In Gd_2In, however, this linear region has a measurable slope even at 4.2 K (inset figure 7.21). This slope increases with increasing temperature, similar to that seen in the $La_{0.5}Ca_{0.5}MnO_3$ perovskite system[130], whereas in the $Ce(Fe_{1-x}Ru_x)_2$ samples this region remains almost completely flat below T_m. As the field is increased further, the linear region is terminated by an abrupt increase in magnetisation as the system becomes ferromagnetic. Once in the ferromagnetic state, the magnetisation levels off once more, but does not completely saturate to the highest available measuring field, even at the lowest measuring temperature of 2 K, as shown in more detail in the inset in figure 7.20. The failure of the magnetisation to reproduce the complete saturation evident at and below 4.2 K in the magnetorestance data (figure 7.20) is not unexpected, since the magnetisation measures correlations on a

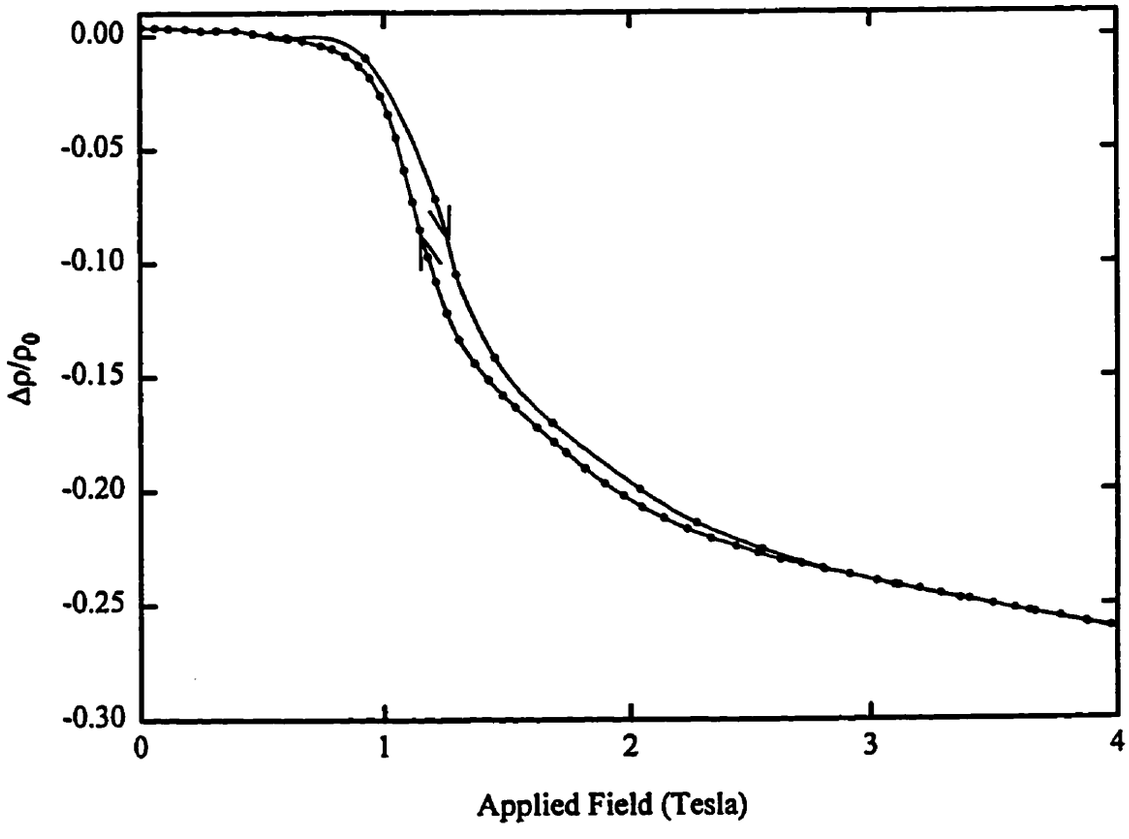

Figure 7.19: Hysteresis in the magnetoresistance in Gd_2In at a fixed temperature of 4.2 K.

longer length scale than the magnetoresistance, suggesting that saturation should be apparent in the magnetisation at fields higher than the 50–60 kOe required for the magnetoresistance. As in the previously discussed materials, the field needed to induce the transition decreases with increasing temperature, as can be clearly seen in figure 7.21. At temperatures above the transition (eg. 99 K, the highest temperature curve in figure 7.21), the magnetisation increases sharply initially, and then approaches saturation at high field, exhibiting none of the low field structure associated with the low temperature regime. A number of curves measured in the ferromagnetic regime are plotted in figure 7.22. As Jee et al.[147] observed, these curves seem to have a limiting low field slope, with different temperature data lying on the same line. Calculation of the demagnetisation factor for this sample give N$\sim$1.2 g-Oe/emu, consistent with a low-field limited slope of 1/N=0.86 emu/g-Oe. This slope is higher than the observed limiting slope of 0.6 emu/g-Oe; however, the non-uniformity of the sample causes inaccuracies in the calculated demagnetisation factor, as well as inducing non-uniform internal fields. For this reason we can not state definitively that our data are not demagnetisation limited in this region. As well, data taken in the same temperature range by McAlister[64] on a spherically shaped sample are clearly demagnetisation limited at low field, suggesting that the low field behaviour is due to demagnetisation constraints rather than the structural considerations cited by Jee et al., especially considering that our limiting slope is an order of magnitude larger than that found by these latter authors.

The high field slope of the M(H) plots is large, the average slope (estimated between 4.5–5.5T) decreasing from $2\text{x}10^{-4}$ emu/g-Oe at 140 K to some $0.5\text{x}10^{-4}$ emu/g-Oe at 2 K. This latter value is an order of magnitude larger than that of Pd, a well-known example of a Pauli paramagnet with substantial exchange enhancement. These slopes are thus more likely to originate from some non-collinearity in the Gd spin configuration rather than from band structural sources. Although the high field magnetisation in these plots does not saturate, a value for the saturation moment can be obtained by extrapolating the data to 1/H=0. The moments obtained in this manner decrease from approximately 7.2 μ_B/Gd at 4.2K to 5.5μ_B/Gd at 140K.

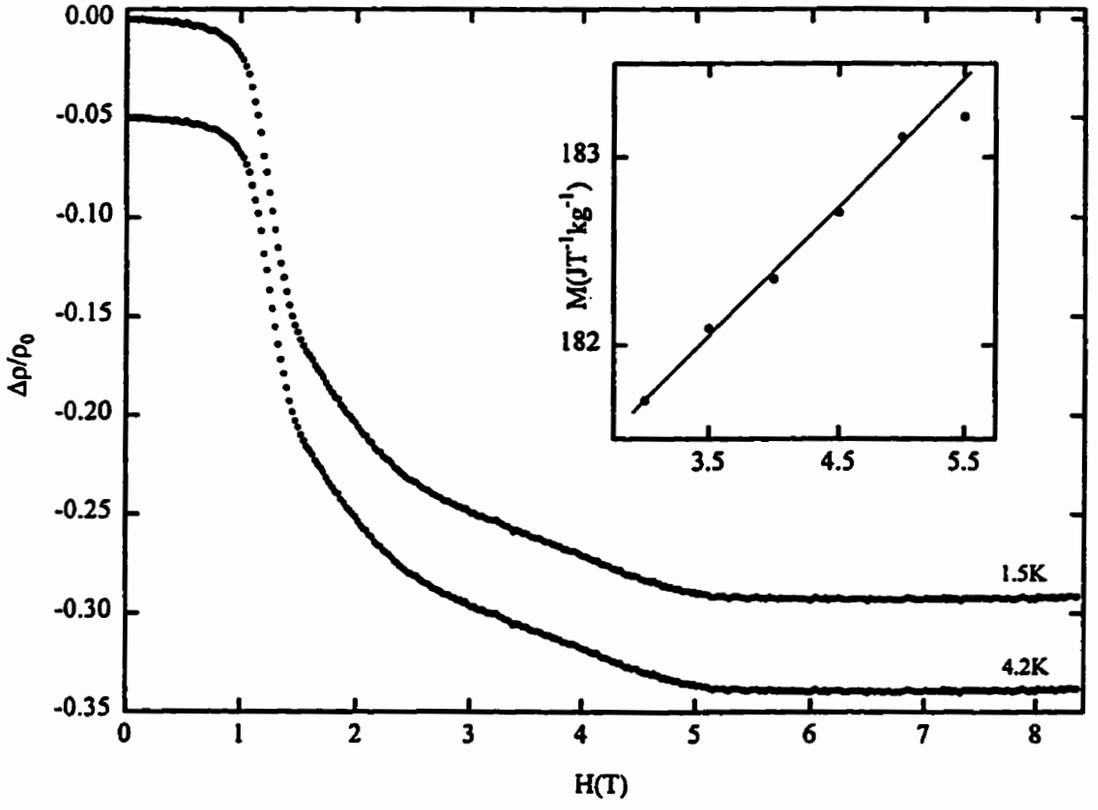

Figure 7.20: Magnetoresistance in Gd_2In at fixed temperatures of 1.5 and 4.2K, showing clearly the high field saturation. The 4.2 K data is offset by 0.05 for clarity. The magnetisation at 2K, in the inset, shows no evidence of saturation.

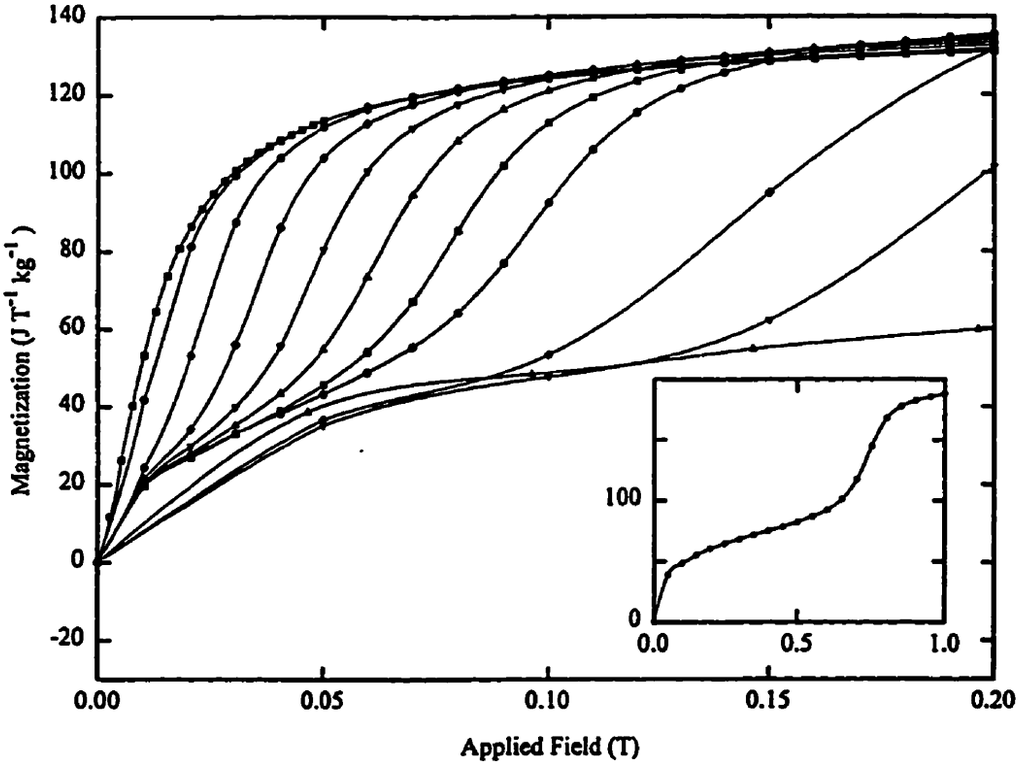

Figure 7.21: Magnetisation of Gd_2In at a number of fixed temperatures, from left to right: 99, 97, 95, 93, 91, 89, 87, 85, 80, 75 and 15 K. The inset shows the magnetisation measured at 4.2 K.

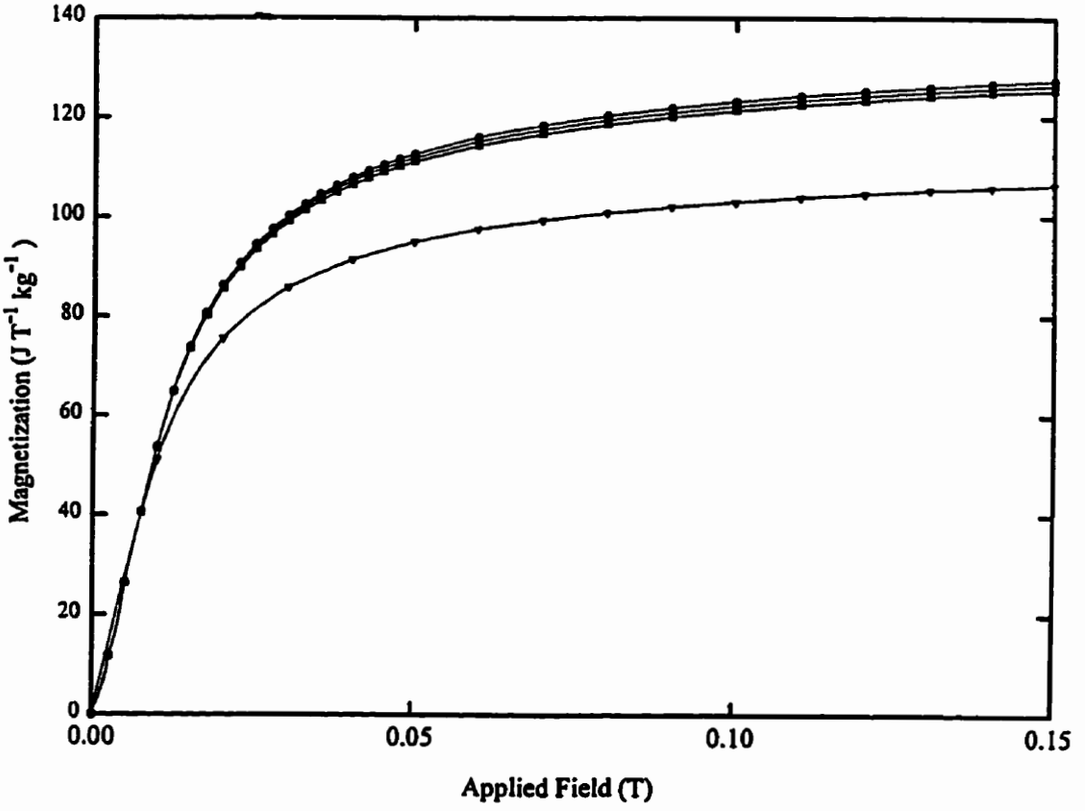

Figure 7.22: Magnetisation data for Gd_2In in fixed temperatures of (from top to bottom) 101 K, 103 K, 105 K and 140K.

The former value is slightly higher than that expected from the Gd moment. These values are comparable to moments of 6–7.5μ_B/Gd atom, found earlier[64, 147].

7.3.3 Temperature Dependence of H_m

Values for the metamagnetic field as a function of temperature were extracted from the data using the same procedure as for the doped $CeFe_2$ samples analyzed in the previous section. Figure 7.23 shows the slope of the magnetoresistance and magnetisation curves. As observed in the doped $CeFe_2$ samples, the point of maximum slope moves to lower field as the temperature approaches T_m from below. The magnetoresistance derivatives are shown in figure 7.23(a) at a number of temperatures close to T_m. This plot shows more structure than similar plots for $Ce(Fe_{1-x}Ru_x)_2$[152, 153]. In the latter materials, the maximum slope remained approximately constant for temperatures below T_m, and then dropped rapidly to zero as the temperature was raised above T_m. In Gd_2In, the maximum slope increases smoothly with temperature until $\simeq$93K, at which point it begins to drop smoothly to zero as the temperature increases further. The presence of this anomaly in Gd_2In suggests some intrinsic difference in the transition mechanism in the two layered systems, perhaps the result of a spiral antiferromagnetic structure in the Gd_2In. It is interesting to note that the temperature at which the maximum slope is the largest (93$\pm$1K) is close to the temperature at which the anomaly in the zero field resistivity (figure 7.17(a)) reaches its largest value.

The magnetisation derivatives in figure 7.23(b) show that, at a given temperature, H_m is smaller in the magnetisation data than in the magnetoresistance data, as observed in the previous compounds. Again, however, the variation of the maximum slope with temperature is different than in the systems measured previously. In $Ce(Fe_{1-x}Ru_x)_2$[152, 153], the maximum slope of the magnetisation data was constant at low temperatures and dropped slightly as the temperature approached T_m. Gd_2In shows remarkably different behaviour–the maximum slope of the magnetisation curves increases steadily with temperature, approaching the ferromagnetic limiting slope of 0.6 emu/g-Oe at 4.2K. This change in behaviour is another indi-

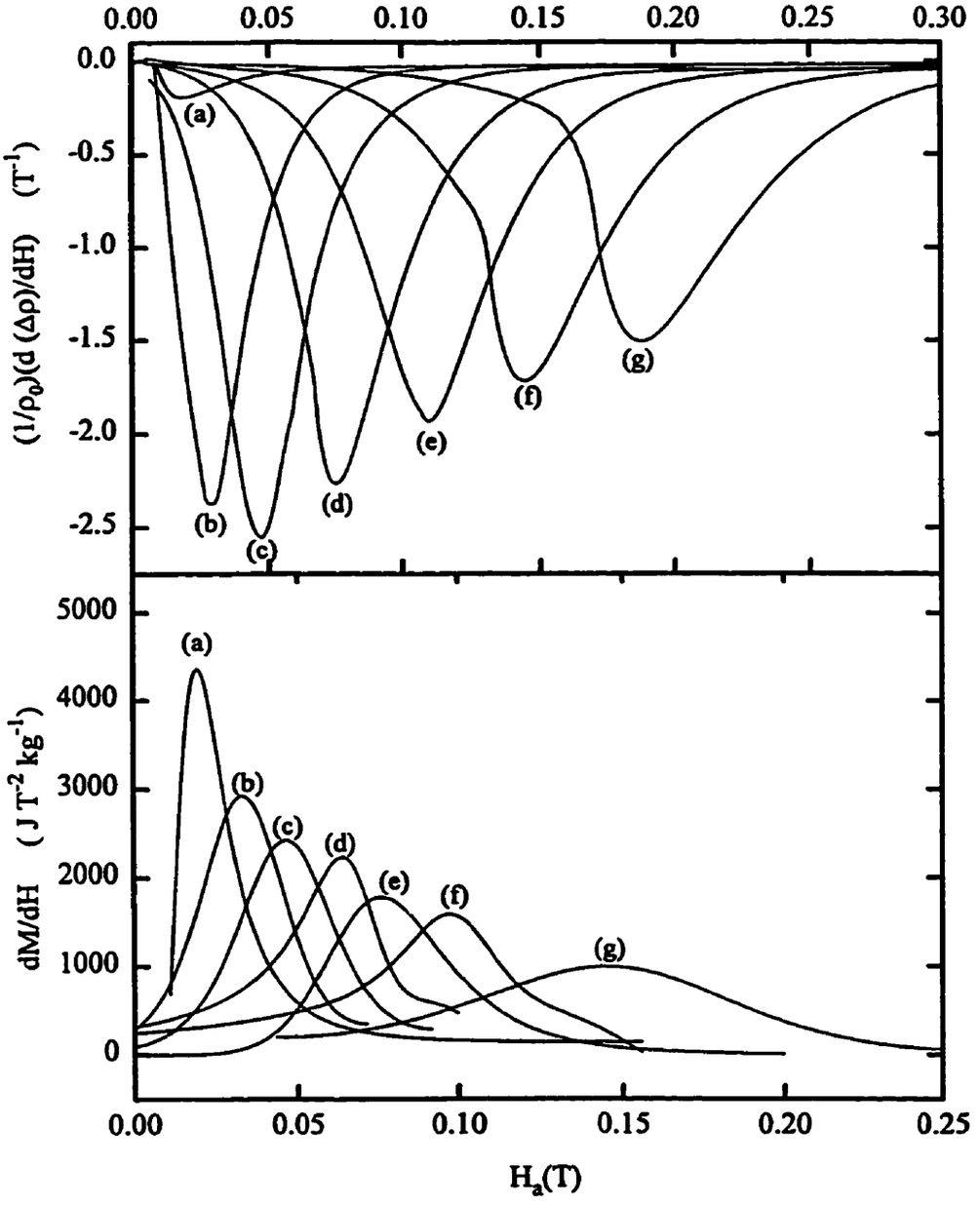

Figure 7.23: Derivatives of $\Delta\rho/\rho_0$(H) (upper curves) at fixed temperatures: (a) 98.8 K, (b) 96.0 K, (c) 92.7 K, (d) 90.2 K, (e) 87.9 K, (f) 84.6 K and (g) 81.3 K and M(H) (lower curves) at a number of fixed temperatures: (a) 95 K, (b) 93 K, (c) 91 K, (d) 89 K, (e) 87 K, (f) 85 K and (g) 80 K.

cation that the magnetic ordering in Gd_2In may not be the same as in the previous layered compounds.

The estimates of H_m from the two sets of data are summarised in figure 7.24. The H_m(T) phase diagram deduced from the magnetisation data is approximately linear, with the values of H_m found using the two methods described previously lying on approximately the same line. In general these data, when corrected for demagnetizing effects agree well with values of H_m deduced from previously published magnetisation data[64, 147]. Fitting this data to the equation $a(T - T_m)$ yields a value for T_m=94±1K, with a slope of 0.09 kOe/K. The magnetoresistance data show a larger difference between the two sets of estimates for H_m(T),as well as greater curvature than the magnetisation data. H_m(T) as derived from the peak slopes of the magnetoresistance plots is nevertheless sufficiently linear to allow a fit to be done. This fit yields a =0.15 kOe/K with a value for T_m=96±1K, the latter temperature in excellent agreement with the onset of the anomaly in the zero field resistivity and the midpoint of the lower transition in the *ac* susceptibility[151]. The values of a found in Gd_2In are an order of magnitude lower than those found in doped $CeFe_2$[152, 153], which is not surprising since the metamagnetic fields in Gd_2In are also much lower than in the other layered systems. The difference in H_m between these systems suggests that the two systems have different spin ordering.

7.4 Summary and Comparison

The general behaviour of the magnetisation and magnetoresistance in the vicinity of the metamagnetic transition of $Ce(Fe_{1-x}Ru_x)_2$ and Gd_2In are remarkably similar. The detailed behaviour in the transition region is quite different in these systems, however, suggesting an intrinsic difference in the magnetic structure of the low temperature states in these systems. Despite these differences, it is interesting to investigate the mechanism of the metamagnetic transition by attempting to relate the behaviour of the magnetisation and magnetoresistance in this regime. An understanding of how these properties relate could lead to a better understanding

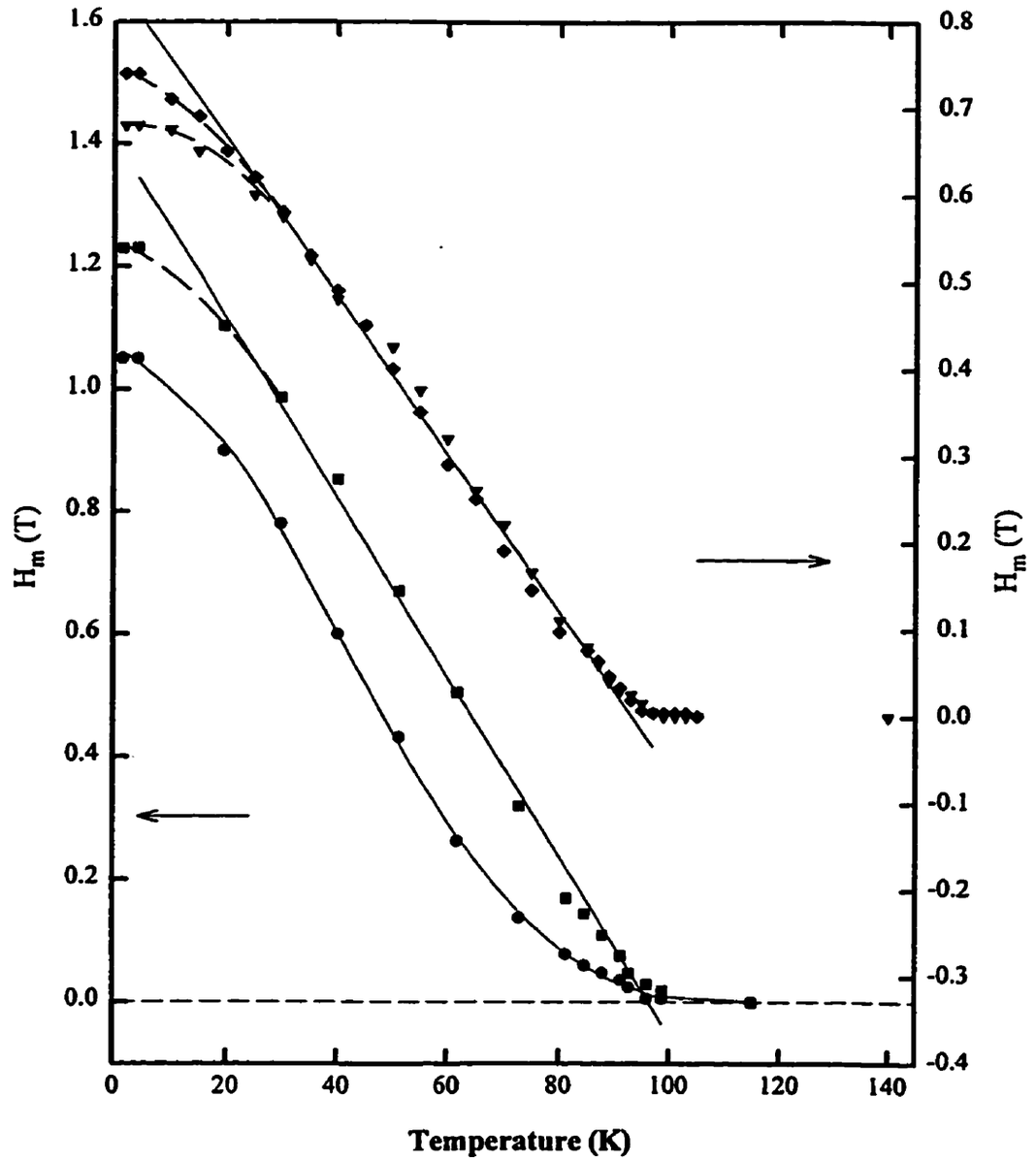

Figure 7.24: H-T phase diagram for Gd_2In. The left axis corresponds to the $H_m(T)$ estimates from magnetoresistive data, while the right corresponds to those from the magnetisation data. Linear fits to the data near T_m are shown as well as the low temperature curvature.

of the giant magnetoresistance process.

Itinerant models have been used to successfully reproduce the general behaviour of the magnetoresistance in magnetic multilayer systems, although they are unable to explain the detailed behaviour in the vicinity of the transition. Attempts to correlate the behaviour of the magnetoresistance and the magnetisation in the transition region using a localised s-f model have shown some success in granular GMR systems[85], although the mechanics of such systems are quite different than in both multilayers and intermetallics. The s-f model predicts the following relationship between $\Delta\rho(H,T) = \rho(0,T) - \rho(H,T)$ and $\langle S_z \rangle$ $\propto$M(H,T) [155]:

$$\Delta\rho(H,T) = Ac\left[J^2\langle S_z\rangle \tanh\left(\frac{\alpha}{2}\right) + \frac{4V^2J^2\langle S_z\rangle^2}{V^2 + J^2[S(S+1) - \langle S_z\rangle \tanh\left(\frac{\alpha}{2}\right)]}\right] \quad (7.1)$$

where $A = \frac{3m^*\Omega}{2\hbar e^2 E_F}$ depends on the detailed band structure (Ω is atomic volume, m^* is the conduction electron effective mass, and E_F is the Fermi energy), c is the atomic fraction of scattering sites, and $\alpha = \frac{g\mu_B H_i}{k_B T}$. To fit equation 7.1 to our GMR data, we used the value Ac=200, a reasonable estimate for the present materials. Since these systems are not ferromagnetic at low temperature, the sublattice magnetisation should be used in the calculation. These data, however, are not available, and thus a value of $\langle S_z \rangle$ scaled to the total magnetisation was used. The measured magnetoresistance as well as three different fits to equation 7.1 are shown at temperatures below T_m in figures 7.25–7.27 for the three systems examined respectively. The different fits in each of these figures utilize three different estimates of the field H_i:(a) H_i=H_a;(b) (c) H_i=H_a+k_BT_m/μ_B; and (c) H_i=H_a+$\lambda\langle S_z\rangle$, with the molecular field constant $\lambda = k_BT_m/\mu_B$. The above fits are obtained using a routine which minimizes the deviation between the measured and fit $\Delta\rho(H,T)$. However, since the magnetisation data begins to change at fields lower than in the magnetoresistance data, the deviations in the transition region become very important, and the overall change in resistivity can not be reproduced.

An alternative approach was taken in the fits of figures 7.28–7.30. Instead of choosing values of |J| and |V| which minimize the deviations between the measured data and the fit, |J| and |V| were chosen to obtain the correct overall change in

Table 7.2: Fitting Parameters for $s-f$ model

Sample	H_i	minimise deviations		match $\Delta\rho$	
		|J|	|V|	|J|	|V|
$Ce(Fe_{0.93}Ru_{0.07})_2$	H_a	1.45 eV	0.05 eV	1.41 eV	0.31 eV
	H_a+H_{mol}	0.22 eV	0.19 eV	0.34 eV	0.11 eV
	$H_a+\lambda\langle S_z\rangle$	0.24 eV	0.14 eV	0.33 eV	0.10 eV
$Ce(Fe_{0.92}Ru_{0.08})_2$	H_a	1.61 eV eV	0.07 eV	1.05 eV	0.15 eV
	H_a+H_{mol}	0.21 eV	0.18 eV	0.30 eV	0.11 eV
	$H_a+\lambda\langle S_z\rangle$	0.24 eV	0.13 eV	0.30 eV	0.10 eV
Gd_2In	H_a	0.45 eV	0.11 eV	0.33 eV	0.12 eV
	H_a+H_{mol}	0.13 eV	0.11 eV	0.13 eV	0.12 eV
	$H_a+\lambda\langle S_z\rangle$	0.13 eV	0.12 eV	0.13 eV	0.11 eV

$\Delta\rho(H,T)$. Curves (b) and (c) in these figures reproduce the field dependence of the resistivity very well although in all of these samples, the calculated curves begin to drop at a field lower than in the measured magnetoresistance, due to the difference in H_m given by $\Delta\rho(H,T)$ and M(H,T). Knowledge of the sublattice magnetisation might improve this fit, although it is difficult to understand how the sublattice magnetisations could have a field dependence which is substantially different from that of the total magnetisation. The values of |J| and |V| found using these various approaches are compared in table 7.2. In general, the fit to using H_i=H_a requires large values of |J|, while smaller |J| are obtained using the larger fields, as would be expected from the equation. The two different fitting methods resulted in large changes in the magnitude of |J| in the doped $CeFe_2$ samples but not in Gd_2In, a result most likely due to the smaller metamagnetic fields and thus smaller deviations in the latter material. The values for |V| remain fairly constant for all samples, as it is the least important fitting parameter.

The failure of this model to relate the MR to the magnetisation is likely a result of the change in ordering from antiferromagnetic to ferromagnetic ordering as a function of applied field. As discussed previously, the transition to antiferromagnetism results in the opening of superzone gaps on the Fermi surface at T_N, decreasing the

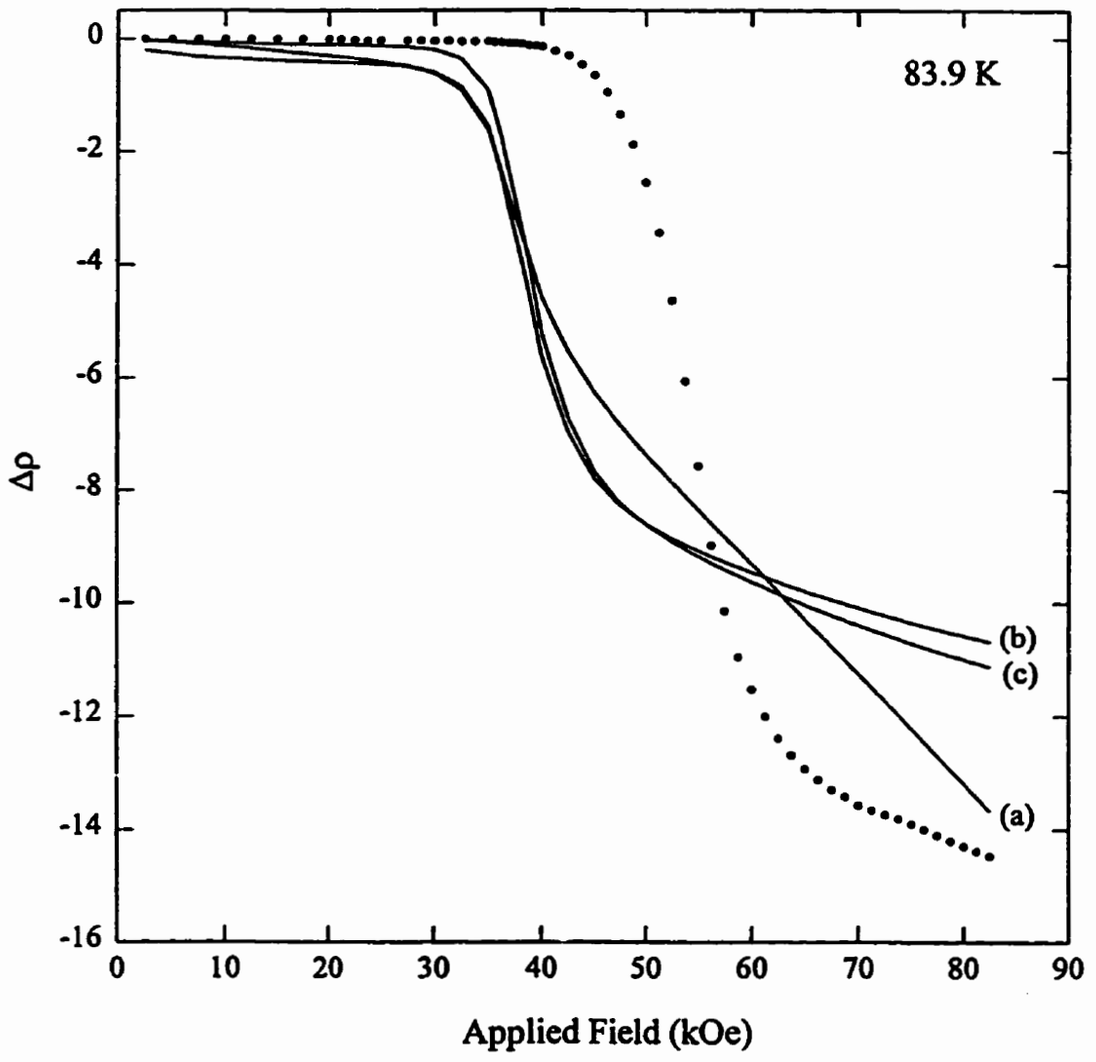

Figure 7.25: Fits to the magnetoresistance in $Ce(Fe_{0.93}Ru_{0.07})_2$ at a fixed temperature of 83.9 K using the s-f model, and minimizing the deviations between the fit and the measured magnetoresistance. The fits labelled (a),(b) and (c) are as described in the text.

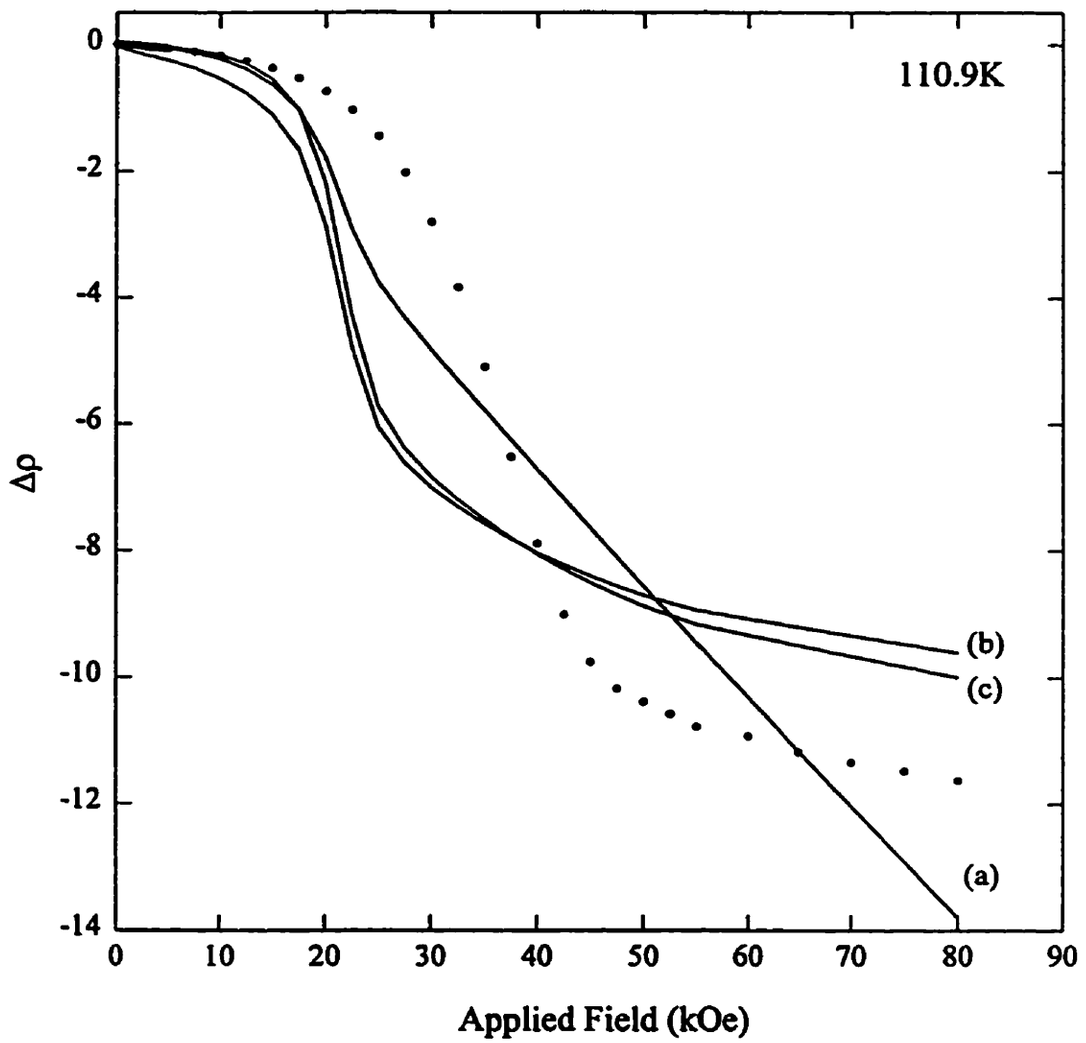

Figure 7.26: Fits to the magnetoresistance in $Ce(Fe_{0.92}Ru_{0.08})_2$ at a fixed temperature of 110.9 K using the s-f model, and minimizing the deviations between the fit and the measured magnetoresistance. The fits labelled (a),(b) and (c) are as described in the text.

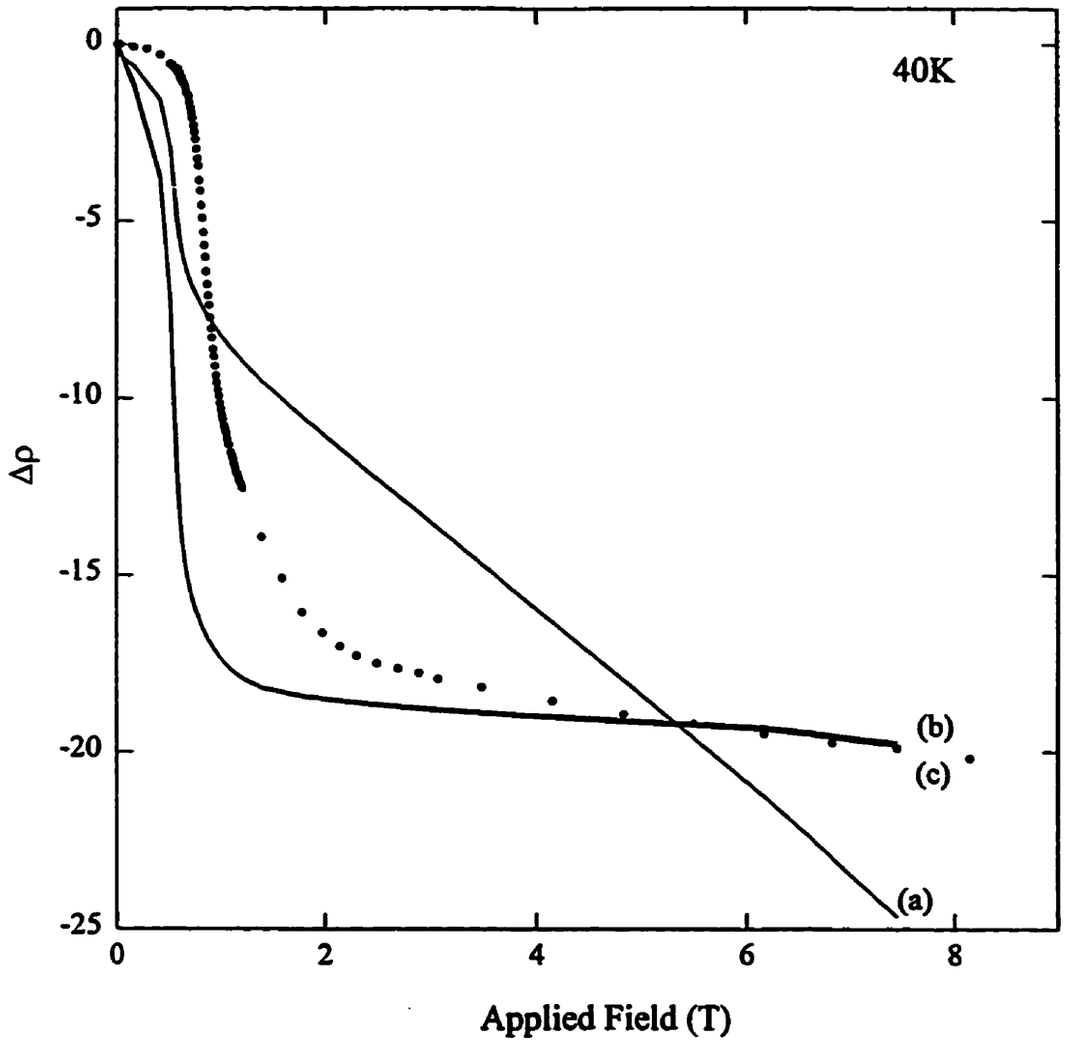

Figure 7.27: Fits to the magnetoresistance in Gd_2In at a fixed temperature of 40 K using the s-f model, and minimizing the deviations between the fit and the measured magnetoresistance. The fits labelled (a),(b) and (c) are as described in the text.

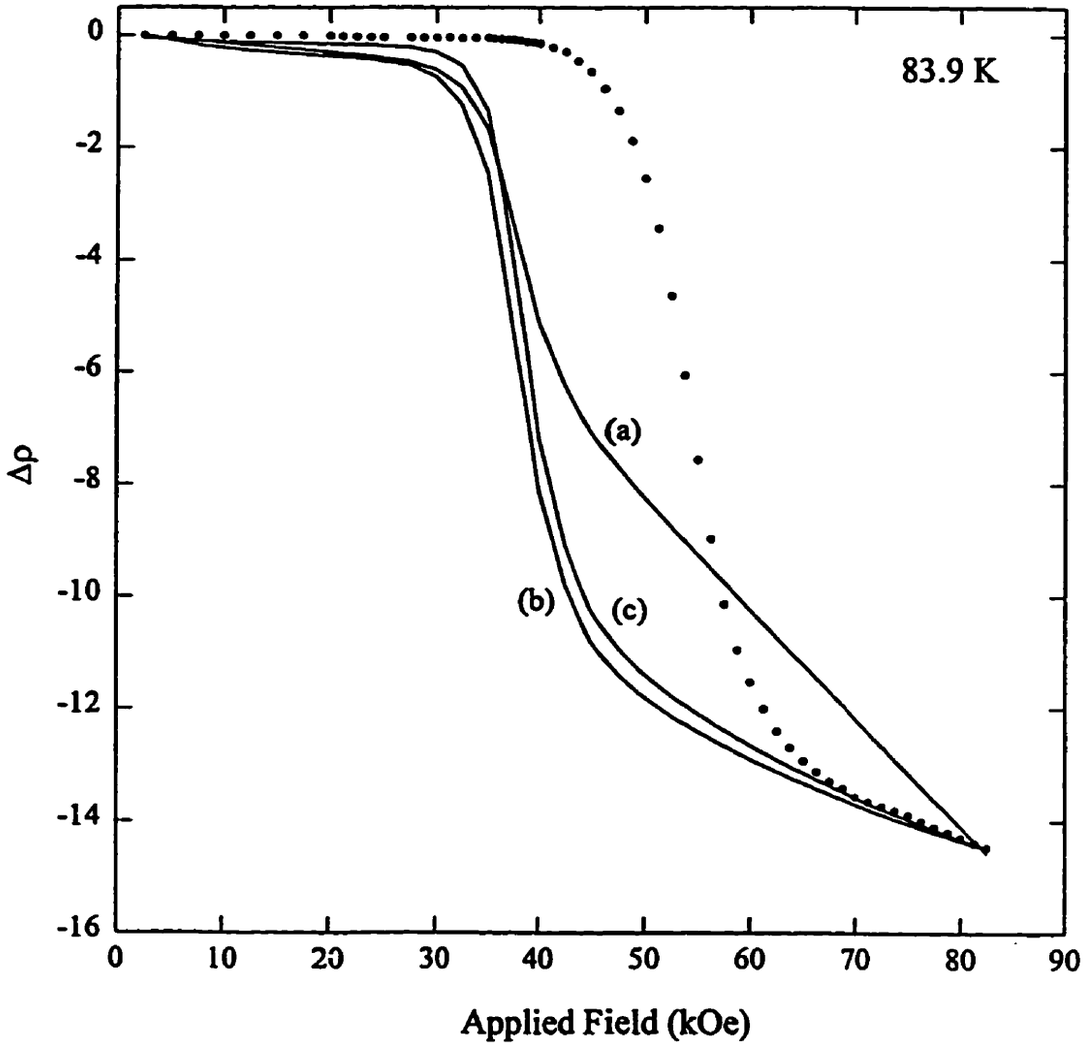

Figure 7.28: Fits to the magnetoresistance in $Ce(Fe_{0.93}Ru_{0.07})_2$ at a fixed temperature of 83.9 K using the s-f model, and matching the overall change in the measured magnetoresistance. The fits labelled (a),(b) and (c) are as described in the text.

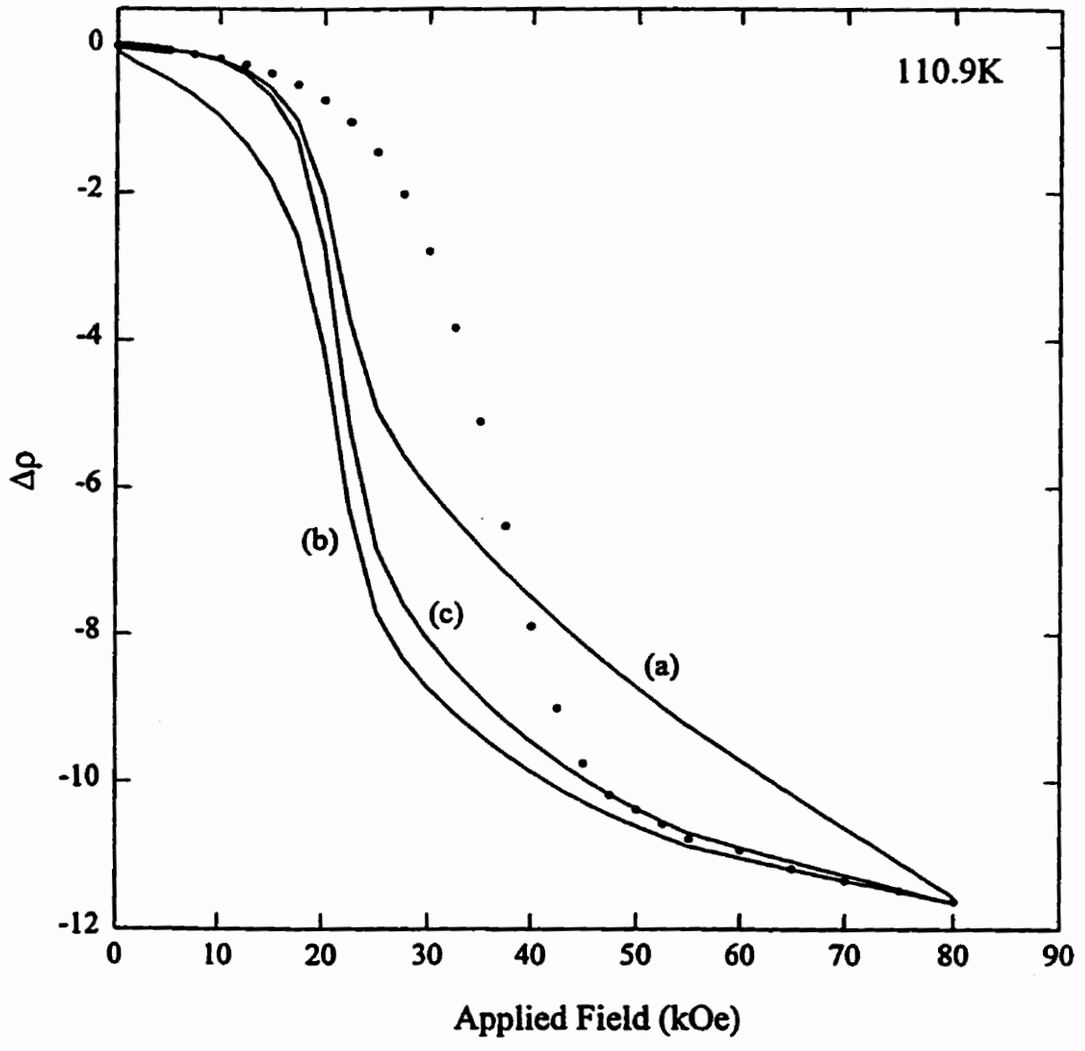

Figure 7.29: Fits to the magnetoresistance in $Ce(Fe_{0.92}Ru_{0.08})_2$ at a fixed temperature of 110.9 K using the s-f model, and matching the overall change in the measured magnetoresistance. The fits labelled (a),(b) and (c) are as described in the text.

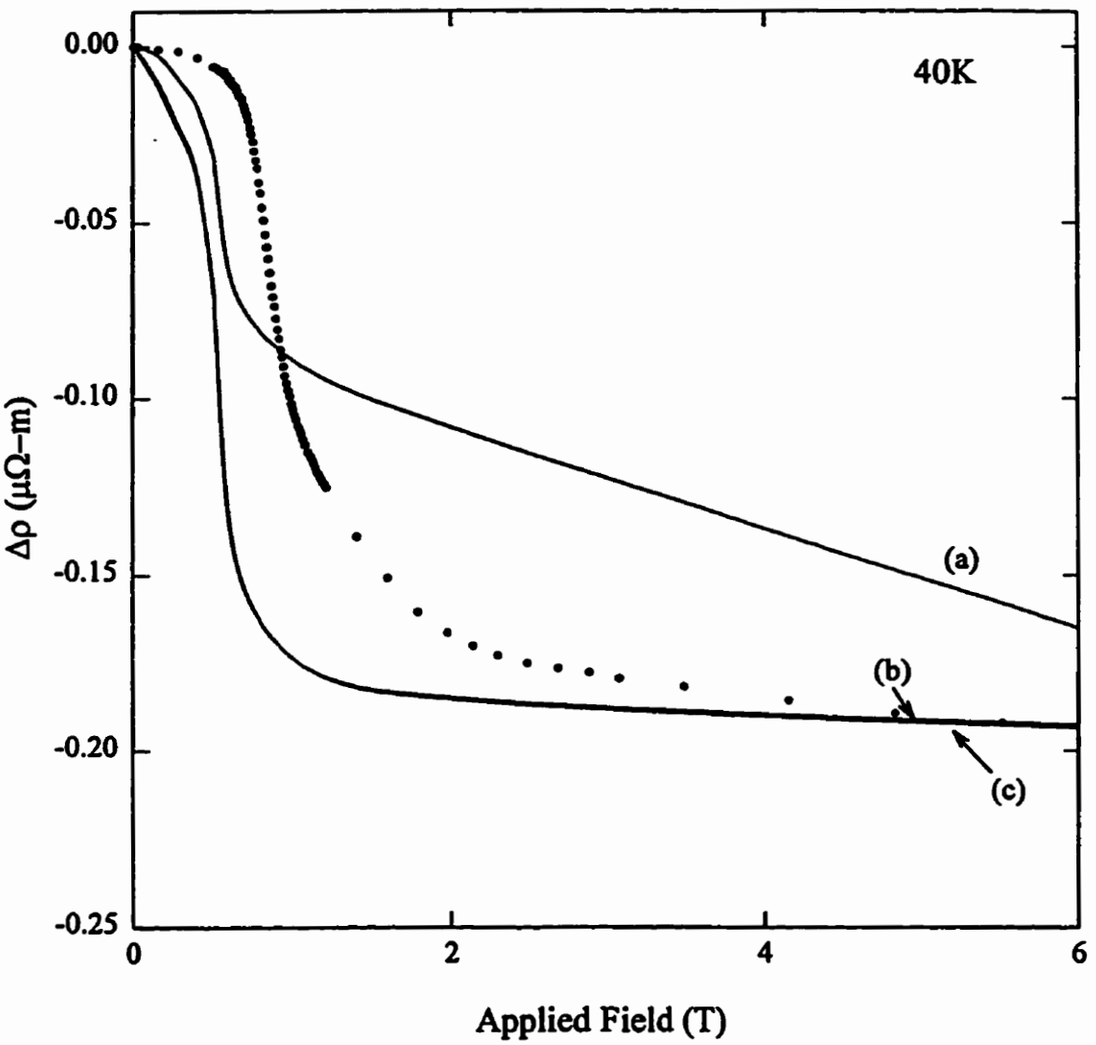

Figure 7.30: Fits to the magnetoresistance in Gd_2In at a fixed temperature of 40 K using the s-f model, and matching the overall change in the measured magnetoresistance. The fits labelled (a),(b) and (c) are as described in the text.

number of current carrying electrons and thus increasing the resistivity significantly from that in the ferromagnetic state, as in equation 2.42, viz,

$$\rho(T) = \frac{\rho_i(T) + \rho_l(T) + \rho_m(T)}{1 - gM(T)} \tag{7.2}$$

where, $\rho_i(T)$, $\rho_l(T)$ and $\rho_m(T)$ are the impurity, phonon and magnetic contributions to the resistivity and M(T) is the sublattice magnetisation. The factor g is related to the decrease in the Fermi surface, and is zero in the ferromagnetic state. As well as these considerations, in the doped $CeFe_2$ samples this transition also involves a distortion of the crystal lattice, which would also affect the band structure. The $s-f$ model discussed above is dependent on the detailed band structure of the material, and assumes this structure (and thus the constant A, amongst others) remains constant throughout, which is probably not the case in these intermetallics. Recently, Antonov et al.[156] have completed first-principles calculations of the band structure in a single crystal of UNiGa, an intermetallic which has a colossal magnetoresistance such as seen in the previously mentioned perovskite materials. They find a 26% reduction of the Fermi surface at the transition from ferromagnetism to antiferromagnetism, which in itself would introduce a giant magnetoresistance. As well, they find considerable changes in the shape of the Fermi surface which also contribute to the overall change in resistivity. By calculating the resistivity in both states, and setting the resistivity in the ferromagnetic state equal to ρ(H) and that in the antiferromagnetic state to $\rho(0)$, they obtain magnetoresistances in semi-quantitative agreement with experimental results. Although the behaviour of the resistance as a function of field can not be so easily calculated, these results suggest that the mechanism for the giant magnetoresistance in intermetallics may be better understood by studying the changes in band structure, and their variation with field. Nevertheless, it is still difficult to appreciate how large changes in the magnetisation, surely reflecting changes in sublattice magnetisation correlated with modifications in the band structure, can occur at fields which are substantially different from those inducing changes in the resistivity if the latter are also driven by band structure modifications.

In conclusion, small differences in behaviour in the vicinity of the lower transition support the hypothesis that the low temperature structure in Gd_2In is different from the simple antiferromagnetism present in doped $CeFe_2$–a result of the more complicated crystallographic structure of Gd_2In. Despite the inability of a localised model to describe the behaviour of these systems in the transition regions, band structure calculations may yield an explanation of the magnetoresistive behaviour in these intermetallic systems.

Chapter 8

Conclusion

Although extensive experimental and theoretical work has been done on the effects of exchange bond disorder on magnetic ordering[80, 157], the principal focus of this work has been on magnetic, rather than transport properties. Furthermore much of the experimental work that has been done concentrated on systems in which impurity moments were treated as having no orbital moments. In systems which undergo ferromagnetic ordering, many measurements suggest that disorder is an irrelevant scaling field *at* the critical point, in agreement with the Harris criterion, but that this disorder manifests itself in the variation of effective critical exponents away from this point. Indeed in a great many systems experiments suggest that the asymptotic critical exponents are those given by the 3D Heisenberg model. Much of this evidence is provided by *ac* susceptibility results.

This thesis concentrates on two particular problems. The first is the influence of an orbital component in the total impurity moment, the presence of which renders the above approaches—particularly *ac* susceptibility studies—ineffective. Spin-orbit coupling induces coercivity in the material, which obscures the emerging critical peaks and precludes observation of the true asymptotic behaviour of the exponents. As well, since estimates for the critical temperature are made from the low field susceptibility behaviour, substantial error exists in T_c found using these data. New approaches have to be introduced, therefore, to investigate the influence of bond disorder on systems with orbital moments. We have demonstrated two

such approaches here. Firstly the temperature dependence of the low field resistive anisotropy (the existence of this anisotropy relies on the presence of an orbital moment), and the coefficients describing this dependence, have been shown conclusively to give information on the underlying bond-disorder. Using the low field resistive anisotropy, however, one can obtain the relative amounts of disorder in a series of alloys, and, if the absolute disorder in one of these samples is known, i.e. the ratio $\eta = J_0/J$, quantitative estimates for the disorder can be found. Although estimates of the disorder in these systems can be obtained in principle using the ratio of the critical temperatures for the paramagnetic to ferromagnetic transition and the ferromagnetic to spin-glass transition, these latter temperatures can not be conclusively defined, partly for the reasons outlined above; this introduces error into these estimates, so the techniques introduced here remain comparative. Secondly, the unusual critical behaviour of the zero temperature spontaneous resistive anisotropy has offered evidence on a universality class of the exponent which governs the concentration dependence of this effect near a ferromagnetic percolation threshold. This exponent appears to depend on whether an orbital moment exists at the magnetic site, as opposed to effects originating in exchange-split band structures. This is supported by previous measurements on PdFe[5] and PdNi[6] alloys which exhibited different exponents. Experimental measurements of the concentration dependence of the SRA in other systems with orbital moments would help to verify this suggestion, however difficulties could arise due to the extremely low critical concentration of, say Co-impurity systems, making reliable estimates for the reduced concentration $(x - x_0)/x_0$ very difficult to obtain near x_0. Currently no theoretical prediction for this exponent exist; it is hoped that the present work will act as a stimulus for further theoretical effort on this problem. In addition, measurements were done on a new superconductor which has a high T_c for its class of materials. We were interested primarily in the role of Ni in this material, since it was unclear whether the high Ni-concentration placed it above or below the ferromagnetic percolation threshold. Studies of the parent compound and of the effects of Fe substitution at the Ni site lead us to conclude that this system is

below the ferromagnetic percolation threshold for nickel. This study was motivated principally by our work on the anisotropy in transport properties of Ni substituted systems.

The second aspect of this work concentrated on giant magnetoresistance. In particular we studied this effect in systems which exhibit a *single* reorientation transition rather than the cascade of transitions that appears to occur in perovskite systems which exhibit a colossal magnetoresistance and are the subject of much recent activity. We have demonstrated that the *s-f* model may not be appropriate for describing this reorientation transition, and suggest that band-structural changes associated with the metamagnetic transition are of principal importance in these systems. A similar conclusion may be reached in the perovskite materials, in which the colossal magnetoresistance is associated with a metal-insulator transition, presumably an indication of significant band-structural changes. Indeed recent measurements in perovskites substituted with Mg and Ca have shown that whereas both exhibit second order (continuous) paramagnetic to ferromagnetic phase transitions on cooling[158], the former system displays insulating/superconducting behaviour on cooling over the entire range examined, while the latter system undergoes a metal-insulator transition near the magnetic phase transition. Furthermore, the former system displays the largest fractional magnetoresistance at T_c while the latter displays little field dependence in the resistivity near T_c, with the magnetoresistance peaking well below the metal-insulator/magnetic phase transition temperature. These results indicate an even more complicated interplay between magnetic phase change and transport properties in substituted perovskites compared with the natural multilayer materials studied here.

Bibliography

[1] A.H. Morrish, "The Physical Principles of Magnetism". John Wiley & Sons. New York 1965.

[2] P. Weiss. J. Phys. Radium. **6**(1907) 661.

[3] W. Heisenberg, Z. Phys. **49**(1928) 619.

[4] J.C. Ododo and B.R. Coles. J. Phys. F.: Metal Phys.,**7**(1977) 2393.

[5] H.P. Kunkel, Z. Wang and Gwyn Williams, J. Phys.: Condens. Matter. **4**(1992), 10 399.

[6] H.P. Kunkel, Z. Wang and Gwyn Williams, J. Phys.: Condens. Matter. **1**(1989), 3381.

[7] K. Fischer. Landolt-Börnstein New Series Group III, Vol 15. Springer, Berlin 1982 p282 et seq.

[8] R.J. Cava, H. Tagaki, H.W. Zandbergen, J.J. Krajewski, W.F. Peck Jr, T. Siegrist, B. Batlogg, R.B. van Dover, R.J. Felder, K. Mizuhashi, J.O. Lee, H. Eisaki and S. Uchida. Nature **367**(1994) 252.

[9] M. El Massalami, B. Giordanengo, J. Mondragon, E.M. Baggio-Saitovitch, A. Takeuchi, J. Voiron and A. Sulpice. J. Phys.: Condens. Matter **7**(1995) 10015.

[10] A. Bartélémy, A. Fert, R. Morel and L. Steren. Physics World, **7** pg 34.

[11] D. Wang, H.P. Kunkel and Gwyn Williams. Phys. Rev. B **51**(1995) 2872.

[12] S.B. Roy and B.R. Coles, Phys.Rev.B **39**(1989) 9360.

[13] E. Fawcett, H.L. Alberts, V. Yu Galkin, D.R. Noakes and J.V. Yakhmi. Rev. Mod. Phys. **66**(1994) 25.

[14] L. Onsager. Phys. Rev. **65**(1944) 117.

[15] H. Eugene Stanley, "Introduction To Phase Transitions and Critical Phenomena". Oxford University Press, Oxford, 1971.

[16] L.P. Kadanoff, Physics **2**(1966) 263.

[17] B. Widom, J. Chem. Phys. **43**(1965) 3898.

[18] Gwyn Williams, in "Magnetic Susceptibility of Superconductors and Other Spin Systems". Plenum Press, New York 1991, p. 475-502.

[19] S.C. Ho, I. Maartense and Gwyn Williams. J. Phys. F.: Metal Phys. **11**(1981) 699; S.C. Ho, I. Maartense and Gwyn Williams. J. Phys. F.: Metal Phys. **11**(1981) 1107; M. Saran and Gwyn Williams. J. Phys. F.: Metal Phys. **17**(1987) 731.

[20] S.N. Kaul. Phys. Rev. B **38**(1988) 9178.

[21] Stuart S.C. Burnett and Solomon Gartenhaus. Phys. Rev. B **49**(1994) 1137.

[22] S.F. Edwards and P.W. Anderson, J. Phys. F **5**(1975) 965.

[23] M.A. Ruderman and C. Kittel, Phys. Rev. **96**(1954) 99; T. Kasuya, Prog. Theor. Phys. **16**(1956) 45; K. Yosida, Phys. rev **106**(1957) 893.

[24] D. Sherrington and S. Kirkpatrick. Phys. Rev. Lett. **B5**(1975) 1792.

[25] B.W. Southern, J. Phys. C **9**(1976) 4011.

[26] R.M. Roshko and Gwyn Williams, J. Mag. Mag. Mat. **50**(1985) 311.

[27] R.M. Roshko and Gwyn Williams. J. Phys. F.: Metal Phys. **14**(1984) 703.

[28] C. Kittel, "Introduction to Solid State Physics". John Wiley & Sons,Inc. New York 1986.

[29] A. Mattheissen and G. Vogt, Pogg. Ann.**122**(1864) 19.

[30] F. Bloch, Z. Phys. **52**(1929) 555; *ibid* **53**(1929) 216; *ibid* **59**(1930) 208.

[31] G.J. Van den Berg, Ch. IV. "Magnetism: Selected Topics". Gordon and Breach Science Publishers, New York 1976.

[32] J. Smit, Physica XVI **6**(1951) 613.

[33] M. Kohler. Ann. Phys. **32**(1938) 211.

[34] F.C. Schwerer and J. Silcox, Phys. Rev. B**1**(1970) 2391.

[35] J. Kondo. Prog. Theoret. Phys. **32**(1964) 37.

[36] P.G. De Gennes and J. Friedel, J. Phys. Chem. Solids **4**(1958) 71.

[37] M.E. Fisher and J.S. Langer, Phys. Rev. Lett. **20**(1968) 665.

[38] R.J. Elliot. "Magnetism Vol IIA", Ed. G.T. Rada and H. Suhl, Academic Press, New York 1965.

[39] V. Sechovsky, L. Havela, K. Prokes, H. Nakotte, F.R. de Boer and E. Bruck. J. Appl. Phys. **76**(1994) 6913.

[40] A. Fert, R. Asomoza, D.H. Sanchez, D. Spanjaard and A. Friederich. Phys. Rev. B **16**(1977) 5040.

[41] I.A. Campbell and A. Fert, Ch 9, "Ferromagnetic Materials" Vol. 3. ed. E.P. Wohlfarth. North Holland, Amsterdam 1982.

[42] N.F. Mott, Proc. Roy. Soc. **A153**(1936) 699.

[43] A.P. Malezemoff, Phys. Rev. B**32**(1985) 6080; Phys. Rev. B**34**(1986) 1853.

[44] S. Nagai, J. Phys. Soc. Jpn. **53**(1984) 3532.

[45] P.A. Stampe, X. Chen, Z. Wang, H.P. Kunkel and Gwyn Williams, J. Phys: Condensed Matter **6**(1994) 3045.

[46] A. Fert and I.A. Campbell, J. Phys. F **6**(1976) 849.

[47] J.W.F. Dorleijn, Philips Res. Rep. **31**(1976) 287.

[48] Neil W. Ashcroft and N. David Mermin, "Solid State Physics". Saunders College Publishers, Fort Worth 1976.

[49] F. London and H. London. Proc. Roy. Soc.(London) **A149** (1935) 71.

[50] J. Bardeen, L.N. Cooper and J.R. Schrieffer, Phys. Rev. **106**(1957) 162;J. Bardeen, L.N. Cooper and J.R. Schrieffer , Phys. Rev. **108**(1957) 1175.

[51] M. Tinkham, "Introduction to Superconductivity". McGraw-Hill, New York 1975.

[52] R. Prozarov, E.R. Yacoby, I. Felner and Y. Yeshurun. Physica C **233**(1994) 367.

[53] Charles P. Bean, Rev. Mod. Phys. **36**(1964) 31.

[54] P.W. Anderson. Phys. Rev **124**(1961) 41.

[55] A.B. Kaiser, J. Phys. C **3**(1970) 410.

[56] M.J. Zuckermann, Phys. Rev **140**(1965) A899; C.F. Ratto and A. Blandin, Phys. Rev. **156**(1967) 513; K. Takanaka and F Takano, Prog. Theor. Phys., Japan. **36**(1966) 1080.

[57] F.C.C. Kao and Gwyn Williams, J. Phys F **4**(1974) 419.

[58] K.P. Sinha and S.L. Kakani, "Magnetic Superconductors: Recent Developments". Nova Science Publishers Inc., New York 1989.

[59] A.A. Abrikosov and L.P. Gorkov, Sov. Phys JETP **12**(1961) 1243.

[60] X.Z. Xhou, H.P. Kunkel, P.A. Stampe and Gwyn Williams, J. Appl. Phys. **79**(1996) 6561.

[61] Z. Altouinian, E. Batalla, and J.O. Ström-Olsen, J. Appl. Phys. **59**(1986) 2364.

[62] D.H. Ryan, J.M.D. Coey, Z. Altouinian, E. Batalla, and J.O. Ström-Olsen, Phys. Rev. B. **35**(1987) 8630.

[63] Z. Wang, Ph.D. Thesis, University of Manitoba, 1991.

[64] McAlister S P 1984 J.Phys.F **14** 2167.

[65] H.E.N Stone, J. Phys. E. **4**(1971) 1058.

[66] K.C. Thompson-Russell and J.W. Edington, "Electron Microscope Specimen Preparation Techniques in Materials Science". Philips: Eindhoven 1977.

[67] W.B. Muir and J.O. Ström-Olsen, J. Phys. E **9**(1976) 163.

[68] I. Maartense, Rev. Sci. Instrum. **41**(1970) 657.

[69] R.M. Roshko, Ph.D. Thesis, University of Manitoba, 1979.

[70] C.J. Schinkel and W.D. Van Amstel, Phys. Lett., 44A,**7**(1973) 467.

[71] D. Wang, Master's Thesis, University of Manitoba, 1994.

[72] J.A. Osborn, Phys. Rev. **67**(1945) 351.

[73] Lillian Hoines, Ph.D. Thesis, Michigan State University, 1994.

[74] B.R. Coles in "Amorphous Ferromagnetism". ed. H. Hooper and A. de Graaf. Plenum Press, New York 1973.

[75] P. Hansen, "Handbook of Magnetic Materials" Vol. 6. ed. E.P. Wohlfarth. North Holland, Amsterdam 1991.

[76] B.M. Boerstel, J.E. Van Dam and G.J. Nieuwenhuys, Ch VI, "Magnetism: Selected Topics". Ed. Simon Foner, Gordon and Breach Scientific Publishers, New York 1976.

[77] J.A. Mydosh and G.J. Nieuwenhuys, Ch. 2, "Ferromagnetic Materials" Vol. 1. Ed. E.P. Wohlfarth, North-Holland Publishing Co., Amsterdam 1980.

[78] D.H. Ryan, J.O. Ström-Olsen, R. Provencher and M. Townsend. J. Appl. Phys. **64**(1985) 5787.

[79] A.B. Harris, J. Phys. C. **7**(1974) 1671.

[80] S.N. Kaul, J. Mag. Mag. Matter. **53**(1985) 5.

[81] S.C. Ho, I. Maartense and Gwyn Williams. J. Phys. F: Metal Phys. **11**(1981) 1107.

[82] H. Ma, Master's Thesis, University of Manitoba, 1989.

[83] G.K. White and S.B. Woods. Phil. Trans. R. Soc. A **251**(1959) 273.

[84] A. Hamzić, Ph.D. Thesis, Universite de Paris-Sud, 1980.

[85] Jian-Qiang Wang, Peng Xiong and Gang Xiao. Phys. Rev. B **47** (1993) 8341.

[86] S.Senoussi, I.A. Campbell, and A. Fert, Solid State Commun. **21**(1977) 269.

[87] P. Lederer and D.L. Mills. Phys. Rev. **165**(1968) 837; A.B. Kaiser and S. Doniach. Int. J. Mag. **1**(1970) 11; A. Blandin,"Magnetism" Vol. 5. Ed. G.T. Rado and H Suhl. Academic Press, New York, 1973.

[88] L.L. Hirst. Phys. Kondens. Matt. **11**(1970) 255; G. Williams. Sol. State Commun. **19** 821.

[89] J.B. Perrier, B. Tissier and R. Tournier. Phys. Rev. Lett. **24**(1970) 313.

[90] G.G. Robbins, H. Claus and P.A. Beck. Phys. Rev. Lett. **22**(1969) 1307.

[91] A. Amamou, F. Gautier and B. Loegel. J. Phys F: Metal Phys. **5** (1975) 1342.

[92] T.J. Hicks, B. Rainford, J.S. Kouvel, G.G. Low and J.B. Comly. Phys. Rev. Lett. **22**(1969) 531.

[93] P.A. Beck and H. Claus. J. Research (NBS). **74A**(1970) 449.

[94] F. Acker and R. Huguenin. Physics Letters. **33A**(1972) 343.

[95] H. Claus. Phys. Lett. **51A**(1975) 283.

[96] C.J. Tranchita and H. Claus. Solid. State Commun. **27**(1978) 583.

[97] L.E. Hedman and R.D. Mattuck. J. Phys. Chem. Solids. **23**(1962) 955.

[98] D.W. Carnegie, Jr, C.J. Tranchita and H. Claus. J. Appl. Phys. **50**(1979) 7318.

[99] R.M. Catchings III, R.J. Borg and C.E. Violet. J. Appl. Phys. **57**(1985) 3435.

[100] H.M. Ahmad and D. Grieg. J. de Phys. **C4**(1974) 223.

[101] J. Crangle and P.J.L. Butcher. Phys. Lett. **32A**(1970) 80.

[102] R.W. Houghton, M.P. Sarachik and J.S. Kouvel. Phys. Rev. Lett. **25**(1970) 238.

[103] H. Boghossian, B.V.B. Sarkissian and B.R. Coles. Inst. Phys. Conf. Ser. **55** Ch. 4 pg 303 (1981).

[104] H. Claus and C.J. Tranchita, J. de Phys. Colloq. **C6**(1978) 858.

[105] S.C. Ho, I. Maartense and Gwyn Williams, J. Phys. F: Metal Phys. **11**(1981) 1107.

[106] M. Saran and Gwyn Williams. J. Phys. F: Metal Phys. **17**(1987) 731.

[107] Z. Wang, H.P. Kunkel and Gwyn Williams. J. Phys.: Condens. Matter **2**(1990) 4173.

[108] S.N. Kaul. J. Phys. F.: Metal Phys. **7**(1977) 2091.

[109] S. Legvold, D.T. Peterson, P. Burgardt, R.J. Hofer, B. Lundell, T.A. Vyrostek and H. Gärtner. Phys. Rev. B **9**(1974) 2386.

[110] R.J. Cava, H. Tagaki, B. Batlogg, H.W. Zandbergen, J.J. Krajewski, W.F. Peck Jr, R.B. van Dover, R.J. Felder, T. Siegrist, K. Mizuhashi, J.O. Lee, H. Eisaki, S.A. Carter and S. Uchida. Nature **367**(1994) 146.

[111] T. Siegrist, H.W. Zandbergen, R.J. Cava, J.J. Krajewski and W.F. Peck Jr. Nature **367**(1994) 254.

[112] N.M. Hong, H. Michor, M. Vybornov, T. Holubar, P. Hundegger, W. Perthold, G. Hilscher and P. Rogl. Physica C **227**(1994) 85.

[113] A. Yatskar, N.K. Budra, W.P. Beyermann, P.C. Canfield and S.L. Bud'ko. Phys. Rev. B **54**(1996) R3772.

[114] R.M. Kadam, M.D. Sastry, Zakir Hossain, Chandan Mazumdar, R. Nagarajan, L.C. Gupta, C. Godart and R. Vijayaraghavan. Physica C **232**(1994) 359.

[115] J.L. Sarrao, M.C. de Andrade, J. Hermann, S.H. Han, Z. Fish, M.B. Maple and R.J. Cave. Physica C **229**(1994) 163.

[116] David J. Singh. Phys. Rev. B **50**(1994) 6486.

[117] B.K. Cho, Ming Xu, P.C. Canfield, L.L. Miller, D.C. Johnston, W.P. Beyermann and A. Yatskar. Phys. Rev. B **52**(1995) 3684.

[118] B.K. Cho, P.C. Canfield, L.L. Miller and D.C. Johnston. Phys. Rev. B **52**(1995) 3676.

[119] P.C. Canfield, B.K. Cho, D.C. Johnston, D.K. Finnemar and M.F. Hundley. Physica C **230**(1994) 397.

[120] R. Movshovich, M.F. Hundley, J.D. Thompson, P.C. Canfield, B.K. Cho and A.V. Chubukov. Physica C **227**(1994) 381.

[121] S.B. Roy, Z. Hossain, A.K. Pradhan, C. Mazumdar, P. Chaddah, R. Nagarajan, C. Godart and L.C. Gupta. Physica C **228**(1994) 319.

[122] H. Takagi, R.J. Cava, H. Eisaki, J.O. Lee, K. Mizuhashi, B. Batlogg, S. Uchida, J.J. Krajewski and W.F. Peck, Jr. Physica C **228**(1994) 389.

[123] L.F. Mattheiss. Phys. Rev. B **49**(1994) 13279.

[124] S.L. Bud'ko, M. El Massalami, M.B. Fontes, J. Mondragon, W. Vanoni, B. Giordanengo and E.M. Baggio-Saitovitch. Physica C **243**(1995) 183.

[125] C.C. Hoellworth, P. Klavins and R.N. Shelton. Phys.Rev. B**53**(1996) 2579.

[126] H. Schmidt, M. Müller and H.F. Braun. Physica C**235**(1994) 779.

[127] Ming Xu, P.C. Canfield, J.E. Ostenson, D.K. Finnemore, B.K. Cho, Z.R. Wang and D.C. Johnston. Physica C**227**(1994) 321.

[128] J.I. Lee, T.S. Zhao, I.G. Kim, B.I. Min and S.J. Youn. Phys. Rev. B **50**(1994) 4030.

[129] J.C. Phillips. "High T_c Superconductors". Academic Press, Inc. Boston 1989.

[130] G. Xiao, G.Q. Gond, C.L. Canedy, E J McNiff,Jr. and A Gupta , J. Appl. Phys., to be published)

[131] K.H.J. Buschow, in "Ferromagnetic Materials" Vol. 1. Ed. E.P. Wohlfarth. North-Holland Press, Amsterdam, 1980.

[132] H.P. Kunkel, M.S. Westmore and Gwyn William. Philos. Mag. B **65**(1992) 1207.

[133] S.J. Kennedy, P.J. Brown and B.R. Coles, J.Phys.:Condens. Matter **5**(1993) 5169.

[134] O. Eriksson, L. Nordström, M.S.S. Brooks and B. Johansson. Phys. Rev. Lett. **60**(1988) 2523.

[135] Hirofumi Wada, Masahito Nishigori and Masayuki Shiga, J. Phys. Soc. Jpn. **62**(1993) 1337.

[136] S.J. Kennedy, A.P. Murani, B.R. Coles and O. Moze, J. Phys. F:Met. Phys. **18**(1988) 2499.

[137] S.J. Kennedy, A.P. Murani, J.K. Cockroft, S.B. Roy and B.R. Coles,J. Phys.: Condens. Matter 1(1989) 629.

[138] S.J. Kennedy and B.R. Coles, J. Phys. :Condens. Matter **2**(1990) 1213.

[139] A.K. Grover, R.G. Pillay, V. Balasubramanian and P.N. Tandon, J. de Phys. Colloq. **49**(1988) C8-281.

[140] Naushad Ali and Xianfeng Zhang, J. Phys.: Condens. Matter 4(1992) L351.

[141] D.F. Franceschini and S.F. da Cunha, J. Mag. Mag. Mater. **51**(1985) 280.

[142] S. Mukherjee, R. Ranganathan and B.R. Coles, Phys. Rev. B **50**(1994) 1084.

[143] S. Radha, S.B. Roy, A.K. Nigam and Girish Chandra, Phys. Rev. B **50**(1994) 6866.

[144] A Palenzona. J. Less-Comm. Metals **16**(1968) 379.

[145] H. Gamari-Seale, T. Anagnostopoulos and J.K. Yakinthos. J.Appl.Phys. **50**(1979) 434.

[146] S. Parviainen and S. Penttilä. Phys. Stat. Sol. **60**(1980) K119.

[147] C.S. Jee, C.L. Lin, T. Mihsalin and X.Q. Wang. J. Appl. Phys. **79**(1996) 5403.

[148] N.N. Delyagin, G.T. Mudzhiri, V.I. Nesterov and S.I. Reiman. Sov.Phys. JETP **59**(1982) 592.

[149] K. Motoya, H. Yasuoka, Y. Nakamura and J.H. Wernick. J. Phys. Soc. Jpn. **44**(1996) 1525.

[150] S.P. McAlister. J.Appl.Phys. **55**(1984) 2343.

[151] M. Saran, Gwyn Williams and S.P. McAlister. Solid State Comm. **57**(1986) 53.

[152] H.P. Kunkel, X.Z. Zhou, P.A. Stampe, J.A. Cowen and Gwyn Williams. Phys. Rev. B **53**(1996) 15099.

[153] H.P. Kunkel, X.Z. Zhou, P.A. Stampe, J.A. Cowen and Gwyn Williams. Phys.Rev. B **54**(1996) 16039.

[154] J.A. Cowen and Gwyn Williams, J. Mag. Mag. Mat. (in press).

[155] J Bews, A.W. Sheikh and Gwyn Williams. J. Phys. F: Metal Phys. **16**(1986) 1537.

[156] V.N. Antonov, A. Ya. Perlov, P.M. Openeer, A.N. Yaresko and S.V. Halilov. Phys. Rev. Lett. **77**(1996) 5253.

[157] Binder and Young

[158] Zhao et al., to be published

[159] F.T. Hedgecock, J.O. Ström-Olsen and D.F. Wilford, J. Phys. F: Metal Phys. **7**(1977) 855.

[160] Y. Ishikawa, R. Tournier and J. Filippi, J. Phys. Chem. Solids **26** (1965) 1727.

[161] B. Babic, F. Kajzar and G. Parette, J. Phys. Chem. Solids **41** (1980) 1303.

[162] S. Arajs and G.R. Dunmyre, J. Appl. Phys **37**(1966) 1017; S. Arajs and G.R. Dunmyre, J. Appl. Phys **38**(1967) 1892; S. Arajs, G.R. Dunmyre and S.J. Dechter, Phys. Rev. **154**(1967) 448.

[163] A. Hamzić, S. Senoussi, I.A. Cambell and A. Fert, Solid. State. Commun. **26** (1978) 617; A. Hamzić, S. Senoussi, I.A. Cambell and A. Fert, J. Mag. Mag. Mat. **15–18** (1980) 921; S. Senoussi, I.A. Cambell and A. Fert, Solid. State. Commun. **21** (1977) 269.

Appendix A

$Cu_{1-x}Ni_x$: Data Appendix

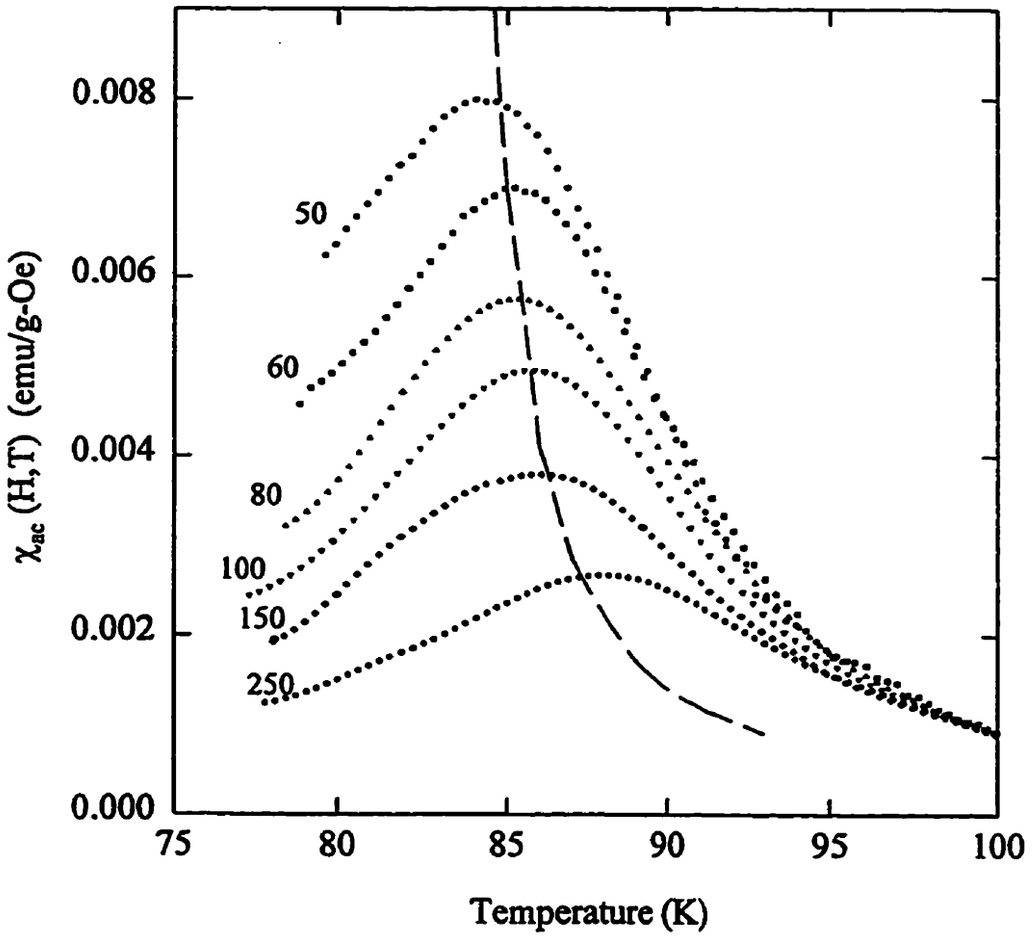

Figure A.1: The temperature dependence of the *ac* susceptibility in fixed biasing fields as labelled, in Oe, for the x=0.55 sample. The dashed line represents the crossover line, as discussed in the text.

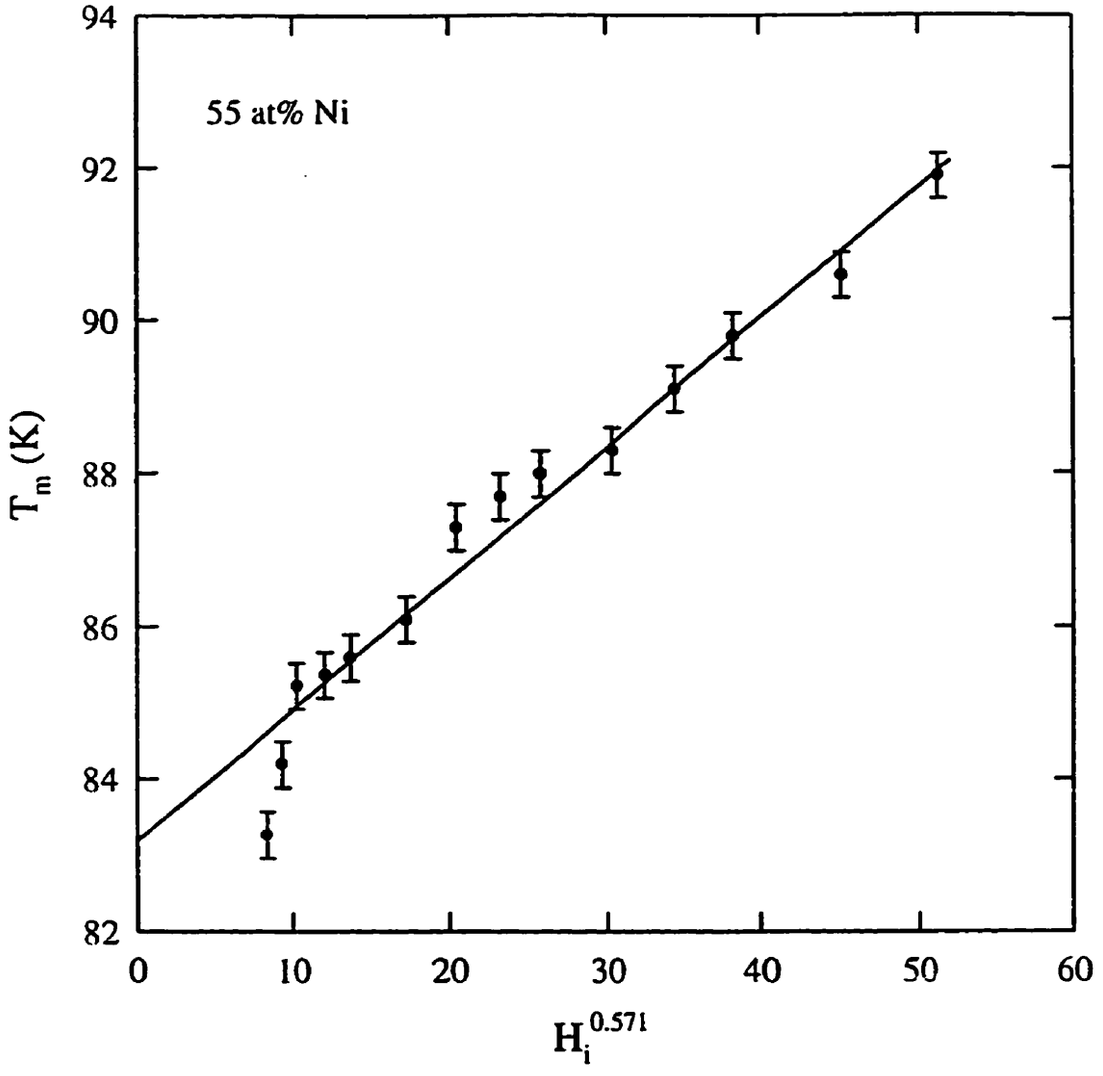

Figure A.2: Peak temperature as a function of internal field to the power of 0.571 for $Cu_{100-x}Ni_x$ with x=0.55. The superimposed line represents a fit to the data with T_c=83.2K.

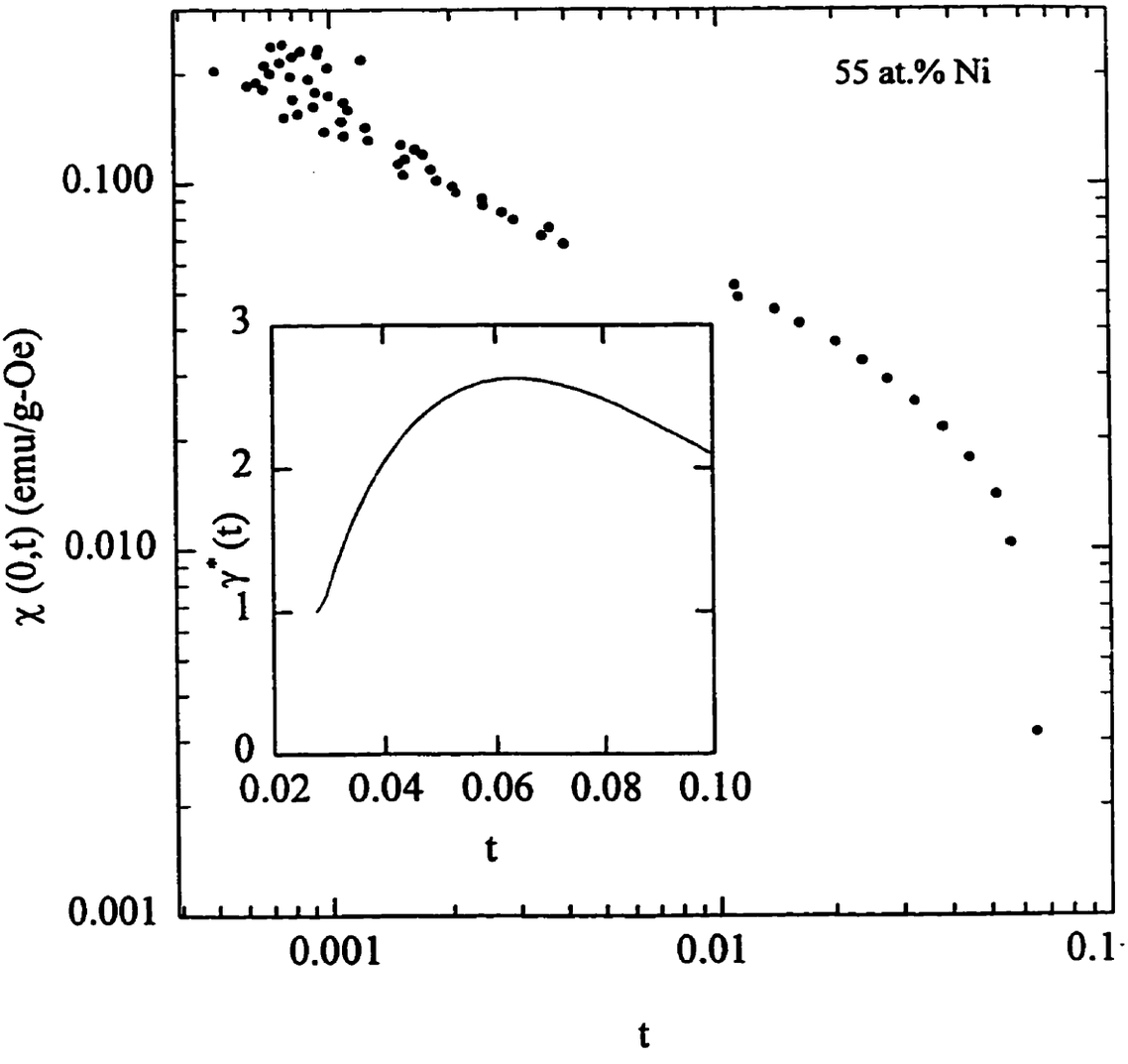

Figure A.3: The zero field susceptibility as a function of reduced temperature for the 55 at.% Ni sample. The inset shows the calculated effective exponent, $\gamma^*(t)$.

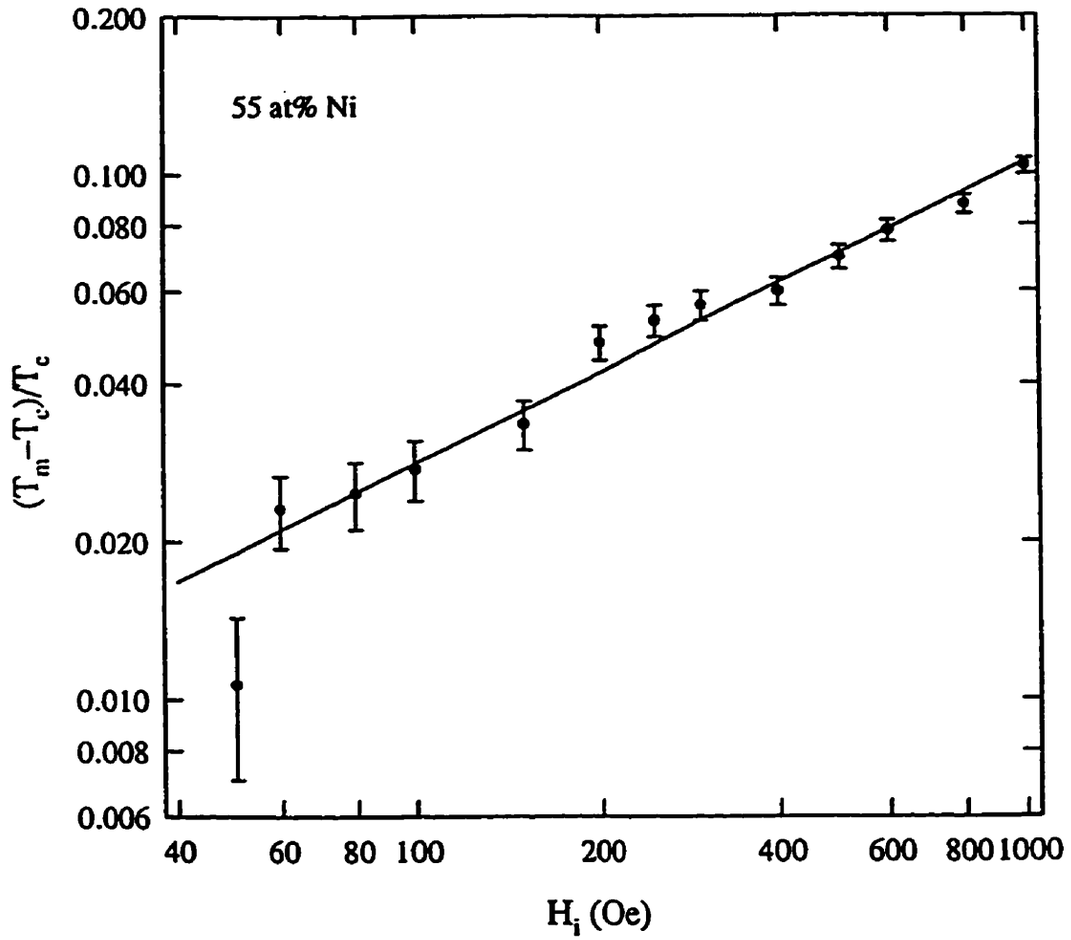

Figure A.4: Reduced peak temperature as a function of internal field for x=0.55. The superimposed line represents the 3D Heisenberg prediction, $1/(\gamma+\beta)$=0.571.

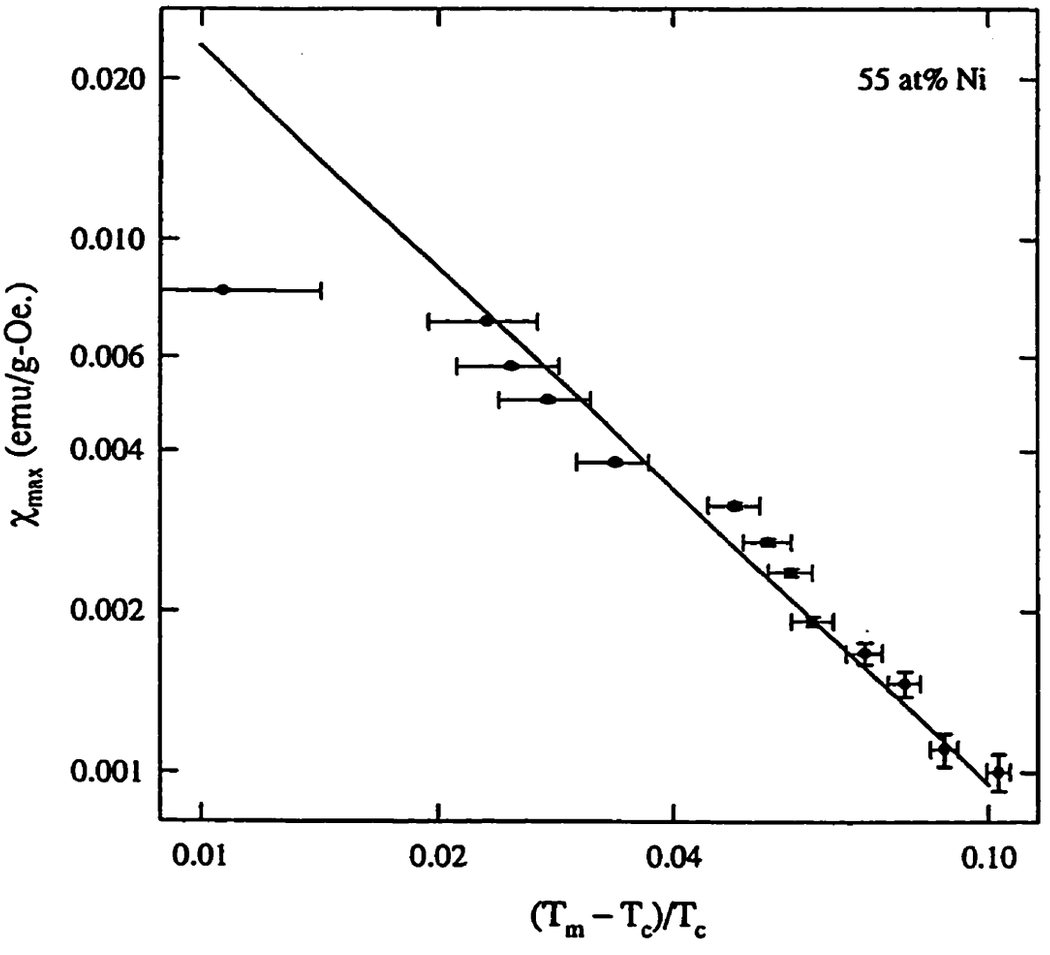

Figure A.5: Peak susceptibility as a function of reduced peak temperature for the 55 at.% Ni sample. The superimposed line represents the 3D Heisenberg value for γ=1.386.

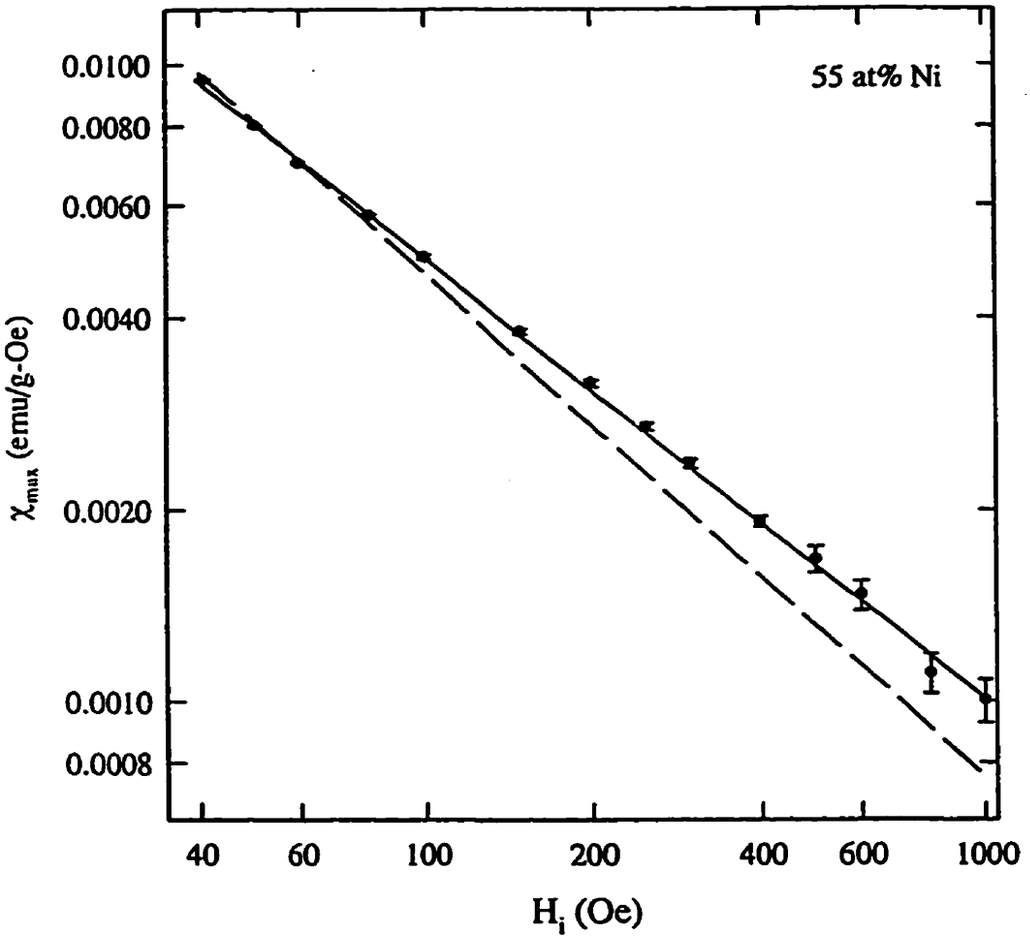

Figure A.6: Peak susceptibility as a function of internal field for the 55 at.% Ni sample. The solid line represents a fit to the data with δ=3.3(1). The dashed line shows a fit calculated using the 3D Heisenberg exponent, δ=4.8.

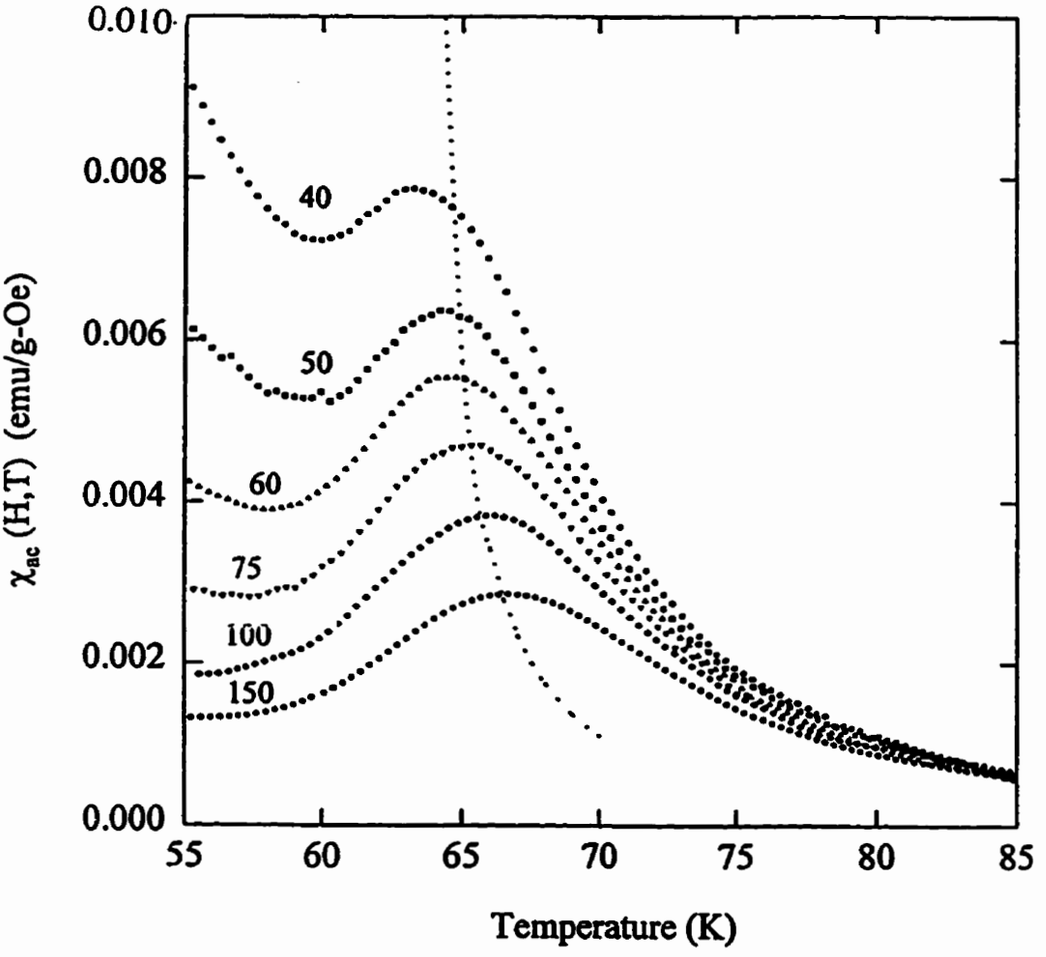

Figure A.7: The temperature dependence of the *ac* susceptibility in fixed biasing fields as labelled, in Oe, for the x=0.53 sample. The dotted line represents the crossover line, as discussed in the text.

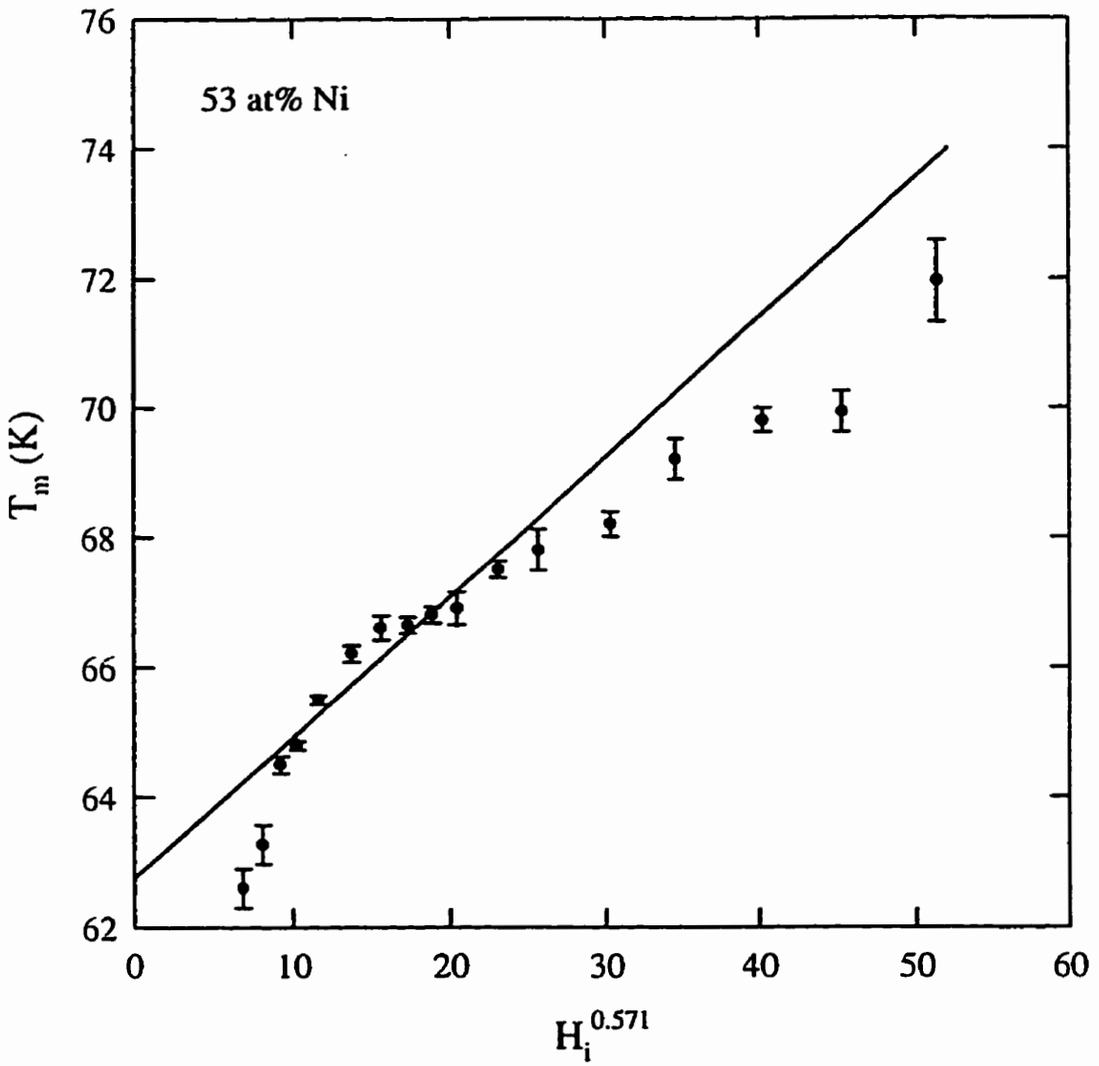

Figure A.8: Peak temperature as a function of internal field to the power of 0.571 for $Cu_{100-x}Ni_x$ with x=0.53. The superimposed line represents a fit to the data with T_c=62.8K.

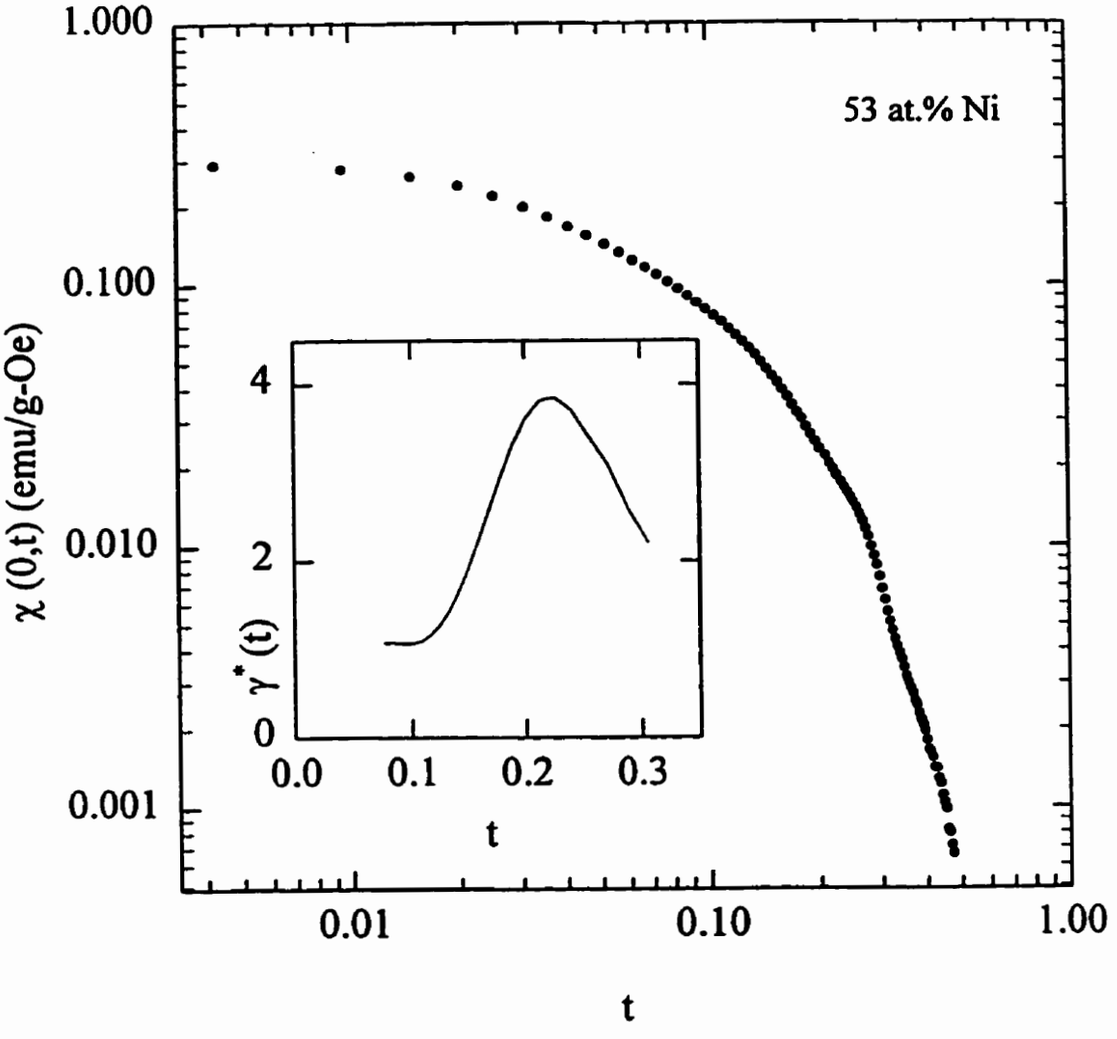

Figure A.9: The zero field susceptibility as a function of reduced temperature for the 53 at.% Ni sample. The inset shows the calculated effective exponent, $\gamma^*(t)$.

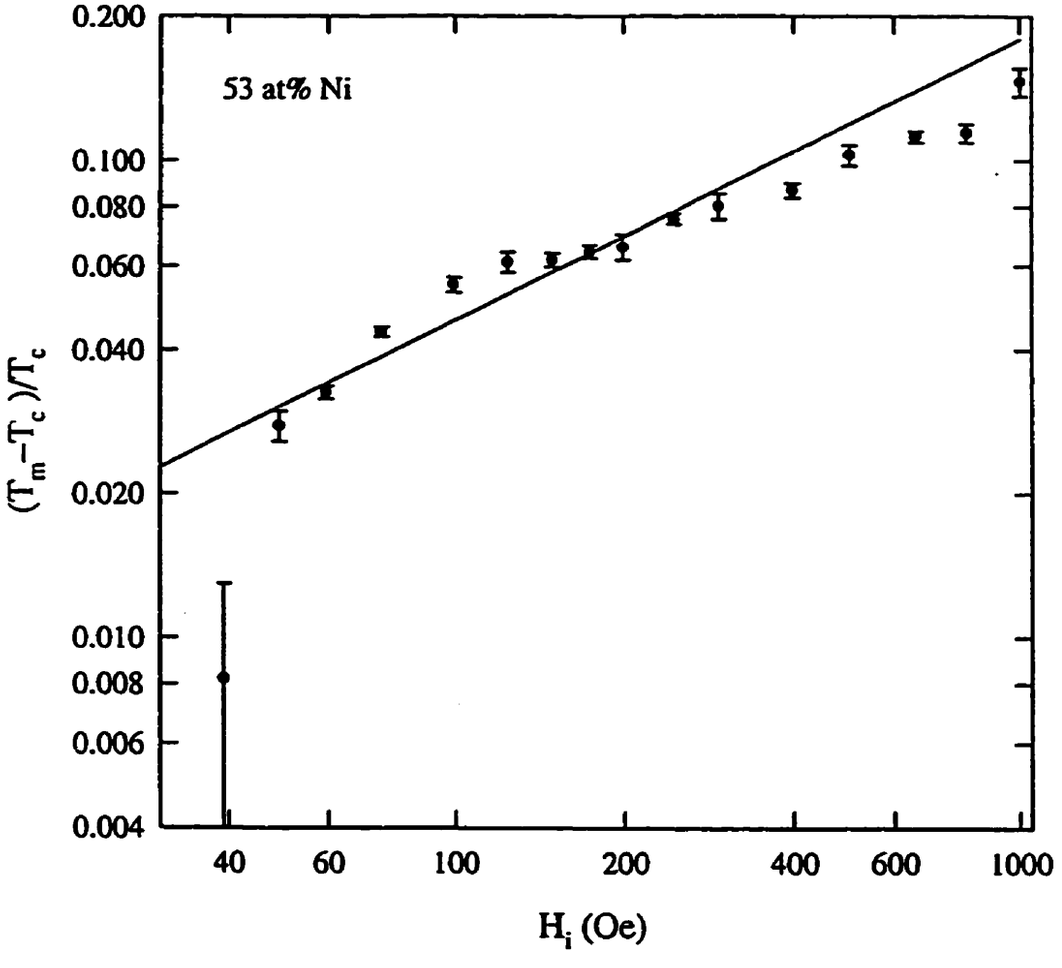

Figure A.10: Reduced peak temperature as a function of internal field for x=0.53. The superimposed line represents the 3D Heisenberg prediction, $1/(\gamma+\beta)$=0.571.

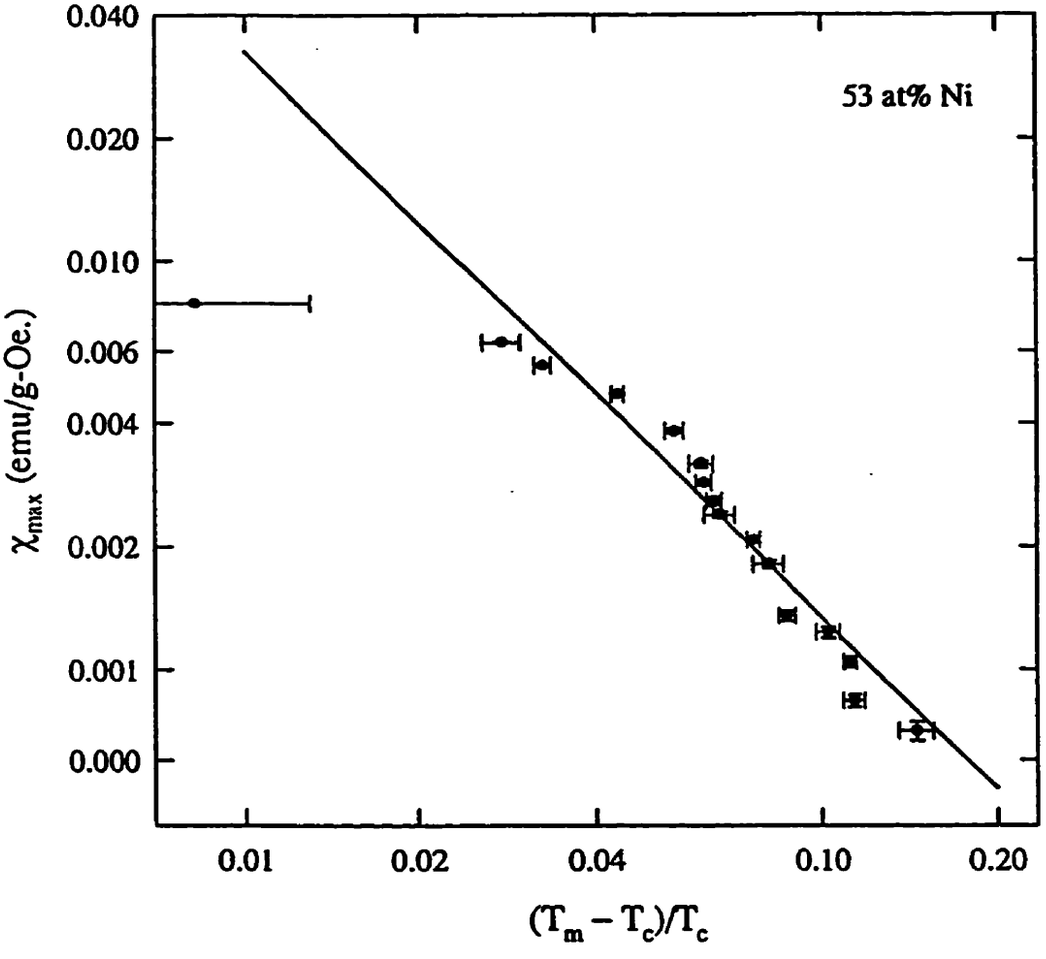

Figure A.11: Peak susceptibility as a function of reduced peak temperature for the 53 at.% Ni sample. The superimposed line represents the 3D Heisenberg value for γ=1.386.

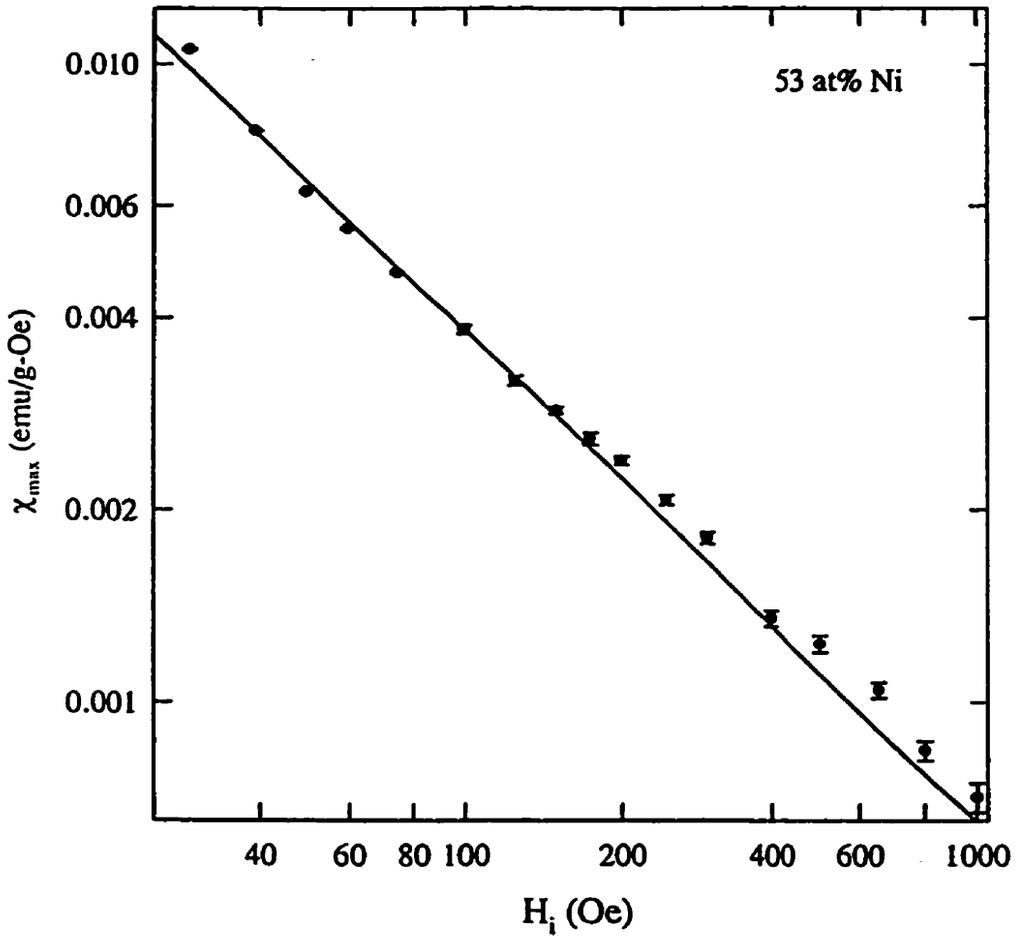

Figure A.12: Peak susceptibility as a function of internal field for the 53 at.% Ni sample. The solid line represents a fit to the data with δ=4.2(2).

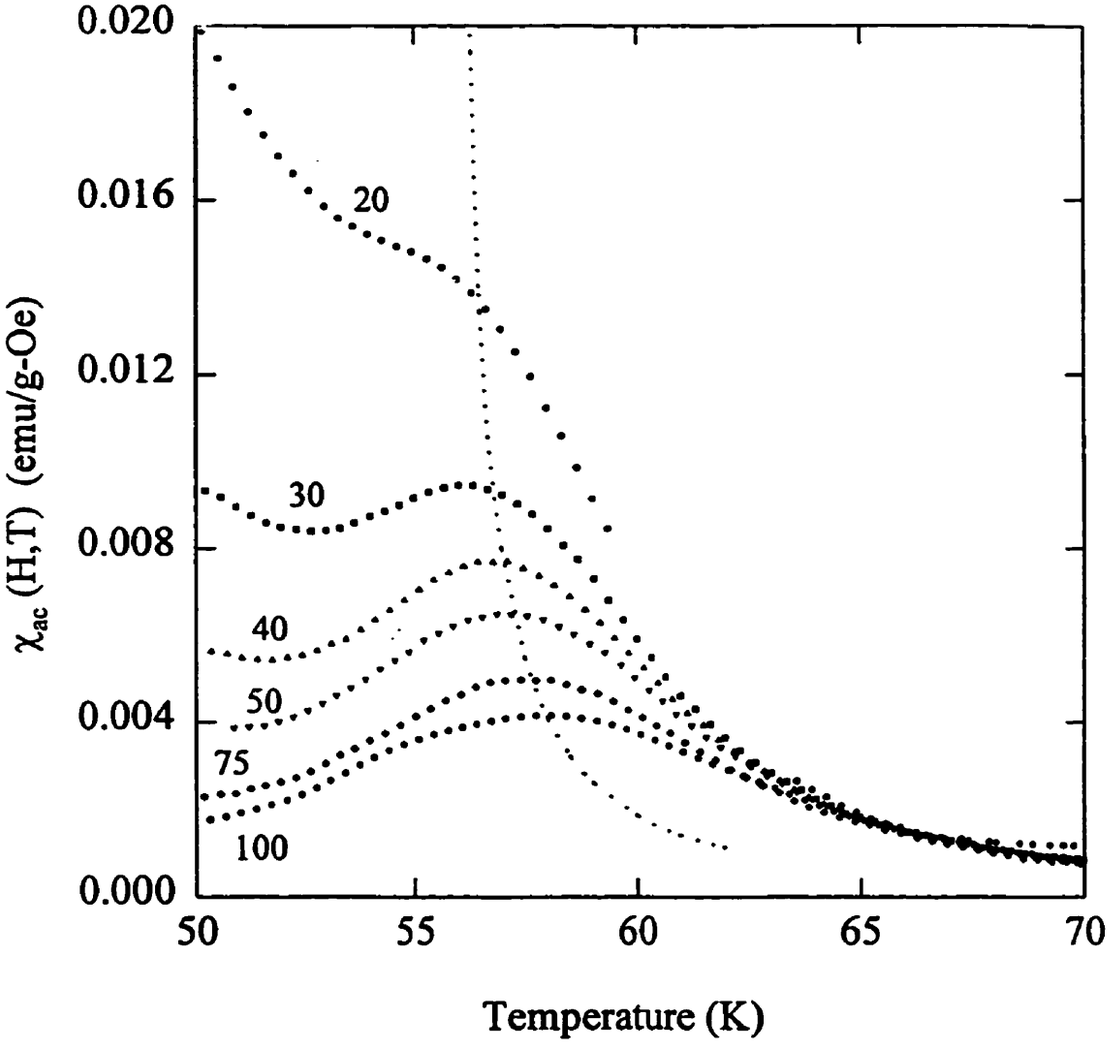

Figure A.13: The temperature dependence of the *ac* susceptibility in fixed biasing fields as labelled, in Oe, for the x=0.52 sample. The dotted line represents the crossover line, as discussed in the text.

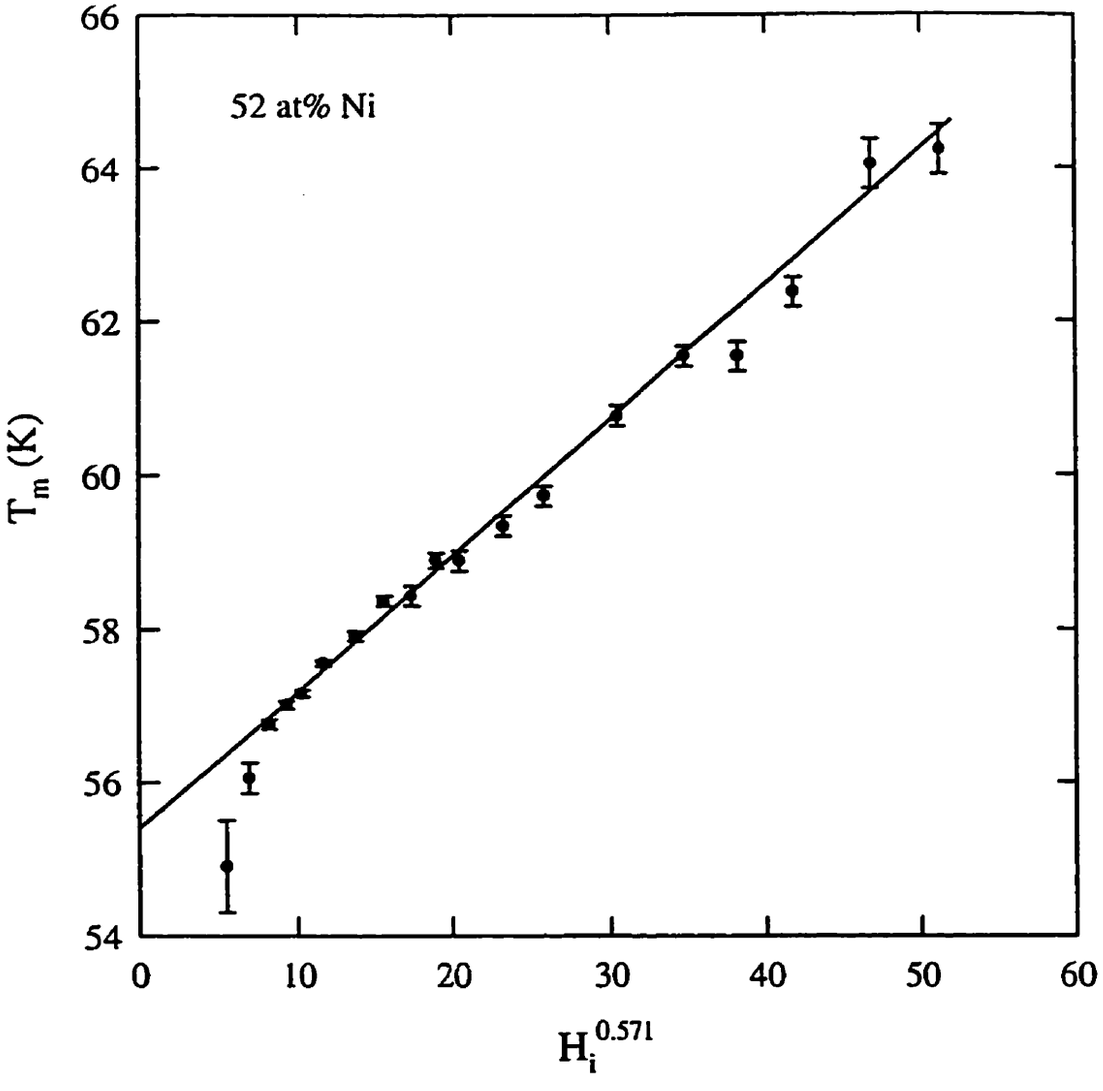

Figure A.14: Peak temperature as a function of internal field to the power of 0.571 for $Cu_{100-x}Ni_x$ with x=0.52. The superimposed line represents a fit to the data with T_c=55.4K.

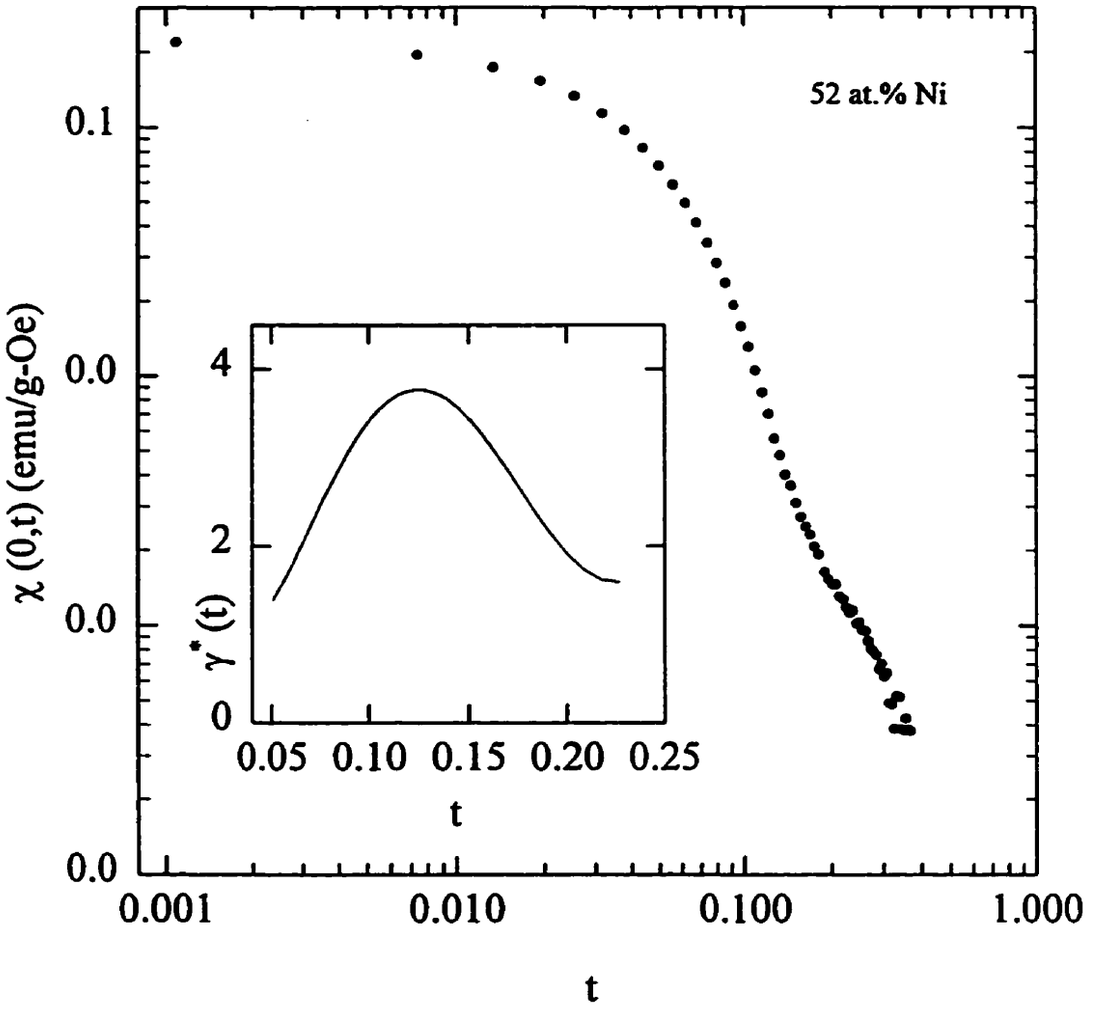

Figure A.15: The zero field susceptibility as a function of reduced temperature for the 52 at.% Ni sample. The inset shows the calculated effective exponent, $\gamma^*(t)$.

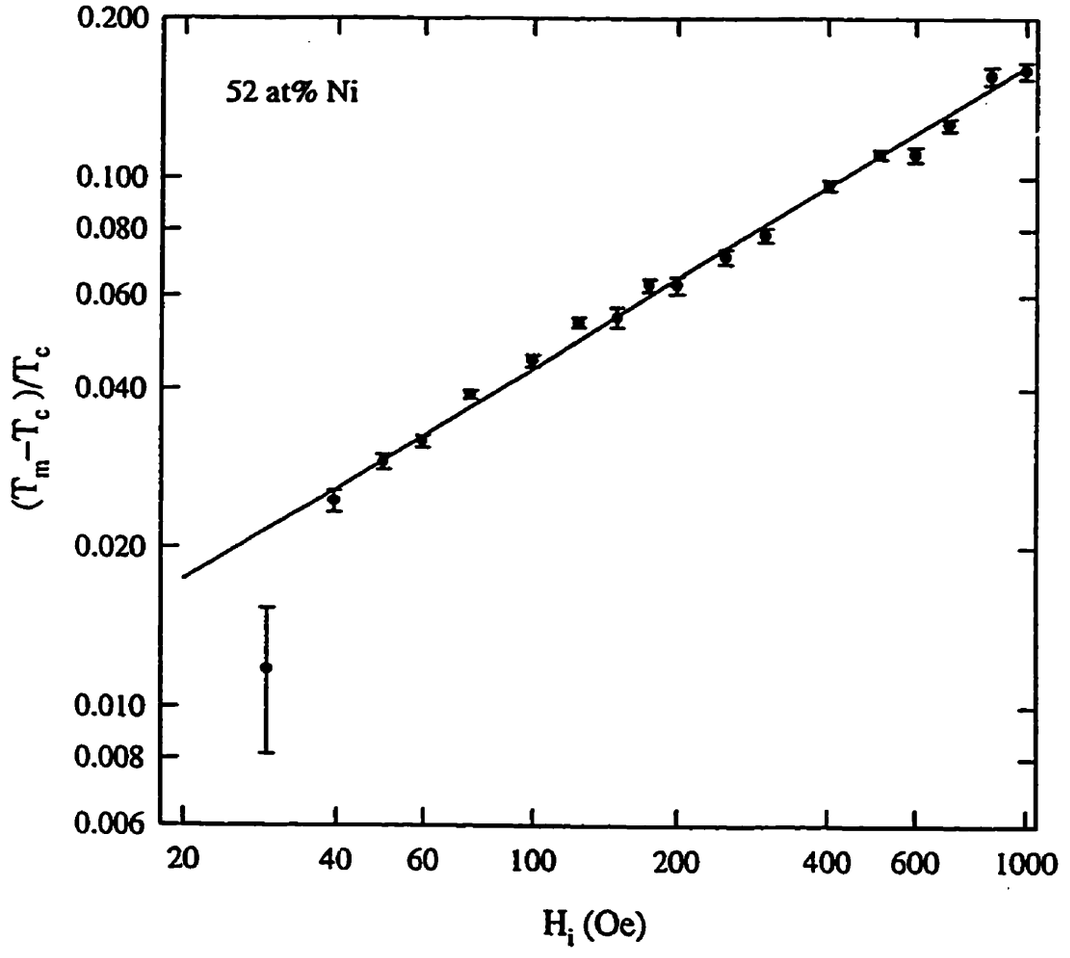

Figure A.16: Reduced peak temperature as a function of internal field for x=0.52. The superimposed line represents the 3D Heisenberg prediction, $1/(\gamma + \beta)$=0.571.

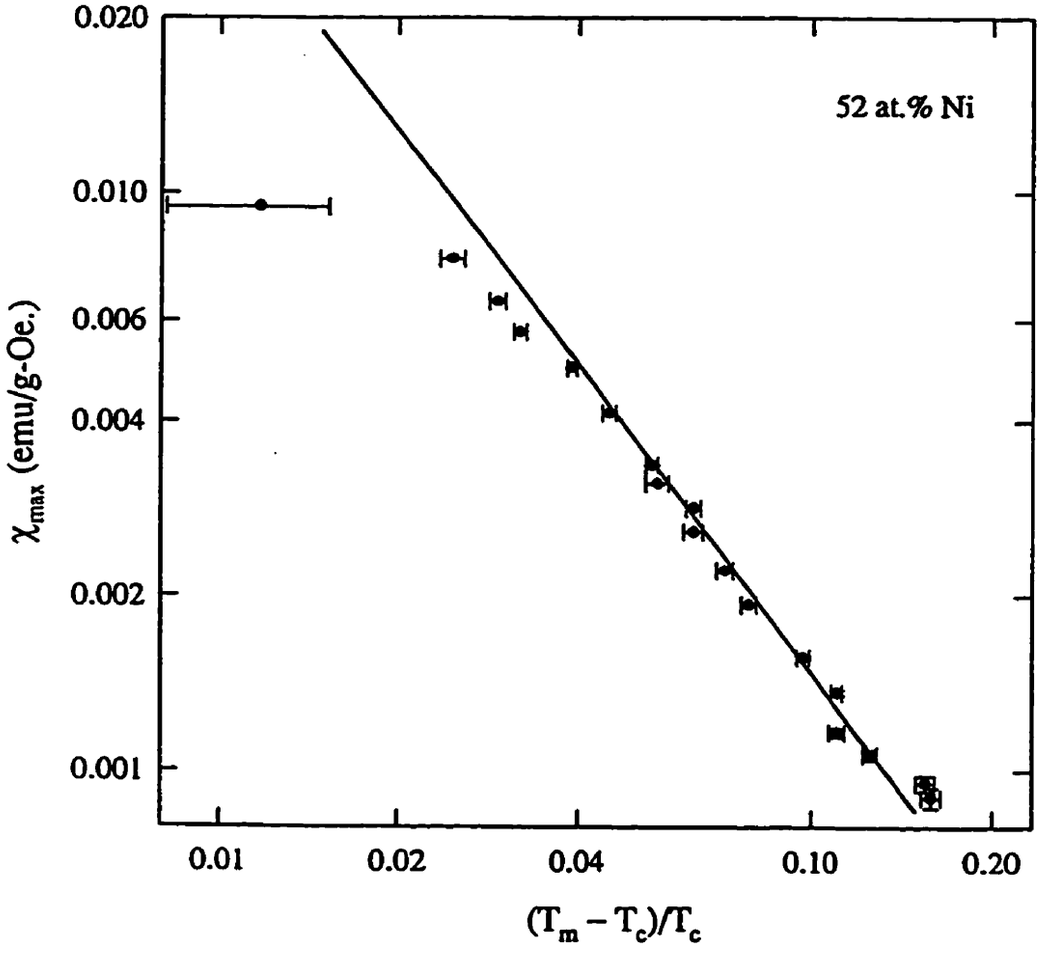

Figure A.17: Peak susceptibility as a function of reduced peak temperature for the 52 at.% Ni sample. The superimposed line represents the 3D Heisenberg value for γ=1.386.

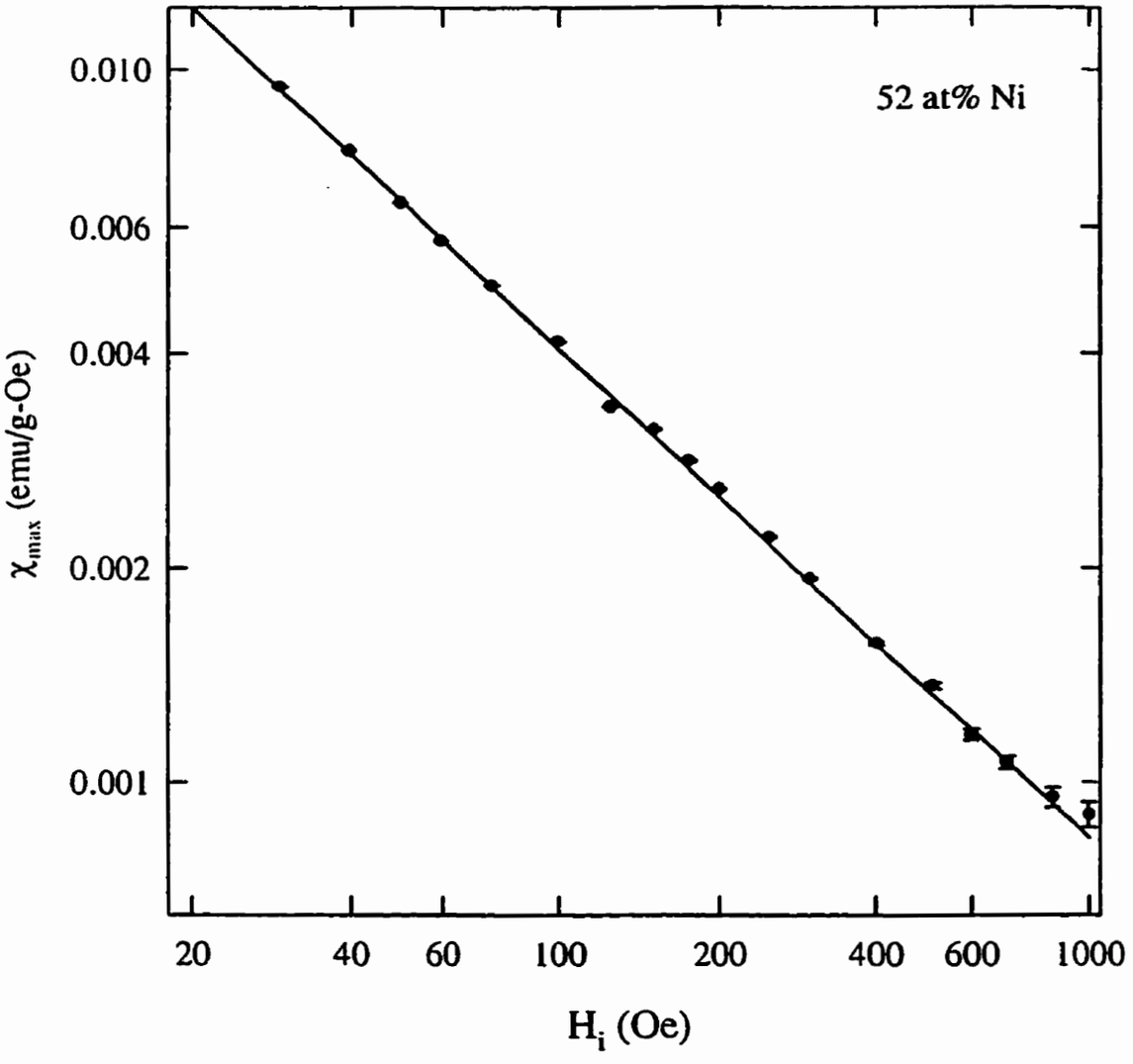

Figure A.18: Peak susceptibility as a function of internal field for the 52 at.% Ni sample. The solid line represents a fit to the data with δ=3.18(1).

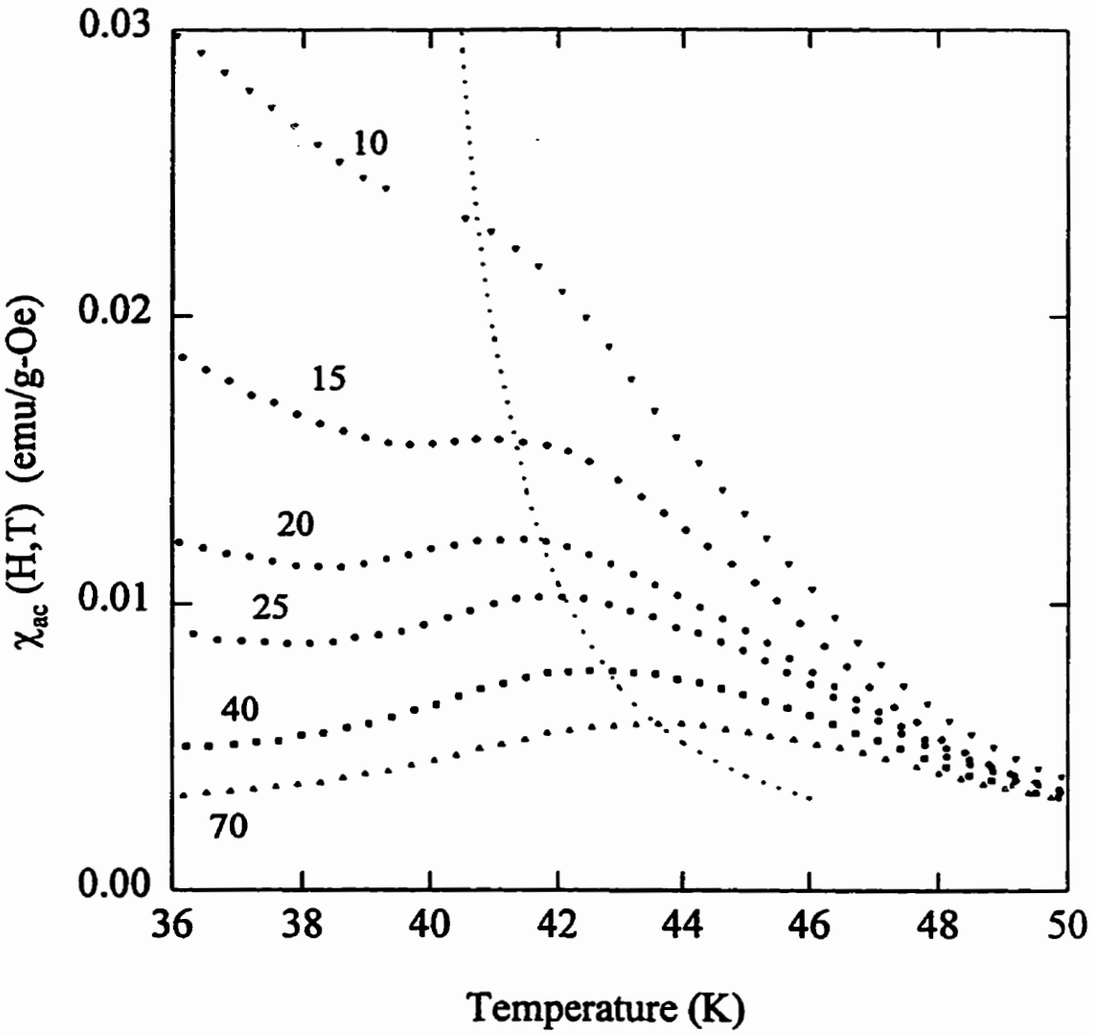

Figure A.19: The temperature dependence of the *ac* susceptibility in fixed biasing fields as labelled, in Oe, for the x=0.51 sample. The dotted line represents the crossover line, as discussed in the text.

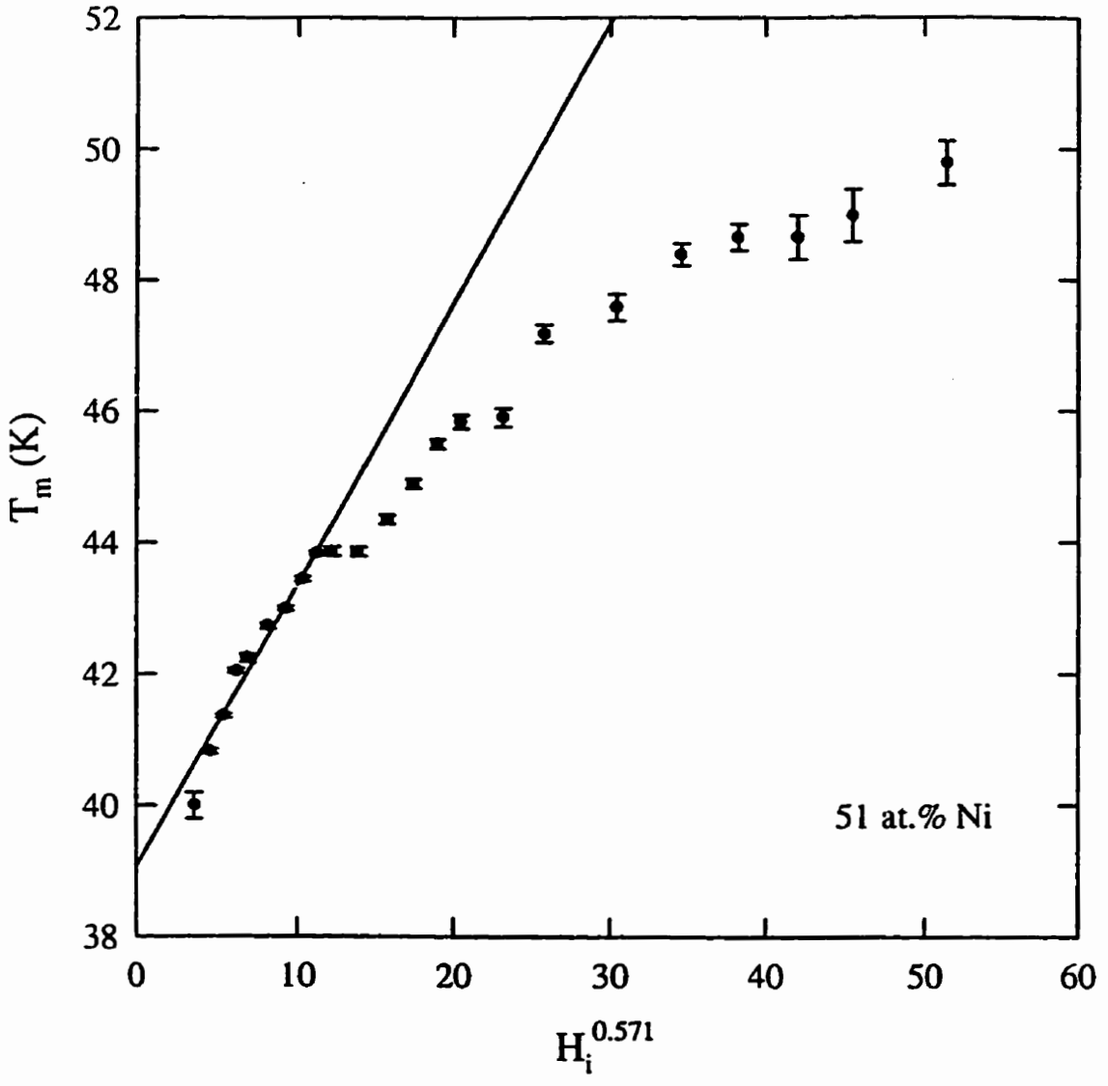

Figure A.20: Peak temperature as a function of internal field to the power of 0.571 for $Cu_{100-x}Ni_x$ with x=0.51. The superimposed line represents a fit to the data with T_c=39.1K.

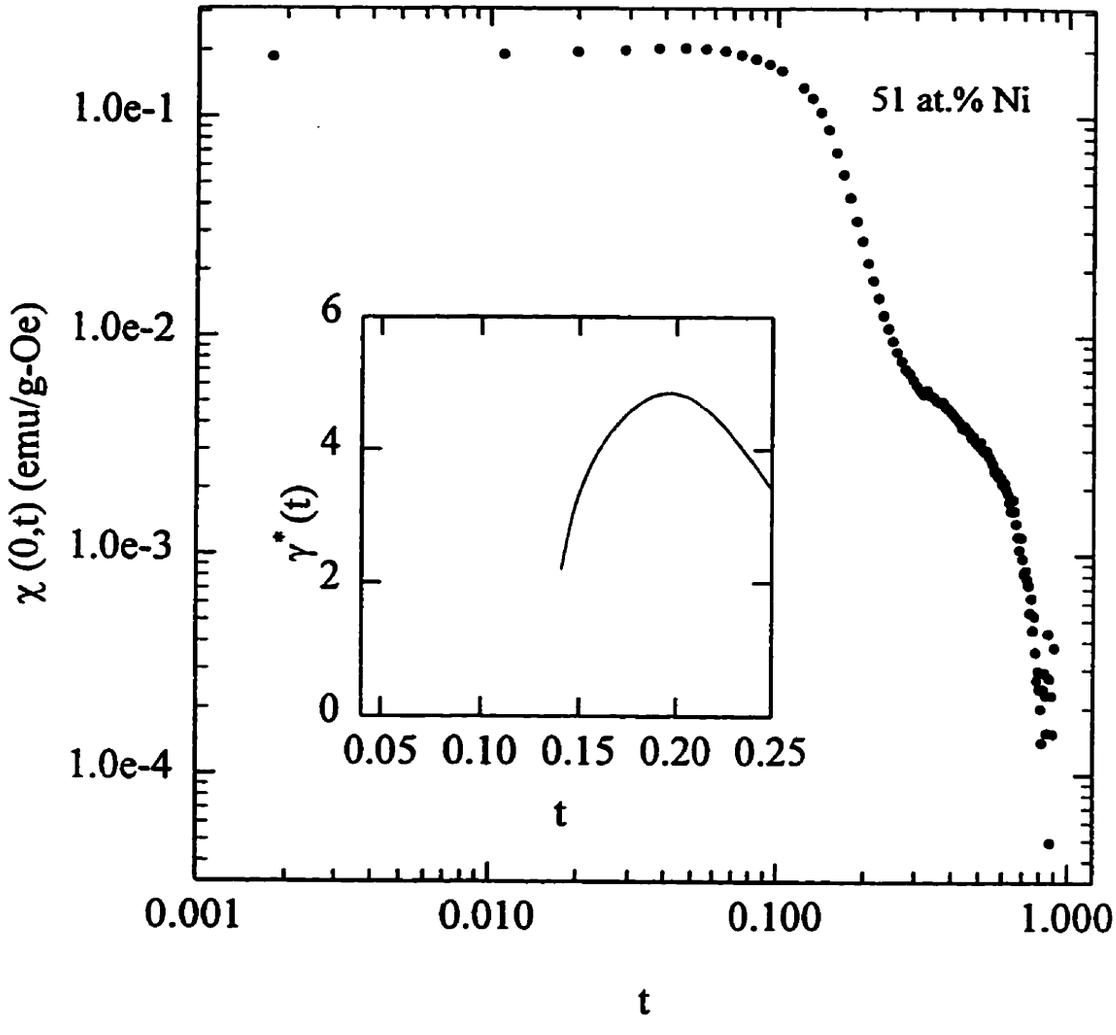

Figure A.21: The zero field susceptibility as a function of reduced temperature for the 51 at.% Ni sample. The inset shows the calculated effective exponent, $\gamma^*(t)$. The kink in the zero field data at high temperature is not understood.

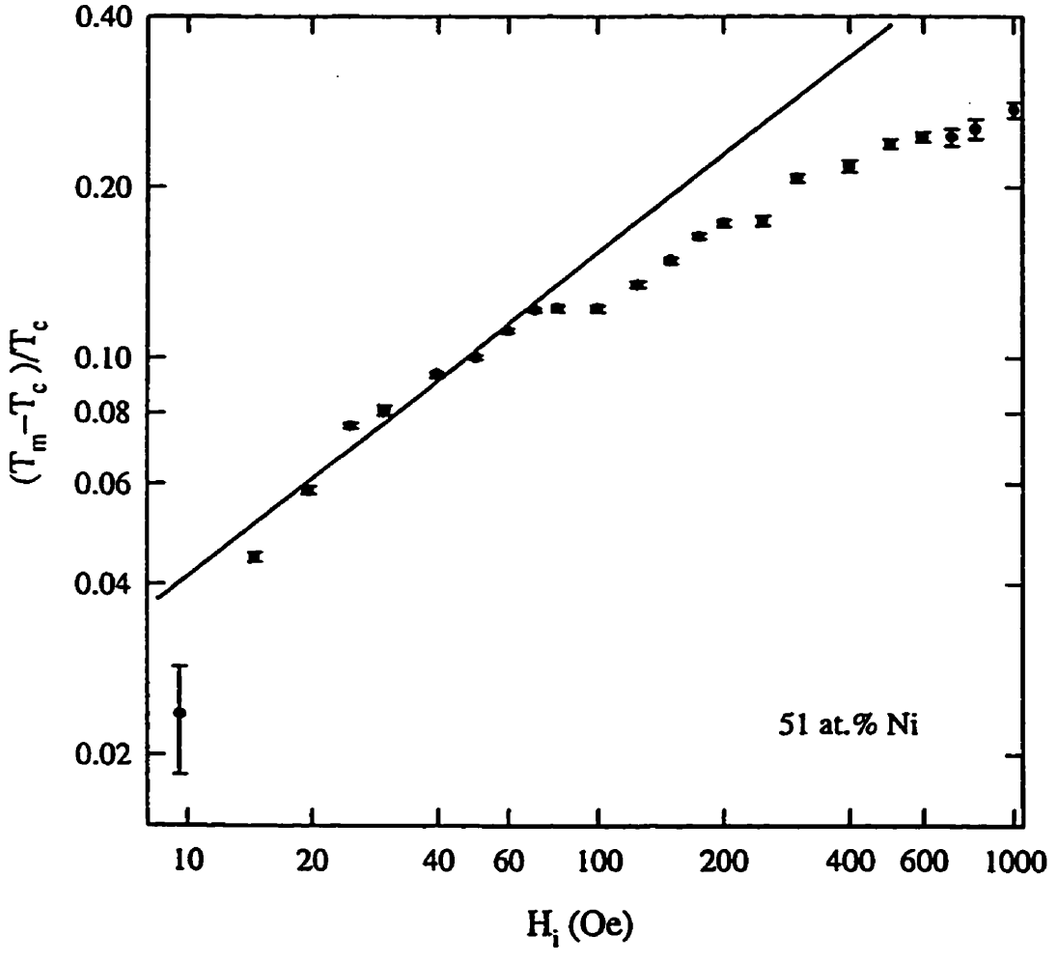

Figure A.22: Reduced peak temperature as a function of internal field for x=0.51. The superimposed line represents the 3D Heisenberg prediction, $1/(\gamma + \beta)$=0.571.

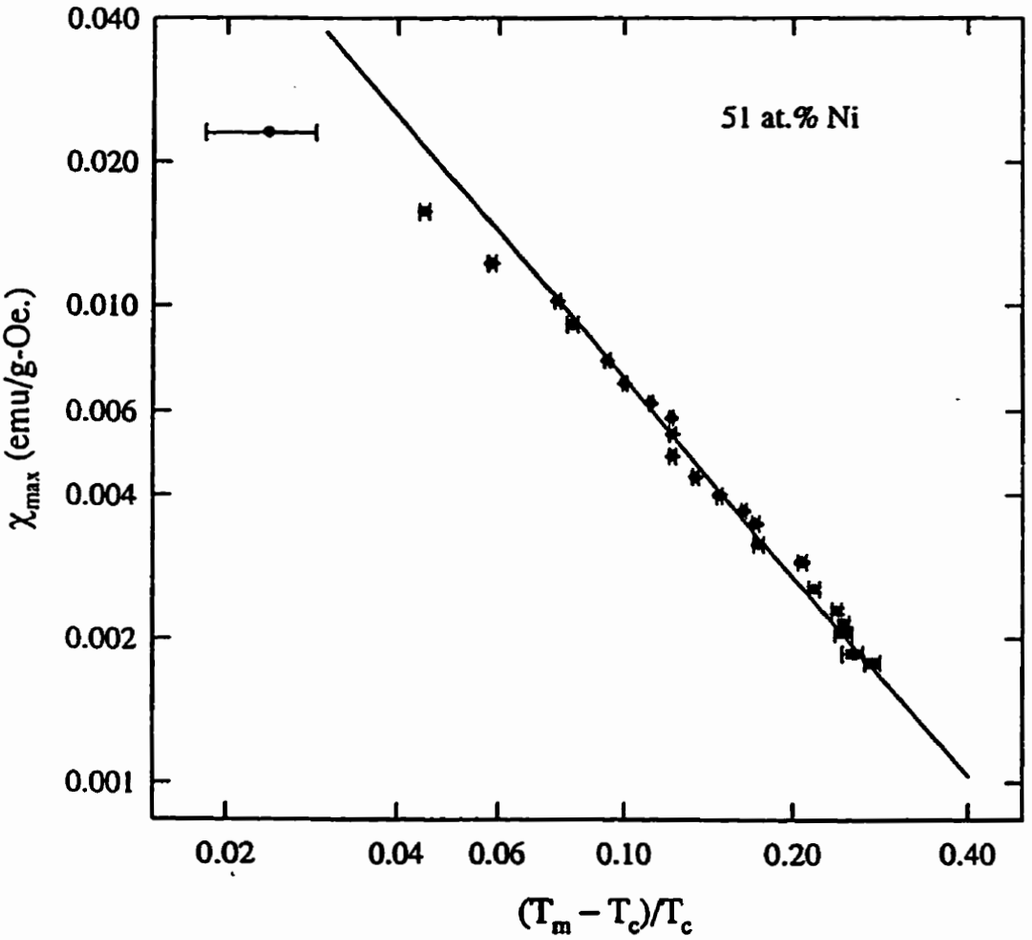

Figure A.23: Peak susceptibility as a function of reduced peak temperature for the 51 at.% Ni sample. The superimposed line represents the 3D Heisenberg value for γ=1.386.

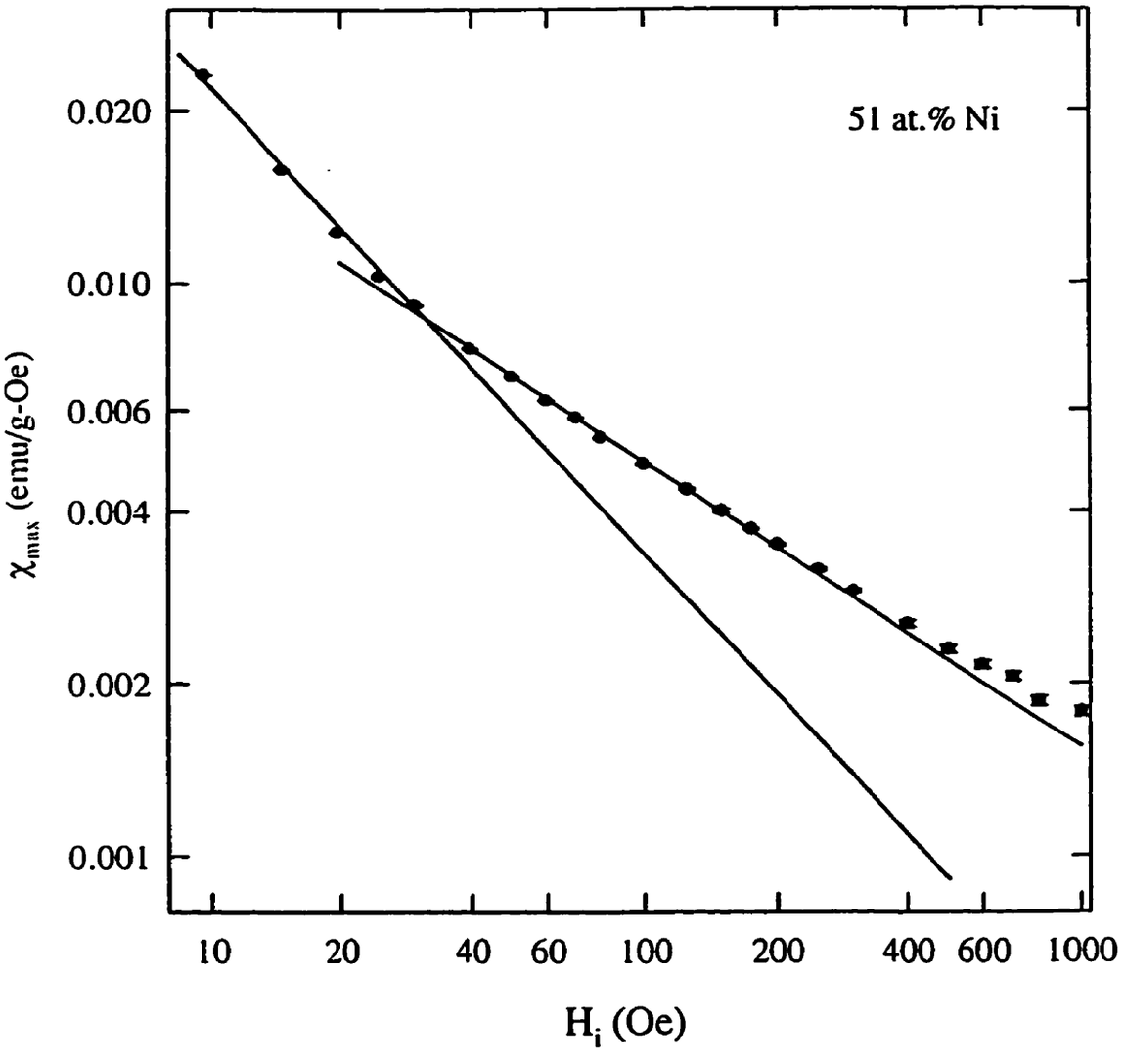

Figure A.24: Peak susceptibility as a function of internal field for the 51 at.% Ni sample. The solid line represents a fit to the high field data with δ=1.98(2). The dashed line shows a fit to the low field data using the 3D Heisenberg exponent, δ=4.8(1).

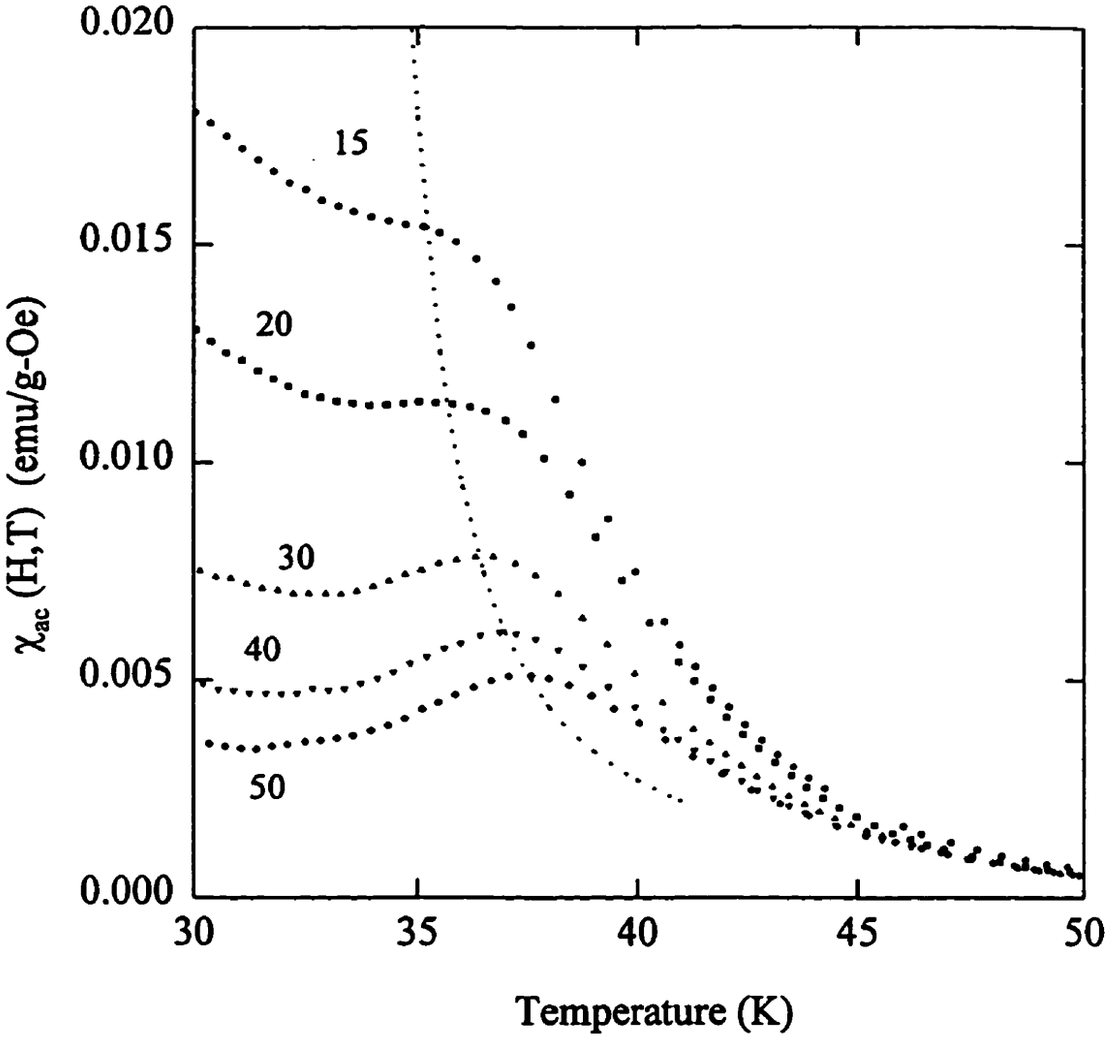

Figure A.25: The temperature dependence of the *ac* susceptibility in fixed biasing fields as labelled, in Oe, for the x=0.50 sample. The dotted line represents the crossover line, as discussed in the text.

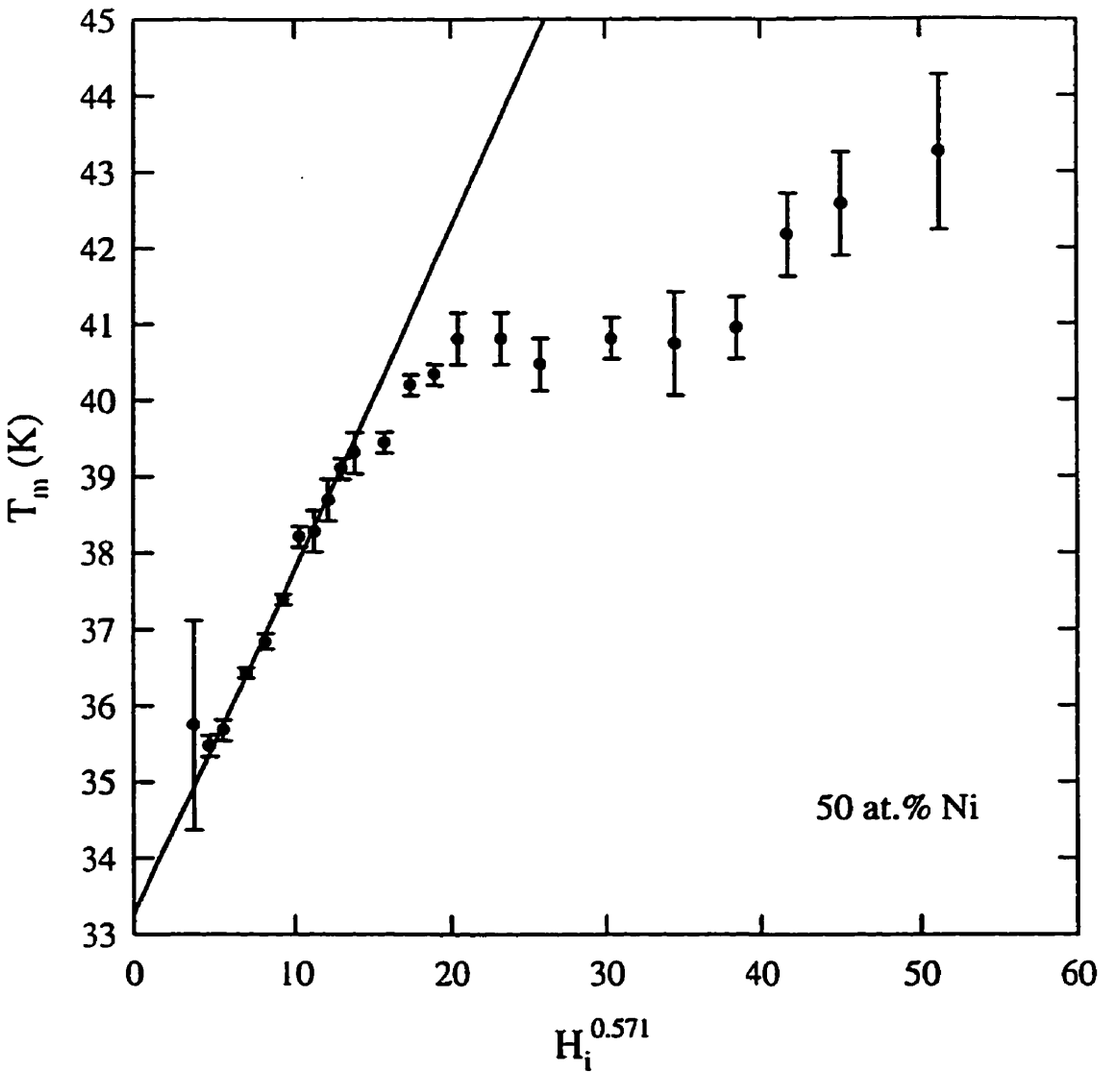

Figure A.26: Peak temperature as a function of internal field to the power of 0.571 for $Cu_{100-x}Ni_x$ with x=0.50. The superimposed line represents a fit to the data with T_c=33.3K.

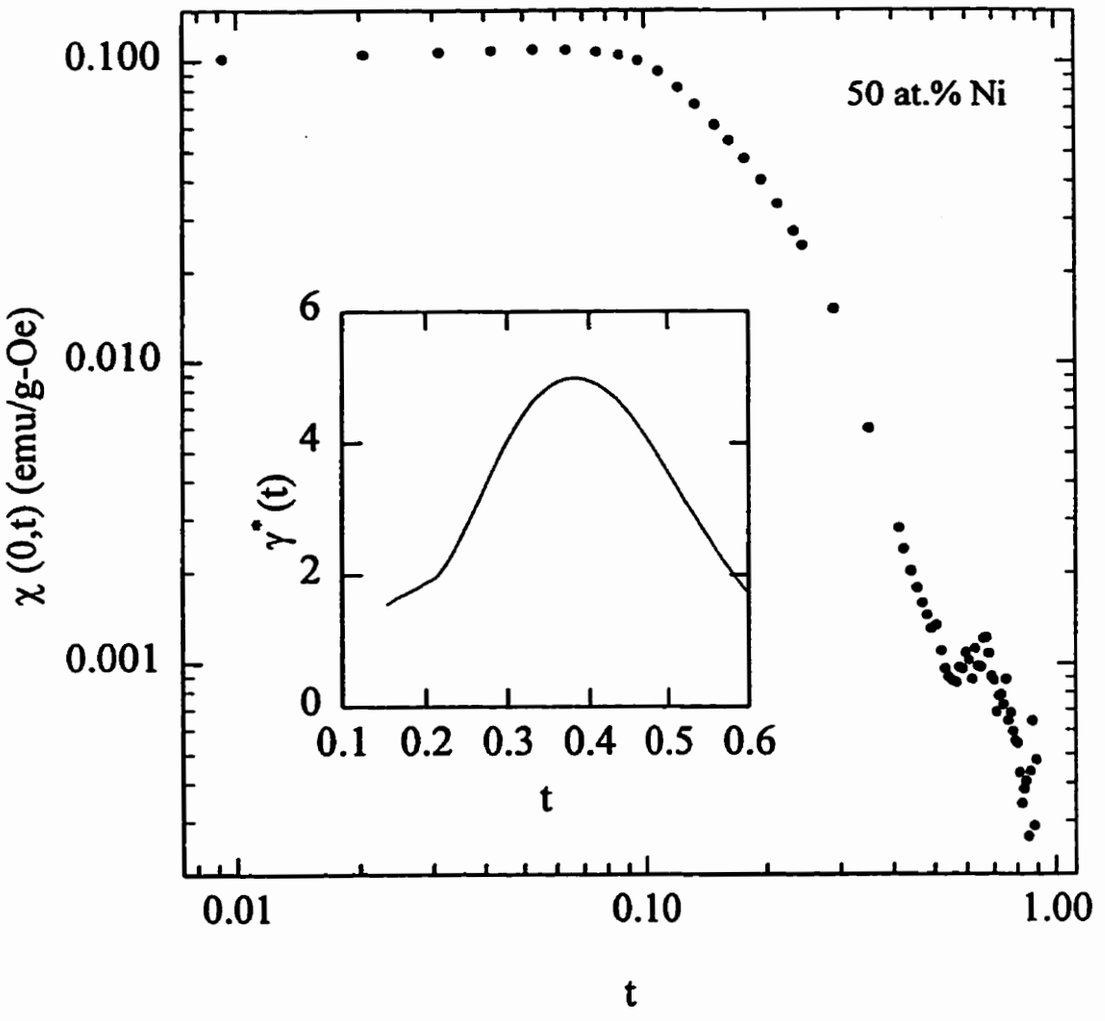

Figure A.27: The zero field susceptibility as a function of reduced temperature for the 50 at.% Ni sample. The inset shows the calculated effective exponent, $\gamma^*(t)$.

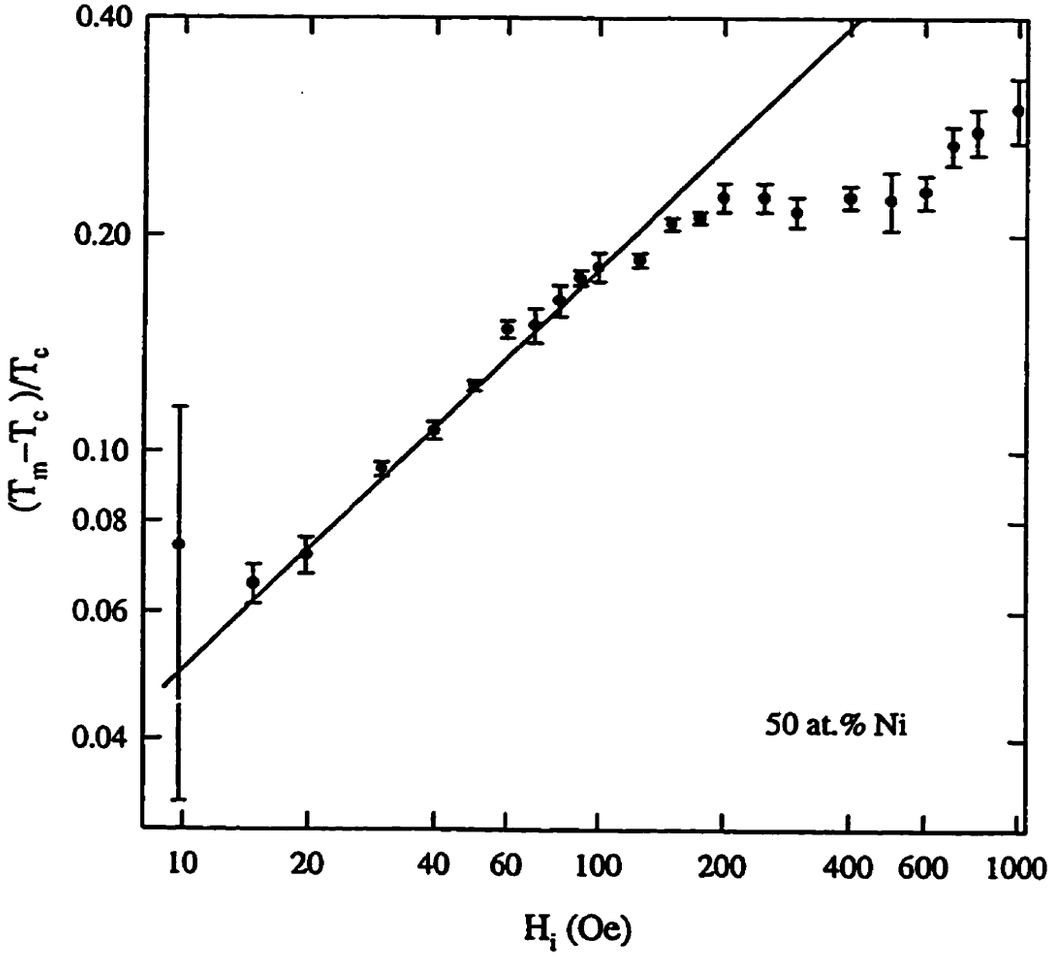

Figure A.28: Reduced peak temperature as a function of internal field for x=0.50. The superimposed line represents the 3D Heisenberg prediction, $1/(\gamma + \beta)$=0.571.

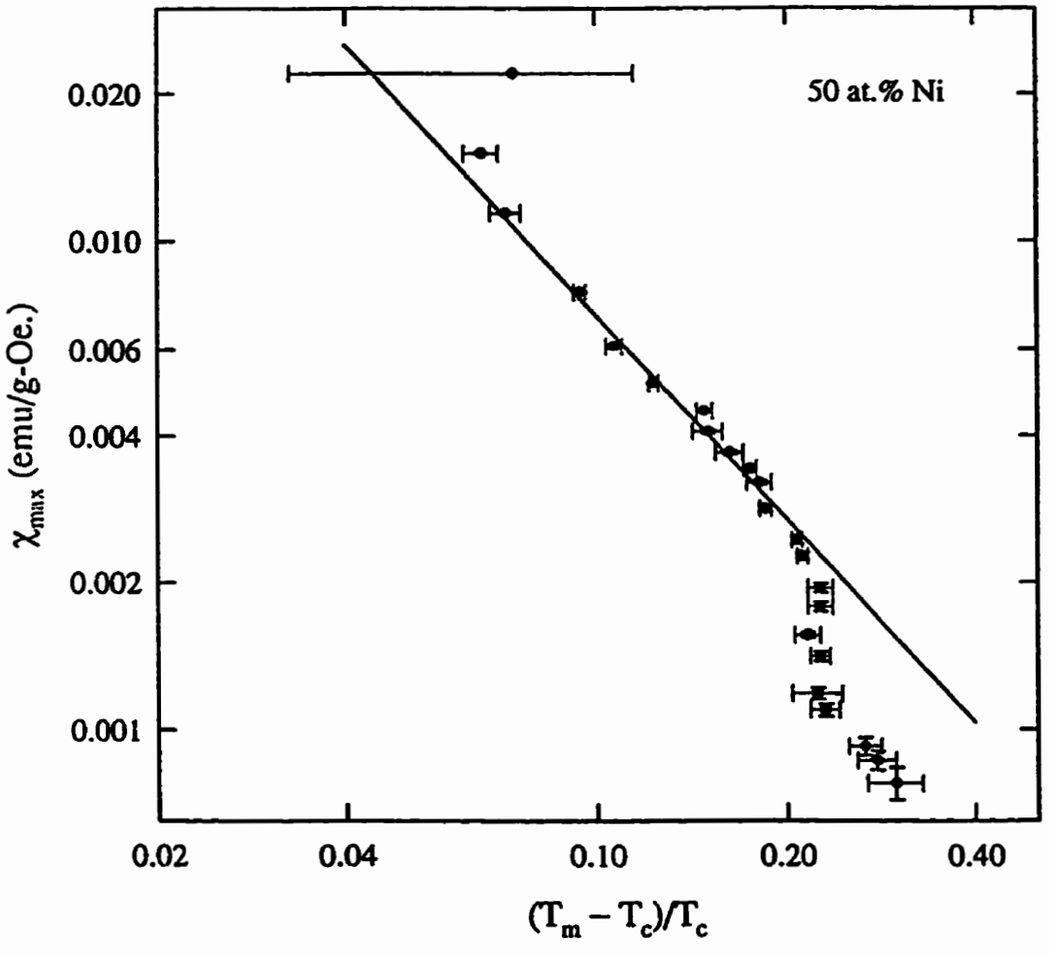

Figure A.29: Peak susceptibility as a function of reduced peak temperature for the 50 at.% Ni sample. The superimposed line represents the 3D Heisenberg value for γ=1.386.

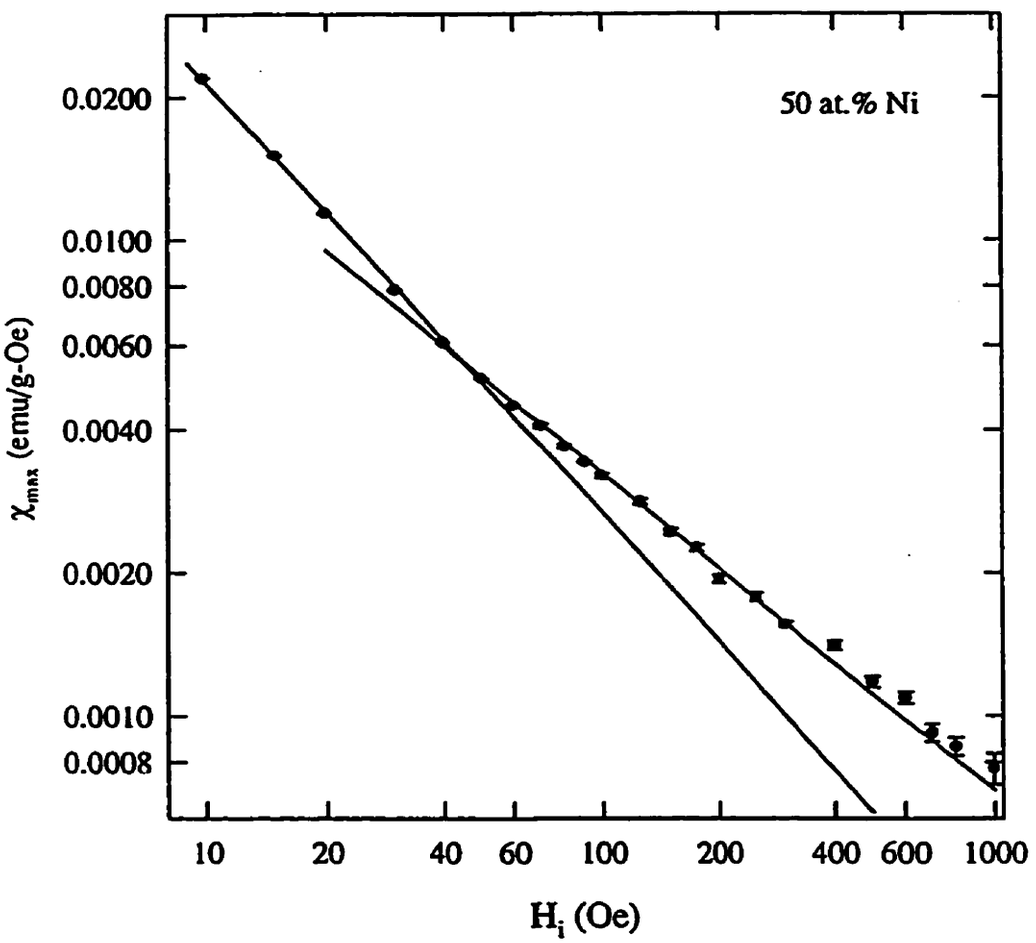

Figure A.30: Peak susceptibility as a function of internal field for the 50 at.% Ni sample. The solid line represents a fit to the high field data with δ=3.0(1). The dashed line shows a low field fit yielding δ=10.2(4)

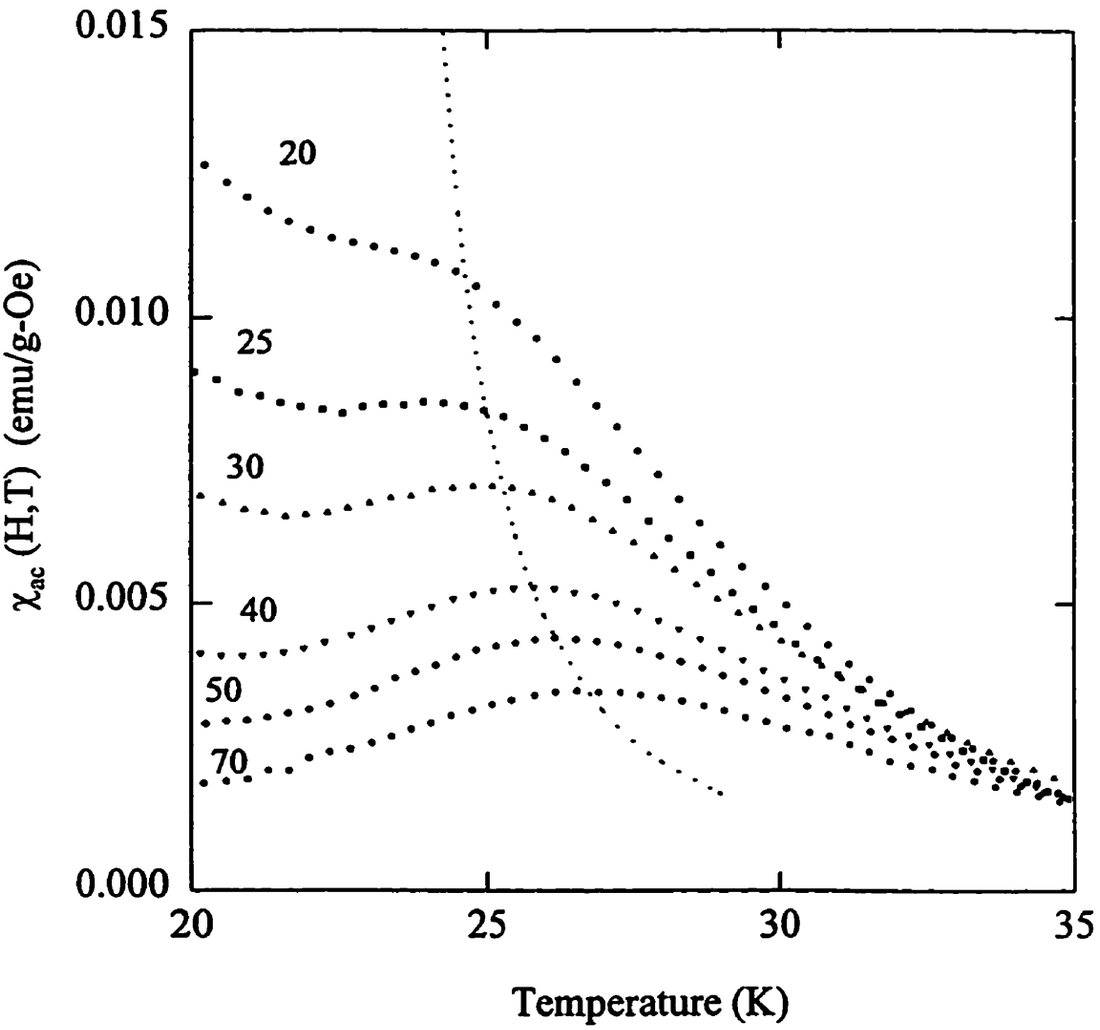

Figure A.31: The temperature dependence of the *ac* susceptibility in fixed biasing fields as labelled, in Oe, for the x=0.49 sample. The dotted line represents the crossover line, as discussed in the text.

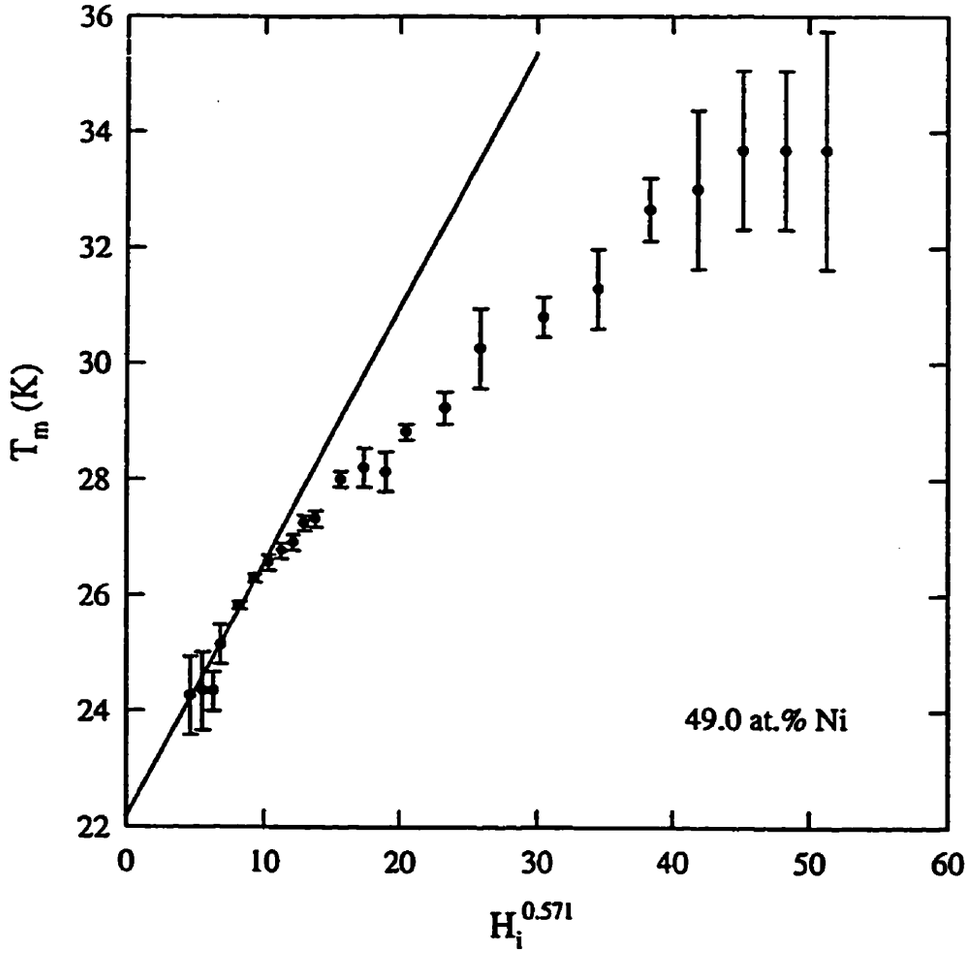

Figure A.32: Peak temperature as a function of internal field to the power of 0.571 for $Cu_{100-x}Ni_x$ with x=0.49. The superimposed line represents a fit to the data with T_c=22.2K.

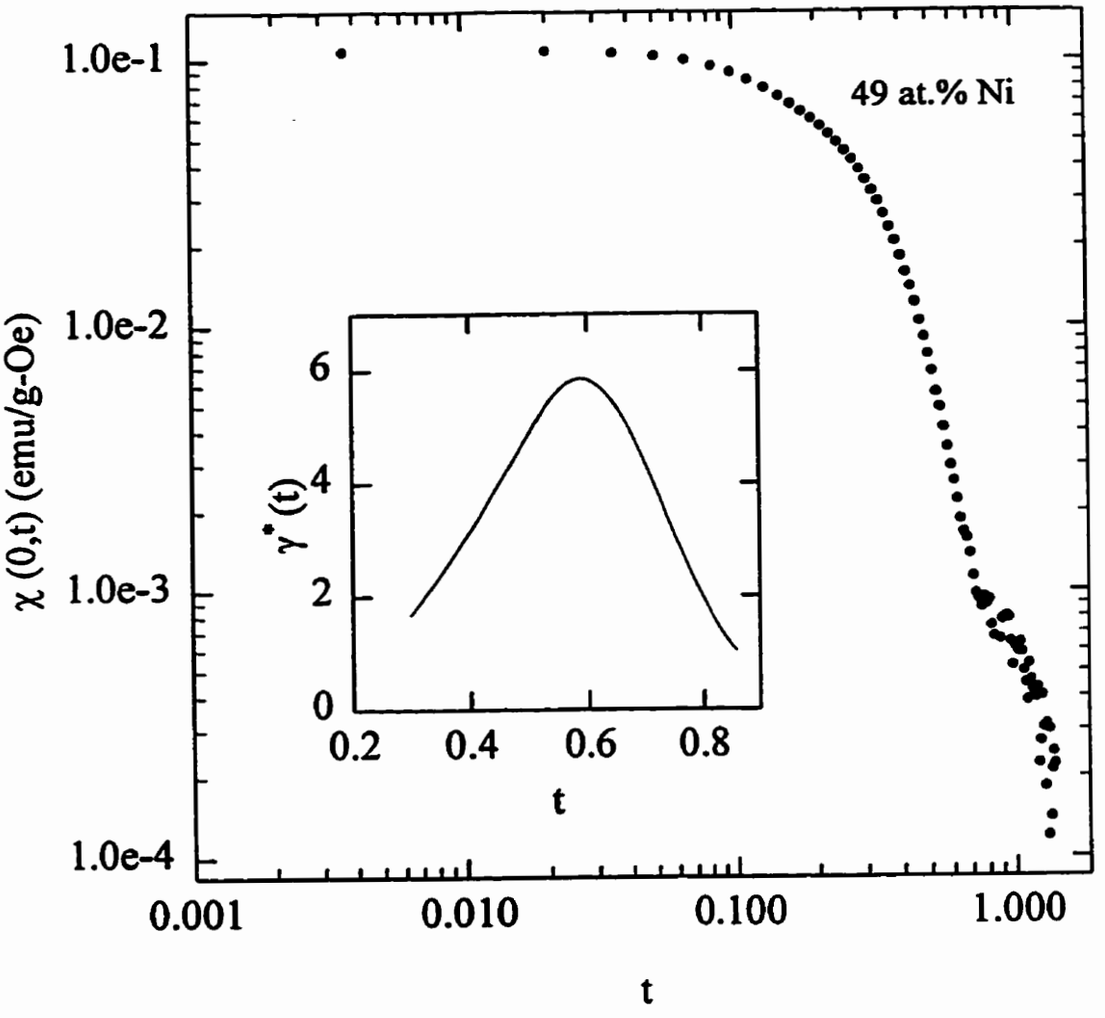

Figure A.33: The zero field susceptibility as a function of reduced temperature for the 49 at.% Ni sample. The inset shows the calculated effective exponent, $\gamma^*(t)$.

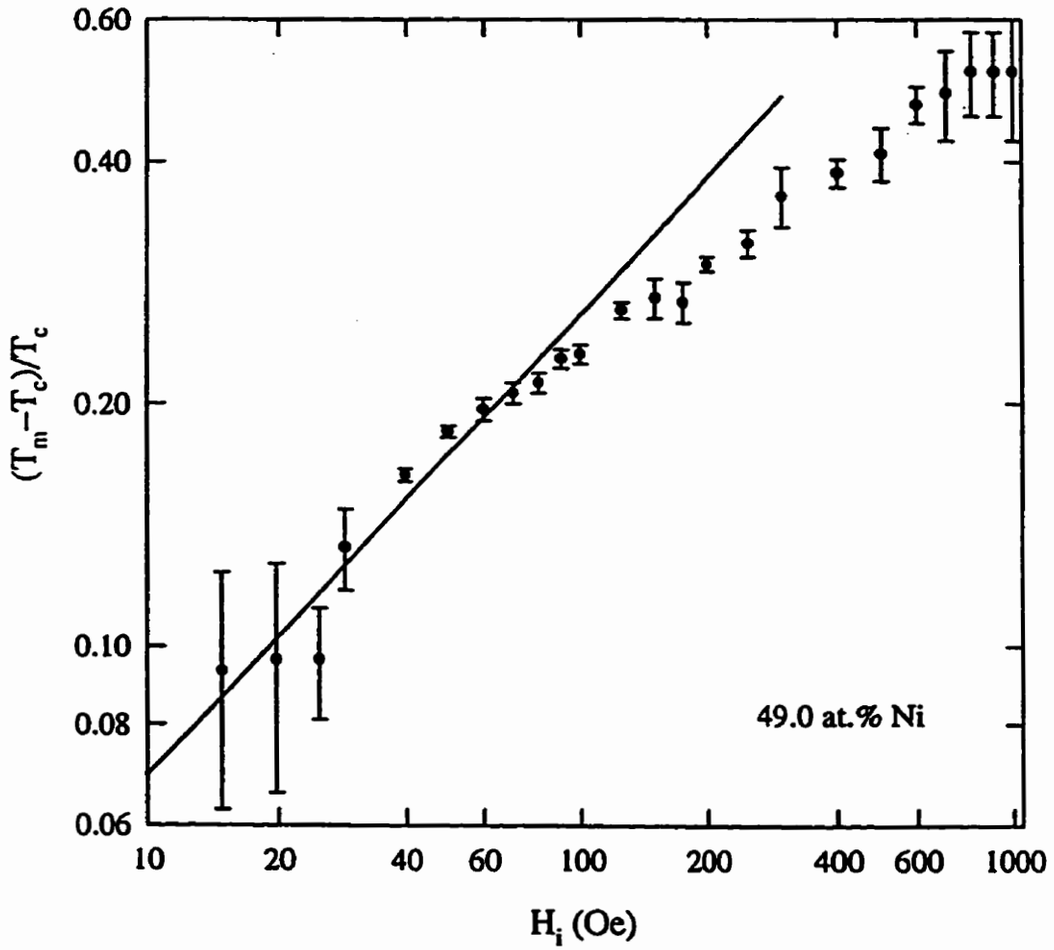

Figure A.34: Reduced peak temperature as a function of internal field for x=0.49. The superimposed line represents the 3D Heisenberg prediction, $1/(\gamma+\beta)$=0.571.

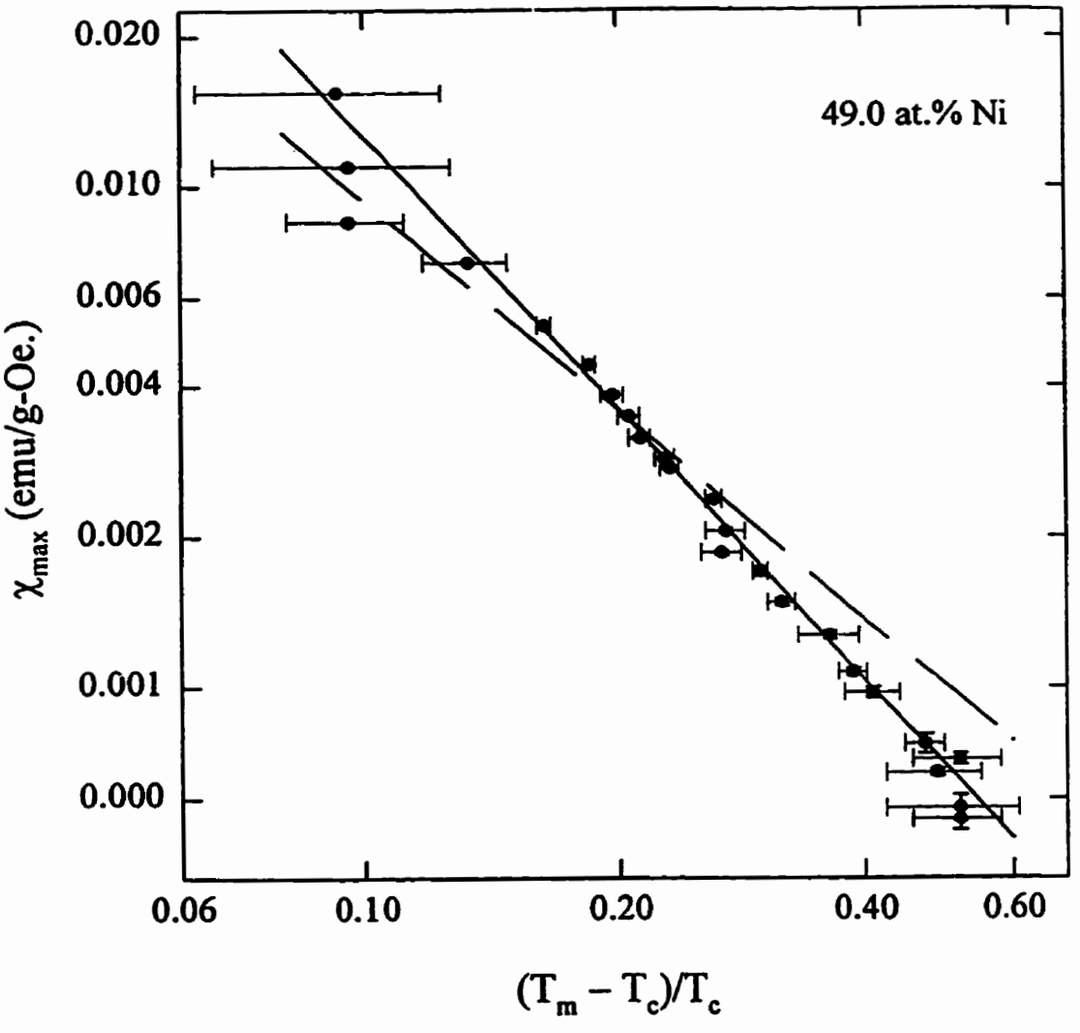

Figure A.35: Peak susceptibility as a function of reduced peak temperature for the 49 at.% Ni sample. The dashed line represents the 3D Heisenberg value for γ=1.386, while the solid line is the best fit, with γ=1.88(1).

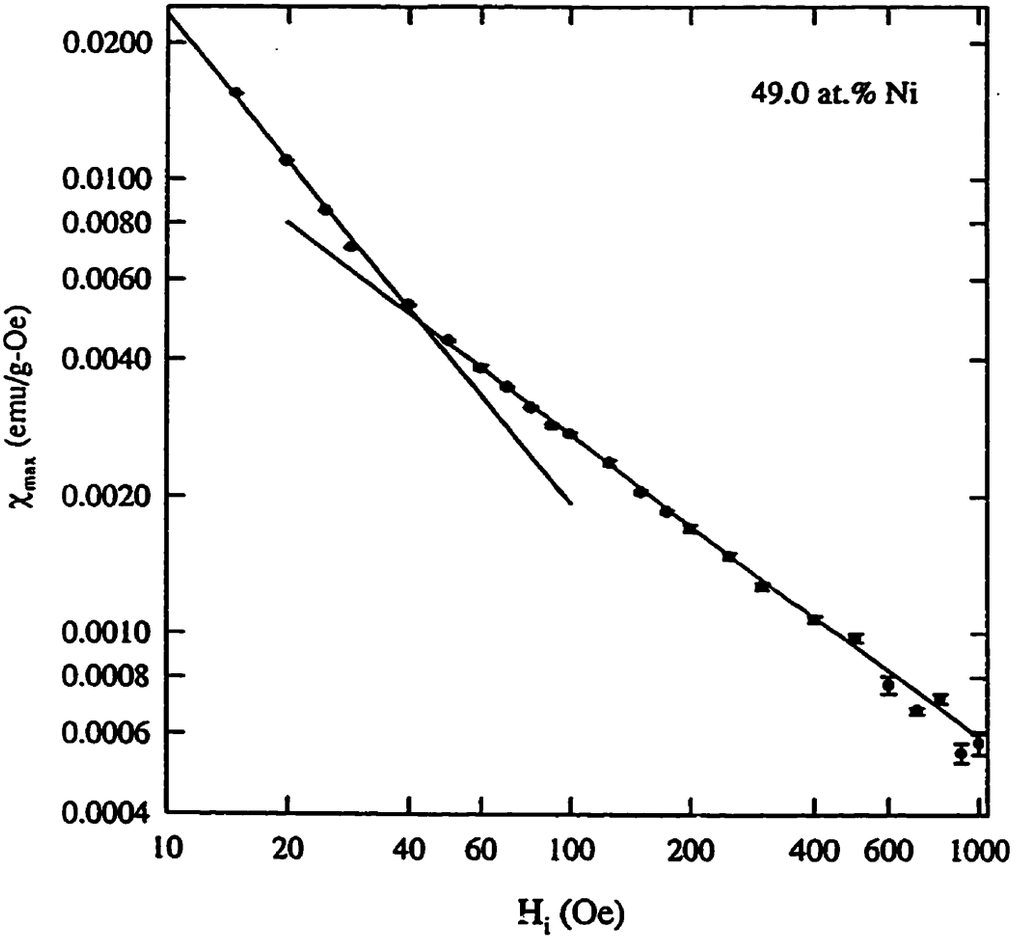

Figure A.36: Peak susceptibility as a function of internal field for the 49 at.% Ni sample. The lines represent fits to the data with $\delta_{lf} < 0$ and δ_{hf}=3.00(8).

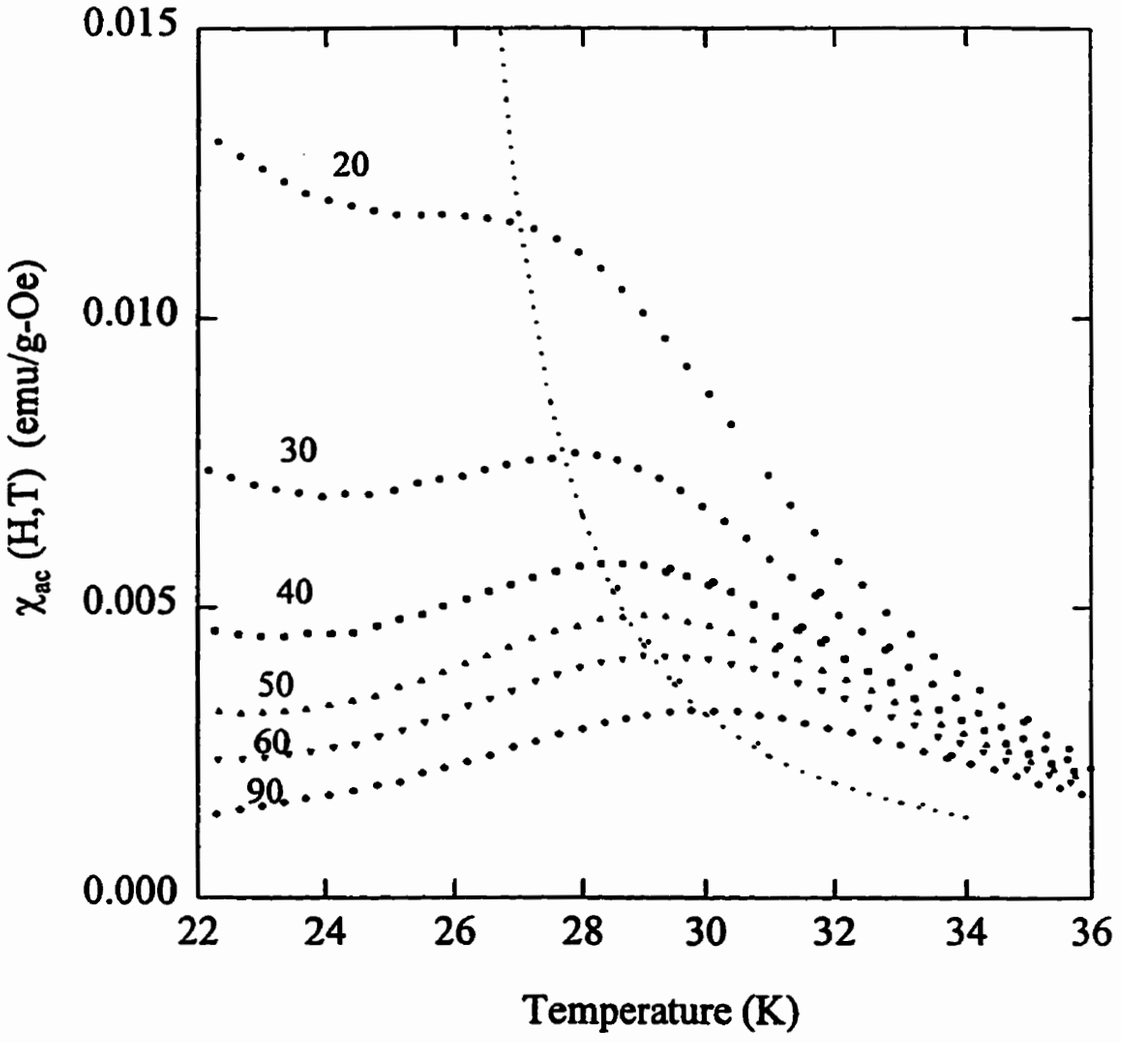

Figure A.37: The temperature dependence of the *ac* susceptibility in fixed biasing fields as labelled, in Oe, for the x=0.485 sample. The dotted line represents the crossover line, as discussed in the text.

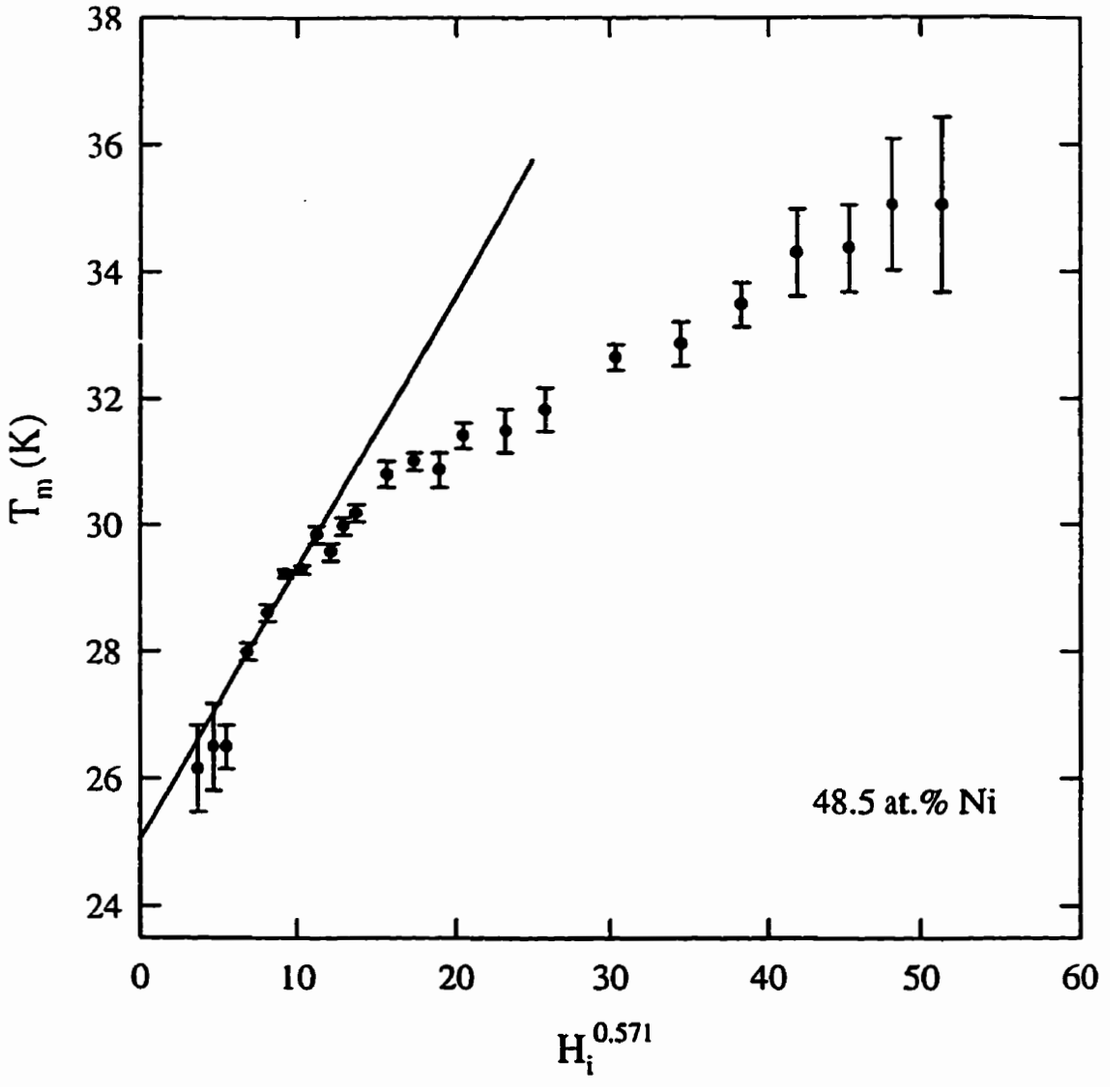

Figure A.38: Peak temperature as a function of internal field to the power of 0.571 for $Cu_{100-x}Ni_x$ with x=0.485. The superimposed line represents a fit to the data with T_c=25.1K.

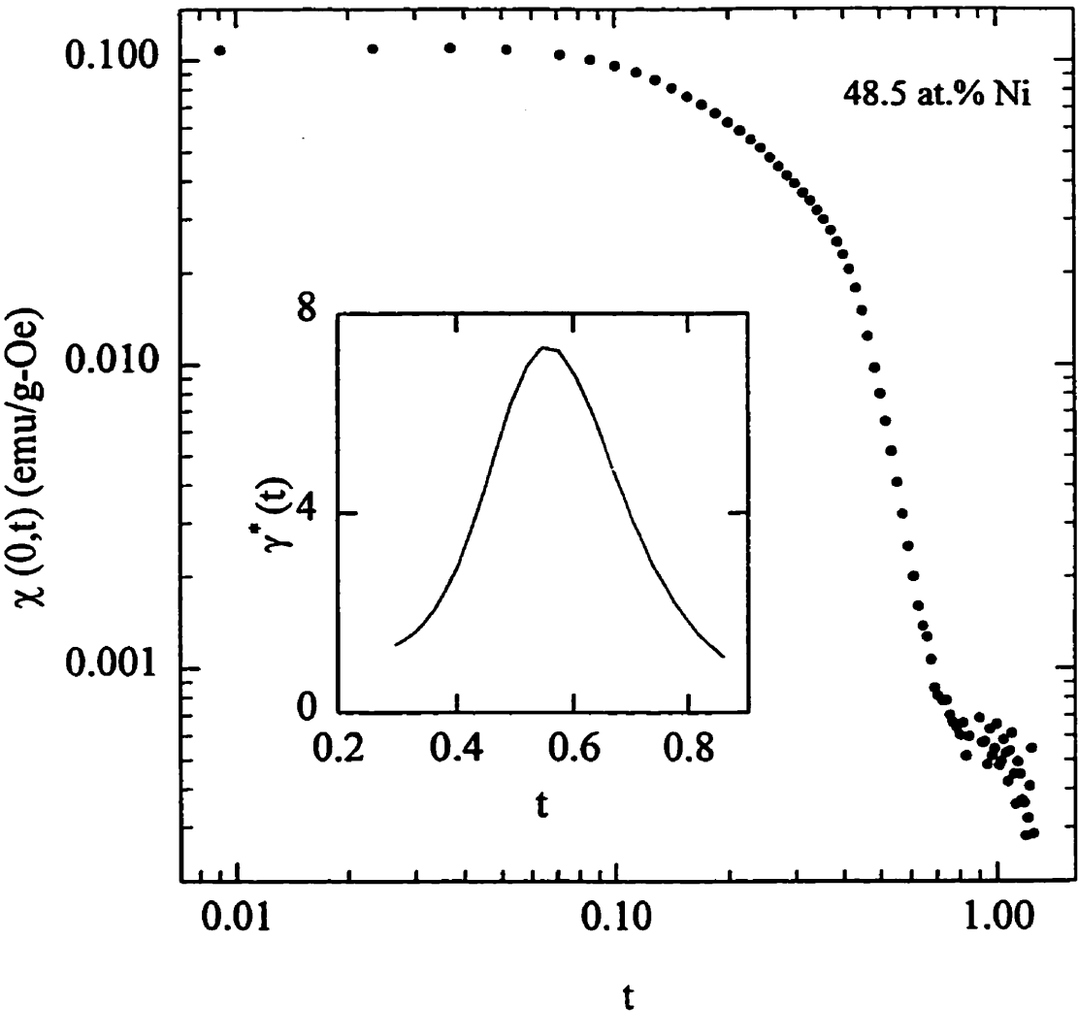

Figure A.39: The zero field susceptibility as a function of reduced temperature for the 48.5 at.% Ni sample. The inset shows the calculated effective exponent, $\gamma^*(t)$.

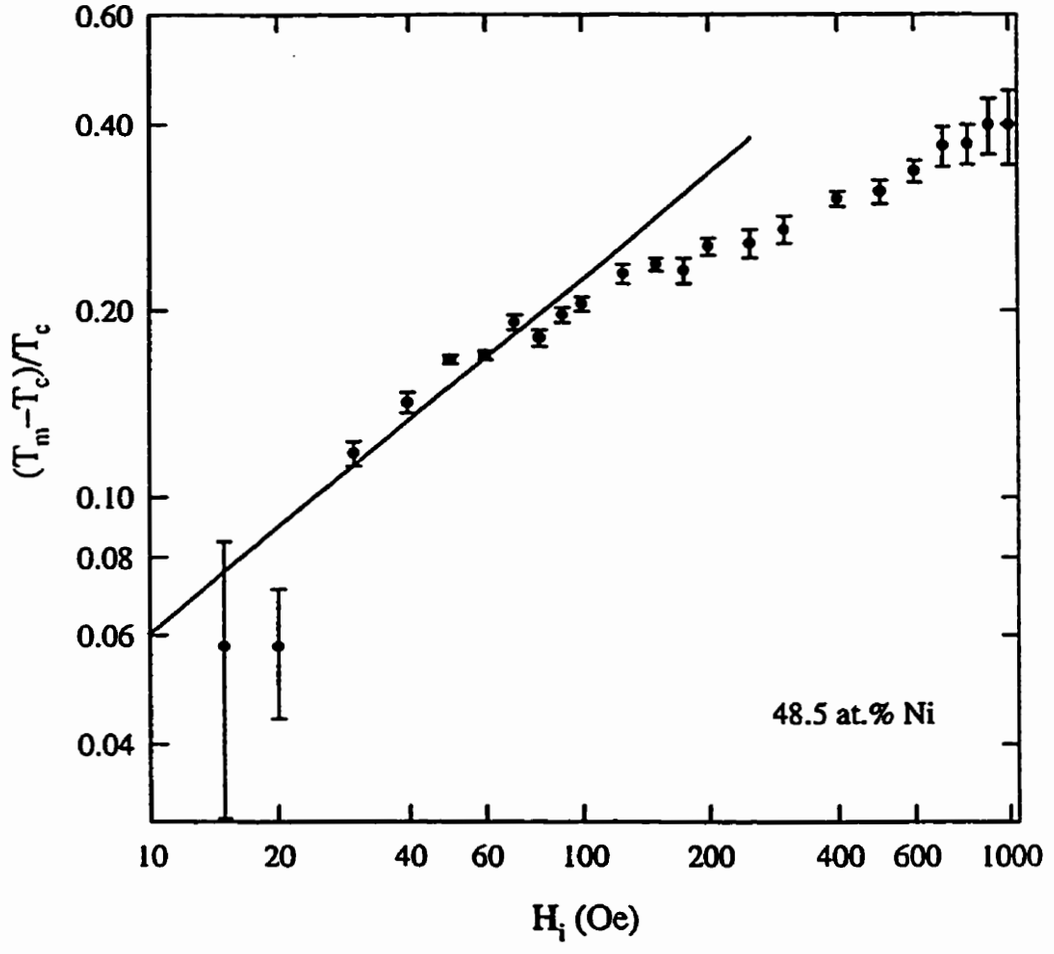

Figure A.40: Reduced peak temperature as a function of internal field for x=0.485. The superimposed line represents the 3D Heisenberg prediction, $1/(\gamma+\beta)$=0.571.

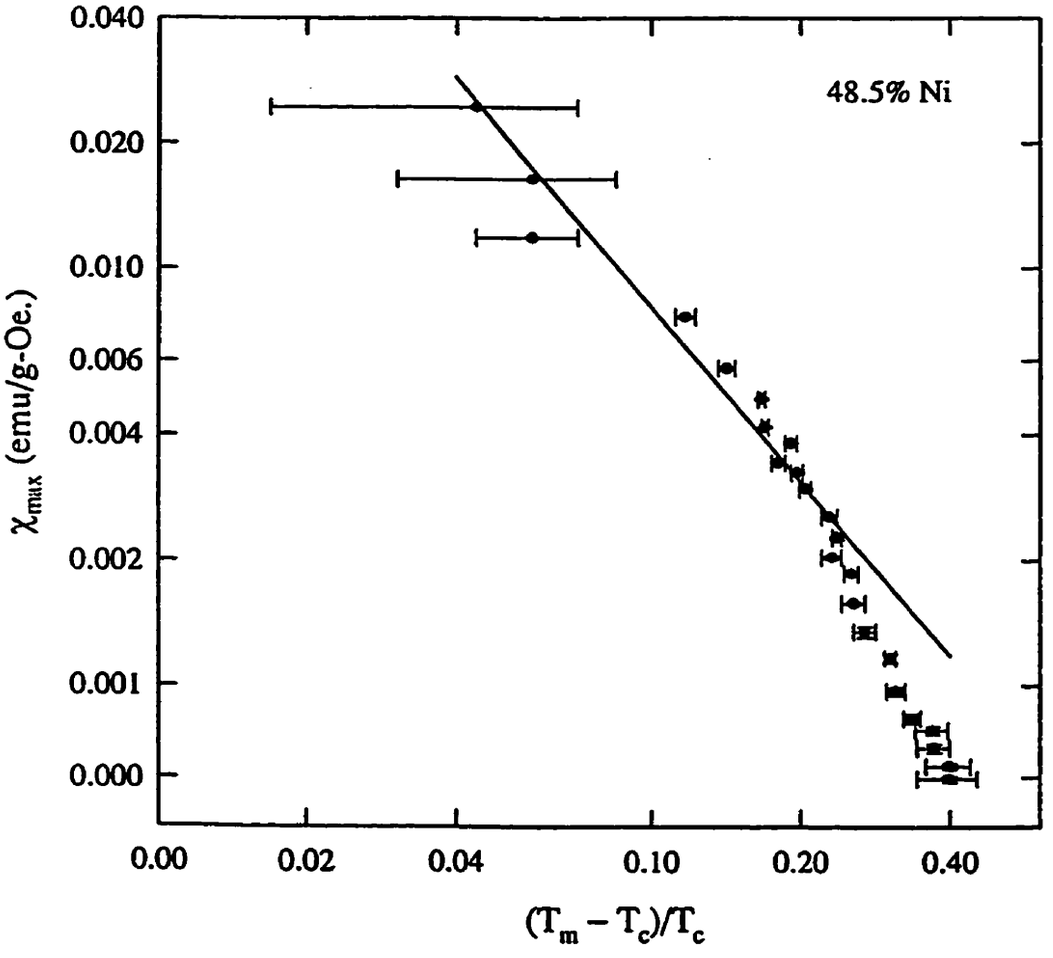

Figure A.41: Peak susceptibility as a function of reduced peak temperature for the 48.5 at.% Ni sample. The superimposed line represents the 3D Heisenberg value for γ=1.386.

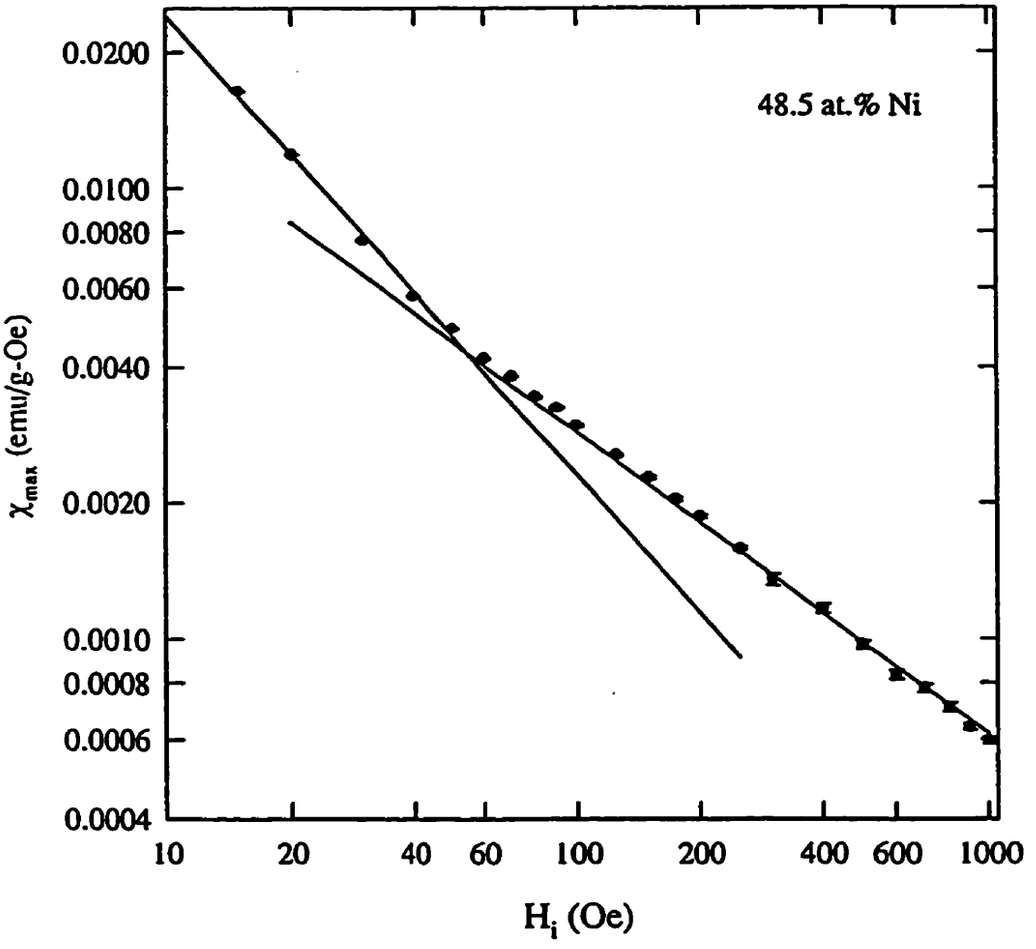

Figure A.42: Peak susceptibility as a function of internal field for the 48.5 at.% Ni sample. The lines represent fits to the data with $\delta_{lf} < 0$ and δ_{hf}=3.73(5).

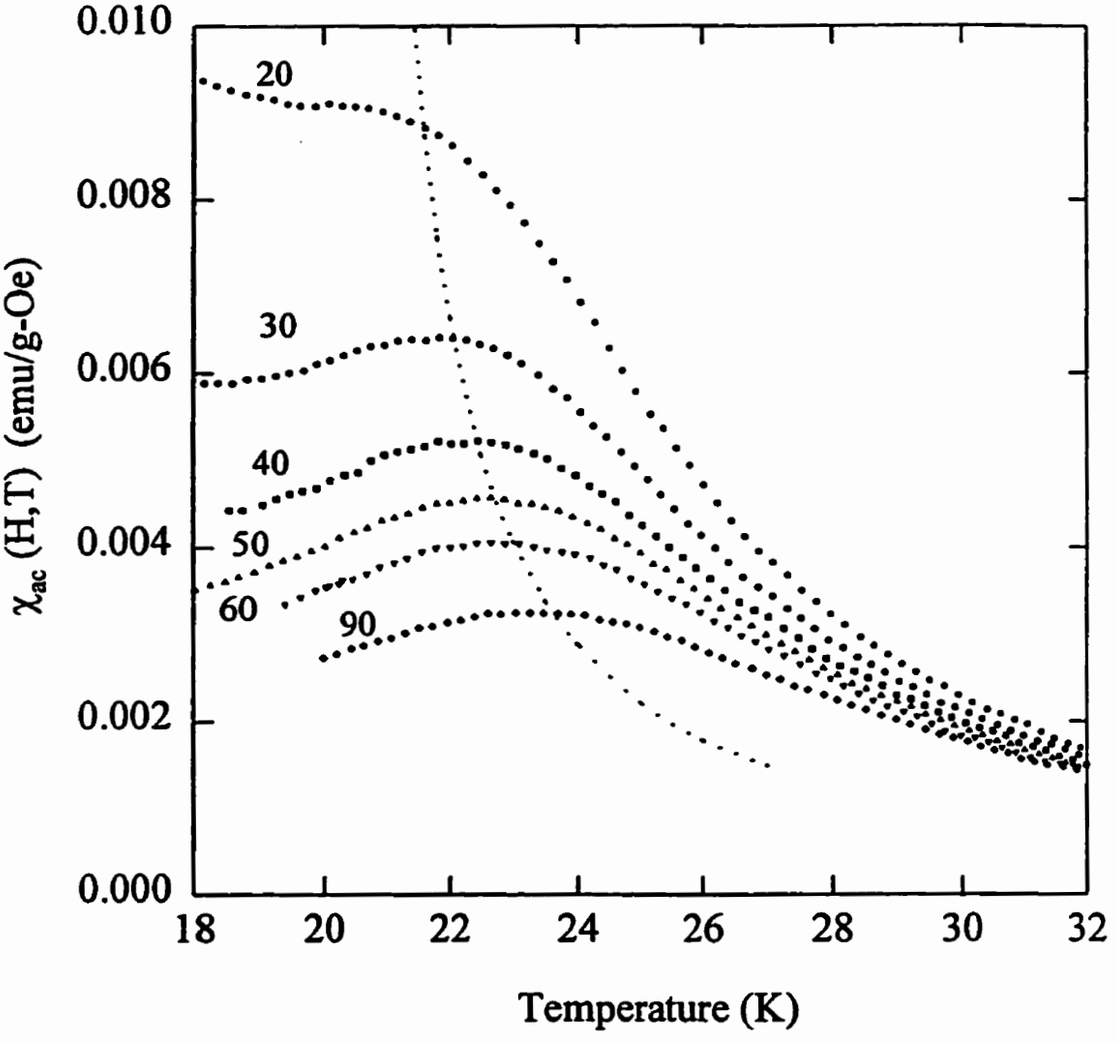

Figure A.43: The temperature dependence of the *ac* susceptibility in fixed biasing fields as labelled, in Oe, for the x=0.48 sample. The dotted line represents the crossover line, as discussed in the text.

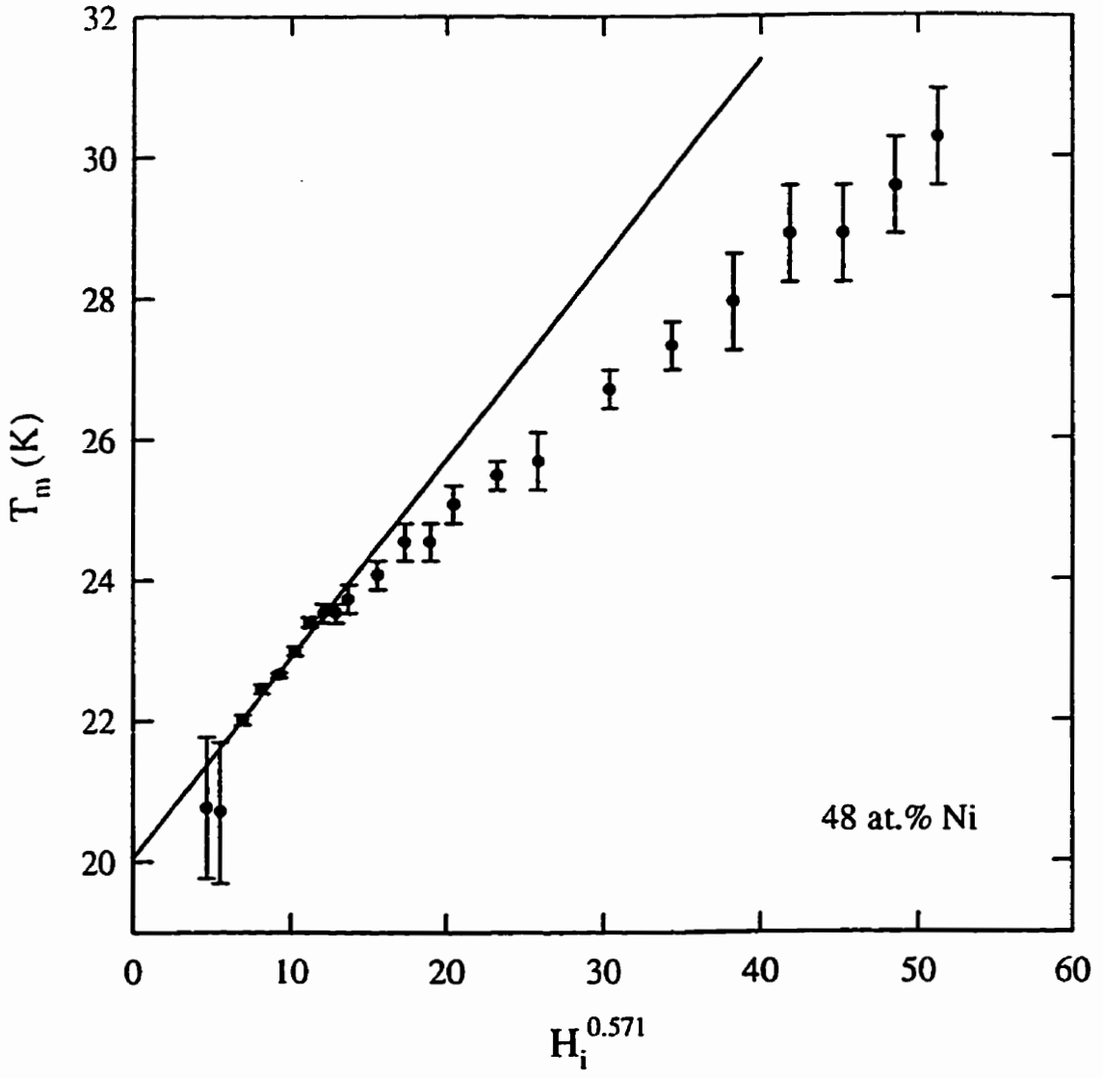

Figure A.44: Peak temperature as a function of internal field to the power of 0.571 for $Cu_{100-x}Ni_x$ with x=0.48. The superimposed line represents a fit to the data with T_c=20.1K.

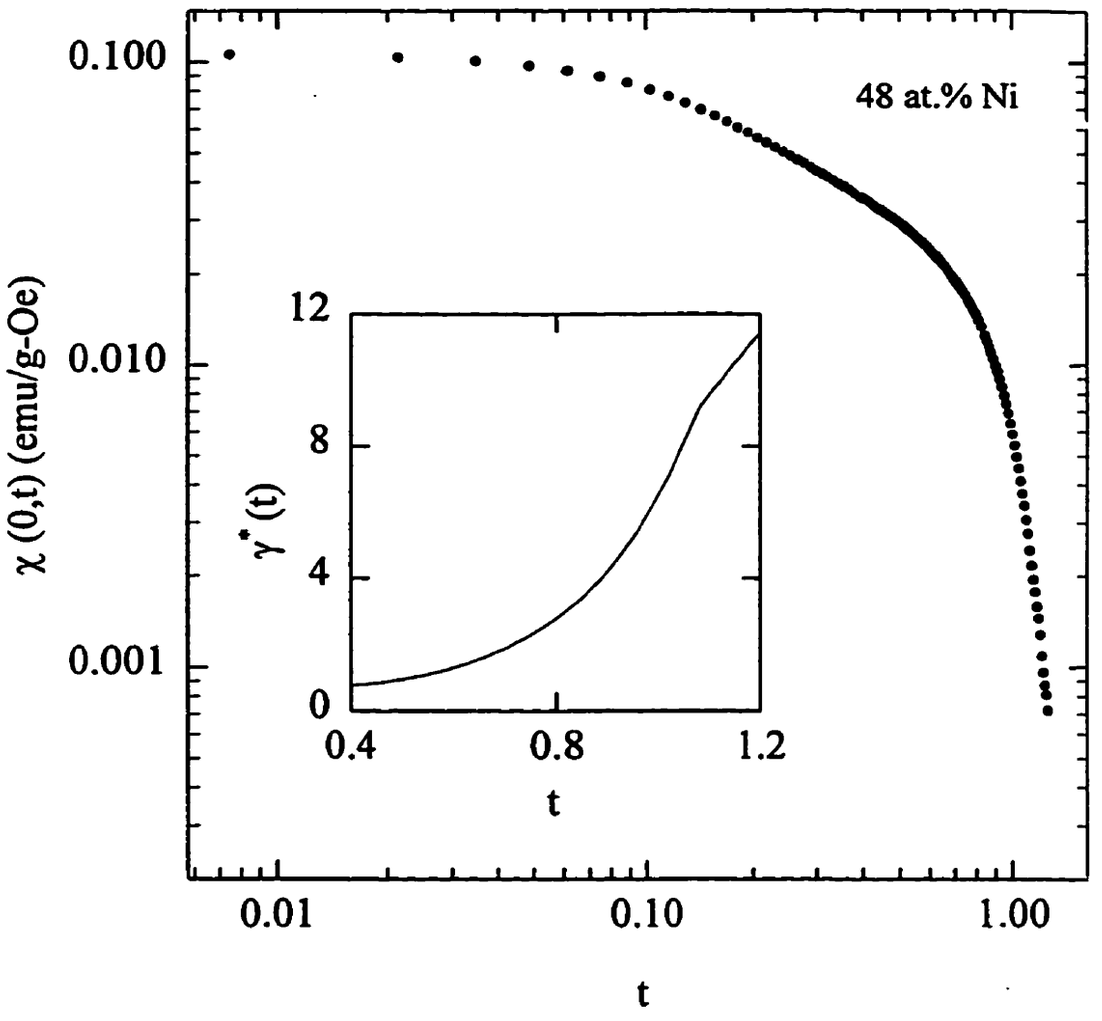

Figure A.45: The zero field susceptibility as a function of reduced temperature for the 48 at.% Ni sample. The inset shows the calculated effective exponent, $\gamma^*(t)$.

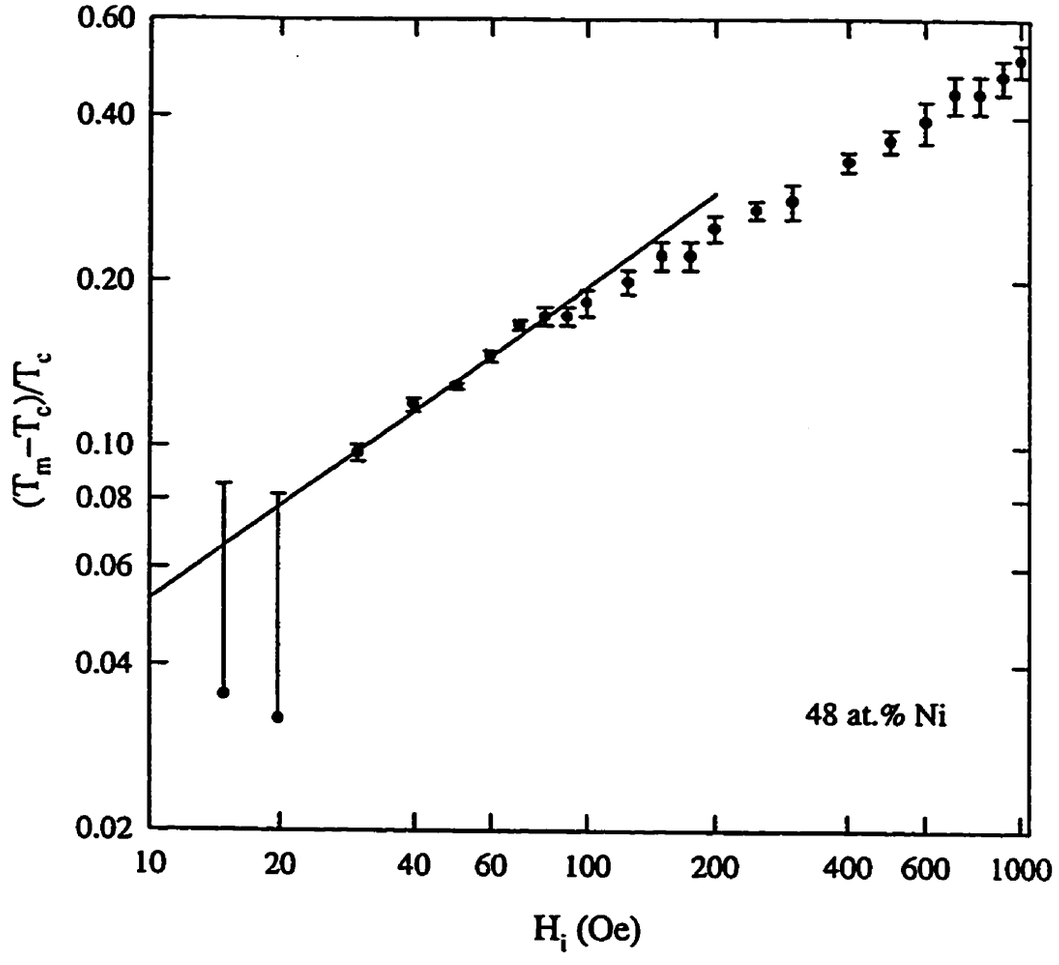

Figure A.46: Reduced peak temperature as a function of internal field for x=0.48. The superimposed line represents the 3D Heisenberg prediction, $1/(\gamma + \beta)$=0.571.

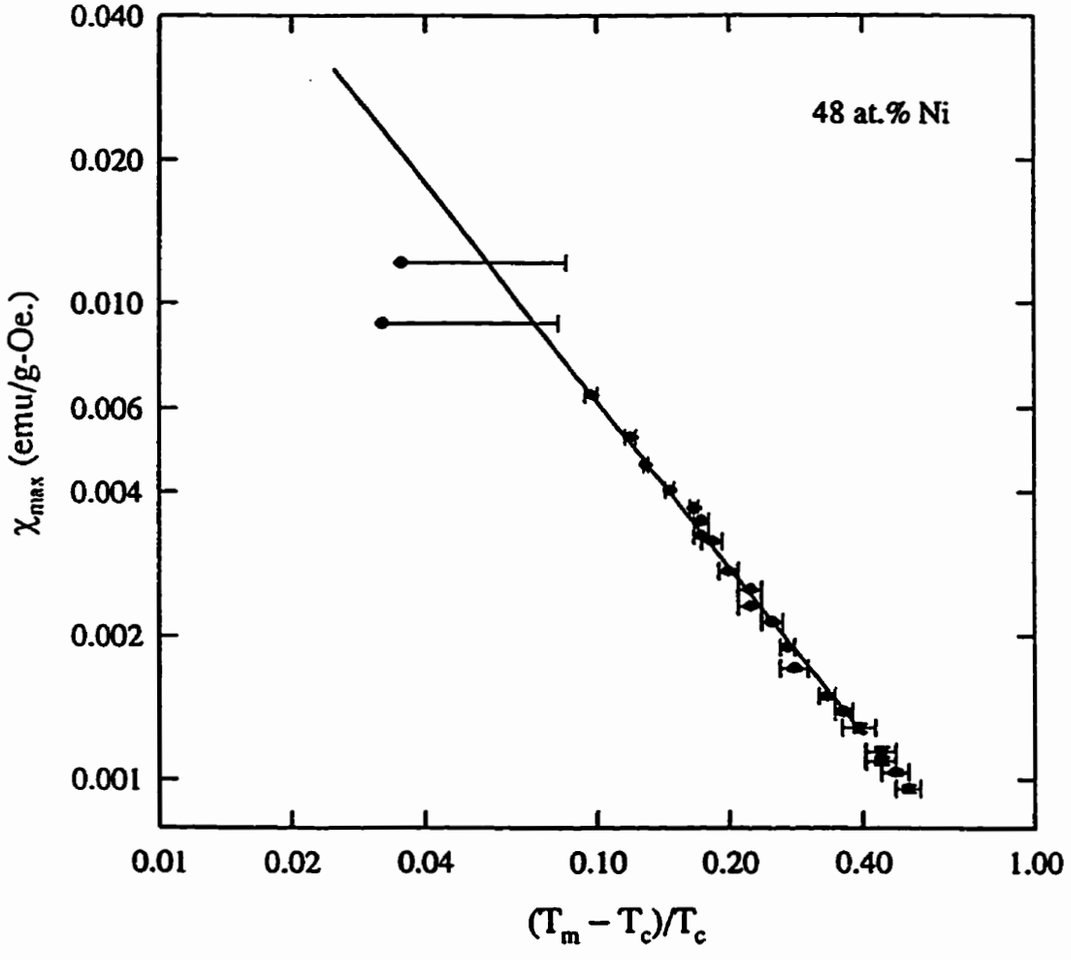

Figure A.47: Peak susceptibility as a function of reduced peak temperature for the 48 at.% Ni sample. The superimposed line represents the best fit for γ=1.16(6).

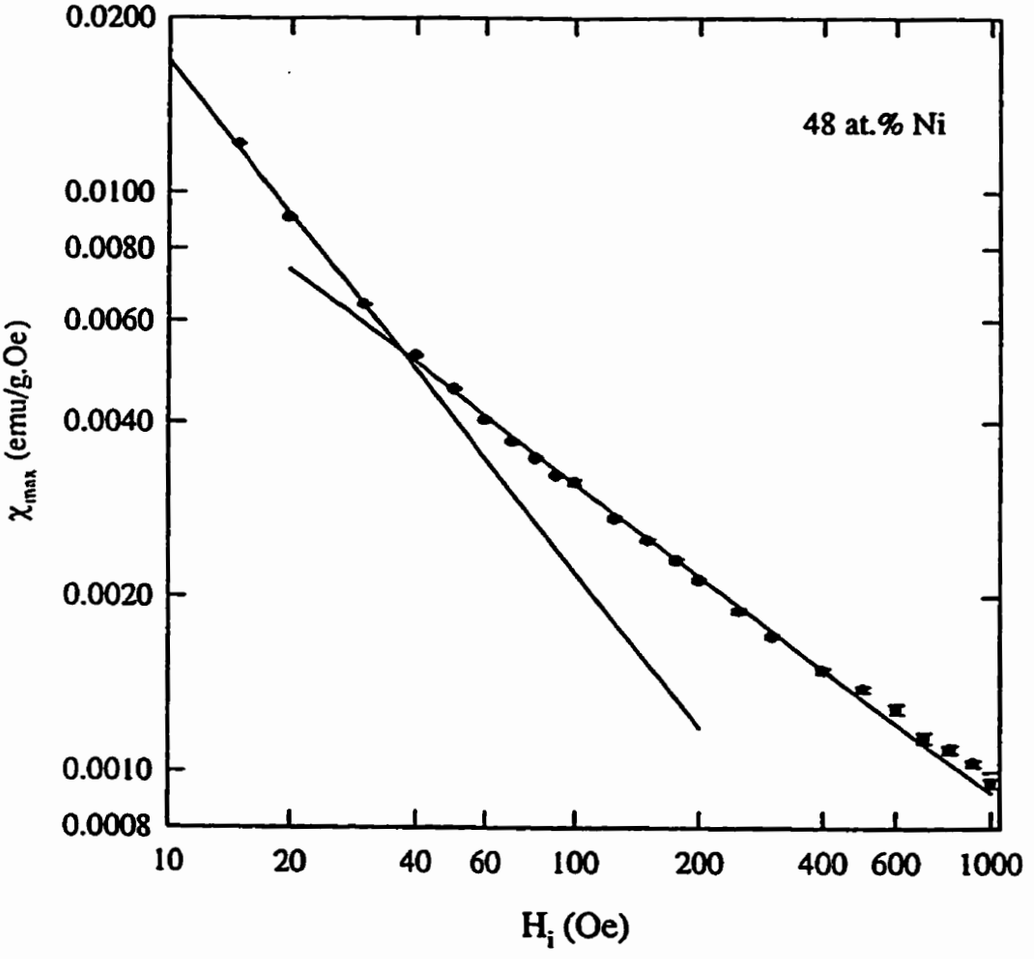

Figure A.48: Peak susceptibility as a function of internal field for the 48 at.% Ni sample. The lines represent fits to the data with $\delta_{lf} = 8.6(6)$ and $\delta_{hf} = 2.13(2)$.

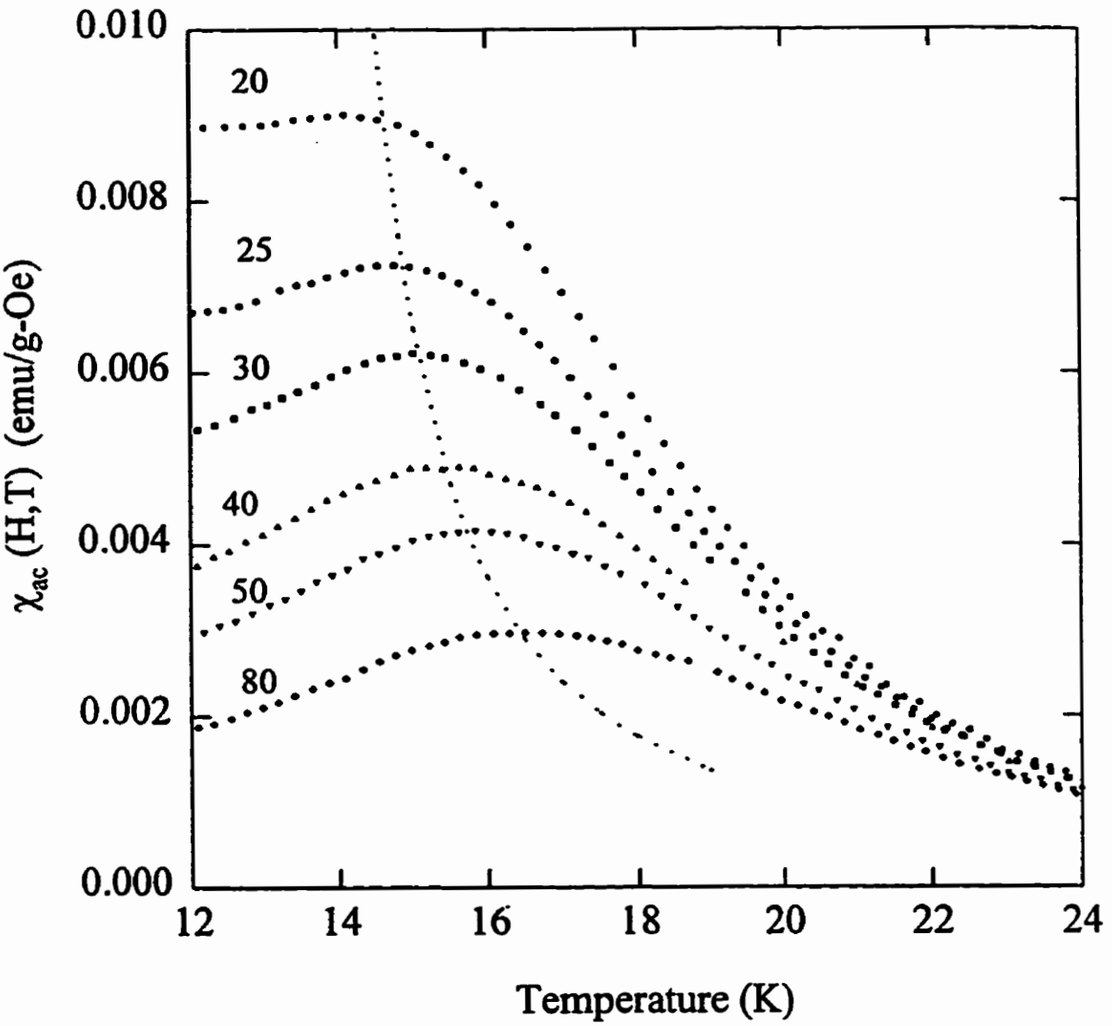

Figure A.49: The temperature dependence of the *ac* susceptibility in fixed biasing fields as labelled, in Oe, for the x=0.475 sample. The dotted line represents the crossover line, as discussed in the text.

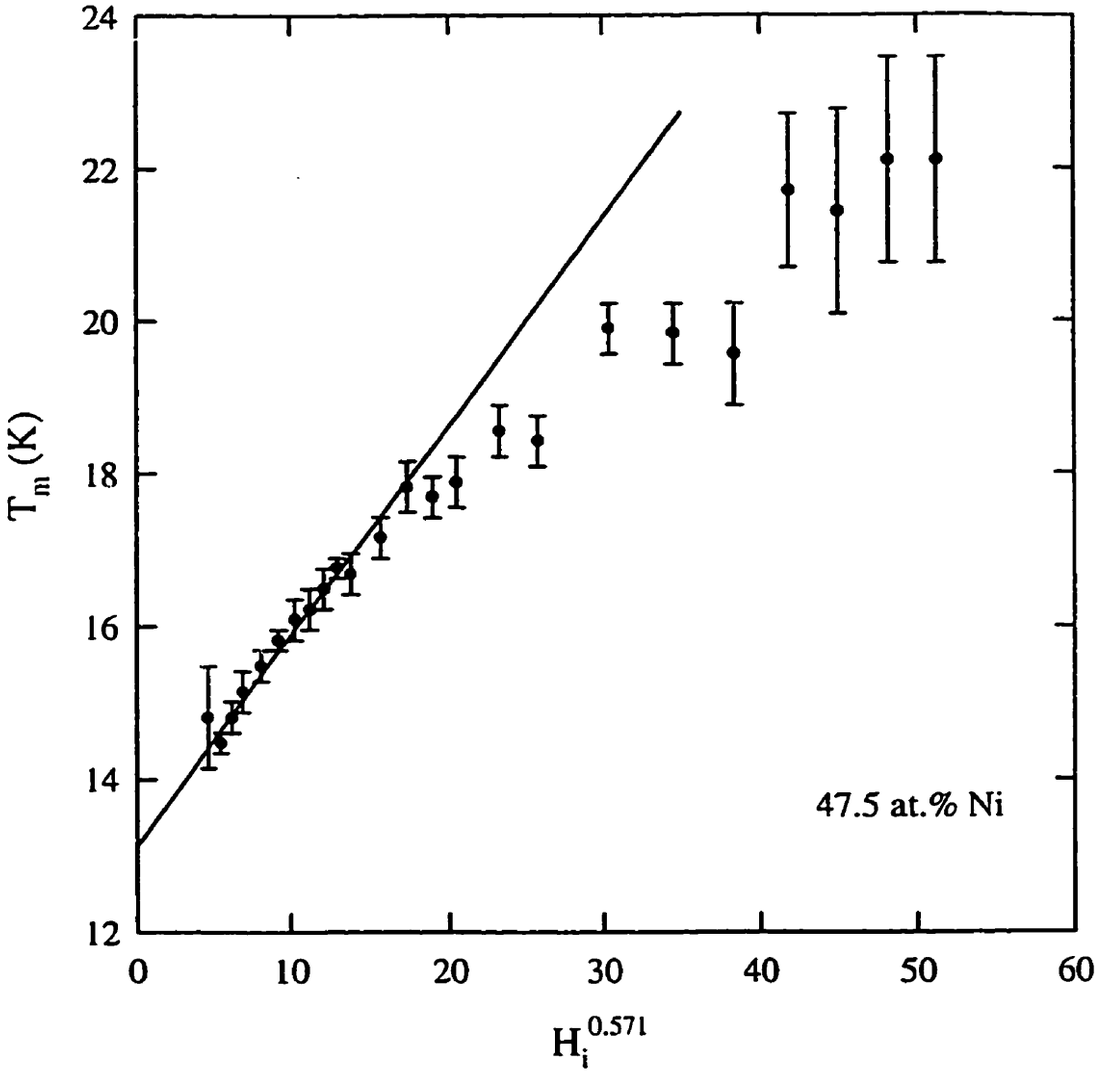

Figure A.50: Peak temperature as a function of internal field to the power of 0.571 for $Cu_{100-x}Ni_x$with x=0.475. The superimposed line represents a fit to the data with T_c=13.1K.

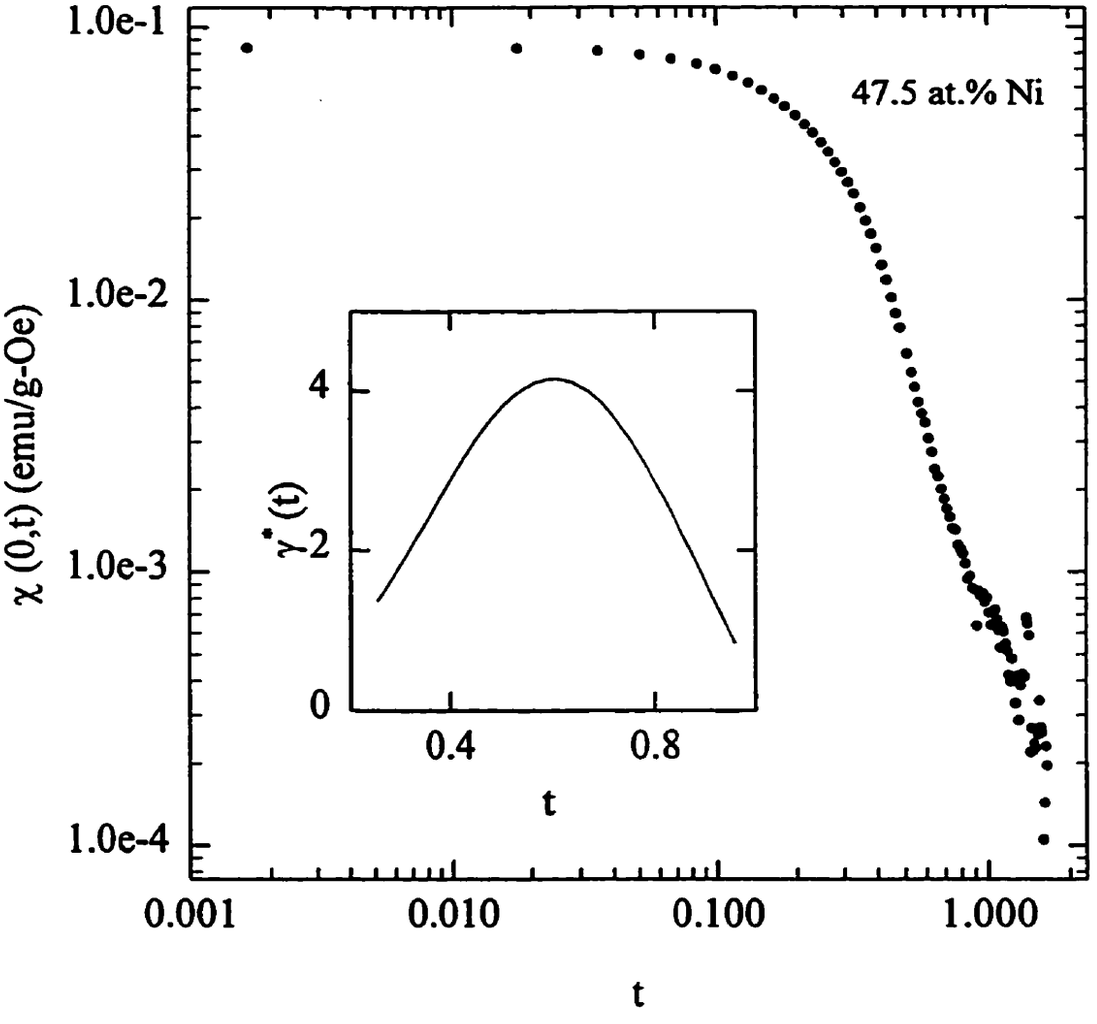

Figure A.51: The zero field susceptibility as a function of reduced temperature for the 47.5 at.% Ni sample. The inset shows the calculated effective exponent, $\gamma^*(t)$.

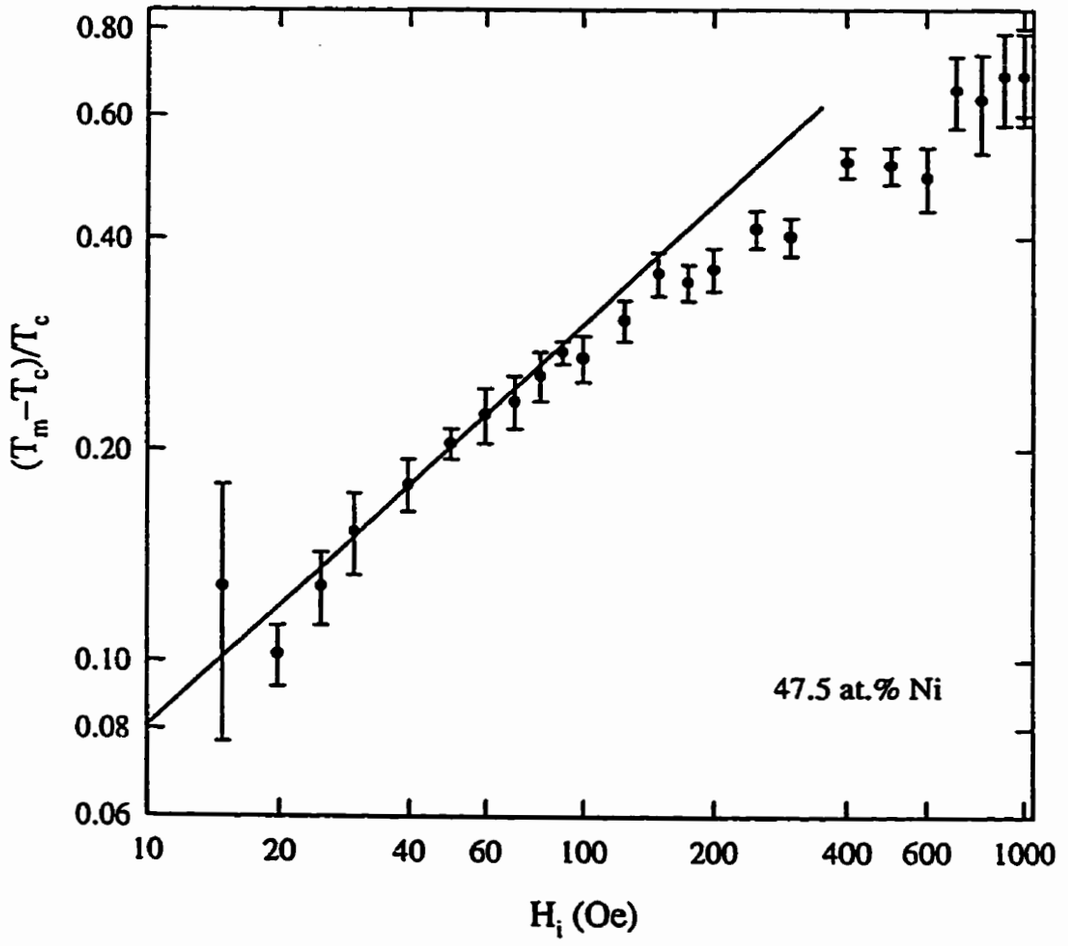

Figure A.52: Reduced peak temperature as a function of internal field for x=0.475. The superimposed line represents the 3D Heisenberg prediction, $1/(\gamma+\beta)$=0.571.

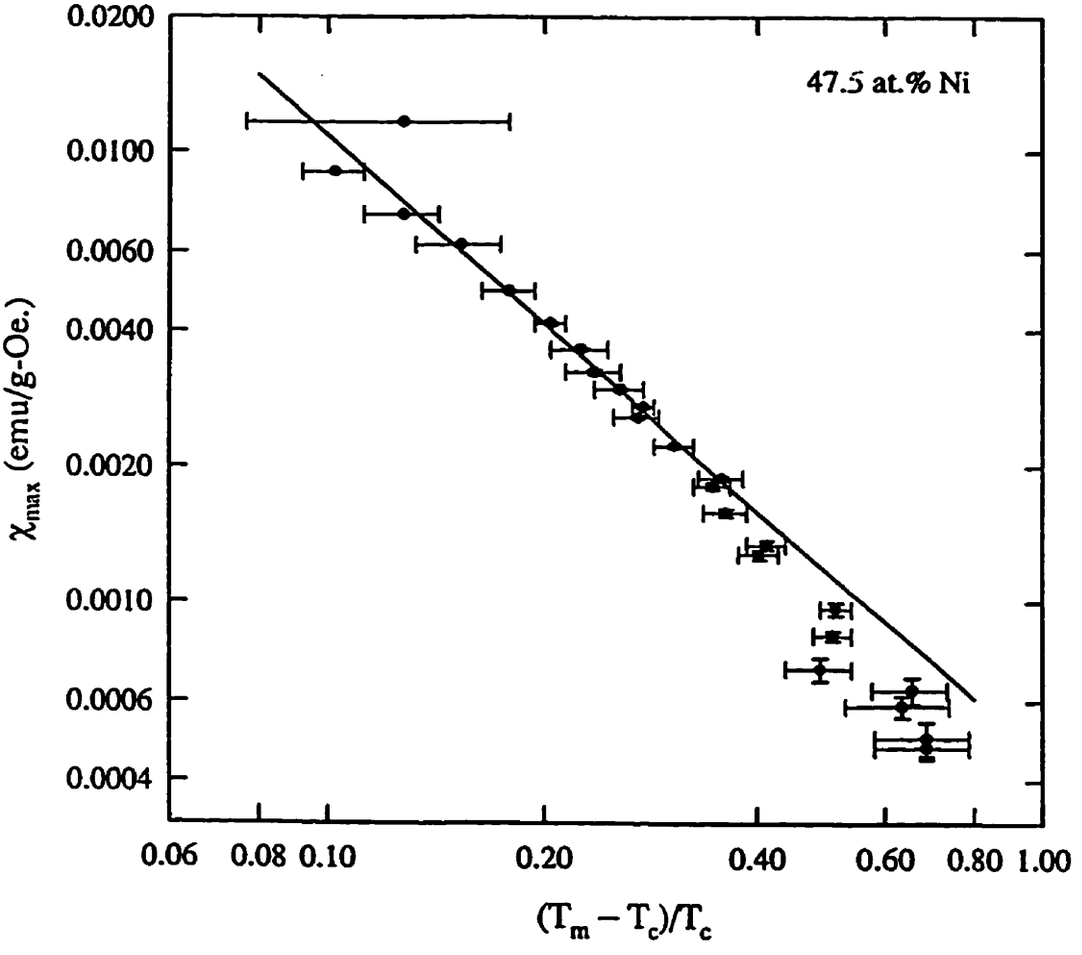

Figure A.53: Peak susceptibility as a function of reduced peak temperature for the 47.5 at.% Ni sample. The superimposed line represents the 3D Heisenberg value for γ=1.386.

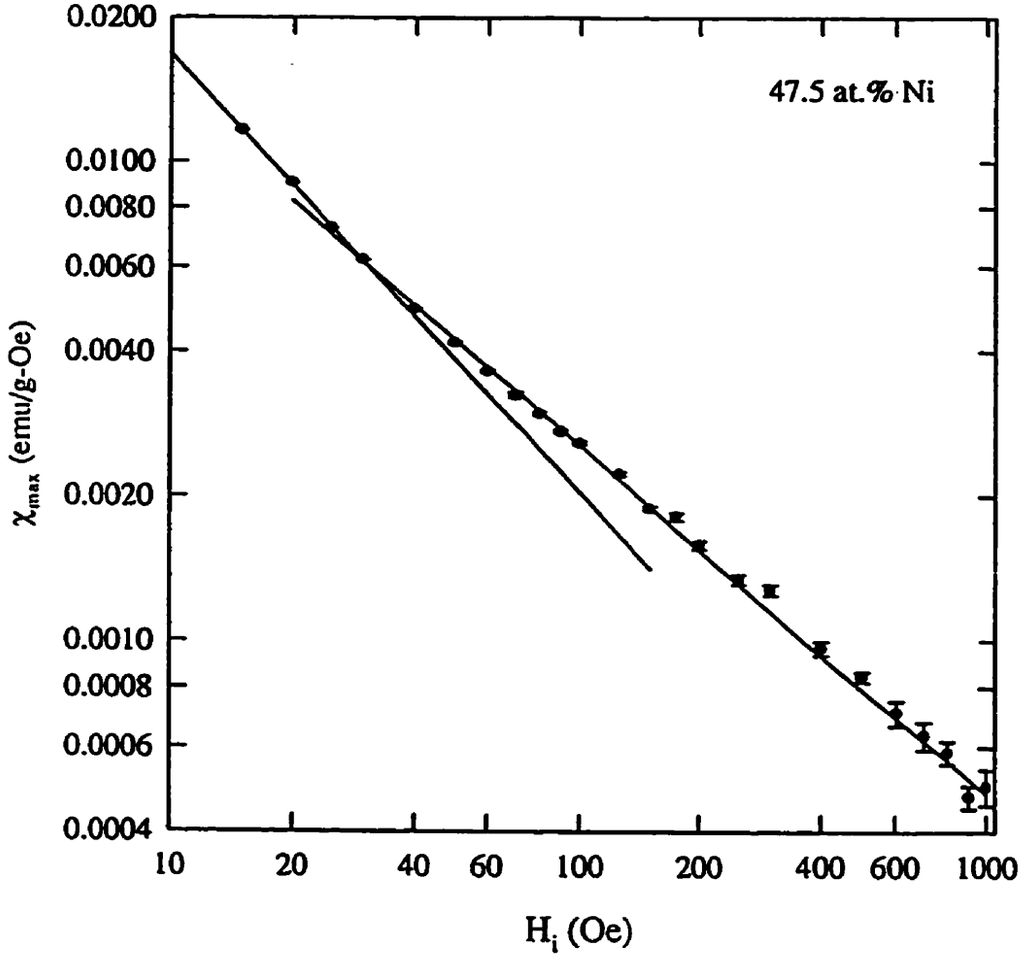

Figure A.54: Peak susceptibility as a function of internal field for the 47.5 at.% Ni sample. The lines represent fits to the data with $\delta_{lf} = 12(1)$ and δ_{hf}=3.7(1).

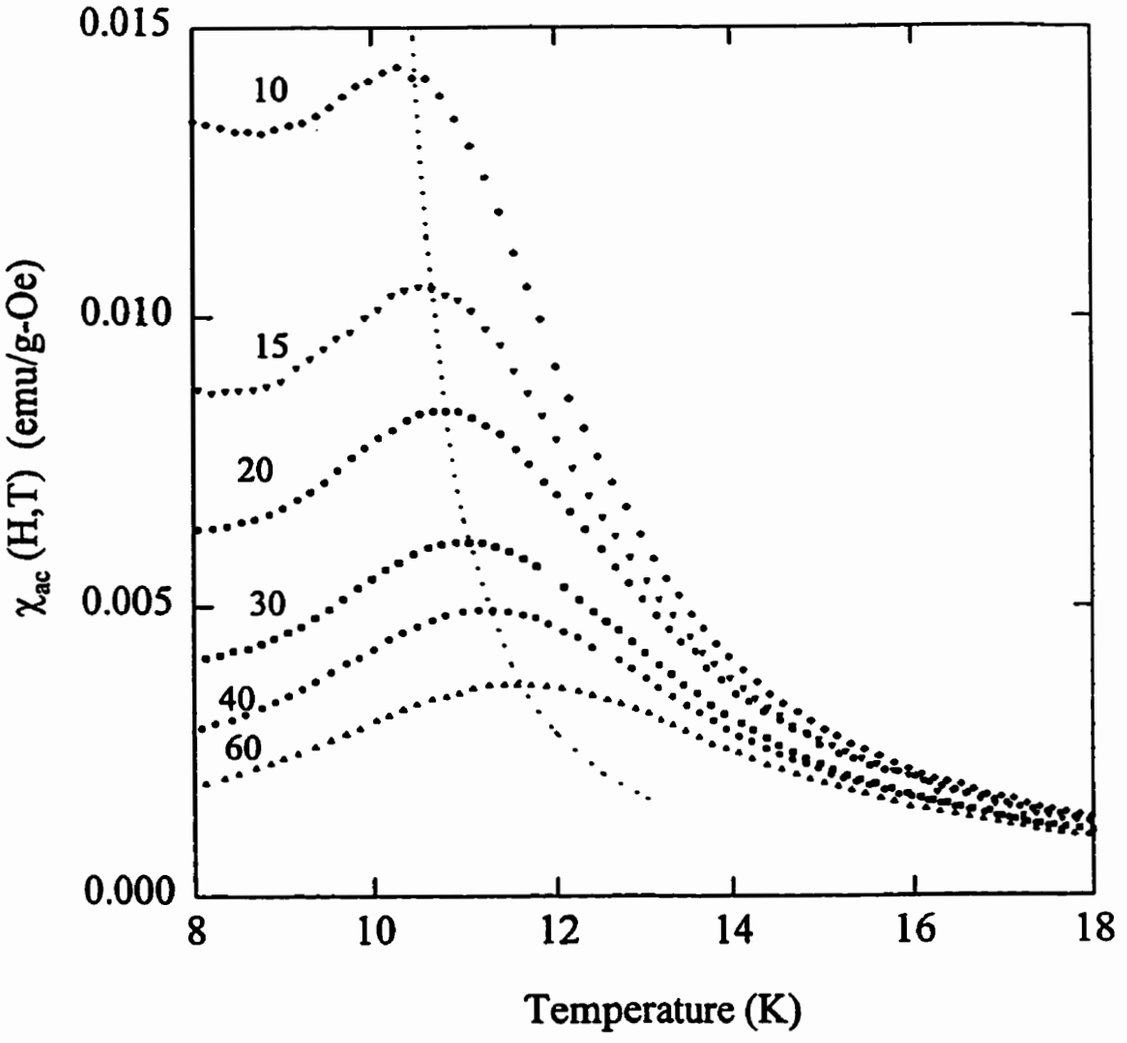

Figure A.55: The temperature dependence of the *ac* susceptibility in fixed biasing fields as labelled, in Oe, for the x=0.47 sample. The dotted line represents the crossover line, as discussed in the text.

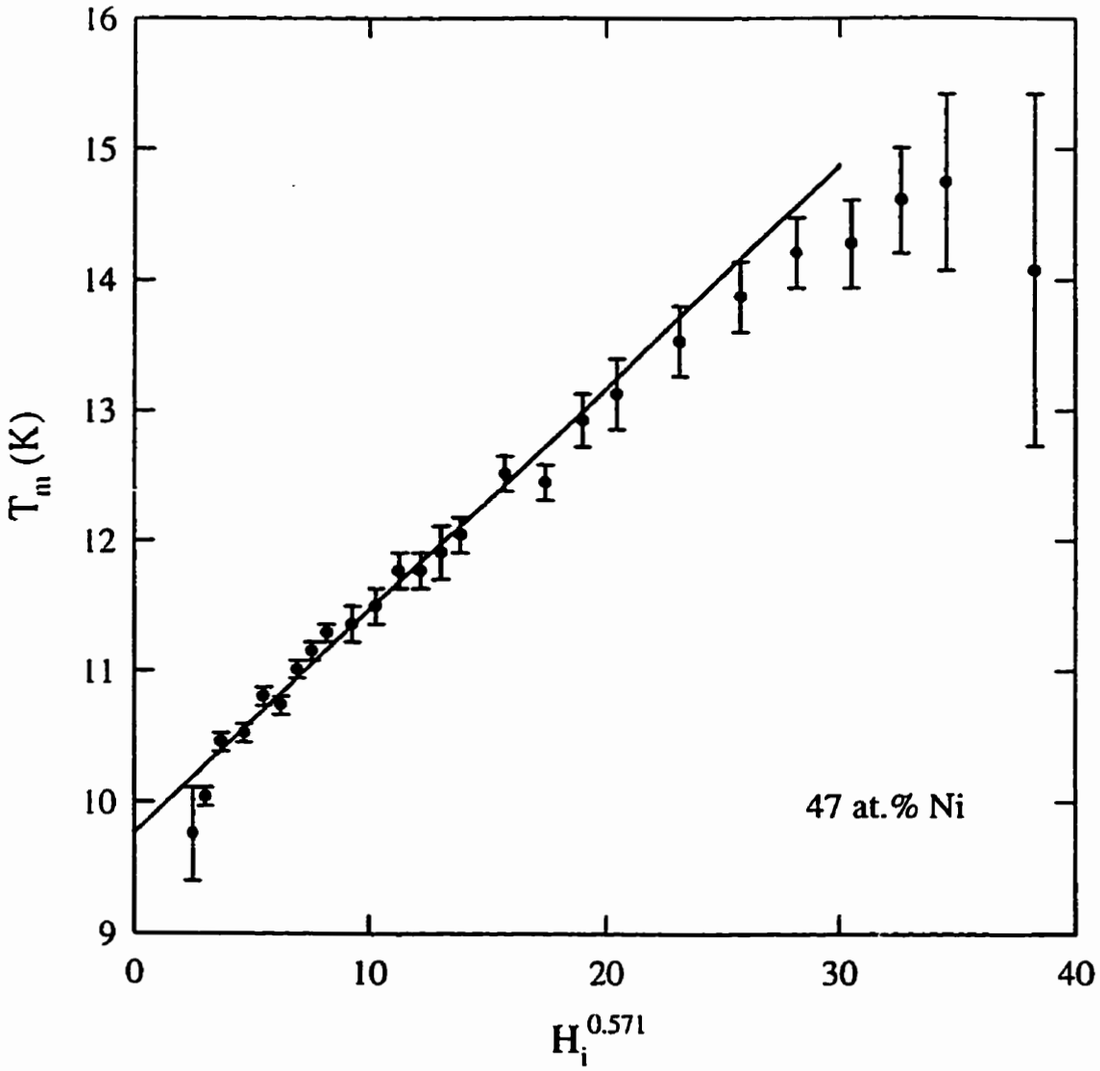

Figure A.56: Peak temperature as a function of internal field to the power of 0.571 for $Cu_{100-x}Ni_x$ with x=0.47. The superimposed line represents a fit to the data with T_c=9.8K.

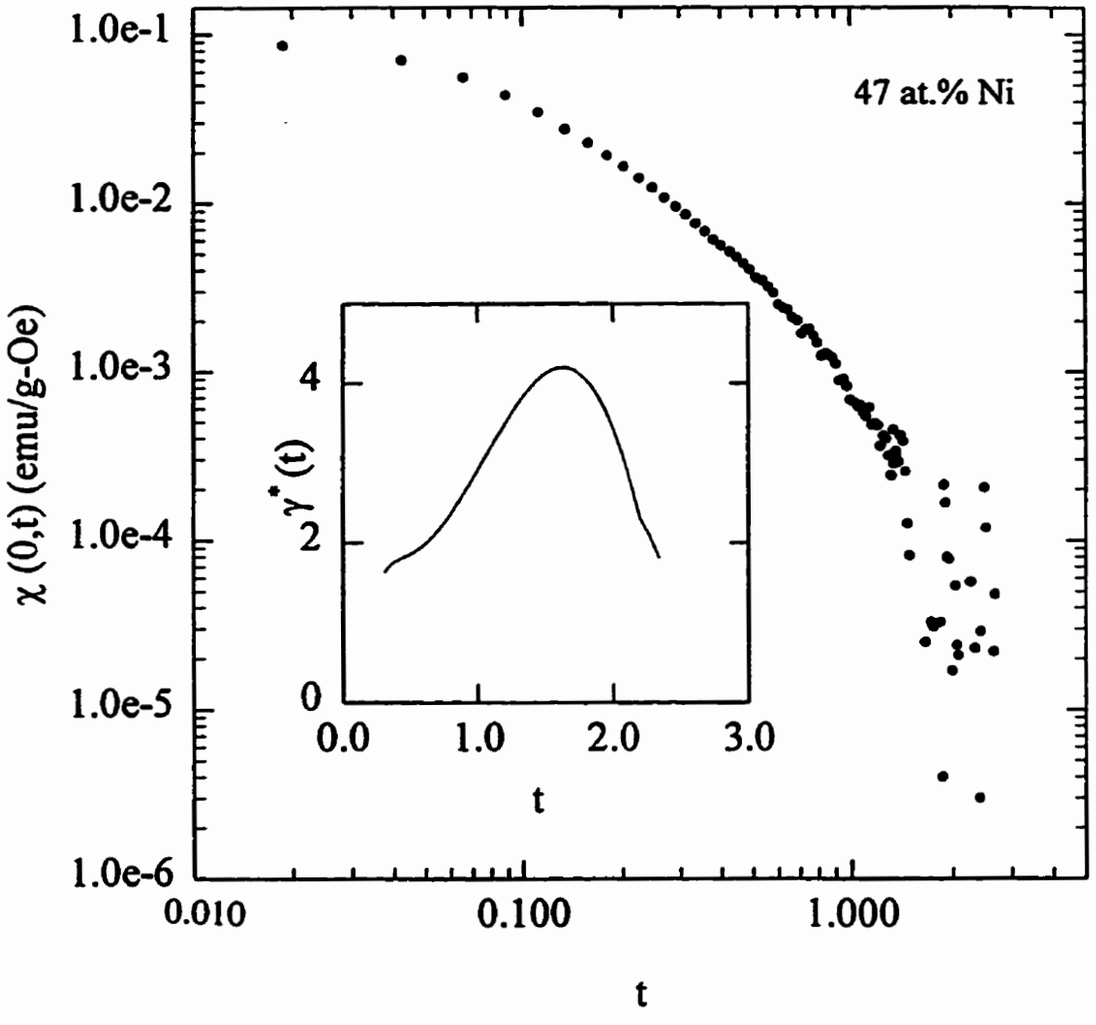

Figure A.57: The zero field susceptibility as a function of reduced temperature for the 47 at.% Ni sample. The inset shows the calculated effective exponent, $\gamma^*(t)$.

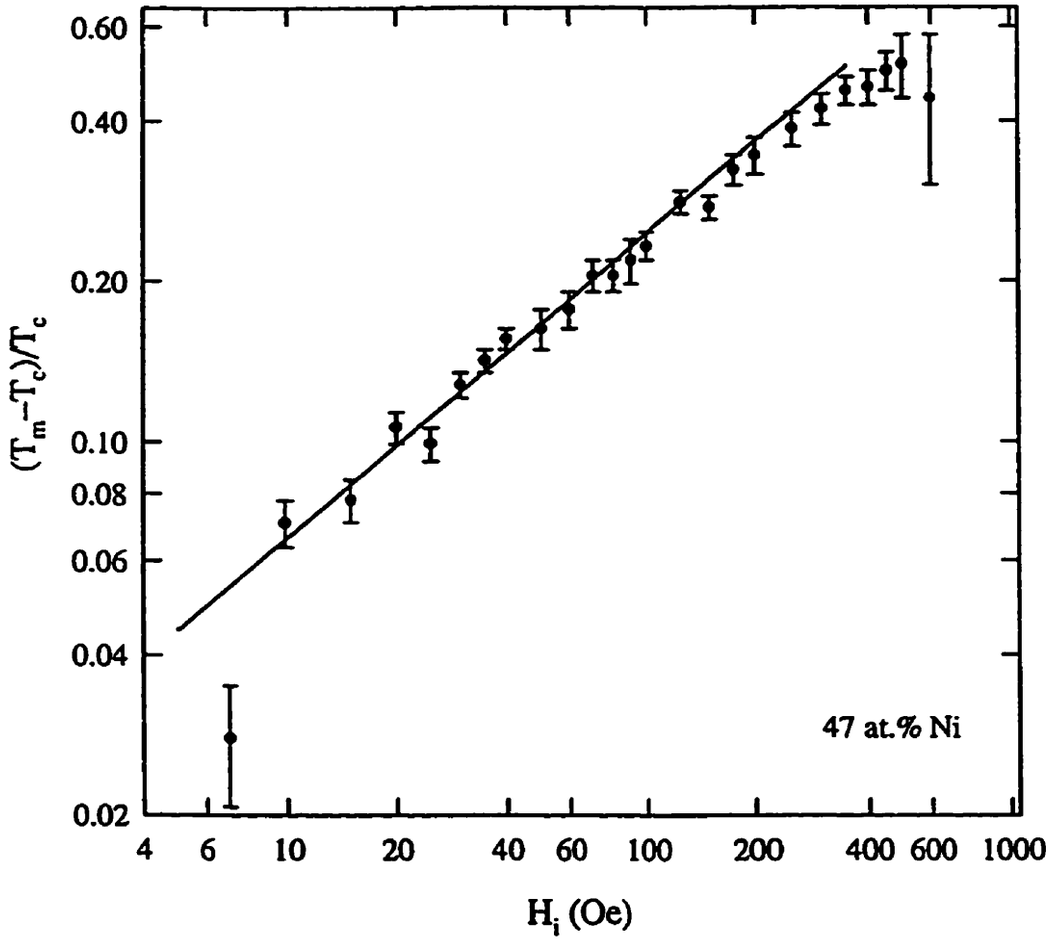

Figure A.58: Reduced peak temperature as a function of internal field for x=0.47. The superimposed line represents the 3D Heisenberg prediction, $1/(\gamma + \beta)$=0.571.

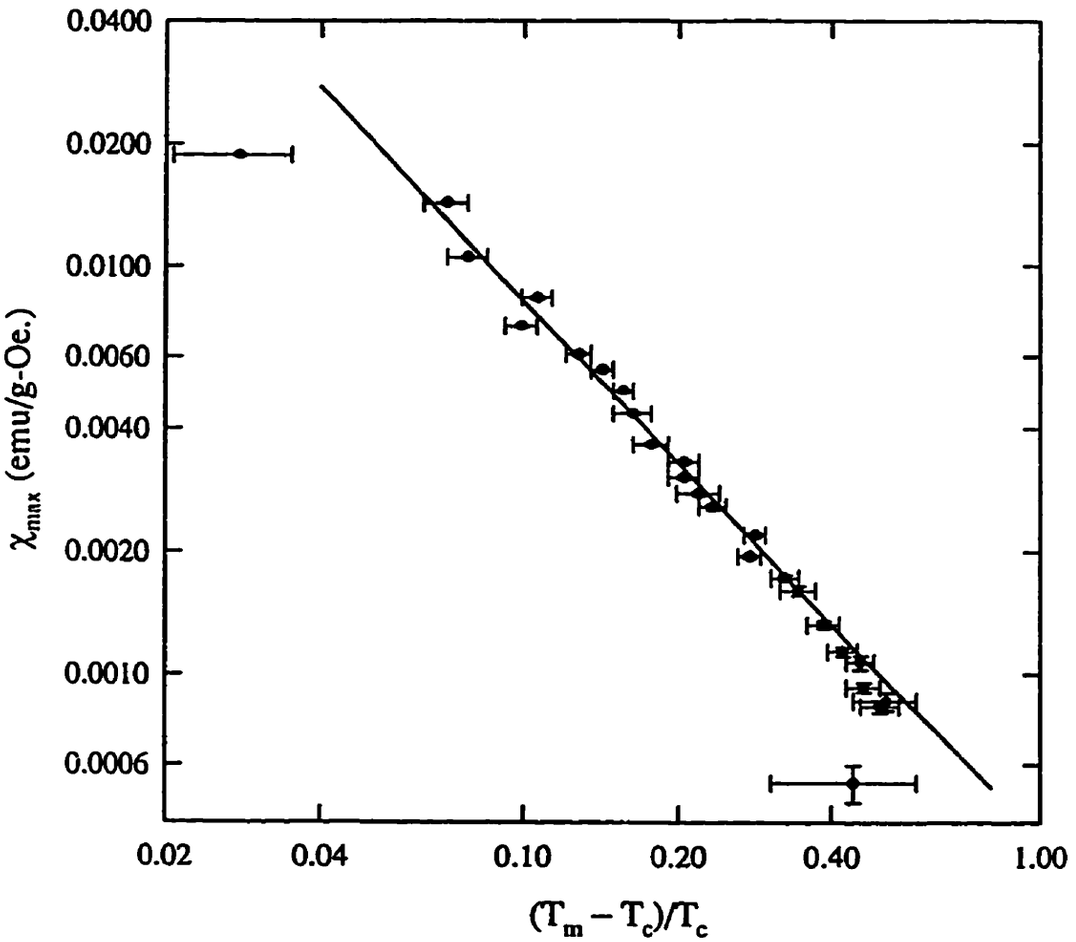

Figure A.59: Peak susceptibility as a function of reduced peak temperature for the 47 at.% Ni sample. The superimposed line represents the 3D Heisenberg value for γ=1.386.

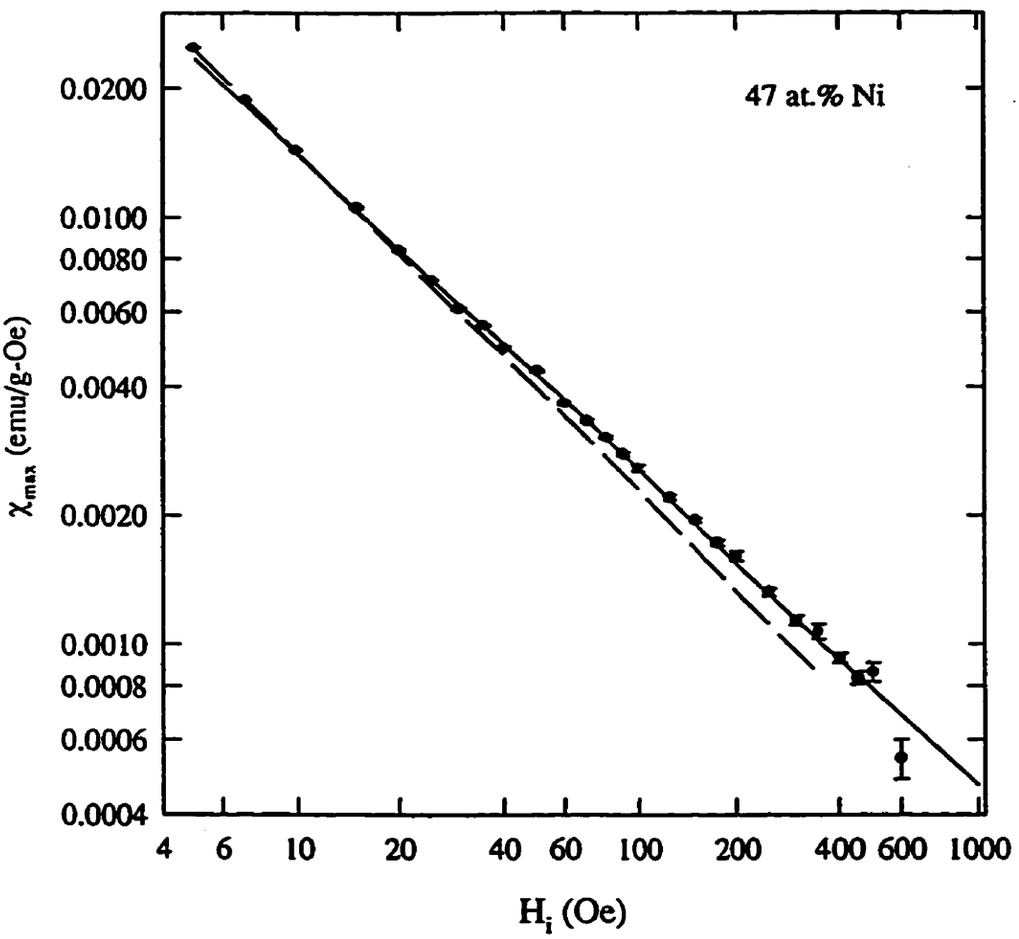

Figure A.60: Peak susceptibility as a function of internal field for the 47 at.% Ni sample. The solid line represents a fit to the high field data with δ=3.8(1). The dashed line shows a fit calculated using the 3D Heisenberg exponent, δ=4.8(3).

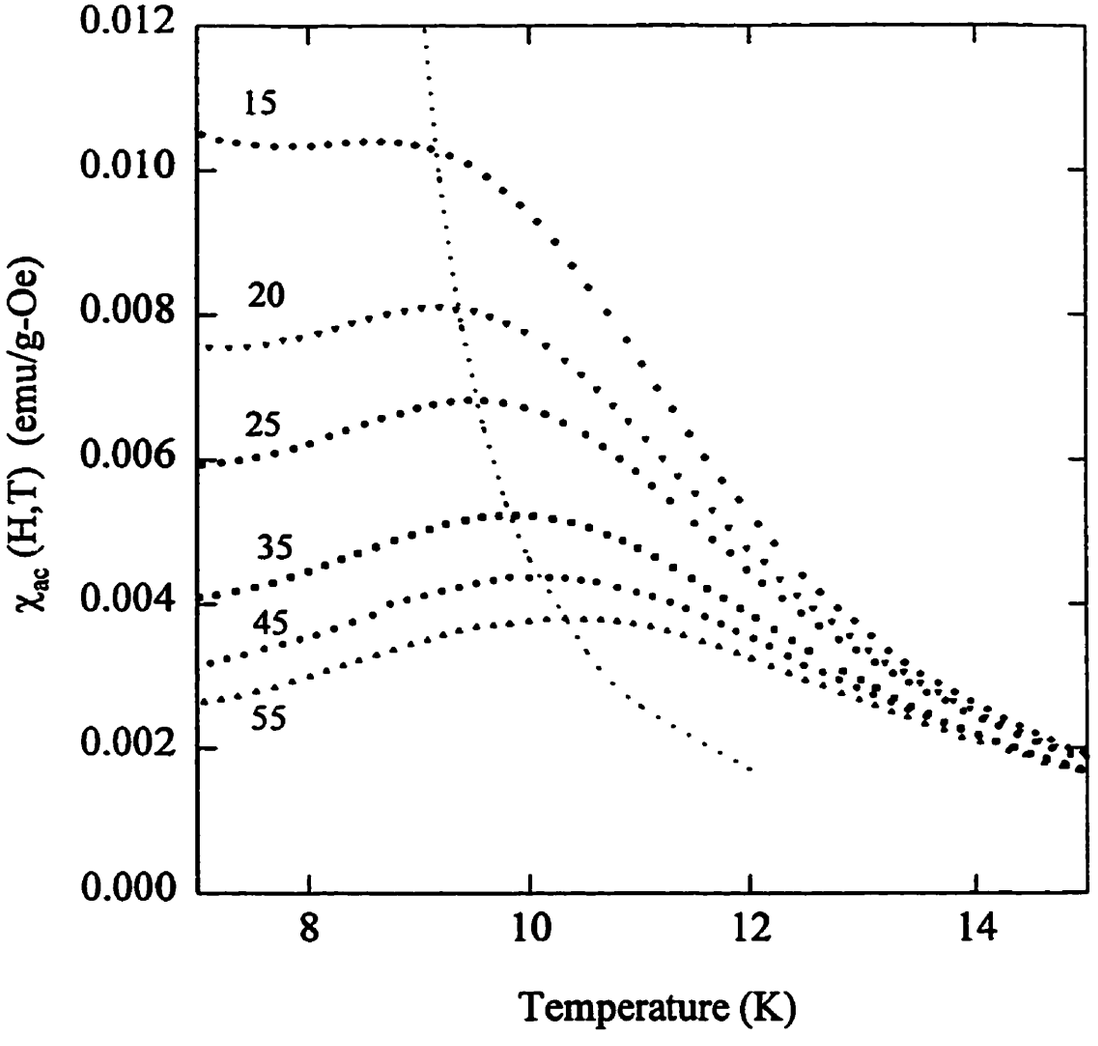

Figure A.61: The temperature dependence of the *ac* susceptibility in fixed biasing fields as labelled, in Oe, for the x=0.465 sample. The dotted line represents the crossover line, as discussed in the text.

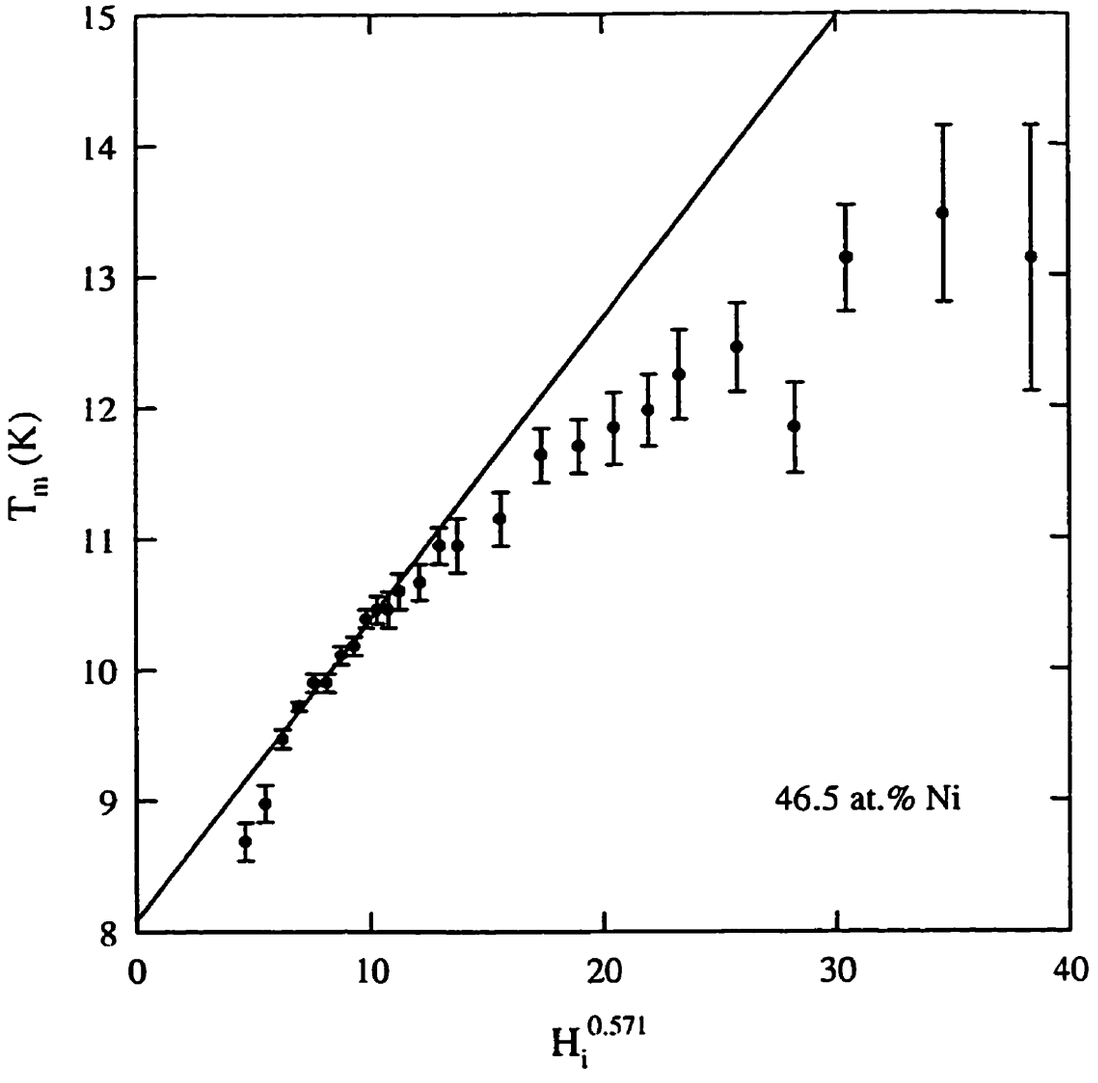

Figure A.62: Peak temperature as a function of internal field to the power of 0.571 for $Cu_{100-x}Ni_x$ with x=0.465. The superimposed line represents a fit to the data with T_c=8.1K.

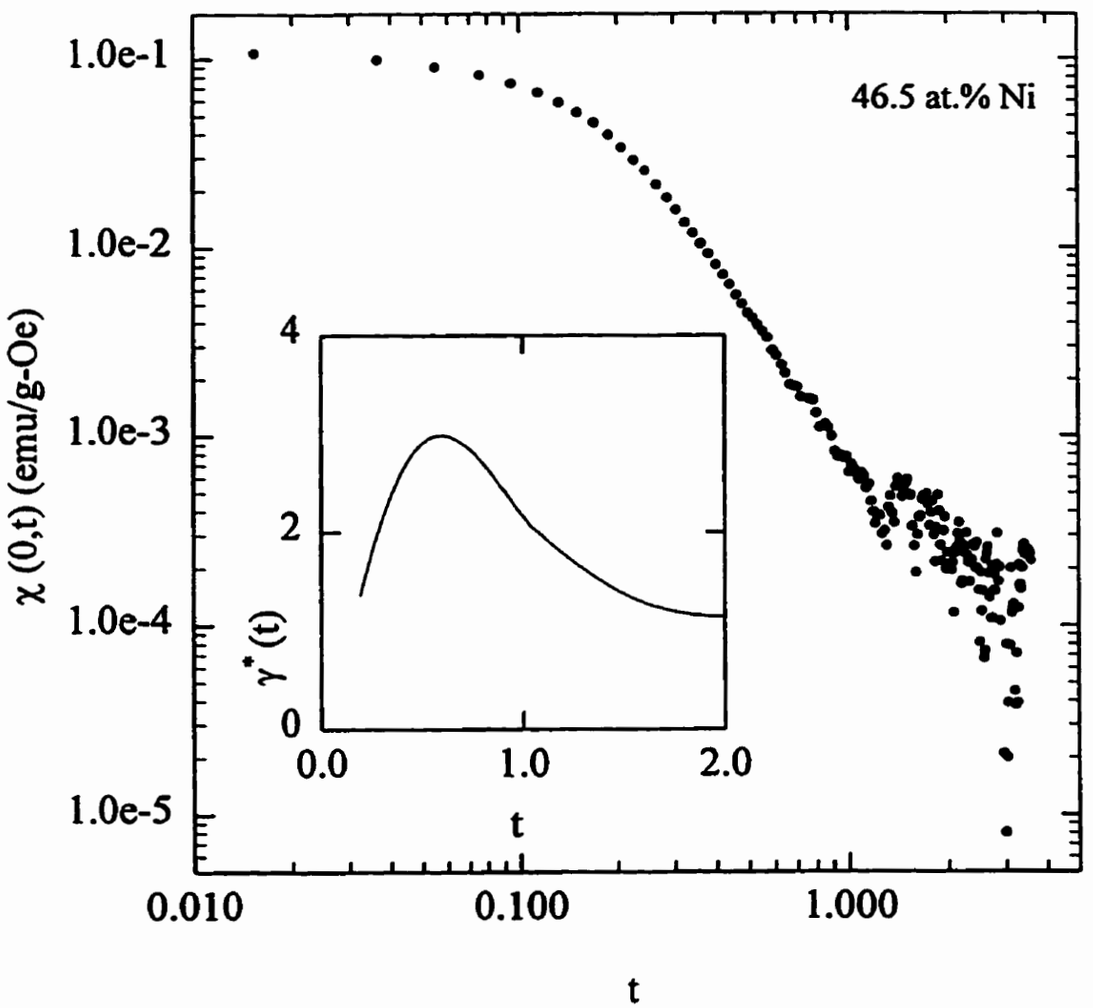

Figure A.63: The zero field susceptibility as a function of reduced temperature for the 46.5 at.% Ni sample. The inset shows the calculated effective exponent, $\gamma^*(t)$.

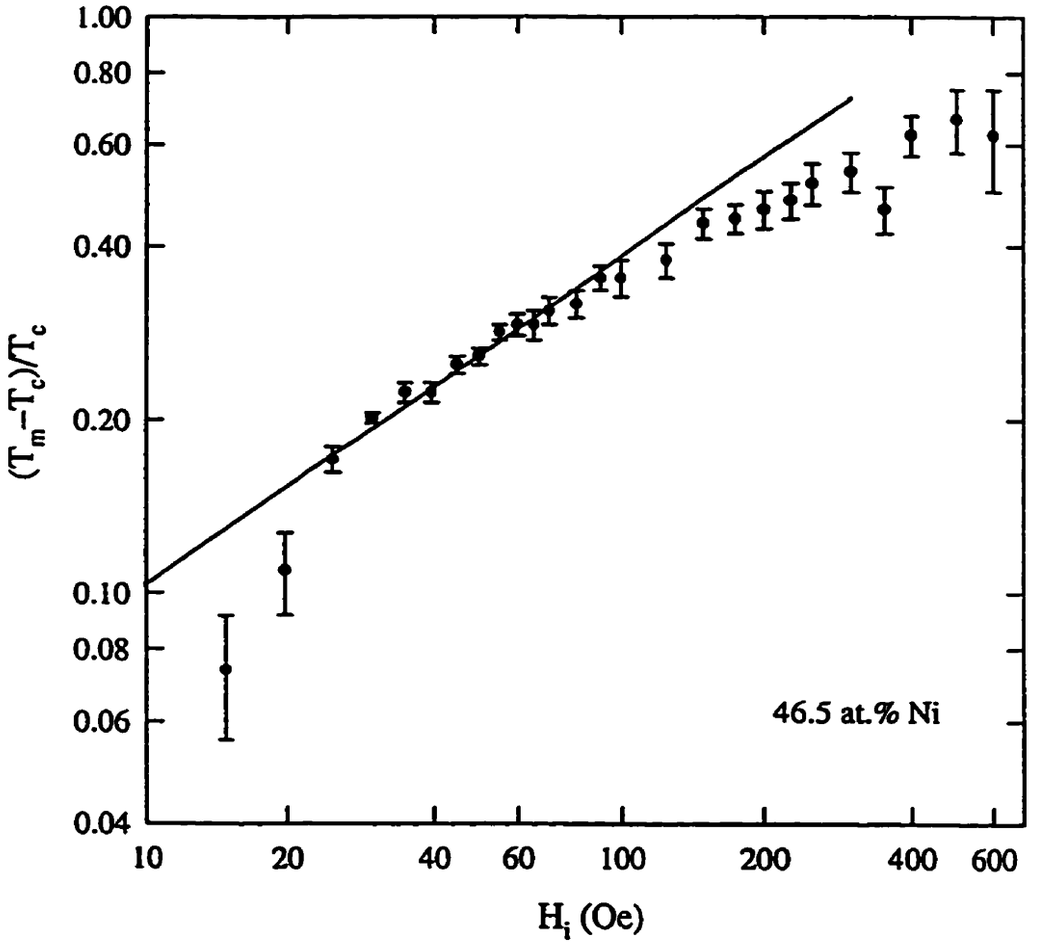

Figure A.64: Reduced peak temperature as a function of internal field for x=0.465. The superimposed line represents the 3D Heisenberg prediction, $1/(\gamma+\beta)$=0.571.

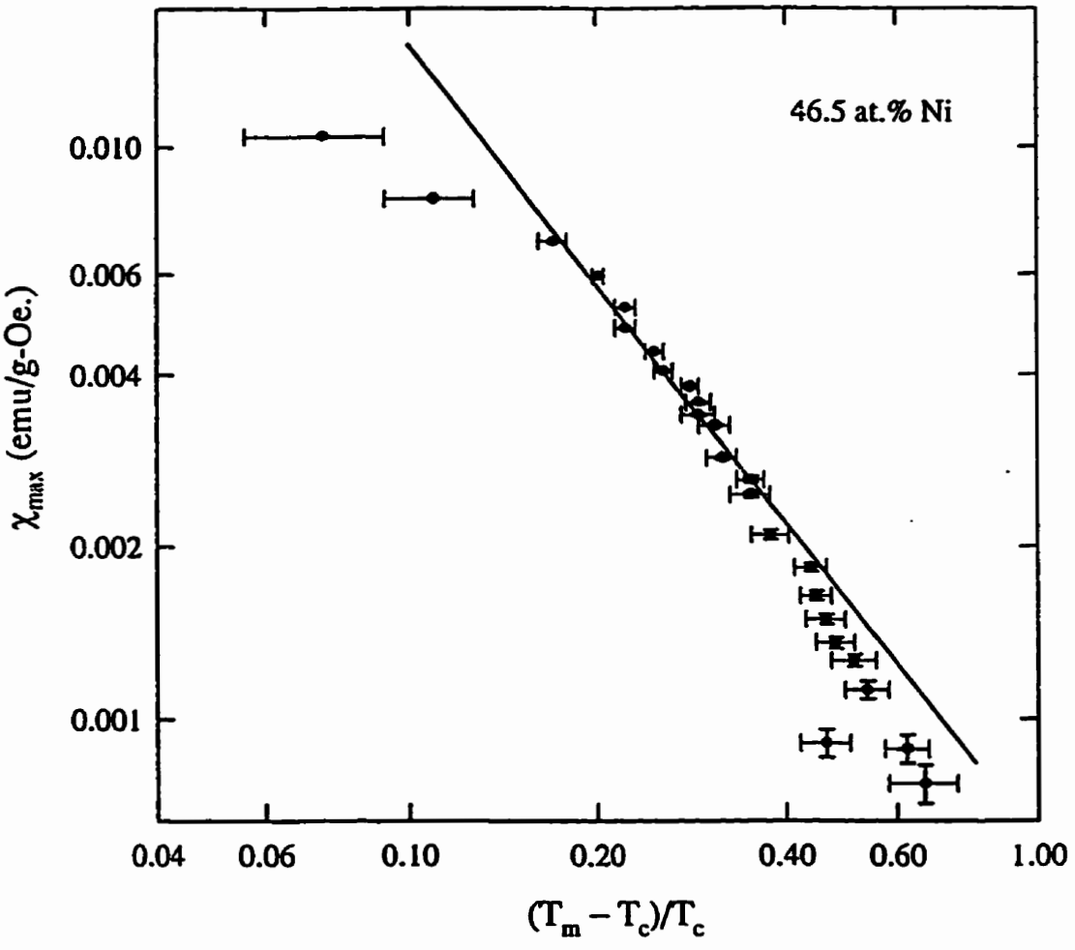

Figure A.65: Peak susceptibility as a function of reduced peak temperature for the 46.5 at.% Ni sample. The superimposed line represents the 3D Heisenberg value for γ=1.386.

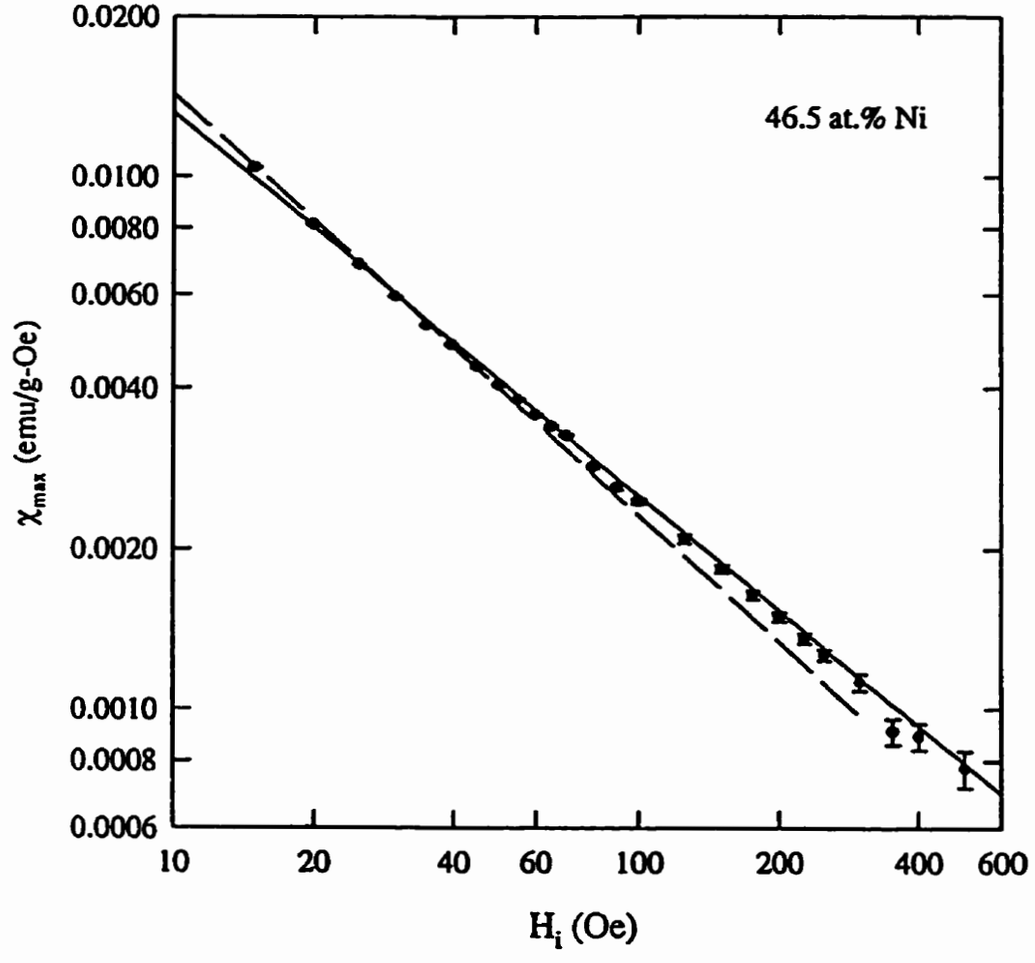

Figure A.66: Peak susceptibility as a function of internal field for the 46.5 at.% Ni sample. The lines represent fits to the data with $\delta_{lf} = 5.8(2)$ and δ_{hf}=3.56(5).

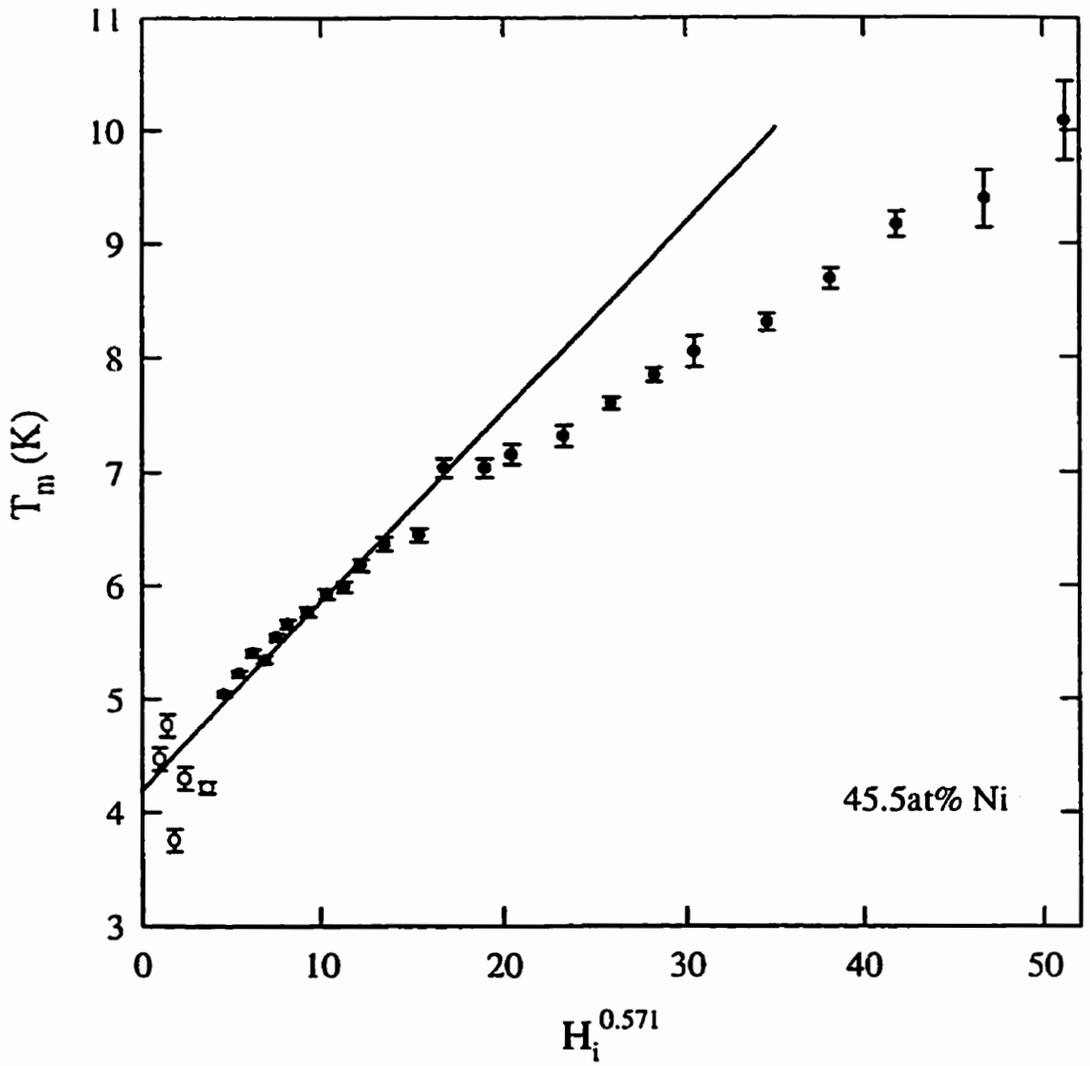

Figure A.67: Peak temperature as a function of internal field to the power of 0.571 for $Cu_{100-x}Ni_x$with x=0.455. The superimposed line represents a fit to the data with T_c=4.2K.

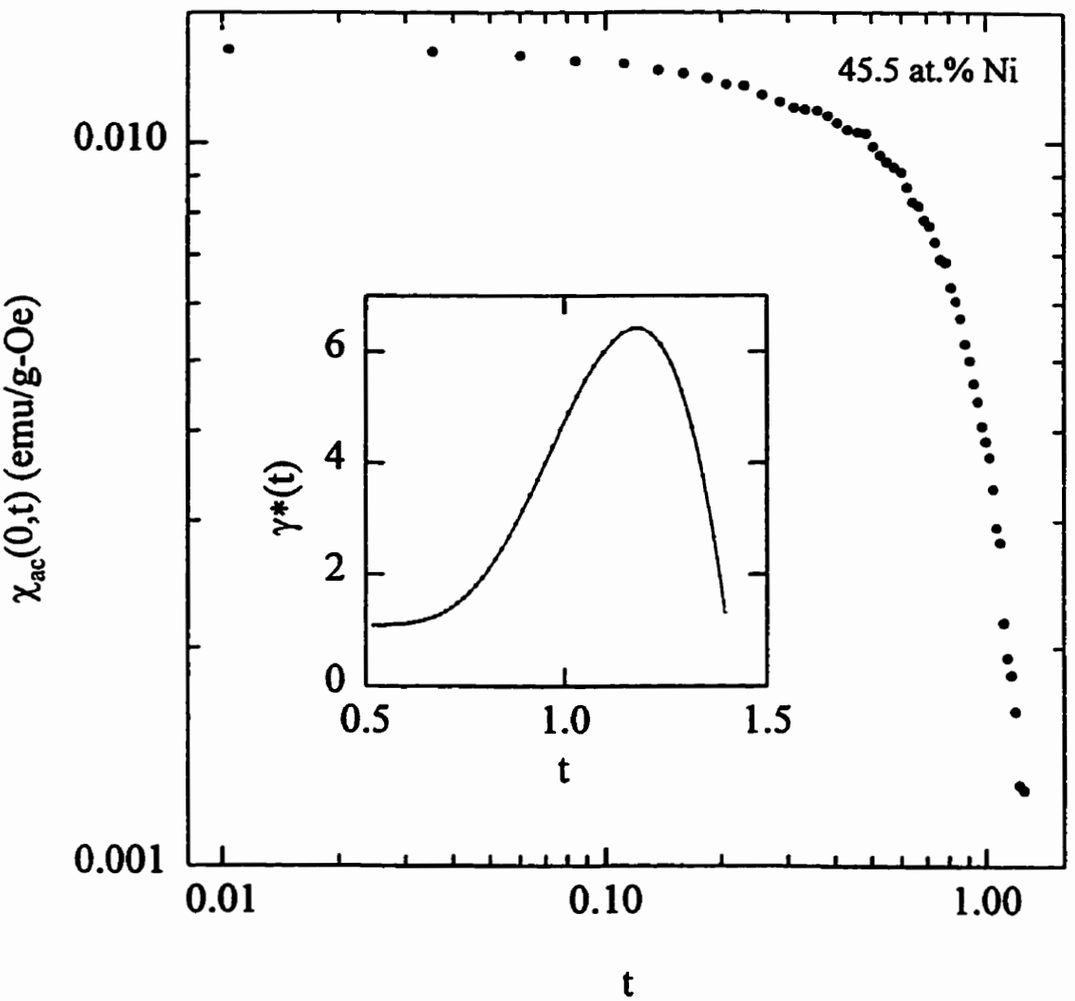

Figure A.68: The zero field susceptibility as a function of reduced temperature for the 45.5 at.% Ni sample. The inset shows the calculated effective exponent, $\gamma^*(t)$.

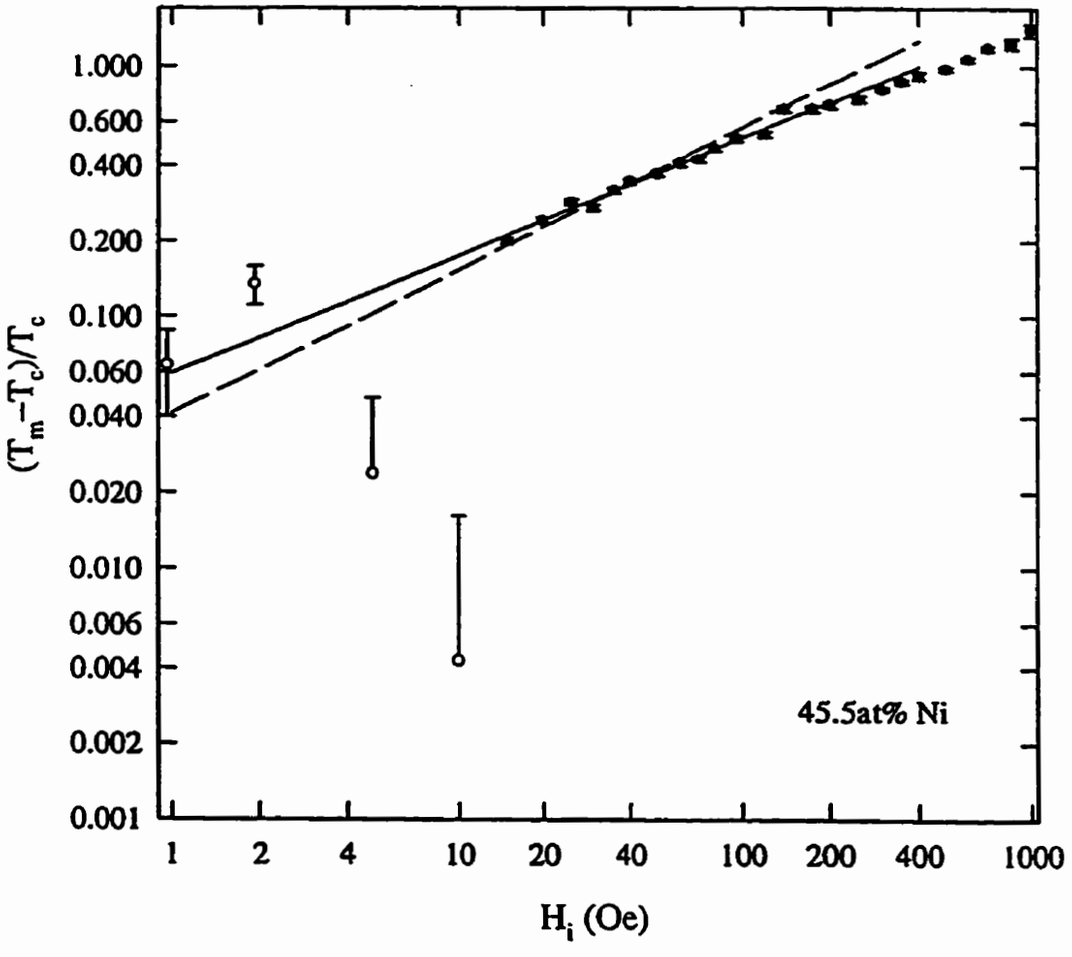

Figure A.69: Reduced peak temperature as a function of internal field for x=0.455. The solid line represents the best fit, $1/(\gamma+\beta)$=0.48(2), and the dashed line is the 3D Heisenberg prediction, $1/(\gamma+\beta)$=0.571.

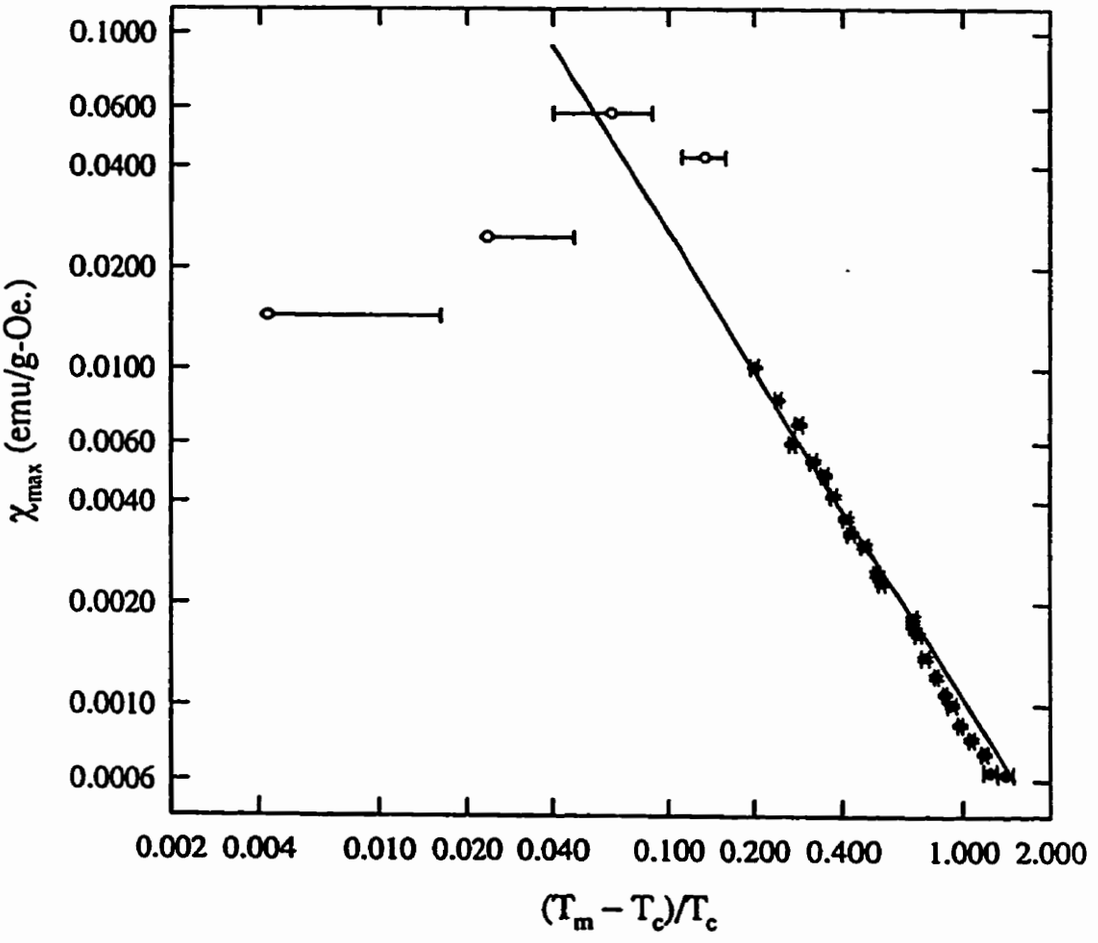

Figure A.70: Peak susceptibility as a function of reduced peak temperature for the 45.5 at.% Ni sample. The superimposed line represents the 3D Heisenberg value for γ=1.386.

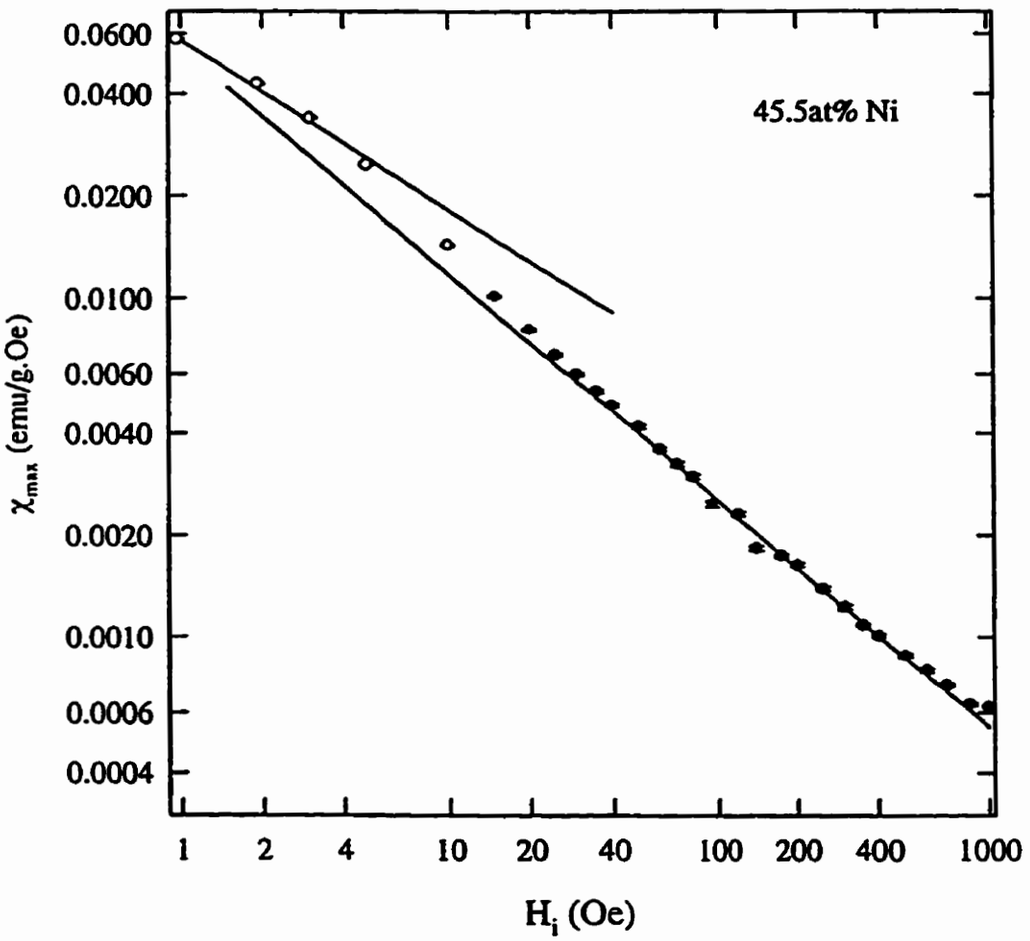

Figure A.71: Peak susceptibility as a function of internal field for the 45.5 at.% Ni sample. The lines represent fits to the data with $\delta_{lf} = 2.00(4)$ and δ_{hf}=3.00(2).

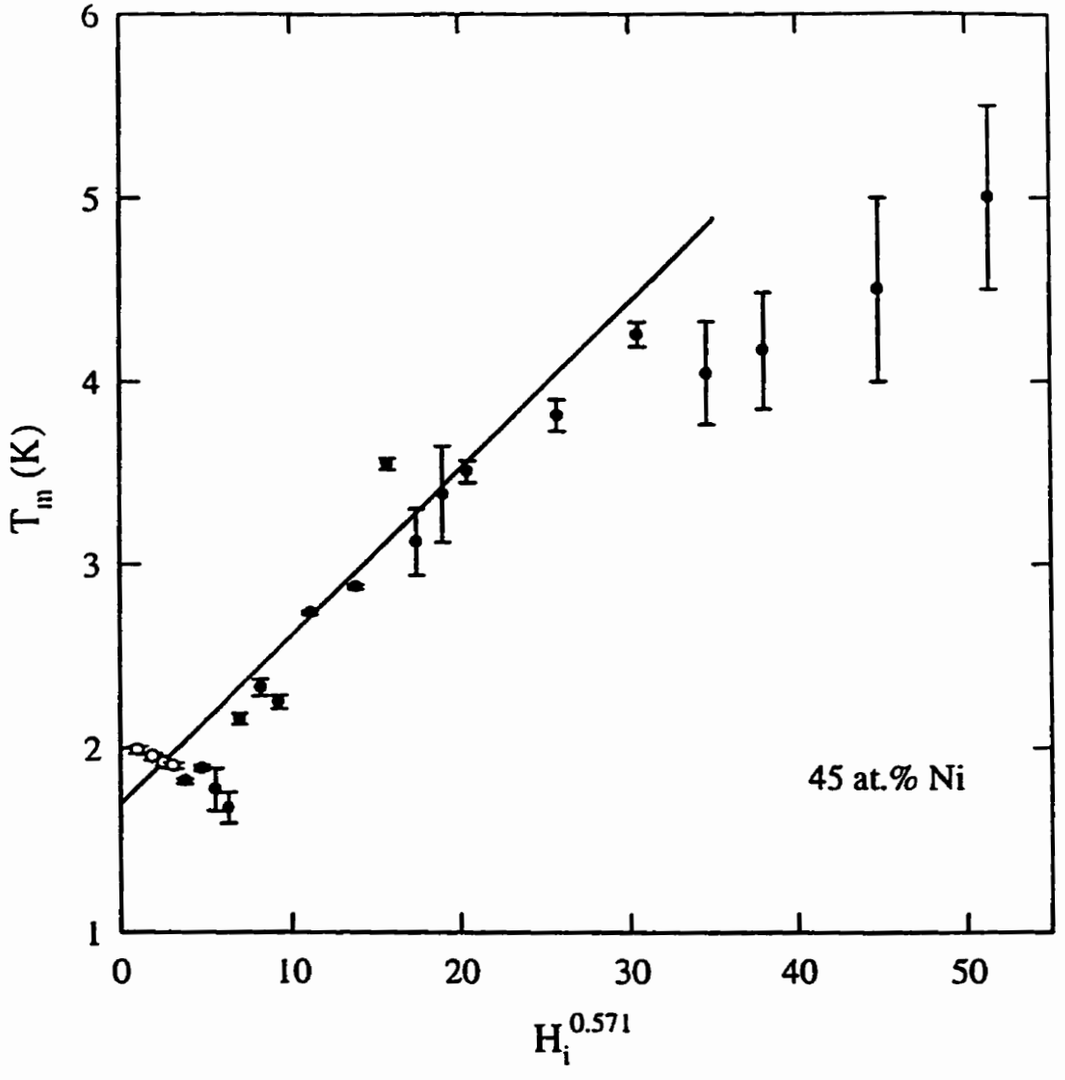

Figure A.72: Peak temperature as a function of internal field to the power of 0.571 for $Cu_{100-x}Ni_x$ with x=0.45. The superimposed line represents a fit to the data with T_c=1.7K.

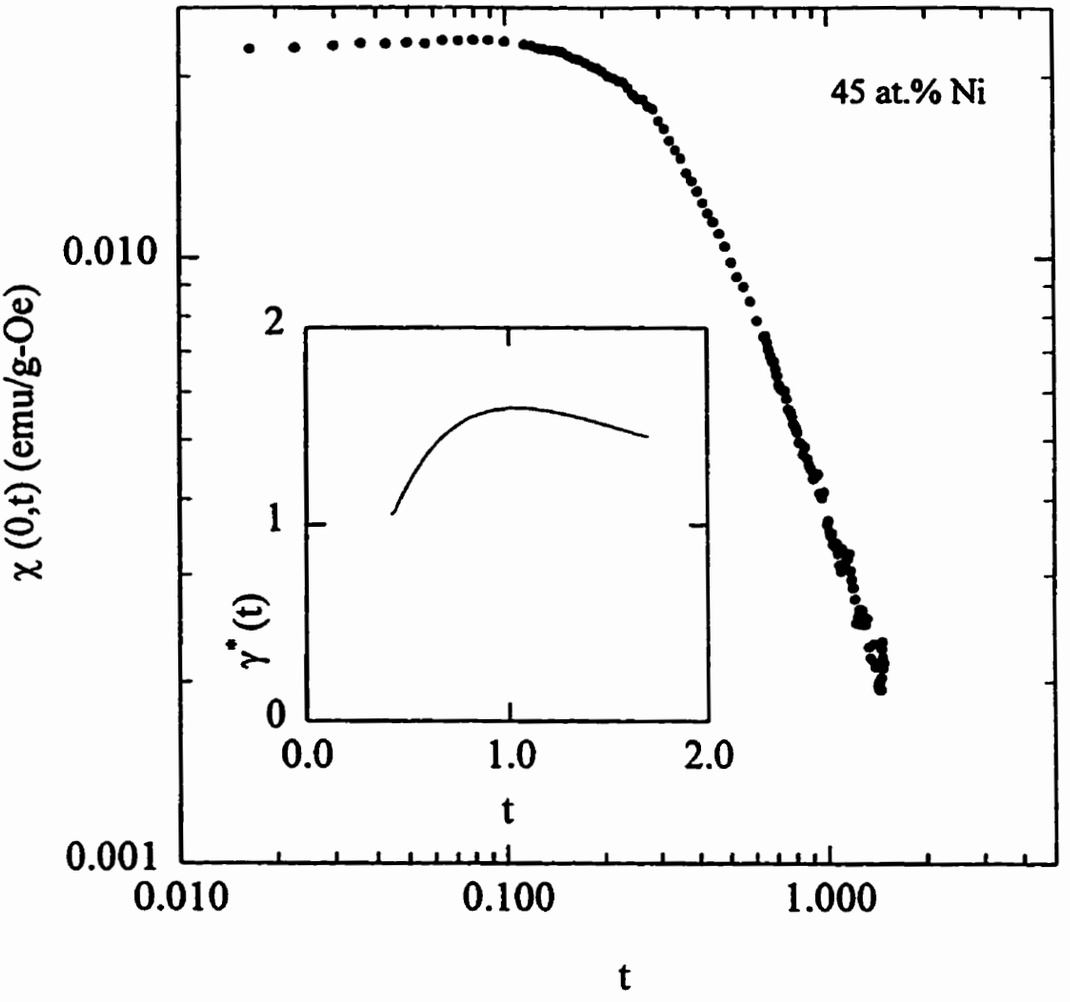

Figure A.73: The zero field susceptibility as a function of reduced temperature for the 45 at.% Ni sample. The inset shows the calculated effective exponent, $\gamma^*(t)$.

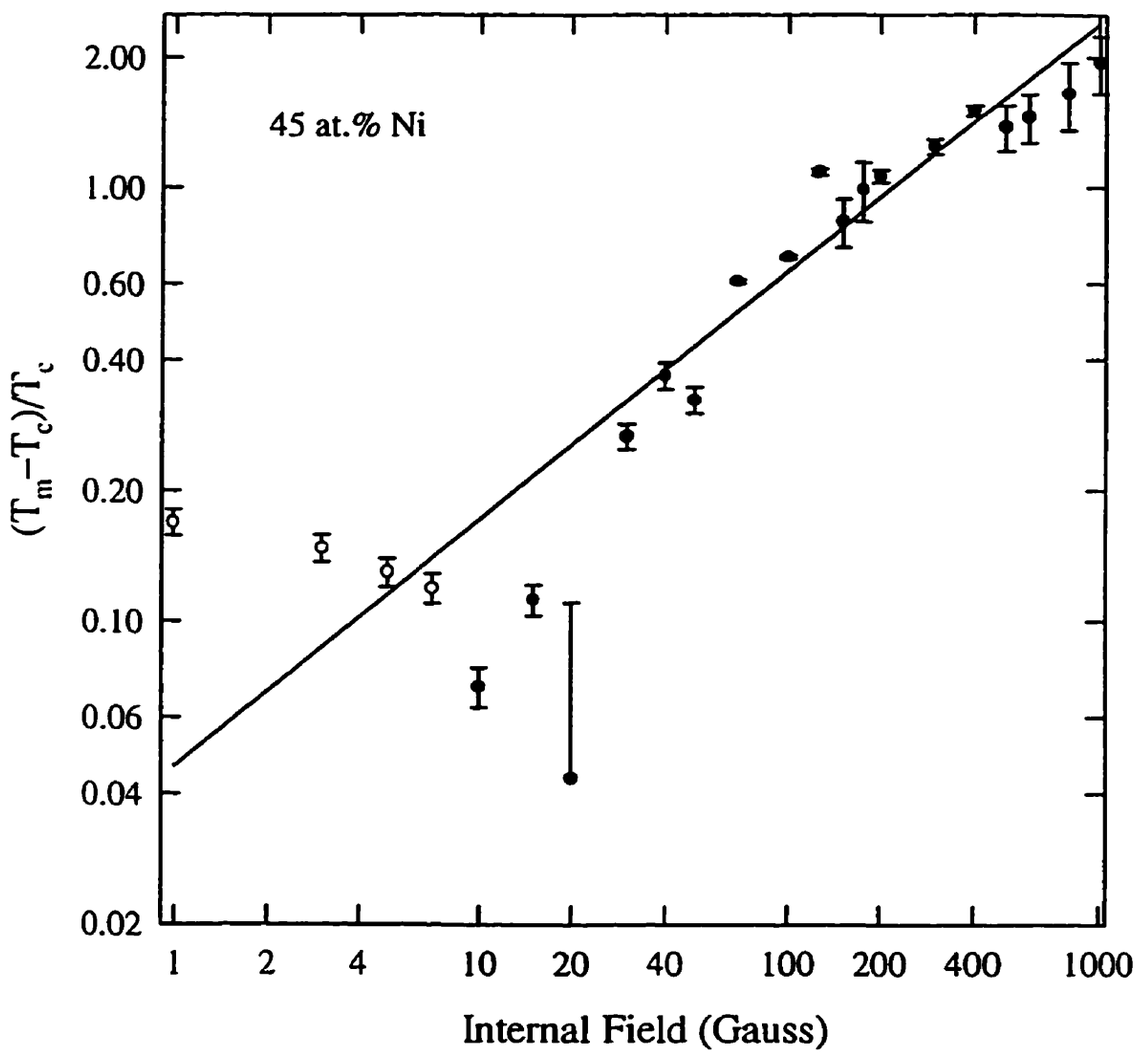

Figure A.74: Reduced peak temperature as a function of internal field for x=0.45. The superimposed line represents the 3D Heisenberg prediction, $1/(\gamma+\beta)$=0.571.

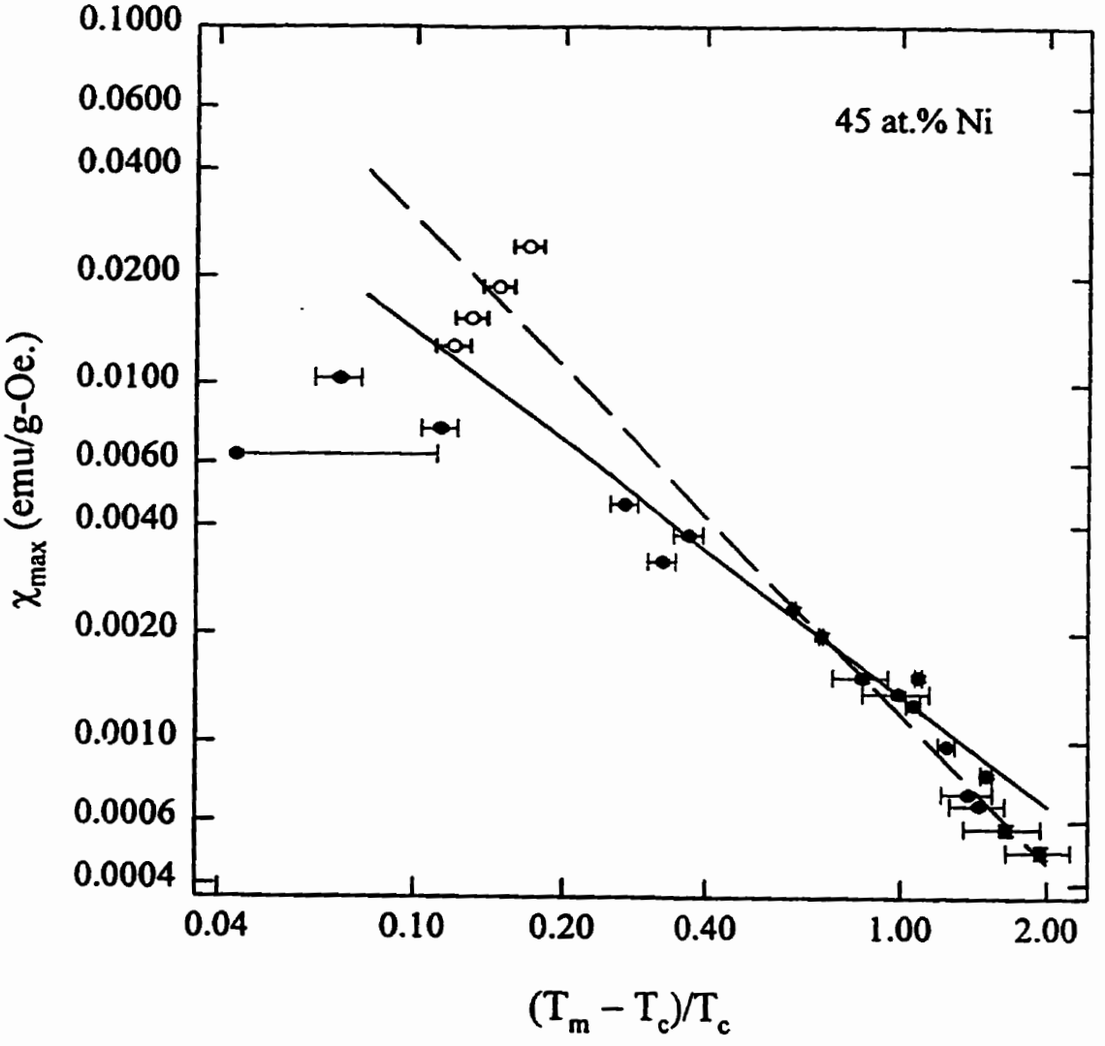

Figure A.75: Peak susceptibility as a function of reduced peak temperature for the 45 at.% Ni sample. The dashed line represents the 3D Heisenberg value for γ=1.386, while the solid line represents the best fit, $\gamma = 1.00(5)$.

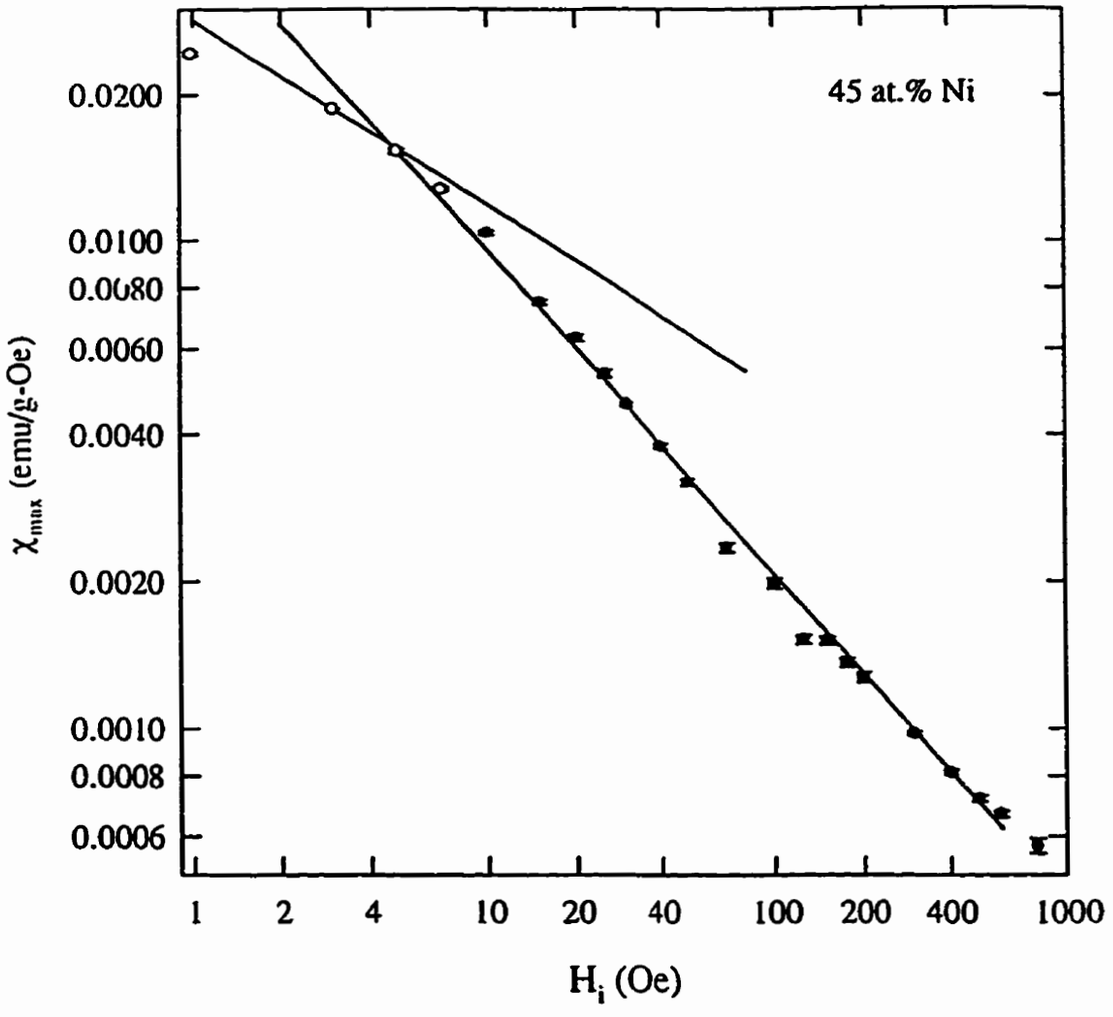

Figure A.76: Peak susceptibility as a function of internal field for the 45 at.% Ni sample. The lines represent fits to the data with $\delta_{lf} = 1.47(2)$ and δ_{hf}=3.00(1).

Resistivity Data and Analysis Plots

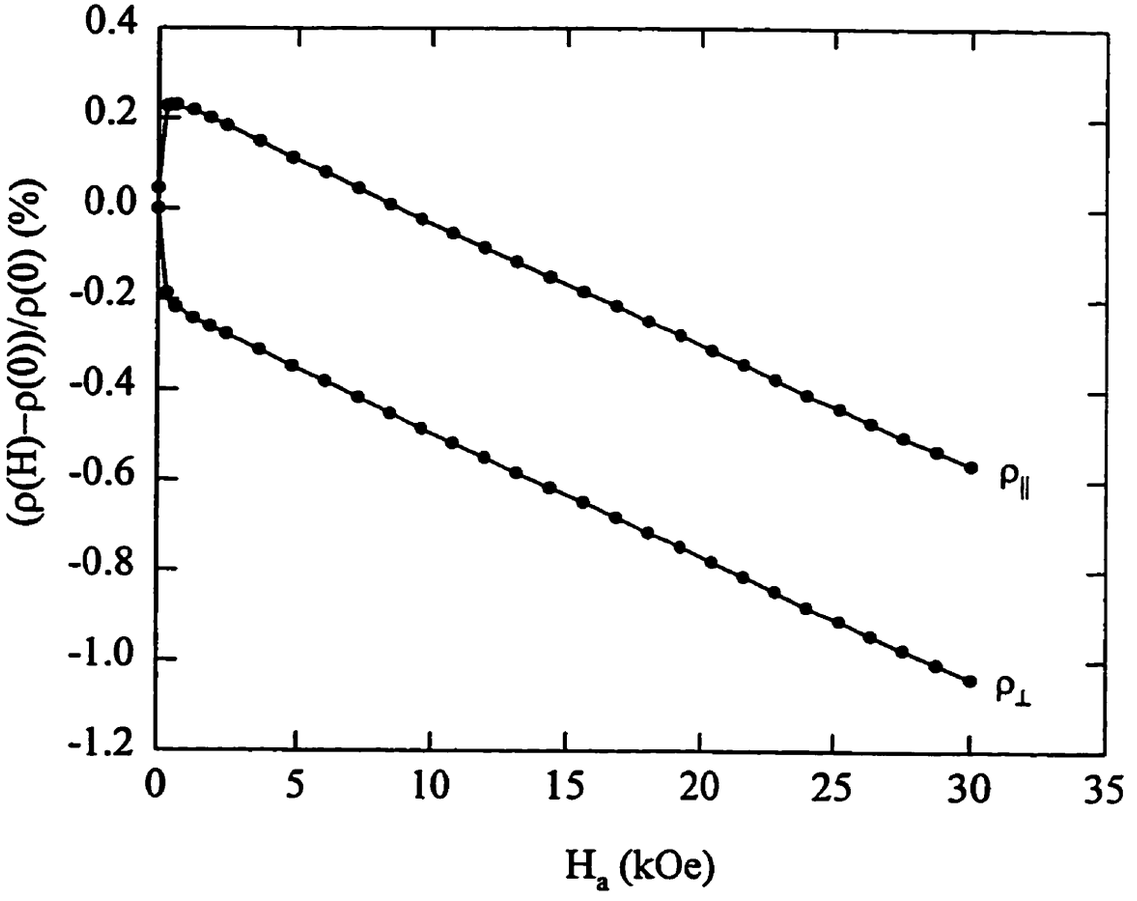

Figure A.77: Magnetoresistance as a function of applied field for the 54 at.% sample, as measured at a fixed temperature of 1.5K.

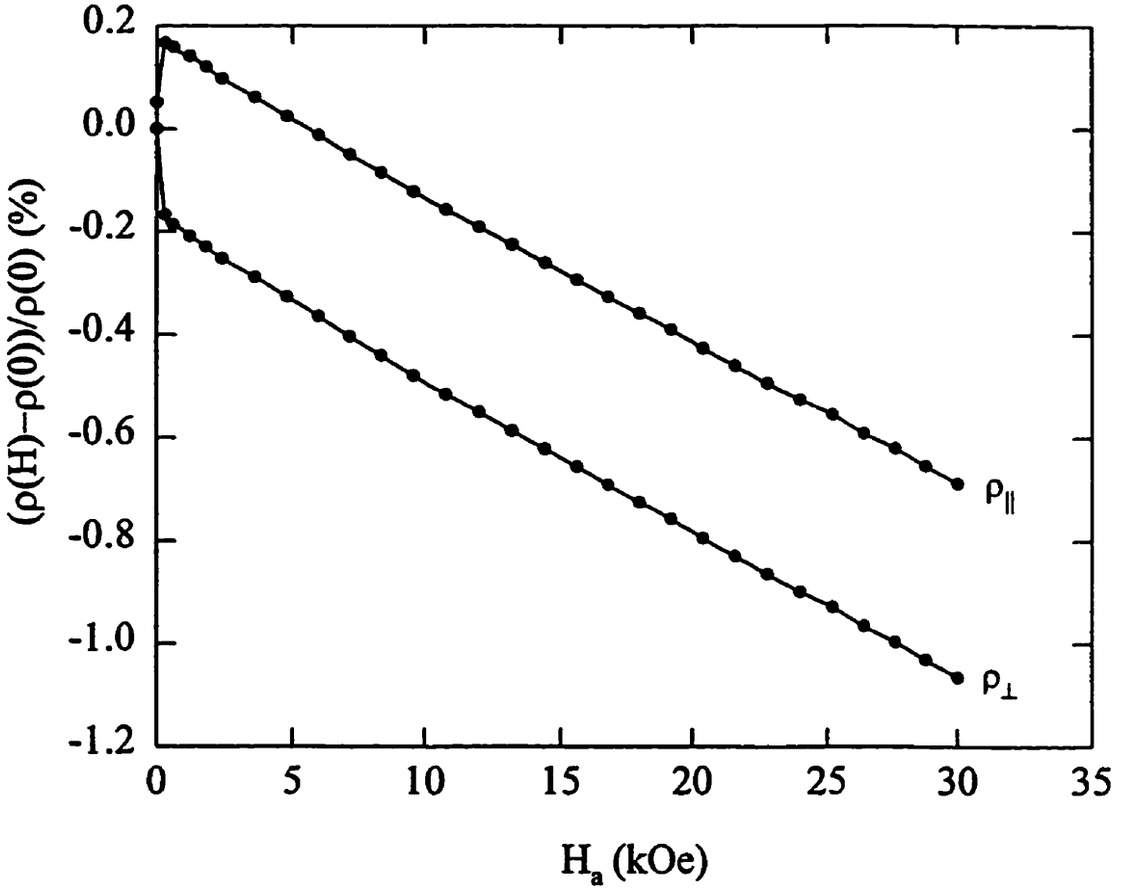

Figure A.78: Magnetoresistance as a function of applied field for the 53 at.% sample, as measured at a fixed temperature of 1.5K.

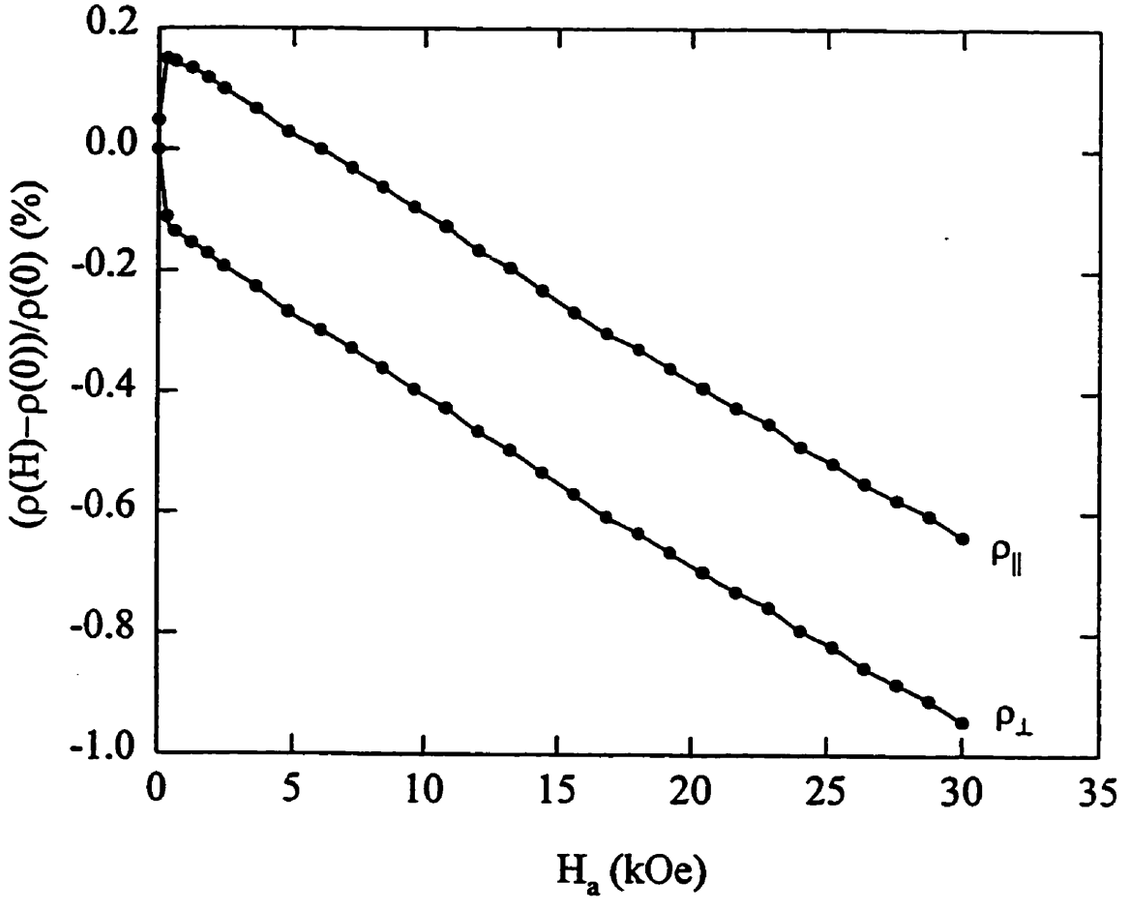

Figure A.79: Magnetoresistance as a function of applied field for the 52 at.% sample, as measured at a fixed temperature of 1.5K.

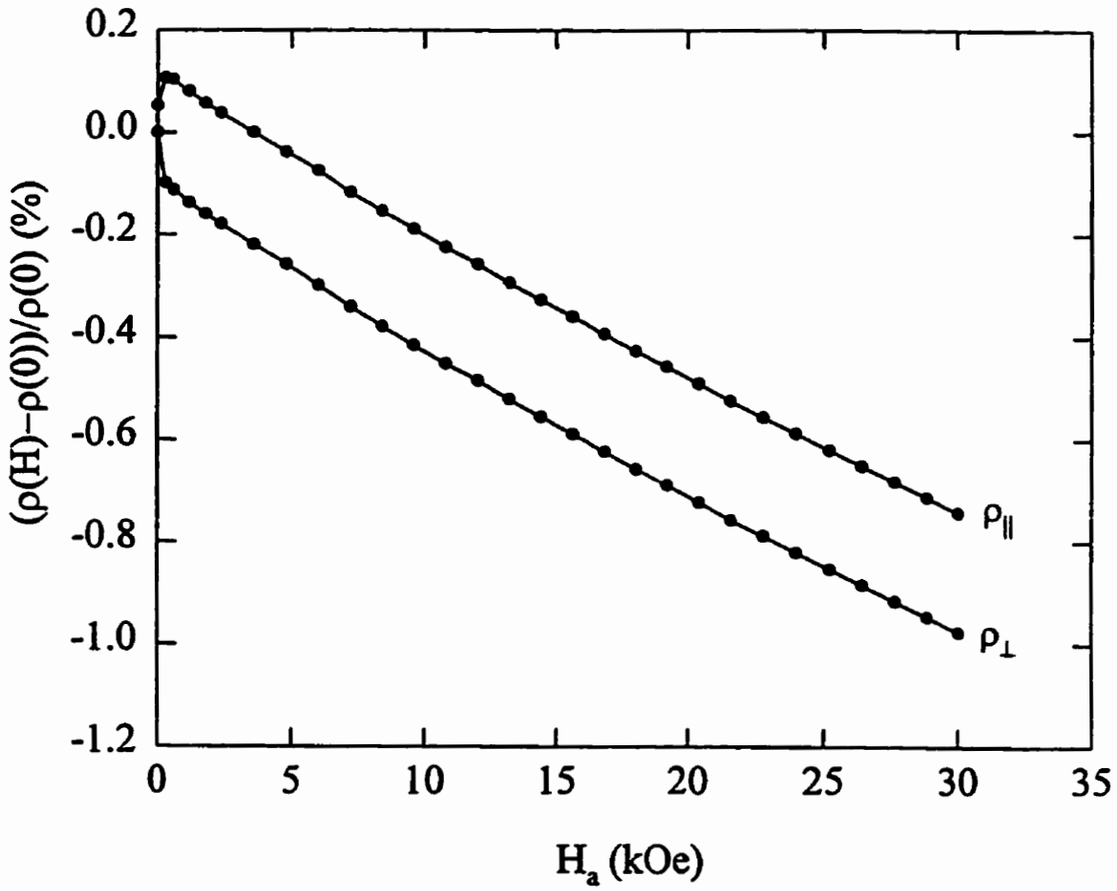

Figure A.80: Magnetoresistance as a function of applied field for the 51 at.% sample, as measured at a fixed temperature of 1.5K.

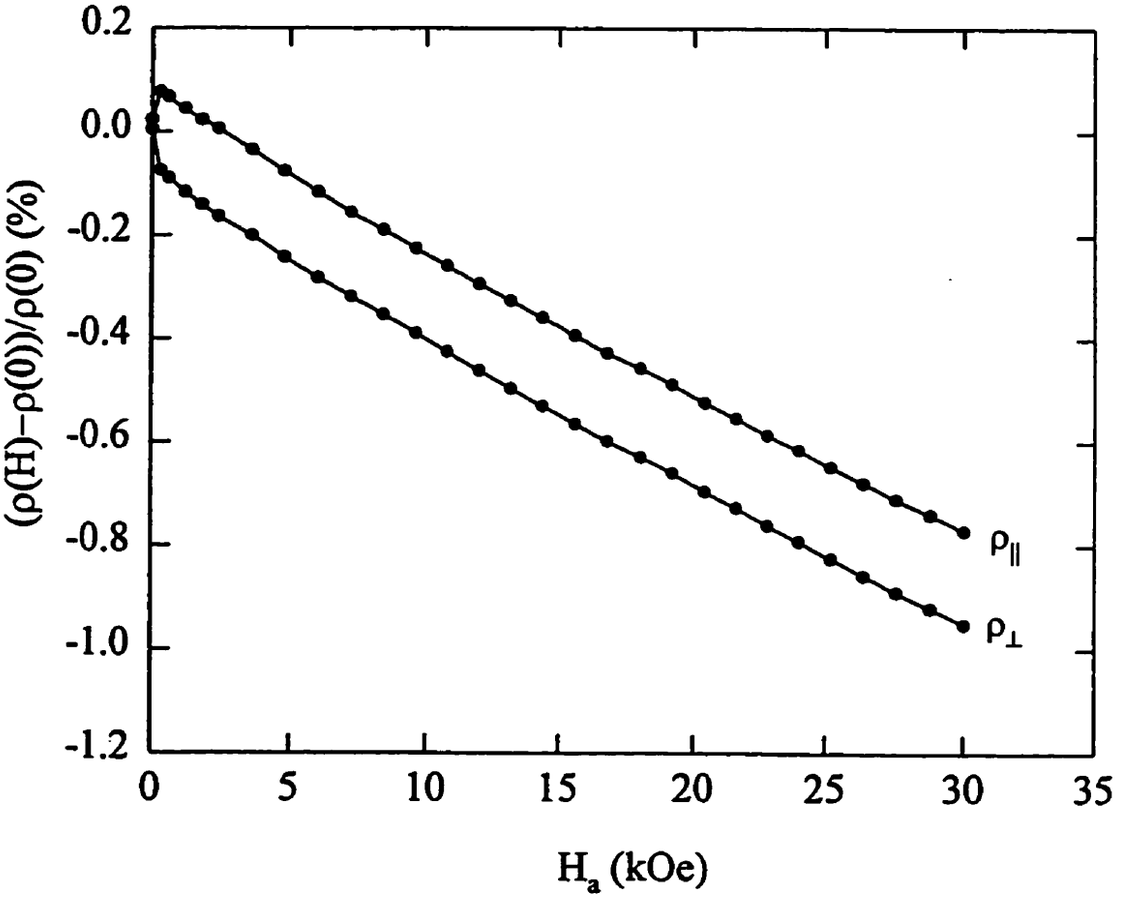

Figure A.81: Magnetoresistance as a function of applied field for the 50 at.% sample, as measured at a fixed temperature of 1.5K.

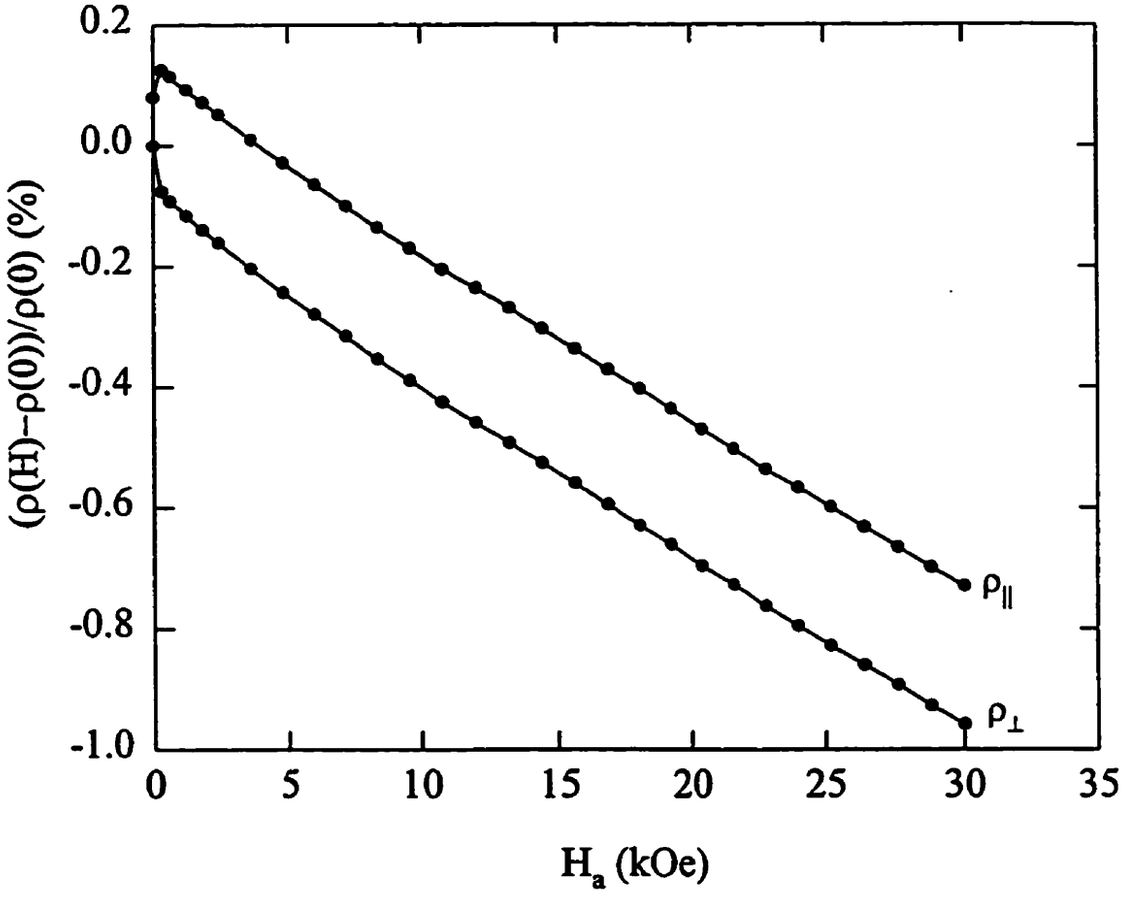

Figure A.82: Magnetoresistance as a function of applied field for the 49.5 at.% sample, as measured at a fixed temperature of 1.5K.

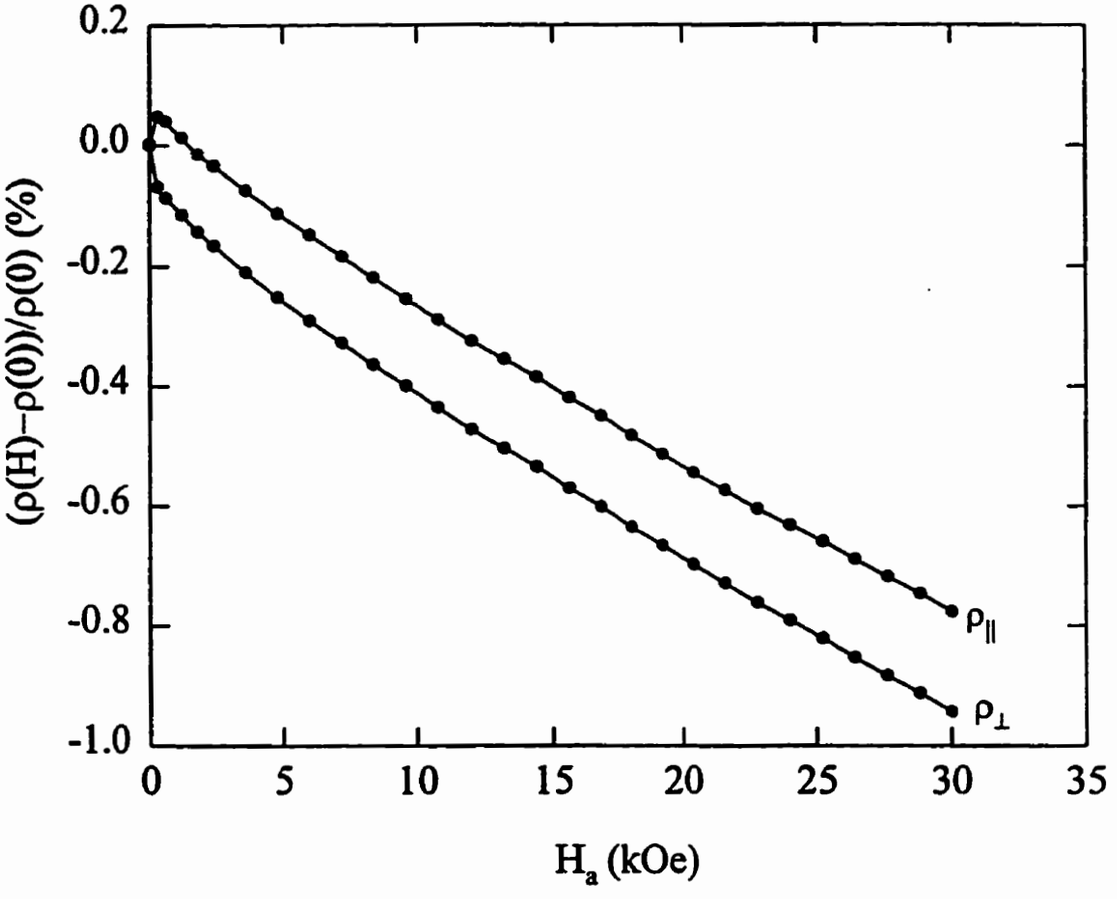

Figure A.83: Magnetoresistance as a function of applied field for the 49 at.% sample, as measured at a fixed temperature of 1.5K.

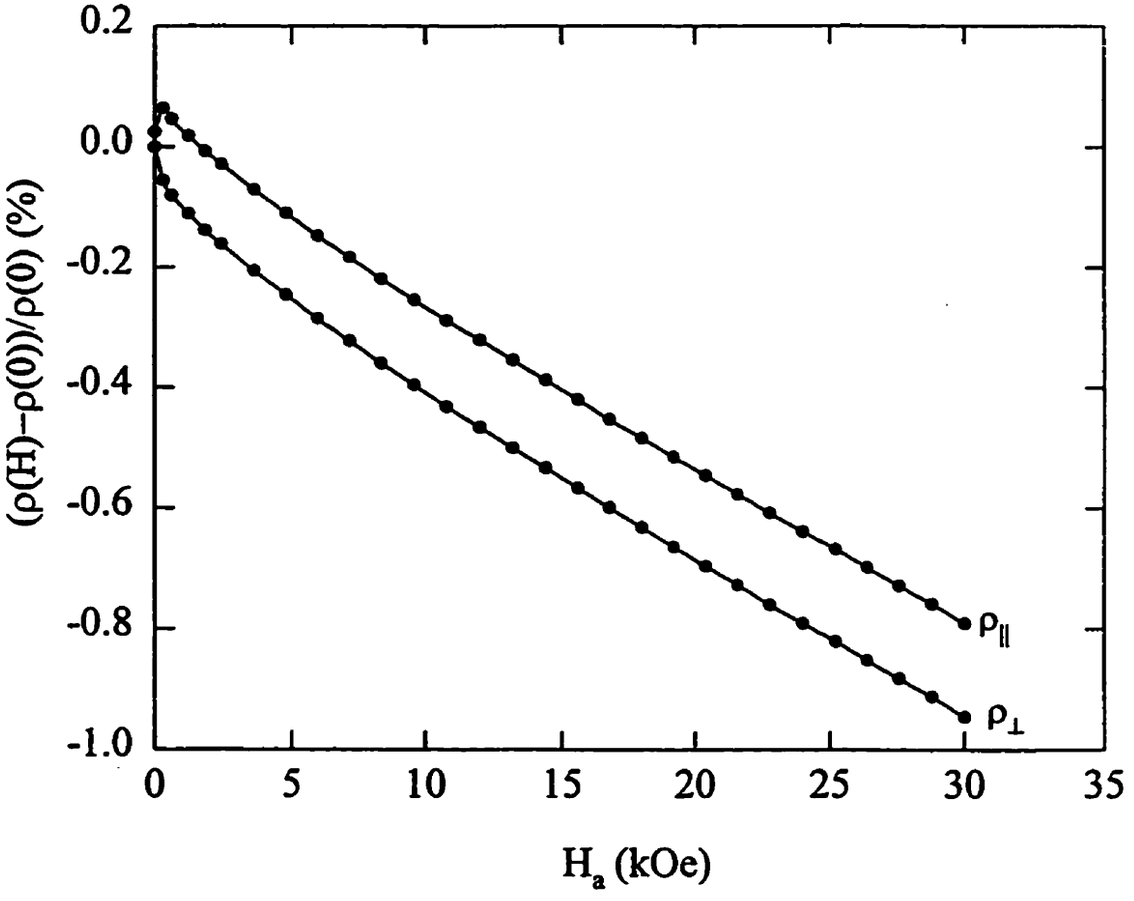

Figure A.84: Magnetoresistance as a function of applied field for the 48.5 at.% sample, as measured at a fixed temperature of 1.5K.

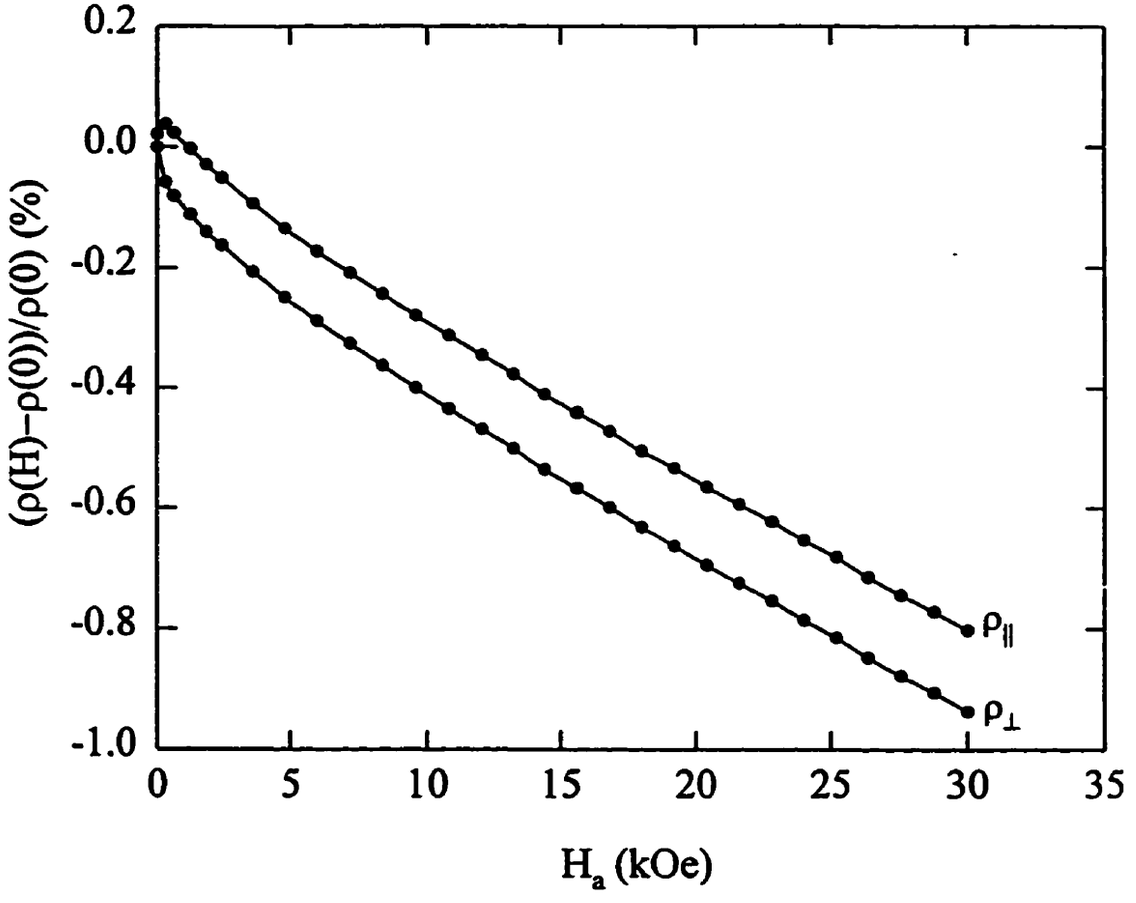

Figure A.85: Magnetoresistance as a function of applied field for the 48 at.% sample, as measured at a fixed temperature of 1.5K.

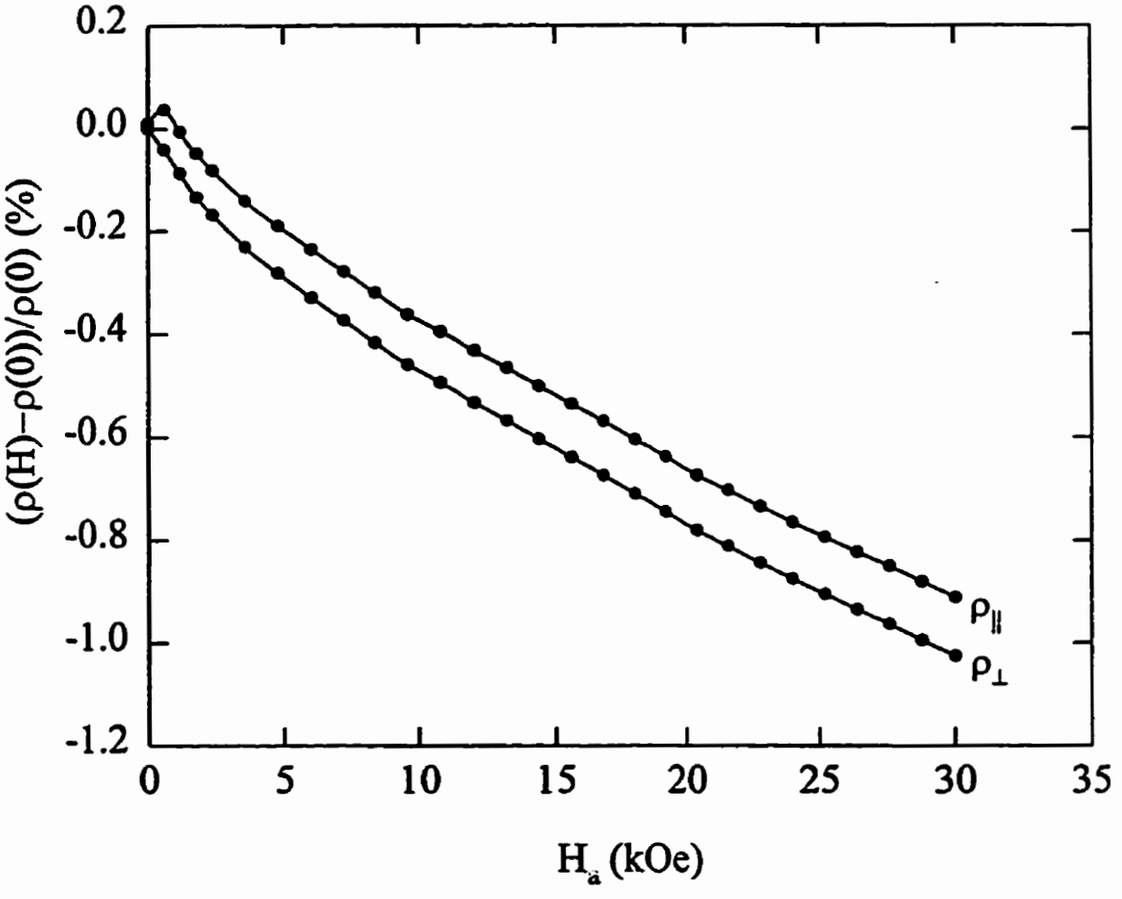

Figure A.86: Magnetoresistance as a function of applied field for the 47.5 at.% sample, as measured at a fixed temperature of 1.5K.

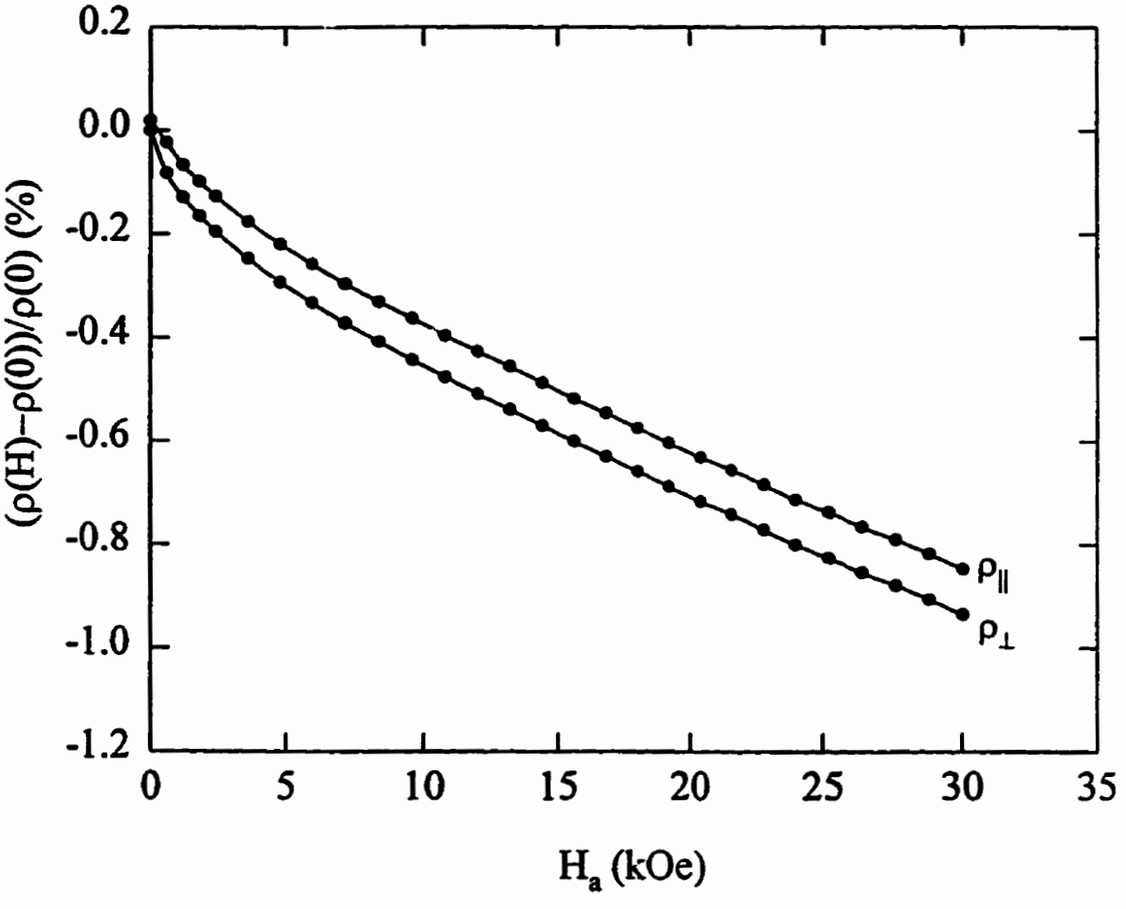

Figure A.87: Magnetoresistance as a function of applied field for the 46.5 at.% sample, as measured at a fixed temperature of 1.5K.

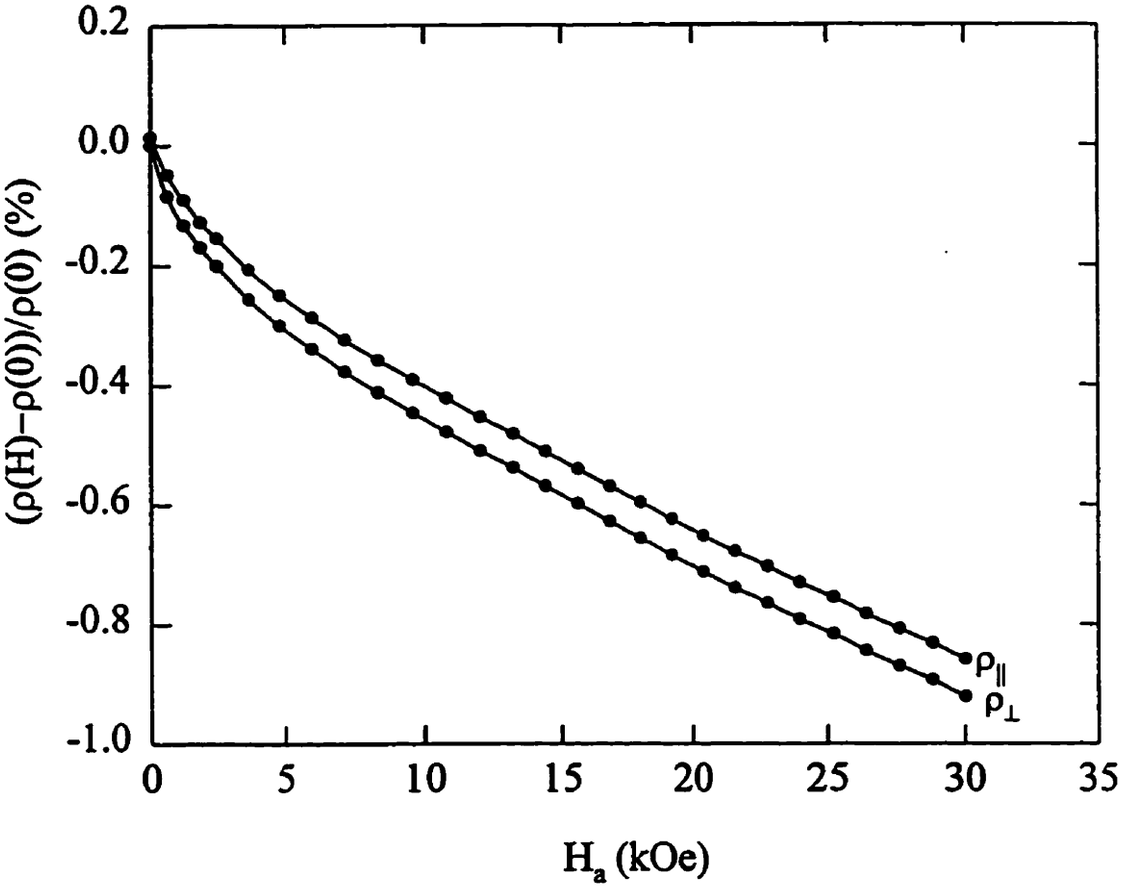

Figure A.88: Magnetoresistance as a function of applied field for the 46 at.% sample, as measured at a fixed temperature of 1.5K.

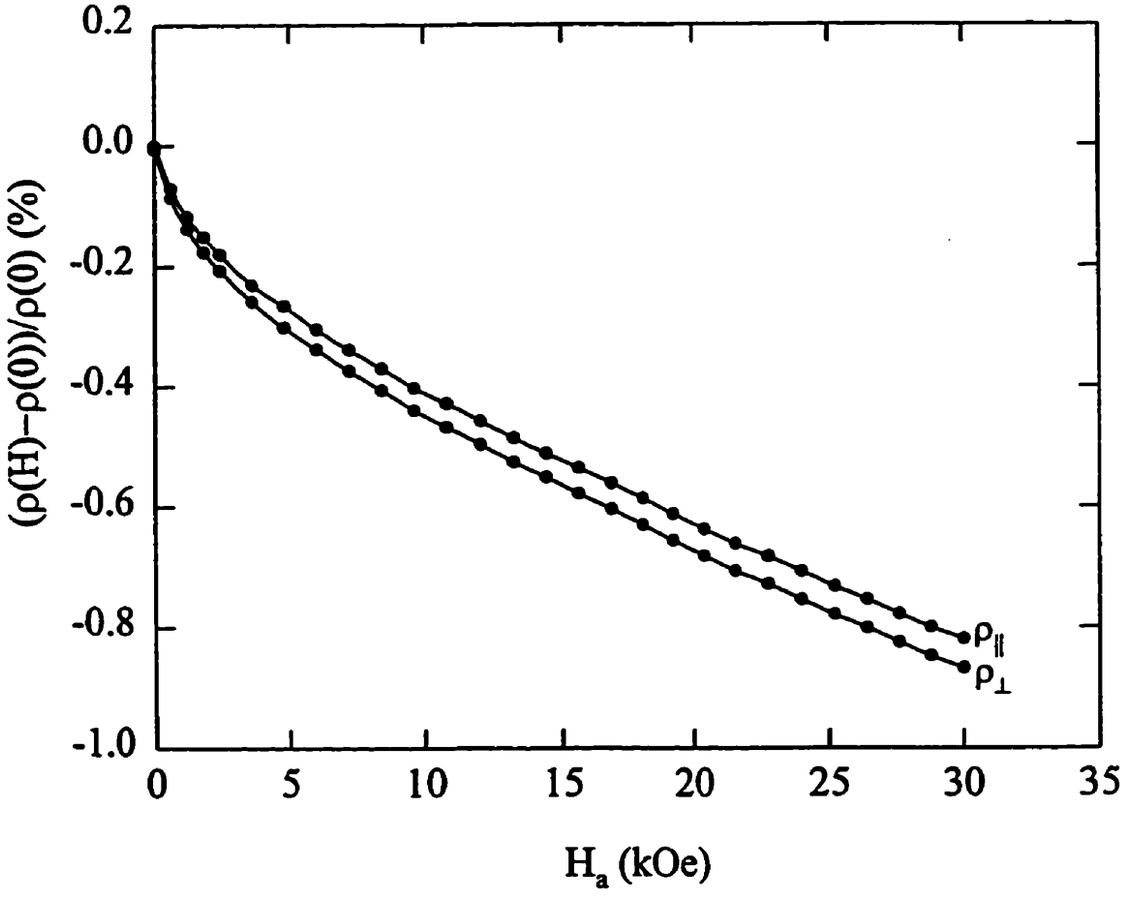

Figure A.89: Magnetoresistance as a function of applied field for the 45.5 at.% sample, as measured at a fixed temperature of 1.5K.

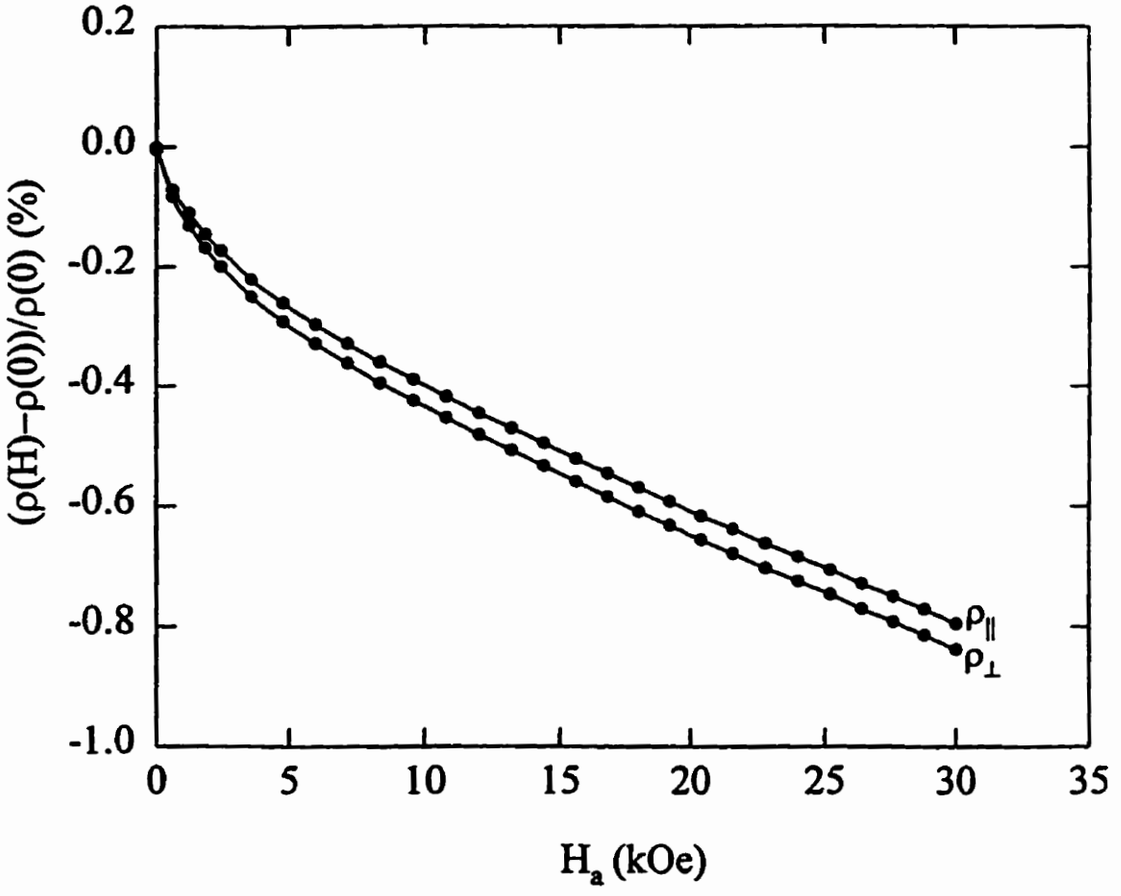

Figure A.90: Magnetoresistance as a function of applied field for the 45 at.% sample, as measured at a fixed temperature of 1.5K.

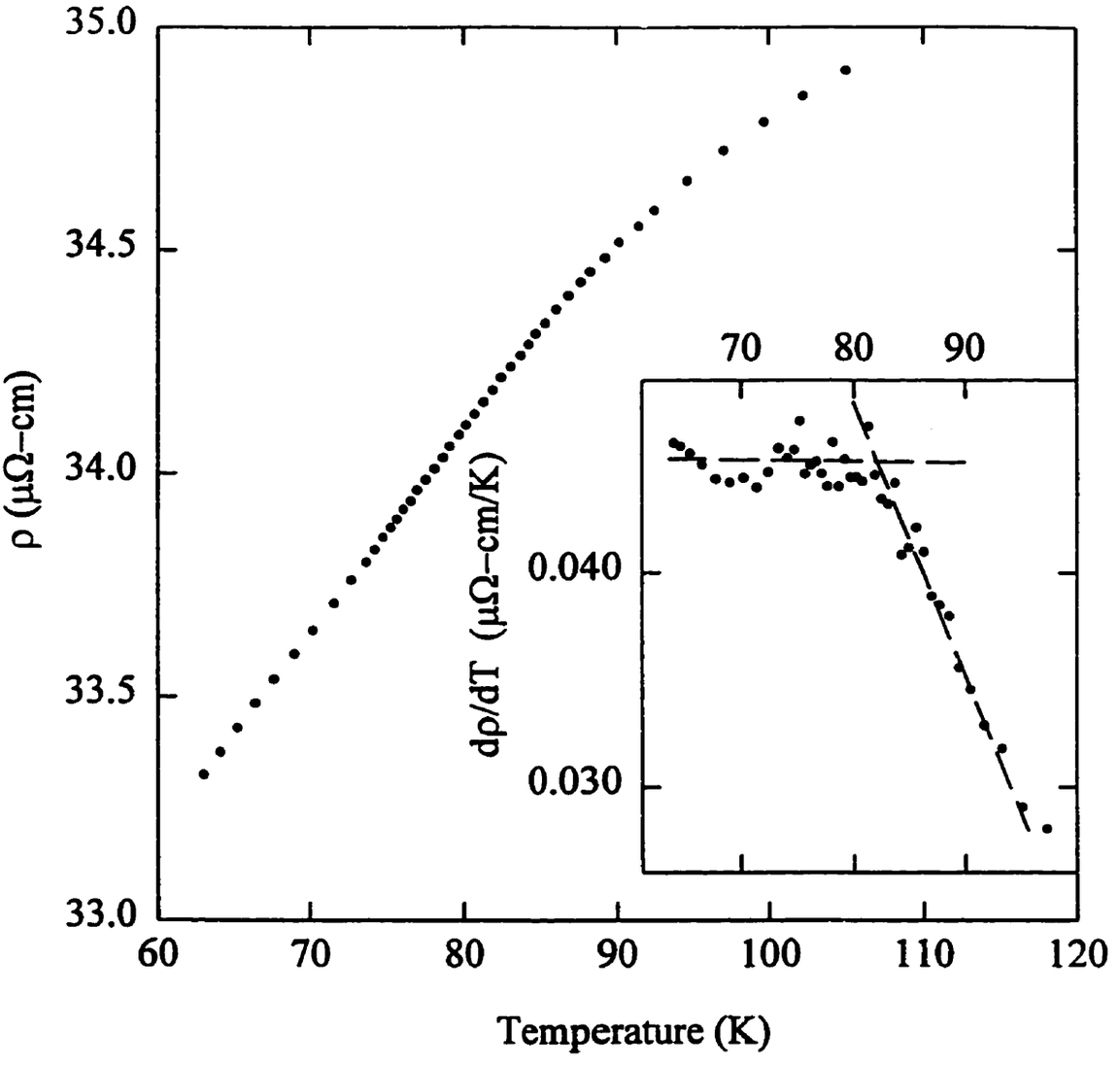

Figure A.91: $\rho(T)$ for the 54 at.% Ni sample. The inset shows the temperature derivative of the resistivity, giving T_c=82.5(8)K.

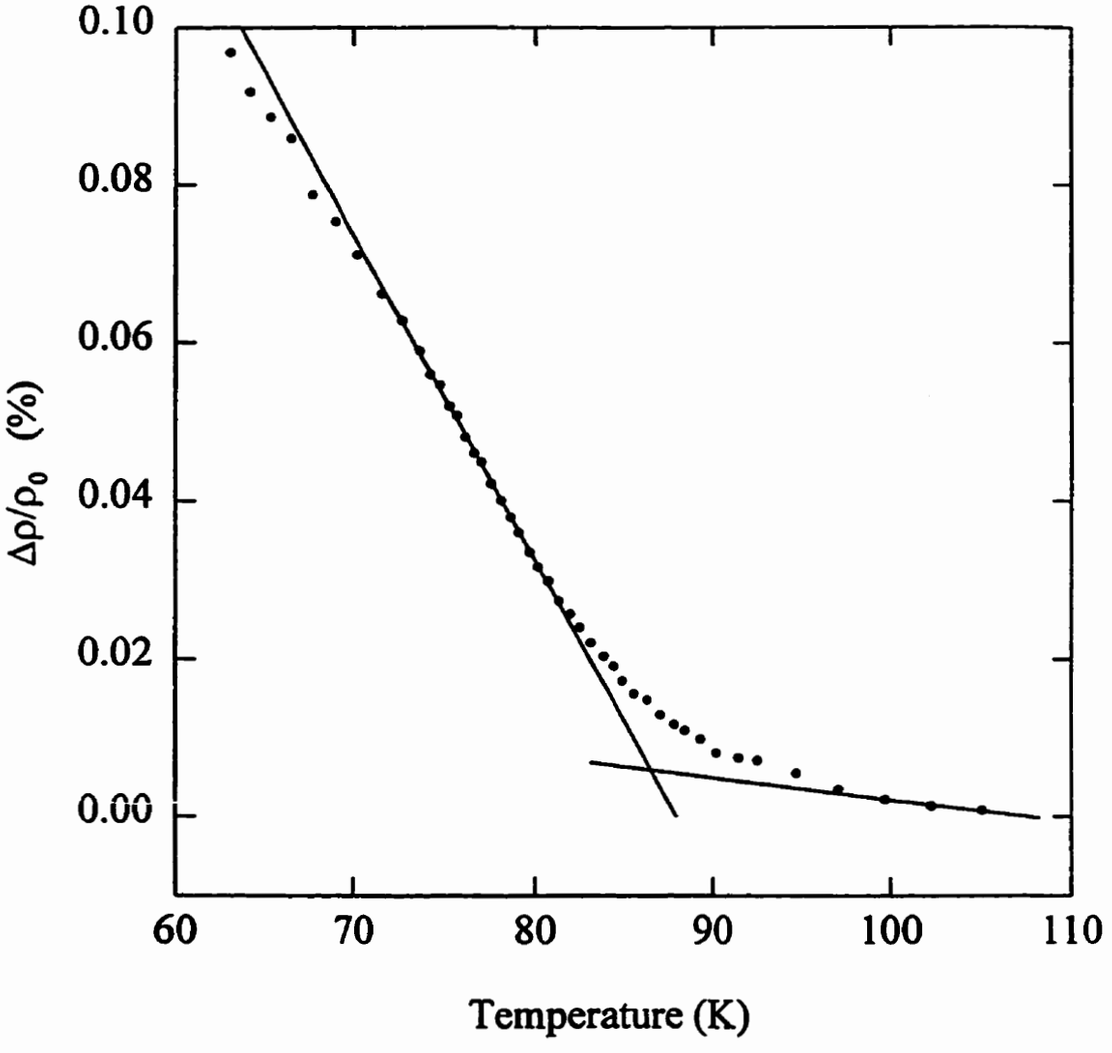

Figure A.92: The low field resistive anisotropy (LFRA) for the 54 at.% Ni sample. The superimposed lines give T_c=86(1) K.

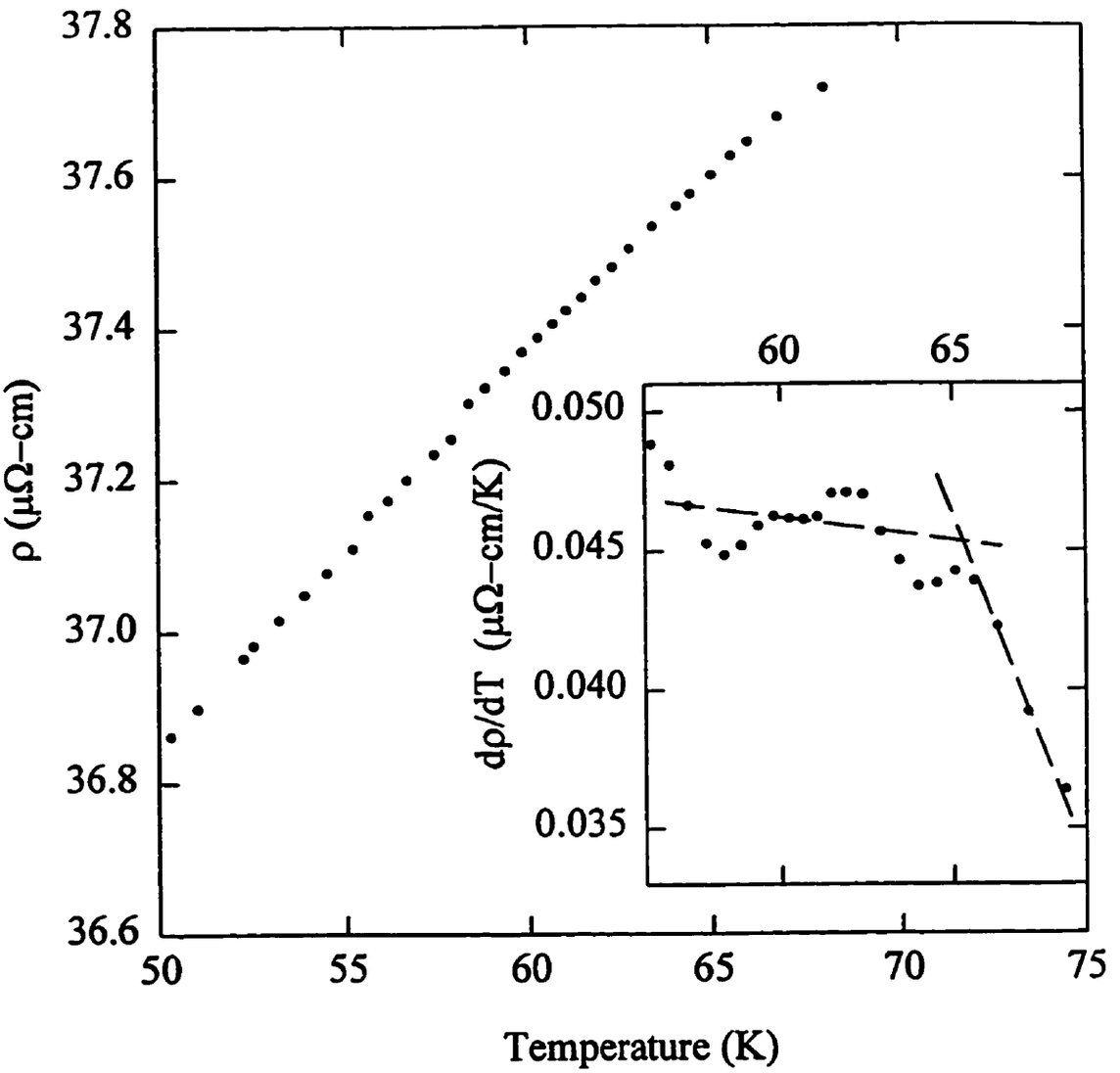

Figure A.93: $\rho(T)$ for the 53 at.% Ni sample. The inset shows the temperature derivative of the resistivity, with T_c=68.3(8)K.

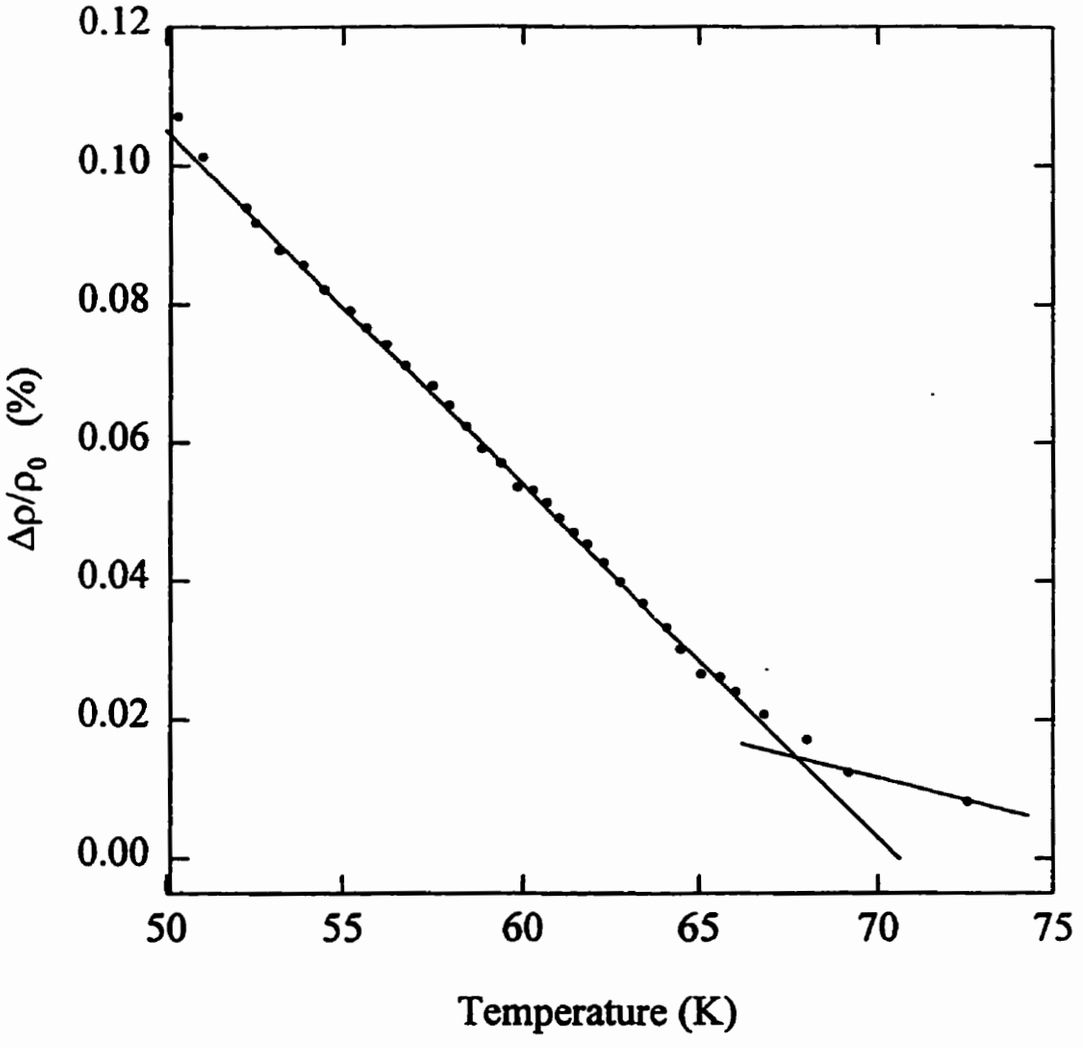

Figure A.94: The low field resistive anisotropy (LFRA) for the 53 at.% Ni sample. The superimposed lines give T_c=67.6(10) K.

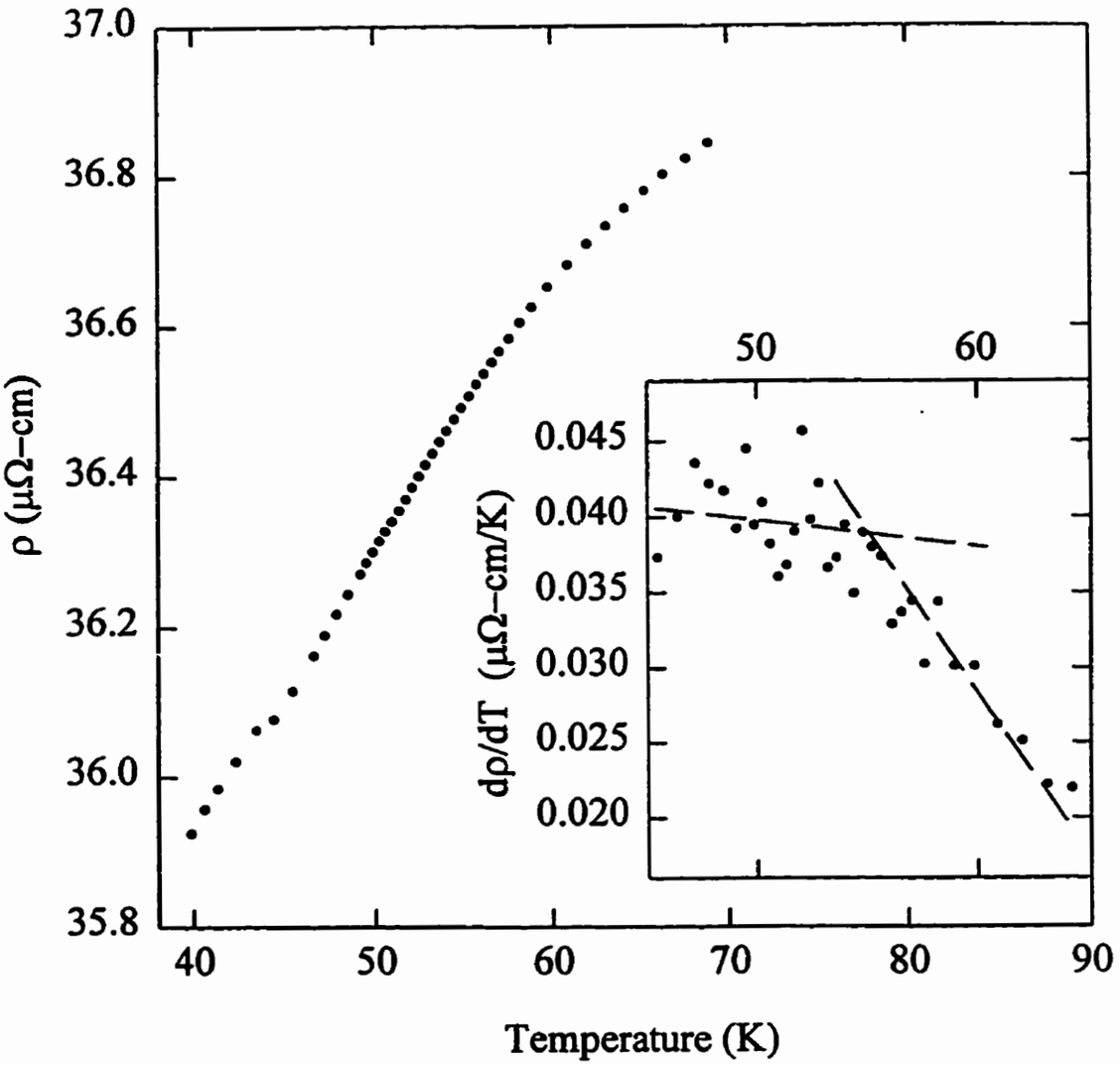

Figure A.95: $\rho(T)$ for the 52 at.% Ni sample. The inset shows the temperature derivative of the resistivity, with T_c=55.0(8)K.

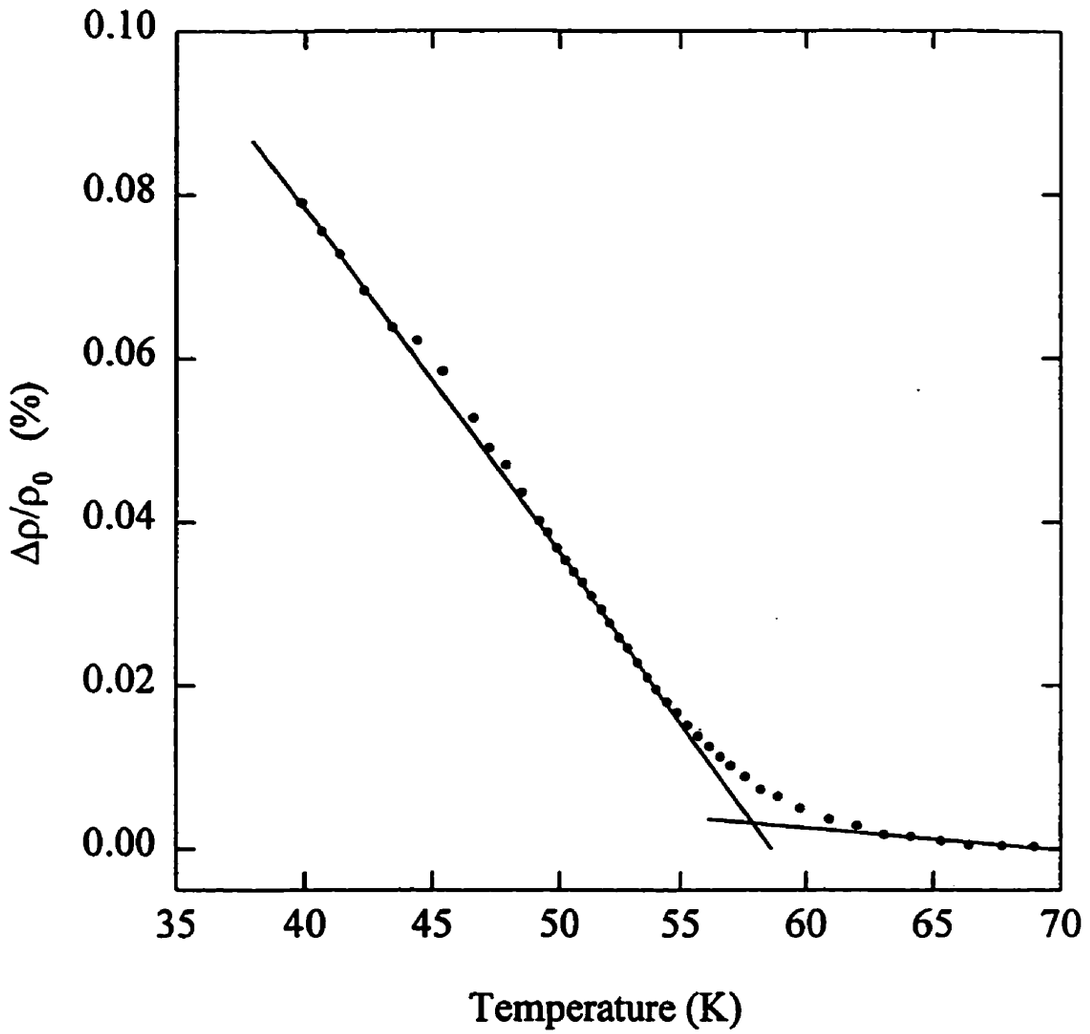

Figure A.96: The low field resistive anisotropy (LFRA) for the 52 at.% Ni sample. The superimposed lines give T_c=57.9(10) K.

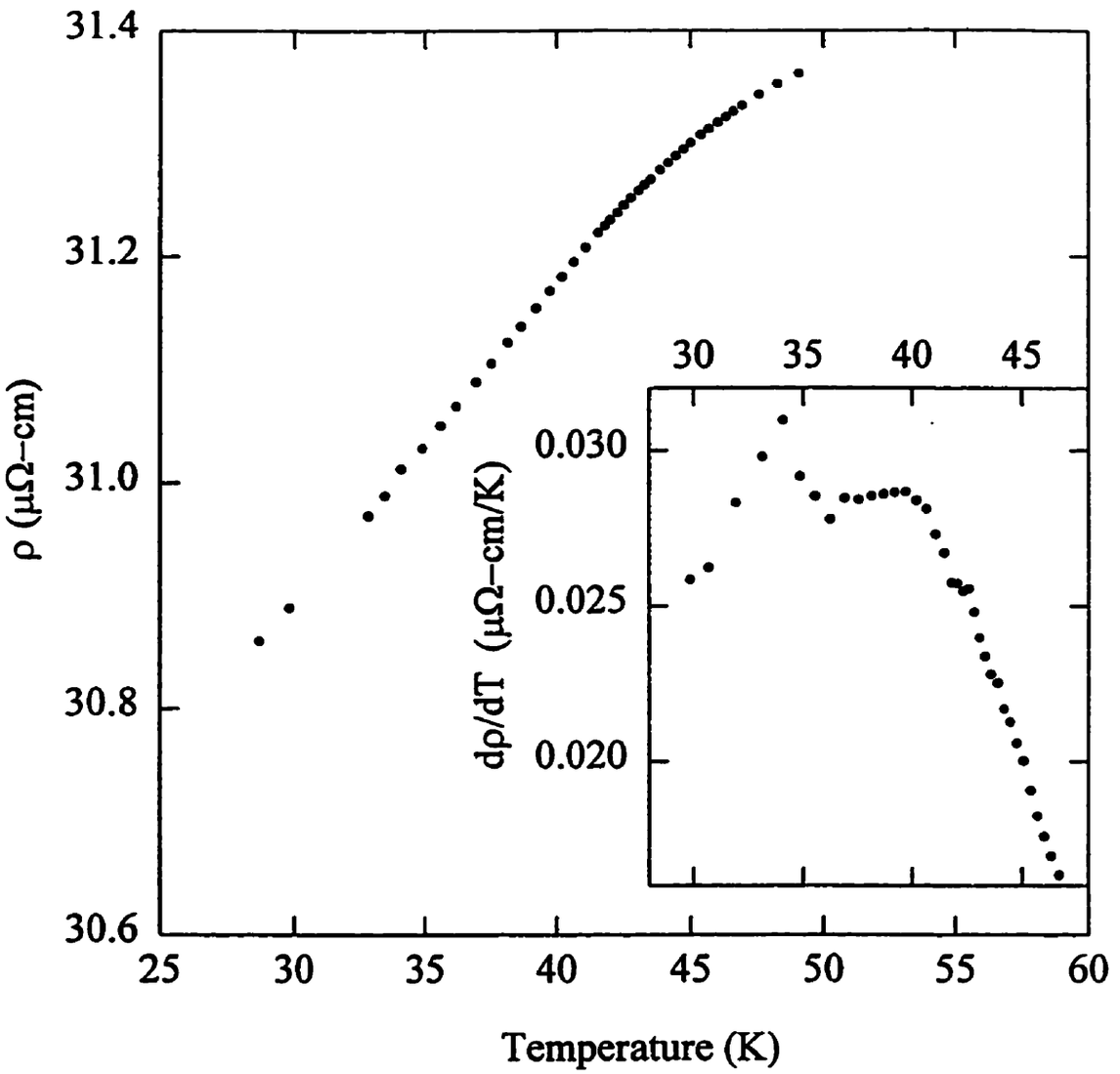

Figure A.97: $\rho(T)$ for the 51 at.% Ni sample. The inset shows the temperature derivative of the resistivity, with T_c=40.6(7)K.

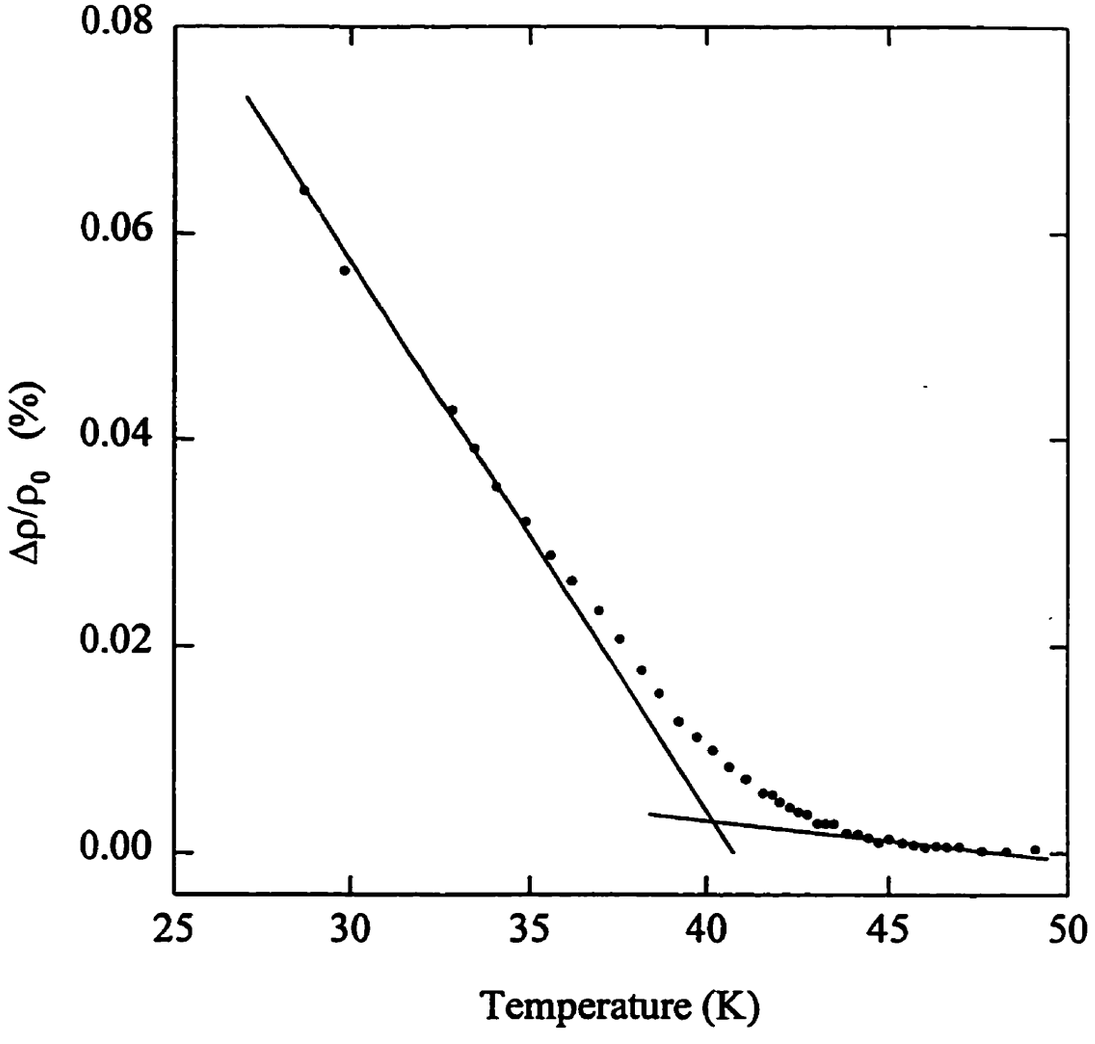

Figure A.98: The low field resistive anisotropy (LFRA) for the 51 at.% Ni sample. The superimposed lines give T_c=40.4(10) K.

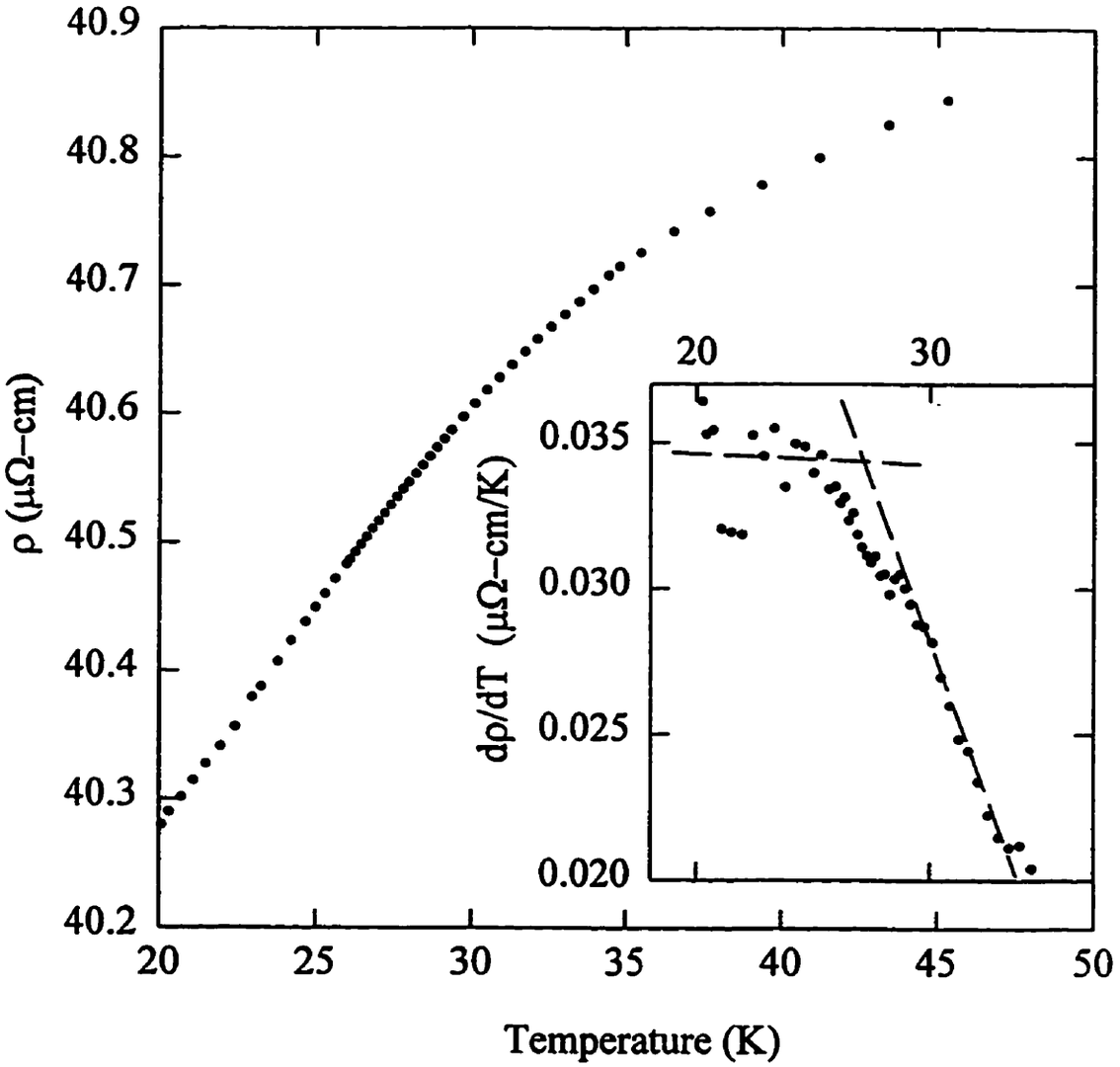

Figure A.99: $\rho(T)$ for the 49.5 at.% Ni sample. The inset shows the temperature derivative of the resistivity, with T_c=28.8(6)K.

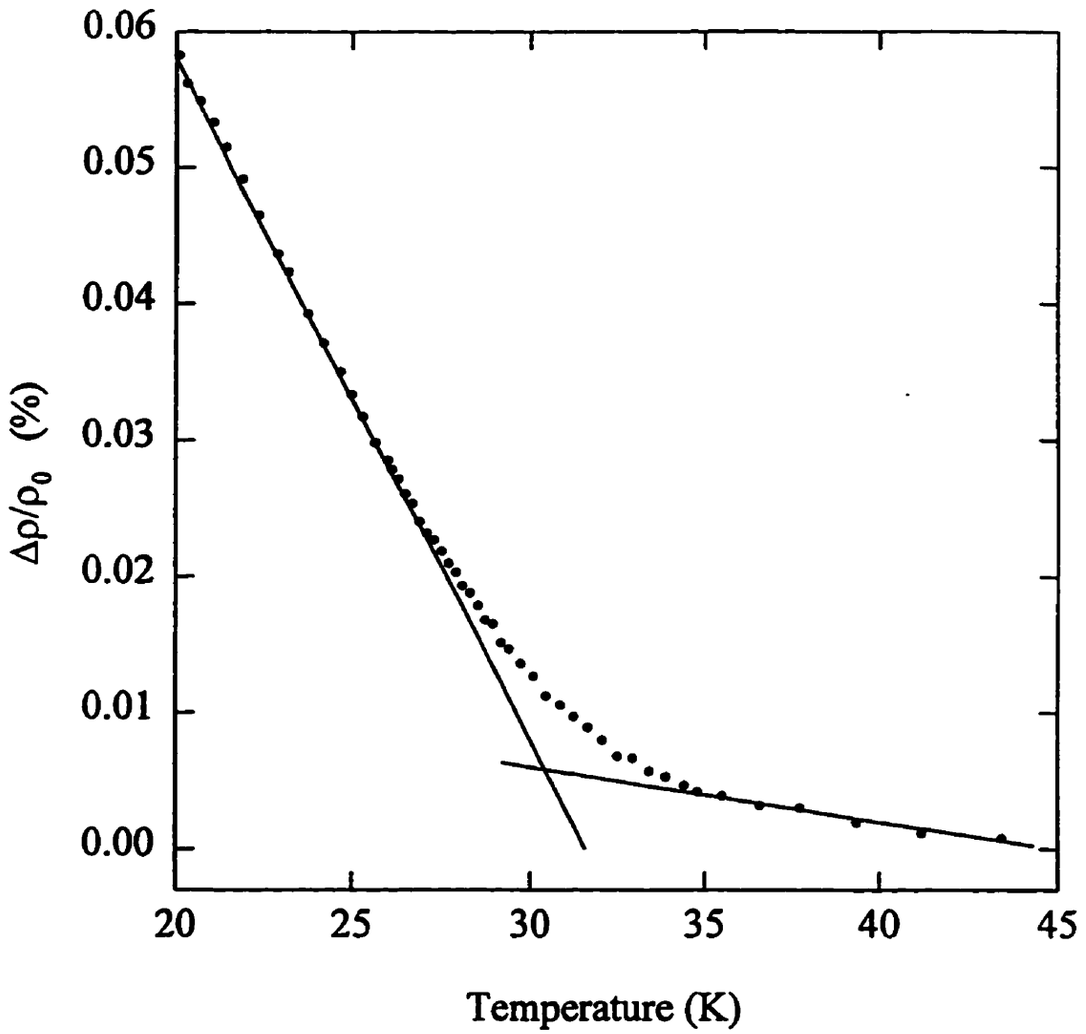

Figure A.100: The low field resistive anisotropy (LFRA) for the 49.5 at.% Ni sample. The superimposed lines give T_c=30.4(9) K.

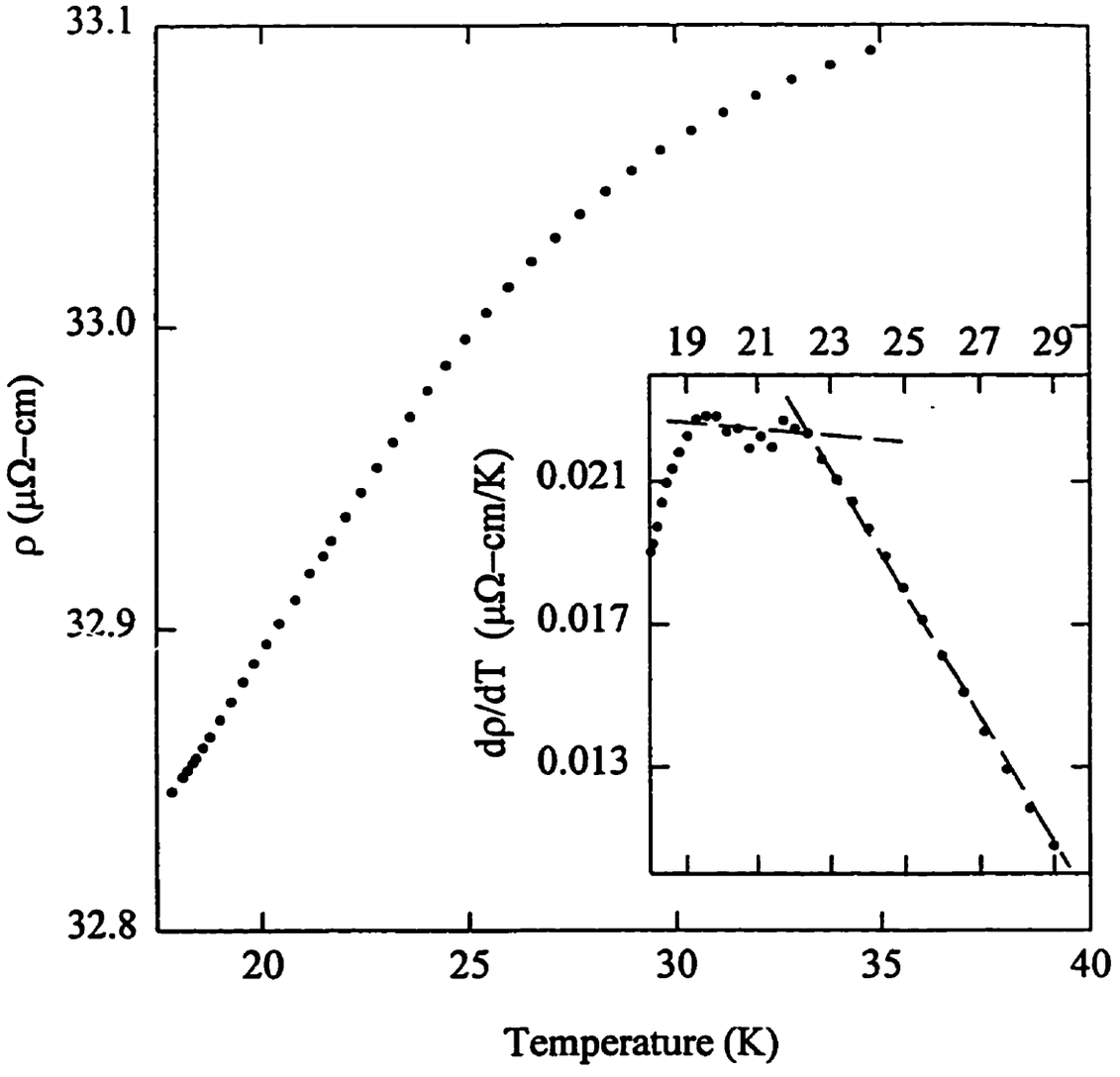

Figure A.101: $\rho(T)$ for the 49 at.% Ni sample. The inset shows the temperature derivative of the resistivity, with T_c=22.4(6)K.

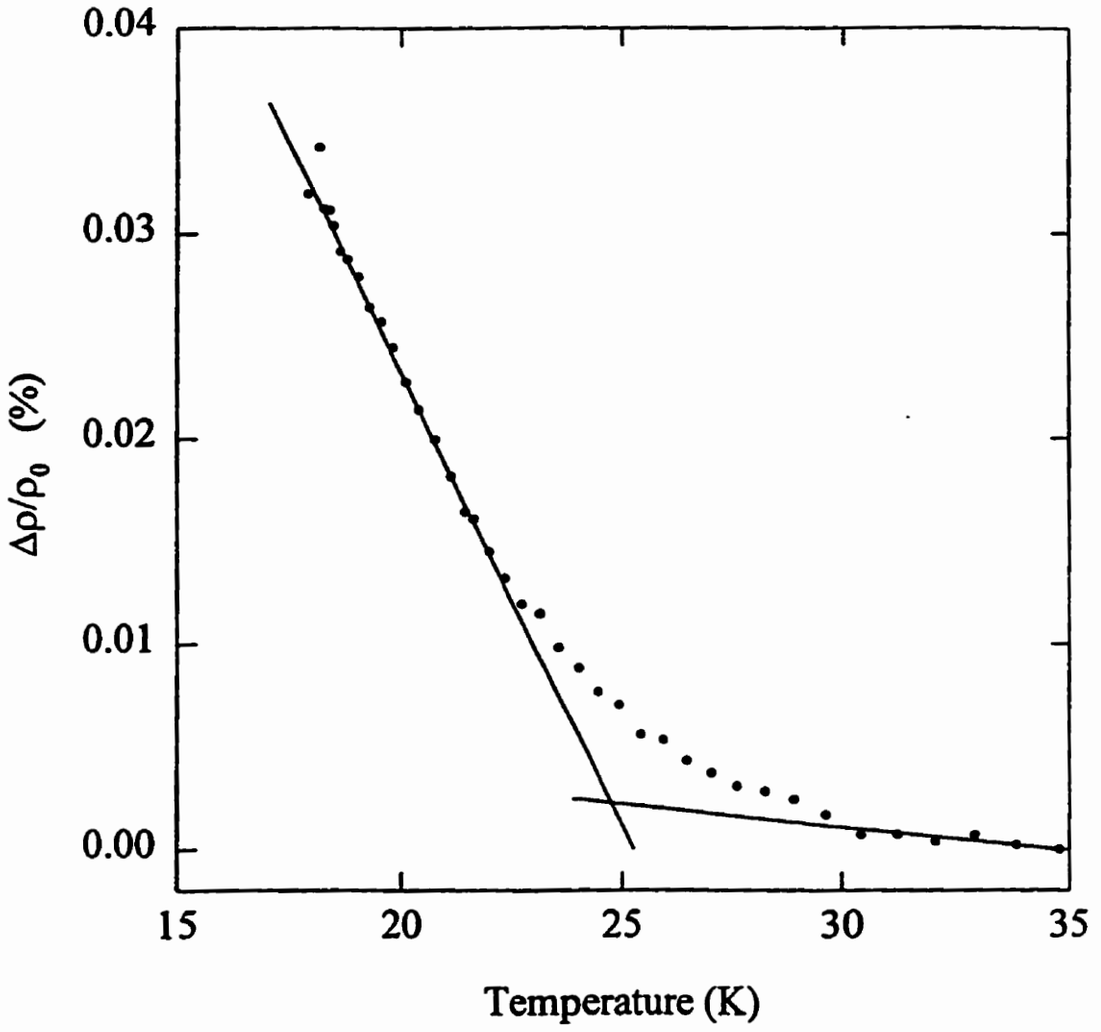

Figure A.102: The low field resistive anisotropy (LFRA) for the 49 at.% Ni sample. The superimposed lines give T_c=24.8(9) K.

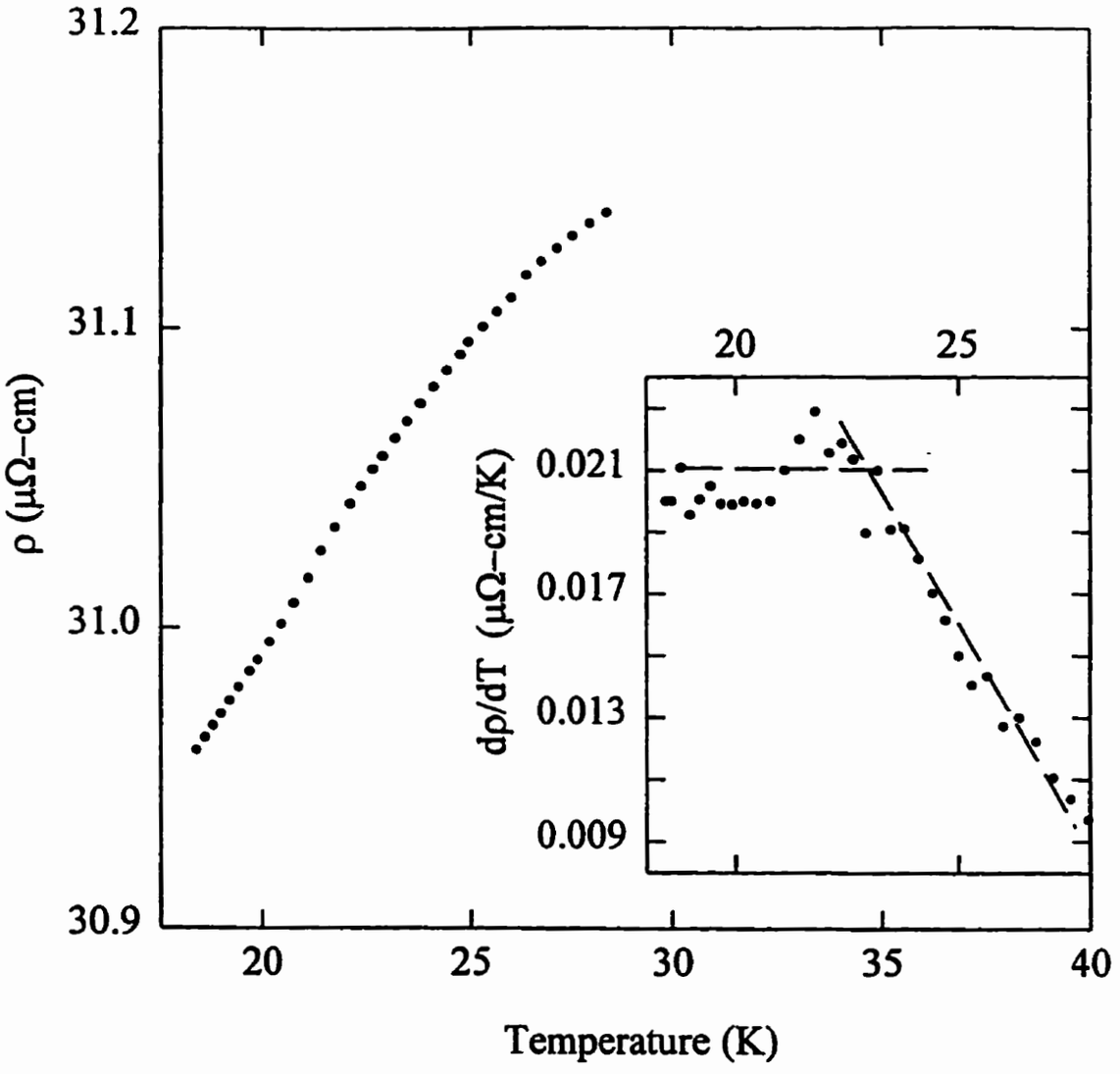

Figure A.103: $\rho(T)$ for the 48.5 at.% Ni sample. The inset shows the temperature derivative of the resistivity, with T_c=23.0(5)K.

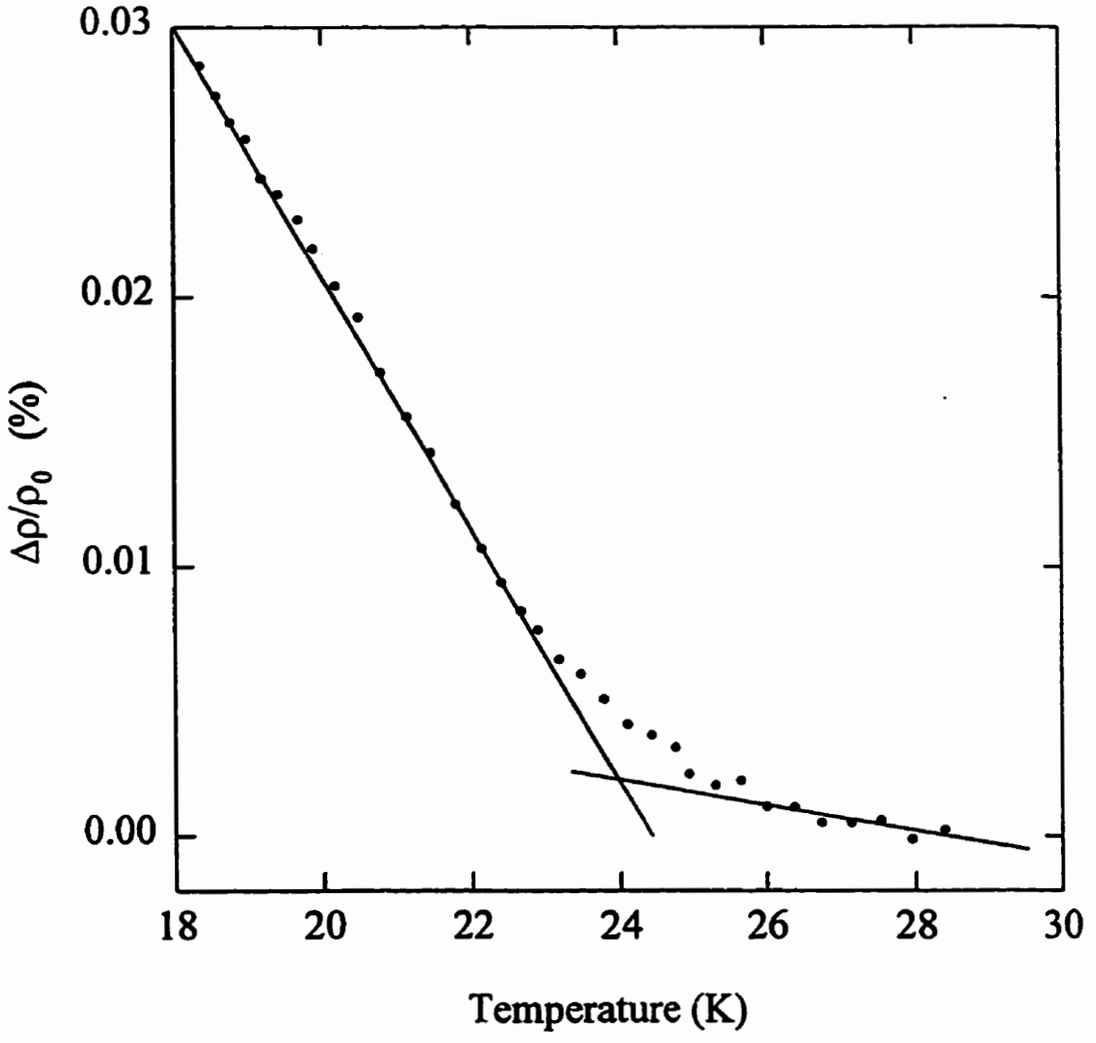

Figure A.104: The low field resistive anisotropy (LFRA) for the 48.5 at.% Ni sample. The superimposed lines give T_c=23.9(8) K.

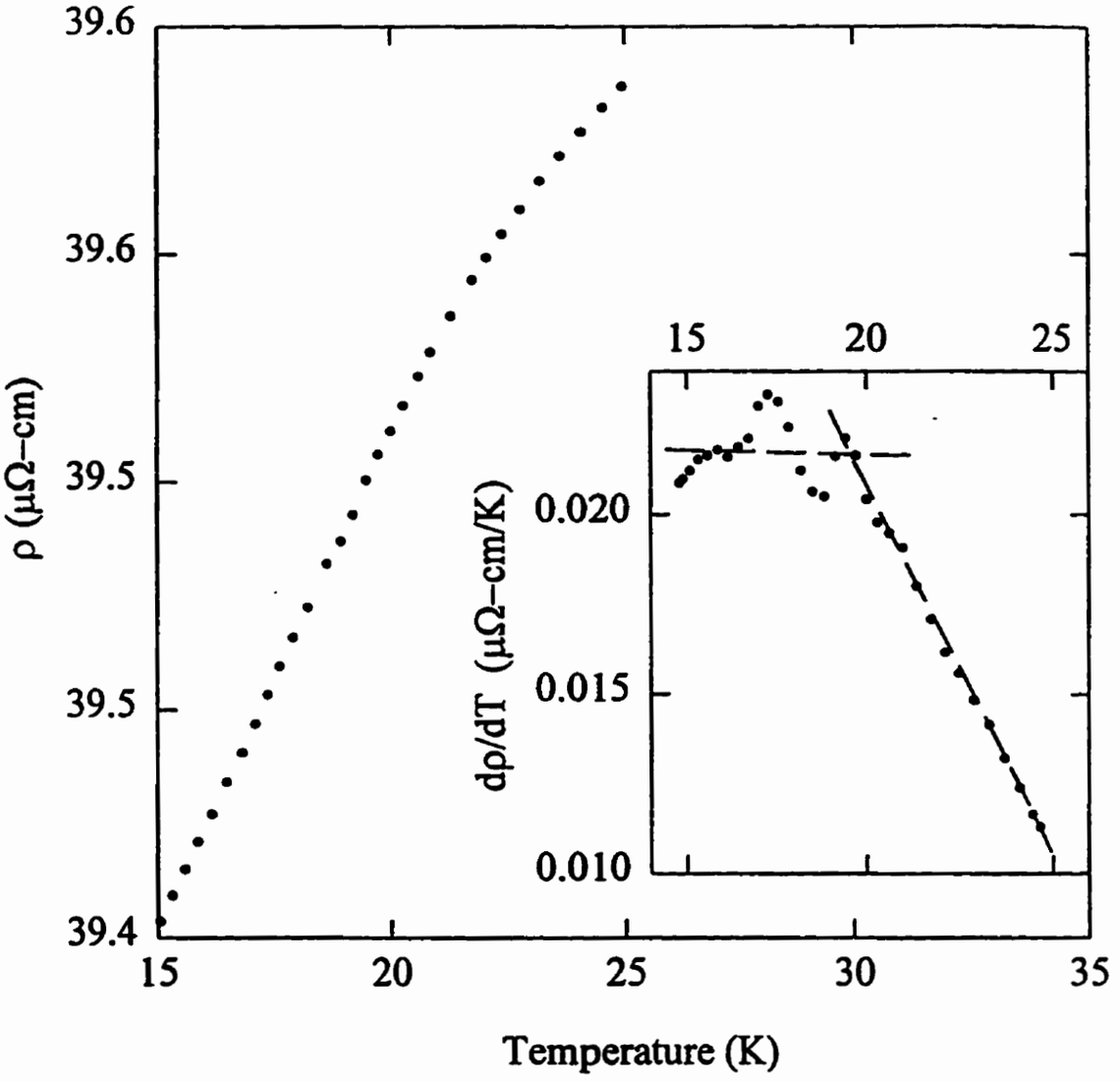

Figure A.105: $\rho(T)$ for the 48 at.% Ni sample. The inset shows the temperature derivative of the resistivity, with T_c=19.6(5)K.

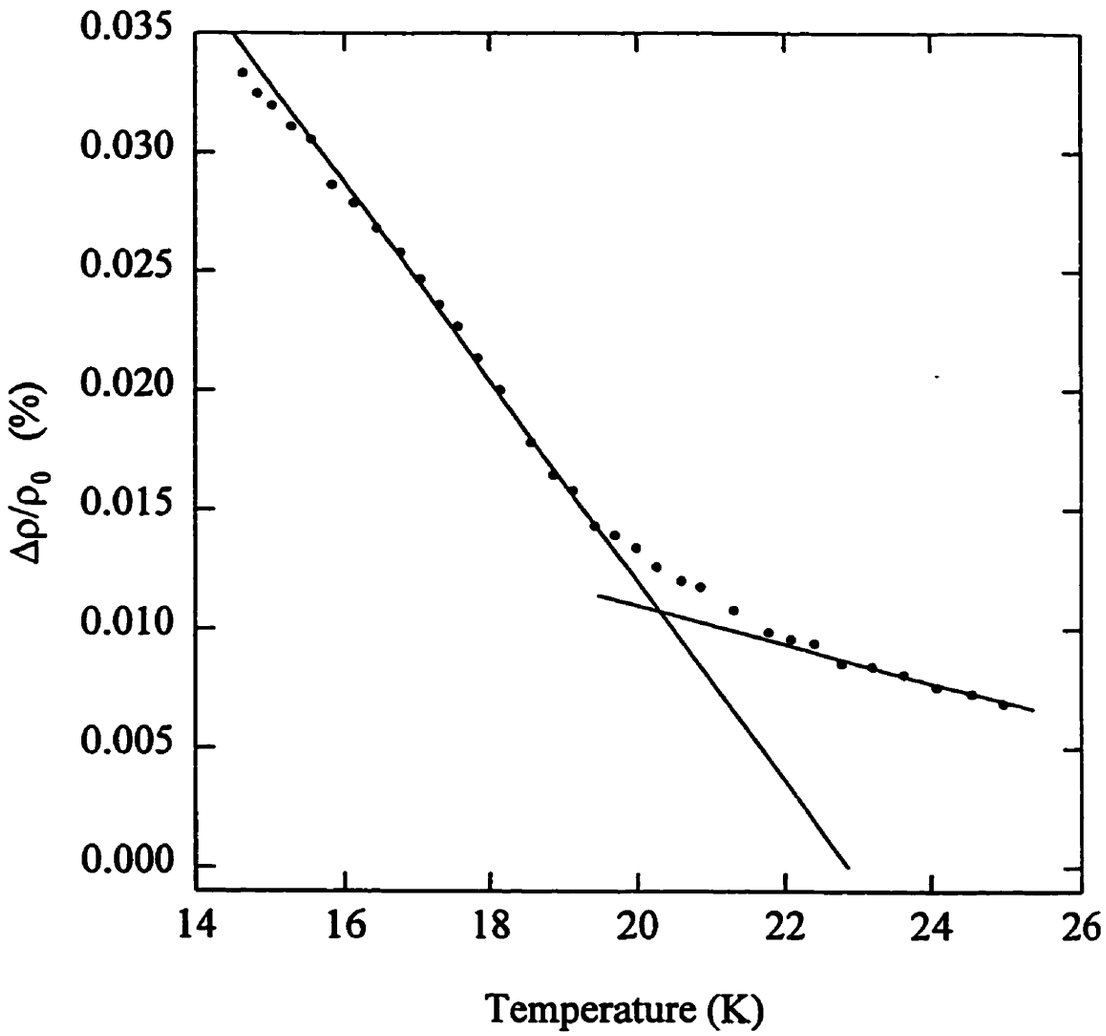

Figure A.106: The low field resistive anisotropy (LFRA) for the 48 at.% Ni sample. The superimposed lines give T_c=20.2(8) K.

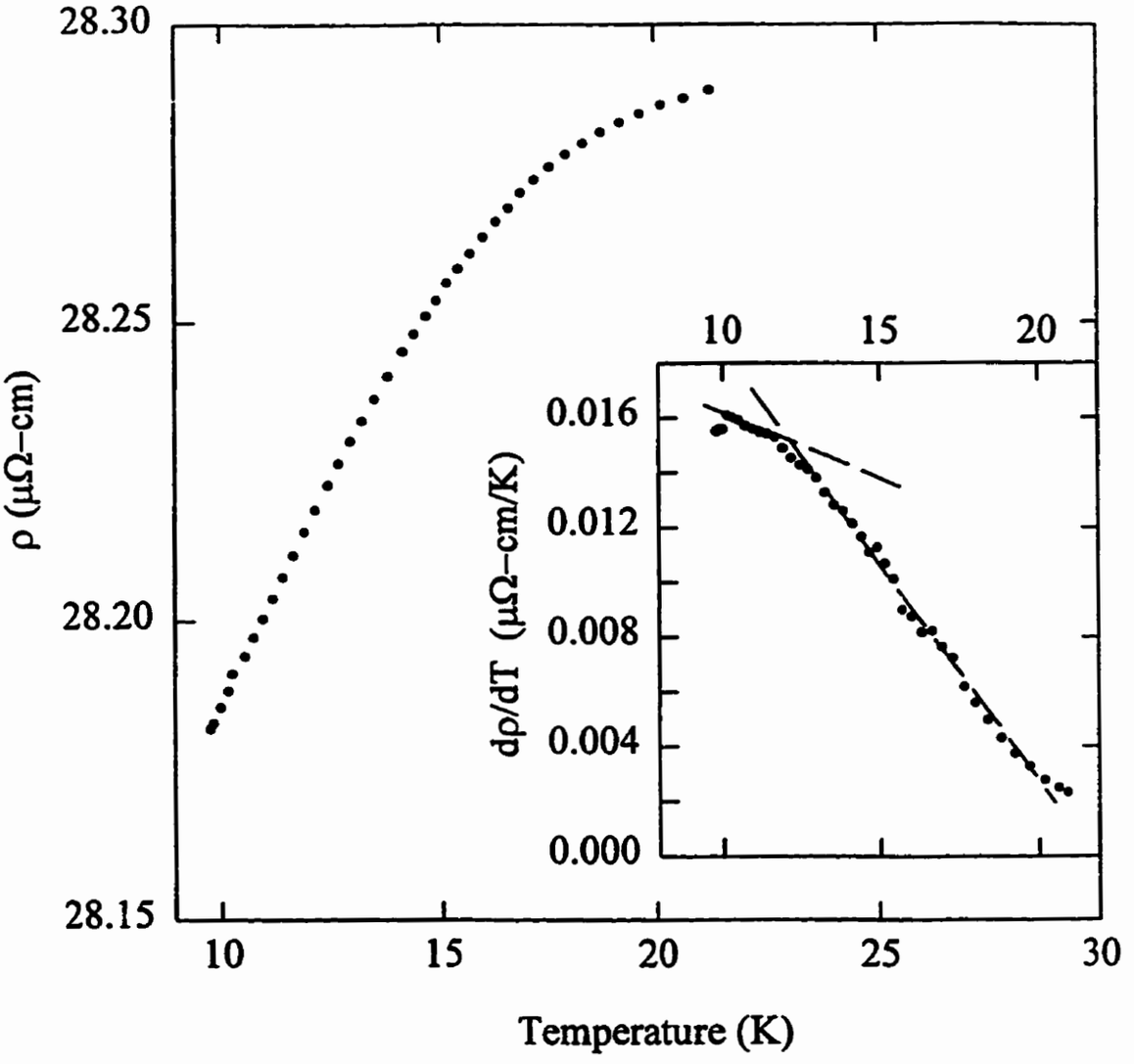

Figure A.107: $\rho(T)$ for the 47.5 at.% Ni sample. The inset shows the temperature derivative of the resistivity, with T_c=11.9(10)K.

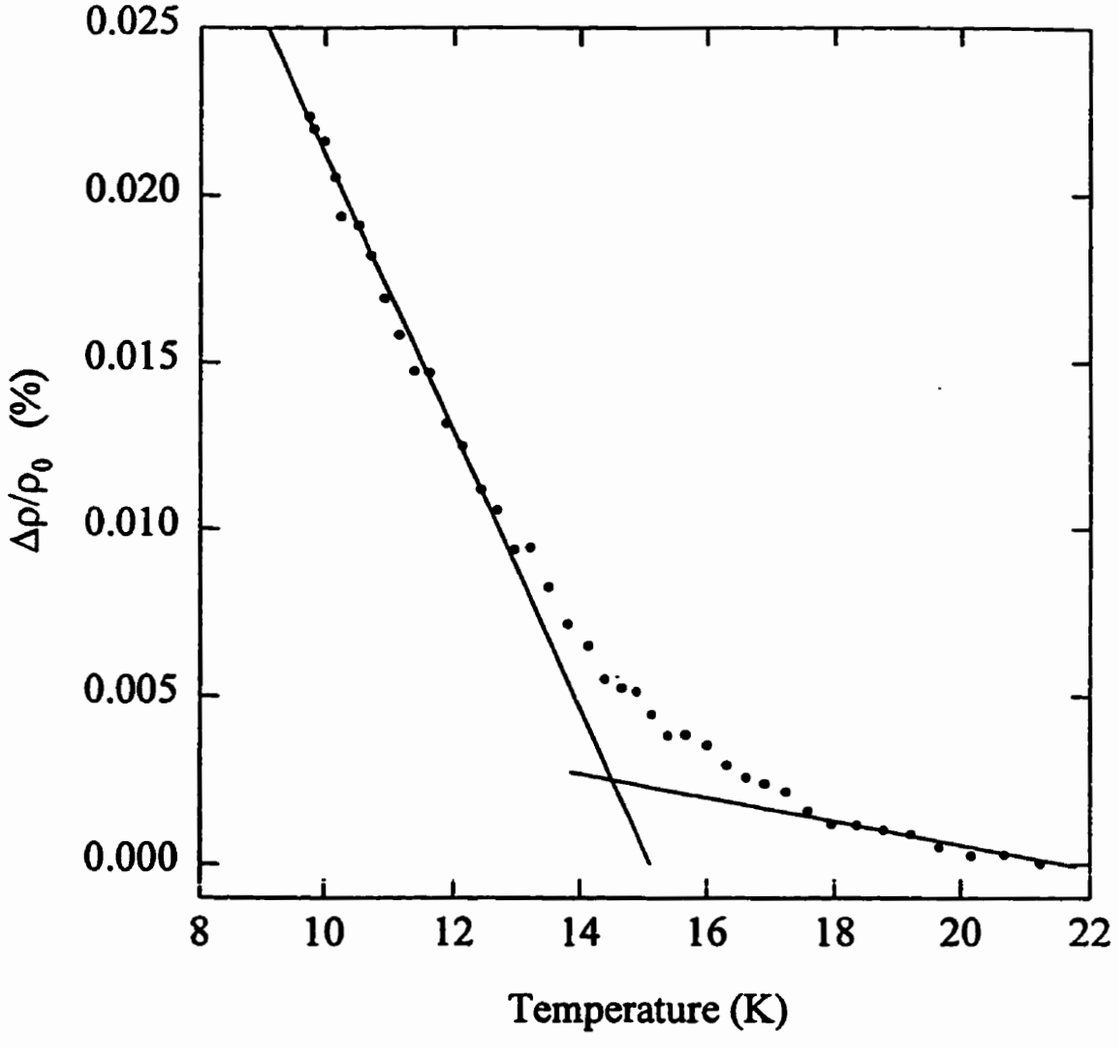

Figure A.108: The low field resistive anisotropy (LFRA) for the 47.5 at.% Ni sample. The superimposed lines give T_c=14.6(20) K.

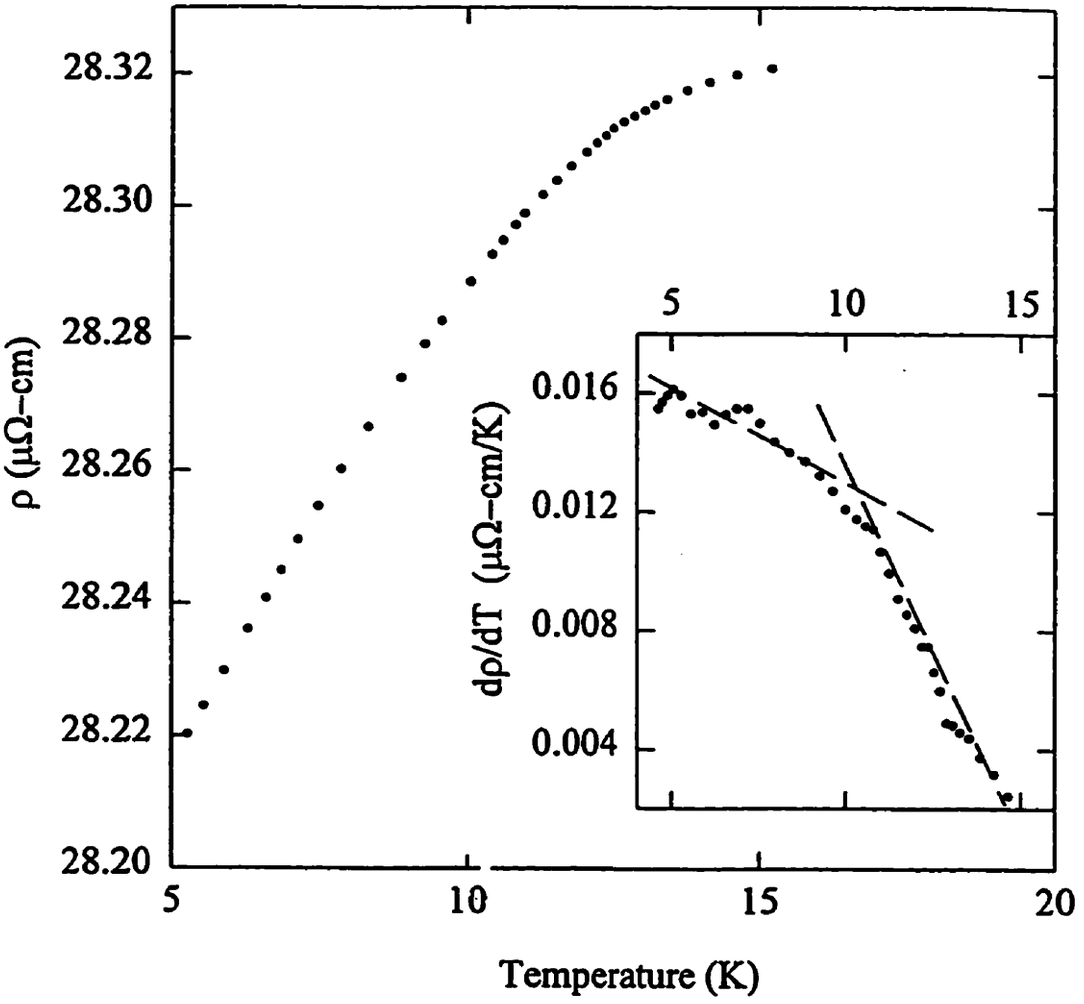

Figure A.109: $\rho(T)$ for the 47 at.% Ni sample. The inset shows the temperature derivative of the resistivity, with T_c=10.3(5)K.

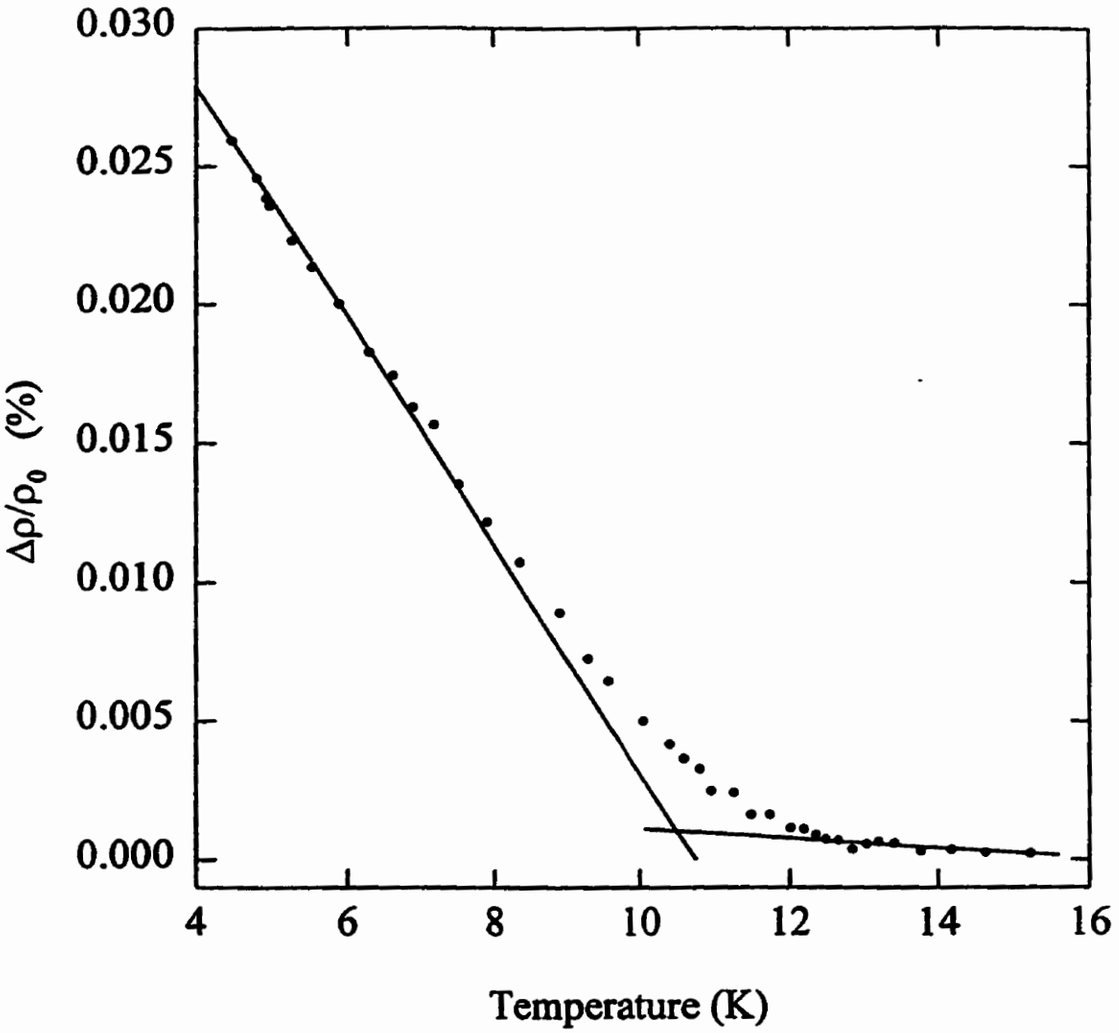

Figure A.110: The low field resistive anisotropy (LFRA) for the 47 at.% Ni sample. The superimposed lines give T_c=10.4(7) K.

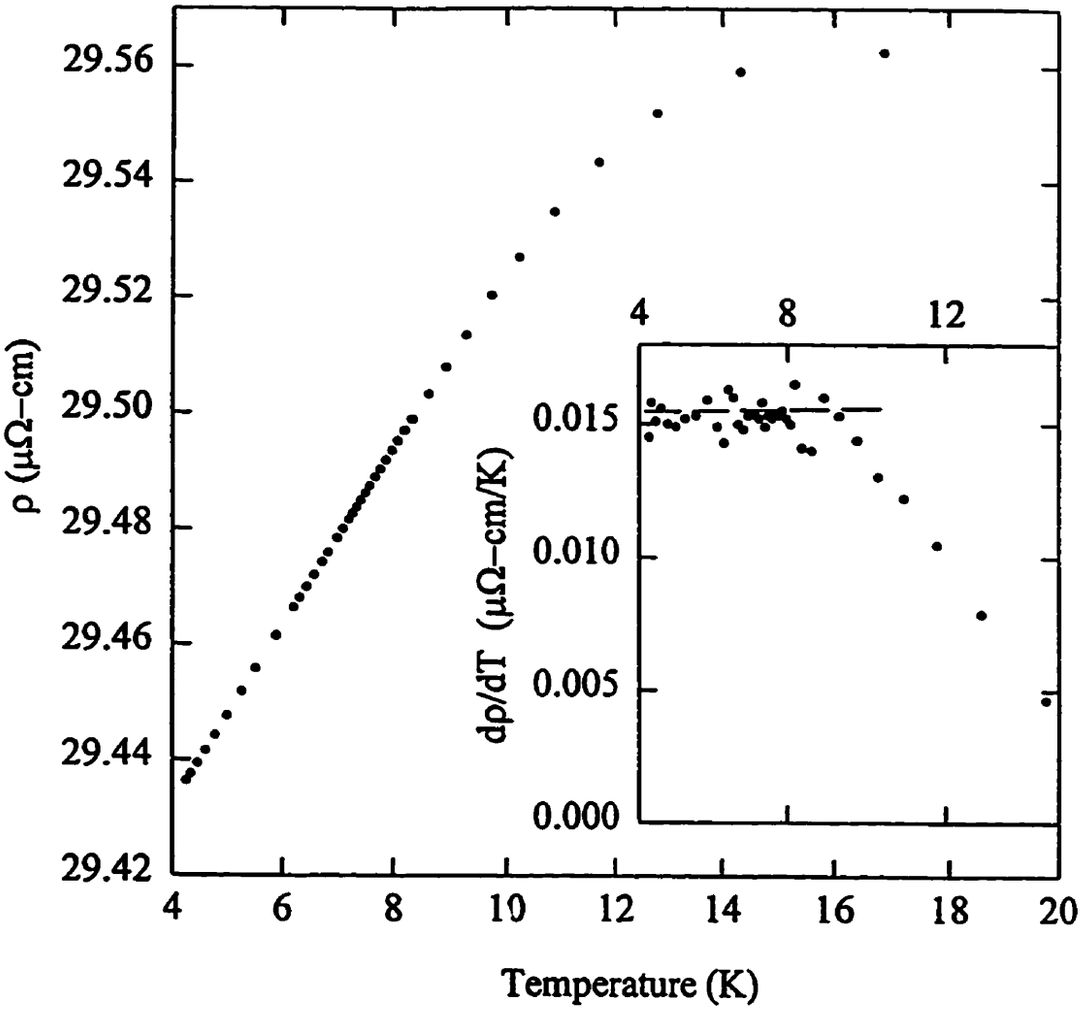

Figure A.111: $\rho(T)$ for the 46.5 at.% Ni sample. The inset shows the temperature derivative of the resistivity, with T_c=9.3(5)K.

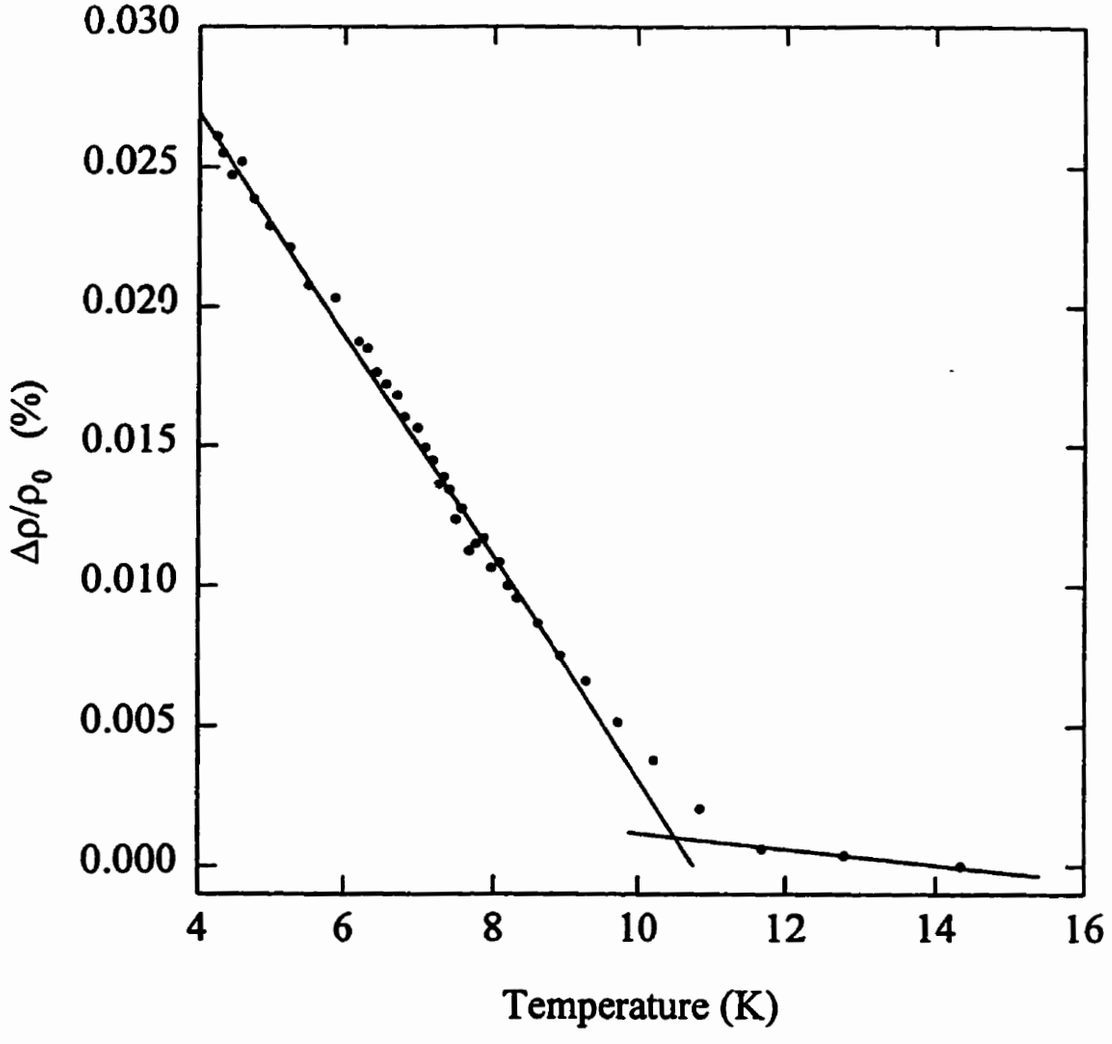

Figure A.112: The low field resistive anisotropy (LFRA) for the 46.5 at.% Ni sample. The superimposed lines give T_c=10.5(6) K.

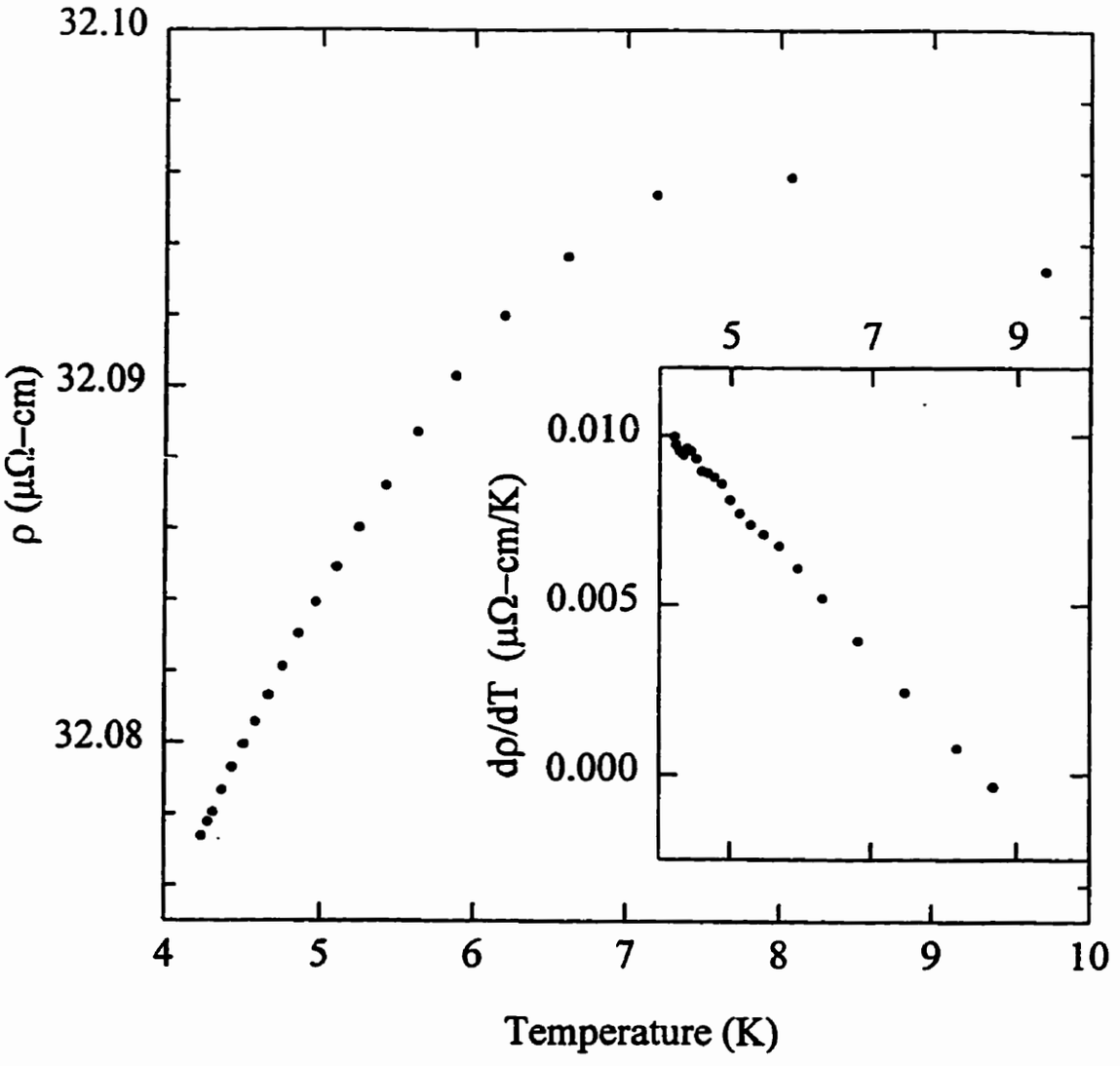

Figure A.113: $\rho(T)$ for the 45.5 at.% Ni sample. The inset shows the temperature derivative of the resistivity, which exhibits no critical features.

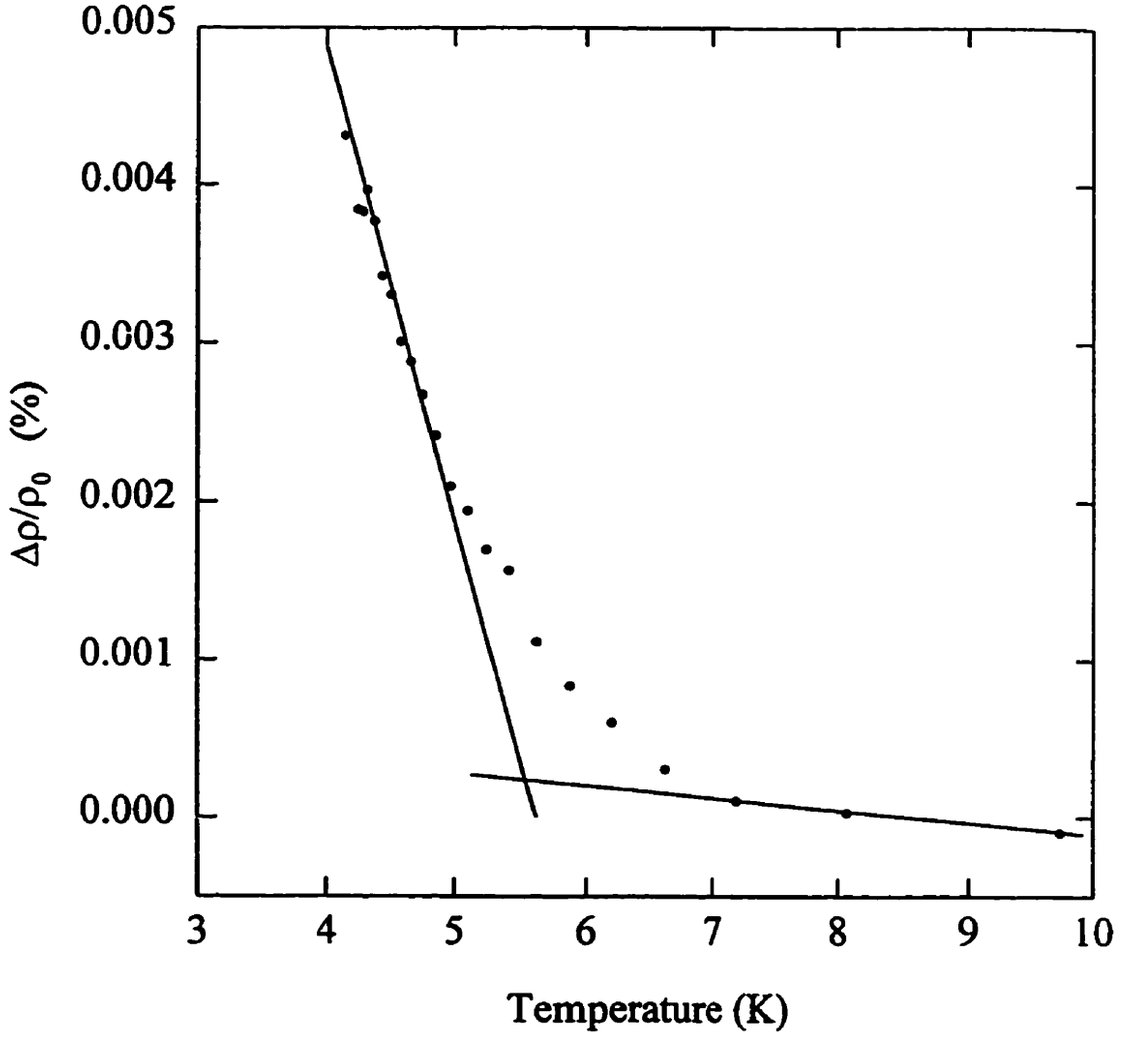

Figure A.114: The low field resistive anisotropy (LFRA) for the 45.5 at.% Ni sample. The superimposed lines give T_c=5.6(10) K.

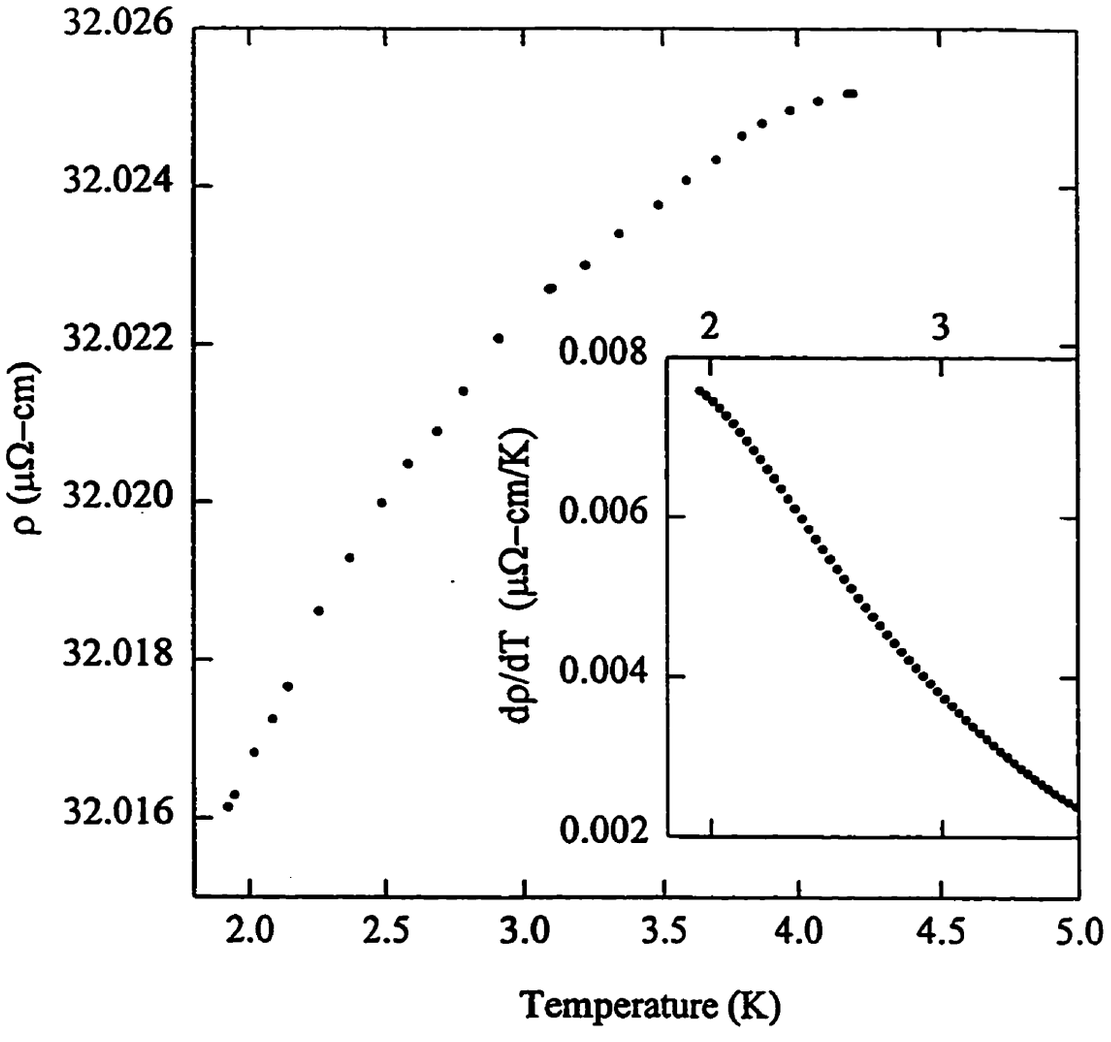

Figure A.115: $\rho(T)$ for the 45 at.% Ni sample. The inset shows the temperature derivative of the resistivity, which exhibits no critical features.

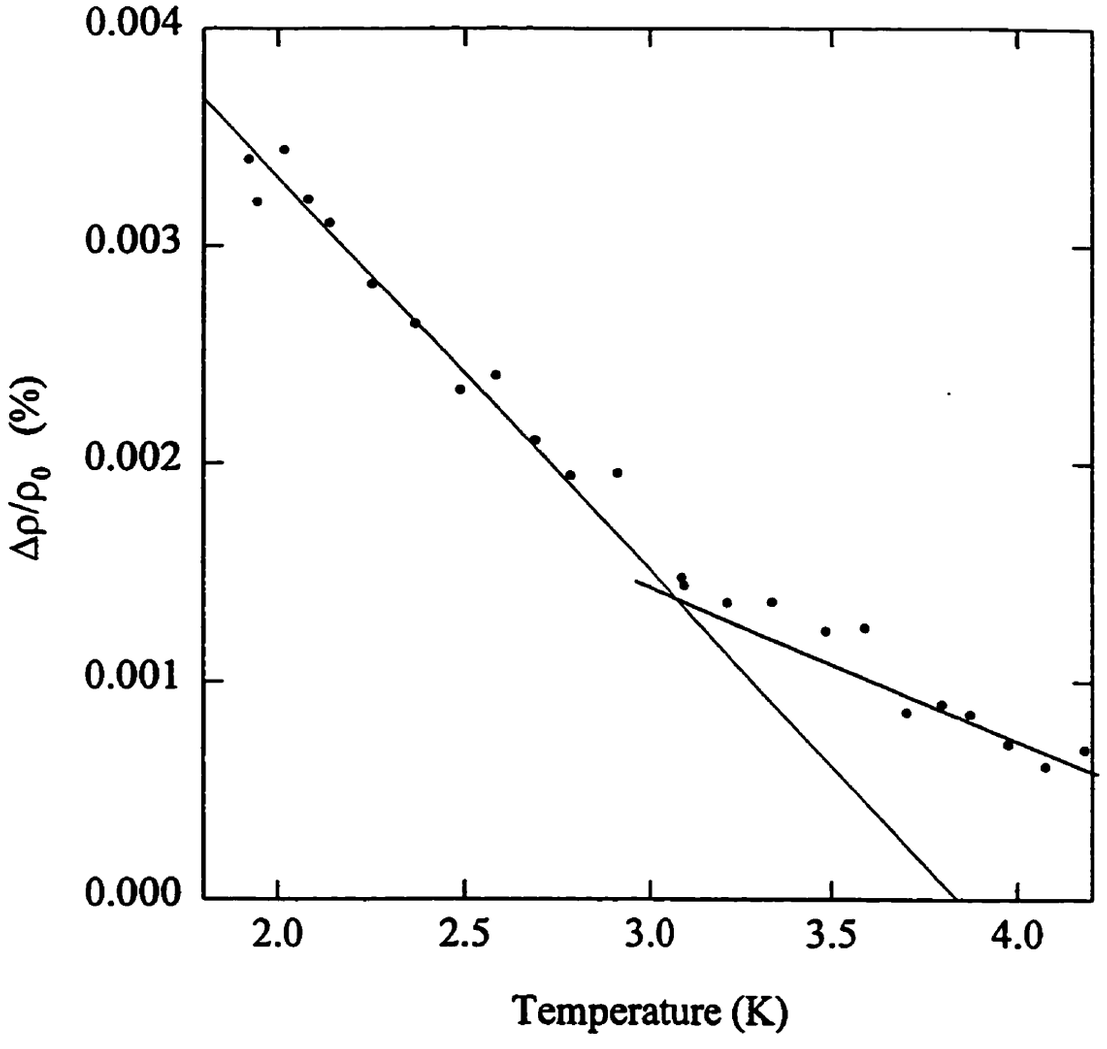

Figure A.116: The low field resistive anisotropy (LFRA) for the 45 at.% Ni sample. The superimposed lines give T_c=3.8(10) K.

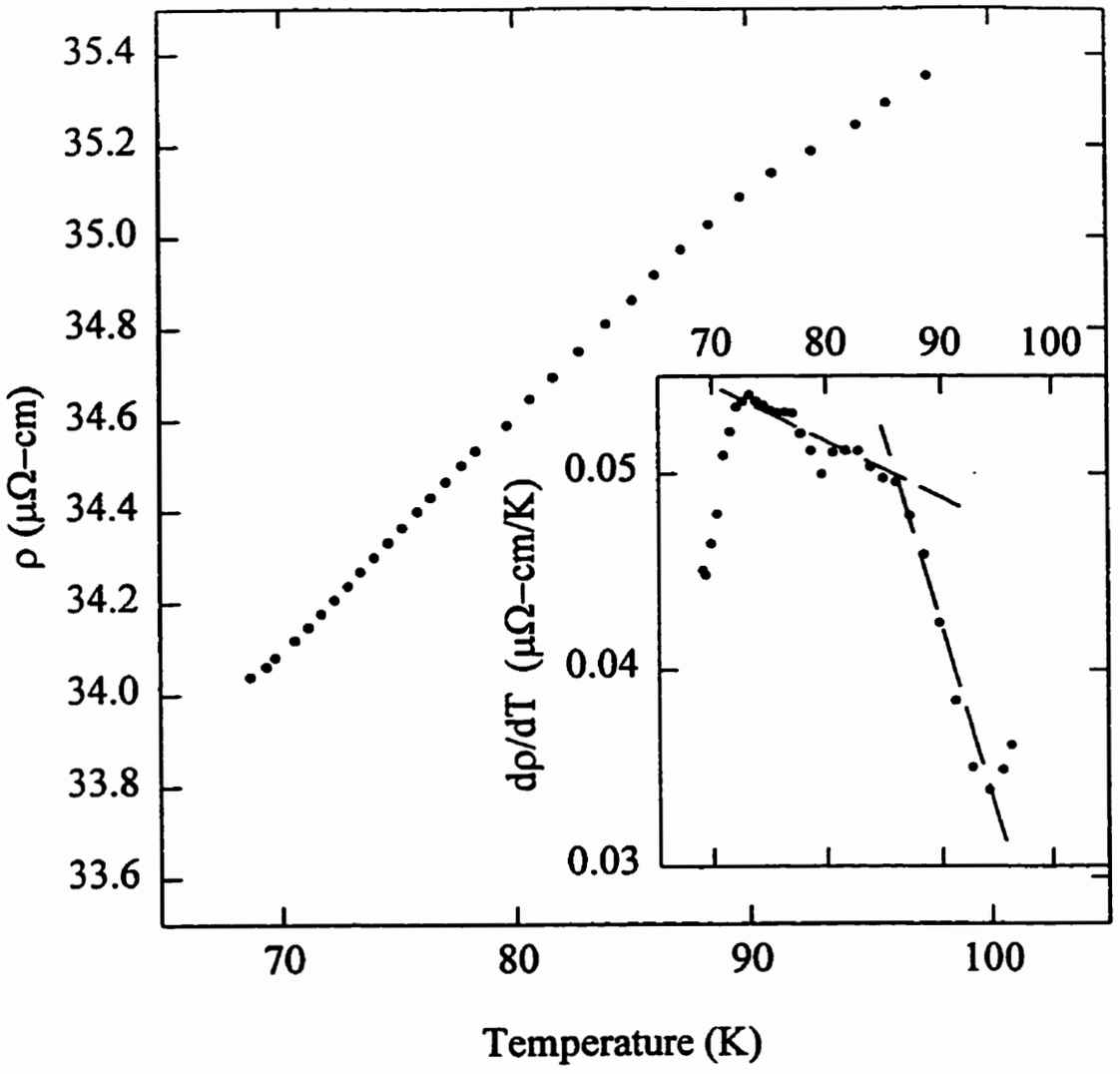

Figure A.117: $\rho(T)$ for the 55 at.% Ni sample after aging. The inset shows the temperature derivative of the resistivity, with T_c=86.4(8)K.

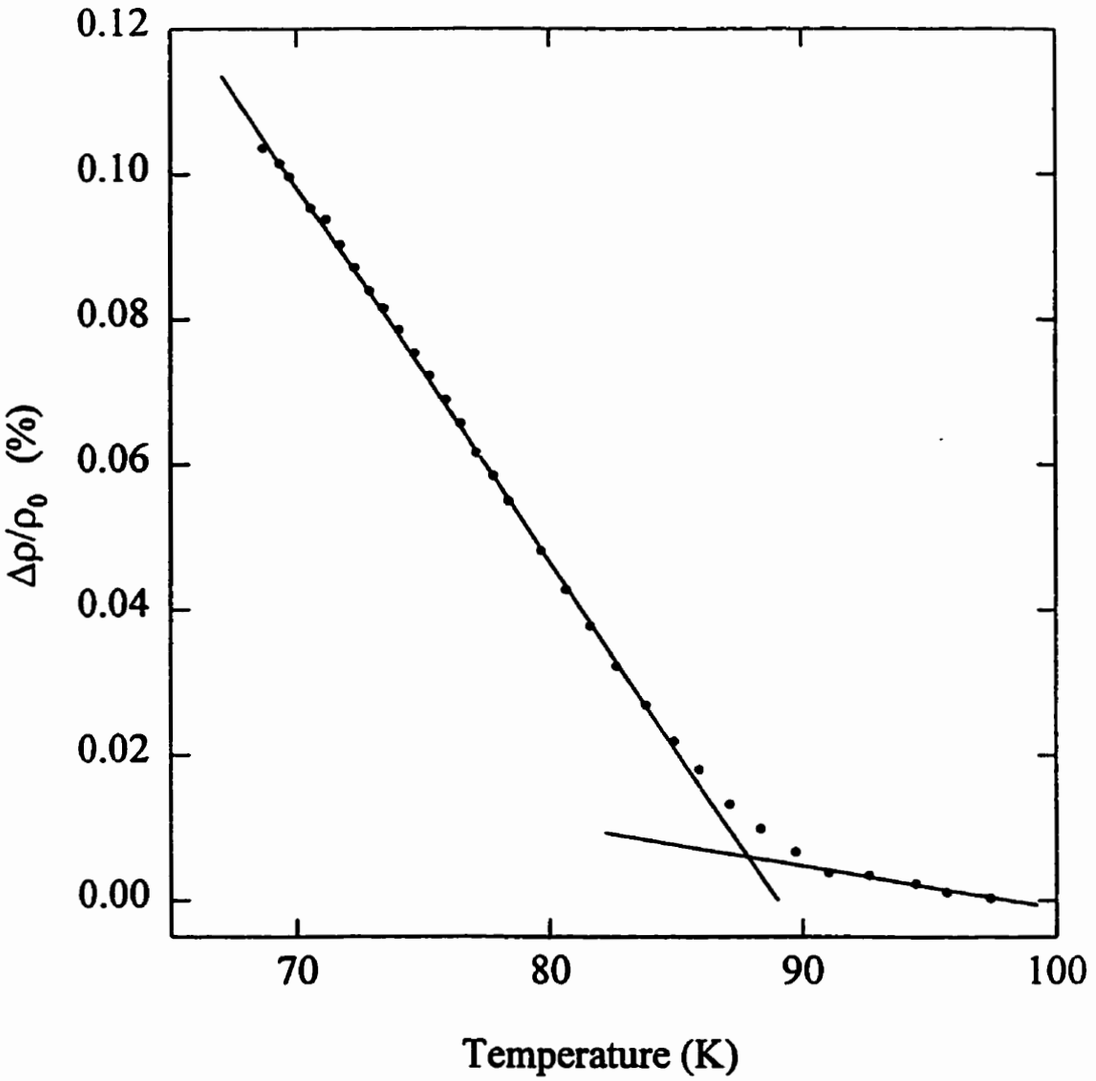

Figure A.118: The low field resistive anisotropy (LFRA) for the 55 at.% Ni sample after aging. The superimposed lines give T_c=87.5(8)K.

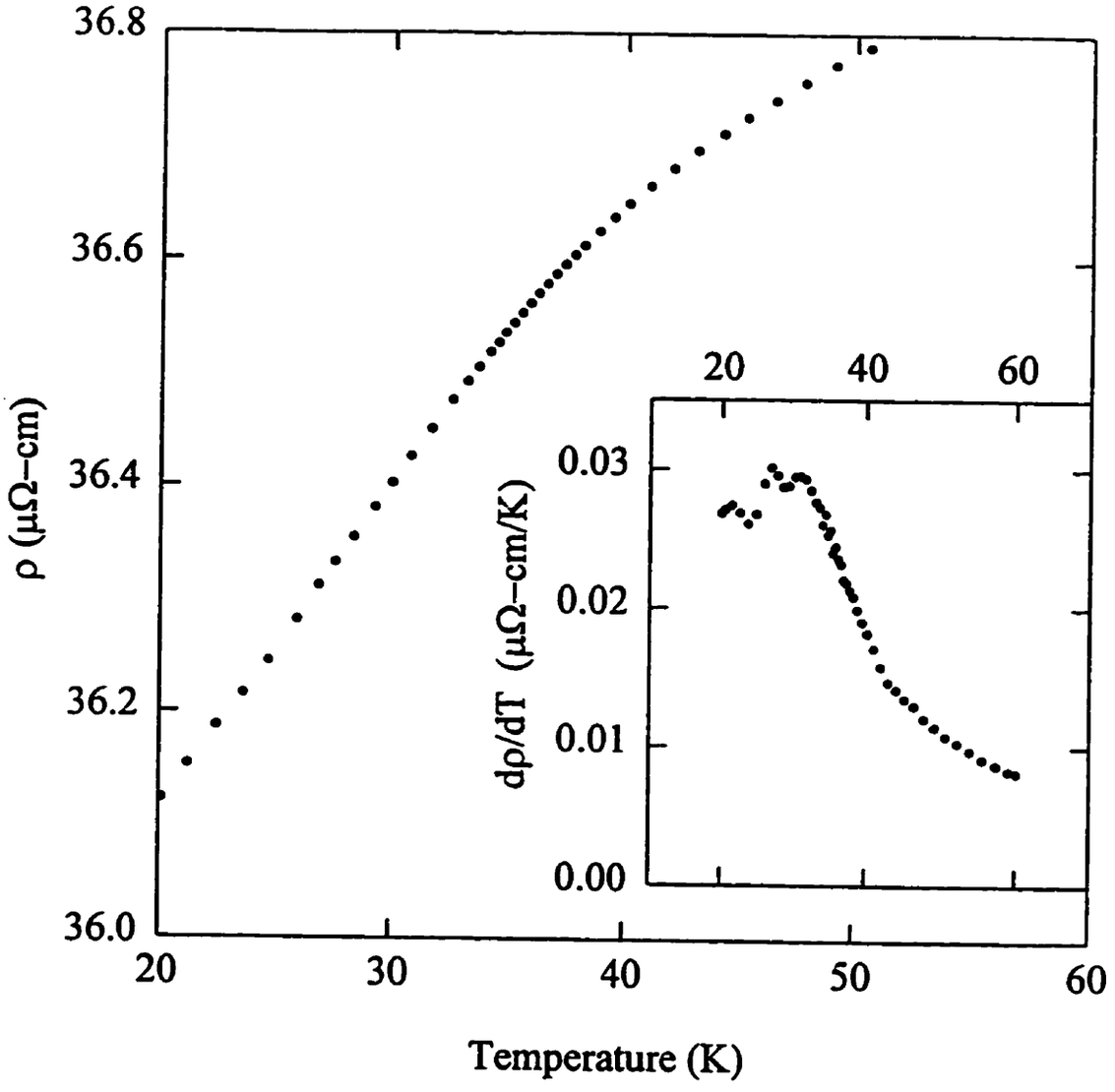

Figure A.119: $\rho(T)$ for the 50 at.% Ni sample after aging. The inset shows the temperature derivative of the resistivity, with T_c=31.1(6)K.

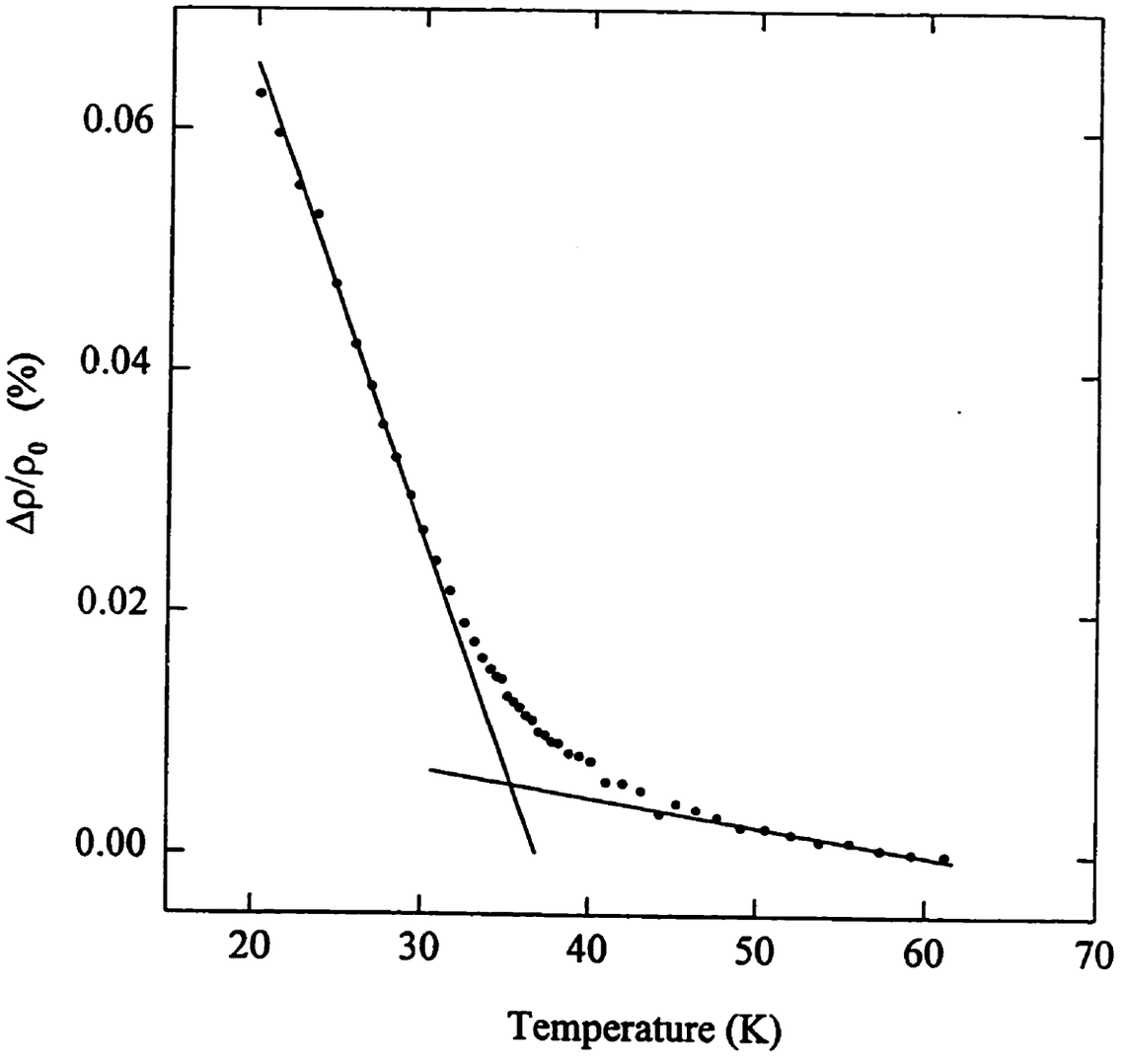

Figure A.120: The low field resistive anisotropy (LFRA) for the 50 at.% Ni sample after aging. The superimposed lines give T_c=35.2(6)K.

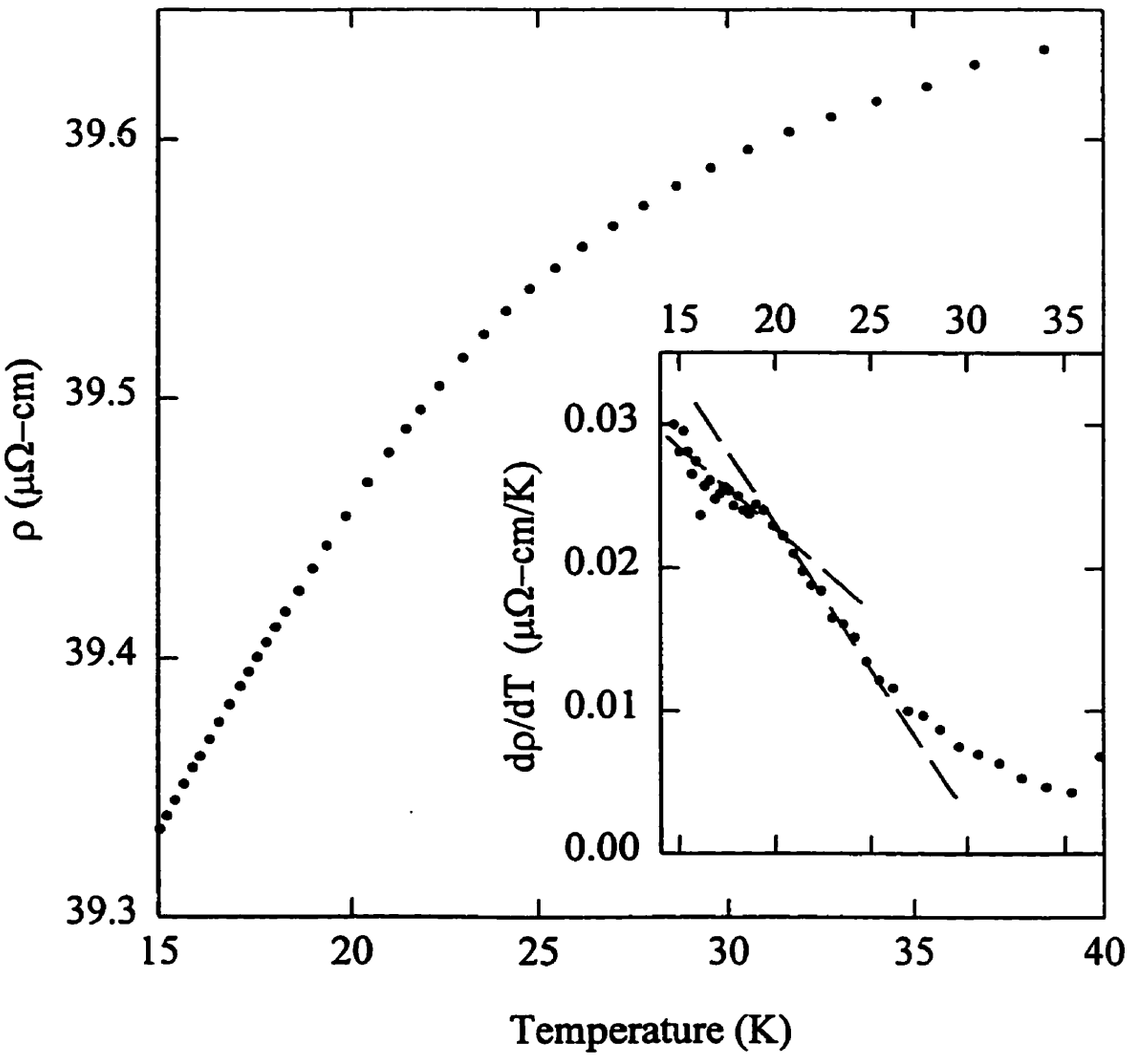

Figure A.121: $\rho(T)$ for the 48 at.% Ni sample after aging. The inset shows the temperature derivative of the resistivity, with T_c=19.5(5)K.

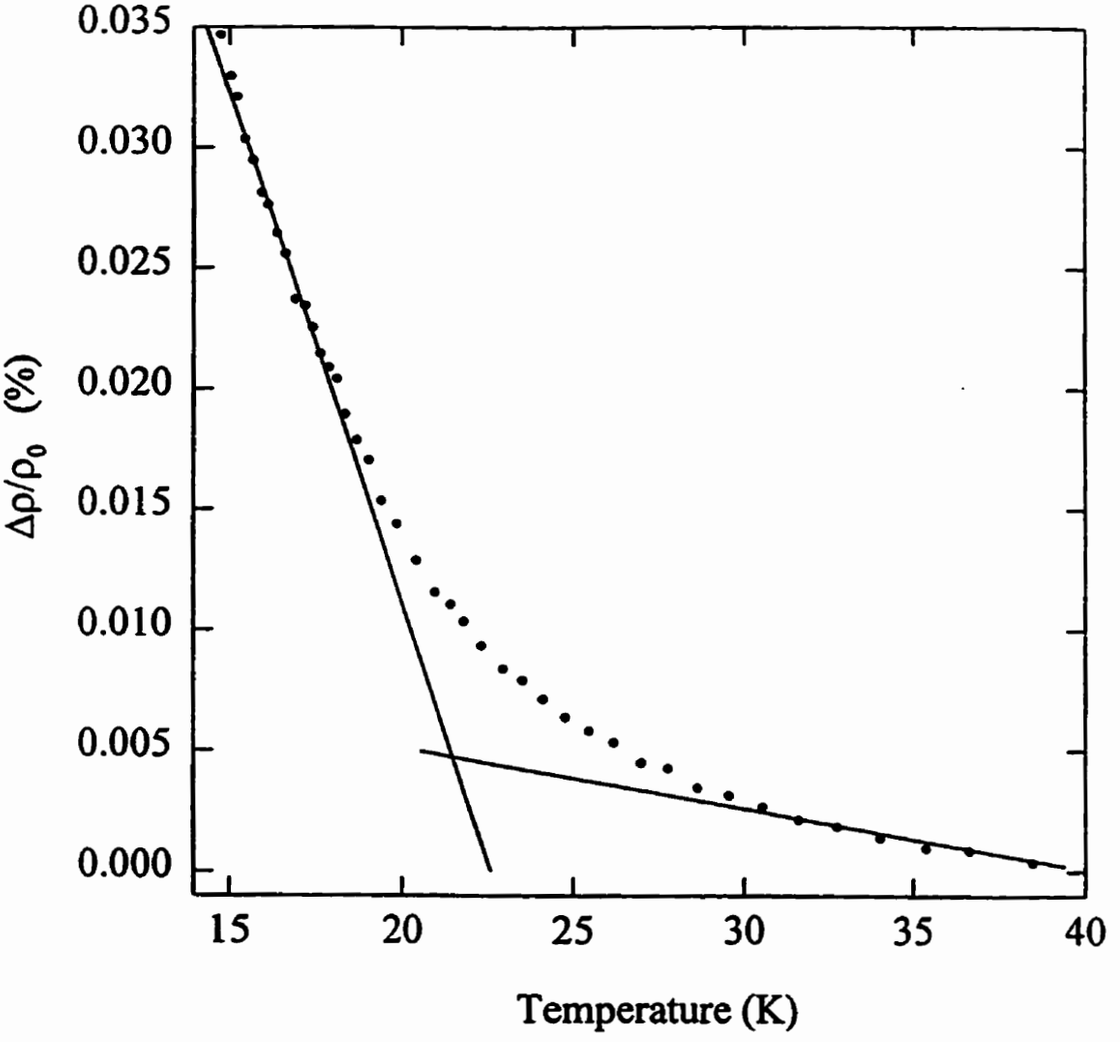

Figure A.122: The low field resistive anisotropy (LFRA) for the 48 at.% Ni sample after aging. The superimposed lines give T_c=21.4(5)K.

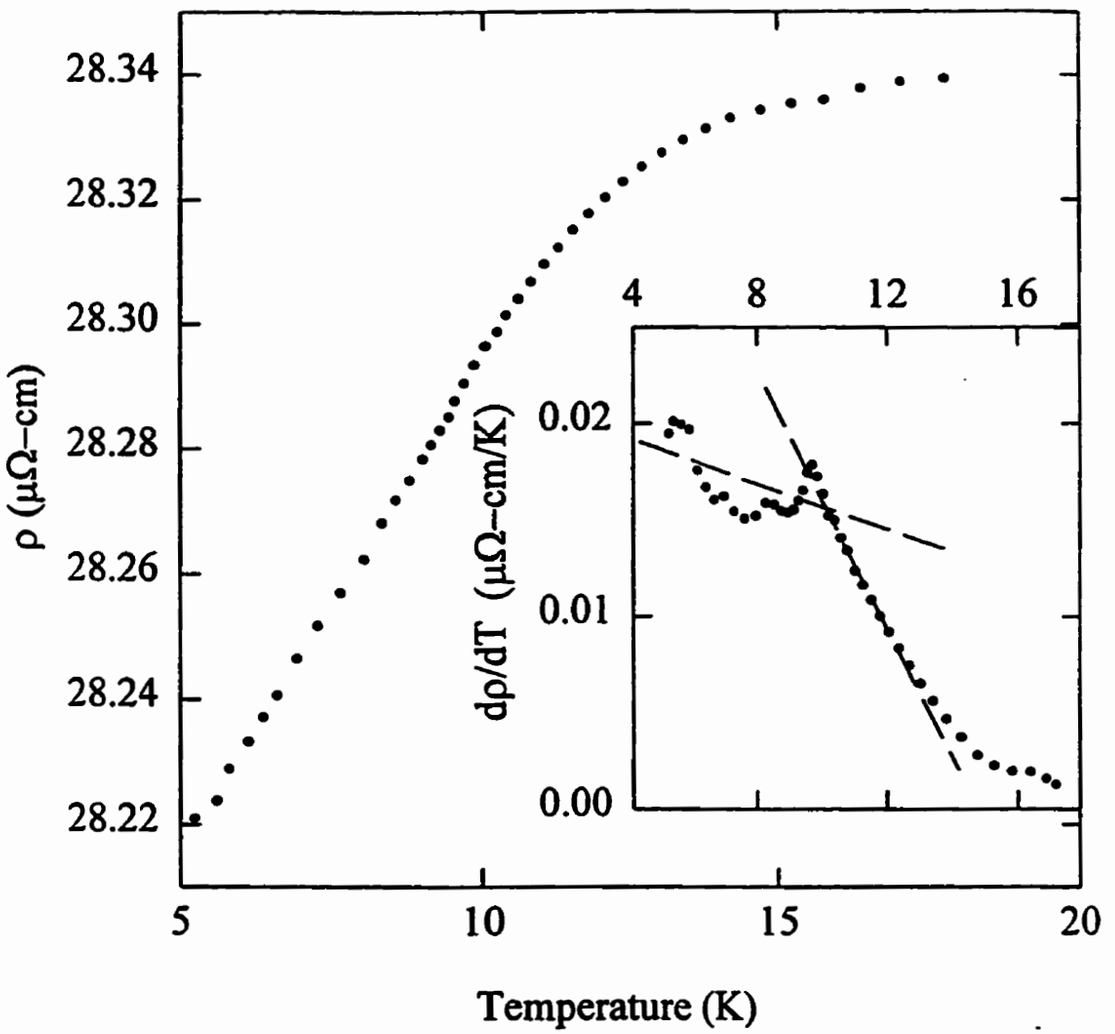

Figure A.123: $\rho(T)$ for the 47 at.% Ni sample after aging. The inset shows the temperature derivative of the resistivity, with T_c=9.8(5)K.

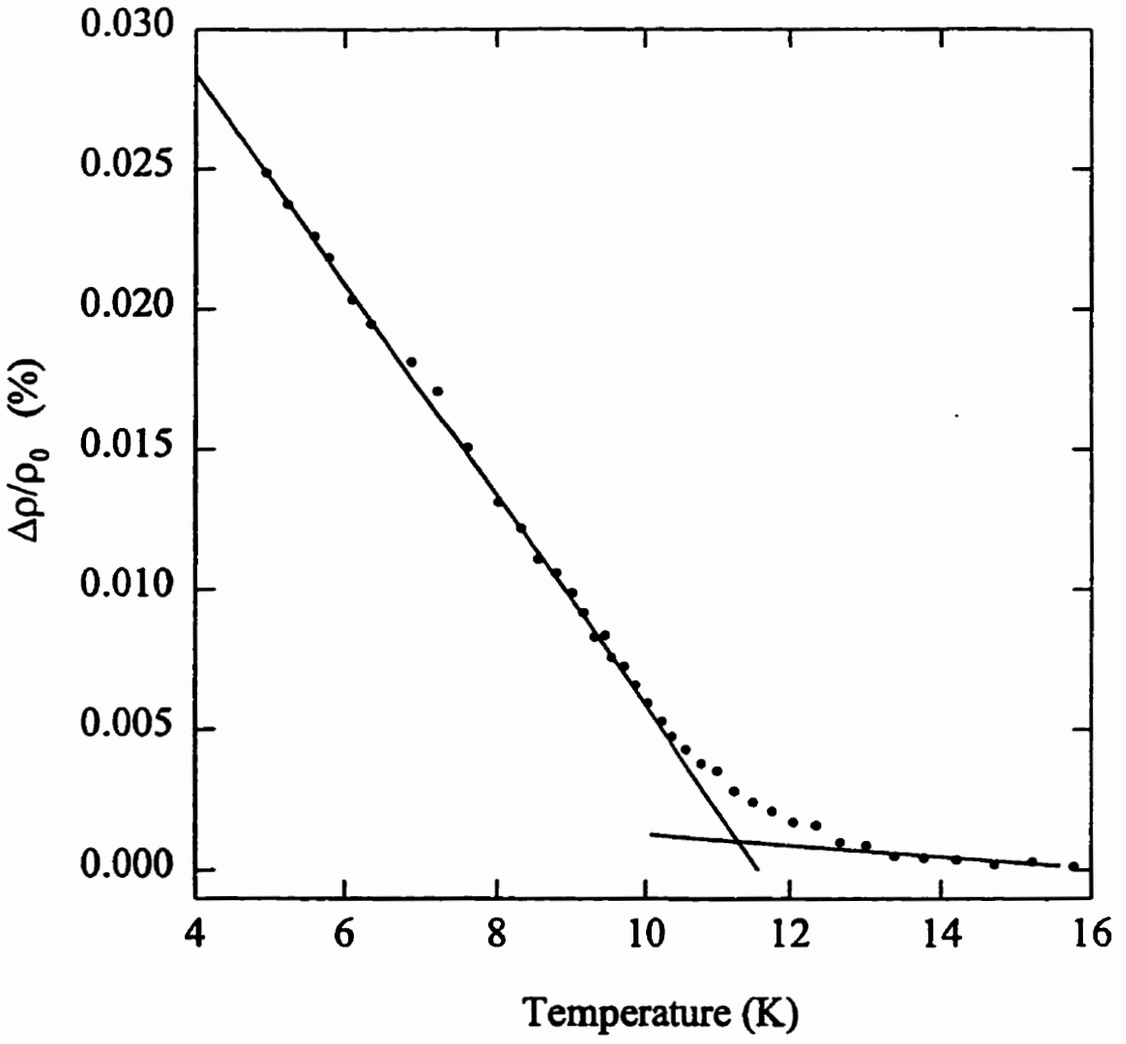

Figure A.124: The low field resistive anisotropy (LFRA) for the 47 at.% Ni sample after aging. The superimposed lines give T_c=11.3(5)K.

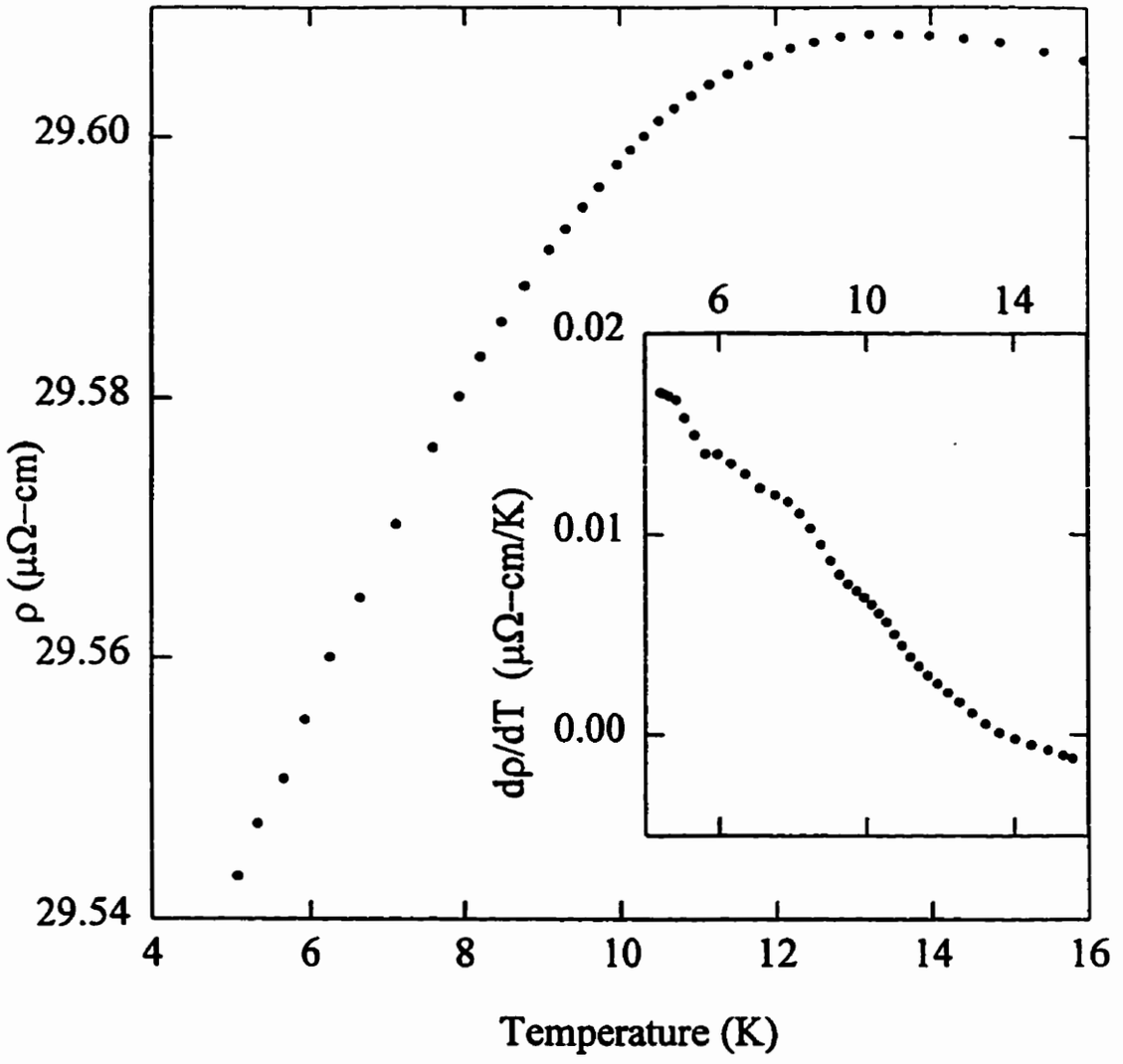

Figure A.125: $\rho(T)$ for the 46 at.% Ni sample after aging. The inset shows the temperature derivative of the resistivity, with no critical behaviour.

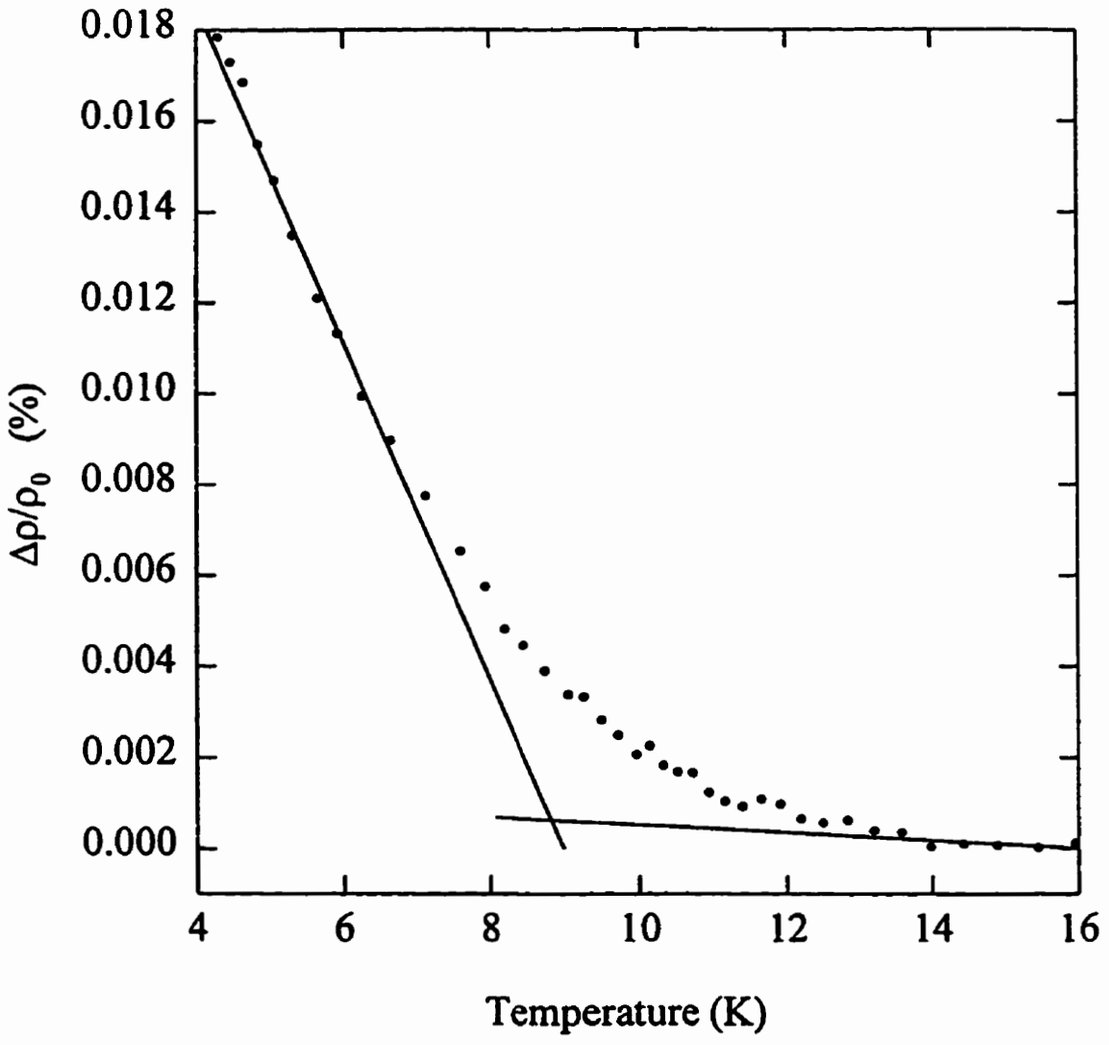

Figure A.126: The low field resistive anisotropy (LFRA) for the 46 at.% Ni sample after aging. The superimposed lines give T_c=8.6(3)K.

Appendix B

SRA in Dilute Cr Alloys with Fe and Co

B.1 Review

Cr is an antiferromagnet whose ground state consists of a spin density wave (SDW) stabilised by Fermi surface nesting, with a wave vector incommensurate with the lattice[13]. The addition of impurities to the Cr lattice not only introduces scattering centres for the electron pairs in the SDW, but can also change the Fermi surface and thus modify the SDW structure. Non-magnetic transition metal elements isoelectronic with Cr result in only a slight depression of the Néel temperature when added to Cr, since only scattering effects need be considered. In general, the addition of elements with higher electron concentration than Cr stabilise the SDW and increase T_N, while those with lower concentration destabilise the SDW. Alloys with magnetic impurities, such as Fe and Co, are more difficult to understand, since not only does the Fermi surface change (increasing T_N), but the SDW electrons are strongly scattered from the magnetic moments of these impurities, causing depairing and destabilisation of the SDW (decreasing T_N). Magnetic susceptibility measurements indicate that both Fe and Co have local moments in a Cr host[157], however, while CrFe shows a paramagnetic susceptibility at all temperatures, CrCo only has a paramagnetic moment for temperatures above T_N, indicating that the Co moments may be coupled into the SDW in the low temperature state. This is

supported by measurements of the magnetisation and magnetoresistance in these two alloys: CrFe has a strong field dependent magnetisation and magnetoresistance, while those in CrCo are much weaker. Mössbauer spectra of CrFe alloys also indicate the presence of a local moments below T_N, however they suggest that below T_N a large fraction of these moments are coupled into the SDW[13]. The difference between the behaviour of Fe and Co impurities is difficult to explain. We suggest that this difference *may* be linked to an orbital component in the total impurity moment. As discussed previously, the presence of an orbital moment can be deduced from measurements of non-zero spontaneous resistive anisotropies (SRA) in a material. This study measures the magnetoresistance of several CrFe and CrCo alloys in an attempt to determine whether such a moment does exist in either of these systems.

B.2 Data and Analysis

$Cr_{1-x}Fe_x$ samples with x=0.1, 0.05, 0.025, and 0.13 and $Cr_{1-x}Co_x$ samples with x=0.08, 0.05 and 0.025 were prepared as described in section 3.1.1 of the text. The magnetoresistance was measured in both longitudinal and transverse modes in fields of up to 3T in the SRA system (section 3.2.2) and up to 10T in the high field magnetoresistance system (section 3.2.4).

Using previously published magnetization data[158, 159], the applied field was converted to induction, using $B=H_a+4\pi M-NM$, where N is the demagnetisation factor calculated as described in Section 3.3.3. The magnetoresistance (MR) of pure Cr is extremely large (as shown in figure B.1), in agreement with previous data[160], as is the anisotropy, plotted in the inset of Figure B.1. This strong MR in pure Cr means that in order to find the magnetic contribution to the magnetoresistance in the alloys, this orbital contribution from the host must be removed. This is done using Kohler's rule, which states that the magnetoresistance in a system is a universal function of the induction and the residual resistivity, i.e.

$$\frac{\Delta\rho}{\rho_0} = f\left(\frac{B}{\rho_0}\right) \tag{B.1}$$

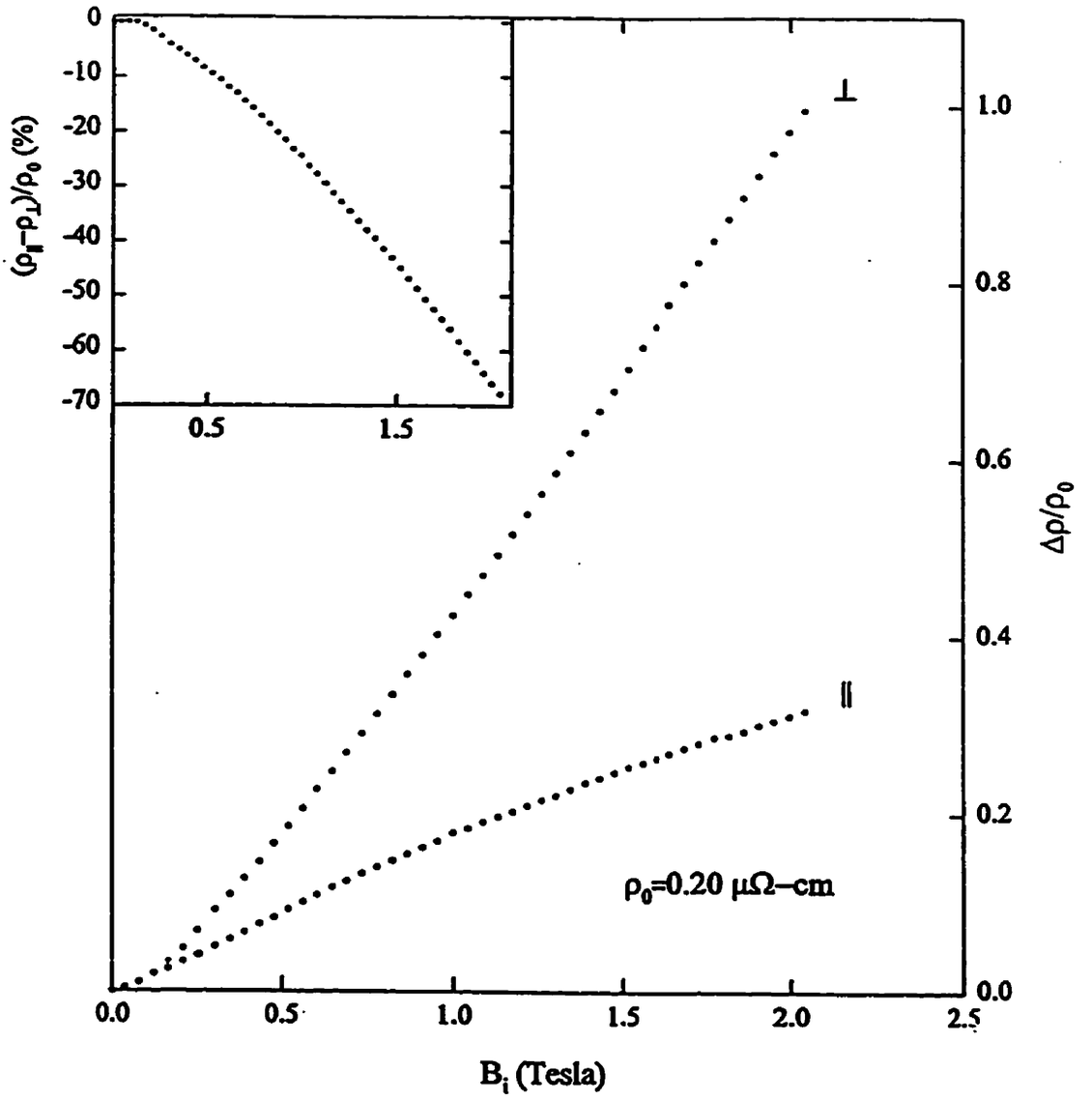

Figure B.1: The longitudinal ($\rho_{\parallel}$), and transverse ($\rho_{\perp}$), magnetoresistances of pure Cr at 4.2K as a function of internal field. The inset shows the anisotropy $(\rho_{\parallel}-\rho_{\perp})/\rho_0$ expressed in percent.

The effect of this correction is demonstrated for the MR in the 2.5 at% Fe sample at 4.2K in figure B.2, which shows the data before and after correction. Although the uncorrected data appear to have saturated, or turned upwards at high field, the corrected data show a strong negative magnetoresistance at all fields. The 1.3% Fe sample has MR curves with a strange shape (Figure B.3), resulting from the competition between the host and the magnetic contributions to the MR. Due to their large residual resistances, the 5 and 10% Fe samples are affected very little by the correction, (Figures B.4 and B.5), and the transverse and longitudinal magnetoresistances are both strongly negative, with little anisotropy between the two modes. The magnetoresistance at 2K is very similar, with slightly larger anisotropy, and are not shown here. The anisotropy between the longitudinal and transverse magnetoresistances at 2K are plotted in Figure B.6 as a function of internal field. Obviously the anisotropy is small at all concentrations, and extrapolations to B=0 result in very small SRA values.

Similar plots are shown for the Co data. The MR in the 5% Co sample is shown before and after correction in figure B.7. The correction results in a weak negative logitudinal magnetoresistance, consistent with previously published data[157]. Figures B.8 and B.9 show the corrected magnetoresistance in the 2.5 and 10% Co samples at 2K, and the corresponding anisotropies are plotted in figure B.10. Although the anisotropy becomes more strongly negative with increasing Co concentration, the SRA is still very small in this system.

Estimates of the SRA as a function of impurity concentration are shown in figure B.11 (with error bars arising primarily from uncertainties in ρ_0), along with previously published SRA values for a number of transition metal-Fe, Ni, Co alloys[161]. The SRA in the PdCo, PdNi, PtCo and PtFe systems approaches a non-zero plateau region as the impurity concentration decreases, consistent with the presence of an orbital moment at the impurity sites. In PdFe, however, which does *not* have an impurity moment, the SRA approaches zero at zero Fe concentration. The CrFe and CrCo SRA estimates are also very small, and within the error bars shown seem to indicate that neither of these systems has an orbital contribution to its total

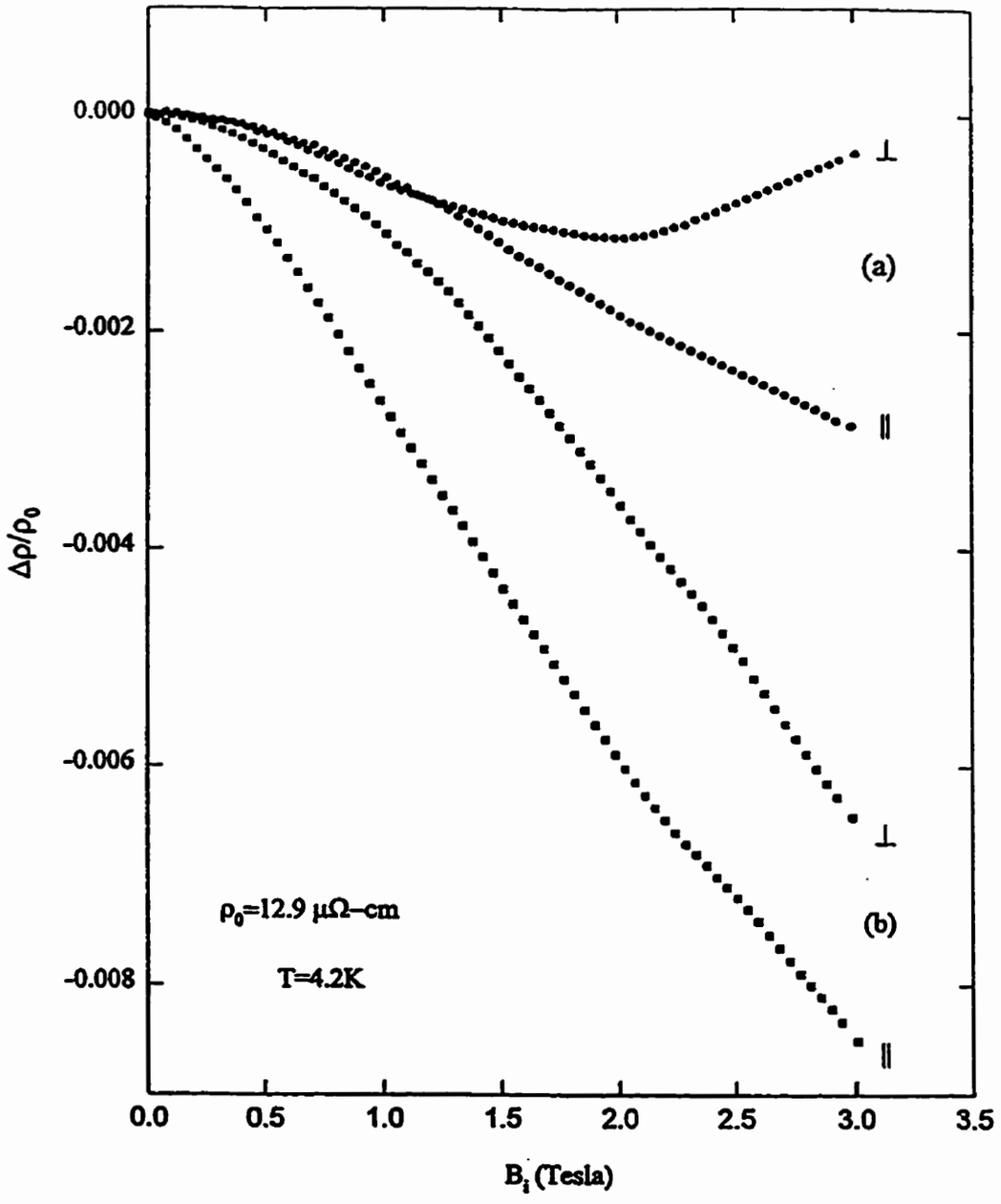

Figure B.2: (a) The measured $\rho_{\parallel}$ and $\rho_{\perp}$ for the 2.5 at.% Fe sample at 4.2K. (b) The magnetoresistance in (a) after correction. The residual resistivity for this sample is in good agreement with previous estimates[157].

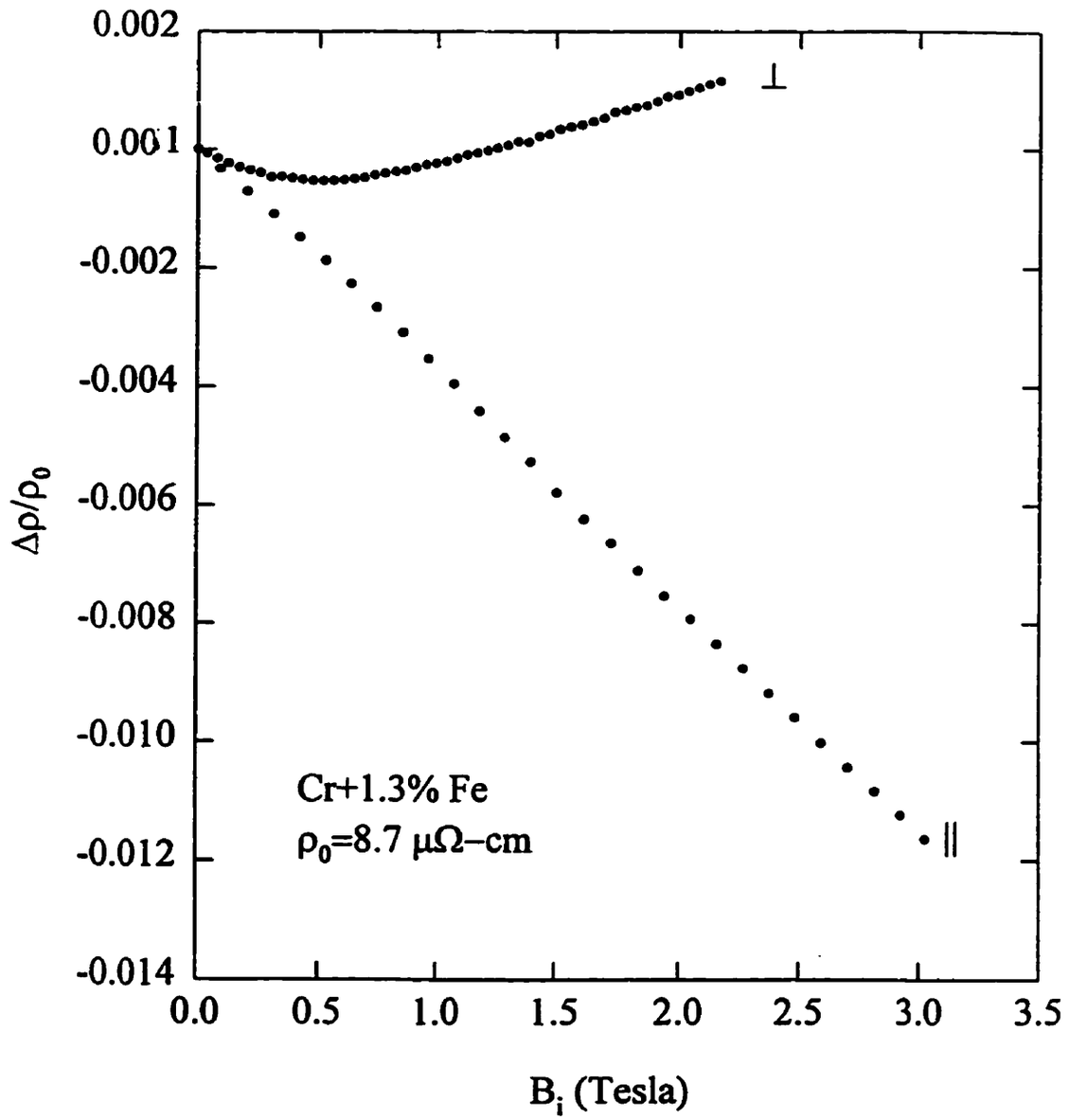

Figure B.3: The corrected $\rho_{\parallel}$ and $\rho_{\perp}$ for the 1.3 at.% Fe sample at 4.2K. The residual resistivity for this sample is in good agreement with previous estimates[157].

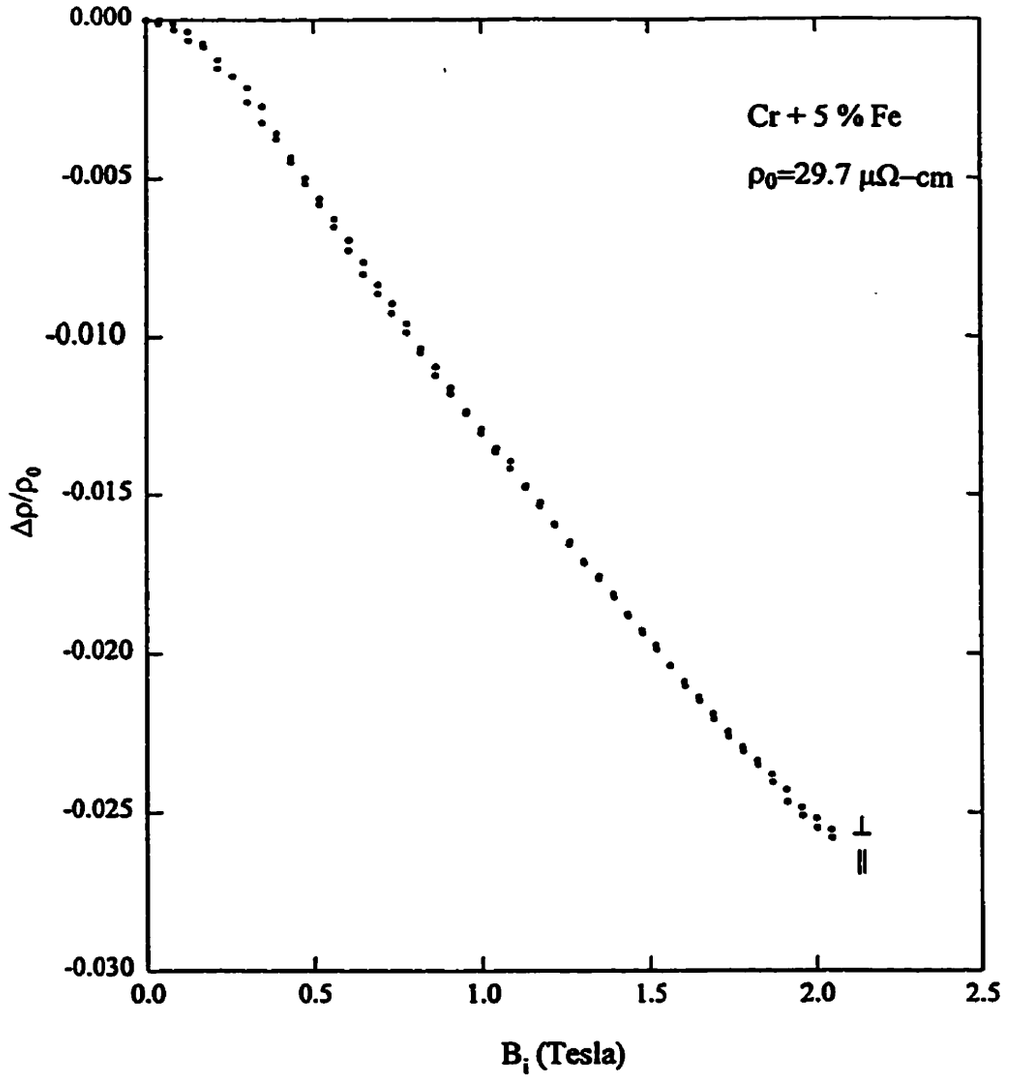

Figure B.4: The corrected $\rho_{\parallel}$ and $\rho_{\perp}$ for the 5 at.% Fe sample at 4.2K. The residual resistivity for this sample is in good agreement with previous estimates[157].

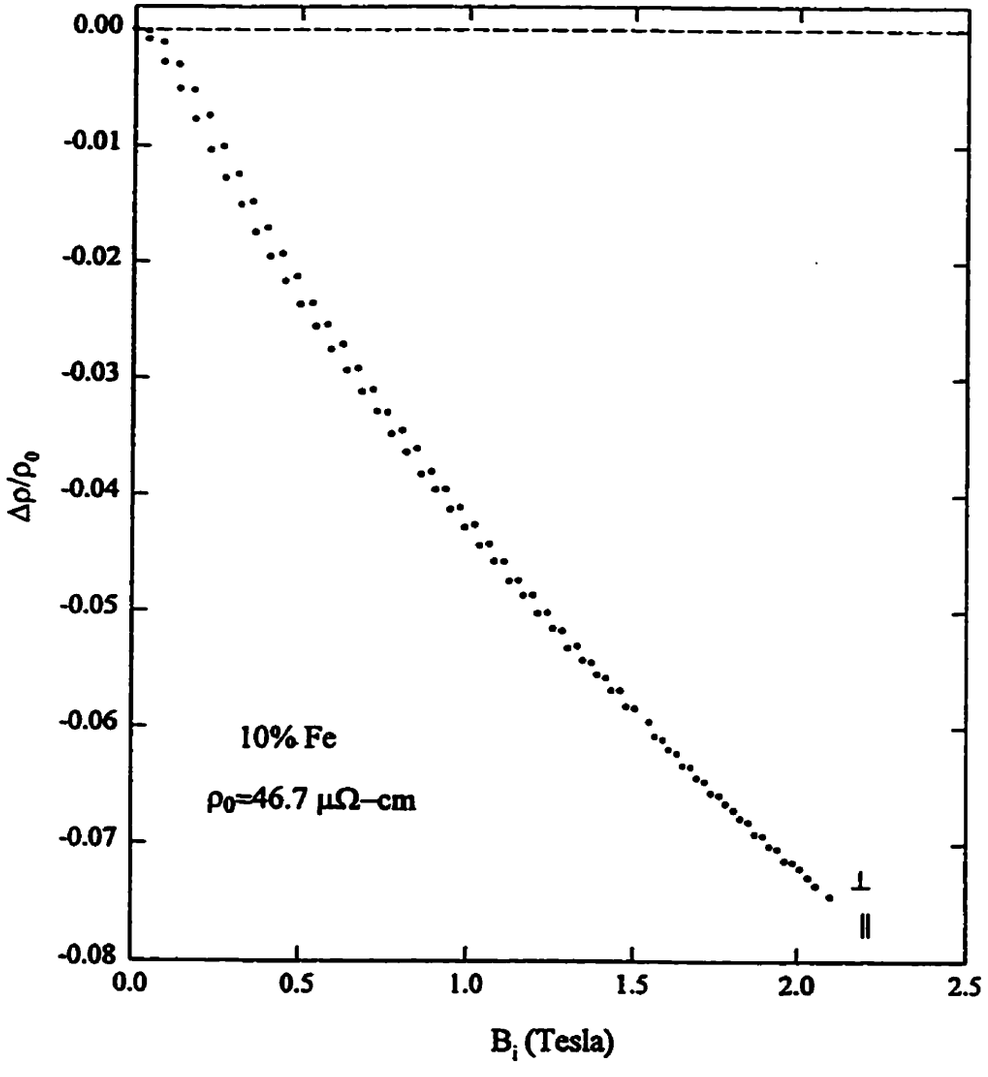

Figure B.5: The corrected $\rho_{\parallel}$ and $\rho_{\perp}$ for the 10 at.% Fe sample at 4.2K. The residual resistivity for this sample is in good agreement with previous estimates[157].

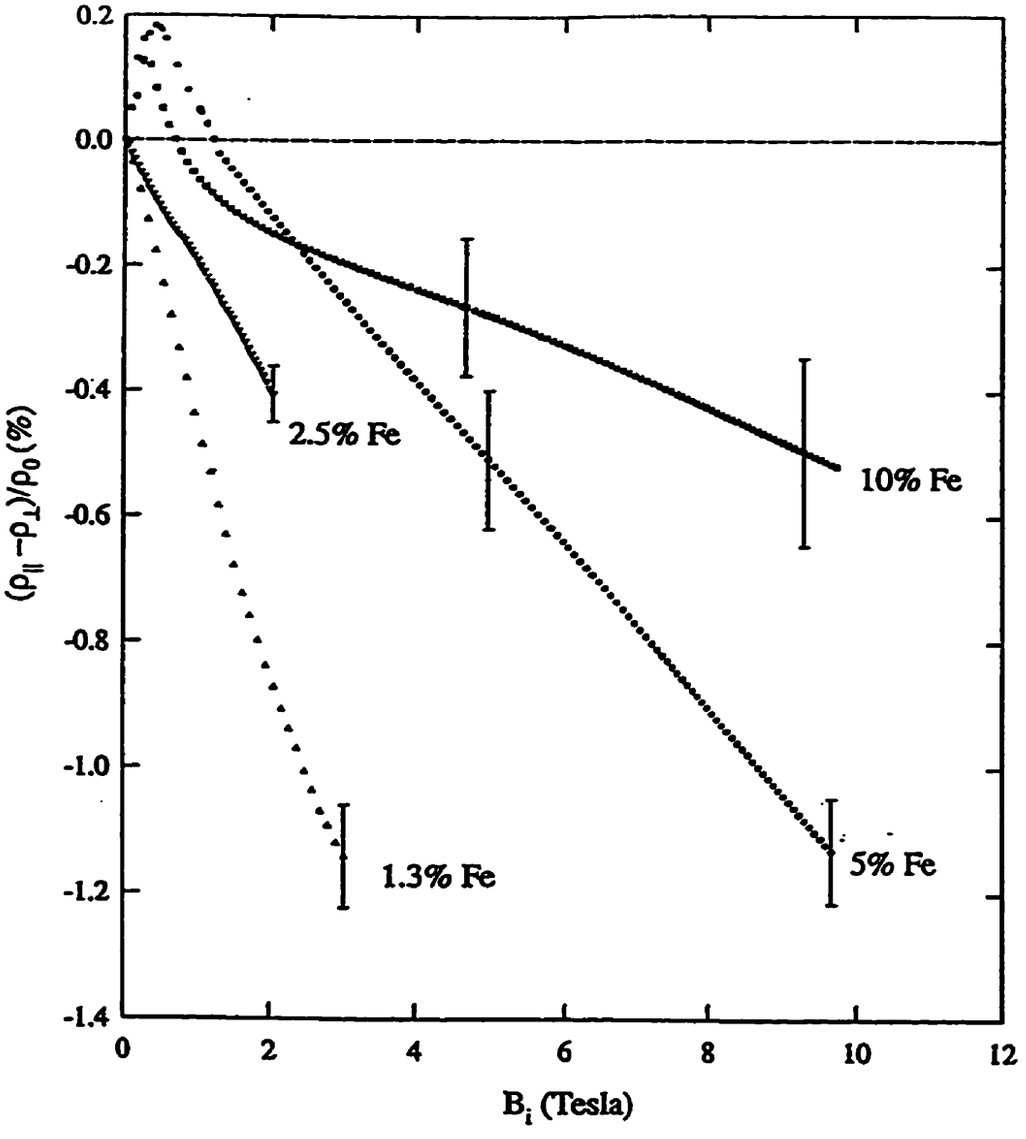

Figure B.6: The anisotropies $(\rho_{\parallel}-\rho_{\perp})/\rho_0$ in percent for the 1.3, 2.5, 5 and 10 at.% Fe samples at 2K. The error bars shown result primarily from uncertainties in ρ_0.

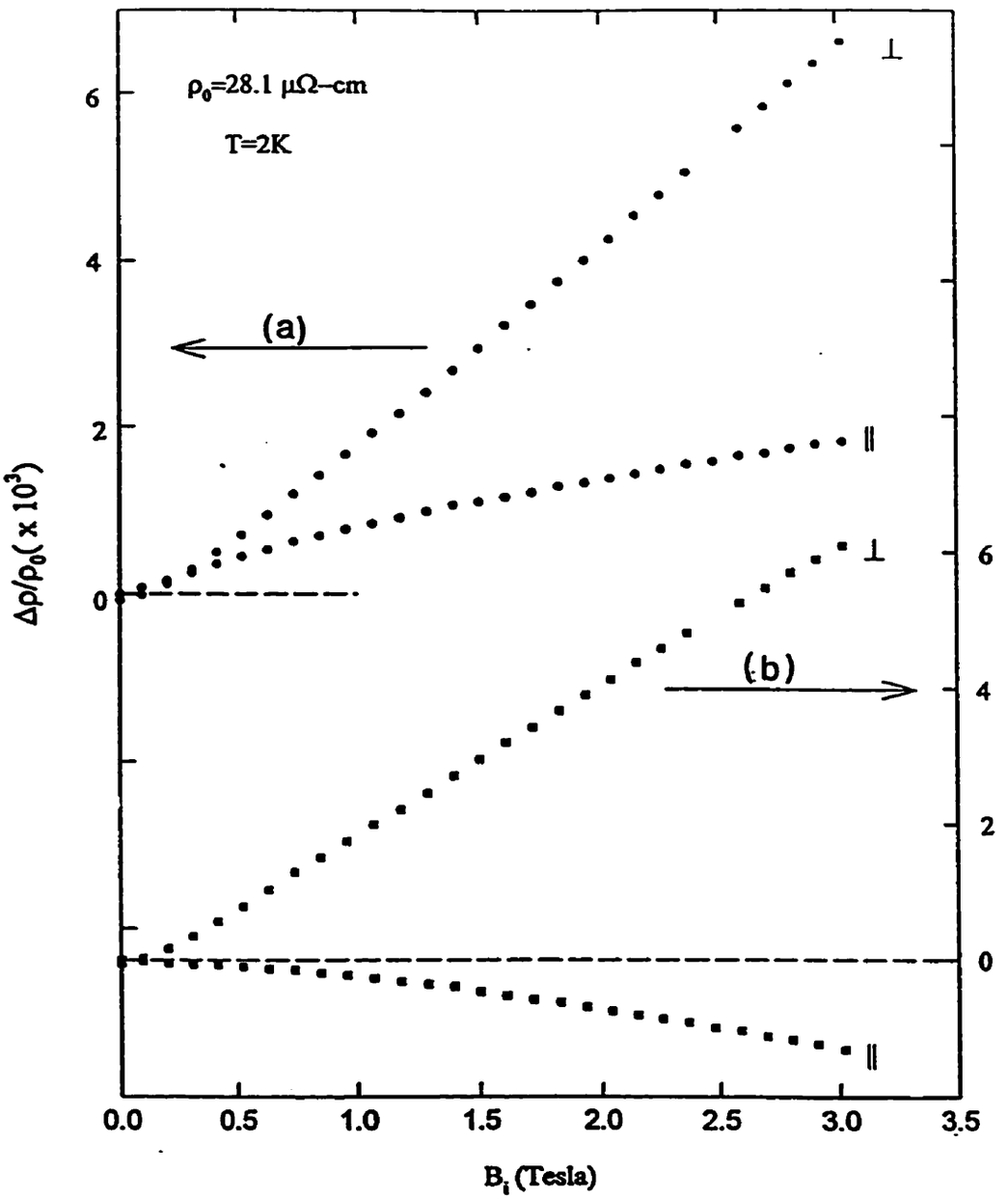

Figure B.7: (a) The measured $\rho_{\parallel}$ and $\rho_{\perp}$ for the 5 at.% Co sample at 2K. (b) The magnetoresistance in (a) after correction. The residual resistivity for this sample is slightly lower than previous estimates [160], indicating that the true composition may be lower.

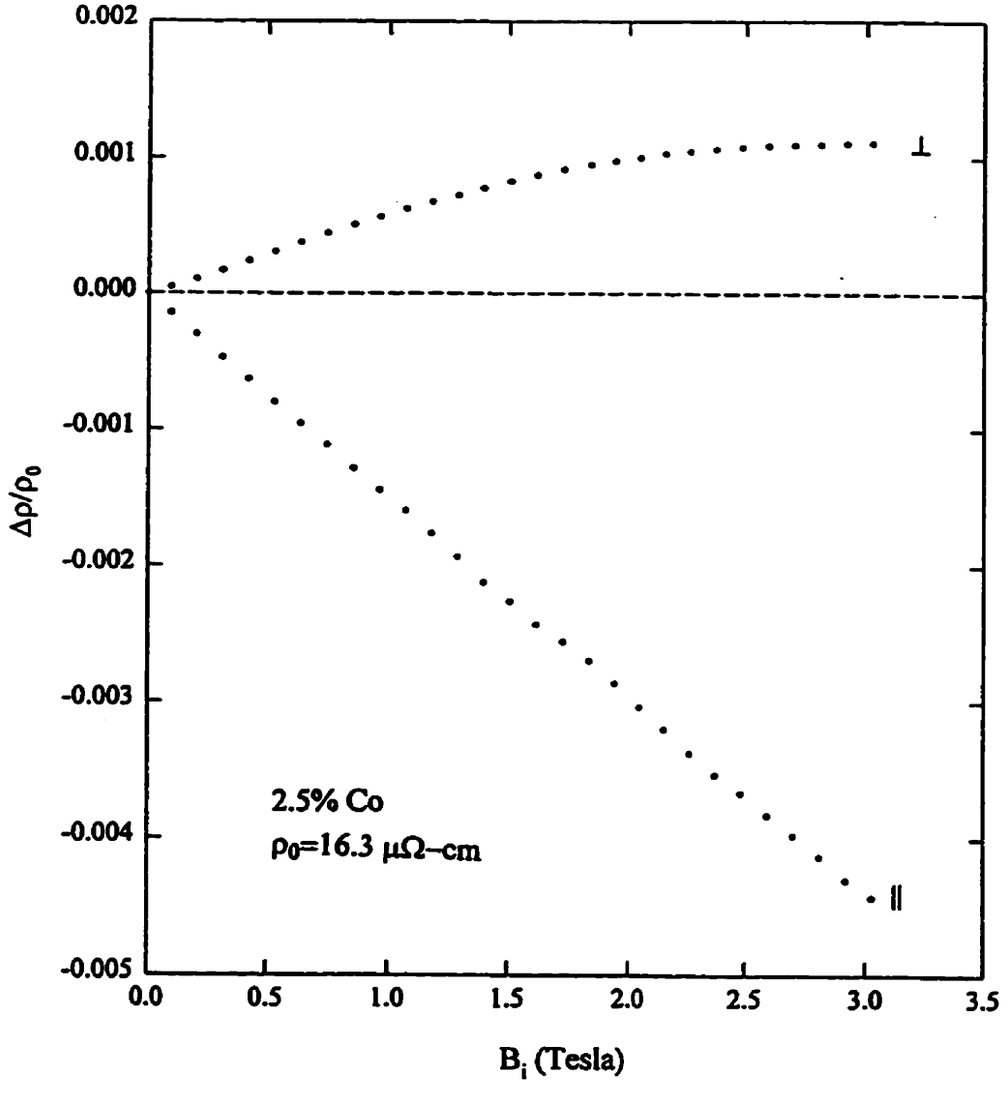

Figure B.8: The corrected $\rho_{\parallel}$ and $\rho_{\perp}$ for the 2.5 at.% Co sample at 2K. The residual resistivity for this sample is slightly lower than previous estimates [160], indicating that the true composition may be lower.

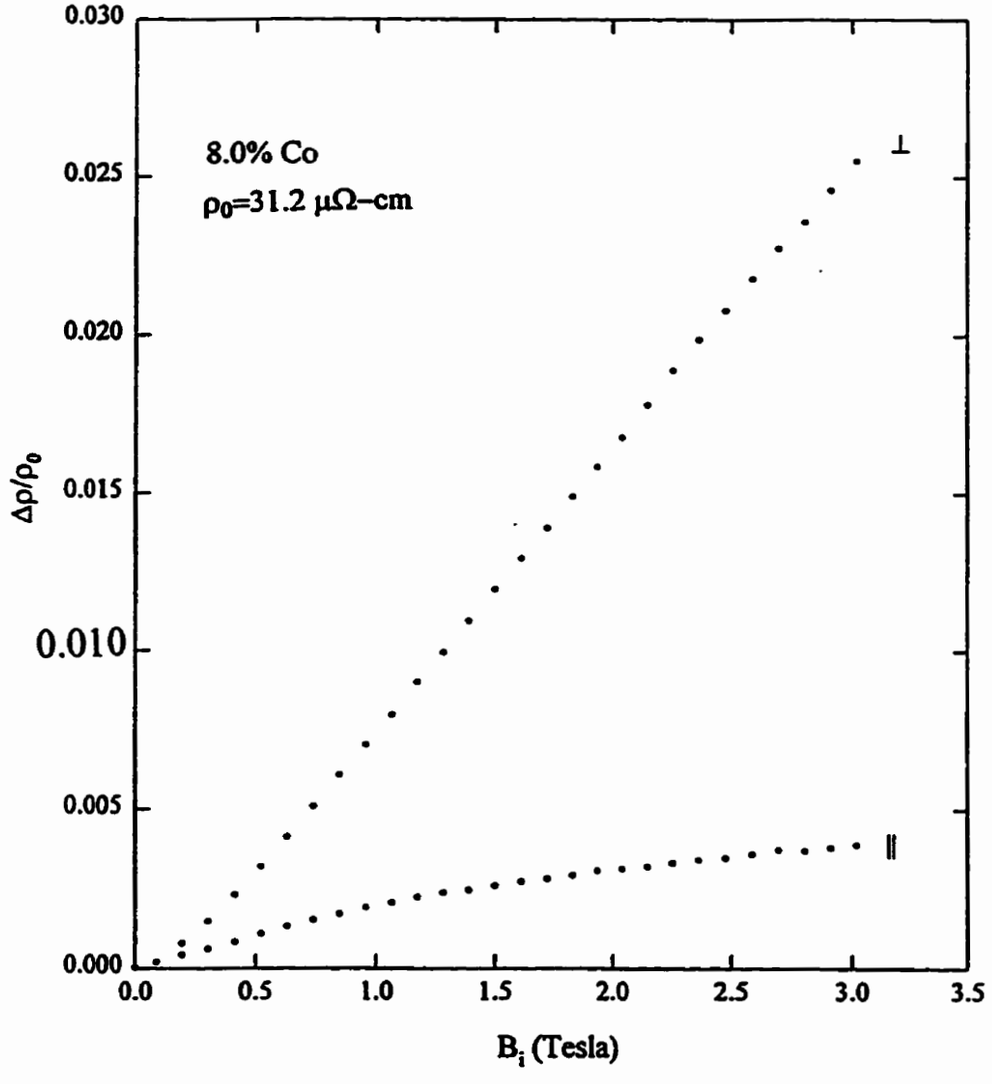

Figure B.9: The corrected $\rho_{\parallel}$ and $\rho_{\perp}$ for the 8 at.% Co sample at 2K. The residual resistivity for this sample is slightly lower than previous estimates [160], indicating that the true composition may be lower.

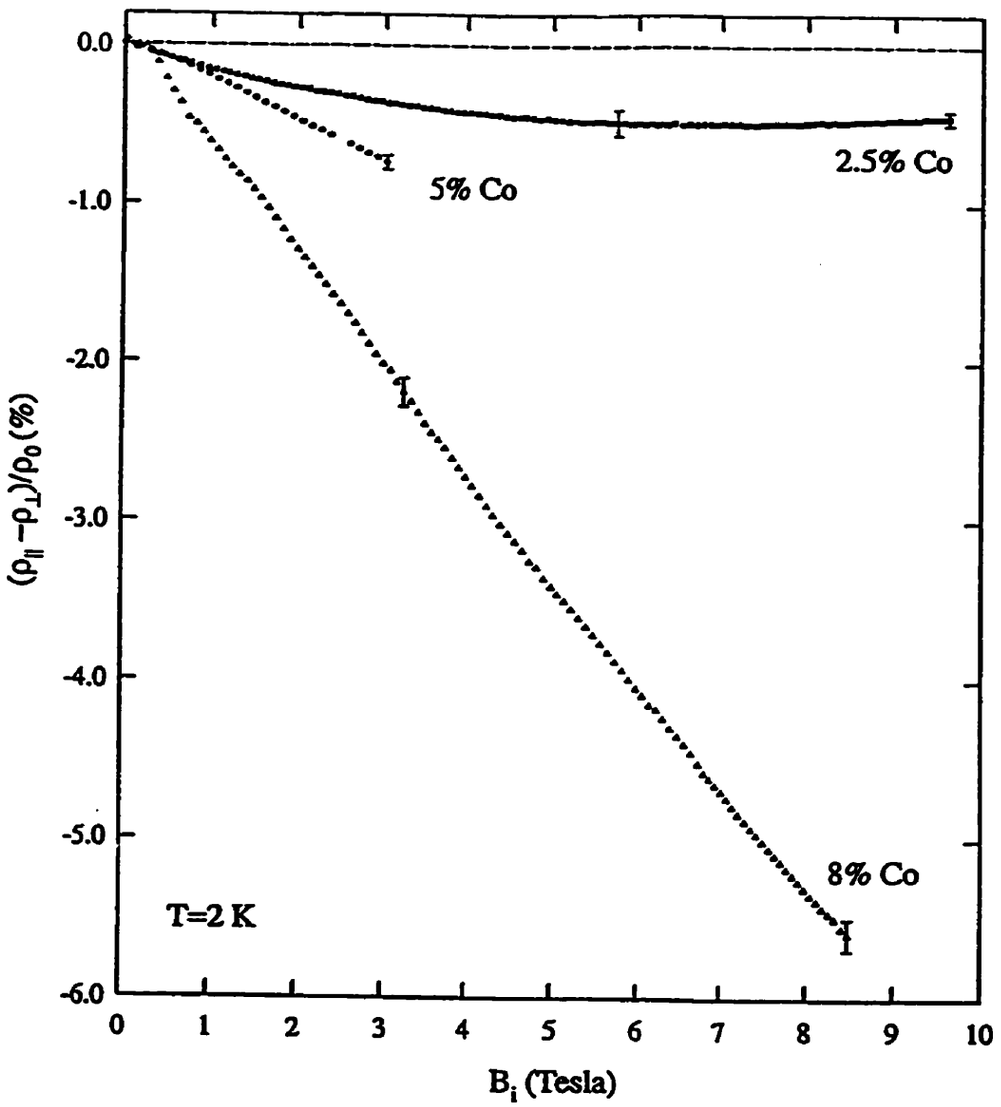

Figure B.10: The anisotropies $(\rho_{\parallel}-\rho_{\perp})/\rho_0$ in percent for the 2.5, 5 and 8 at.% Co samples at 2K. The error bars shown result primariliy from uncertainties in ρ_0.

magnetic moment.

B.3 Conclusion

In summary, the magnetoresistances in the CrFe and CrCo systems are quite different, supporting the claim that the Fe moments are not coupled to the SDW while the Co moments are. As discussed in chapter 2, the existance of a non-zero SRA depends both on the existence of an orbital moment and on the presence of a polarising field strong enough to align the orbital moments. The SRA data indicate that neither of these impurities have orbital contributions to the magnetic moment, unless the Fe and Co orbital moments, these are coupled so strongly to the SDW that the large applied fields can not align them. If this were the case, this coupling might be weaker in CrFe this coupling might be weaker than in CrCo, resulting in the different features noticed, ie. that the Fe moments do not appear coupled to the SDW while the Co moments do. In conclusion, unless this postulated strong orbital moment-SDW coupling exists, the measurements of the SRA in these alloys indicates that neither the Fe or the cobalt have orbital contributions to their total moments when in a Cr host.

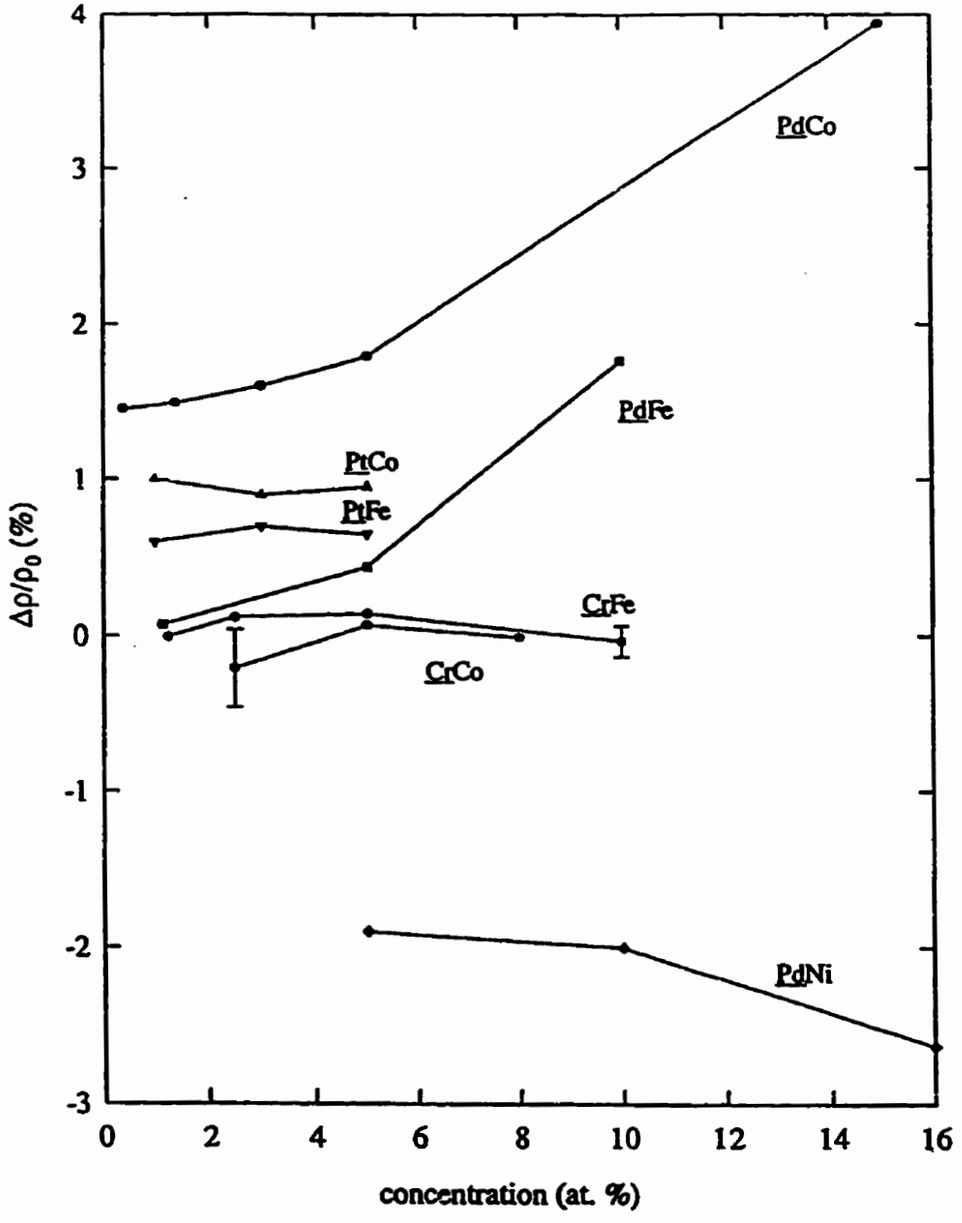

Figure B.11: The SRA as a function of concentration in CrFe and CrCo, as well as values for PdCo, PdNi, PdFe, PtCo and PtFe[161].